XVII INTERNATIONAL CONGRESS OF THE MEXICAN HYDROGEN SOCIETY

Sociedad Mexicana del Hidrógeno A. C.

# XVII International Congress of the Mexican Hydrogen Society

# BOOK OF PROCEEDINGS

**Guanajuato, Mexico - September 19th to 22nd, 2017**

# Acknowledgments

The Mexican Hydrogen Society acknowledge the contribution and the participation of the Reviewers in the peer-review process of the Abstracts and Full paper works:

Alonso Lemus Ivonne Liliana (CINVESTAV-CONACYT)
Contreras López David (Universidad de Guanajuato)
Collins Martínez Virginia (CIMAV)
Fuentes Ramírez Rosalba (Universidad de Guanajuato)
Galindo Esquivel Ignacio (Universidad de Guanajuato)
Galindo González María del Rosario (UGto-CONACYT)
Gamiño Arroyo Zeferino (Universidad de Guanajuato)
González Huerta Rosa de Guadalupe (IPN)
López Ortiz Alejandro (CIMAV)
Medina Ramírez Adriana (Universidad de Guanajuato)
Morales Rodríguez Ricardo (Universidad de Guanajuato)
Ramos Sánchez Guadalupe (UAM I-CONACYT)
Rodríguez Carvajal Ricardo (Universidad de Guanajuato)
Rodríguez Varela Javier (CINVESTAV)
Ruiz Camacho Beatriz (Universidad de Guanajuato)
Solorza Feria Omar (CINVESTAV)
Suarez Alcántara Karina (IIM_UNAM)

We also want to thank the Guanajuato University, the Division of Natural and Exact Sciences (DCNE), Chemical Engineering Department and the Direction and Support to Research and Postgraduate (DAIP) for the economical support.

Finally, thanks to the sponsors: ISASA Instrumentacion, SAIDE and Solartron Analytical and Princeton Applied Research.

# Content

## CHAPTER 4

## Modelling and Design ..... 307



## CHAPTER 5

## Renewable Energy Systems ..... 363

# CHAPTER 1
# Hydrogen Production, Storage and Applications

## 1.1 Theoretical study of the thermodynamic properties of calcium hydride

Teresa Ramírez-Rodríguez, William Ramírez-Carbellido, Fray de Landa Castillo-Alvarado

[1]Instituto Politécnico Nacional, Unidad Profesional Adolfo López Mateos, Zacatenco, Delegación Gustavo A. Madero, C.P. 07738, Ciudad de México, México.

* Corresponding author: 04455 43520891, teresa.ramirez7715@gmail.com

## ABSTRACT

The theoretical study of the thermodynamic properties of calcium hydride has been performed to find the conditions necessary to store hydrogen in solid phase, since it is a feasible solution, because it is a safer mode; Hydride metal hydrides for hydrogen storage may employ chamber temperatures (close to ambient) in the absorption / desorption of hydrogen, a benefit may be that calcium hydride is insoluble in most organic solutions. For reversible hydrogen storage, however, calcium hydride by volume is too thermodynamically stable to be used, as reported in some studies.

The objective of this work is to give a basic perspective on the structure-link-properties relationships to investigate whether calcium hydride has thermodynamic properties useful for storing hydrogen. Calculations based on the theory of density functional (DFT) using pseudopotentials PW91 and PBE, the approximation of the generalized gradient, GGA, used for the energy functional exchange correlation, is achieved in a range of ambient temperature. The nature of the bonds in can $H_{2n}$ clusters shows that Ca-H bonds are stronger than calcium-calcium bonds, this probably due to the position of the hydrogen atoms in a metal hydride. The size of the hydrogen ion (proton) is much smaller than the metal ion, the hydrogen ions tend to occupy the interstitial position around the metal ions.

***Keywords:*** storage of hydrogen, calcium hydride, DFT, thermodynamic properties

## Introduction

As potential for obtaining energy from; Solar, wind, nuclear, tidal, hydroelectric, biofuel and geothermal energy, hydrogen seems to be the best option due to a higher energy density per unit mass (120 MJ / kg), without environmental and abundant involvement in the universe . Hydrogen has a means of storing electricity through hydrogen bonds. 6 kilograms of hydrogen for a light vehicle to run for 500 kilometers.

Hydrogen can be stored physically as a gas or a liquid. To be stored as gas, it requires high pressure tanks (350-700bar) [5000-10000psi]. To be stored as a liquid, it requires cryogenic temperatures due to the boiling point of hydrogen and an atmospheric pressure of minus 252.8 °C. Hydrogen can also be stored on the surface of the solids (by adsorption) or inside the solids (by absorption) [1]

Using DFT, researchers have shown that an electron polarization occurs in hydrogen molecules when applied to an electric field and the electrostatic interactions between hydrogen molecules and substrates with a considerable capacity to store hydrogen. Most significant is that by removing the applied electric field, the system returns to its original state and the hydrogen molecules are desorbed, resulting in good reversibility and rapid kinetics. It has also been noted that hydrogen storage in quasi-molar (quasi-molecular) form by the exposure of metallic cations occurred through a polarization mechanism where the $H_2$ molecule is polarized by the electric field associated with dot ions [2]

## 2. Materials and Methods

Calculate the electronic properties of calcium hydride using the program CASTEP (Cambridge Serial Total Energy Package) which uses (density functional theory). The PW91 functional is used for the correction with density gradients to the local exchange-correlation functional, trying, in some way, to simulate the Non-locality effects of the exact functional. It has also been used the PBE functional it belongs to the class of generalized gradient approximation (GGA) functional for the exchange-correlation energy $E_{xc}$. Considering that the requirement $E_{xc}$ [ρ] may be non-local, i.e. $E_{xc}$ may depend on the density ρ at a given point (locality).

Calculations of geometric optimization and state density were obtained based on a unit cell with the above parameters:

**Table 1**. Unit cell of calcium hydride.

| Real Lattice(Å) | | | Reciprocal Lattice(1/Å) | | |
|---|---|---|---|---|---|
| 5.9250000 | 0.0000000 | 0.0000000 | 1.0604532 | 0.0000000 | 0.0000000 |
| 0.0000000 | 3.5810000 | 0.0000000 | 0.0000000 | 1.7545896 | 0.0000000 |
| 0.0000000 | 0.0000000 | 6.7760000 | 0.0000000 | 0.0000000 | 0.9272706 |

**Table 2**. Parameters of unit cell of calcium hydride.

| Lattice parameters(Å) | Cell Angles |
|---|---|
| a = 5.925000 | alpha = 90.000000 |
| b = 3.581000 | beta = 90.000000 |
| c = 6.776000 | gamma = 90.000000 |

Current cell volume = 143.769272 $Å^3$
Total number of ions in cell is 8
Total number of species in cell is 2
Max number of any one species is 4

It indicates the zone of Brillouin that corresponds to the primitive cell in the space K

Number of kpoints used is16

**Table 3**.K-Points for BZ Sampling.

| Number | Fractional coordinates | | | Weight |
|---|---|---|---|---|
| 1 | 0.375000 | 0.428571 | 0.375000 | 0.0714286 |
| 2 | 0.375000 | 0.428571 | 0.125000 | 0.0714286 |
| 3 | 0.375000 | 0.285714 | 0.375000 | 0.0714286 |
| 4 | 0.375000 | 0.285714 | 0.125000 | 0.0714286 |
| 5 | 0.375000 | 0.142857 | 0.375000 | 0.0714286 |
| 6 | 0.375000 | 0.142857 | 0.125000 | 0.0714286 |
| 7 | 0.375000 | 0.000000 | 0.375000 | 0.0357143 |
| 8 | 0.375000 | 0.000000 | 0.125000 | 0.0357143 |
| 9 | 0.125000 | 0.428571 | 0.375000 | 0.0714286 |
| 10 | 0.125000 | 0.428571 | 0.125000 | 0.0714286 |
| 11 | 0.125000 | 0.285714 | 0.375000 | 0.0714286 |
| 12 | 0.125000 | 0.285714 | 0.125000 | 0.0714286 |
| 13 | 0.125000 | 0.142857 | 0.375000 | 0.0714286 |
| 14 | 0.125000 | 0.142857 | 0.125000 | 0.0714286 |
| 15 | 0.125000 | 0.000000 | 0.375000 | 0.0357143 |
| 16 | 0.125000 | 0.000000 | 0.125000 | 0.0357143 |

Calculating total energy with cut-off of 320.000eV

Density of states: Electronic eigenvalues on a fine Monkhorst-Pack grid are calculated non-self-consistently for both valence and conduction bands, using electronic charge densities and potentials generated during the simulation.

Electronic states are allowed only at a set of k-points determined by the boundary conditions that apply to the bulk solid. The occupied states at each k-point contribute to the electronic potential, so that in principle an infinite number of calculations are needed. However, the electronic wave functions at k-points that are very close together will be almost identical. This suggests that the DFT expressions that contain a sum over k-points (or, equivalently, an integral over the Brillouin zone) can be efficiently evaluated using a numerical scheme that performs summation over a small number of special points in the Brillouin zone. [3]

Band structure: Electronic eigenvalues along high symmetry directions in the Brillouin zone are calculated non-self-consistently for both valence and conduction bands, using electronic charge densities and potentials generated during the simulation.

Phonons: For phonon dispersion runs, phonon frequencies and eigenvectors along high symmetry directions in the Brillouin zone are calculated. In the case of phonon density of states calculations, phonon frequencies and eigenvectors are computed on a Monkhorst-Pack grid. This information is required during analysis to display total and projected (partial) phonon densities of states. It is also used to calculate thermodynamic properties.

## 3. Results and Discussion

The final configuration of the optimization geometry [4] of the calcium hydride is

**Table 4**.Calcium hydrogen unit cell with optimized geometry.

| Real Lattice(Å) | | | Reciprocal Lattice(1/Å) | | |
|---|---|---|---|---|---|
| 4.8108989 | 0.0000000 | 0.0000000 | 1.3060315 | 0.0000000 | 0.0000000 |
| 0.0000000 | 6.4003026 | 0.0000000 | 0.0000000 | 0.9817013 | 0.0000000 |
| 0.0000000 | 0.0000000 | 5.4168082 | 0.0000000 | 0.0000000 | 1.1599424 |

**Table 5**. Parameters of unit cell of calcium hydride with optimized geometry.

| Lattice parameters(Å) | Cell Angles |
|---|---|
| a = 4.810899 | alpha = 90.000000 |
| b = 6.400303 | beta = 90.000000 |
| c = 5.416808 | gamma = 90.000000 |

Current cell volume is 166.790073 $Å^3$

**Table 6**. Cell contents.

| Element | Atom number | Fractional coordinates of atoms | | |
|---|---|---|---|---|
| | | u | v | w |
| H | 1 | 0.250000 | 0.250000 | 0.250000 |
| H | 2 | 0.250000 | -0.250000 | 0.750000 |
| H | 3 | -0.250000 | 0.750000 | -0.250000 |
| H | 4 | 0.750000 | 0.250000 | 0.250000 |
| Ca | 1 | 1.000000 | 1.000000 | 1.000000 |
| Ca | 2 | -0.500000 | -1.000000 | 1.500000 |
| Ca | 3 | -1.000000 | 1.500000 | -1.000000 |
| Ca | 4 | 1.500000 | -0.500000 | -0.500000 |

Final Enthalpy = -4.07947274E+003 eV

Maximum deviation from symmetry = 0.263123E-14Å
Final energy, E = -4030.984391373 eV
Final free energy (E-TS) = -4030.999842991eV

**Fig. 1.** Brillouin zone of calcium hydride

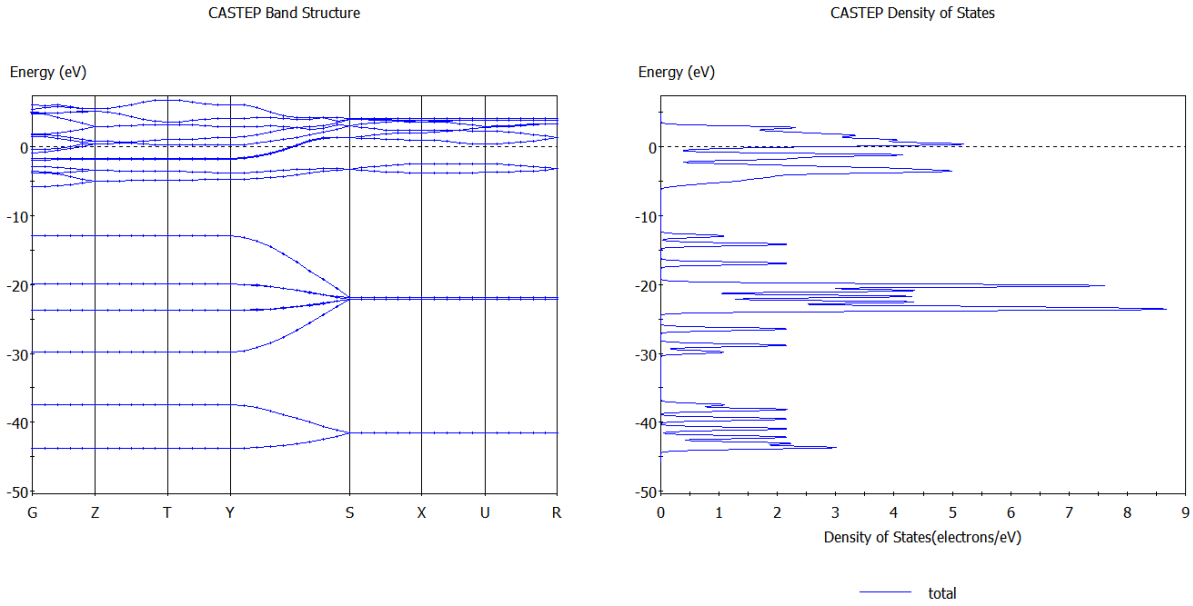


**Fig. 2.** Band structure and density of states from calcium hydride

Calcium hydride is a set of crystals of orthorhombic structure, white when it is pure, lacks a characteristic odor. Its molecular weight is 42.094g / mol. [5]. The Brillouin zone, Fig. 1, provided us thermodynamic properties, which is useful for further research and corroborated by other researchers.

The DOS curves are given in Fig. 2. The DOS for the calcium hydride shown can we see that the energy bands are more or less uniformly dispersed along the axis but in the energy there is a large energy separation of about 3 eV between the highest Occupied Fermi energy levels (0 eV) and the energy bands Corresponding to higher excited states.

## 4. Conclusion

Calcium hydride has two ionic bonds between calcium and the two hydride ions, it is a saline hydride, and that is, its structure is similar to salt. Its crystal structure is the same as lead chloride, which belongs to the orthorhombic crystal system.

After obtaining the optimization of the calcium hydride geometry the state density and the band structure have been calculated, showing that the calcium hydride crystal is a material with affinity to be able to absorb hydrogen.

**References**

[1]Ren, Jianwei, et al. Current research trends and perspectives on materials-based hydrogen
storage solutions: a critical review. International Journal of Hydrogen Energy, 2016.
[2] Zhou, J., et al. Electric field enhanced hydrogen storage on polarizable materials substrates. Proceedings of the National Academy of Sciences, 2010, vol. 107, no 7, p. 2801-2806.
[3] Monkhorst, Hendrik J.; Pack, James D. Special points for Brillouin-zone integrations. Physical review B, 1976, vol. 13, no 12, p. 5188.
[4] Milman, V., et al. Electronic structure, properties, and phase stability of inorganic crystals: A pseudopotential plane-wave study. International Journal of Quantum Chemistry, 2000, vol. 77, no 5, p. 895-910.
[5] Dixit, Deepesh Kumar; GANDHI, Krishna; DIXIT, Brajesh Kumar. Theoretical calculation of hydrogen desorption energies of calcium hydride clusters. International journal of hydrogen energy, 2012, vol. 37, no 4, p. 3767-3771.

# 1.2 Low-cost charging station for hydride hydrogen storage tanks

J.R. Tena Garcia, J.C. Carrillo-Bucio, K. Suárez Alcántara

Unidad Morelia del Instituto de Investigaciones en Materiales de la Universidad Nacional Autónoma de México.

Antigua Carretera a Pátzcuaro No. 8701.Col. Ex Hacienda de San José de la Huerta C.P. 58190, Morelia, Michoacán, México.

* Corresponding author: E-mail: karina_suarez@iim.unam.mx

---

## ABSTRACT

A hydrogen charging station was designed and constructed. The station is used for characterizing the tanks constructed by the research group. The tanks were constructed on the basis of different hydrogen storage materials. The station consists of inert gas and hydrogen pipes for hydrogen charging/ discharging; and, pressure, temperature and flow meters. The determination of the hydrogen storage/ release is based on the careful measurement of gas flow during programmed heating under a fixed initial pressure. The gas flow measures are translated to hydrogen release or storage in wt.% by means of real gas state equations and suitable mass balance. The station is solving a specific need of the research group: a reliable and low-cost equipment for the characterization of hydrogen storage tanks and it constitute the prototype for bigger hydrogen charging stations.

Acknowledgment: The present work was supported by the UNAM-DGAPA-PAPPIT IA100817 Estudio del comportamiento masivo de $NaAlH_4$ como material de almacenamiento de hidrógeno obtenido a partir de Al reciclado

***Keywords:*** hydrogen storage, charging station, hydrogen tanks

# 1.3 Biohydrogen production in a lab-scale low-recirculation upflow anaerobic sludge blanket reactor using different feeding strategies

Santiago Rodríguez-Valderrama, Carlos Escamilla-Alvarado, Héctor Amézquita-García

Laboratory of Engineering and Sustainable Bioprocesses, Chemical Sciences Faculty, Universidad Autónoma de Nuevo León, UANL, Av. Universidad S/N Ciudad Universitaria, San Nicolás de los Garza, NL 66455, México

* Corresponding author: Tel: +521 55 27 31 6440. E-mail address: cea_escamilla@yahoo.com.mx

## ABSTRACT

Hydrogen has been produced for commercial applications from gas natural, oil, coal gasification and water electrolysis, but these processes require high energy and cause air pollution and global warming. Hydrogen can be produced from biological processes such as dark fermentation or photo-fermentation. Biohydrogen production has gained considerable attention as a sustainable and renewable alternative, because less energy is required and it is more environmental friendly. Amidst the biohydrogen production technologies, dark fermentation is the most studied owing to its treatment capacity for different organic wastes, yet its development at industrial scale is still limited due to low yields. Therefore, the aim of this study was to evaluate the biohydrogen production in an upflow anaerobic sludge blanket reactor (UASB) using different feeding strategies as a mean to further increase yields.

The 0.4 L UASB reactor was fed with sucrose as carbon source, whereas methanogenic granules were used as inoculum (heat-treated at 90 °C for 1 h to inhibit methane producing microflora and select hydrogen producing microbes). Five feeding strategies were used to evaluate biohydrogen production: *i)* intermittent feeding with sucrose concentration 25 g/L, *ii)* neutralization and feeding with sucrose concentration 25 g/L, *iii)* diary feeding (400 mL: sucrose concentration 25-37 g/L), *iv)* diary feeding (800 mL: sucrose concentration 19 g/L) and *v)* continuous feeding (2400 mL: sucrose concentration 8.3 g/L). Recirculation speed was the lowest attainable by the peristaltic pump (30 rpm, 0.1 L/h). The pH was analyzed before feeding, whereas biogas production was determined by water displacement. Hydrogen composition was measured by adsorption in NaOH (4N) and gas chromatography.

The UASB reactor operated for 98 days. The total volume of biogas accumulated was 129.59 L. The average biogas production in strategies *i, ii and iii* was lower than 1300 mL/d whereas the maximum production was 2775 mL/d, achieved in strategy *v*. The

average yield in all operation was 110 mL biogas/g sucrose.d and average hydrogen composition in biogas was 85.83 %. The average hydrogen yield compared to its theoretical maximum (3 mol $H_2$/mol glucose) was 0.87 mol $H_2$/mol glucose.

In conclusion, dark fermentation proved to be a competent technology for biohydrogen production and continuous feeding resulted a better strategy than intermittent feeding.

***Keywords:***Dark fermentation, methanogenic inhibition, sucrose.

## 1. Introduction

The global energy is mainly produced from fossil fuels as petroleum, coal and natural gas. Their exploration, exploitation, refining, transportation and combustion affect negatively the environment and health. However, this fuels are decreasing, while energy demand is increasing due to population growth, urbanization and modernization [1,2]. To increase the energy and reduced the problems related to fossil fuels, the use of renewable sources are promising to diminish the air pollution and greenhouse gas emissions [3]. The principal renewable energy sources include the solar energy, geothermal energy, ocean energy and bioenergy [4]. Modern bioenergy are produced from biomass through industrial process an used in industries, power plants, and transport sectors. Thermochemical, thermal and biochemical processes are the ways to transform biomass to bioenergy [5].

Biohydrogen, bioethanol, biodiesel and methane are biofuels and can be produced by biochemical processes as dark fermentation (DF), fermentations, transesterification and anaerobic digestion [6]. Biohydrogen has advantages over other alternatives because is a carbon, nitrogen and sulfur free biofuel and is considered as a good energy carrier due to its high energy content 122 MJ $kg^{-1}$. Hydrogen has been produced for commercial applications from gas natural, oil, coal gasification and water electrolysis, but these processes require high energy and cause air pollution and global warming [7]. Biotechnologies such as DF and photo-fermentation provide an environmentally way of hydrogen production from diferent organic wastes and wasterwaters as a feedstock, but DF has higher hydrogen production rates compared to photo-fermentation because this bioprocess is independen of weather conditions [3].

Various fermentation systems have been developed for hydrogen production, such as the batch, semi-continuous, continuous, and one or multiple stages. The best process configurations have reported are anaerobic sequencing batch (ASBR) and upflow anaerobic sludge blanket (UASB) reactors [7]. Hydrogen production in continuous mode is more stable and has higher volumetric rate than batch mode, but larger scale systems have not yet been reported in the literature mainly due the low stability of DF, low organic matter removal (formation of by-products: organic acids and alcohols), low energy efficiency and low yields [8,9]. To increase the hydrogen yields, some authors have assessed the effect of inoculum pretreatment on microbial community structure[10], pH influence [11], effect of hydraulic retention time (HRT) [12], and batch and continuous operation mode [13,14]. The aim of this study was to evaluate the biohydrogen production

in an UASB reactor using different feeding strategies as a mean to explore and further increase yields.

## 2. Materials and Methods

### 2.1. Inoculum

Methanogenic granules were obtained from brewery industry anaerobic sludges (Obregón, Sonora, Mexico) and stored at 4 °C. Before use, inoculum was rinsed with distillated water and heat-treated at 90 °C for 1 h in a water bath to inhibit methane producing microflora and enrich hydrogen producing microbes [15]. The inoculum was characterized in terms of pH, humidity, total solids, volatile solids and ashes (Table 1). Humidity, total solids, volatile solids and ashes were carried out in triplicate using standard techniques [16].

*Table 1**. Characteristics of inoculum.***

| **Parameter** | |
|---|---|
| pH | 6.66 |
| Humidity (%$^{wb}$) | 93.80 ± 0.07 |
| Total solids (%$^{wb}$) | 6.20 ± 0.07 |
| Volatile solids (%$^{db}$) | 34.82 ± 3.59 |
| Ash (%$^{db}$) | 65.18 ± 3.59 |

Notes: wb, wet basis; db, dry basis

### 2.2. Experimental system and procedure

A plexiglass 0.4 L working volume UASB reactor (0.056 m diameter, 0.23 m height) was fed with sucrose as carbon source, with a peristaltic pump as shown in Fig 1. The initial volume of inoculum, mineral medium and phosphate buffer solution were 77, 40 and 283 mL respectively. The mineral medium was described by Cisneros-Pérez et al. [10] (mg $L^{-1}$): $ZnCl_2$, 75; $MgCl_2 \cdot 6H_2O$, 100; $MnCl_2 \cdot 4H_2O$, 10.77; $FeCl_3 \cdot 6H_2O$, 25.97; $CuCl_2 \cdot 2H_2O$, 3.41; and $NiCl_2 \cdot 6H_2O$, 101.25. In order to keep the operation pH at 5.5-6.5 a phosphate buffer of 30 g $K_2HPO_4$ $L^{-1}$ and 20 g $KH_2PO_4$ $L^{-1}$ and was used. The system had a recirculation peristaltic pump (323, Watson Marlow, England) that operated at the lowest attainable speed (30 rpm, 0.1 L $h^{-1}$).

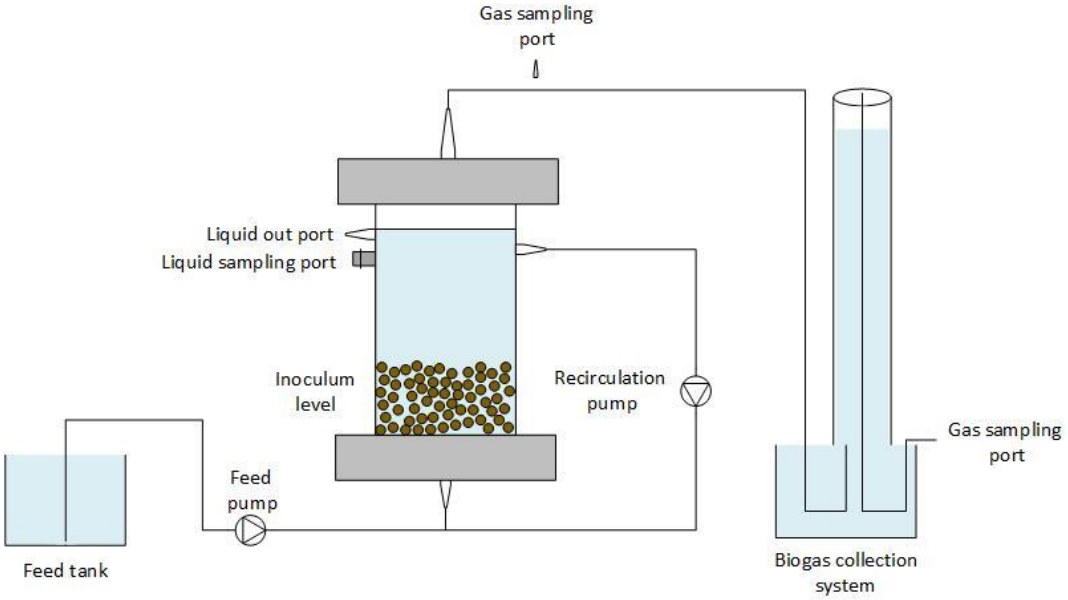


***Fig 1. Schematic diagram of the experimental apparatus***

Five feeding strategies were used to evaluate biohydrogen production: *i)* semi-continuous feeding of 100 mL at 25 $g_{sucrose}$ $L^{-1}$ twice a week (average loading rate 1.785 g $L^{-1}$ $d^{-1}$), *ii)* neutralization with NaOH 4N of the reactor and semi-continuous feeding of 200 mL at 25 $g_{sucrose}$ $L^{-1}$ every two days (6.25 g $L^{-1}$ $d^{-1}$), *iii)* feeding of 400 mL at either 25 or 37 $g_{sucrose}$ $L^{-1}$ during 8 h daily (25 and 37 g $L^{-1}$ $d^{-1}$ respectively), *iv)* feeding of 800 mL at 19 $g_{sucrose}$ $L^{-1}$ during 8 h daily (38 g $L^{-1}$ $d^{-1}$ ) and *v)* continuous feeding of 2400 mL $d^{-1}$ at 8.3 $g_{sucrose}$ $L^{-1}$ (49.8 g $L^{-1}$ $d^{-1}$). For strategies (*iii*), (*iv*) and (*v*), the mineral medium and phosphate buffer volumes were 40 and 360 mL respectively; the final feeding volume was completed with distilled water.

### 2.3. Analytical methods.

The pH was analyzed before ($pH_r$) and after feeding ($pH_{adj}$) with a pH-meter (PC18, Conductronic, Mexico), whereas biogas production was determined by water displacement (3 L column) method everyday using NaCl saturated and pH 3.0 acidified (sulfuric acid) solution to inhibit microbial growth and avoid $CO_2$ dissolution. Hydrogen composition was measured by adsorption in NaOH (4N) and gas chromatography. The gas chromatograph (GC-15A, Shimadzu Corporation, Kioto, Japan) was equipped with thermal conductivity detector and a Porapak N column. The oven, injector and detector temperatures were 35, 150 and 150 °C, respectively. Helium was used as carrier gas. The total volatile fatty acids (VFA) concentration was determined by Anderson et al. [17] titration method. Sucrose concentration was determined by total sugars method with sulfuric acid and phenol compared against a calibration curve obtained using dextrose [18]. Moreover, concentration of total sugars during feeding in strategies (*iii*), (*iv*) and (*v*) were correlated through linear regression and expressed through the following function:

$$Y = b_0 + b_1 X \qquad (1)$$

Where Y denotes the total sugars (g $L^{-1}$), X the time during feeding (h), $b_0$ is the offset term and $b_1$the slope term.

## 3. Results and discussion

The UASB reactor was operated for 98 days at room temperature. In Fig. 2A the performance of the UASB reactor in respect to biogas production and hydrogen yield may be observed. The pH and VFA variations during the operation of the UASB can be seen in Fig 2B. In this figure, the $pH_r$ was the pH recorded daily and previous any feeding, whereas $pH_{adj}$ was the pH recorded after feeding was completed and the reactor content was homogenized.

After inoculation, the reactor presented a three-day lag phase due to inoculum adaptation to substrate. The biogas production in the strategy (*i*) ranged from 0 to 1275 mL $d^{-1}$ during the first 11 days and then decreased to 1000 mL $d^{-1}$ at day 14. Sucrose concentration above 19 g $L^{-1}$ might have influenced in inhibition by VFAs accumulation [19]. Regarding the pH profile, it drastically dropped after the first day, however buffering capacity in the system raised its value to 5.8-6. VFAs also raised noticeably after start-up (8334 mg $L^{-1}$), but decreased to 6500 mg $L^{-1}$ as the UASB was adapting to substrate and operation.

During strategy (*ii),* the biogas production decreased from day 14 to 22. Even though pH in the UASB reactor ($pH_r$) was maintained above 5.5 units, the neutralization performed through shocks of concentrated NaOH might have altered microbial metabolism and communities, reducing in consequence the biogas production [20]. Effectively, the addition of alkaline compounds helps the rapid neutralization of the generated VFA but reduces the activity of hydrogen producing bacteria. According to Li et al. [21], pH values of 6-7 operation were detrimental to dark fermentation, whereas values in the range of 5.3-5.7 are beneficial for hydrogen production.In our operation, pH after feeding ($pH_{adj}$) was maintained over 6, although it diminished day after day.

Strategy (*iii*) began with the heat shock of the microbial granules (90 °C, 1h) as a means to counteract the diminishing in biogas production observed during strategy (*ii*) that was ascribed to an unbalance in microbial communities, likely a lactic acid deviation [22,23]. After the heat shock, biogas production and hydrogen yields were increasingly regained. This behavior could also be due to the increase in organic load from 25 g $L^{-1}$ $d^{-1}$ to 37 g $L^{-1}$ $d^{-1}$; an increase in the organic load allows the formation of a new environment to which microorganisms must adapt [22]. The average biogas production was 544 mL $d^{-1}$, reaching a maximum of 916 mL $d^{-1}$ at the end of the strategy. Altogether pH had noticeably variations that corresponded with alterations in VFA concentration. The $pH_{adj}$ after feedings were <6.5, whereas the minimum $pH_r$ was 5.6. At the end of this stage the biogas production was increasing constantly.

In strategy (*iv)* biogas production ranged from 916 mL $d^{-1}$ at the beginning of the strategy to 1780 mL $d^{-1}$ at the end, after 52 d of operation. Indeed, the maximum biogas production was 2375 mL $d^{-1}$ on day 70. The $pH_r$ was lower than 5.5 and decreasing over time, whereas VFAs followed an inverse trend, amounting up to 7400 mg $L^{-1}$. After day 75 the biogas production started to decrease down to a minimum in the period of 1250 mL $d^{-1}$.

Strategy (*v*) showed an average daily increase of 259 mL $d^{-1}$. Indeed, the maximum biogas production in this strategy and during all UASB operation was 2775 mL $d^{-1}$; after 7 days biogas production decreased to a value of 1800 mL $d^{-1}$. According to the continuous operation followed in this strategy, the $pH_r$ and $pH_{adj}$ were the same in this strategy. Its value was lower than 5.5 whereas the VFAs increased up to a maximum of 7473 mg $L^{-1}$. This trend was similar to that observed in strategy (*iv*).

Conventional (UASB) operation is mainly dependent on the pH, carbon source, sludge type, organic loading rate (OLR) and HRT [24]. Determining the optimal HRT (that is the time required for an infinitesimal particle of feed to traverse the reactor through its ejection) and OLR, could maximize the biogas and hydrogen production [25]. In strategies (*iii*), (*iv*) and (*v*) the UASB reactor operated at HRT of 24 h, 12 h and 4 h respectively, and OLR of 25 and 37 g $L^{-1}$ $d^{-1}$, 38 g $L^{-1}$ $d^{-1}$, and 49.8 g $L^{-1}$ $d^{-1}$,correspondingly.

Amidst all strategies the $H_2$ yield had three maximums: 72.5 mL $H_2$ $g_{sucrose}^{-1}$ $d^{-1}$ for strategy (*i*), 90.4 mL $H_2$ $g_{sucrose}^{-1}$ $d^{-1}$ for strategy (*iv*) and 77.7 mL $H_2$ $g_{sucrose}^{-1}$ $d^{-1}$ in (*v*). The lowest yields during overall operation were obtained in strategy (*iii*). The average hydrogen yields in the strategies were 39.9 mL $H_2$ $g_{sucrose}^{-1}$ $d^{-1}$ for (*i*), 26.6 mL $H_2$ $g_{sucrose}^{-1}$ $d^{-1}$ for (*ii),* 26.4 mL $H_2$ $g_{sucrose}^{-1}$ $d^{-1}$ for (*iii),* 68 mL $H_2$ $g_{sucrose}^{-1}$ $d^{-1}$ for (*iv),* and 68.2 mL $H_2$ $g_{sucrose}^{-1}$ $d^{-1}$ for (*v*). Comparing to the hydrogen yields in our research, Si et al. [12] reported that at 24, 12 and 4 h HRT, the yields were 155, 362.5 and 527.5 mL $H_2$ $g_{sucrose}^{-1}$ $d^{-1}$ using glucose as the carbon source in a UASB reactor, these values were significantly higher than the best obtained in our research (90.4 mL $H_2$ $g_{sucrose}^{-1}$ $d^{-1}$). These disparities could be ascribed to the differences in the operation volume and temperature, 2.5 L and 35 °C for them, and 0.4 L and room temperature for us. Moreover, Si et al. [12] also included carbon nanotubes to accelerate the formation of granules, and a preadaptation of 150 days at 12 HRT of the inoculum to the substrate (in our work the whole operation time was 98 days), which favored the formation of substrate-specific hydrogenogenic granules.

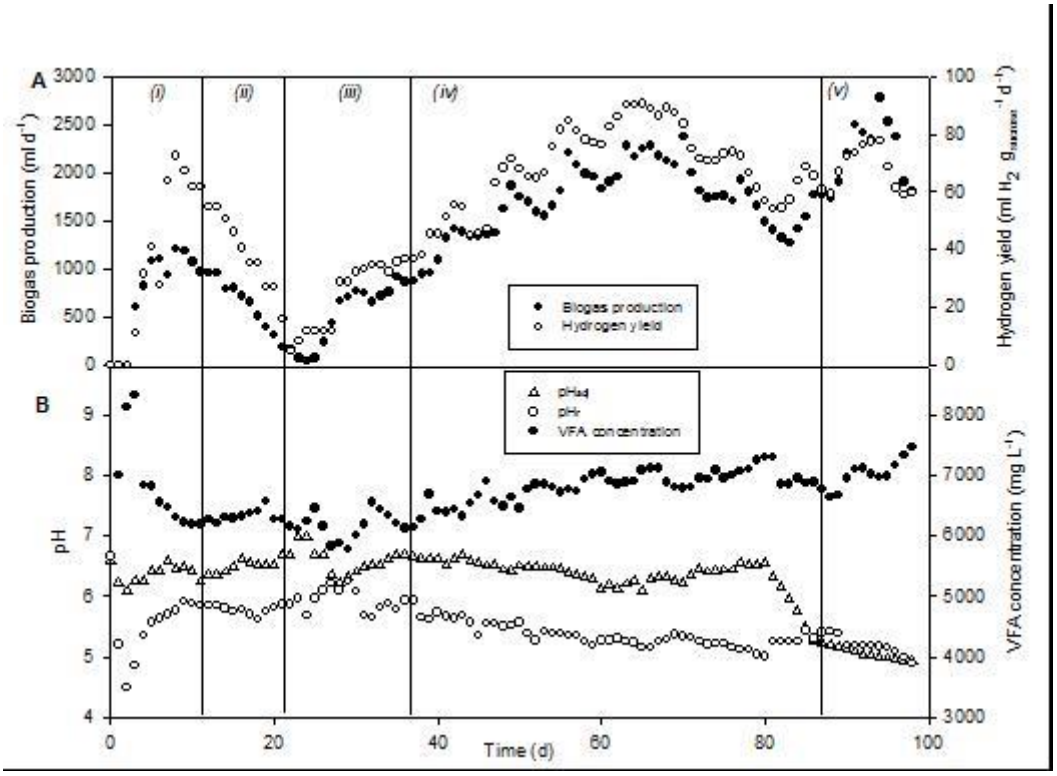


*Fig 2. UASB reactor performance (A) biogas and hydrogen production, (B) pH and VFAs profiles*

The total volume of accumulated biogas after the 98 days operation was 129.59 L and the average performance in the whole operation was 57.6 mL $H_2$ $g_{sucrose}^{-1}$ $d^{-1}$. The average hydrogen yield compared to its theoretical maximum (3 mol $H_2$ $mol^{-1}$ glucose) was 0.87 mol $H_2$ $mol^{-1}$ glucose; when low yields are obtained it could be ascribed to part of the substrate being used to microbial growth and maintenance [26] . Still, our value was higher than that obtained by Feng-Yung et al. [24]: 0.75 mol $H_2$ $mol^{-1}$ hexose, who fed the same carbon source (sucrose). They found that hydrogen production depended greatly on the HRT, obtaining their highest hydrogen production at 8 h HRT with an average hydrogen content of 42.4% (v/v), which was lower than the one found in this research (72.5%).

In general, the reactor operated in a $pH_r$ range of 4.48 to 6.6. The minimum $pH_r$ values were registered at the beginning of strategy (*i)* as consequence of fast VFA production and accumulation that could be due to microbial community acclimatization to substrate. The $pH_{adj}$ in strategy (*i), (ii)*, (*iii)* were over 6. At the end of strategy (*iii*) $pH_{adj}$ was decreasing due to rapid consumption of substrate and production of metabolites. In strategy (*v),* the $pH_r$ and $pH_{adj}$ were similar due they were measured at the same time. The $pH_r$ had variations in the strategies (*i*) and (*ii*) due to the semi-continuous feeding. In strategies (*iii*), (*iv*) and *(v),* the $pH_r$ values decreased due to the accumulation of VFA, which was corresponded by the increase in the concentration of VFA that exceeded 6500 mg $L^{-1}$. In strategies (*iv)* and *(v)* the $pH_r$ had values lower than 5.5; at lower pH values the presence of lactic acid bacteria is acknowledged, these compete with the hydrogenogenic

microorganisms for the carbon source. A reason why in strategy (*i*) when the pH decreased the hydrogen production also decreased, might have been due to the accumulation of AGVs since at this stage certain part of the volume of operation was replaced by means of feeding twice a week. The pH of the fermentation systems also has consequences on biogas composition. De Gioannis et al. [11] reported that the hydrogen concentration was 53 % vol and 86 % vol at pH 6.5-7.5, also at pH 5.5 and 8.5 the hydrogen content in the biogas was 1.5 and 22% vol, which confirmed the inhibition of hydrogen producing microorganisms at alkaline and acid pH values.

The maximum concentration of VFAs was 8334 mg $L^{-1}$ in strategy (*i)* mainly due to VFA accumulation by initial sugar feeding. For strategy (*ii)* the average VFA concentration was 6304 mg $L^{-1}$, the $pH_r$ during this strategy did not show important variations. For strategy (*iii),* the VFA concentration was more unstable than strategy (*ii*), The minimum VFA concentration in strategy (*iii)* was 5780 mg $L^{-1}$ at day 29. From day 38, the concentration of VFA increased significantly until the end of strategy (*iv*), obtaining an average concentration of 6800 mg $L^{-1}$; this increase was corresponded with the decrease of daily values of $pH_r$. The VFA concentration at the end of the operation time was variable but increased in the last 4 days until attaining a maximum of 7470 mg $L^{-1}$. Feng-Yung et al. [24] found that the concentration of VFAs increased as the HRT decreased, obtaining a concentration of 11 083 ± 236 mg $L^{-1}$ at a HRT of 4 h, and a yield of 100 mL $H_2$ $g_{sucrose}^{-1}$ $d^{-1}$ at low hydrogen composition of ca. 20%.

In Fig. 3 it is shown the total sugars consumption for strategies (*iii)*, (*iv)* and (*v)* during their first 10 h after feeding, considering that in these strategies the feeding time was over 8 hours. The sucrose concentration in strategies (*iii)* and (*iv)* was increasing over time, however for strategy (*v)* the concentration continuously decreased, which is indicative of a higher consumption rate of the sugars. In strategies (*iii)* and (*iv)* the consumption of sugars was given during the 14 hours following the feed due to the recirculation of medium. According with Eker et al. [19]at low initial sugars concentration (3.84 to 18.9 g $L^{-1}$) the sugar consumption is faster. The initial sugar concentration in strategy (*v*) was 8.3 g $L^{-1}$, in strategy (*iii*) was 25 and 37 $g_{sucrose}L^{-1}$, and 19 $g_{sucrose}L^{-1}$ for (*iv*); after 10 h of feeding the sugar utilization was 43.08%. The regression coefficients are presented in Table 2 for each strategy analyzed in Figure 3. It can be observed that the fitting is very good for strategies (*iii)* and (*v)*, but for strategy (*iv*) the linear regression was poor.

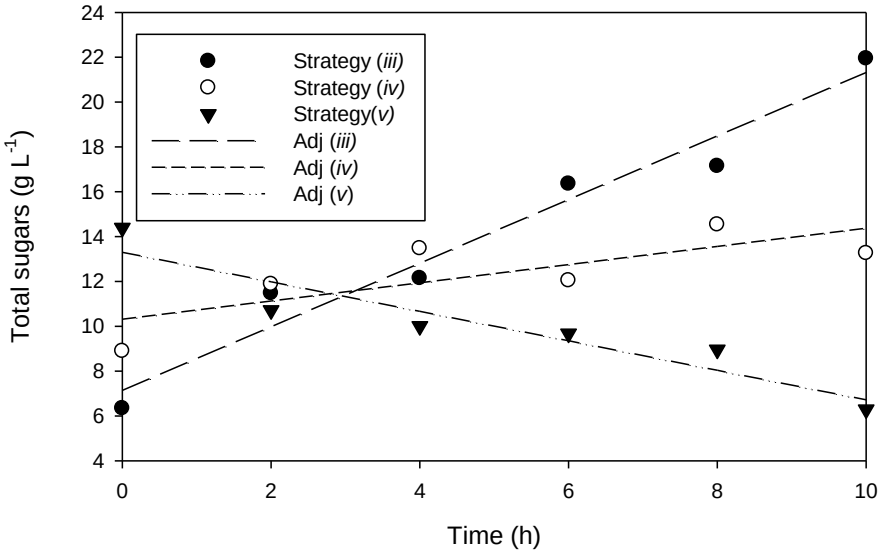


***Fig 3. Total sugars consumption***

*Tabla 2.**Linear regression coefficients***

| Strategy | $b_0$ | $b_1$ | $R^2$ |
|---|---|---|---|
| ***(iii)*** | 7.14 | 1.41 | 0.96 |
| ***(iv)*** | 10.32 | 0.40 | 0.60 |
| ***(v)*** | 13.29 | -0.66 | 0.87 |

## 4. Conclusion

Semi-continuous and continuous feeding in UASB achieved hydrogen generation and accumulation of VFAs. Neutralization with NaOH caused low biogas productivities and hydrogen yields, since the activity of the microorganisms was affected. The average yield for the whole operation of the UASB was 110 mL biogas $g_{sucrose}^{-1}$ $d^{-1}$, whereas average hydrogen content was 72.95 %. The average hydrogen yield compared to its theoretical maximum (3 mol $H_2$ $mol^{-1}$ glucose) was 0.87 mol $H_2$ $mol^{-1}$ glucose.

Dark fermentation proved to be a competent technology for biohydrogen production.

## Acknowledgements

The authors express their gratitude to the Dr. Eduardo Soto Regalado, Dr. Felipe Cerino Córdova, Dr. Ángel Martínez Hernández, Dr. Pasiano Rivas García, Dr. Margarita Loredo

Cancino and Dr. Luis Humberto Alvarez Valencia for their advising and facilitating the use of laboratory equipment.

**References**

[1] Asif M, Muneer T. Energy supply, its demand and security issues for developed and emerging economies. Renew Sustain Energy Rev. 2007;11:1388–413.

[2] Paris: International energy agency. World energy outlook 2010. 2010.

[3] Elbeshbishy E, Dhar BR, Nakhla G, Lee HS. A critical review on inhibition of dark biohydrogen fermentation. Renew Sustain Energy Rev. 2017;79:656–68.

[4] IPCC. Renewable Energy Sources and Climate Change Mitigation. 2011. p. 246

[5] Rahman MM, Paatero J V., Lahdelma R. Wide Spread Exploitations of Bioenergy: Are the Ways towards Sustainable Energy?. J Clean Energy Technol. 2015;4:209–12.

[6] Escamilla-alvarado C, Ponce-noyola MT, Poggi-Varaldo HM, Ríos-Leal E, García-Mena J, Rinderknecht-Seijas N. Energy analysis of in-series biohydrogen and methane production from organic wastes. Int J Hydrogen Energy. 2014;39:16587–94.

[7] Uçkun E, Trzcinski AP, Jern W, Liu Y. Bioconversion of food waste to energy : A review. 2014;134:389–99.

[8] Tapia-Venegas E, Ramirez-Morales JE, Silva-Illanes F, Toledo-Alarc??n J, Paillet F, Escudie R, Lay CH, Chu CY, Leu HJ, Marone A, Lin CY, Kim DH, Trably E, Ruiz-Filippi G. Biohydrogen production by dark fermentation: scaling-up and technologies integration for a sustainable system. Rev Environ Sci Biotechnol. 2015;14:761–85.

[9] Hawkes FR, Hussy I, Kyazze G, Dinsdale R, Hawkes DL. Continuous dark fermentative hydrogen production by mesophilic microflora: Principles and progress. Int J Hydrogen Energy. 2007;32:172–84.

[10] Cisneros-p C, Carrillo-reyes J, Celis LB, Etchebehere C, Alatriste-mondrag F, Etchebehere C, Razo-F E. Inoculum pretreatment promotes differences in hydrogen production performance in EGSB reactors. Int J Hydrogen Energy. 2015;40:6329–39.

[11] De Gioannis G, Friargiu M, Massi E, Muntoni A, Polettini A, Pomi R, Spiga D. Biohydrogen production from dark fermentation of cheese whey: Influence of pH. Int J Hydrogen Energy [Internet]. 2014;39:20930–41.

[12] Si B, Li J, Li B, Zhu Z, Shen R, Zhang Y, Liu Z. The role of hydraulic retention time on controlling methanogenesis and homoacetogenesis in biohydrogen production using upflow anaerobic sludge blanket (UASB) reactor and packed bed reactor (PBR). Int J Hydrogen Energy [Internet]. 2015;40:11414–21.

[13] Pattra S, Sangyoka S, Boonmee M, Reungsang A. Bio-hydrogen production from the fermentation of sugarcane bagasse hydrolysate by Clostridium butyricum. Int J Hydrogen Energy. 2008;33:5256–65.

[14] Khongkliang P, Kongjan P, Utarapichat B, Reungsang A, O-Thong S. Continuous hydrogen production from cassava starch processing wastewater by two-stage thermophilic dark fermentation and microbial electrolysis. Int J Hydrogen Energy. 2017;1–9.

[15] Zinatizadeh AA, Mirghorayshi M, Birgani PM, Mohammadi P, Ibrahim S. Influence of thermal and chemical pretreatment on structural stability of granular sludge for high-rate hydrogen production in an UASB bioreactor. Int J Hydrogen Energy. 2017;1–8.

[16] APHA/AWWA/WEF. Standard Methods for the Examination of Water and Wastewater. Stand Methods. 2012; p. 541.

[17] Anderson GK, Yang G. Determination of bicarbonate and total volatile acid concentration in anaerobic digesters using a simple titration. Water Environ Res. 1992;64:53–9.

[18] DuBois M, Gilles K a., Hamilton JK, Rebers P a., Smith F. Colorimetric method for determination of sugars and related substances. Anal Chem. 1956;28:350–6.

[19] Eker S, Sarp M. Hydrogen gas production from waste paper by dark fermentation: Effects of initial substrate and biomass concentrations. Int J Hydrogen Energy. 2017;42:2562–8.

[20] Lee C, Lee S, Han S-K, Hwang S. Effect of operational pH on biohydrogen production from food waste using anaerobic batch reactors. Water Sci Technol. 2014;69:1886–93.

[21] Li Z, Wang H, Tang Z, Wang X, Bai J. Effects of pH value and substrate concentration on hydrogen production from the anaerobic fermentation of glucose. Int J Hydrogen Energy. 2008;33:7413–8.

[22] Etchebehere C, Castelló E, Wenzel J, del Pilar Anzola-Rojas M, Borzacconi L, Buitrón G, Cabrol L, Carminato VM, Carrillo-Reyes J, Cisneros-Pérez C, Fuentes L, Moreno-Andrade I, Razo-Flores E, Filippi GR, Tapia-Venegas E, Toledo-Alarcón J, Zaiat M. Microbial communities from 20 different hydrogen-producing reactors studied by 454 pyrosequencing. Appl Microbiol Biotechnol. 2016;100:3371–84.

[23] Noike T, Takabatake H, Mizuno O, Ohba M. Inhibition of hydrogen fermentation of organic wastes by lactic acid bacteria. Int J Hydrogen Energy. 2002;27:1367–71.

[24] Chang FY, Lin CY. Biohydrogen production using an up-flow anaerobic sludge blanket reactor. Int J Hydrogen Energy. 2004;29:33–9.

[25] Kumar G, Sivagurunathan P, Park J, Park J, Park H, Yoon J, Kim S. Bioresource Technology HRT dependent performance and bacterial community population of granular hydrogen-producing mixed cultures fed with galactose. Bioresour Technol. 2016;206:188–94.

[26] Argun H, Kargi F. Bio-hydrogen production by different operational modes of dark and photo-fermentation: An overview. Int J Hydrogen Energy. 2011;36:7443–59.

# 1.4 Kinetic Study of the Decomposition of Methane over Pt Catalysts supported on γ-alumina doped with $Nd_2O_3$ for the Production of $H_2$

Marina Caballero, Gloria Del Angel.

[1]Universidad Autónoma Metropolitana-Unidad Iztapalapa. Departamento de Química, Área de Catálisis, Av. San Rafael Atlixco No. 186, C.P. 09340, A.P 55-534. México D. F. México.

* Corresponding author: marcabdi@yahoo.com.mx

## ABSTRACT

This paper presents results for the catalytic decomposition of methane using Pt catalysts supported on γ-alumina and on γ-alumina doped with neodymium. All catalysts were prepared by wet impregnation using $Nd(NO_3)_3{\cdot}6H_2O$ and $H_2PtCl_6.6H_2O$ as precursors. The concentrations for the catalysts were for Pt, 1.0 wt%, and for Nd, 1 and 10wt%. The reaction was done from 400 to 750°C.

All the catalysts reduced methane decomposition temperature by 400-750 °C relative to noncatalytic thermal decomposition, the Pt catalysts supported on γ-alumina doped with neodymium exhibited higher activity than Pt supported on alumina alone. All catalysts showed high activity and selectivity at 750°C, with conversions around 57-80 %vol and productions of hydrogen over 21,922, 20,000, 14,000 ppm for PtANd10, PtANd1 and PtA catalyst respectively, also were observed in the stream output unconverted methane, and small amounts of $C_2H_4$ y $C_2H_6$ (less than 1%).

The last stage the is paper includes a kinetic study of methane cracking, the temperature range used was 400-750ºC, for this purpose two experiments were carried out, the first consisted of varying the amount of catalyst (25, 50, 75 and 100 mg), keeping the feed flow constant (2 mL/min), in the second experiment the flow rate was varied (2, 4, 6 and 8 ml/min), keeping the mass of the catalyst constant (50 mg). With these experiments the pseudo-order of reaction was determined (order 1). The activation energy of methane cracking is estimated at 35.5, 37.9 and 33 kJ/mol for the Pt/A, Pt/ANd1 and Pt/ANd10 catalysts, respectively. The characterization was done by X-ray diffraction, $N_2$ adsorption-desorption, $H_2$-TPR, FTIR of CO adsorption, FTIR Pyridine of adsorption XPS, HRTEM, SEM-EDS, Catalytic activity and TPO analysis after reaction.

***Keywords:*** Platinum, Neodymium, carbon, Kinetic, activation energy

# 1.5 Quantum Dot Sensitized Photoelectrodes Used for Hydrogen Generation

A. Cerdán-Pasarán, I. Zarazúa, R. Fuentes-Ramírez, A. Alatorre-Ordaz, T. López-Luke, E. De la Rosa.

Universidad de Guanajuato, División de Ciencias Naturales y Exactas, Noria Alta s/n, Guanajuato, Gto. 36050, México.
Centro de Investigaciones en Óptica, A.P 1-948, León, Gto. 37160, México.
Facultad de Ciencias, Universidad de Colima, Colima, Col. 28045, México.

* Corresponding author: tzarara@cio.mx (+52 477 4 41 42 00 ext. 144)

## ABSTRACT

The splitting of water by sunlight to generate hydrogen is one form to obtain clean energy. One of the most promising options is the construction of photoelectrochemical cells using semiconductor nanoparticles as photocatalysts and photoelectrodes. Herein, we report the study of cadmium chalcogenide quantum dots (QDs) sensitized $TiO_2$ photoanodes and its application in hydrogen generation system. The QDs were deposited in the photoelectrodes as single layer and as co-sensitized layers with the combination of two different QDs. CdS was deposited by successive ionic layer absorption and reaction (SILAR) method, while CdSe and CdTe were deposited by electrophotesis (EPD). The electrodes were tested in a photoelectrochemical cell with two electrodes configuration using a Pt wire as counter electrode. The sacrificial reagent used in the electrolyte was sulfide. The hydrogen generation and photocurrent response was obtained using a solar simulator and a potentiostat. The highest photocurrent obtained in the single layer configuration was with the CdSe QDs. The co-sensitized photoelectrodes with CdS/CdSe and CdTe/CdS show increased photocurrent response compared with single layer deposited. The improvement observed with the addition of CdS was attributed to the increased light absorption and protection role of the CdS over the QDs.

***Keywords:*** hydrogen photoelectrogeneration; CdS; CdSe; CdTe

## 1. Introduction

Sunlight is an inexhaustible clean energy source available in the most parts of the world. Due to its intermittency, many efforts have been done in order to store it into chemical energy in the form of hydrogen through photoelectrochemical and photocatalytic methods. The photoelectrochemical decomposition of water under irradiation with light by semiconductor electrodes have been assessed. These materials require to perform three fundamental functions: light harvesting of the maximal possible part of the solar energy spectrum, charge generation and separation processes and catalytic function for efficient water oxidation and reduction.

The $TiO_2$ semiconductor has been tested, however only absorbs ultraviolet light, owing to its large bandgap (3 eV) [1,2]. One approach to increase the light absorption in the visible range is use dyes or inorganic semiconductors as sensitizers [3,4]. The nanostructured semiconductor materials provide attractive opportunities to enhance the light absorption, so the charge carriers generated can be used to drive the chemical reactions through two approaches: by size and shape engineering related to the quantum confinement, or by optical confinement allowing better management of the light flowing into the active region of the devices [5]. Furthermore, quantum dots (QDs) based on cadmium have been evaluated in photoelectrodes with $TiO_2$ and ZnO nanowires or nanotubes using easy deposition methods, such as chemical bath deposition (CBD) or successive ionic layer absorption and reaction (SILAR) [6–11].

In this work, we have analyzed the hydrogen generation of a photoelectrochemical cell with $TiO_2$ photoelectrodes sensitized with different quantum dot semiconductors based on cadmium chalcogenides: CdS, CdSe and CdTe. The QDs were deposited as a single layer and as co-sensitized layer combining two QDs. The improvement was observed in the photelectrochemical cell using co-sensitized electrodes, related to the light absorption enhancement and protection role of the CdS QDs.

## 2. Materials and Methods

### *2.1. $TiO_2$ films preparation*

$TiO_2$ films were deposited on fluorine-doped tin oxide (FTO) glass. $TiO_2$ compact layer was deposited by spray pyrolysis with a solution of titanium isopropoxide (0.2 M) using acetylacetone/etanol. After that, the $TiO_2$ active layer was deposited with a $TiO_2$ paste (DSL 18-NRT) by blading. Finally, the $TiO_2$ scattering layer was deposited with a $TiO_2$ paste (Wer2-O reflector) by blading. The films were sintered for 30 min at 450 °C.

### *2.2. Synthesis of CdSe and CdTe*

Colloidal CdSe QDs were synthesized based in Peng method [12]. 0.05 g of CdO, 0.3 g of 1-tetradecylphosphonic acid (TDPA) and 4 g of trioctylphosphine oxide (TOPO) were blended and heated to 320 °C under nitrogen flow in a flask. A solution of Se powder 0.026 g in 4.25 mL of trioctylphosphine (TOP) was injected in the flask when the temperature decreased at 275 °C. The temperature was increased again. The CdSe solution was cooled and dissolved in 10 mL of toluene. The QDs were cleaned using

methanol and centrifugation at 3000 rpm. The QDs were dissolved in toluene. The synthesis of CdTe QDs was similar, changing the TeTOP solution instead SeTOP with Te powder as precursor of tellurium.

*2.3. SILAR deposition*

CdS and ZnS QDs were deposited by SILAR method. The precursor solutions for CdS were 0.05 M $Cd(CH_3COO)_2 \bullet 2H_2O$ dissolved in ethanol and 0.05 M $Na_2S$ dissolved in methanol:water. The SILAR method consist in 1 min dip-coating the $TiO_2$ substrate into the Cd solution and subsequently into the S solution. Between each dipping step, the electrodes were rinsed by immersion in the corresponding solvent to remove the excess of precursor. Seven SILAR cycles were done. ZnS was deposited with 0.1 M $Zn(CH_3COO)_2 \bullet 2H_2O$ and 0.1 M $Na_2S$ dissolved in water. Two SILAR cycles were done for ZnS.

*2.4. Electrophoretic deposition*

The CdSe and CdTe QDs were deposited by electrophoretic deposition (EPD). The $TiO_2$ electrodes were immersed in the colloidal QDs using an FTO glass as counter electrode. A power supply was used to apply 200 V constant voltage for 105 min.

*2.5. Characterization*

The SEM images were obtained with a JEOL microscope JSM-7800F equipped with an energy dispersive spectrometer (EDS). The UV-Vis absorption was measured with an Agilent Technologies Spectrophotometer Cary 5000. The photoelectrochemical characterization was done with a Gamry reference 600 potentiostat/galvanostat and a solar simulator Oriel Sol 3A. The light intensity was 100 $mW/cm^2$. The photoelectrochemical cell consist in two-electrodes using the $TiO_2$/QDs photoelectrode as working electrode and Pt wire as counter electrode. The electrolyte was 0.25 M $Na_2SO_3$ and 0.35 M $Na_2S$ in water. The hydrogen generated was collected in a container locked on top.

## 3. Results and Discussion

The SEM image and the EDS map of the cross section corresponding to the photoelectrode with the QDs sensitizing the $TiO_2$ is shown in figure 1. It is possible to see the homogeneous distribution of the QDs in the $TiO_2$ active and scattering layers. The S and Se appear to be deposited mainly in active layer, while the Te was deposited homogeneously in both layers.

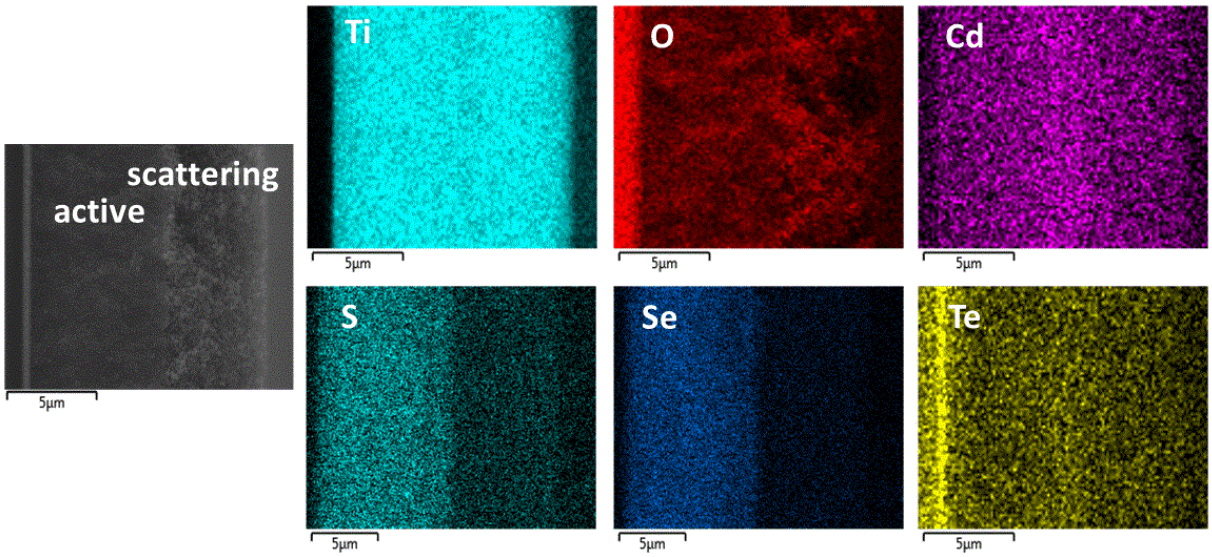


**Fig. 1.** SEM image and EDS mapping of the cross section of the quantum dot sensitized $TiO_2$ photoelectrode.

The UV-Vis absorption spectra of the colloidal CdSe and CdTe and the CdS and $TiO_2$ films are shown in figure 2. It is observed that the $TiO_2$ absorbs light in the UV region. The CdS has absorption at 550 nm corresponding to the visible region. The CdSe has absorption at 650 nm and the absorption of CdTe is at 690 nm. As can be seen, the CdSe and CdTe have absorption in longer wavelength compared to the CdS, therefore the combination of CdS QDs with CdSe or CdTe could broaden the light absorption range.

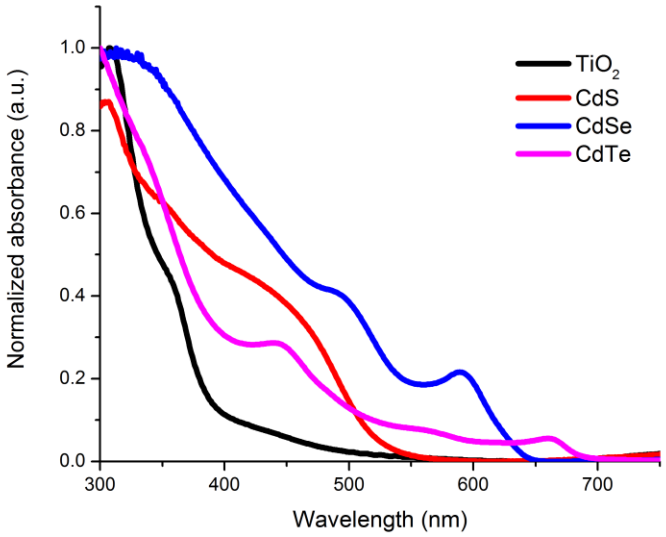


**Fig. 2.** Absorption spectra of the QDs used as sensitizers in the $TiO_2$ photoelectrodes.

The linear sweep voltammetry of the photoelectrochemical cell with the quantum dot sensitized photoelectrode is shown in figure 3. The stable photocurrent densities of the electrodes $TiO_2$/CdS/ZnS, $TiO_2$/CdSe/ZnS and $TiO_2$/CdTe/ZnS were 1.23 mA/cm$^2$, 10 mA/cm$^2$ and 16.7 mA/cm$^2$, respectively, reached at 0.5 V with CdTe and CdS and at 0.75 V with CdSe.

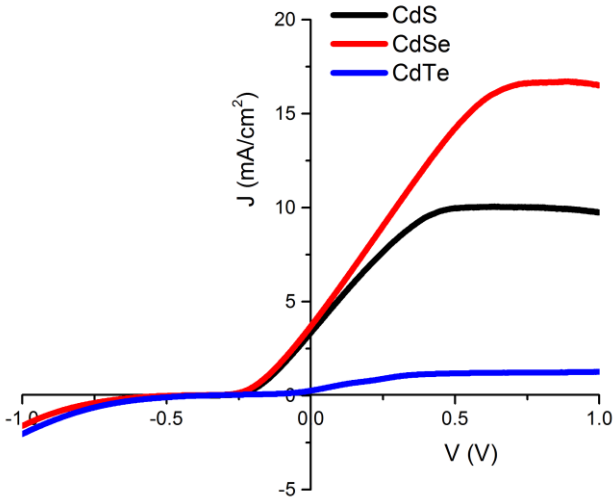


**Fig. 3.** J-V curve of the $TiO_2$ photoelectrodes deposited with QDs semiconductors.

Due to the stable photocurrent was obtained at 0.75 V, the photocurrent response measurements of the photoelectrochemical cell were evaluated at 0.75 V bias voltage applied, as is shown in figure 4. It is observed that the photoelectrodes with CdS and CdSe QDs were stable during the turn-on and turn-off cycles. The photoelectrode with CdTe seems to suffer degradation caused by the presence of the sacrificial agent added to the electrolyte.

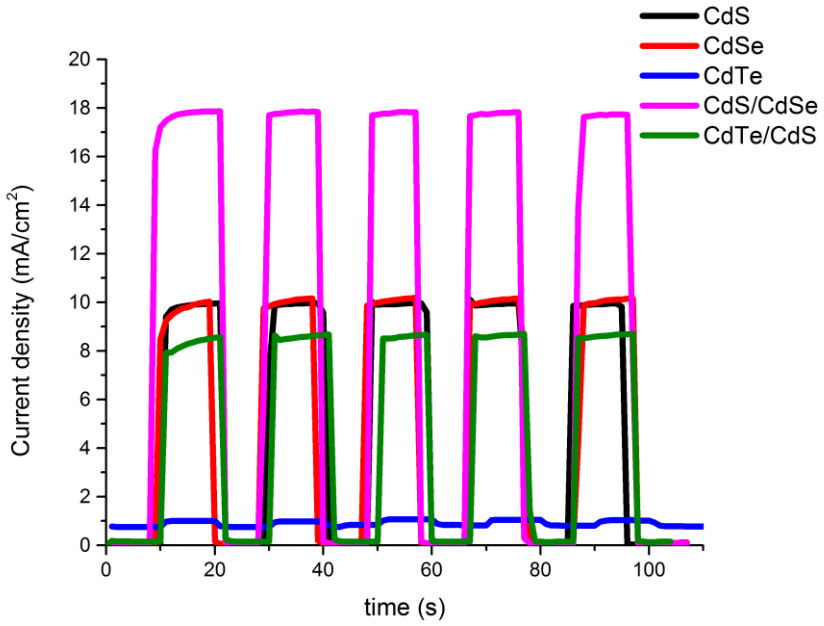


**Fig. 4.** Photocurrent response under pulsed illumination of the photoelectrochemical cell at 0.75 V bias voltage.

When CdS QDs were deposited as co-sensitizer with CdSe and CdTe QDs, the current density was improved (figure 4), thus the current obtained with $TiO_2$/CdTe/CdS/ZnS was 8.6 mA/cm$^2$ and with $TiO_2$/CdS/CdSe/ZnS was 17.9 mA/cm$^2$. It shows a considerable increment in the current obtained with the co-sensitized photoelectrodes in comparison to the electrode with only one QDs sensitizer.

## 4. Conclusion

We present the study of quantum dot-sensitized $TiO_2$ photoanodes used to generate hydrogen in a photoelectrochemical cell with a sacrificial electrolyte of sulfur. We obtained high and stable current density with the CdS and CdSe QDs, while with CdTe the current density was lower. The co-sensitization of CdSe and CdTe with CdS increased considerably the photocurrent response in both cases, attributed to the complementary light absorption and protection caused by CdS QDs. These photoelectrodes present potential applications in photoelectrochemical systems for hydrogen generation.

## Acknowledgements

We acknowledge financial support from CEMIE-Solar consortium projects P27 and P28 and to CONACYT for PhD scholarship for A. Cerdán-Pasarán.

## References


[1] Khan SUM. Efficient Photochemical Water Splitting by a Chemically Modified n-TiO2. Science (80- ) 2002;297:2243–5. doi:10.1126/science.1075035.

[2] Ni M, Leung MKH, Leung DYC, Sumathy K. A review and recent developments in photocatalytic water-splitting using TiO2 for hydrogen production. Renew Sustain Energy Rev 2007;11:401–25. doi:10.1016/j.rser.2005.01.009.

[3] Yu Z, Li F, Sun L. Recent advances in dye-sensitized photoelectrochemical cells for solar hydrogen production based on molecular components. Energy Environ Sci 2015;8:760–75. doi:10.1039/C4EE03565H.

[4] Gan J, Lu X, Tong Y. Towards highly efficient photoanodes: boosting sunlight-driven semiconductor nanomaterials for water oxidation. Nanoscale 2014;6:7142–64. doi:10.1039/c4nr01181c.

[5] Gür TM, Bent SF, Prinz FB. Nanostructuring Materials for Solar-to-Hydrogen Conversion. J Phys Chem C 2014;118:21301–15. doi:10.1021/jp500966u.

[6] Kim DH, Han HS, Cho IS, Seong WM, Park IJ, Park JH, et al. CdS-sensitized 1-D single-crystalline anatase TiO2 nanowire arrays for photoelectrochemical hydrogen production. Int J Hydrogen Energy 2015;40:863–9. doi:10.1016/j.ijhydene.2014.09.174.

[7] Wang G, Yang X, Qian F, Zhang JZ, Li Y. Double-Sided CdS and CdSe Quantum Dot Co-Sensitized ZnO Nanowire Arrays for Photoelectrochemical Hydrogen Generation. Nano Lett 2010;10:1088–92. doi:10.1021/nl100250z.

[8] Seol M, Jang J, Cho S, Lee JS, Yong K. Highly Efficient and Stable Cadmium Chalcogenide Quantum Dot/ZnO Nanowires for Photoelectrochemical Hydrogen Generation. Chem Mater 2013;25:184–9. doi:10.1021/cm303206s.

[9] Seol M, Kim H, Kim W, Yong K. Highly efficient photoelectrochemical hydrogen generation using a ZnO nanowire array and a CdSe/CdS co-sensitizer. Electrochem Commun 2010;12:1416–8. doi:10.1016/j.elecom.2010.07.035.

[10] Chen HM, Chen CK, Chang Y-C, Tsai C, Liu R, Hu S, et al. Quantum Dot Monolayer Sensitized ZnO Nanowire-Array Photoelectrodes: True Efficiency for Water Splitting. Angew Chemie 2010;122:6102–5. doi:10.1002/ange.201001827.

[11] Rodenas P, Song T, Sudhagar P, Marzari G, Han H, Badia-Bou L, et al. Quantum Dot Based Heterostructures for Unassisted Photoelectrochemical Hydrogen Generation. Adv Energy Mater 2013;3:176–82. doi:10.1002/aenm.201200255.

[12] Peng ZA, Peng X. Nearly Monodisperse and Shape-Controlled CdSe Nanocrystals via Alternative Routes : Nucleation and Growth. J Am Chem Soc 2002;124:3343–53.

# 1.6 Modified electrodes whit Ni electrodeposition to eliminate $Cr^{+6}$ in alkaline electrolysis process

Nahúm Hernández Pérez, Juan Manuel Sandoval Pineda, Claudia Alicia Cortes Escobedo, Usiel Sandino Silva Rivera, Rosa de Guadalupe González Huerta.

Instituto Politécnico Nacional -ESIQIE, Laboratorio de Electroquímica y Corrosión, UPALM, CP 07738, México,

Instituto Politécnico Nacional-ESIME-Azc, SEPI, Av. de las Granjas, No. 682, Azcapotzalco, CP 02250, México

CIITEC Instituto Polite´cnico Nacional, Cda. Cecati s/n, Col. Sta. Catarina, CP 02250 Azcapotzalco, D.F., Mexico

* Corresponding author:57296000 ext 54246, rosgonzalez_h@yahoo.com.mx

## ABSTRACT

Alkaline water electrolysis is one of the easiest methods for hydrogen production, offering the advantage of simplicity and lower cost. The challenges for widespread use of water electrolysis are to reduce energy consumption, cost and maintenance, as well as increase the reliability, durability and safety of the process. Alkaline electrolysis of water has been used for many years to obtain $H_2$ and $O_2$, however, the design of cheaper, more active and endurable electrodes is necessary.

Stainless steel (SS) is considered as one of the cheapest electrodes materials for alkaline electrolysers since it is relatively chemically stable and has low overpotential. Nevertheless, SS anodes do not withstand high concentration alkaline solutions because they undergo a corrosion process. If the electrolyser operates up 1.6 V, it can generate $Na_2FeO_4$ and hazardous hexavalent chromium ($Cr^{6+}$) in the anode. Hexavalent chromium is generated when the chromium containing stainless steel electrodes undergo an electro-oxidation process, to minimize this process, a low potential (1.6 V) and low electrolyte concentration (5%) must be applied, but the typical voltage value is normally 1.6 – 4.0 V for the monopolar configuration for electrolysis processes. In this work an alkaline electrolyser was design, in the first step six electrodes were manufactured of stainless steel. In the second step, nickel with matte or dull finish was deposited on SS surfaces to improve it is resistance to corrosion and wear. Then, the performance curve efficiency and the production of hexavalent chromium were determined. The performance curve after 70 h of operation, with nickel-plated electrodes showed an overpotential of 0.5 V at 10 A, compared with stainless steel electrodes. With SS electrodes $Cr^{6+}$was detected, in electrolyte and bubbler water, out of standard (>0.5 mg $L^{-1}$). When the electrolyser used Ni

Electroplating Electrodes, $Cr^{6+}$ was detected in quantities between the normativity (< 0.1 mg $L^{-1}$).

***Keywords:*** *Alkaline electrolyser, hydrogen, hexavalent chromium, modified electrodes, nickel-plated electrodes*

## 1. Introduction

Alkaline water electrolysis is one of the easiest methods for hydrogen production, offering the advantage of simplicity. The challenges for widespread use of water electrolysis are to reduce energy consumption, cost and maintenance and to increase reliability, durability and safety. Water alkaline electrolysis has been used during many years as a way to produce $H_2$ and $O_2$. However the development of cheaper, active and stable cathodic and anodic electrodes is necessary

Water electrolysis comprises two reactions: hydrogen evolution reaction (HER) at the cathode, and oxygen evolution reaction (OER) at the anode. Both reactions must have a low overpotential to increase the efficiency. The overvoltage of the OER has been identified as the greatest source of energy loss in water electrolysis. In addition, the anode can suffer electro-corrosion processes resulting in higher overpotentials [1]. This over potential is directly related to the potential difference necessary to drive the system at a given current density and therefore is directly related to the cost of the hydrogen production [2].

Stainless steel is considered as one of cheaper electrodes material for alkaline electrolysers, since it is relatively chemically stable with low over-potential. However, although stainless steel has a good stability at alkaline media, anodes undergo an electro-corrosion process due to the electrochemical reactions carring out. Electrolyser operates above 1.6 V can generate $Na_2FeO_4$, $Ni(OH)_2$ and $Cr^{6+}$ (which is a hazardous ion) in the anode, . Hexavalent chromium ($Cr^{6+}$) is generated when the chromium containing stainless steel electrodes undergo an electro-oxidation process. Stainless steel (304 y 316) has between 20-22% w of metallic chromium. Low potential (1.6 V) must be applied to minimize this process, but the typical voltage value is normally 2.2-4.0 V for the monopolar configuration for electrolysis processes. The review of the state of art showed little information about $Cr^{6+}$ generation during the operation of a low power alkaline electrolyser. Some electrolyser designs have been discussed in literature, for example M. Hammoudi et. al. present a multi-physics model used for the design and diagnosis of the alkaline electrolysers; K.C. Sandeep et. al. said that the commercial hydrogen production by water electrolysis is limited by the high cost of electricity. In that study, porous nickel electrodes were developed indigenously on an engineering scale to minimize the cell voltage. Ch. Ziems et. al. built two pressurized alkaline electrolyser-prototypes to investigate the influence of different temperatures and pressures. The purpose of that work was to design

an small alkaline electrolyser with a KOH 25% solution as an electrolyte, and a maximum power of 60 W, to integrate it to an hybrid wind–photovoltaic hydrogen system. E. Amores, et. al. designed new advanced alkaline electrolysers to optimize their combination with renewable energies. In pursuing this goal, modeling of alkaline electrolysers becomes a powerful design tool. It is necessary to establish a small-scale manufacturing process for electrolysers that can offer design security, installation, and operation of these devices.

Nickel is considered as the most suitable material for alkaline electrolysers, since it is highly chemically stable, relatively cheap and can be applied as catalytic material for cathodic and anodic reactions. The development method of electrodes is an important factor in terms of effecting electrode surface properties such as roughness. One of the methods used for metal deposition over metallic subtracts is the electrodeposition. Material selection and electrode modifications in cell design are important in water electrolysis. In this work, an alkaline electrolyser was design, in first step six electrodes were manufactured of stainless steel. The second step nickel with matte or dull finishes are deposited on stainless steel surfaces to improve corrosion and wear resistance. The Performance curve and production of hexavalent chromium were determined.

## 2. Materials and Methods

### 2.1 Preparation modified electrodes

Stainless steel was used as a substrate material for electrodes (anodes and cathodes). Nickel with matte or dull finishes was deposited on stainless steel surfaces to improve corrosion and wear resistance. Electrodeposition method is an electrochemical technique, where a thin layer of elemental nickel is deposited on a substrate based on Faraday's laws. Electrodeposition process consists of three steps, each involving a specific solution and requires electrochemical system:

a) Cleaning: this process includes polishing of the basis metal and anodic electrolytic cleaning (AEC) of the electrodes to eliminate dust, grease and particles remain on the surface. In AEC,anode is the working electrode into an alkaline electrolyte (9% w)and the electrolysis of water occurs at 5-7 A $dm^{-2}$. The oxygen formed in the reaction produces a cleaning on the surface and dirt dragging.
b) Surface pretreatment (SP): a high degree of adhesion between the deposit and the substrate is critical in all electrodeposit applications. In this case, the adhesion of nickel onto the stainless steel support becomes a very difficult task, for that is necessary a surface pretreatment before nickel deposit. Good adhesion of nickel is achieved on stainless steel surface by means of electrochemical pretreatment with solution: $NiCl_2$ (240 g $L^{-1}$), HCl (120 ml $L^{-1}$). In SP, cathode is the working electrode into an acid electrolyte and the electrolysis of water occurs at 2.5 V.The hydrogen formed in the reaction produces an electrolytic pickling on electrode surface, and the high presence of $Cl^-$ ion in the media produce the dissolving of the nickel anode material of the cell.

c) Deposit nickel: In this work was used Watts method to nickel electrodeposit. Electrodepositing bath was prepared by adding 300 g $L^{-1}$ $NiSO_4*6H_2O$, 60 g $L^{-1}$ $NiCl_2*6H_2O$, 45 g $L^{-1}$ $H_3BO_3$ at 55-60 °C, pH 4.5 at 6 $Adm^{-2}$ and time of 10 min.An expression for calculating nickel thickness, *s* in micrometers, can be used equation (1).

$$s = \frac{m*100}{d*A} = \frac{109.5*a*I*t}{8.097*A} = \frac{12.294*a*I*t}{A} \quad (1)$$

where m *(g)* is the amount of nickel deposited at the cathode (or dissolved at the anode), *I*(A) is the electric current that flows through the plating tank, *t (h)* is the time that the current flows, 8.907 (g $cm^{-3}$) is density of nickel, and $\eta$ is the current efficiency ratio. The proportionality constant 1.095 in g/Ah is equals $M$/nF, where $M$ is the atomic weight of nickel (58.69 gr $mol^{-1}$), n is the number of electrons in the electrochemical reaction (2), and F is Faraday's constant, equal to 26.799 A-h (more commonly given as 96,500 C).

## 2.2 Physical characterization

Scanning electron microscopy (SEM) was used to determine surface morphology of platining nickel, this was done in a Sirion FEG-SEM (from FEI). XDR was used to analyze the surface of stainless steel electrodes after 70 h of operation.

## 2.3 Design of Electrolyser and Performance Curves

Electrolyser system was designed to support above 100 W. In order to evaluate the electrolysis systems, it is necessary to identify parameters related to the performance: (a) Cell monopolar configurations, (b) electrodes gap 2.3 mm and (b) Operating conditions: voltage range (from 1.5 V to 6V), applied current (from 0.1 A to 10 A), temperature (from 25 °C to 80 °C), pressure (atm), type and electrolytes concentration (NaOH 5% w solution prepared from deionized water).

In a first stage, a total of 6 stainless steel (304-19 gauge) electrodes (3 anodes and 3 cathodes, each with 74 $cm^2$) were in contact with a 5% alkaline solution (NaOH), this concentration was chosen to avoid drag NaOH and that gas purification system was simpler. In a second stage, 3 anodes were modified by electrodepositing of Ni onto stainless steel substrates. Figure 1 shows electrolyser CAD diagram.

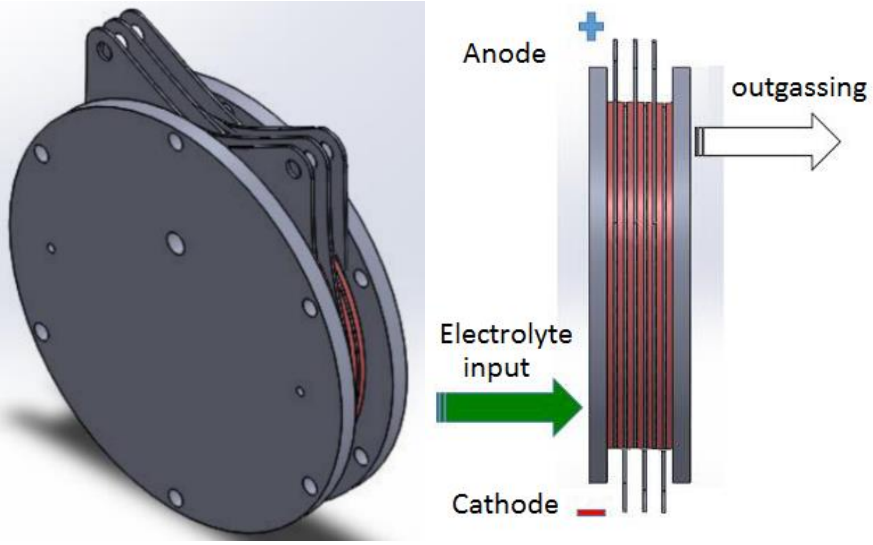


**Fig. 1.** Alkaline electrolyser design of, CAD diagram

The performance curve was obtained using test system which included a power source, recirculation tank, bubbler, dryer, mass flow meter and electrolyser, Figure 2. A controlled current was applied from 0.1 to 10 A. The hydrogen gas production was measured with a flowmeter ALICAT, by definition a water electrolysis always produces hydrogen at twice the volumetric rate as oxygen (gas oxyhydrogen). The electrolyser was operated for 70 h, and performance curves were obtained every 10 h.

Hexavalentchromium ($Cr^{6+}$) dissolved in the electrolyte and water bubbler was determined by photometric technique using 1.5-Diphenylcarbazide, the spectrophotometer (UV/VIS) is an equipment to measure the absorption of light. The sample is measured against a specified blank solution. $Cr^{6+}$ oxidizes 1.5-Diphenylcarbazide to 1.5 diphenylcarbazone, which forms a violet colored complex with the developed $Cr^{3+}$. At 550 nm the extinction of the dye is in linear relationship to $Cr^{6+}$ concentration. The evaluation was carried out by means of the calibration function as well as with a reference solution.

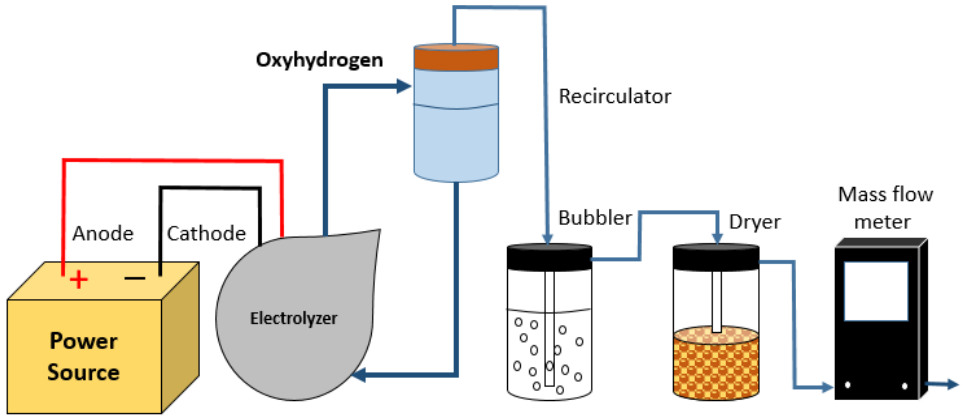


**Fig. 2.** Diagram of test system

## 3. Results and Discussion

Figure 3 shows the test system and a photograph of the stack electrolyser. It is important that the test of electrolyser must be in a ventilated place without flammable materials (solvents, paper, etc.) around the area. The gas produced must be bubbled in distilled water and pass through a desiccant to remove electrolyte dragged.

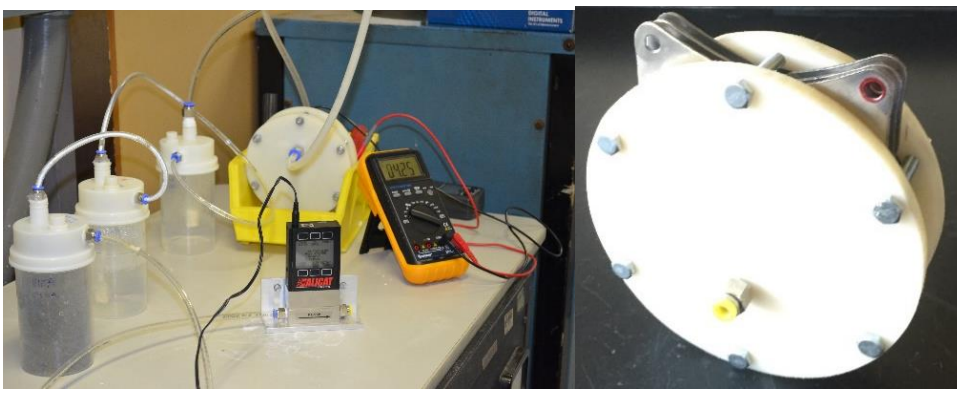

**Fig. 3.** Test system and stack alkaline electrolyser

Figure 4 (a) shows the performance curve of the alkaline electrolyser (EA) stack with Stainless steel electrodes (SSE). The initial experimental results showed that the system requires 4.1 V at 10 A. Figure 4 (b) shows performance curve with nickel electrodeposit electrodes (NiEE). Initial performance curve shows:the system requires 4.1 V at 10 A, in the first 30 h of operation, the performance curves show a better behavior, but after 40 h of operation applied voltage increases, after 70 h of operation at 10 A the system requires 3.9 V. Two possibilities were presented to explain the change in performance curves: 1) change in the electrode surface and 2) surface oxidation.

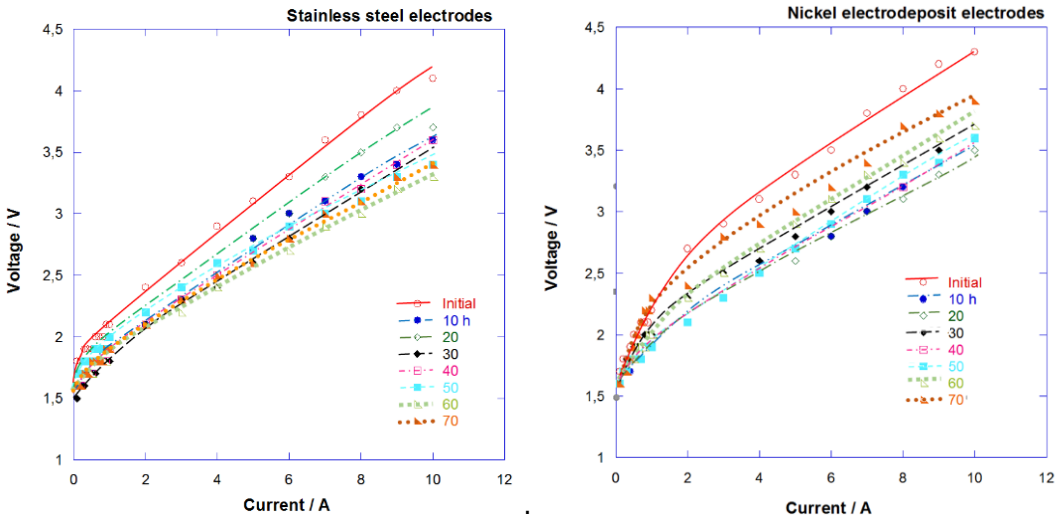


**Fig. 4.** Electrolyser performance curves: a) SS electrodes and b) NiE electrodes

Figure 5 show that performance of electrolyser with stainless steel electrodes is better than electrolyser with nickel electrodeposit electrodes, at 10 A the applied voltage is higher than in second arragement, this is attributed to the Nickel electrodeposit with matte or dull finishes which had lower conductivity than the stainless steel.

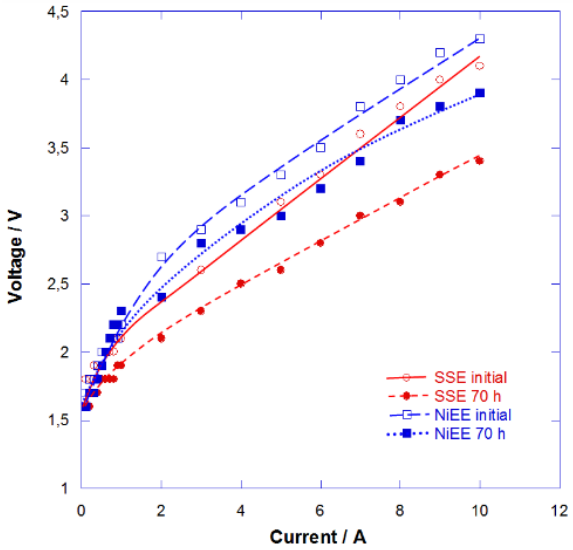


**Fig. 5.** Electrolyser performance: initial results and after 70 h of operation, with SSE and NiEE

Electrodes material should be stable (do not corrode) in the alkaline media (pH 10-14) and at intermediate temperature (30 – 80 °C). Pourbaix diagrams are commonly used in chemistry for detecting the thermochemical stable phases of an aqueous electrochemical system. The diagrams are plotted with the pH of the electrolyte on the x-axis and the potential of the metal on the y-axis. Figures 6 (a) and (b) show the literature Pourbaix diagrams for Iron-chromium and Nickelrespectively.

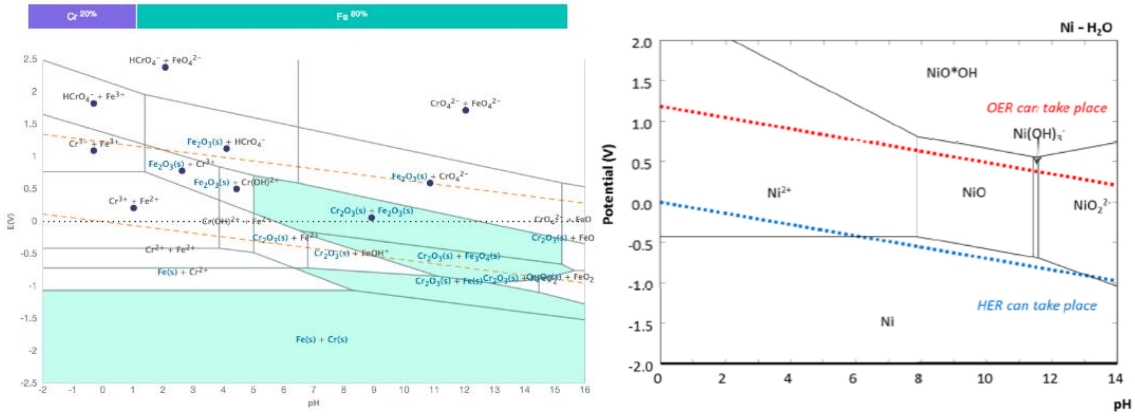


**Fig. 6.** Literature Pourbaix diagrams for a) Iron-chromium and b) Nickel

The following compound are formed according to Pourbaix diagrams if working electrodes are operated in alkaline medium and potential above 1.6 V,on SS Anode $CrO_4^{2-}$($Cr^{6+}$) and $FeO_4^{2-}$ is formed and on NiE anode NiO*OH is formed.

Figure 7 (a) shows an image of the SS cathodeafter 70h of operation. Electrode surface shows a dark layer, which was analyzed by X-rays. Diffractogram is showed in Figure 7 (b), dark layer is Tetrataenita (Intermetallic alloys $Fe_{0.5}O_7Ni_{0.49}$); so, if stainless steel is used as an anode in alkaline media, iron decomposes and some part of it is deposited on the cathode.

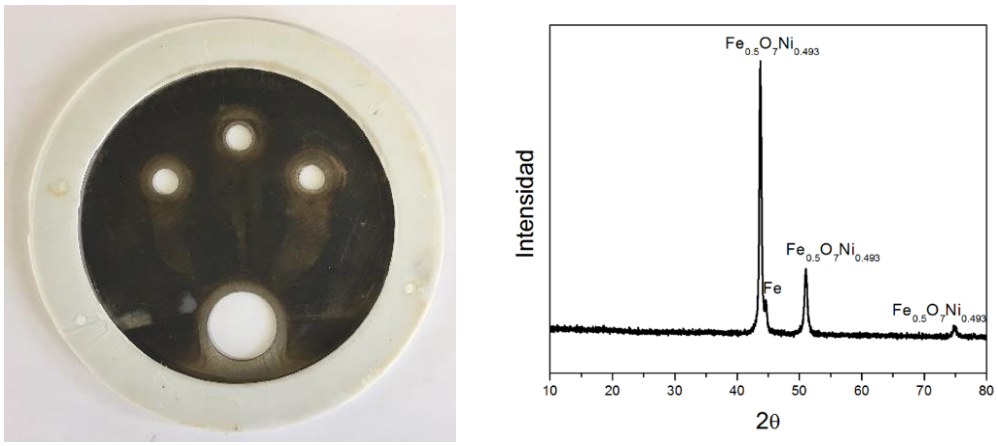


**Fig. 7.** a) Electrolyser cathode from the SSE arrangement after 70 h of operation and b) Tetrataenita diffractogram

Electrode surface of anode shows a brown layer, Figure 8 (a), iron forms a brown precipitate into the electrolyte, Figure 7 (b). According to Pourbaix diagrams it could be sodium ferrate ($Na_2FeO_4$). The electrolyte presents a yellow color, which is attributed to the hexavalent chromium generated in the anode.

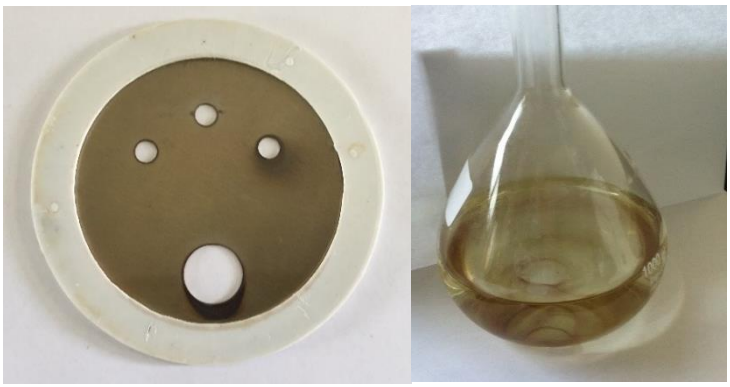

**Fig. 8.** a) Electrolyser anode from the SSE arrangement after 70 h of operation and b) Working electrolyte from the SSE arrangement after 70 h of operation

Hexavalent chromium ($Cr^{6+}$) is listed as number 16 in the Agency for Toxic Substances and Disease Registry, *Priority List of Hazardous Substances* (ATSDR, 1999).

Figure 9 (a) shows nickel plated electrode and Figure 9 (b) shows SEM image before it has been used as electrode in an electrolysis process. The electrodeposition was homogeneous, from equation (1) the nickel thickness was 20 µm. From the literature

(Pourbaix diagrams) it is known that nickel decomposes particularly slowly in alkaline media (equation 2) but although nickel is unstable at some oxygen evolution potentials, this is not expected to give problems in this work.

$$Ni + OH^- \rightarrow NiO^*OH \qquad (2)$$

Figure 10 show cathode, anode and electrolyte of second electrolyser arrangement whit nickel plated electrodes, after 70h in operation. Electrode surface of cathode and anode is clean and the electrolyte is clear, although it forms a yellow precipitate.

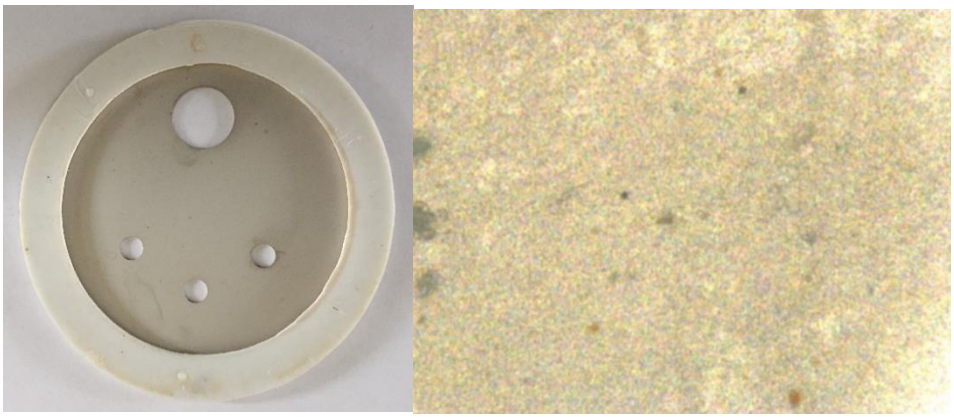

**Fig. 9.** Initial cathode and anode nickel plated

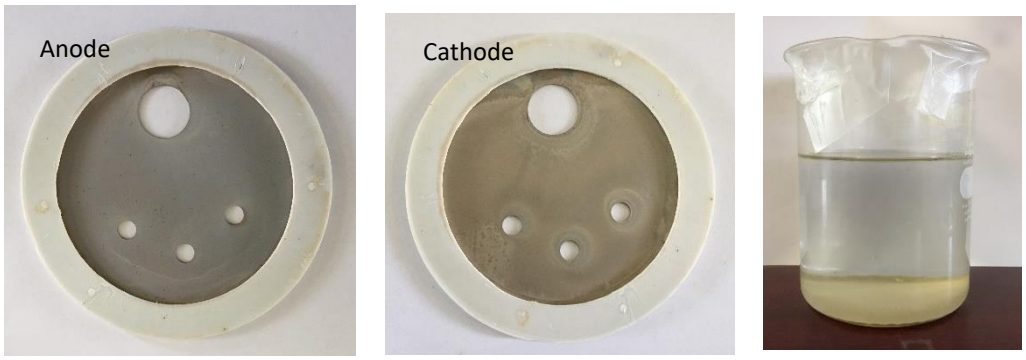


**Fig. 10.** Cathode, anode and electrolyte of second electrolyser whit nickel plated electrodes after 70h of operation.

Electrolyte was analyzed, two samples of 100 ml were taken from the bubbler and recirculation tank. Mexican regulation (NOM-002-SEMARNAT-1996) indicates that 1 mg $L^-$

[1] of $Cr^{6+}$ is the instantaneous maximum limit and 0.5 mg $L^{-1}$ is the maximum weekly average limit.

Table 1 shows$Cr^{6+}$concentration of sample.

**Table 1**. $Cr^{6+}$concentration of sample

| Electrolyser | From | Sample | $Cr^{6+}$(mg $L^{-1}$) |
|---|---|---|---|
| 1(SSE) | Recirculation tank | 1 | 1.766 |
| 1 (SSE) | Bubbler | 2 | 0.800 |
| 2 (NiEE) | Recirculation tank | 3 | 0.077 |
| 2 (NiEE) | Bubbler | 4 | 0.019 |

From Table 1, SSE formed $Cr^{6+}$ out of regulation in recirculation tank and bubbler. It is very dangerous and is necessary make a chemical treatment to eliminate $Cr^{6+}$. On the other hand, NiEE arrangement show $Cr^{6+}$ concentrantion whithin the normative limits in both samples. It shows that NiEE arrangement generates much less $Cr^{6+}$ than SS arrangement. This generation of ions is attributed to defects in nickel electrodeposit, which will be reviewed and reported in future works.

## 4. Conclusion

The challenges for widespread use of water electrolysis are to reduce energy consumption, cost and maintenance, as well as increase the reliability, durability and safety of the process. The review of the state of art showed little information about $Cr^{6+}$ generation during the operation of an alkaline low power electrolyser. The performance curve after 70 h of operation, with nickel-plated electrodes showed an overpotential of 0.5 V at 10 A, compared with stainless steel electrodes. With stainless steel electrodes (SSE) hexavalent chromium was detected in electrolyte and bubbler water out of standard (>0.5 mg $L^{-1}$) and with nickel-plated electrodes (NiEE) the $Cr^{6+}$ concentration was detected within the normative limits. It is expected that this work will serve as a reference for the proper design of low power alkaline electrolysers and the selection of stable non-hazardous materials as electrodes.

## Acknowledgements

The authors thank the financial support from IPN multidisciplinary project SIP-1820 (2017-2018) (modules 20170047 and 20170090) and CONACYT: CEMIE-Ocean project 249795: Transversal Line I-LT1. Authors thank Dra. Mabel VacaMier from UAM-Azc, for the support to hexavalent chromium determination.

## References


[1] KjartansdóttirCK, NielsenLP, and Møller P. Development of durable and efficient electrodes for large-scale alkaline water electrolysis," Int. J. Hydrogen Energ, 2013; 38:8221–8231.

[2] Ge X,Sumboja A, Wuu D, An T, Li B, Goh F, Hor T, Zong Y, Liu Z, ACS Catal. 2015;5:4643–4667.

[3] Marini S, Salvi P, Nelli P, Pesenti R, Villa A, Berrettoni M, Zangari G, Kiros Y,Advanced alkaline water electrolysis, Electrochem acta 2012;82:384–391.

[4] Manabe A, Kashiwase M, Hashimoto T,Hayashida T, Kato A, Hirao K, Shimomura I,Nagashima I, Basic study of alkaline water electrolysis,Electrochim Acta, 2013;100:249–256.

[5] Yde L, Kjartansdóttir C,Allebrod A, Mogensen F, Møller MB,Hilbert P, Dierking A. 2nd Generation Alkaline Electrolysis: Final report. Århus University Business and Social Science – Centre for Energy Technologies, 2013.

[6] Jacobs J, Testa SM, Overview of Chromium(VI) in the Environment: Background and History, L1608_C01.fm, 2004.

[7] Hammoudi M, Henao C, Agbossou K, Dube´ Y, Doumbia ML, New multi-physics approach for modelling and designof alkaline electrolysers, Int. J. Hydrogen Energ 2012;37:13895-13913.

[8] Sandeep KC, Kamath S, Mistry K, Kumar AM, Bhattacharya SK, Bhanja K, Mohan S, Experimental studies and modeling of advancedalkaline water electrolyser with porous nickelelectrodes for hydrogen production, Int. J. Hydrogen Energ 2017;42:12094-12103.

[9] Ziems Ch, Tannert D, Joachim H.Krautz A, Project presentation: Design and installation of advanced highpressure alkaline electrolyser-prototypes, Energy Procedia 2012;29:744 – 753.

[10] Khalilnejad A, Riahy GH, A hybrid wind-PV system performance investigation for the purpose ofmaximum hydrogen production and storage using advanced alkalineelectrolyser, Energy Conversion and Management 2014;80:398–406.

[11] Amores E, Rodrıguez J, Carreras Ch, Influence of operation parameters in the modelingof alkaline water electrolysers for hydrogenproduction, Int. J. Hydrogen Energ 2014;39:13063-13078.

[12] Mohamed M, Kassaby EL, Yehia A. EldrainyA, Mohamed E. KhidrK,Khidr I, Effect of hydroxy (HHO) gas addition on gasoline engine performance and emissions. Alexandria Engineering, 2016;55:243-251.

# 1.7 Test bench development and characterization of $RuO_2$- $IrO_2$ and Ir/Ru/CoOx-$SbSnO_2$ mixtures for MEAs assemblies in PEMWE

P. M. González Puente, R. G. González Huerta, J.R. Vargas García, N. Rojas García-Pardo, E. Amores Vera

IPN-ESIQIE, Laboratorio de Electroquímica y Corrosión, UPALM, 07738, CDMX, MEXICO.
Depto. Ing. Metalurgia y Materiales, Instituto Politécnico Nacional, 07300, CDMX, MEXICO.
Centro Nacional del Hidrógeno (CNH2), 13500, Puertollano (Ciudad Real), SPAIN.
* e-mail: pau_meche@hotmail.com phone number: 52 55 4145 4128

## ABSTRACT

Hydrogen produced by water splitting is a promising solution for an economy based on renewable energy sources. The production of $H_2$ has the potential to bring a local energy solution through the electrolysis of water. Proton Exchange Membrane Water Electrolysis (PEM WE) is one of the most suitable technologies for this purpose. PEM electrolyzer can produce pure $H_2$ continuously by converting electrical energy into chemical energy without any purification process. Membrane Electrodes Assemblies (MEAs) are one of the most important components of PEM electrolyzer. PEM electrolyzer performance depends mainly on the structure and electrochemical characteristics of these MEAs. In this work different MEAs were analyzed using as the cathode platinum commercial catalyst, $RuO_2$-$IrO_2$ mixtures and Ir/Ru/CoOx-Sb-$SnO_2$ at the anode. Before each preparation of MEA, the Nafion 115 membrane is chemically activated with hydrogen peroxide and sulfuric acid. Before spraying, the membranes were dried and flattened. Then, these MEAs were assembled in a 25 $cm^2$ PEM electrolyzer cell in order to characterize and analyze the behavior of the MEAs using a test bench. Polarization curves and durability tests as well as performance evaluation under specific operating conditions were compared with commercial MEAs using the same cell. The results reveal that mixtures of metallic oxides have reasonable stability under PEM water electrolysis conditions. These results suggest that appropriate mixture of theses metallic oxides are attractive for the fabrication of low-cost MEAs. As a consequence, it could improve efficiency and operation at high current densities, for the design and optimization for PEM water electrolysis. The development of durable MEAs for PEM electrolyzers is still a challenge and causes of degradation are yet to be comprehended.

***Keywords:*** PEM water electrolysis; MEAs; metallic oxides; durability tests.

# 1.8 COMPARISSON OF DENSITY OF STATES OF $Mg_xM_{1-x}H$ ALLOYS (M= Al, Ni, Zn; 0.8 ≤ x ≤ 1.0)

O. Ramírez-Rodríguez, G. Ramírez-Dámaso, F. L. Castillo-Alvarado, F. Caballero, I. E. Ramírez-Platón, E. Rójas-Hernández.

Escuela Superior de Ingeniería y Arquitectura "Unidad Ticomán" del Instituto Politécnico Nacional, Av. Ticomán No. 600, Col. San José Ticomán, C. P. 07340, Del. Gustavo A. Madero, CDMX, México.

Tecnológico de Estudios Superiores de Ecatepec, Av. Tecnológico s/n esq. Av. Carlos Hank González, Col. Valle de Anáhuac, C. P. 55210, EDOMEX, México.

Escuela Superior de Física y Matemáticas del Instituto Politécnico Nacional, Av. I. P. N. s/n, Unidad Profesional Adolfo López Mateos, Edificio 9, col. Lindavista, Del. Gustavo A. Madero, C. P. 07738, CDMX, México.

Carrera de Ingeniería Química, Facultad de Estudios Superiores Zaragoza C. II UNAM, Batalla 5 de Mayo s/n, Col. Ejército de Oriente, C.P. 09320, Iztapalapa CDMX, México.

Becario COFAA-IPN, EDD-IPN.

## ABSTRACT

In this work, the electronic density of states of three magnesium alloys: magnesium-zinc, magnesium-nickel and magnesium-aluminum were obtained, for different magnesium concentrations x = 0.80, 0.82,…, 1.0. Density Functional Theory (DFT) was applied. The procedure consists in building a crystal structure which is cleaved in the direction of the plane (110). Further a supercell was built to add on his surface hydrogen molecules. Later the structure was optimized in order to obtain the optimum geometry in alloys with and without hydrogen. Generalized gradient approximations (GGA) contained in CASTEP module, of the molecular simulation program Materials Studio 6.0, let to obtain the electronic density of states of the three magnesium alloys described earlier; finally, the temperature 0 K, magnesium-aluminum alloy was obtained as the best candidate for hydrogen adsorption.

.

***Keywords:*** Density of states, Magnesium-aluminum alloy, magnesium-nickel alloy, magnesium-zinc alloy.

## 1. Introduction

Mexico consumes 60% from oil resources and has 90% dependence of it. It is alarming if we consider the environmental impact, the gradual increase in the difficulty of extracting them and the visible reduction of reserves conventional oil and gas. This problem arises the need to generate new clean sources of energy. The energy obtained of hydrogen is a promising source of energy, but the problem of store and transportation of hydrogen is an important limiting; metal hydrides can store between 5 and 7% hydrogen weight. It is known that pure Mg stores 7.6 mass% hydrogen, but requires elevated temperatures (300 ºC at 1 atm pressure) for absorption and desorption of hydrogen [1]. It is proposed as a practical alternative hydrogen alloy with aluminum, nickel and zinc, in order to decrease the temperatures of adsorption and desorption [2-4].

In previous studies the $Mg_xM1_{-x}$ alloy (M= Al, Ni or Zn; $_x$ = 0.80, 0.82,…, 1.0) were discussed [5] and it was concluded that magnesium-aluminum-alloy is better than the magnesium-nickel or magnesium-zinc for hydrogen storage, because has a bigger binding energy of hydrogen molecule [6].

## 2. Materials and Methods

In this work, the results of the electronic density of states of the alloys with and without hydrogen on the surface (110) of the supercell $Mg_xM1_{-x}$ will be discussed. We build a crystal structure hexagonal closed packed (hcp) of magnesium alloyed with aluminum, nickel or zinc. Figure 1a) show hcp $Mg_{0.8}Ni_{0.2}$ and Figure 1b) shows the same structure but in a unit cell after geometric optimization.

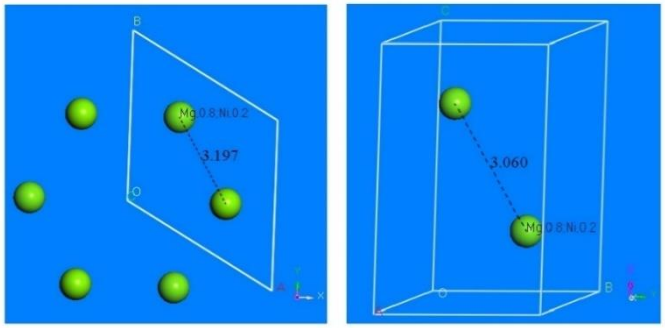


**Fig. 1.** Crystal structure of $Mg_{0.8}Ni_{0.2}$ a) hcp 2-dimensional and b) 3-dimensional unit cell.

Also, it was cleaved the bulk structure in the direction of the plane (110), $H_2$ molecule interacts on this surface and finally we build a supercell of this alloy. All our crystal structures are optimized, we use Castep module of Materials Studio for this purpose.

## 3. Results and Discussion

The hydrogen molecule interacts with the surface of the supercell MgAl, to compare the results before and after that hydrogen is added, we have obtained the partial electronic density of states, it is orbital s (red), orbital p (blue) and orbital d (gray), whose results are shown in figure 2.

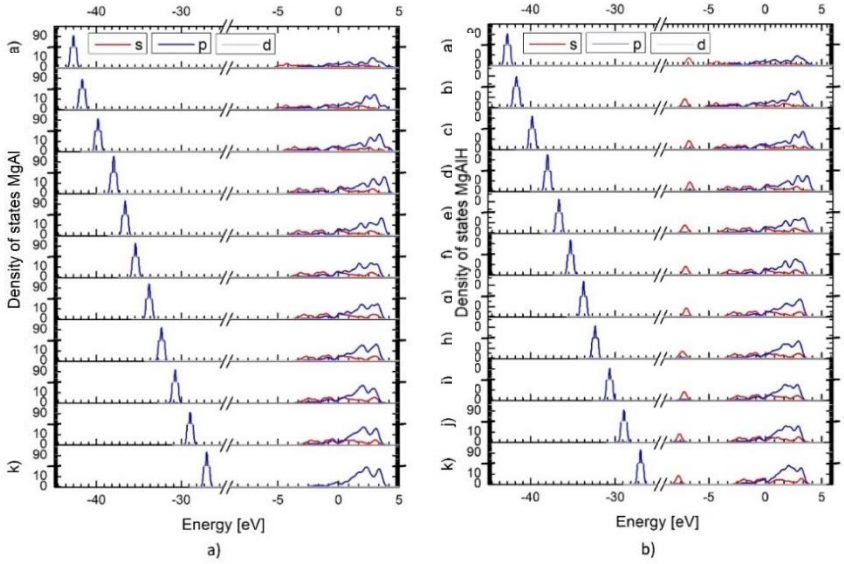


**Fig. 2.** Electronic density of states of $Mg_xAl_{1-x}$ a) without and b) with hydrogen.

In figure 2a) (left) we have the partial density of states, we can see that orbital s practically doesn´t change, but orbital p has peak that is displaced to 0 (Fermi level), it corresponds to a decrease in the gap of about 15 eV for compositions from $Mg_{1.0}Al_{0.0}$ (a) to $Mg_{0.80}Al_{0.20}$ (k). Fig 2b) shows the electronic density of states when hydrogen interacts with the surface. We can observe a peak of the orbital s at -8.0 eV by the hydrogen interaction.

In figure 3 we show the results of MgNi alloy a) without hydrogen and b) with hydrogen, with concentrations of 0.0 Ni (a) until 0.20 Ni (k).

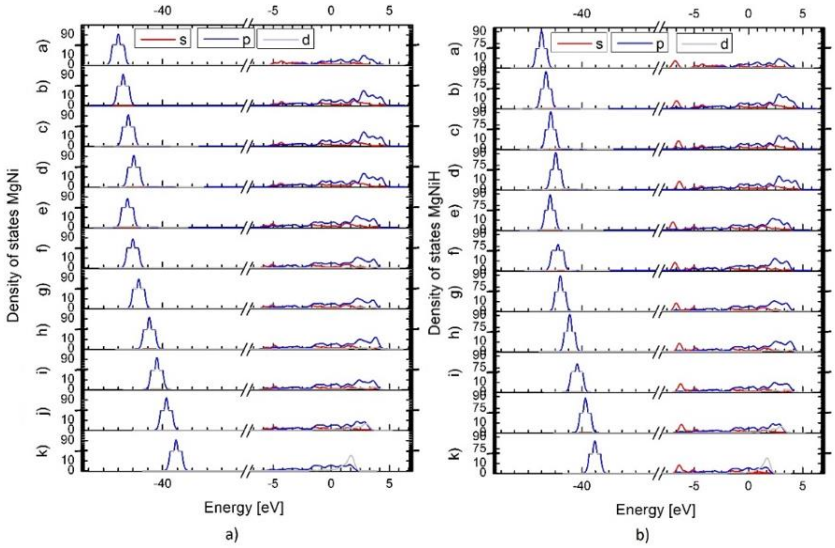


**Fig. 3.** Electronic density of states of $Mg_xNi_{1-x}$ a) without and b) with hydrogen.

The difference in both figures are one peak of the orbital s, at about – 7.0 eV, which appears when hydrogen interacts on the surface. The gap of the orbital p decreases about 5 eV, when concentrations of nickel increase from 0 to 20%.

In Figure 4 we have the density of states of the orbitals s (red), p (blue) and d (gray), a) without and b) with hydrogen, and for concentrations of 0.0-0.20, that corresponds to layers a-k, respectively.

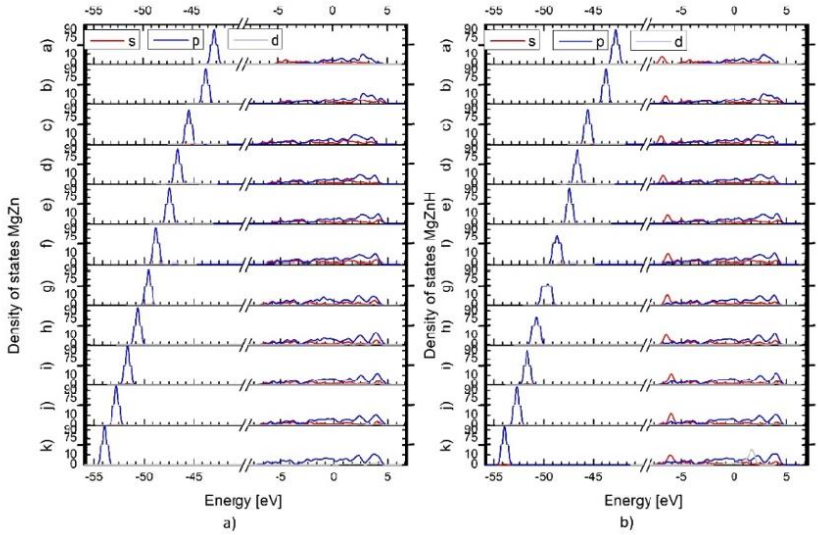


**Fig. 4.** Electronic density of states of $Mg_xZn_{1-x}$ a) without and b) with hydrogen.

In this case the gap of orbital p is increased when the concentrations of zinc are increased by about 12 eV. When hydrogen is added on the surface, a peak of orbital s is appeared by the presence of hydrogen, at about -6.5 eV.

## 4. Conclusion

The density of states of the orbital p, of the magnesium-aluminum alloy has the best behavior because when the concentration of aluminum is increasing, decreases their gap about 15 eV. In the case of magnesium-nickel alloy, the gap of orbital p this decrease is only of 5 eV, when the concentration of nickel is increased. The magnesium-zinc alloy increases their gap of the orbital p by about 12 eV, when the concentration of zinc is increased. Our results let us conclude that magnesium aluminum is the best alloy for hydrogen storage.

## Acknowledgements

F. L. Castillo-Alvarado acknowledges the partial support provided by COFAA-Instituto Politécnico Nacional, EDD- Instituto Politécnico Nacional, MEXICO.

G. Ramírez-Dámaso, acknowledges the partial support provided by SIP-Instituto Politécnico Nacional (SIP-20170593).

## References

[1] Zaluska A., Zaluski L., Strom-Olsen J. O., Nanocrystalline magnesium for hydrogen storage, J. Alloys Comp. (1999) 288: 217–225

[2] Andreasen A., Hydrogenation of Mg-Al alloys. International Journal of Hydrogen Energy 33 (2008) 7489-7497.

[3] Schlapbach L., Seiler A., Stucki F. and Siegmann H. C., Surface effects and the formation of metal hydrides, Journal of the Less-Common Metals, 73 (1980) 145-160.

[4] Milanese C., Girella A., Bruni G., Berbenni V., Cofrancesco P., Marini A., Villa M., Matteazzi P., Hydrogen storage in magnesium–metal mixtures: Reversibility, kinetic aspects and phase analysis, Journal of Alloys and Compounds 465 (2008) 396–405.

[5] Ramírez-Platón I. E., “Almacenamiento de Hidrógeno en Aleaciones Mg1−xMx (M=Al, Ni, Zn) para $0 \leq x \leq 0.2$”, Master Degree Thesis, SEPI-ESIA TICOMAN, Instituto Politécnico Nacional, México (2016), in Spanish.

[6] Ramírez-Dámaso G., Ramírez-Platón I.E., López-Chávez E., Castillo-Alvarado F.L., Cruz-Torres A., Caballero F., Mondragón-Guzmán R., Rojas-Hernández E., A DFT study of hydrogen storage on surface (110) of $Mg1-_xAl_x$ ($0 \leq x \leq 0.1$), Int. J. Hydrogen Energy 41 (2016) 23388-23393.

# 1.9 Development of ZnO based photo-anodes to improve the electrical performance of dye sensitized solar cell as a previous step for hydrogen generation

C. E. Velázquez-González; J. A. Castillo-Robles; J. R. Zapata-Cruz; C. Álvarez-de los Reyes; W. J. Pech-Rodríguez E. Rocha-Rangel

[1]Universidad Politécnica de Victoria, Av. Nuevas Tecnologías 5902, Parque Científico y Tecnológico de Tamaulipas, Ciudad Victoria, Tamaulipas, C.P. 87138, México

*Phone number: (834)1711100 ext; 2315 e-mail: erochar@upv.edu.mx

## ABSTRACT

Due to the constant increase in energy consumption it is necessary to find non-conventional energy sources, considering the impact in the environment and the reduction of natural reserves. Solar cell technologies have attracted great attention because solar light energy is abundant over the surface of the earth. Among them, Dye sensitized Solar Cell (DSSC) is a promising device, owing to the low cost and high theoretical efficiency.

This work presents a study of ZnO based nanostructures as anodes for DSSC. The photo-electrocatalysts were designed and synthesized by using the Reaction bonding of Zinc Oxide (RBZnO).The as-prepared material was characterized using X-ray diffraction (XRD) and differential thermal analysis (DTA) and the results shown that physical properties of ZnO depend on the oxidation temperature. Also, the XRD measurements reveal that the synthesized materials have nanometric grain size. The synthesized ZnO was used to fabricate the anode electrode for DSSC. The DSSC was characterized by photocurrent density and photovoltaic measurements. From the obtained results it can be seen better performance compared with mesoporous $TiO_2$ anode layer, studied by the same group. From the obtained results it is observed that DSSC technology can be use such as an efficient way for hydrogen generation, through the water electrolysis, compared with the traditional water splitting technology. DSSC has the advantage that is cheap, versatile technology, has a useful OCV for hydrogen electrolysis when they are interconnected and have good stability along the time.

***Keywords:*** photo-electrocatalysts; DSSC; RBZnO; hydrogen.

## 1. Introduction

At today the increase in electrical consumption and the environmental pollution makes necessary the research of new removable energy sources. Dye sensitized solar

cell (DSSC) technology are promising devices due to the low cost and high theoretically efficiency. DSSC may be use to contribute in the well know chemical fuel production, storage energy solutions) [1-3]. Hydrogen plays a key role as alternative fuel due to their higher electrical efficiency, when it used as fuel in proton exchange membrane fuel cell (PEMFC) [4]. Nevertheless, hydrogen is not available in free state in nature [5], therefore it is necessary to produce. Water electrolysis is one of the investigated and efficient methods for hydrogen production [6,7] and DSSC technology can by use to generate electrical energy to carry out the water electrolysis in an environmental friendly way.

Nonetheless, DSSC based $TiO_2$ nanoparticles has a serious drawback due to its low photocatalytic activity that results in poor electrical efficiency. ZnO is another electroceramic material that could be used such as photo-anode for DSSC and have similar band gap than $TiO_2$[8]. Furthermore, ZnO has higher electron mobility and also display long life time of electron, under the DSSC operation conditions, increasing the open circuit potential and at the same time its efficiency [9]. The performance and cost-benefit of DSSC with ZnO like photoanode can be improve by using natural dyes [10] as well as by incorporating nanostructures like nanorods or nanotubes [8].

This work focused in the development and study of DSSC by using ZnO nanoparticles synthesized by reaction bonding. Moreover, the effect of deposition and the thickness of the anode were studied.

## 2. Materials and Methods

The samples synthesized in this study were performed by mixture of Metallic powders of Zn and non-activated ZnO (such as seed for ZnO nanoparticles) with and weight ratio of 45/55 wt/wt., respectively. The mixture was transfer in a stainless steel reactor that contain zirconia ball mill with a powder-ball weight ratio of 10:1. The mechanical activation was carried out in a planetary mill with speed of rotation of 300 rpm for 3 and 6 h. To avoid particle agglomeration ethylic alcohol was added. After that, the sample was thermal treated to 1200 °C with the aim to oxidize all the metallic Zn.

The anode for DSSC was conductive glass substrate (fluorine doped Tin oxide with an electrical resistance of 15 $\Omega/cm^2$ and high optical transparency, 82-84 %) coated with ZnO nanoparticles. The coated ZnO was achieved in two steps, one with a thick layer of small particle size (absorbent layer) and another with big particle size (scattering layer). The deposition of ZnO photocatalyst was achieved by using screen printing process, active are of 0.64 $cm^2$. In the first stage a coating solution of 0.5 g of ZnO (small particles) with Terpineol was transfer onto cleaned glass substrate and then was dried at 120 °C for 10 min. Afterwards, a second layer consisted of large particles of ZnO was transferred to the glass substrate. The deposited layer of ZnO was soaked in a RK1 dye solution for 2 h at room temperature. The cathode of DSSC was performed by applying platisol and summited to heat treatment at 400 °C during 5 min. TDE-250 was used as electrolyte.

ZnO samples was characterized by X-Ray measurements performed on a Phillips-X´Pert diffractometer using Cuk$\alpha$ radiation ($\lambda$= 0.15406 nm) source, working voltage of 40 kV and scan rate from 10 to 100° (2$\theta$).

FTIR analysis was performed, with the aim to identify the chemical bonds in the ZnO samples, using a WQF-510A FTIR Rayleígh instrument. The FTIR spectra were taken in transmission mode at 4 cm-1 resolution in the scan range of 4000-400 cm-1 using KBr pellets.

The photocurrent curve was measurement using Gill AC potentiostat under AM1.5G illumination using 11002 Sunlite model from Abet Technologies. The efficiency of the developed DSSC was obtained from the calculate short circuit current density, the open circuit potential and the fill factor.

## 3. Results and Discussion

Fig. 1. shows the X-Ray diffraction pattern for the synthesized ZnO. The reflections peaks near to 31.8°, 34.4°, 36.3°, 47.6°, 56.6°, 62.9°, 66.4°, 68°, 69.1°, 72.6° are attributed to the wurtzite crystalline structure of ZnO (100), (002), (101), (102), (110), (103), (200),(112), (201) and (004) crystalline plane, respectively, according to JCPDS 5-0664. Also, it is observed a weak reflections peaks at 38.9°, 43.22° and 54.4° that are due to the Zn (100), (101) and ((102) crystalline planes JCPDS -65-3358.

The particle size for the sample was calculated by using the Debye-Scherrer equation [11]:

$$D = \frac{0.9\lambda_{k\alpha}}{B_{2\theta}cos\theta} \quad (1)$$

Where *D* is the particle size, 0.9 is the shape factors for spherical particles, $\lambda$ the radiation wavelength (1.5406Å), $B_{2\theta}$ the Full Width at Half Maximum, and $\theta$ the angle at maximum intensity of the ZnO (101) and Zn (101). The value for the particle size for ZnO was 33.87 nm while the Zn has a particle size of 39.9 nm.

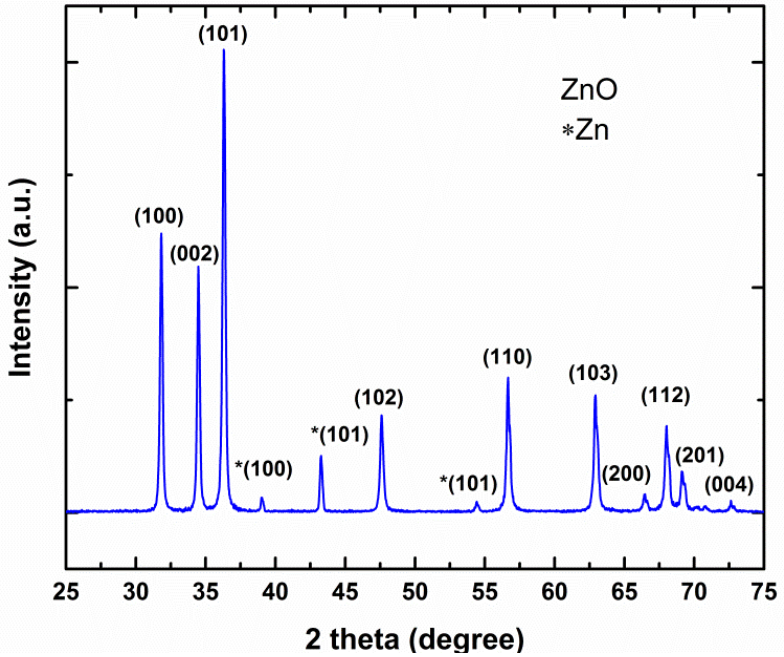


**Fig. 1.** X-Ray diffraction of the synthesized ZnO by the method RBZnO.

Fig. 2. Shows the spectrum for ZnO nanoparticles. At 425 $cm^{-1}$ its observed a sharp peak of the stretching vibration band of Zn-O bonds [12], the high intense peak suggest a high crystallinity of ZnO material. The stretching and bending vibrations of O-H species has been observed close to 3346 and 1630 $cm^{-1}$, respectively [13]. Also, it is observed a double band located at 2921 and 2865 $cm^{-1}$ characteristic of C-H bonds, which may be due to the raw materials.

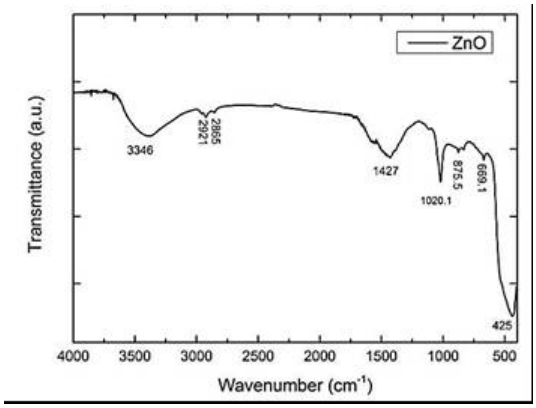


**Fig. 2.** FTIR spectra for the synthesized ZnO nanoparticles.

The photocurrent curve for the fabricated DSSSC using ZnO as photo-anode is presented in fig. 3. As can be observed the open circuit potential is about 149 mV and the short-

circuit current was 15 μA $cm^{-2}$. Meanwhile, the maximum electrical power density is close to 0.6 μA$cm^{-2}$.

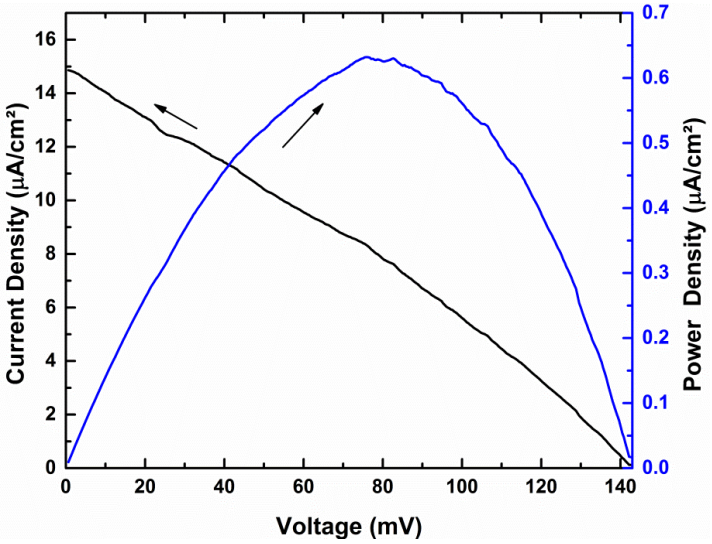


**Fig. 3.** DSSC performance curve of ZnO composite anode.

## 4. Conclusion

X-ray diffraction patterns show the formation of a large amount of ZnO. However, in them are observed some peaks corresponding to zinc, this indicates that the whole zinc is not oxidized by the oxidation conditions worked. Through the study of x-ray diffraction, it was possible to determine that the particle size with which it is being worked is nanometric. The spectrum obtained by infrared analysis shows the formation of the functional groups corresponding to the Zn-O bond. The VI curve reveals that electrical voltages are lower than the required for the $H_2O$ electrolysis. Therefore, series/parallel electrical configurations may be used to carry out the $H_2$ production.

## Acknowledgements

The authors thanks to CONACYT for scholarship provided to the students C.E.V.G, J.R.Z.C and C.A.D.R. We also acknowledgement XVII International Congress of the Mexican Hydrogen Society for the opportunity to accept the exposure of contributions.

## References

[1] Andrade L, Cruz R, Ribeiro HA, Mendes A. Impedance characterization of dye-sensitized solar cells in a tandem arrangement for hydrogen production by water splitting. Int J Hydrogen Energy. 2010;35:8876-83.
[2] Williams JH, DeBenedictis A, Ghanadan R, Mahone A, Moore J, Morrow WR, et al. The Technology Path to Deep Greenhouse Gas Emissions Cuts by 2050: The Pivotal Role of Electricity. Science. 2012;335:53-9.
[3] Torabi N, Behjat A, Jafari F. Dye-sensitized solar cells based on porous conjugated polymer counter electrodes. Thin Solid Films. 2014;573:112-6.
[4] Rousseau S, Coutanceau C, Lamy C, Léger JM. Direct ethanol fuel cell (DEFC): Electrical performances and reaction products distribution under operating conditions with different platinum-based anodes. J Power Sources. 2006;158:18-24.
[5] Blomen LJMJ, Mugerwa MN. Fuel Cell Systems: Springer US; 2013.
[6] Jensen SH, Graves C, Mogensen M, Wendel C, Braun R, Hughes G, et al. Large-scale electricity storage utilizing reversible solid oxide cells combined with underground storage of CO2 and CH4. Energy Environ Sci. 2015;8:2471-9.
[7] Carmo M, Fritz DL, Mergel J, Stolten D. A comprehensive review on PEM water electrolysis. Int J Hydrogen Energy. 2013;38:4901-34.
[8] Quintana M, Edvinsson T, Hagfeldt A, Boschloo G. Comparison of Dye-Sensitized ZnO and TiO2 Solar Cells: Studies of Charge Transport and Carrier Lifetime. The Journal of Physical Chemistry C. 2007;111:1035-41.
[9] Bandara J, Weerasinghe HC. Enhancement of photovoltage of dye-sensitized solid-state solar cells by introducing high-band-gap oxide layers. Sol Energy Mater Sol Cells. 2005;88:341-50.
[10] Guillén E, Casanueva F, Anta JA, Vega-Poot A, Oskam G, Alcántara R, et al. Photovoltaic performance of nanostructured zinc oxide sensitised with xanthene dyes. Journal of Photochemistry and Photobiology A: Chemistry. 2008;200:364-70.
[11] Hsu HY, Tongol BJ. Electrochemical and surface characteristics of carbon-supported PtSn electrocatalysts for ethanol electro-oxidation: possible application for inkjet ink formulations. Adv Nat Sci: Nanosci Nanotechnol. 2013;4:015012.
[12] Salavati-Niasari M, Mir N, Davar F. ZnO nanotriangles: Synthesis, characterization and optical properties. J Alloys Compd. 2009;476:908-12.
[13] Rahim S, Sasani Ghamsari M, Radiman S. Surface modification of titanium oxide nanocrystals with PEG. Scientia Iranica. 2012;19:948-53.

# 1.11 Photocatalytic activity of $TiO_2$-CoO as mixed oxide for improved $H_2$ production by water splitting method

A.Pérez-Larios, E. Pulido, C. Belver

[1]Universidad de Guadalajara, Centro Universitario de los Altos, Depto. Ingenierías, Carretera a Yahualica km. 7.5, Tepatitlán de Morelos, Jalisco, México. 47600.

[2] Universidad Autónoma de Madrid, Sección de Ingeniería Química, Facultad de Ciencias, Campus Cantoblanco, E-28049 Madrid, Spain.

alarios@cualtos.udg.mx

## ABSTRACT

The need to develop new alternatives for sustainable energy has drawn the attention to emergent clean renewable technologies, since they proceed from natural and lasting source like solar light, wind and geothermal energy. The alternative method of photocatalytic water splitting is promising since it involves the absorption of light to produce hydrogen by irradiating oxide semiconductors. Photocatalytic systems for water splitting may contain sacrificial reagents, as methanol, commonly used in the photocatalytic evolution of $H_2$ from water, since its hydroxyl group captures photogenerated holes and minimizes the probability of $e^-/h^+$. The textural properties of the prepared materials show that the metal content as mixed oxide has a significant effect on the textural properties of $TiO_2$ increasing in high proportion of BET specific surface areas from 64 to 156 $m^2/g$ for all the samples. The powder XRD patterns show the formation of anatase as the unique titania phase formed. The anatase (101) peak intensity at $2\Theta$=25.4° and hence the crystallite size diminishes when the amount of Co increases. The diffractograms show peaks denoting the presence of Co or CoO. This result suggest that Co was incorporated to the titania network or that it is present as nano CoO conglomerates highly dispersed on the titania surface.

The energy band gap for the different samples was calculated from the DRS spectra obtained in the UV-Vis region by extrapolating to the X axis the absorbance to Y axis equal zero. The results showed a small shift to the red region (2.06 – 2.30 eV) for the mixed oxide samples while for the $TiO_2$ reference the Eg is 3.2 eV. The results show that the formation of hydrogen with $TiO_2$-CoOis more of ten times (~2400□mol/h) higher than that obtained with the $TiO_2$ bare sample (190 □mol/h).

A discussion about the role of Co in the photocatalytic decomposition of methanol:water will be made in the extended version. For instance the results showed that nanomaterials CoO semiconductors are potential photocatalysts to be used for environment clean energy production

***Keywords:*** Mixed oxide, hydrogen production, photocatalysis, UV-vis light

# 1.12 Improved Mixed oxide as photocatalyst: $TiO_2$-$Fe_xO_y$ for $H_2$ production by water splitting method

A. Pérez-Larios, E. Pulido[1], J. Bedia, C. Belver

[1]Universidad de Guadalajara, Centro Universitario de los Altos, Depto. Ingenierías, Carretera a Yahualica km. 7.5, Tepatitlán de Morelos, Jalisco, México. 47600.

[2] Universidad Autónoma de Madrid, Sección de Ingeniería Química, Facultad de Ciencias, Campus Cantoblanco, E-28049 Madrid, Spain.

alarios@cualtos.udg.mx

## ABSTRACT

The most studied processes at the present for the hydrogen production are electrochemical, steam reforming of alcohols or hydrocarbons and water splitting. Thus, the water splitting using semiconductors materials had recently acquired great relevance because of the low cost for the hydrogen production. The principle of this technique is based on the photoexcitation of the semiconductor using a UV or visible light sources. The electrons-hole pairs formed are capable to split water molecules into gaseous oxygen and hydrogen. The nanomaterials of $TiO_2$ and $TiO_2$-$Fe_xO_y$ (metal load: 1.0, 3.0, 5.0, 10.0 wt. % Fe) samples were prepared by the sol-gel method. The textural properties of the prepared materials has a significant effect on the textural properties of $TiO_2$ increasing in high proportion of BET specific surface areas from 64 to 136 $m^2/g$ for all the samples.

The powder XRD patterns show the formation of anatase as the unique titania phase formed. The anatase (101) peak intensity at $2\Theta=25.4°$ and hence the crystallite size diminishes when the amount of Fe increases. The diffractograms do not show peaks denoting the presence of Fe or $Fe_xO_y$. This result suggest that Fe was incorporated to the titania network or that it is present as nano $Fe_xO_y$ conglomerates highly dispersed on the titania surface.

The energy band gap for the different samples was calculated from the DRS spectra obtained in the UV-Vis region by extrapolating to the X axis the absorbance to Y axis equal zero. The results showed a small shift to the red region (2.09 – 2.60 eV) for the mixed oxide samples while for the $TiO_2$ reference the Eg is 3.2 eV and corresponds to the reported value for the anatase phase. Thus the mixed oxide with Fe and $TiO_2$ only exerts small variations in the Eg energy band gap.

The hydrogen production from the water splitting method for the various photocatalysts is reported. The results show that the formation of hydrogen with $TiO_2$- $Fe_xO_y$is more of ten times (~5586□mol/h) higher than that obtained with the $TiO_2$ bare sample (190 □mol/h).

A discussion about the role of Fe in the photocatalytic decomposition of methanol:water will be made in the extended version. For instance the results showed that nanomaterials

CoO semiconductors are potential photocatalysts to be used for environment clean energy production

***Keywords:*** Mixed oxide, hydrogen production, photocatalysis, UV-vis light

# 1.14 Evaluation of an electrochemical hydrogen compressor-purificator system coupled to an oxy-hydrogen reactor.

Valeria Juárez Casildo, Rosa de Guadalupe González Huerta

[1]ESIQIE-IPN, Lab. Electroquímica y Corrosión, UPALM, CP 07738, Ciudad de México.

* rosgonzalez_h@yahoo.com.mx

55 57296000 ext 54246

## ABSTRACT

It is known that the energetic consumption has been increasing drastically due to uncontrolled grow population and excessive use of technology based in irrational use of traditional energy sources which have been harmful to environment. Since humanity be aware of this problem, the scientists have accepted hydrogen as an energetic vector and they have developed the “Hydrogen technologies” which focus on finding ways to produce, store and use it in a clean and environmentally friendly way.

This paper reports the design of an electrochemical hydrogen compressor- purificator which has been coupled to alkaline electrolyser (AE), the goal is purificate the hydrogen gas by PEM electrolyser (PEME), then clean hydrogen will be used in fuel cells or storage under pressure, both process carry out in PEME: compression and purification. The electrochemical concentration of hydrogen from a hydrogen/oxygen/steam water gas mixture has been investigated by means of an electrochemical PEM electrolyzer, hydrogen being transported as hydrated protons, thorough a Nafion membrane, from the inlet (anode) to the outlet (cathode) compartments of the cell.

From the analysis of an experimental data it is possible to evaluate the current efficiency, the hydrogen recovery, the hydrogen purity, and the performance of the cell. Galvanostatic and tensiostatic mode of operation have been investigated: in second case an erratic behavior of the cell has been observed, mainly because of the uncontrolled water content in the membrane. Under galvanostatic condition the role of the applied current, feed flow rate, water steam amount in the gas mixture feed and the quantity of water in the cathode side has been studied.

In the experimental set up, two compression/purification cell has been evaluated feeding 5 cm3/min of gas mixture from alkaline reactor, it was found that is necessary 1 V at 400 mA for produce 4.1 cm3/min of pure hydrogen. Cell number two is more efficient than cell number one in wide range of current. And was possible to compress pure hydrogen at 26 psi with 0.048 W in 60 minutes.

***Keywords:*** Hydrogen recovery; hydrogen compression; alkaline reactor; purification process.

## 1. Introduction

The use of hydrogen as a secondary energy has two kind of application: stationary and mobile. Based on this, they have developed the “Hydrogen technologies”. The aim of the research is to find different ways of producing, storing and using hydrogen friendly way with the environment.

For some decades they have developed technologies that allow to treat gas mixtures whose main component is hydrogen in order to purify it; such is the case Electrochemical Hydrogen Compressor (EHC). First accurate publications on the working principle of EHC were published by Sedlak in 1981, electrochemically pumping hydrogen from a low to a high pressure and separation of hydrogen from an inert gas to provide high-purity hydrogen. In 1998, Bessarabov explained the possibilities of hydrogen pumping in a paper on electrochemically aided membrane separation, and in the same year Rohland (et.al) reported on application of the principle in a hydrogen compressor. The potential ability of EHC to purify and compress hydrogen was recognized, using the general structure of a fuel cell. [2]

The Electrochemical Hydrogen Compressor Purificator is getting interest due to the hydrogen works as an energy carrier and results very convenient for renewable energy storage. It could be said that the unfavorable properties of the use of this gas can be compensated by the characteristics and flexibility of applying electrochemical compression.

Hydrogen generated in a PEM electrolyser (PEME) is of high purity (99.9999%) only moisture removal is required using a simple process. The gases generated in an oxyhydrogen reactor is a mixture of hydrogen and oxygen, the simultaneous compression of these gases presents some disadvantages. First, the mixing of both gases leads to a highly reactive atmosphere; secondly the compressors are made of titanium plates which turns out to be an expensive metal and its structure is voluminous to achieve high pressures. Therefore, a combination of an electrocatalyst with a subsequent EHC could be safer and more economically attractive with getting pure hydrogen and moderate pressures that optimize storage systems.

In addition to this, something that makes this equipment more interesting is that the implicit purification of a mixture of gases is carried out while being compressed due to the protonic membrane selectivity; these equipment have now been designed in order to purify the hydrogen produced by catalytic reforming because the reactor effluent is a mixture of $H_2$ and $CO_2$ mainly.

The objective of this work is to evaluate the performance of EHCP (Electrochemical Hydrogen Compressor Purifier) coupled to an alkaline reactor.

## 1.1 Principle of work.

The compressor-electrochemical hydrogen purifier is a cell in which membrane electrode assembly is very similar to a PEM electrolyzer.

Molecular hydrogen is fed at the anode where an oxidation is carried out, in which the protons of the electrons are separated, the aim is for the protons to be transported through the proton exchange membrane for further reduction on the cathode side, while the electrons are transferred through the outer circuit to the catalyst layer located on the other side of the membrane, all this is achieved by applying a potential difference to the cell. Indeed, this induces mass transport, generating high purity hydrogen as shown in figure 1. [2]

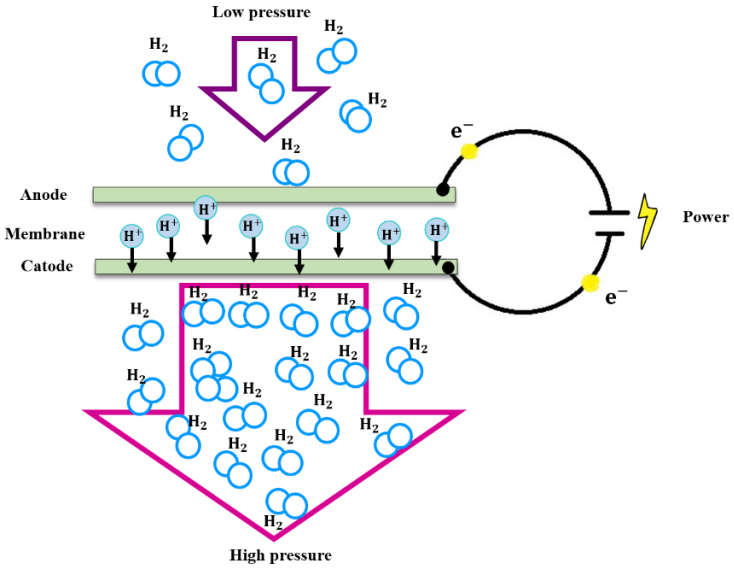


**Fig.1** Principle of work of an Electrochemical Hydrogen Compressor Purifier.

Electrochemical reactions taking place at the electrodes are given by the following equations [3]:

Ánodo $$H_2(LP) \rightarrow 2H^+ + 2e^- E^\circ = 0\,V \quad (1)$$

| | | |
|---|---|---|
| Cátodo | $2H^+ + 2e^- \rightarrow H_2(HP) E^\circ = 0\ V$ | (2) |
| Reacción global | $H_2(LP) \rightarrow H_2(HP) E^\circ = 0\ V$ | (3) |

1.2 Energy requirement for the process.

Hydrogen transport energy is calculated per unit mass (kWh / kg) and can be expressed in relation to its energy content, which is given by the lower heat value (LHV) 33.35 (kWh / kg) of hydrogen because it is necessary to understand that in its use to produce electrical or thermal energy the product to be obtained is always water. For calculation purposes, the lower heat value (if in the combustion is produced steam water) and higher (HHV) (if in the combustion liquid water is produced). [1]

The total cell potential ($V_C$) of the PEM electrochemical compressor includes Nernst or equilibrium voltage, polarization voltage and voltage drops due to ohmic resistance. The equilibrium potential ($V_N$) depends on the pressure difference between the anode and the cathode; the polarization voltage summarizes the potential of anode and cathode, therefore the total voltage of the cell is given by the following equation.

$$V_C = V_N + n_a + n_c + IR' \quad (4)$$

Where

$V_c$ Is the cell potential.

$V_N$ Is the Nernst potential.

$n_a$ Is the anode overvoltage or anodic polarization voltage.

$n_c$ Is the cathode overvoltage or cathodic polarization voltage.

IR' Is the Ohmic resistance.

## 2. Materials and Methods

2.1 Experimental set-up.

The experimental set-up is shown in fig. 2. The effluent from an alkaline reactor consist in a mixture of hydrogen, oxygen, steam water and traces of electrolyte (NaOH 5%), it is fed to two stages of washing gases and later, by means of a needle valve are supplied 5 cm3/m to the anode of a first electrochemical cell (purifier) where at the output of the cathode this is obtained PEM grade hydrogen, which will be fed to a second electrochemical cell (compressor) in order to

compress it. With the aim of analyzing this process, both cells need power that comes from a 3A direct current (DC) source; the input and output streams of the both cells were measurement by a flowmeter of 1 L capacity and the pressure conditions has been monitored by a manometer of 2 bar at the outlet of the compressor.

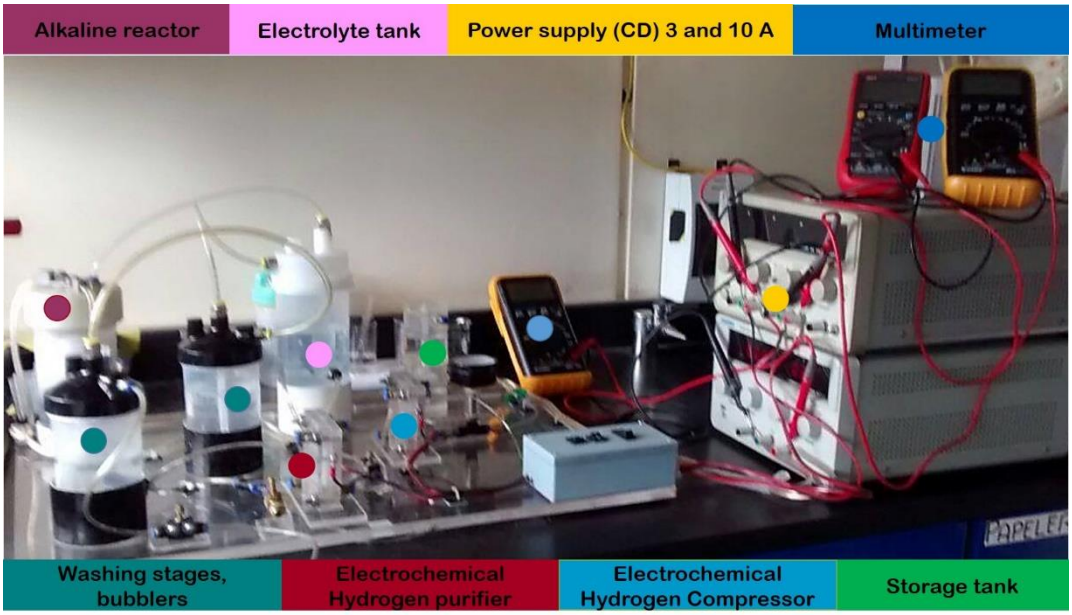


**Fig.2.** Experimental set-up. Electrochemistry and corrosion laboratory ESIQIE-IPN.

2.2 Electrochemical cell

Both cells, purification and compression, are composed of 2 square acrylic plates of 8 x 8 cm and 1 cm thick, two current collector plates (stainless steel) with flow channels, two carbon mesh electrodes, a membrane of Proton exchange and two suitable silicone gaskets. The elements of the electrochemical cell are shown in Fig. 3.

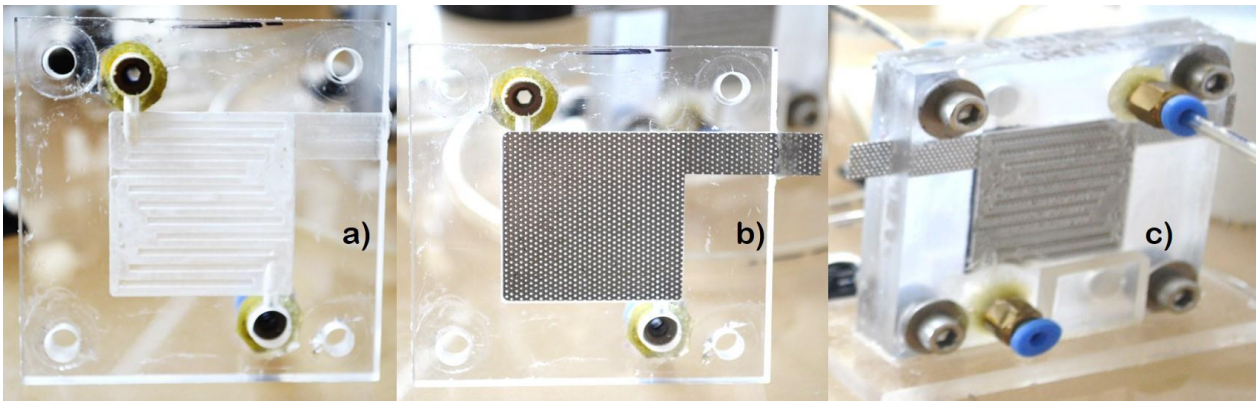

**Fig.3.** a)Acrylic Cell Plates with Flow Fields. b) Current Collectors (Stainless Steel). c) Assembled Electrochemical Cell

## 2.3 Membrane electrode assembly.

The membrane electrode assembly was made with a proton conducting membrane commercial Nafion® 115 (16 $cm^2$), activated before used. The carbon mesh electrode has Pt 10% as catalyst. The membrane and the electrodes form the MEA. It was assembled by hot pressing method. The MEA is shown in Fig. 4.

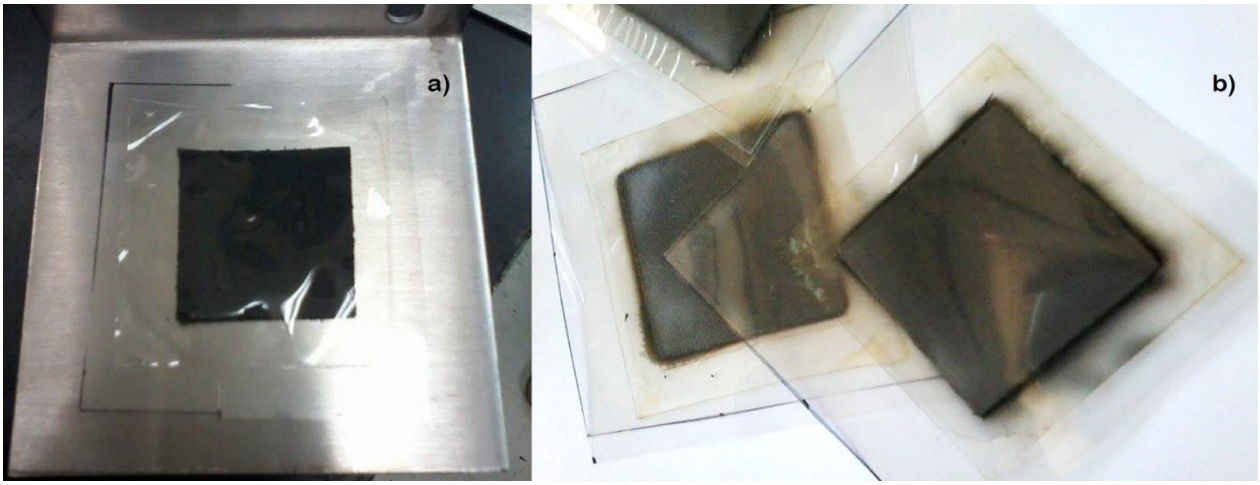


**Fig.4.** a)Elements of the MEA (proton exchange membrane and 10% Pt carbon mesh). b) Membrane Electrode Assembly (MEA)

## 2.4 Test runs

The test runs were made in order to study the next points.

### 2.4.1 Cell operation mode.

There are two modes for operate an electrochemical cell; under tensiostatic and galvanostatic control. In first case one measures the current density for a given value of applied voltage In the second case one measures the cell voltage (driving force) for an assigned current density (rate of the process), which is related to the rate of hydrogen production in the cathodic compartment. In other words, with galvanostatic conditions, the rate of the process is assigned and the driving force is measured; under tensiostatic conditions the driving force is assigned and the rate of hydrogen production is measured.

### 2.4.2 Importance of water in the process.

High ionic conductivity of the proton conducting membrane can be preserved only if the membrane is in hydrated form. In a compression/purification cell water must be added to

the cathodic compartment to preserve the optimal hydration degree of the membrane and to provide a suitable reserve for water saturated hydrogen outflow. [4]

2.4.3 Energy management.

Due to the energy-environmental approach with which this electrochemical cell is investigated, it is essential to analyze how much energy the process is consuming and how much energy it is possible to generate from the purified and compressed hydrogen. And on the other hand analysis of capacity where the utility of pumped hydrogen is established.

## 3. Results and Discussion

3.1 Tensiostatic and galvanostatic measurements.

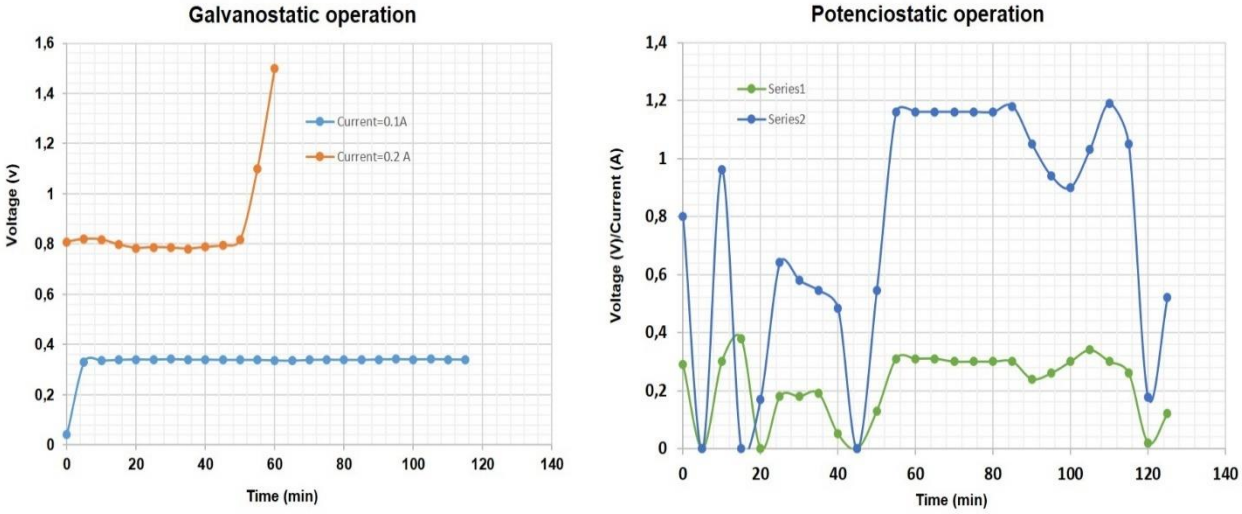


**Fig.5.** Behavior of tensiostatic and galvanostatic cell operation.

The cell was operated under tensiostatic conditions controlling the voltage and it is observed that the behavior of both voltage and current are unstable as a function of time. The potential goes from 0 to 1.2 V and never stays stable; While the current goes from 0 to 0.4 A. During the experiment, it was not possible to regulate the potential, always remained erratic and therefore the current as well. On the other hand, the galvanostatic operation was also performed at two different currents (0.1 and 0.2 A), in both cases the potential remains very stable as a function of time, however it is possible to observe that at low currents the stability is much greater; Based on the graph it is observed that at 0.1 A the cell the potential is constant while at 0.2 A, after almost 1 hour of operation the stability is broken, the potential increases dramatically (Fig. 5).

3.2 Cells characterization.

Two electrochemical cells were evaluated, one as a purifier and the other as a compressor. The graph on the right (Figure 6) shows that the potential of the purification cell is large compared to the compressor that only pumps pure hydrogen. For example, when setting a current density of 0.1 the compressor only requires 600 mV, whereas the purification cell needs 1.3 V to carry out hydrogen transport. It is very important to mention that both cells were characterized as water electrolyzers and it was determined that in the cell destined for purification the electrolysis was carried out in 2 V while in the cell compression is made to 2.4 V.

The clue to the purification of the alkaline reactor effluent has worked correctly is that the compressor was evaluated with pure hydrogen to obtain data of voltage and current that were registered in the left graph (Figure 6). Once the hydrogen was purified, it was fed to the compression cell to be pumped, the data (voltage, current) were also recorded. Curiously when comparing both values, it is observed that they are highly similar so it is possible to say that purification has worked correctly. When the compression cell operates at 0.14A and pure hydrogen, the potential was 0.76 V, while when feeding purified hydrogen the voltage was 0.79 V.

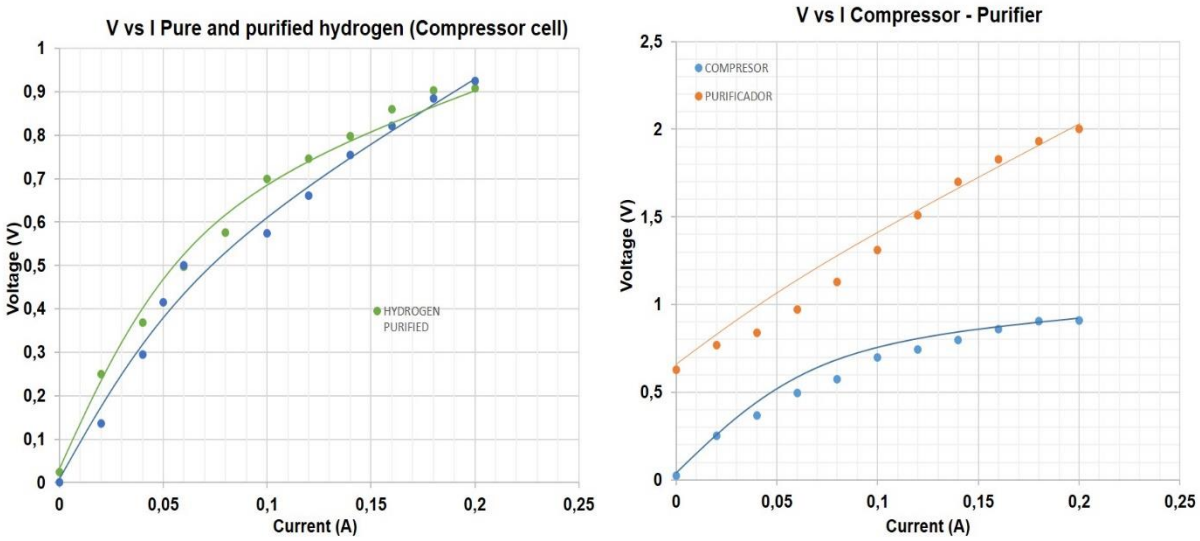


**Fig.6.** Behavior of tensiostatic and galvanostatic cell operation

3.2.1 Energy requirement for the process.

If both electrochemical cells operate in their more stable 0.1 A conditions, a flow at the output of the cathode of 0.7 ml / min will be obtained and for this the purifier needs 0.13 W, while for pumping the same amount the compressor needs 0.048 W by keeping this current for about 1 hours, 26 psi was achieved at the cathode.

3.2.2 Cell Efficiency

Due to the difference in chemical potential between the cathode and anode compartments there is a mass transfer diffusion of molecular hydrogen across the membrane in the direction opposite to the proton transfer. The cell efficiency is defined in equation 5 as a relation between the hydrogen produced ($H_P$) and the theoretical hydrogen ($H_T$) (as a direct relation with Faraday´s law). It is important that the hydrogen produced be the nearer It is important that the amount of hydrogen produced is very similar to the theoretical amount because that will give us an idea of the back diffusion is small.

$$\eta_{cell} = \frac{H_p}{H_T} \quad (5)$$

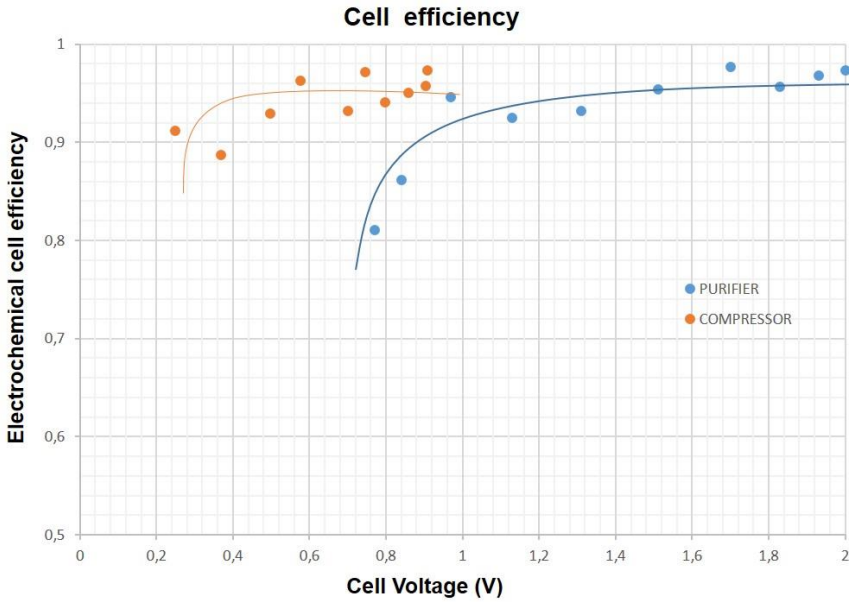


**Fig.6.** Electrochemical cell efficiency.

The efficiency of both cells was calculated, in general the values are above 80%, however the efficiencies of the purifier are more dispersed and function of the voltage than those of the compressor, which always tend to be very similar; Is the effect of the impurities, the amount of hydrogen pumpedº to lower current and therefore to lower potential because the bomb capacity decreases at low current values.

**4. Conclusion**

Galvanostatic operating condition must be preferred to tensiostatic one, since the former allows a self-control of the process kinetics because the kinetic is fix. On the contrary, a free kinetic of the process, as it occurs under tensiostatic condition, generates an erratic behavior results because the system not regulates itself due to the membrane humidity.

For the purposes of this experiment, by feeding to the purification cell a mixture of hydrogen and oxygen with platinum as catalyst, oxygen is adsorbed on the active sites leaving little space for the hydrogen oxidation reaction. This is why a high overpotential is observed.

It is very important to be careful with the overpotential of the purifier, because due to the presence of water above 1.7 V the competition reactions between hydrogen oxidation and water electrolysis begin.

In addition to having the equipment's operating data, it is very important to analyze the utility of the compressed and purified hydrogen and to see if the energy used to carry out the whole process is similar to that which can be supplied by hydrogen for use under electric conditions .

## Acknowledgements

Thanks to the financial support granted: IPN multidisciplinary project SIP-1820 (2017-2018) and CONACYT CEMIE project Ocean 249795: Line Transversal I-LT1 Technologies and strategies of electrical interconnection of ocean energies for the Mexican territorial sea.

## References

1. Aguer M. (2005). *Hydrogen, the foundation of a balanced future*. Spain.Diaz Santos.

2. Bessarabov G., Wang H., Li H., y N. Zhao, (2016), *PEM electrolysis for hidrogen production principles and aplications*, New York, USA: Taylor and Francis group.

3. Camack R., Michael Frey., Robert R., (2001), *Hydrogen as a Fuel,* New York, USA:Taylor and Francis Group.

4. Casati C., Longhi P., Znderighi L. and F. Bianchi, (2008), Some fundamentals aspects in electrochemical hydrogen purification/compression, *Journal of power sources*, 103-113.

# 1.15 Hydrogen storage of Ta(Mg)H prepared by mechanical milling

Juan Bonifacio-Martínez, Jorge A. Ramirez-Gómez, Alberto R. Sandoval-Jiménez, Fernando Ureña-Nuñez

[1]Departamento de Química, Gerencia de Ciencias Básicas, Instituto Nacional de Investigaciones Nucleares, Carretera México-Toluca s/n, La Marquesa, Ocoyoacac, Edo. de México, C.P. 52750, México.
[2]Instituto Tecnológico de Toluca, Av. Tecnológico s/n, Ex-Rancho la Virgen, Metepec, Edo. de México, C.P. 52140, México.
[3]Departamento de Tecnología de Materiales, Gerencia de Ciencias Aplicadas, Instituto Nacional de Investigaciones Nucleares, Carretera México-Toluca s/n, La Marquesa, Ocoyoacac, Edo. de México, C.P. 52750, México.
[4]Departamento de Física, Gerencia de Ciencias Básicas, Instituto Nacional de Investigaciones Nucleares, Carretera México-Toluca s/n, La Marquesa, Ocoyoacac, Edo. de México, C.P. 52750, México.
* Corresponding author: +55 53297200 and e-mail: juan.bonifacio@inin.gob.mx

## ABSTRACT

The Tantalum-magnesium hydride with an orthorhombic structure were prepared “in situ” from the mixture de tantalum and magnesium powders by mechanical milling. The synthesis of the solid solution Ta(Mg)H was obtained in a Spex-type vibratory mill at times of 12, 18 and 24h under controlled atmosphere of ultra-high purity argon. To determine the optimum hydrogen sorption conditions experiments were carried out in a Parr reactor by varying temperature pressure ant time parameters. The obtained solid solution of Ta(Mg)H was characterized by means of X-ray diffraction (XRD), scanning electron microscopy (SEM) coupled to an energy dispersive X-ray spectrometer (EDX), $N_2$ physisorption analysis, thermogravimetric analysis (TGA) and simultaneous differential scanning calorimetry (DSC) coupled with mass spectrometry (MS), the crystal structures, surface morphologies, textural properties, hydrogen storage and dehydrogenation processes. The results of XRD revealed that the solid solution of Ta(Mg)H consist of $Ta_2H$ and $TaH_{0.5}$ phases with nanocrystalline structures. The $N_2$ physisorption analysis showed that the Ta(Mg)H has a high specific surface area, high pore volume and pore area, after the solid solution was desorbed at 250 °C for 1h. After hydrogenation process the samples were also analyzed by the aforementioned techniques. SEM analysis showed that the solid solution has a rough and porous texture. The best hydrogen absorption in the solid solution was obtained when the sample was hydrogenated at 0.2 MPa and 25 °C, with a hydrogen total loss weight of 10.7%. TGA/DSC analysis based on the results of MS showed only a relationship, m/e=2, that corresponds to the $H_2$ gas, indicative of the dehydrogenation processes. The low value of the activation energy ($E_a$=76.8 KJ/mol) obtained by the dehydrogenation processes shows that the solid solution of Ta(Mg)H is a good hydrogen storage material.

***Keywords:*** Hydrogen storage; solid solution; Ta(Mg)H: mechanical milling.

# 1.16 Design and analysis of a monopolar Oxy-hydrogen reactor

Horacio Tapia Baca, Jorge Olmedo González, David Flores Hernández, Juan Manuel Sandoval Pineda, Rosa de Guadalupe González Huerta

[1]Instituto Politécnico NacionalESIQIE, Laboratorio de Electroquímica y Corrosión, UPALM, CP. 07738, CDMX

[2]Instituto Politécnico Nacional-ESIME Azc, SEPI, Av. de las Granjas 682, Azcapotzalco, CP. 02250. CDMX

*Mail: rosgonzalez_h@yahoo.com.mx

## ABSTRACT

At present population is growing up therefore energy consumption is increasing, so it is a determining factor for hydrocarbons depletion together with the environment deterioration that it has produced by the excessive use of these natural and finite resources. One option to solve this problem is hydrogen as fuel that can be used as a bridge between renewable energies and hydrocarbons. Hydrogen is an energy vector, it can be used as a complement to fossil fuels and it is an attractive alternative to reduce greenhouse gases emissions.

It exist too many ways to produce hydrogen such as PEM electrolysis or alkaline electrolysis that produce hydrogen form water electrolysis. These two technologies are really important because they can use electrical energy from renewable energies so $CO_2$ emissions could decrease considerably. The last one has been resulted more economically feasible than the first. Hydrogen production from alkaline electrolysis has a mature technological development and it is used in several industries for hydrogen production at low and medium scale.

In this work is designed and analysed twelve oxyhydrogen reactors that produce hydrogen form water electrolysis using an alkaline technology. The reactor cell configuration is monopolar with wet electrodes and geometric area of 165 $cm^2$. It was found that reactor efficiency is related with the current density so it is really important to have a correct mechanical design. It is presented a new reactor design that improves current density of alkaline electrolysis reaching efficiencies higher to 65%-40%. The reactors show similar performances, at 20 A of current the applied voltage is 3.1 V and its efficiency is 50%, indicating an optimum point of operation. Oxyhydrogen gas volume of 550 sml/min was produced in this point.

***Keywords:*** Alkaline electrolysis; oxyhydrogen production, monopolar and wet electrodes.

# 1.17 Synthesis of crystalline nanocomposites of zinc sulfide ZnS ((ZnS, ZnS/ZnO, ZnS-I/ZnO) with potential photocatalytic activity for hydrogen production

Puentes Prado Laura Elena, Galindo González María del Rosario, Gómez Solís Christian.

[1,2]División de Ciencias Naturales y Exactas de la Universidad de Guanajuato, Campus Guanajuato, Noria Alta s/n. Noria Alta. Guanajuato, Guanajuato.

[3]Centro de Investigación en Óptica, Loma del Bosque 115, Colonia Lomas del Campestre León, Guanajuato, México,37150.

* leppq_92@outlook.com, (477)4057264

## ABSTRACT

A fundamental investigation of the interface properties of coupled semiconductor photocatalysts in view of enhancing visible light activity is presented. As typical semiconducting heterostructures of ZnS, the crystalline zinc sulfide (ZnS) thin films were prepared by chemical bath deposition (CBD). Followed by deposition of zinc oxide (ZnO) nanofilm using spin coating. Electrochemical Impedance Spectroscopy (EIS) and Analysis of Chronoamperometry (CA) characterized the thin films. The as-deposited thin films were surface homogeneous and the optical band gap of the film was estimated to be 3.29 eV. This reduces the photoexcitation threshold energy and thus potentially enhances the solar energy conversion capabilities of such a heterostructure photocatalysts. The Monitoring by Gas Chromatography (GC) of ZnS-ZnO films heterostructures also exhibited a higher photocatalytic performance for $H_2$ evolution from water splitting under visible light irradiation at 25 °C. This study offers a novel way of fabricating semiconductor composites for high-efficiency photocatalysis applications.

***Keywords:*** chemical bath deposition, sputtering, band gap, photocatalysts, water splitting.

---

## 1. Introduction

Formation of hydrogen and oxygen by water splitting using heterogeneous photocatalysts under UV or visible light irradiation is a promising process to achieve recyclable and clean hydrogen production [1]. Zinc sulfide (ZnS) thin films with wide direct band gap and n-type conductivity are promising for optoelectronic device applications, such as electroluminescent devices and photovoltaic cells. In optoelectronics, it can be used as light emitting diode in the blue to ultraviolet spectral region due to its wide band gap of 3.7 eV at room temperature [2]. In the area of optics, ZnS can be used as a reflector and dielectric filter because of its high refractive index (2.35) and high transmittance in the visible range, respectively [3,4]. Several techniques such as molecular beam epitaxy, $H_2$ plasma chemical sputtering [4] and liquid phase techniques such as electrochemical deposition, chemical bath deposition (CBD) [5-6] have been used to produce ZnS thin

films. Among them, chemical bath deposition is the least costly, low temperature technique. Here it was adopted as the generic name for techniques that produce a solid film in a single immersion through control of the kinetics of formation of the solid. The CBD process uses a controlled chemical reaction to effect the deposition of a thin film by precipitation. In the most typical experimental approach, substrates are immersed in an alkaline solution containing the chalcogenide source, the metal ion, added base and a complexing agent. However, generally, the films obtained by CBD method are either amorphous or poorly crystallized. Therefore, annealing at high temperature was needed to improve the crystallinity of the thin films [7,8]. Moreover, the deposition of ZnS by CBD is a more difficult proposition than that of other nanomaterials. It is evident that there is a much wider range of conditions in which the concurrent deposition of zinc sulfide and zinc oxide can occur [9]. In this paper, using tri-sodium citrate as the complexing agent, pure phase of well-crystallized ZnS thin films were directly deposited at a temperature of 90 °C.

ZnS photocatalyst with a band gap wider than ZnO (3.37 eV) can facilitate the fast formation of photogenerated electron-hole pairs. ZnS is used for the photocatalytic degradation of organic molecules and photocatalytic $H_2$ production.

## 2. Materials and Methods

### Chemical bath deposition of ZnS thin film

The substrates used for the deposition of ZnS thin films were commercial microscope glass slides. Before deposition, the substrates were degreased with ethanol, etched with HCl for 10 min, cleaned with deionized water and finally dried in air. Aqueous solutions of 0.2 M zinc acetate ($Zn(CH_3COO)_2$), 0.6 M thiourea ($SC(NH_2)_2$), complexing agent 0.2 M tri-sodium citrate were used to prepare ZnS thin films.

### Deposition of ZnO thin films by spin coating

In this paper, ZnO thin films were prepared by sol–gel method. Zinc acetate dihydrate, 2-methoxyethanol and monoethanolamine (MEA) were used as starting material, solvent and stabilizer, respectively. Zinc acetate dihydrate was first dissolved in a mixture of 2-methoxyethanol and MEA solution at room temperature. The molar ratio of MEA to zinc acetate was maintained at 1.0 and the concentration of zinc acetate was 0.75 M. The solution was stirred at 60°C for 2h to yield a clear and homogeneous solution, which served as the precursor solution.
The solution was dropped onto glass substrates, which were rotated at 3000 rpm for 30s. After deposited by spin coating, the films were dried at several conditions for 10 min over a hot plate to evaporate the solvent and remove organic residuals.

## 3. Results and Discussion

### Photoelectrochemical (PEC) property

The Mott–Schottky plots were conducted in 0.5 M $Na_2SO_3$ aqueous solution at pH 13 in dark condition with electrochemical impedance spectroscopy. The flat band potentials of ZnS, ZnO and ZnS:ZnO mixture was determined by using the Mott–Schottky equation at 25 °C. The estimated flat band potential was found from the average value of the *x*-

intercepts of the linear portion of the Mott–Schottky data from different frequencies and was measured to be 0.7,0.1 *vs*. Ag/AgCl for ZnS and Zn:ZnO respectively and 0.57 V *vs*. Ag/AgCl for ZnO mixture photocatalyst.

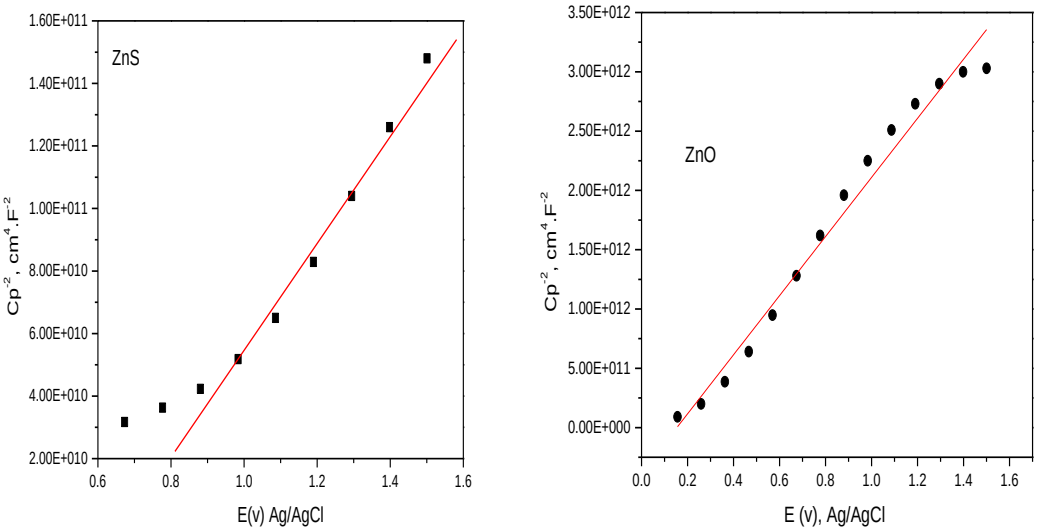


**Fig. 1.** Mott-Schottky plot of ZnS and ZnO films indicates that this material is a n-type semiconductor.

Figure 1 shows the Mott-Schottky plots obtained for ZnS thin films. The positive slope of M-S plot for ZnS and ZnO thin film confirms the n-type semiconductor characteristic, while negative slope of ZnS:ZnO thin film is related to p-type semiconductor.

Photoelectrochemical test using chronoamperometry analysis was carried out, in order to determine the electron/hole pair separation mechanism of the aluminates under UV–vis irradiation. Figure 2 shows the chopped currentetime transient responses of ZnS, ZnO and ZnS:ZnO photocatalysts coated ITO substrates as electrodes under UV light irradiation. When the irradiation light is turned on, the currents for all samples increased drastically. The currents decreased rapidly when the light was turned off. It reveals that incorporating $I_2$ helps to enhance the separation of photogenerated electronehole pairs of ZnS:ZnO composites, leading to larger photocurrent than the pristine ZnS. The results are consistent with the trends of their hydrogen evolution activity.

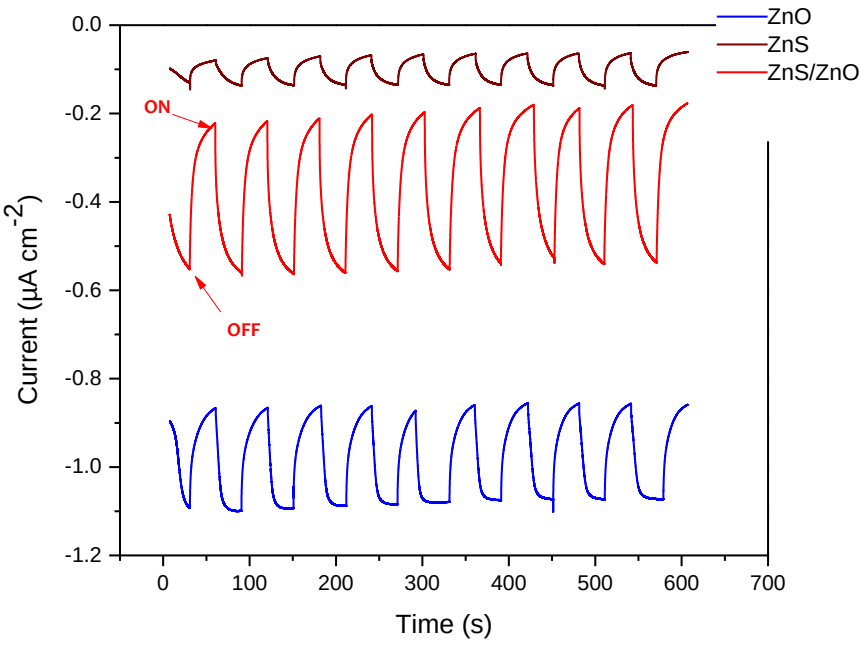


**Fig. 2** Photocurrent response (On-off) for ZnS, ZnO and ZnS/ZnO samples under UV-light irradiation.

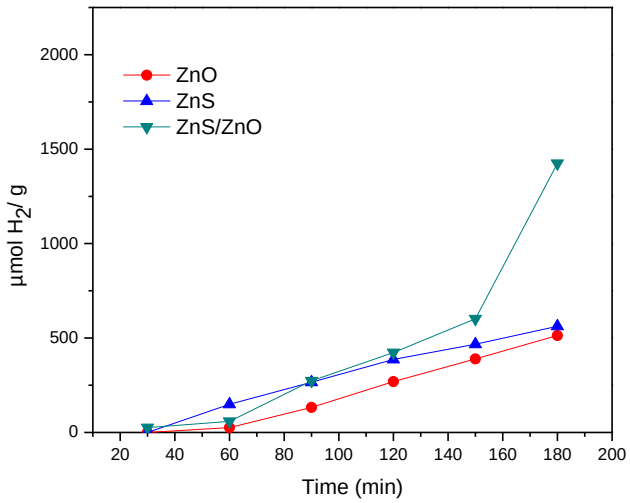


**Fig. 3** Hydrogen production from water splitting using ZnS, ZnO and ZnS/ZnO films as photocatalysts.

As shown in Figure 3, the photocatalytic $H_2$ production of pristine ZnS is 561 μmol $h^{-1}g^{-1}$. The introduction of ZnO can enhance the photocatalytic $H_2$ production activity of ZnS. The

hydrogen production activity of the photocatalyst can be improved by incorporating zinc oxide. Since the zinc oxide semiconductor is a good material for transporting holes, the photogenerated holes can immigrate to the photocatalysts surface easily. Therefore, electronehole pairs can be separated effectively, and the photocatalytic ability can be improved. The photocatalytic $H_2$ production of ZnO became 513 µmol $h^{-1}g^{-1}$. The PZnS:ZnO photocatalyst exhibited the highest photocatalytic $H_2$ production performance (1425 µmol $h^{-1}g^{-1}$).

## 4. Conclusion

ZnS:ZnO was prepared and acted as composite photocatalyst for $H_2$ production. The results of EDS analysis and electrochemistry confirm that the nanocomposites consist of ZnS nanoparticles and ZnO nanoparticles. After incorporating the zinc oxide, the $H_2$ production efficiency of ZnS:ZnO photocatalyst was remarkably enhanced because of improved dispersing property, increased surface area and efficient separation of electron and hole pairs in the excited states of ZnS:ZnO composite photocatalysts.

## Acknowledgements

## References

[1] Pany, S.; Parida, K. M. Sulfate-anchored hierarchical meso-macroporous N-doped TiO2: a novel photocatalyst for visible light H2 evolution. ACS Sustain. Chem. Eng. 2014, 2, 1429–1438.
[2] Yamaga S, Yoshokawa A and Kasain H 1998 *J. Cryst. Growth* **86** 252.
[3] Ruffner J A, Hilmel M D, Mizrahi V, Stegeman G I and Gibson U 1989 *J. Appl. Opt.* **28** 5209.
[4] Ledger A M 1979 *Appl. Opt.* **18** 2979.
[5] Mane R S and Lokhande C D 2000 *Mater. Chem. Phys.* **65** 1.
[6] Brien P O and McAleese J 1998 *J. Mater. Chem.* **8** 2309.
[7] Arenas O L, Nair M T S and Nair P K 1997 *Semicond. Sci. Technol.* **12** 1323–30.
[8] Johnston D A, Carletto M H, Reddy K T R, Forbes I and Miles R W 2002 *Thin Solid Films* **403–404** 102–6.
[9] Brien P O and McAleese J 1998 *J. Mater. Chem.* **8** 2309.
[10] B. Di, et al. “ZnO/ZnS Heterostructur Nanorod Arraysand Their Efficient Photocatalytic Hydrogen Evolution”, Chemistry Europan Journal, 2015, 1-3.
[11] P. Bao, et al. ChemPlusChem 2013, **78**, 1 266 –1 272.
[12] A. Vante, Electroquímica y electrocatálisis. Materiales: aspectos fundamentales y aplicaciones. Vol. Ib. Buenos Aires: s. e., 2013.
[13] M. Barbeni, et al. Hydrogen from hydrogen sulfide cleavage. Improved efficiencies via modification of semiconductor particulates. *International Journal of Hydrogen Energy,* 2003, **10**, 249-253

# 1.18 Effect of advanced synthesis procedures of Nickel Catalysts supported on Cerium modified MCM-41 in ethanol steam reforming

María F. Hernández-Madera, Jorge Tovar-Rodríguez, Emiliano Fratini, Iginio Longo, Carlo Ferrari, Ignacio R. Galindo-Esquivel

[1]Departamento de Ingeniería Química, Universidad de Guanajuato, Noria Alta s/n, Guanajuato 36050, Gto. Mexico.
[2]Dipartimento di Chimica "Ugo Schiff", Università degli Studi Firenze, Via della Lastruccia 3, 1-50019, Sesto Fiorentino, Firenze, Italia.
[3]Istituto Nazionale di Ottica, Area di Ricerca CNR di Pisa, Via G. Moruzzi, 1-56124, Pisa, Italia
* Corresponding author: (+55) 473 732 0006 ext 1425, igalindo@ugto.mx

## ABSTRACT

Catalyst synthesis procedures play a significant role in determining the overall efficiency of any catalyzed process. MCM-41 synthesis involves several steps that include micelle formation of an amphiphilic molecule used as structure-directing agent (CTABr), followed by particle growth and silica polymerization of a Si precursor by ageing the mixture in presence of a mineralizing agent at hydrothermal controlled conditions and detemplation where the structure directing agent is removed generally through calcination. In this research microwaves (MW) and ultrasound (US) were used to modify the supports synthesis and the effect of the synthesis procedure modifications was followed through characterization by SAXS, BET, SEM and ATR-FTIR. The MCM-41 was modified by adding cerium in a constant 0.02 Ce/Si molar ratio during the micelle formation step, to increase cerium dispersion US was applied in some cases, while mechanical mixing was used as reference. The obtained mixture was aged for 4h at ambient conditions and then hydrothermally treated at 100°C applying the conventional method for 24h or a MW assisted method for 2h, in both cases at autogenous pressure. All materials were calcined at 550°C to remove the occluded CTAB and generate the expected porosity. These materials were impregnated with nickel nitrate hexahydrate ($Ni(NO_3)_2 \cdot 6H_2O$) to obtain a 10wt.% Ni content in the catalysts. Prior to reaction the catalysts were activated in-situ at 550°C with $H_2$ flowing at 50 $cm^3$/min. Ethanol SR was performed in a fixed bed catalytic reactor using 50 mg of catalyst, water/ethanol molar ratio of 3, 500°C and 1 atm. Argon was used as carrier flowing at 100 $cm^3$/min. Product analysis was performed online with two GCs equipped with a FID and a TCD. Compared to MCM-41 pure Si support, SAXS reveals that the synthesis assisted by MW and US for Ce-MCM-41 allows for structure conservation, the supports modified with only one advanced strategy or none of them showed a high crystallinity loss. The catalyst synthesized with MW and US did not deactivate during ethanol SR (6 h) and was highly selective to $H_2$; methane, carbon monoxide and carbon dioxide were the only identified byproducts.

***Keywords:*** MCM-41; Ethanol Steam Reforming; Microwaves, Ultrasound

# 1.19 Hydrogen production through ethanol steam reforming over Yttrium modified MCM-41 supported Nickel catalysts

María F. Hernández-Madera, Jorge Tovar-Rodríguez, Emiliano Fratini, Ignacio R. Galindo-Esquivel

[1]Departamento de Ingeniería Química, Universidad de Guanajuato, Noria Alta s/n, Guanajuato 36050, Gto. Mexico.
[2]Dipartimento di Chimica "Ugo Schiff", Università degli Studi Firenze, Via della Lastruccia 3, I-50019, Sesto Fiorentino, Firenze, Italia.
* Corresponding author: (+55) 473 732 0006 ext 1425, igalindo@ugto.mx

## ABSTRACT

Presently, steam reforming (SR) of natural gas is the most cost effective and efficient technology for hydrogen production, but relying on fossil fuels is not a sustainable option. Consequently, the use of ethanol that may be obtained from biomass instead of natural gas is a straightforward evolution for SR technology. Additionally, the catalyst applied in the SR determines the process overall efficiency. Usually SR is performed at temperatures in the range from 600 to 800°C to obtain a high hydrogen yield and low catalyst deactivation. This research presents stable operation and high hydrogen yields in ethanol SR at 500°C when using catalysts of nickel deposited on yttrium modified MCM-41 supports. The effect of different yttrium loadings while keeping nickel loading at 10wt.% was determined. The supports were synthesized using a conventional hydrothermal method for MCM-41 synthesis, but adding different amounts of yttrium precursor ($Y(NO_3)_3 \cdot 6H_2O$) to yield Y/Si molar ratios of 0, 0.02, 0.04, 0.06 and 0.08. The supports were characterized by SAXS, BET and ATR-FTIR. These materials were impregnated with nickel nitrate hexahydrate ($Ni(NO_3)_2 \cdot 6H_2O$) to obtain a 10wt.% Ni content in the catalysts. After impregnation, the catalysts were characterized by BET and TEM. Prior to reaction the catalysts were activated in-situ at 550°C with $H_2$ flowing at 50 $cm^3$/min. Ethanol SR was performed in a fixed bed catalytic reactor using 50 mg of catalyst, water/ethanol molar ratio of 3, 500°C and 1 atm. Argon was used as carrier flowing at 100 $cm^3$/min. Product analysis was performed online with two GCs equipped with a FID and a TCD. As the amount of Y increased in the supports the MCM-41 structure featured a lower degree of hexagonal ordering. The surface area decreased after yttrium incorporation. Compared to the synthesized Ni/MCM-41 catalyst the addition of any amount of Y decreased the catalysts deactivation and favored hydrogen production. The catalyst containing 0.06 Y/Si molar ratio did not deactivate during ethanol SR (6 h) and was highly selective to $H_2$; methane, carbon monoxide and carbon dioxide were the only identified byproducts.

***Keywords:*** MCM-41; Ethanol Steam Reforming; Yttrium oxide.

# 1.20 A scaled system for biohydrogen production from green microalgae

Hernández-Hernández E. M., Cortés-Escobedo C.A., Velasco-Bedrán H.A.

[1]Centro de Investigación e Innovación Tecnológica, Cda. Cecati S/N Col. Santa Catarina, Azcapotzalco, México, 02250.
[2]Escuela Nacional de Ciencias Biológicas, Wilfrido Massieu 399 Nueva Industrial Vallejo, Gustavo A. Madero, México, 07738.
* Corresponding author: +525534792023 e-mail: mariana.hernandez2703@outlook

## ABSTRACT

Today hydrogen is one of the most important energy carriers, $H_2$ production by biological species (Bio-hydrogen) has a number of advantages and could be a cost-effective alternative to current industrial methods. Biohydrogen can be produce through different biological pathways, these are grouped into two distinct categories: light dependent or not light dependent processes, both of them include direct or indirect photofermentación, dark fermentation and biophotolysis. The advantage of direct photolysis is the requirements are only water and light, which is relatively available and economic. In particular, this project is focused to direct biophotolysis and this requires the construction of culture systems that allow the gas production. Therefore, the bioreactors are essential for bio hydrogen production by green microalgae, such production is linked to photosynthetic reactions of dissociation of water and it is possible to use solar energy (light) for this process. There are some reports on bio hydrogen production by green microalgae, but only at laboratory scale photobioreactor (2L). This work explores the operation of a 19.7L solar photobioreactor, which operates in two phases, the growth phase and the gas production phase. The device dimensions are 1x0.70x0.03m and a nominal volume of 0.021$m^3$, and was characterized in mixing time, air volume (aeration), etc. Also *Chlamydomonas* sp. was inoculated in BG-11 culture medium, to know its growth kinetics, compared to the growth of the same strain in flask. Finally, the hydrogen tests were realized in sulfur free culture medium and anaerobiosis caused by the introduction of nitrogen gas. The use of photobioreactors considerably improves biomass productivity and favors the production and uptake of gas, this technique stands out for the implementation of systems of production of electric energy in situ by coupling fuel cells.

***Keywords:*** biohydrogen; photobioreactor; green microalgae.

# 1.21 Sizing of electrolyzer for application in combustion engines

G. Becerra, E. Osorio, V. M. Sanchez, RG. Gonzalez-Huerta, R. Barbosa

[1]CONACYT - Universidad de Quintana Roo, Boulevard bahía S/N, esq. Ignacio Comonfort, Col. del Bosque, Chetumal, Quintana Roo CP 77019, Mexico

[2]Universidad de Quintana Roo, Boulevard bahía S/N, esq. Ignacio Comonfort, Col. del Bosque, Chetumal, Quintana Roo CP 77019, Mexico

[3]Instituto Politécnico Nacional - ESIQUIE, Laboratorio de Electroquímica y Corrosión UPALM, Ciudad de México, CP 07738, Mexico.

* Corresponding author: e-mail: romelix1@gmail.com,

## ABSTRACT

The combustion engine vehicles are still the most used in the market and new technologies are being incorporated, while new tools are planned for the transition. In the present work, it is proposed to substitute a percentage of the usual fuel by hydrogen. We analyzed the size and the operating range of the electrolyzer, according to the power profiles of the combustion engine, with the aim of establishing a production control.

The objective is to design the intake system of an internal combustion engine, including hydrogen injection, which increases the fuel calorific value.

This through by mixing the oxyhydrogen gas generated by electrolyzer with the intake air, without making major modifications of its components, construction materials and operation. The advantage of the above-mentioned proposal is to improve the engine efficiency and reduce pollutant emissions.

The internal combustion engine under dual fuel mode with added hydrogen increases its thermal efficiency and reduces carbon based emissions. However, the hydrogen in the present proposal enters the intake manifold to be mixed with air and then to the combustion chamber, where it is mixed and detonated together with the fuel.

The amount of gas to be mixed depends on the power at which the engine should be operated. At the same time, the power difference available to increase the efficiency of the engine is arranged to produce the oxyhydrogen gas.

***Keywords:*** Electrolyzer; hydrogen, internal combustion engine; thermal efficiency.

## 1. Introduction

Humanity has developed different ways of moving. Currently, the mobility market is dominated by vehicles with internal combustion engines (ICE).
The most efficient engine in the combustion engine's use the diesel as fuel [1] and it has been the most popular conveyance used mainly for the versatility and great range of applications.
However, nowadays, big cities have many problems related to transportation, road traffic, poor quality air and so forth.
So that, the research is focused on changing the usual oil fuels, save fuels, reduce the emissions in order to save the environmental and help the energetic transition [2,-4].
Some works are developing models and control to combustion engine's, these are focused on finding dose the amount of fuel for obtaining the speed and power demanded by the operator [5-7].
On the other hand, hydrogen has be used for combustion engines, mainly in dual mode, by replacing a percentage of the usual fuel with hydrogen or oxyhydrogen gas (HHO).
Some works to ICE's with dual-mode fuel can be mentioned in compression ignition (CI) engine where is applied different proportion of HHO, it is obtained from water electrolysis [8-10].
These works mentioned that, the engine output power is incremented by summation of hydrogen. Horcasitas et al. have been used an alkaline electrolyzer for a CI engine to prove dual fuel HHO gasoline experimentally [11]. Test are performed on different operation points in speed and analyzed the gasoline fuel consumption and the carbon dioxide ($CO_2$) emissions, which are reduced. Moreover, research have been developed when using diesel - hydrogen in dual mode, again the main point of interest is analyzed the gas pollutants and the output power [12-14].
In this work we link the control systems with the production and injection of hydrogen in dual mode, and analyzed the necessary energy to produce the hydrogen, what normally, it is not analyzed on the mentioned papers.

## 2. Engine model

The CI engine model is from [5] and some relevant features are detailed for dual fuel HHO – diesel.

1. **Manifold**. From the mass conservation law, the dynamics in the intake manifold for the air mass rate $m_a$

$$\frac{dm_a}{dt} = \dot{m}_{ai} - \dot{m}_{ao}, \quad m_a = \frac{p_a V_a}{r T_a} \quad (9)$$

the subscripts *i* and *o* are for the input - output air flow respectively; $p_a$ is the intake manifold pressure, $V_a$ the volume, *r* the gas constant for air and $T_a$ temperature.

The expression $\dot{m}_{ao}$ depends on speed and pressure

$$(\dot{m}_{ao}) = \eta_v (\dot{m}_{ao})_{calc}, \qquad (\dot{m}_{ao})_{calc} = \frac{nV_d}{4\pi r}\frac{\omega p_a}{T_a}$$

Where *n* is the number of cylinders; $V_d$ cylinder volume; $\eta_v$ volumetric efficiency,

$$\eta_v = \alpha_0 + \alpha_1 \omega + \alpha_2 \omega^2$$

coefficients $\alpha_0$, $\alpha_2 > 0$ and $\alpha_1 < 0$.

2. **Combustion**. The engine can be modeled from the energy perspective

$\frac{1}{2}J\omega^2=E_i-E_b$ (1)

Considering *J* inertia, ω speed, $E_i$ fuel energy and $E_b$ the total break energy. Thus, it in power (*P*) terms

$\frac{d}{dt}\left(\frac{1}{2}J\omega^2\right)=P_i-P_b$ (2)

where the subscripts *i* and *b* are the chemical and load, respectively. $P_i$ is expressed as

$P_i=\eta_i p_{th}\dot{m}_f$ (3)

Where $\eta_i$ is the conversion efficiency chemical - mechanical energy, $p_{th}$ the lower heating value and $\dot{m}_f$ the fuel flow. The lower heating value is modified by the quantity of HHO gas that input in the admission manifold; because in combustion chamber it will be mixed with diesel to detonate and provide the mechanical power in the crankshaft. The efficiency from two terms is obtained; the first integrates the losses by the friction of the wall and effects that depend on the speed of the motor; and the second losses due to unburned products.

$\eta_i=\mathrm{a}_\lambda+b_\lambda+c_\lambda\lambda^2, \quad \lambda=\frac{\dot{m}_{a0}}{\dot{m}_f}$ (4)

With $a_\lambda$, $b_\lambda>0$, $c_\lambda<0$ and λ is the air-fuel relation.

It is substituted the eq. (4) in (3),

$P_i=\left[\mathrm{a}_\lambda+b_\lambda\left(\frac{\dot{m}_{a0}}{\dot{m}_f}\right)+c_\lambda\left(\frac{\dot{m}_{a0}}{\dot{m}_f}\right)^2\right]p_{th}\dot{m}_f$ (5)

and the speed dynamic eq. (2), with (5),

$\frac{d\omega}{dt}=\frac{1}{J\omega}\left\{\left[\mathrm{a}_\lambda+b_\lambda\left(\frac{\dot{m}_{a0}}{\dot{m}_f}\right)+c_\lambda\left(\frac{\dot{m}_{a0}}{\dot{m}_f}\right)^2\right]p_{th}\dot{m}_f-P_b\right\}$ (6)

The final model is

$\frac{d\omega}{dt}=p_{th}\mathrm{a}_\lambda\frac{1}{J\omega}\dot{m}_f+\frac{1}{J\omega}b_\lambda\left(\frac{p_{th}V_d n}{4rT_\mathrm{a}\pi}\right)\eta_v p_a+\frac{1}{J\omega}c_\lambda\left(\frac{p_{th}V_d^2n^2}{16r^2{T_\mathrm{a}}^2\pi^2}\right)\frac{p_\mathrm{a}^2\eta_v^2\omega}{\dot{m}_f}-\frac{1}{J\omega}P_b$ (7a)

$\frac{dp_\mathrm{a}}{dt}=\frac{T_\mathrm{a}r}{V_\mathrm{a}}\dot{m}_{ai}-\frac{V_d n\eta_v}{4V_\mathrm{a}\pi}\omega p_\mathrm{a}$ (7b)

It is possible to represent the static map if dω/dt = 0

$\eta_i=\frac{P_b}{p_{th}\dot{m}_f}$ (8)

The above analysis is required the amount of HHO gas that is considered to be added in the intake manifold, which will be a percentage of the air entering the combustion chamber.

## 3. Diesel hydrogen air mixture

In this section, fuel air ratio for the percentages of gas is intended to be supplied as secondary fuel in the combustion chamber is analyzed, in addition to the oil-based liquid [14]. The air fuel ratio is determined by the molar structure of the components in *mol/cm*$^3$.

For the analysis, it is first considered that for the mixture only oxygen ($O_2$) is used, by diesel ($C_yH_z$) eq. (11) and hydrogen ($H_z$) eq.(12) separately[1]

$$C_xH_y + \left(x + \frac{y}{4}\right)(O_2) \rightarrow xCO_2 + \left(\frac{y}{2}\right)H_2O \quad (11)$$
$$H_z + \frac{z}{4}O_2 \rightarrow \frac{z}{2}H_2O \quad (12)$$

Eq. (11) and eq.(12) shown that if use oxygen to combustion hydrogen, the residue obtained is water ($H_2O$), while carbon dioxide ($CO_2$) in diesel combustion, is present.
On the other hand, ambient air contains a large percentage of nitrogen and oxygen is the next component. For mobility, ambient air is used. In the following analysis, air with the main components is considered, again for diesel eq. (13) and hydrogen eq. (14)

$$C_xH_y + \left(x + \frac{y}{4}\right)(O_2 + 3.773N_2) \rightarrow xCO_2 + \left(\frac{y}{2}\right)H_2O + \left(\frac{y}{4}\right)3.773N_2 \quad (13)$$
$$H_Z + \frac{z}{4}(O_2 + 3.773N_2) \rightarrow \left(\frac{z}{2}\right)H_2O + \left(\frac{z}{2}\right)3.773N_2 \quad (14)$$

For the mixture air, diesel and hydrogen,

$$\mathrm{a}(C_xH_y) + bH_z + \left(\mathrm{a}x + \frac{\mathrm{a}y+bz}{4}\right)(O_2 + 3.773N_2) \rightarrow \mathrm{a}xCO_2 + \left(\frac{\mathrm{a}y+bz}{2}\right)H_2O + \left(\mathrm{a}x + \frac{\mathrm{a}y+bz}{4}\right)3.773N_2 \quad (15)$$

where 0 <*a*< 1 is the quantity of diesel and 0 <*b*< 1 hydrogen for the mix, finally (*a*+*b*=1).

## 4. Study of cases

Using the ideal air-to-fuel ratio in the diesel engine, the fuel does not burn completely and it is results in lower efficiency coupled with considerable emissions. For the above, turbocharged engines are used to increase the fuel air ratio and there by improve the burning of the fuel, which causes excess air in the combustion chamber [6]. In the present work, it is intended to use excess air to change a portion by oxy-hydrogen gas (produced by an electrolyzed), thus improving combustion and using less diesel fuel.

### 4.1 Case 1

Dates taken from [5] (see Table 1), to BMW 524 TD (diesel engine) 2443cm$^3$. In the same work, the output power with the different parameters (input and output) such as speed and torque present in the Table 2 and Table 3. However, the air and fuel inlet flow does not correspond to the units and the following data are proposed, so that it is physically feasible.

Table1. Simulation parameters used in [5].

[1] x=12, y=26, z=2. The $p_{ht}$ =120*MJ/kg* to $H_2$ and $p_{th}$ = 43 *MJ/kg* to $C_{12}H_{26}$

| | | |
|---|---|---|
| $a_\lambda$= 0.072 | $b_\lambda$= 0.018 | $c_\lambda$= -0.00017 |
| $p_{th}$= 40 X $10^6$ | *J=0.15* | $V_d$ =0.0024 |
| n =6 | r = 0.287 | $T_a$ = 315 |
| $\alpha_0$= 0.773 | $\alpha_1$= -1.54 X $10^{-3}$ | $\alpha_2$= 2.49 X $10^{-6}$ |
| $V_a$=1.4 X$10^{-3}$ | | |

Table 2. Dates presented in engineer out power analysis to BMW 524 TD 2443 $cm^3$ [5].

| Tr[NM] | wr[RPM] | wr[rad/s] | Power[W] |
|---|---|---|---|
| 500 | 800 | 83.70 | 41,888.0 |
| | 1400 | 146.61 | 73,304.0 |
| | 1900 | 198.97 | 99,484.0 |
| 800 | 800 | 83.78 | 67,020.8 |
| | 1400 | 146.61 | 117,286.4 |
| | 1900 | 198.97 | 159,174.4 |

Table 3. Input power proposed in [5]

| $\dot{m}_{ai}$ | $\dot{m}_{ao}$ | AFR | $\dot{m}_f$ | Mfp*Hv | $\eta$ |
|---|---|---|---|---|---|
| 0.1282 | 0.0826 | 41.4848 | 0.00193 | 77,355.2 | 0.5415 |
| 0.246935 | 0.1352 | 37.4647 | 0.00360 | 144,000.0 | 0.50906 |
| 0.3697 | 0.1727 | 33.7131 | 0.00510 | 204,000.0 | 0.48767 |
| 0.20507 | 0.1321 | 41.4845 | 0.00320 | 128,000.0 | 0.5236 |
| 0.3951 | 0.2164 | 37.465 | 0.00580 | 232,000.3 | 0.50554 |

| | | | | | |
|---|---|---|---|---|---|
| 0.5915 | 0.2763 | 33.7126 | 0.00820 | 328,000.0 | 0.48529 |

These values at steady state, the fuel flow (*mfp*)[*kg/s*] is calculated and multiplied with the calorific value of the fuel $H_v$ it is results in power at the engine input (*mfp*H*$_v$[*W*]) to provide power output.
In order to avoid high efforts in the combustion chamber, jacket, piston, piston ring, valves, ventilation, lubricating oil and other elements, only the enrichment of 5% to 15%, and thereby help reduce emissions, without major changes to the original system [15].
Further, by the density of the oxy-hydrogen gas and the form of production by the electrolyze. The following table corresponds to the determination of the electrolyze for the mentioned motor: electrolyze output power ($P_{out}Elec[\omega]$) to 5% and 15%, as well as the electric power required at the electrolyze input ($P_{in}Elec[\omega]$), for the two percentages, considering that it has a fixed efficiency (input intakes) of 80%, respectively.

Table 4. Data power by sizing of electrolyzed

| 5.00% | 5.00% | 15.00% | 15.00% |
|---|---|---|---|
| $P_{inElec}$ | $P_{outElec}$ | $P_{inElec}$ | $P_{outElec}$ |
| 4,835 | 3,868 | 14,504 | 11,603 |
| 9,00 | 7,200 | 27,000 | 21,600 |
| 12,750 | 10,200 | 38,250 | 30,600 |
| 8,000 | 6,400 | 24,000 | 19,200 |
| 14,500 | 11,600 | 43,500 | 34,800 |
| 20,500 | 16,400 | 61,500 | 49,200 |

### 4.2 Case 2

Figure 1 shown, the proposed of a usually driving cycle used in test vehicles, for confined bus lanes on Mexico City (metrobus). The vehicles parameters are masa = 15,000 Kg and diesel engine = 205 kW. More details about the parameters are shown in [4] and [16].

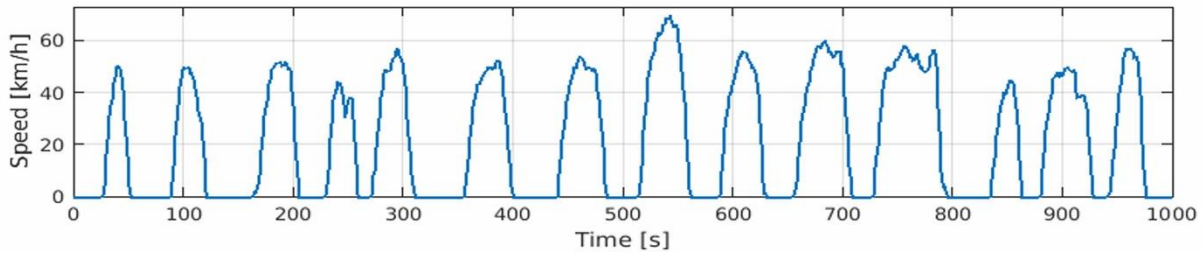


Figure 1. Profile test usually of driving cycle in vehicles for high velocity bus on México City.

To reach the test profile in the vehicle, according of velocity and torque, its motor will operate at three operating points. The above moves to radio of the tire and gear ratios between differential and changing box. The scheme proposed to increase the efficiency of the combustion engine and increase the output power for subsequent use. In the following approach, the engine operating points are presented to enable the vehicle to follow the path of the driving cycle. However, the points of operation of the regime are transferred implying little torque and efficiency to values in which efficiency is improved. Beside the speed is maintained to comply with the driving cycle. Figure 2 shown speed versus torque at correspondent operation point to supply the driver power demands. Figure 2a shown point below 200 Nm, theses points are multiplied by 5 to drive them to operate at the maximum efficiency allowed for that speed. Figure 2b and Figure 2c is similar to the previous one but for the points below 225 Nm and 250nm, respectively. Only the operating points are moved on the torque axis, since the speed must be met and therefore not increased or decreased. It can be observed that at speed constant (@ 1700 rpm) in three conditions, the torque have proportional increasing by 5 factor, however the increased of percentage efficiency have increasing by 1.3 factor.

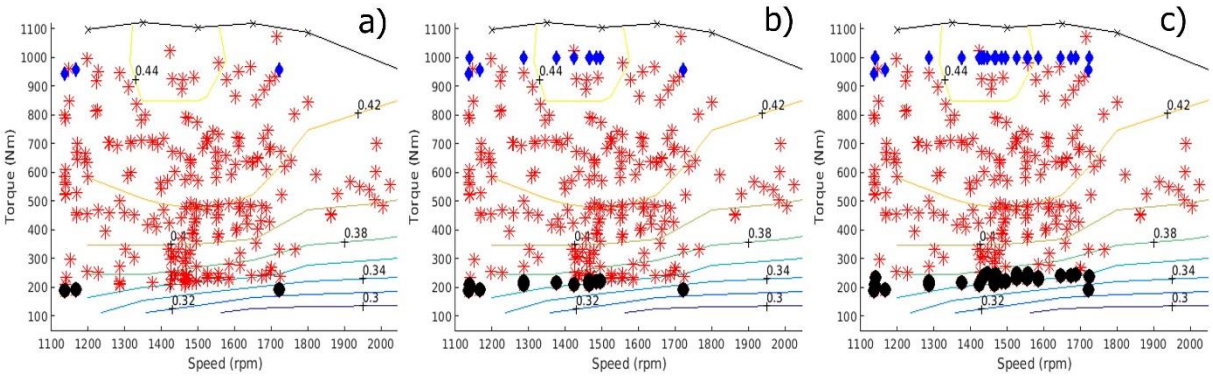


Figure 2. Speed versus torque at different operation point, black point show the points selected at change and blue point shown new point. Operation point above a) 200 Nm, below b) 225 Nm and c) 250 Nm.

The strategy for increased the output torque in the operating points, increases engine effinciency, which is shown in the table 5. However, if the increased power is used to couple a generator (90% efficiency) and with this an electrolyser (80%), then the hydrogen is injected into the engine, the efficiency decreases (0.3041, 0.3165 and 0.3390) respectively.

Table 5 Values of the total energy of the system to case two.

| System modification in torque [N] | Input energy | Output energy | Mean efficiency |
|---|---|---|---|
| without | 51,686.0 | 21,712.0 | 0.4201 |
| <200 | 52,164.0 | 22,033.8 | 0.4224 |
| <225 | 54,927.0 | 24,143.8 | 0.4396 |
| <250 | 59,372.0 | 27,951.6 | 0.4708 |

## 5. Conclusions

The conclusions so far with the simulations and calculations made using diesel combustion engine data indicate that it is possible to improve engine efficiency by about 10% by replacing the 15% of the power at the input, To the reduction of $CO_2$ with the same percentage and that only gives product of water vapor, which is a significant percentage that in a certain time period helps the environment and the economy of the user, by the prices of the gas[2].
On the other hand, if Hydrogen is produced with high efficiency of the engine and injected again, the final efficiency does not fall so drastically, but it must be considered for the cost - benefit, according to the desired operation of the machine, in addition to the reduction of the exhaust gases.

## 6. References

[1] Heywood J.B. Internal combustion engine fundamentals. McGraw-Hill: New York; 1988.

[2] Caliskan H. Environmental and enviro-economic researches on diesel engines with diesel and biodiesel fuels. Journal of Cleaner Production 154(1) (2017), pp. 125–129.

[3] Becerra G., Alvarez-Icaza L., Pantoja-Vazquez A. Power flow control strategies in parallel hybrid electric vehicles. Journal of Automobile Engineering 230(14) (2016), pp. 1873–1890.

[4] Becerra G., Alvarez-Icaza L., De La Mota I.F., Mendoza-Soto, J.L. Simulation and optimization applied to power flow in hybrid vehicles. In Applied Simulation and Optimization 2, Springer International Publishing (2017), pp. 185–224.

[2] In the market it is possible to find electrolyzes of different material, however, does not mention a corresponding analysis to test the performance.

[5] Outbib R., Dovifaaz, X. Rachid A., Ouladsine M. A theoretical control strategy for a diesel engine. Journal of Dynamic Systems, Measurement, and Control 128 (2006), pp. 453–457.

[6] Mendoza-Soto J., Alvarez-Icaza L. Passivity based control of a turbocharger-diesel engine system with exhaust gas recirculation. In 10th International Conference on Electrical Engineering, Computing Science and Automatic Control, CCE. Mexico City; Mexico: 2013.

[7] Guzman E., Becerra, G. Moreno J., Alvarez-Icaza L. Controladores para motores diésel con incertidumbres paramétricas. In XVI Congreso Latinoamericano de Control Automatico, Cancun, QRoo, Mexico. (2014) pp. 965–970.

[8] Falahat A., Hadman M., Yamin J. Engine performance powered by a mixture of hydrogen and oxygen fuel obtained from water electrolysis. International Journal of Automotive Technology 15(1) (2014), pp. 97–101.

[9] Ji C., Wang S. Effect of hydrogen addition on the idle performance of a spark ignited gasoline engine at stoichiometric condition. International Journal of Hydrogen Energy 8(34) (2009), pp. 3546–3556.

[10] Ji C., Wang S., Zhang B. (2010). Combustion and emissions characteristics of a hybrid hydrogen–gasoline engine under various loads and lean conditions. International Journal of Hydrogen Energy 11(35) (2010), pp. 5714–5722.

[11] Horcasitas-Verdiguel M., Sandoval-Pineda J., Grunstein-Ramírez B., Teran-Balaguer L., Gonzalez-Huerta R. Design and manufacture of ice test module to reduce gasoline consumption using oxyhydrogen gas from an alkaline electrolyzer. Energy and fuels 30(1) (2016), pp. 6640–6645.

[12] Tsujimura T., Suzuki Y. The utilization of hydrogen in hydrogen/diesel dual fuel engine. The utilization of hydrogen in hydrogen/diesel dual fuel engine 42(19) (2017), pp. 14019–14029.

[13] Chintala V. Subramanian K. Experimental investigations on effect of different compression ratios on enhancement of maximum hydrogen energy share in a compression ignition engine under dual-fuel mode. Energy 87(1) (2015), pp. 448–462.

[14] Chintala V., Subramanian K. Cfd analysis on effect of localized in-cylinder temperature on nitric oxide (no) emission in a compression ignition engine under hydrogen-diesel dual-fuel mode. Energy 116(1) (2016), pp. 470–488.

[15] Rojas-Mena M.A. Estudio de factibilidad del uso de hidrogeno como combustible en máquinas de combustión interna para generación de electricidad. Master's thesis, Universidad Nacional Autonoma de Mexico; 2006.

[16] Becerra Guillermo, Pantoja-Vazquez A., Alvarez-Icaza L. Comparación de estrategias para flujo de potencia en vehículos híbridos. In Memoria del congreso nacional de control automático; (2012) C. Del Carmen, Campeche, Mexico, 17-19 Oct.

# 1.22 Synthesis and characterization of $IrO_2$-$WO_3$ nanoparticles as electrocatalytic material in a PEM electrolyzer

C. E. Ochoa-Dorantes, M.M. Ley Samos, J.C. Cruz, D.L. Trejo Arroyo, G. Rodriguez-May B. Escobar, A. M. Valenzuela Muñiz

[1]Instituto Tecnológico de Chetumal, Av. Insurgentes s/n, 77013,Chetumal, Quintana Roo, México

[2]Centro de Investigación Científica de Yucatán, A.C., Calle 43 No. 130 Colonia Chuburná de Hidalgo, Mérida, Yucatán 97200, México

[3] Instituto Tecnológico de Cancun, Avenida Kabah, Km. 3, Centro, 77515 Cancún, Q.R. México

* Corresponding author: 442 32 90 609, jcruz@itchetumal.edu.mx

---

## ABSTRACT

In the future energy scenario based on renewable energies, hydrogen is an attractive energy carrier and electrolysis of water is the most efficient and practical hydrogen production process. There are different methods for obtaining the fuel, but the most commonly used is the electrolysis of water. PEM type electrolyzers are used for this; however, the oxygen evolution reaction in the anode is the limiting reaction being the case of study. For this reason in the present work materials based on $IrO_2$ and $WO_3$ were developed in different mechanical mixing 100, 70:30, 50:50, 30:70 wt., respectively, by means of a mechanical mixture from two chemical reduction syntheses. The $IrO_2$ was obtained by 6.25 mM of $IrCl_3$ dissolved in isopropyl alcohol by adjusting the pH with 1 M NaOH and a 0.5 mol $NH_4OH$ reductant was applied by adjusting a basic pH of 13. The obtained precursor was filtered and calcined at 400°C for 1hr. $WO_3$ was obtained from 10mM WCl6 dissolved in isopropyl alcohol and polyethylene glycol, generating a precursor of $W(OH)_x$ followed by a calcination process at 500 ° C for 1hr. The material was characterized by electrochemical techniques of cyclic voltammetry, linear voltammetry and electrochemical impedance spectroscopy. The material that presented a better efficiency was the mixture 50:50 IrO2: WO3. The material has a lower activation energy being this 23mV of overpotential at room temperature, and a maximum current density close to 20mA /$cm^2$ at 2.4 V vs NHE.

***Keywords:*** Electrolyzer, IrO2 nanoparticles, WO3 nanoparticles

# 1.22 Hydrogen Storage as $MgH_2$: Current Situation and Perspectives

J. G. Cabañas Moreno, O. Hernández Silva, C. Ramírez-Herrera, K. Suárez-Alcántara

[1]Centro de Investigación y de Estudios Avanzados del IPN, Programa de Nanociencias y Nanotecnología, Av. Instituto Politécnico Nacional No. 2508, Colonia San Pedro Zacatenco, CP 07360, Ciudad de México, México

[2]Unidad Morelia del Instituto de Investigaciones en Materiales de la Universidad Nacional Autónoma de México,

Antigua carretera a Pátzcuaro 8701, Col. Ex-hacienda de San José de la Huerta, Morelia, Michoacán, 58190, México

* Corresponding author: 55-57473800 ext 6785, jcabanasm@cinvestav.mx

---

**ABSTRACT**

One of the biggest challenges in the development of renewable energy technologies is the one related to energy storage. Magnesium hydride ($MgH_2$) has been considered for several decades - with varying degrees of interest - as an attractive option for hydrogen storage in the solid state. Its relatively high gravimetric capacity (7.6 wt.% H), the availability and eco-friendliness of Mg, and the reversibility and apparent simplicity of the reaction $Mg + H_2 \leftrightarrow MgH_2$ are obvious advantages of this possible hydrogen storage material. On the other hand, it has usually been considered that the high temperatures (>300 °C) needed to produce acceptable rates of $MgH_2$ decomposition represent a serious disadvantage for practical applications.

The discovery that nanostructured Mg and $MgH_2$ powders can show enhanced rates of hydriding and dehydriding, respectively, has been the starting point of sustained efforts to reduce the operating temperatures for this hydrogen storage system. In combination with nanostructuring, a large number and variety of additives have been tried with the same purpose, in the belief that they may serve as catalysts for the decomposition of the hydrogen molecule and/or the nucleation of Mg or $MgH_2$ in the early stages of the hydriding/dehydriding processes. More recently, attempts at producing nanosized particles of $Mg/MgH_2$ have led to interesting academic results.

After two decades of research with $Mg/MgH_2$ nanostructures, how likely is that this system will be used in hydrogen storage applications?

We will review the work that is currently being done in this area, as well as the many interesting questions still left to explain the hydriding and dehydriding processes in the $Mg/MgH_2$ system. From these considerations, we will attempt to identify the most pressing problems in pursuing the practical use of $MgH_2$ as a hydrogen storage material.

***Keywords:*** hydrogen storage, $MgH_2$, nanostructures

# 1.23 Synthesis, characterization and photocatalytic evaluation of potassium hexatitanate ($K_2Ti_6O_{13}$) fibers

M.A. González Lozano, V. Collins Martínez, A. López Ortiz, M. Meléndez Zaragoza, R.H. Lara, M.A. Escobedo Bretado

[1]Facultad de Ciencias Químicas, Universidad Juárez del Estado de Durango, Av. Veterinaria s/n, Circuito Universitario, C.P. 34120, Durango, Dgo., Mexico

[2]Centro de Investigación en Materiales Avanzados S. C., Miguel de Cervantes 120, C. P. 31136, Chihuahua, Chih.,

Mexico

* M.A. Escobedo Bretado: phone number: +52 618 1301120, e-mail: miguel.escobedo@ujed.mx

---

## ABSTRACT

Potassium hexatitanate have been scarcely studied as a photocalalytic material for the hydrogen production from water splitting. The aim of the present study is to synthetized and characterized $K_2Ti_6O_{13}$ fibers in order to evaluate their photocatalytic activity towards the efficient production of hydrogen. Materials were characterized by XRD, BET, UV–Vis and SEM. The viability of obtaining $K_2Ti_6O_{13}$ via the flux method using boric acid subjected to different melting temperatures and cooling media (air or water) was carried out. The amount of used flux enabled the production of a liquid phase in which the $TiO_2$ and $K_2O$ reacted to form $K_2Ti_6O_{13}$ with various morphologies, according to results. The melting temperature did not significantly influence the microstructure presented by the materials. Fibers were produced with sizes varying from 12 to 35 µm in length and 260 – 530 nm in diameter as well as with a specific surface area of 4.1 $m^2/g$ and 2.3 $m^2/g$ for a heat treatment at 900 °C (C21) and 1000 °C (C22), respectively. Band gap energies of these titanates fell within the electromagnetic spectrum from 3.2 eV for both samples. Maximum hydrogen production was achieved by (C21) with 2,387 µmol$H_2$/gcat, while the lowest production was observed for sample (C22) with 1,538 µmol$H_2$/gcat at 8 hours of irradiation. From these results the crystals of potassium hexatitanate exhibited high photocatalytic activity for water splitting and they can be considered as potential photocatalysts for $H_2$ production.

***Keywords:*** $H_2$ production; Water splitting; Photocatalysis; Titanates.

---

## 1. Introduction

Hydrogen production through an environmentally clean process is regarded as a promising energy carrier to achieve a sustainable energy system. Specifically, photocatalytic water splitting using with UV-Vis irradiation has attracted significant interest because such a system is capable of hydrogen production without greenhouse emissions and the use of solar irradiation [1]. Many studies have been carried out to develop highly active photocatalysts, some of the advantages of the photocatalysis are: low processing costs, the evolution of hydrogen and oxygen during the water splitting reaction and suitable small reactor systems for domestic applications [2].

Therefor the development of materials with appropriate band gap, crystallinity and morphological features allow the development of active photocatalysts and efficient processes for hydrogen production in the water splitting reaction. A method of synthesis which is widely used for semiconductor production for this purpose is the molten salts (Flux method). Agreements of synthesis condition and the kinds of molten salts used is posible to obtain nanometric particles or small fibers.

Some examples of photocatalysts used for water splitting or $H_2/O_2$ evolution from aqueous solution with a sacrificial reagent prepared by this route and theoretical research are: $SrTiO_3$ treated with the KCl flux exhibited higher activity by 20 times than the non-flux-treated [3], $La_2Ti_2O_7$ showed $H_2$ evolution from an aqueous methanol solution [4,5] $PbTiO_3$ nanospheres, flakes, hierarchical flowers and thin microbelts show excellent optical absorbance, fine band gap tuning and high surface area [6] $CaZrTi_2O_7$ powder with high crystallinity and 100–300 nm showed a broad photoluminescence band around 580 nm [7,8], $K_3Ta_3Si_2O_{13}$ and $Ba_3Ta_6Si_4O_{26}$ with one-dimensional and linear pillared structure [9], La-doped $Ag_{1.4}K_{0.6}Ta_4O_{11}$ makes use of Ag nanoparticles on the surface to enhance absorption in the visible region [10], $RbLaNb_2O_7$ prepared in platelet-shaped morphologies using a RbCl flux [11], strontium sodium tantalite (SNT) mesocrystals exhibit an outstanding photocatalytic performance due to their nanosteps, high porosity and preferred oriented direction [12] and graphitic carbon nitride (g-$C_3N_4$) showed the enhanced photocatalytic activity for water reduction and oxidation under visible light irradiation with wavelength > 420 nm [13].

So far, there is little research about potassium titanates as photocatalyst, some have been synthesized to assess the reduction of carbón dioxide with mixture of Cu/ZnO under concentrated solar irradiation [14]. However, there is scarce research related to their photocatalytic activity towards the splitting of the water molecule [15]. Therefore, the objective of the present research is the synthesis by flux method, characterization and photocatalytic evaluation of potassium hexatitanate through the water splitting reaction towards the hydrogen production under the visible light irradiation.

## 2. Materials and Methods

*2.1 Synthesis*

In this work, two samples of $K_2Ti_6O_{13}$ were obtained by the method described by Ponce et al., [16]. Mixtures of raw materials (purity > 99%), $TiO_2$ (Sigma-Aldrich), $K_2CO_3$ (Fermont) and $H_3BO_3$ (Fermont) with composition (mol %) $30K_2O$-$60TiO_2$-$10B_2O_3$ were molten in a platinum crucible in an electrical furnace (Lindberg Blue BF51433). The furnace program included heating up to 400°C (to decompose boric acid and avoid losses due to volatilization[17]), which was maintained for 1 hour, followed by heating up to 1250°C and maintaining the temperature for another hour. Each of the melts was poured into water, after cooling, the samples were dried at 80°C in a stove (Lab-line 3475) for three hours and then powdered into an agate mortar (-80 mesh, 180 □m). The remnant flux was dissolved in hot water (95°C) using a ratio of powder: water of 1:20 under magnetic stirring at a rate of 150 rpm for two hours, the solutions were filtered and the powders were dried at 70°C for two hours, after powders were thermally treated to growth fibers at 900 (C21) and 1000 °C (C22) for 2 h, using a heating rate of 10 °C/min.

*2.2 Characterization of materials*

Powdered samples were analyzed by X-ray diffraction (XRD, Rigaku MiniFlex) using Cu-Kα radiation, measurements were performed in a 2θ interval from 5 to 80 ° and using a step size of 0.011 °/sec; likewise, they were attached to a metallic cylinder and coated with graphite and then characterized by scanning electron microscopy (SEM, Philips XL30ESEM) equipped with an X-ray micro-analyzer for energy dispersive spectroscopy (EDS, EDAX Pegasus). Specific surface area (BET, Brunauer–Emmett–Teller) was calculated from the amount of $N_2$ adsorption at 77 K, in a Quantachrome Instrument. For the measurement of the band gap energy a UV–vis Perkin Elmer (Lambda-10) spectrophotometer equipped with an integration sphere for the diffuse reflectance studies was used.

*2.3 Photocatalityc evaluation*

Photocatalytic evaluation of the synthesized samples towards the hydrogen production by water splitting was performed using a 250 W mercurial lamp and 0.2 g of each tungstate sample suspended in 200 mL of DI water and 4mL of methanol in the reactor system as sacrificial agent (2% vol). The suspension was placed inside a quartz photoreactor with a length and diameter of 19 and 5 cm, respectively, then it was hermetically sealed and placed 7 cm away from the 250 W mercury lamp. The photoreactor was kept under constant stirring and irradiated for 8 h [18]. The reaction was monitored by gas chromatography (GC) using a Perkin Elmer Clarus 500 GC.

In order to monitor the photocatalytic reaction, gas samples were taken at regular time intervals using a gas syringe through a septum located at the upper section of the photoreactor, where a small gas headspace was located. A sample under darkness was

taken at the initial concentration and then the sampling took place every hour up to a total of 8 h of continuous irradiation.

## 3. Results and Discussion

### *3.1 X-ray diffraction*

X-ray diffraction patterns for synthetized samples are shown in Figure 1. Accordingly, it was found the single formation of crystalline $K_2Ti_6O_{13}$ phase based on heat treatment at 900 °C (C21) and 1000 °C (C22), as indicated by ICSD Card pattern no. 74-0275. Additionally, samples were analyzed by Scherrer' procedure to investigate about size of crystals (Table 1). Size of crystals is scarcely bigger for samples after heating treatment at 1000 °C, regarding to samples heated at 900 °C, thus indicating the influence of heating process during crystals aggregation and size. A range from 38 to 52 nm was identified for C22 crystal samples, which is similar to that reported in elsewhere [15].

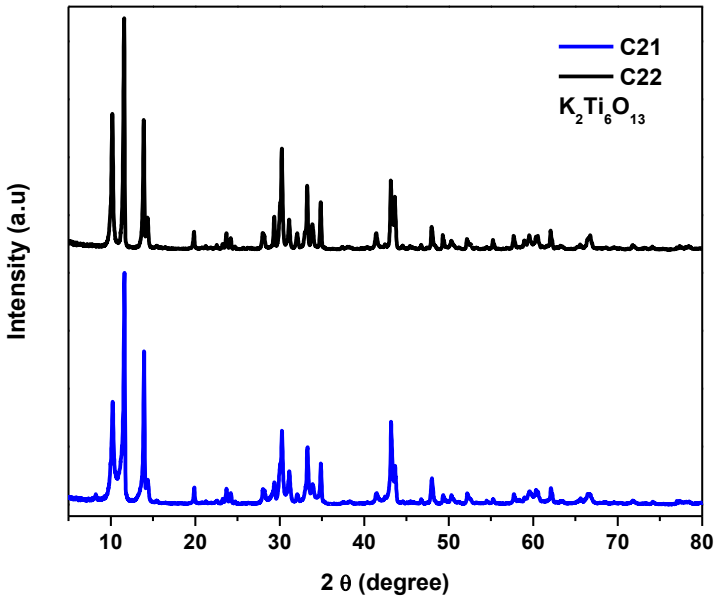


**Fig. 1.** XRD of the synthesized titanate.

### *3.2 BET surface area*

Table 1 shows results concerning to surface area determined for synthetized samples. A surface area for C21 sample was 4.1 $m^2/g$, while 2.3 $m^2/g$ was identified for C22 samples, which was associated to growth of $K_2Ti_6O_{13}$ phase. According to literature, a surface area of 1.08 $m^2/g$. [14] and 1.2 -2.9 [15] has been reported, which is in the same order of magnitude that results reported in Table 1. This finding is highlighted considering necessity of hydrogen production efficiency by water splitting process [2].

**Table 1.** Crystal size, surface area, band gap energy and hydrogen production.

| Sample | Crystallites size (nm) | Surface area ($m^2/g$) | Band Gap Energy (eV) | $H_2$ Production µmols ($H_2/g_{cat}$ ) |
|---|---|---|---|---|
| C21 | 45.8 | 4.1 | 3.28 | 2,387 |
| C22 | 46.5 | 2.3 | 3.23 | 1,538 |

*3.3 UV – Vis spectra*

Figure 2 shows the tungstate diffuse reflectance spectra (UV–Vis) of $K_2Ti_6O_{13}$ samples; results were converted to Kubelka – Munk units [18] through to the following expression:

$$F(R) = (1–R)^2/2R \quad (1)$$

where R is diffuse reflectance and F(R) is the Kubelka – Munk function.

In order to determine the direct band gap energy of the samples, a lineal region from the inflection point of the diffuse reflectance spectrum is considered, which represents the absorption energy above the border. Extrapolating the lineal slope up to the interception of the photonic energy axis (X axis), this point provides the band gap value of the material. The calculated values are presented en Table 1.

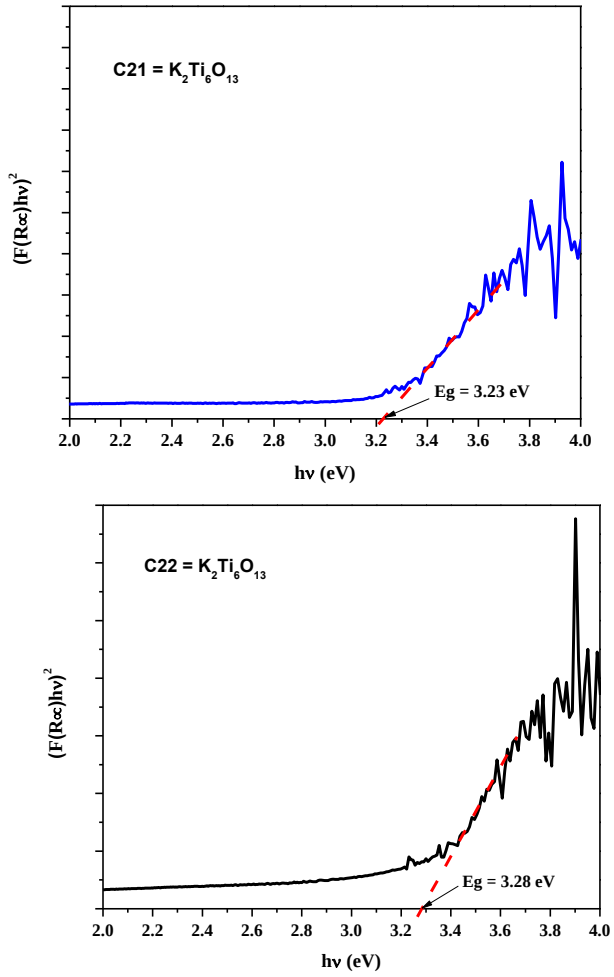


**Fig. 2.** UV–Vis spectra of the synthesized titanate.

Most of band gap energies found for these materials are somewhat bigger than the observed values reported in the literature for similar synthesis techniques. For example, Pt and Cu/ZnO on $K_2Ti_6O_{13}$ has no significant effect on the light absorption behavior of $K_2Ti_6O_{13}$ since is reported to have Eg = 3.6 eV [14], while $K_2Ti_6O_{13}$ exhibited a Eg = 3.5 – 3.6 eV [15], finally α-$K_2Ti_6O_{13}$ show a Eg = 3.3 eV [19] which is very close to the value obtained in the present work.

*3.4 Scanning electron microscopy*

Scanning electron microscopy provided important information related to samples morphology as well as the fiber size and elemental composition present in the samples. Figure 3 shows SEM images of the obtained titanate treated at 900 °. Accordingly, well

defined synthetized fibers are observed (30 µm long, 261-341 thick), while a similar morphology is observed for synthetized samples after 1000 °C treatment involving 12 µm long and 360-530 nm thick parameters (Figure 4). These findings suggest a longitudinal growth decrement, as well as thick increment for >900 °C treated samples. In addition, not any porosity is observed for C21 and C22 samples. Furthermore, the EDS analysis resulted in the expected molar ratios of the crystalline phase for each sample, thus verifying the obtained XRD results.

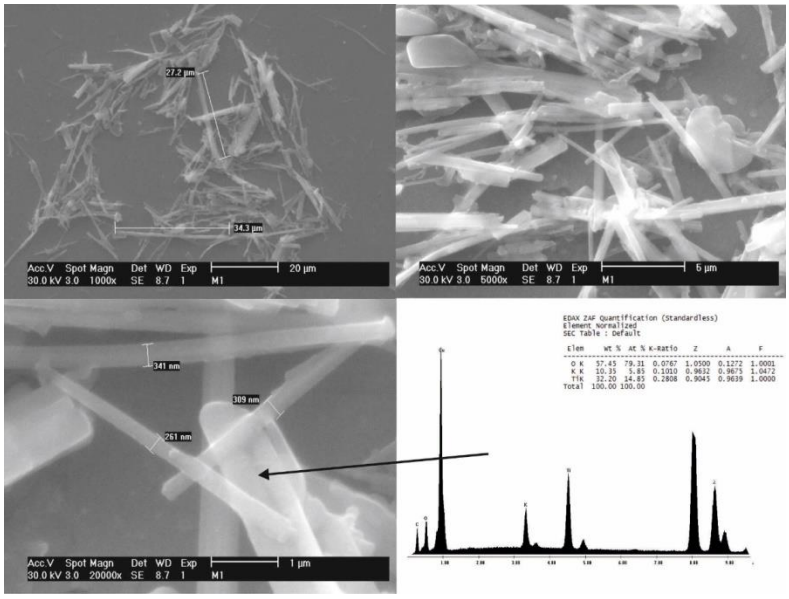

**Fig. 3.** SEM images of the C21 sample.

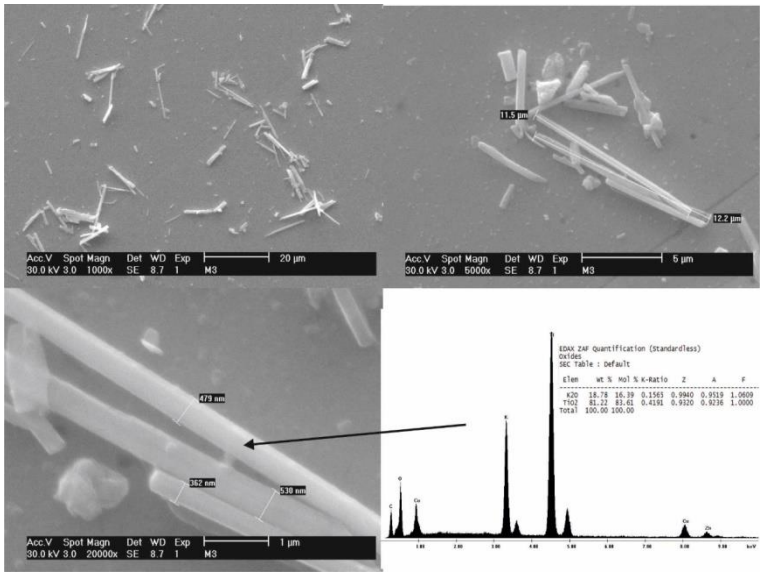

**Fig. 4.** SEM images of the C22 sample.

*3.5 Photocatalytic evaluation*

Photocatalytic analyses for C21 and C22 samples were carried in order to determine hydrogen evolution during 8 h of splitting water molecule reaction and results are shown in Table 1. Highest hydrogen production was determined for C21 sample (2,387 µmoles $H_2$/gcat) while minor rendering was identified for C22 sample (1,538 µmoles $H_2$/gcat). These finding were mainly associated to surface area, shape and size and agglomeration properties for synthetized $K_2Ti_6O_{13}$ phases.

## 4. Conclusion

Potasium titanates fibers were successfully synthetized using an effective synthesis method, followed by calcination at 900 and 1000 °C. The photocatalytic activity of $K_2Ti_6O_{13}$ was investigated. Of the two samples prepared in the present study, C21 sample exhibited the best performance for the photocatalyst with the highest $H_2$ production under visible light spectrum according to experimental results. The synthesis method allowed to obtain the desired crystalline phase. According to the photocatalytic evaluation towards the water splitting of the water molecule, it can be concluded that $K_2Ti_6O_{13}$ is a promising and innovative photocatalytic material that needs to be further studied, especially on the proper surfaces on the fine crystals would provide the independent reaction field for either reductive or oxidative reaction to minimice the reverse reaction to create a more active and efficient photocatalyst toward the $H_2$ production.

## Acknowledgements

The authors acknowledge QFB. Sandra V. Reyes Aguilera for the assistance in this work. Special thanks are given to PROFOCIE 2016 (Programa de Fortalecimiento de la Calidad en Instituciones Educativas), and Laboratorio Nacional de Nanotecnología in Centro de Investigación en Materiales Avanzados, S.C., for their support in funding and infrastructure.

## References

[1] Honda Y, Watanabe M, Hagiwara H, Idaa S, Ishihara T. Inorganic/whole-cell biohybrid photocatalyst for highly efficient hydrogen production from wáter. Appl. Catal., B 2017;210:400–6.

[2] López XA, Fuentes AF, Zaragoza MM, Guillen JAD, Gutiérrez JS, Ortiz AL, Martínez VC. Synthesis, characterization and photocatalytic evaluation of $MWO_4$ (M = Ni, Co, Cu and Mn) tungstates. Int. J. of Hydrogen Energy 2016;41:23312–17.

[3] Kato H, Kobayashi M, Hara M, Kakihana M. Fabrication of $SrTiO_3$ exposing characteristic facets using molten salt flux and improvement of photocatalytic activity for water splitting. Catal. Sci. Technol 2013;3:1733-38.

[4] Hu S, Jia L, Chi B, Pu J, Jian L. Visible light driven (Fe, Cr)-codoped $La_2Ti_2O_7$ photocatalyst for efficient photocatalytic hydrogen production. J. Power Sources 2014;266:304-312.

[5] Wang Q, Hisatomi T, Moriya Y, Maeda K, Domen K. Physicochemical properties and photocatalytic $H_2$ evolution activity of Rh-doped $La_2Ti_2O_7$ prepared by molten salt synthesis. Catal. Sci. Technol 2013;3:2098–2103.

[6] Chandrasekaran S, Kim EJ, Chung JS, Yoo I, Senthilkumar V, Kim YS, Bowen CR, Adamaki V, Hur SH. Structurally tuned lead magnesium titanate perovskite as a photoelectrode material for enhanced photoelectrochemical water splitting. Chem. Eng. J 2017;309:682-690.

[7] Yugo M, Kenji S, Akihiko K. Nanocrystalline $CaZrTi_2O_7$ photocatalyst prepared by a polymerizable complex method in the presence of $Cs_2CO_3$ flux for water splitting. Chem. Lett. 2009;38:180–1.

[8] Liu J, Chen S, Zhu Y. Electronic structures and effective masses of photogenerated carriers of $CaZrTi_2O_7$ photocatalyst: First-principles calculations. Solid State Commun 2012;152:1650–54.

[9] Takayama T, Iwase A, Kudo A. Photocatalytic water splitting over rod-shaped $K_3Ta_3Si_2O_{13}$ and block-shaped $Ba_3Ta_6Si_4O_{26}$ prepared by flux method. Chem. Lett 2015;44:306–8.

[10] Wang R, Zhu Y, Liu G, Lau T. Synthesis of La-doped $Ag_{1.4}K_{0.6}Ta_4O_{11}$ nanocomposites as efficient photocatalysts for hydrogen production and organic pollutants degradation. Appl. Catal., A 2013;467:335-341.

[11] Arney D, Maggard PA. Effect of platelet-shaped surfaces and silver-cation exchange on the photocatalytic hydrogen production of $RbLaNb_2O_7$. ACS Catal 2012;2:1711–17.

[12] Sun J, Chen G, Pei J, Jin R, Wang Q, Guang X. A simple approach to strontium sodium tantalite mesocrystals with ultra-high photocatalytic properties for water splitting. J. Mater. Chem. 2012;22:5609–14.

[13] Zhang J, Zhang M, Zhang G, Wang X. Synthesis of carbon nitride semiconductors in sulfur flux for water photoredox catalysis. ACS Catal 2012;2:940–48.

[14] Guana G, Kida T, Harada T, Isayama M, Yoshida A. Photoreduction of carbon dioxide with water over $K_2Ti_6O_{13}$ photocatalyst combined with Cu/ZnO catalyst under concentrated sunlight. Appl. Catal., A 2003;249:11–8.

[15] Yoshida H, Takeuchi M, Sato M, Zhang L, Teshima T, Chaskar MG. Potassium hexatitanate photocatalysts prepared by a flux method for water splitting. Catal. Today 2014;232:158–164.

[16] Peña PP, Lozano MAG, Bretado MAE, Gómez PD, Sánchez EG, Rivera E, Alexandrova L. Synthesis and characterization of potassium hexatitanato using boric acid as the flux, Ceram. Int 2015;41:10051–56.

[17] Pernice P, Esposito S, Aronne A., Structure and nonisothermal crystallization of glasses in the BaO-$TiO_2$-$B_2O_3$ system, Phys. Chem. Glasses 1998;39:222.

[18] Back S, Wenderich K, Mul G. Synthesis of bimetallic tungstates for finding photocatalytic active compounds with a smaller band gap than tungsten oxide. University of Twente; 2014. Student Theses.

[19] Meng X, Wang D, Liu J, Lin B, Fu Z. Effects of titania different phases on the microstructure and properties of $K_2Ti_6O_{13}$ nanowires. Solid State Commun 2006;137:146–49.

# 1.24 Synthesis and evaluation of the phases $SrFe_2O_4$ and $SrFe_{12}O_{19}$ for Hydrogen production from photocathalytic water spliting.

J. A. Jiménez-Miramontes, M. J. Meléndez-Zaragoza, J. M. Salinas-Gutiérrez, A. López-Ortiz, V. Collins-Martínez

Centro de Investigación en Materiales Avanzados, S.C. Chihuahua, Chih. México

* Tel: +52 6144391129; e-mail: virginia.collins@cimav.edu.mx

## ABSTRACT

The use of materials whose properties are suitable for hydrogen production by the water splitting via photocatalysis is one of the most promising strategies to solve the current energy demand. These materials must be photoactive under sunlight, inexpensive, eco-friendly and have a band gap that fulfill the water dissociation potential of 1.23 eV. Ferrite systems present adequate optical properties to be used in this type of process, so strontium ferrite was synthesized in two of its most known phases to evaluate its performance in the evolution of hydrogen by water splitting under visible light irradiation. The strontium ferrite in its spinel phase $SrFe_2O_4$ and the hexagonal phase $SrFe_{12}O_{19}$ have active band gaps in the visible light spectrum of ~ 2 eV. Synthesis of the two phases from nitrates were achieved by using the modified Pechini's method at temperatures of 700-900 °C. The characterization of the materials consisted in the use of different techniques such as X-Ray Diffraction (XRD), Scanning Electron Microscopy (SEM) and UV-vis spectroscopy. The diffractograms obtained by XRD indicate the presence of pure phases of the strontium ferrite and by applying the Scherrer's equation crystallite sizesof approximately 15 and 30 nm for the spinel and hexagonal phases were obtained, respectively. The two phases have a morphology of sintered irregular polygons with a BET surface area of 18 $m^2/g$ for the spinel and 14 $m^2/g$ for the hexagonal and present a band gap of 1.77 eV and 1.82 eV, respectively.The photocatalytic evaluation was performed by monitoring the evolution of hydrogen through gas chromatography, showing the best performance for the spinel phase of 730 µmol $H_2$/gcat·h.

***Keywords:*** *Water splitting; Photocatalysis; $SrFe_2O_4$; $SrFe_{12}O_{19}$*

## 1. Introduction

There is a considerable need to find environmentally friendly alternative energy sources to supply the high-energy demand covered nowadays by fossil fuels. It is well

known that energy sources coming from oil and its derivatives cause strong consequences on the environment with an alarming increase of $CO_2$ amounts produced by factories, cars, etc. as well as many other pollutants that are harmful to human health. The remarkable climate change, among many other concerns, is one of the main reasons that aims to find new solutions to this problem.

One of the most promising alternatives is the solar energy. In a year, earth absorbs 3,850,000 EJ (exajoules) of solar radiation in comparison with the 474 EJ consumed. This suggests that an efficient use of this source could provide enough clean and renewable energy to be used indefinitely[1],in order to substitute the aforementioned fossil fuels. Hydrogen production throughout photocatalytic water splitting is a viable technology, since greenhouse gases are not produced, however, this remains as mayor technological challenge.

Photocatalytic water splitting is a chemical reaction produced by the interaction of a semiconductor material with the electromagnetic radiation. This process begins with the material irradiation through a photon with enough energy to promote an electron from its valence band (VB) to the conduction band (CB), thus generating an electron – hole pair ($e^-$ -$h^+$). The difference between these energetic levels is known as band gap ($E_g$) and the photon energy must be equal or greater than the $E_g$ value. The electron – hole pair is responsible forthe oxidation or reduction of the chemical species on the semiconductor surface, unless a recombination process that may occur, where the pair returns to its original state, thus releasing energy as light or heat.[2]

In the water splitting process, electrons reduce the water molecule to produce hydrogen, while holes oxidize it to form oxygen. Thus, to achieve the separation, the CB level must be more negative than the redox potential of the $H^+/H_2$ electrode and the VB level be more positive than the redox potential of the $O_2/H_2O$ electrode. So the band gap of the photocatalyst must be equal or greater than 1.23 eV [1,3]

The search of a photocatalytic semiconductor with an appropriate $E_g$ for water splitting has been an important research topic, where semiconductor materials with high band gap energy (~3.0 eV) are typical to be found [4]. The UV light spectrum comprises near 5% of the solar light, while another 46% corresponds to visible light. Therefore, an efficient and visible light active photocatalyst, must have a band gap energy between 1.1 to 3.0 eV (1100 nm to 400 nm respectively) taking into account the 1.23 eV over potential corresponding to a 237 KJ/mol Gibbs free energy. It is difficult for this reaction to occurthermodynamically by itself, and consequently, band gap values must be between 1.6 and 2.5 eV according to reported results.[1,5]

One of the most promising candidates as photocatalysts are ferrite systems for being environmentally friendly, in addition to generally present a band gap range suitably low to be photocatalytically active under visible light irradiation. Spinel ferrites ($MFe_2O_4$) have the capacity to absorb more visible light than other similar catalysts because of their stable and unique structural properties. This work, is aimed to study strontium ferrite as a photocatalyst for the production of hydrogen from the splitting of the water molecule. The $SrFe_2O_4$ spinel phase of strontium ferrite has adequate optical properties, although there

are no relevant studies for this application, even though different phases of this ferrite have been used as catalysts in organic oxidation and degradation processes[5–8].

Strontium ferrite such as spinel ($SrFe_2O_4$) and hexagonal ($SrFe_{12}O_{19}$) phases have interesting optical properties such as low band gap energies within the visible spectrum. These systems can be formed at very high temperatures (700-1200°C) with band gaps obtained from 2.1 eV and 1.8 eV for each of the strontium phases.[5,9]

Typical synthesis methods for ferrites include: controlled precipitation, combustion, SSR (solid state reaction), sol-gel, ball milling, hydrothermal and Pechini [10–12]. Each method presents its advantages and disadvantages with respect to one another, for example, the SSR method, although very simple and cheap for this type of preparation, presents the disadvantage of employing very high reaction temperatures and longtimes, which causes low surface area and photocatalytic activity materials [13].

A very suitable method to obtain nanoparticles and thin films, very important features for a good photocatalyst, is the Pechini's procedure [14]proving to be a cheap and easy to perform method, in addition to present good physical, optical and photocatalytic results[12].The Pechini's method, known as the citrate or modified Pechini's method, is a process to oxidize materials from the mixture of an aqueous solution containing the cations, in stoichiometric proportions, into another solution of an α-hydrocarboxylic acid such as citric acid and polyhydric alcohol such as ethylene glycol often in a 1:1 ratio. This solution is homogenized under constant stirring and then evaporated to obtain a rigid cross-linked polymer, which prevents segregation of the cations.

Citric acid has the ability to chelate the metal ions and homogeneously distributing them, while by the addition of ethylene glycol results in a polystyrifaction, thus forming a polymer network. By heat treatment, this polymer is converted into a homogeneous oxidized powder to obtain the desired material[15].

The main objective in this study is the synthesis of $SrFe_2O_4$ and $SrFe_{12}O_{19}$nanoparticles by the modified Pechini's method to determine their efficiency in the evolution of hydrogen from a photocatalytic process of the water molecule separation, as well as to correlate the textural and optical properties of the phases with their performance.

## 2. Materials and Methods

*Synthesis process.*

In order to obtain different phases of the strontium ferrite, $Fe(NO_3)_3 \cdot 9H_2O$ and $Sr(NO_3)_2$ Sigma-Aldrich® were used as precursors. The synthesis used was the modified Pechini's Method using citric acid as the chelating agent and ethylene glycol for the polymer network (Sigma-Aldrich®). The ratio of Citric acid and metals depends on the valences of these, being 1:3 with $Fe^{3+}$ and 2:1 with $Sr^{2+}$. The molar ratio for AC-EG was

1:1. The calculated amount of ethylene glycol was heated at 70°C under continuous stirring until evaporation was observed. The citric acid dissolved in distilled water is then added, maintaining the same conditions. The required amounts of nitrates were diluted in distilled water to homogenize and then added to the CA-EG gel by raising the temperature to 80°C. Once part of the water and the nitrates are evaporated, a viscous solution is obtained, which is allowed to dry until a polymer resin is produced. This resin is then calcined at different temperatures for each phase to obtain a powder.

*Characterization*

In order to determinate the calcination temperature, resin thermal decomposition was performed in a thermogravimetric analyzer equipment TA Q500. The characterization of the material consisted of its analysis in a Panalytical XpertPRO X-ray diffractometer with copper radiation (αCu). For the study of the morphology and particle size an analysis by Field Emission scanning electron microscopy was carried out on aJEM-2200FSmicroscope. The determination of the surface area was by nitrogen physisorptionthrough BET method (Brunauer-Emmett-Teller) in aQuantachrome model NOVA1000equipment. To obtain the absorption spectra and diffuse reflectance of the powders, a Visible Evolution 220 Thermo UV spectrophotometer with integration sphere was used. The same procedure was performed for the two phases.

*Photocatalytic activityevaluation*

The evaluation of the phases as photocatalysts was performed by measuring the evolution of hydrogen with the gas chromatography technique in a Clarus 500 Perkin Elmer Chromatograph with a TCD (Thermal Conductivity Detector) using nitrogen as the carrier gas. The system used to carry out the separation of the molecule from the water consisted of a reactor equipped with a quartz tube. Inside the reactor a magnetic stirrer is placed, 200 ml of distilled water with a 4% methanol solution as sacrificial agent and 0.2 grams of sample for each evaluation. The reactor is kept under constant stirring for a period of 8 hours by gas sampling every hour. The system is maintained irradiated by a 250 W mercury vapor lamp that emits light in the visible range.

## 3. Results and Discussion

*Thermogravimetric Analysis*

The obtained material is a mixture of the metal ions of strontium and iron with some organic compounds, so a thermogravimetric analysis is performed to know the suitable temperature to decompose organic compounds present to obtain the expected oxidized phases. Figure 1 shows the thermograms of each phase, with the weight losses ranging between 80-90 % of the initial weight due to the combustion of organics at temperatures around 400-600°C. According to the data of the thermograms and the information reported in the literature, temperatures required to obtain organic-free oxidized phases are very high, in the order of 700-1200 °C. So that for each one of them an optimum temperature was used to achieve the crystallinity, being of 400°C and 700°C for the $SrFe_2O_4$ in an interval of 2 hours at each temperature for a total time of 4 hours and in the $SrFe_{12}O_{19}$phase was 900°C for 2 hours, enough time to obtain a crystalline phase.

*X-ray diffraction*

The diffractograms obtained from each material were indexed using the ICDD database (*International Center for Diffraction Data*) and compared by means of the program MATCH, verifying that the resulting phases were the desired ones. Figure 2 shows the diffractograms compared with the ICDD cards where the peaks obtained are indexed and where it is observed that there is no sign of impurities, indicating that pure phases were obtained. While, in the spinel phase broad peaks are observed, thus suggesting small crystallite sizes. Otherwise, the hexagonal phase, present very intense and sharp peaks, indicating the presence of possibly bigger crystal sizesthan the spinel phase.

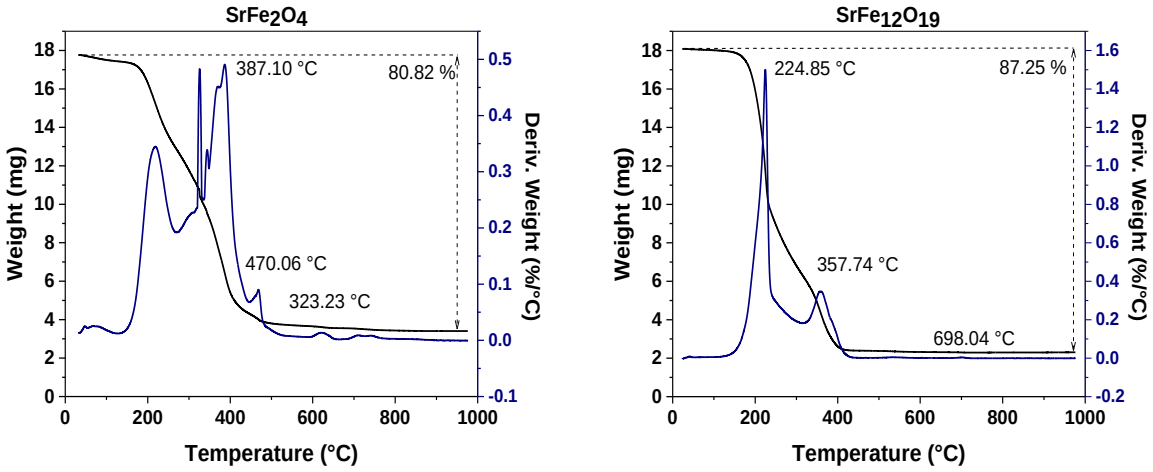


Figure 1.***Thermograms of each strontium ferrite sample prior to calcination.***

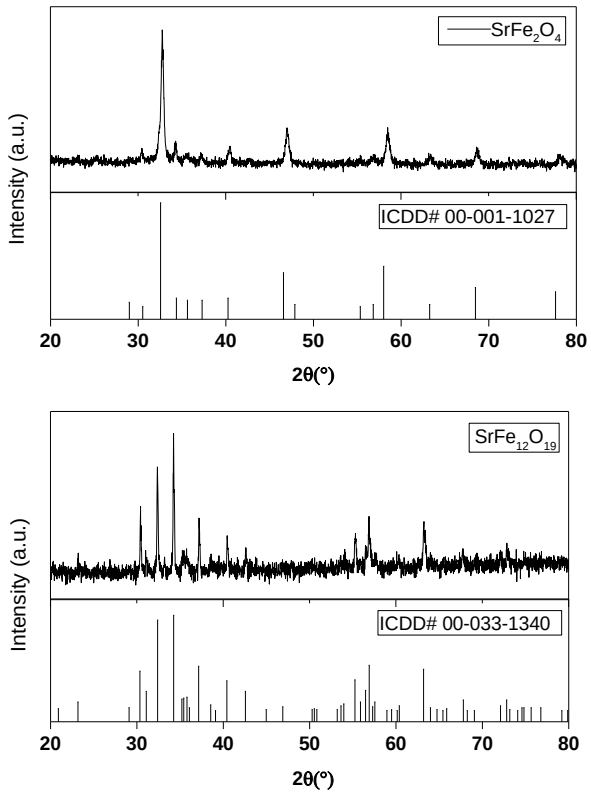


**Figure 2**. Diffractograms of the synthesized phases indexed with ICDD patterns.

Based on the diffractogramsfound from each phase the crystallite size using the Scherrer equationwas calculated by:

$$D = \frac{0.94\lambda}{\beta\cos(\theta)} \qquad (1)$$

where λ is the wavelength of the radiation from the copper lamp of the diffractometer (0,154 nm αCu), β is the Full Width at Half Maximum (FHWM) in radians, θ is the angle of the peak with greatest intensity in radians, and D is the crystallite size calculated in nanometers. Table 1 shows the approximate size obtained by equation (2) in each phase, where it can be seen that a crystallite size of the spinel phase is smaller in comparison with the hexagonal phase. From the analysis of Table 1, it can be inferred that the difference in the size of the spinel crystal with respect to the hexagonal was expected, since the temperature used in the latter was considerably higher than that of the spinel, thus favoring crystalgrowth of this phase.

Table 1.***Approximate crystallite size calculated for the strontium ferrite phases.***

| CrystalSize | |
|---|---|
| Phase | D (nm) |
| $SrFe_2O_4$ | 15 |
| $SrFe_{12}O_{19}$ | 30 |

*Scanning electron microscopy*

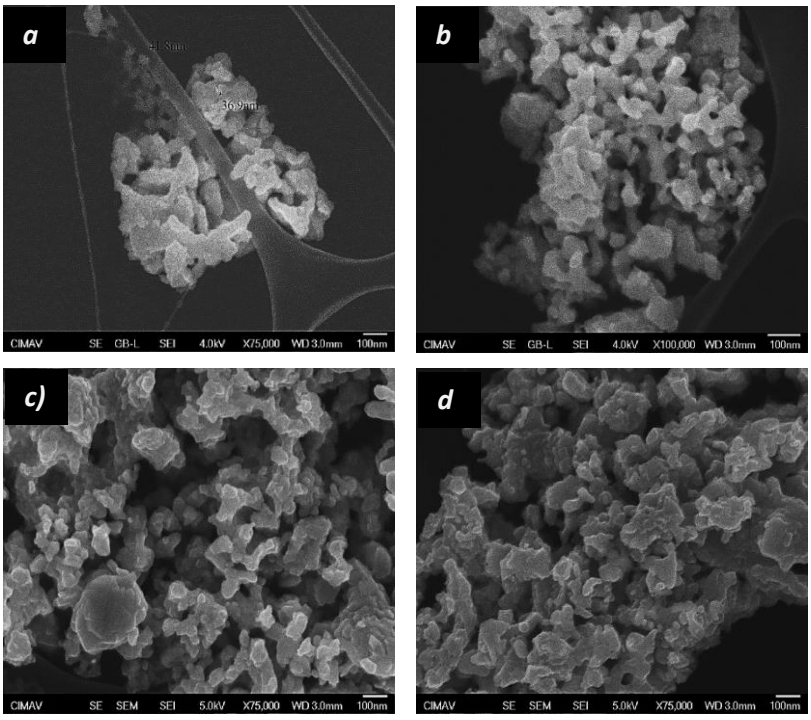


Figure 3.***FE-SEM micrographs for samples: $SrFe_2O_4$ a) and b) and $SrFe_{12}O_{19}$ c) and d).***

An analysis of the particle size and shape of each phase was carried out with a field emission scanning electron microscope, where it was very remarkable the evidence of a sintering process associated with the times and high temperatures employed for the crystallization of the samples. These sintering did not allow to observe a defined particle

morphology in the spinel and hexagonal phases, suggesting that irregular polygonal forms were obtained.

In Figure 3 c) and d) images of the hexagonal phase are found, where clearly particles with a size greater than those of the spinel phasecan be observed, with an average size of 70 nm. It can also be appreciated the formation of agglomerates of greater sizes reaching nearly 300 nm. As previously mentioned, these results were expected due to the high temperatures used to obtain these phases. Although some particles with nanometric sizes were obtained the sintering effect over these particles may affect the performance of the materials

*Surface Area*

For the analysis of the surface area, the method BET was used [16]. Table 2 presents the surface area obtained from the adsorption isotherms of each material, whose values are between 4 and 20 $m^2/g$. These relatively small areas can be explained by the high grade of sintering in the sample and this is presumably due to the effect of particle size, since the smaller the size, the greater its surface area.

Table 2.***BET surface area of the strontium ferrite synthesized samples.***

| Phase | A ($m^2/g$) |
|---|---|
| $SrFe_2O_4$ | 18 |
| $SrFe_{12}O_{19}$ | 14 |

Figure 4 shows BET isotherms obtained from each material. These isotherms can be classified as type III, since they have low interaction between the adsorbate and adsorbent, where in addition the lack of hysteresis indicates non-porous materials.

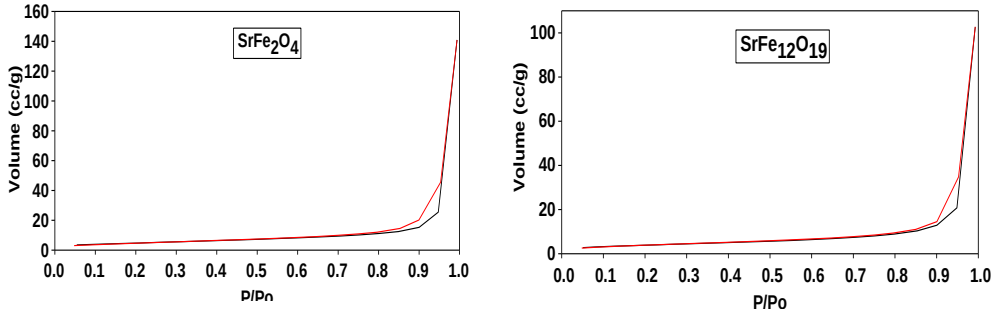


Figure 4.***BET isotherms for the synthesized strontium ferrites.***

*Uv-Visible Spectroscopy*

An analysis of UV-Vis spectroscopywas performed on the samplesto know in which part of the electromagnetic spectrum absorblight. The diffuse reflectance spectrais employed to determine the band gap of each material by using the Kubelka Munk method. Reflectance *R,* obtained from each phase is substituted in *(3)* the Kubelka Munk equation [17]:

$$f(R) = \frac{(1-R)2}{2R}$$

where *f(R)* is multiplied by *hv*, thus obtaining the graphs in figure 5. In the "y" axis is $(f(R)*hv)^n$ where n is 2 for direct band gap semiconductors and ½ for indirect materials. A band gap of approximately 1.77 eV and 1.74 eV were obtained for the $SrFe_2O_4$ and $SrFe_{12}O_{19}$ phases, respectively.

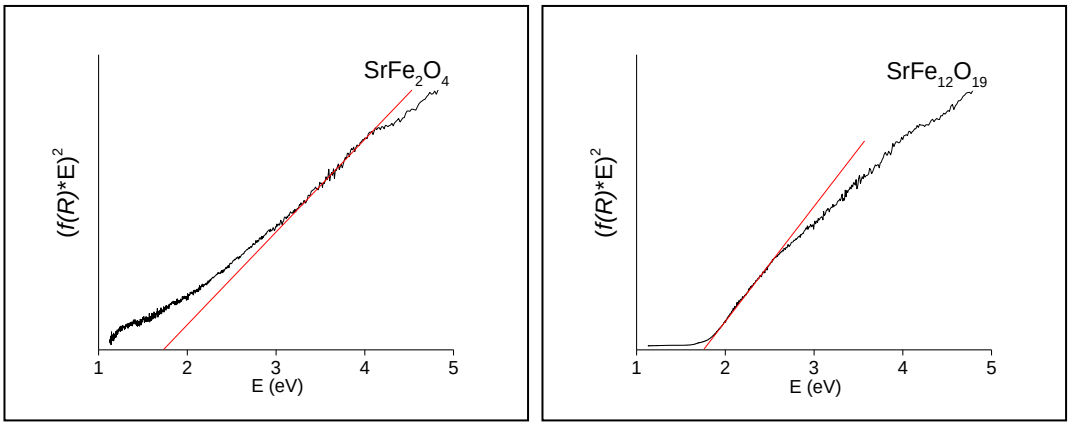


Figure 5.***Calculated band gap for the strontium ferrite phases based on the Kubelka Munk method.***

Table 3 presents a comparison of the obtained band gap by the synthesis method of this work with respect to values reported in the literature. Here, it can be observed that there is a difference of 0.33 eV forthe spinel phase and 0.11 eV for the hexagonal that may be due to the size of the particles obtained, as well as to changes in the structure and defects caused by the synthesis method, as reported by Mohanta and collaborators.

**Table 3.**Band gap energies of the strontium ferrite phases compared to those reported in the literature.

| Band Gap | | |
|---|---|---|
| Phase | Obtained (eV) | Reported (eV) |
| $SrFe_2O_4$ | 1.77 | 2.1 [5] |
| $SrFe_{12}O_{19}$ | 1.74 | 1.88 [9] |

*Photocatalytic evaluation*

Hydrogen evolution within the reactor was measured every hour for a total time of 8 hours resulting in a production of 5837 µmol $H_2/g_{cat}$ for$SrFe_2O_4$ and 34 µmol $H_2/g_{cat}$ for$SrFe_{12}O_{19}$ (Figure 6). Table 4 presents the photocatalytic performance of the two phases of strontium ferrite for hydrogen generation per mass and surface area of the catalyst, also in production per hour.

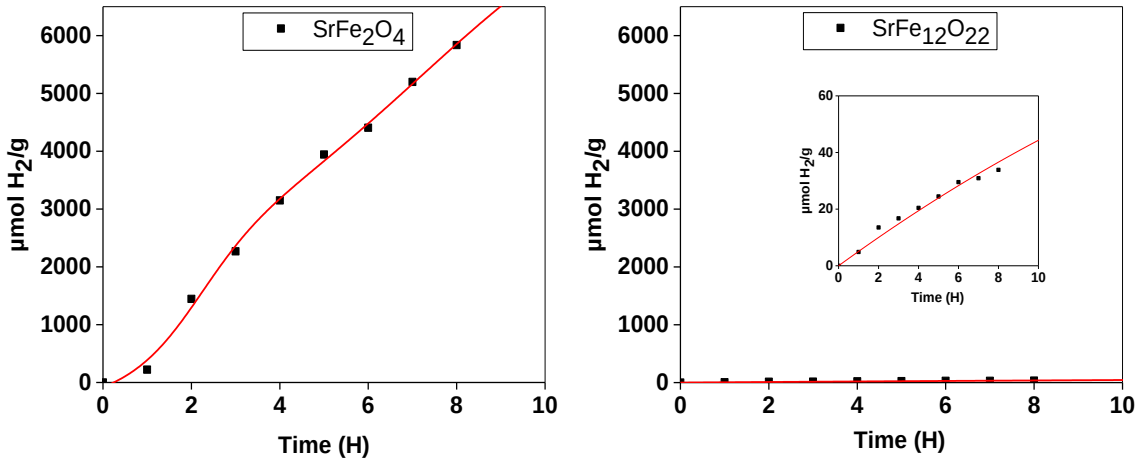


Figure 6.***Photocatalytic evaluation of the strontium ferrite phases towards the $H_2$ production.***

In this table it is very remarkable the low performance presented by the hexagonal ferrite with respect to the spinel phase. This can be explained by the band gap potential of its conduction band, which although falls within the visible range spectrum, it does not fulfill the potential levels required for the separation of the water molecule[9]. Vijayaraghavan et al. reported that the potential of the conduction band of the spinel phase is above the $H_2$potential, thus achieving a fundamental requirement for the separation of the water molecule. While the potential of the hexagonal ferrite falls below the level required and

although it is a very small value, it considerably impactsover the photocatalytic performance of this strontium phase[9].

**Table 4.** Photocatalytic performance of the strontium ferrite phases with respect to the evaluation time and surface area.

Phase evaluation

| Phase | µmol $H_2/g_{cat}$ in 8 hrs | µmol $H_2/m^2$ | µmol $H_2/g_{cat}$·h |
|---|---|---|---|
| $SrFe_2O_4$ | 5837 | 324 | 730 |
| $SrFe_{12}O_{19}$ | 34 | 2 | 4 |

Up to date, there are no studies where the performance of these phases has been reported for this application. Therefore, the obtained results in this work are compared with some studies that report the photocatalytic performance towards the hydrogen production of well-known photocatalysts, which were evaluated under similar conditions. A comparison in µmol $H_2/g_{cat}$·hproduction is shown in table 5, where it is observed that the performance of the spinel phase allows to consider this ferrite system as a potential candidate to be further studied as a water splitting photocatalysts under visible light irradiation.

**Table 5.** Photocatalysts performance comparison of the strontium ferrite phases obtained in thiswork with some known materials for $H_2$ production by water splitting.

| Photocatalysts Performance Comparison | | | |
|---|---|---|---|
| Phase | µmol $H_2/g$·h | Light source (W) | Reference |
| $SrFe_2O_4$ | 730 | 250 Hg | Thiswork |
| $TiO_2$ | 68 | 400 Hg | [18] |
| $TiO_2$ –ZnO (Ti/Zn = 10) | 203 | 400 Hg | [18] |
| 0.1 wt% Pt/$TiO_2$ –ZnO | 1789 | 400 Hg | [18] |
| Ni–N–$TiO_2$ | 490 | 400 Hg | [3] |

## 4. Conclusion

- Strontium ferrite phases were synthesized by the modified Pechini's method, obtaining pure $SrFe_2O_4$ y$SrFe_{12}O_{19}$phases.
- The two strontium ferrite synthesized phases are nanocrystalline, with particles sizes of approximately 40 and ~70 nm for the spinel and hexagonal phase, respectively.
- Synthesized materials were nonporous and shown the presence of sintered agglomerates and consequently smaller surface areas than 20 $m^2$/g.
- The $SrFe_2O_4$ y$SrFe_{12}O_{19}$ phases present a band gap of 1.77 and 1.74 eV, respectively, which are suitable for the process of water splitting under visible light.
- Performance for the hydrogen generation per hour and catalyst mass of the ferrites was 730 µmol $H_2/g_{cat}$·hfor the spinel phase and 4 µmol $H_2/g_{cat}$·hfor the hexagonal phase.

## Acknowledgements

The authors acknowledge M.Sc. Ernesto Guerrero Lestarjette, M. Sc. Karla Campos Venegas, Eng. Wilber Antunez Flores, and Eng. Luis de la Torre Saenz for their contributions to the XRD, SEM, BET, results. Special thanks are given to Laboratorio Nacional de Nanotecnología in Centro de InvestigaciónenMaterialesAvanzados, S. C., for their support in the use of the facilities.

## References

[1] Martin DJ. Investigation into High Efficiency Visible Light Photocatalysts for Water Reduction and Oxidation. Springer T. Switzerland: Springer International Publishing; 2015. doi:10.1007/978-3-319-18488-3.

[2] Liao C, Huang C, Wu JCS. Hydrogen Production from Semiconductor-based Photocatalysis via Water Splitting. Catalysts 2012;2:490–516. doi:10.3390/catal2040490.

[3] Selcuk MZ, Boroglu MS, Boz I. Hydrogen production by photocatalytic water-splitting using nitrogen and metal co-doped $TiO_2$ powder photocatalyst. React Kinet Mech Catal 2012;106:313–24. doi:10.1007/s11144-012-0434-4.

[4] Acar C, Dincer I, Zamfirescu C. A review on selected heterogeneous photocatalysts for hydrogen production. Int J Energy Res 2014;38:1903–1920. doi:10.1002/er.

[5] Vijayaraghavan T, Suriyaraj SP, Selvakumar R, Venkateswaran R, Ashok A. Rapid and efficient visible light photocatalytic dye degradation using $AFe_2O_4$ (A = Ba, Ca and Sr) complex oxides. Mater Sci Eng B 2016;210:43–50. doi:10.1016/j.mseb.2016.04.005.

[6] Jia T, Yan S, Liu Z. Preparation and Catalytic Properties of $SrFe_2O_4$ in Selective Oxidation. Adv Mater Res 2012:751–4. doi:10.4028/www.scientific.net/AMR.396-

398.751.

[7] Pardeshi SK, Pawar RY. $SrFe_2O_4$ complex oxide an effective and environmentally benign catalyst for selective oxidation of styrene. J Mol Catal A Chem 2011;334:35–43. doi:10.1016/j.molcata.2010.10.020.

[8] Mohanta O, Singhbabu YN, Giri SK, Dadhich D, Das NN, Sahu RK. Degradation of Congo red pollutants using microwave derived $SrFe_{12}O_{19}$: An efficient magnetic photocatalyst under visible light. J Alloys Compd 2013;564:78–83. doi:10.1016/j.jallcom.2013.02.074.

[9] Dom R, Borse PH, Cho CR, Lee JS, Yu SM, Yoon JH, et al. Synthesis of $SrFe_{12}O_{19}$ and $Sr_7Fe_{10}O_{22}$ systems for visible light photocatalytic studies. J Ceram Process Res 2012;13:451–6.

[10] González G, Carrillo FR, Zamarripa MG, Parga JR, Galván DH. Síntesis de Ferrita de Estroncio a partir de $SrCO_3$ y Polvo Precursor Magnético. 2010.

[11] Yourdkhani A, Seyyed Ebrahimi SA, Koohdar HR. Preparation of strontium hexaferrite nano-crystalline powder by carbon monoxide heat treatment and re-calcination from conventionally synthesized powder. J Alloys Compd 2009;470:561–4. doi:10.1016/j.jallcom.2008.03.021.

[12] Solarte NJ, Ramírez AE, Villaquirán CF, Tirado-Mejía. L, Gaona S. Síntesis de Polvos Cerámicos de Hexaferrita de Estroncio por los Métodos Pechini y Combustión. Rev Lat Met Mat 2015;35:276–84.

[13] Chen W, Liu H, Li X, Liu S, Gao L, Mao L, et al. Polymerizable complex synthesis of $SrTiO_3$:(Cr/Ta) photocatalysts to improve photocatalytic water splitting activity under visible light. Appl Catal B Environ 2016;192:145–51. doi:10.1016/j.apcatb.2016.03.057.

[14] Masoudpanah SM, Seyyed Ebrahimi SA. Structure and magnetic properties of nanocrystalline $SrFe_{12}O_{19}$ thin films synthesized by the Pechini method. J Magn Magn Mater 2013;343:128–33. doi:10.1016/j.jmmm.2013.05.016.

[15] Olav T, Sunde L, Grande T, Einarsrud M. Handbook of Sol-Gel Science and Technology. Handb. Sol-Gel Sci. Technol., Switzerland: Springer International Publishing; 2016, p. 1–30. doi:10.1007/978-3-319-19454-7.

[16] Brunauer S, Emmett PH, Teller E. Adsorption of Gases in Multimolecular Layers. J Am Chem Soc 1938;60:309–19. doi:10.1021/ja01269a023.

[17] Pike Technologies. Diffuse Reflectance – Theory and Applications. Appl Note 2011:2. doi:10.1016/j.soilbio.2011.02.019.

[18] Xie MY, Su KY, Peng XY, Wu RJ, Chavali M, Chang WC. Hydrogen production by photocatalytic water-splitting on Pt-doped $_{TiO2}$-ZnO under visible light. J Taiwan Inst Chem Eng 2017;70:161–7. doi:10.1016/j.jtice.2016.10.034.

# 1.25 Type and moment of injection of the mixture Hydrogen-Gasoline in an internal combustion engine

R.A. Vega Parra, D. Alemán Meza, G.A. Radovich Quiroz

[1]Department of Mechanical & Automotive Engineering, Universidad Politécnica de Chihuahua, Av. Téofilo Borunda No. 13200 Col. Labor de Terrazas, Chihuahua, Chih., 31220, México

* Corresponding author: +52 (614) 2142424, dania.aleman@gmail.com

## ABSTRACT

In 1966 was the origin of the idea that an Internal Combustion Engine (ICE) could be thrust by Hydrogen now that it can substitute the carbohydrates that are used to fuel ICE. The present investigation wishes study that hydrogen can be mixed with gasoline to fuel ICEs, increasing its efficiency and reducing contaminations to the atmosphere. This work consists of various analyses comparing the use of gasoline, of Hydrogenand of a mixture of Hydrogen-Gasoline to determine the type and moment of injection of the selected fuel, also for timing advance and delays calculations of both admission and exhaust valves for the Hydrogen injection.

***Keywords:*** injection; hydrogen-gasoline; ICE

## 1. Introduction

### Review: Internal combustion engines (CIE): injection

Speaking of internal combustion engines (ICE), with pulse injection, the elevation of the needle valve from its seat is constant, making the pressure in the flute is also constant. The amount of fuel injected depends only on the amount of time that the voltage is applied by the control unit to the injector, this time it is knew as Pulse Width Modulated (PWM) and can vary between 2 and 1 milliseconds. The injector time is ~ 1 millisecond and describes its duration in opening[1].

The voltage of the injectors is characterized by the pulse width which will have a maximum duration equivalent of the pulse period, which, in turn, depends on the engines

RPM. The normal pulse period for standard pulse systems in two-stroke engines is equivalent to two crankshaft revolutions.

The manifold pressure and the pulse of the injector dependon the variation of the position of the throttle. When the maximum manifold pressure corresponding to the maximum acceleration is reached, the injector must remain open for a certain time to supply a maxim load, or maximum torque per setting[2].

Increasing engine RPM decreases the time available for injection and the injector takes longer a longer portion of time available, increasing engine speed, increases. It's possible to reach a point where the engine cycle time equals the time needed by the injector to release the total fuel required. However, the maximum duration of the pulse must not be greater than the "Duty Cycle", which is the percentage ratio of the time required by the injector and the time available. The duration of the pulse oscillates between ½ and 2/3 of the maximum RPM.

The determination of the fuel fed moment by the injector in relation to the engine operating cycle is defined by the design of the injector control circuit and the electronic control module (ECM) programming. If the injectors are activated according to the positioning angle of the crankshaft, it's called a synchronous injection, the three main types of synchronous injection being the simultaneous, grouped or sequential, where the voltage is supplied to the injectors from the ignition switch or relay Main EFI and the injector's operation controller ECM[3].

Asynchronous injection occurs when the ECM needs to increase fuel injection in the engine (at start and acceleration) regardless of the crankshaft position angle and by injecting all cylinders at the same time.

In addition, the amount of fuel injected depends on the pressure of the fuel system and the duration/ pulse width or time, the injector is turned on. The fuel pressure of the system is controlled by the pressure regulator. The injector time is controlled by the ECM. Cold start required the maximum pulse width, which depends on the load and the temperature of the engine coolant[4].

During startup, the battery voltage is low, causing the injector valve to rise slowly; however, the ECM corrects this by increasing the duration of the injection. When the ECM receives the signal from the crankshaft position sensor (CKP), all injectors are activated simultaneously, ensuring sufficient fuel to start the engine, where the total fuel injection time is determined by the duration of the base injection, as well as injection and voltage corrections.

Another aspect of paramount importance with the characteristic angles in the engine[5,6], as well as the angle of rotation of the crankshaft:

- The angle formed by the crankshaft arm with the vertical axis of the cylinder ($\alpha$), where $\alpha = 0$at the top dead center (TDC) corresponding to the valve crossing; $\alpha = \pi$in the bottom dead center (BTC) after admission; $\alpha = \pi$ at the top dead center (TDC) during combustion.

- Advance to the Intake Aperture ($\alpha_{AAA}$), that is to say that the angle that rotates the crankshaft from the start of the intake valve until it passes through the BTC.
- Admission Closure Delay ($\alpha_{RCA}$) - angle at which the crankshaft rotates as it passes through the TDC until the intake valve is closed. Therefore, the admission interval is$-\alpha_{AAA} \leq \alpha \leq (\pi + \alpha_{RCA})$.
- Ignition Advancement ($\alpha_{AI}$) - Angle corresponding to the start of the combustion reaction until the crankshaft passes through the second BTC of the cycle, the compression being found in$(\pi + \alpha_{RCA}) \leq \alpha \leq (\pi - \alpha_{AI})$.
- Advance to the exhaust opening ($\alpha_{AAE}$) - Crankshaft Angle rotation from the exhaust valve until it passes through the BTC, where combustion and expansion occurs when$(\pi - \alpha_{AI}) \leq \alpha \leq (3\pi - \alpha_{AAE})$.
- Exhaust closing delay($\alpha_{RCE}$) - angle from the PMS to the complete closing of the exhaust valve: $(3\pi - \alpha_{AAE}) \leq \alpha \leq (4\pi + \alpha_{RCE})$, or $\alpha = \alpha_{RCE}$ of the next cycle.

The above can be plotted by two circumferences showing the complete cycle of a four-stroke engine or two turns per cycle (Fig. 1), where the outer circumference represents the first cycle turn and contains the intake, compression and part of combustion; the interior is the second round, where combustion ends, as well as expansion and exhaust. The first section of the outer circumference and the last of the interior are represented by the same color because they are the valve cross, when admission and exhaust are open.

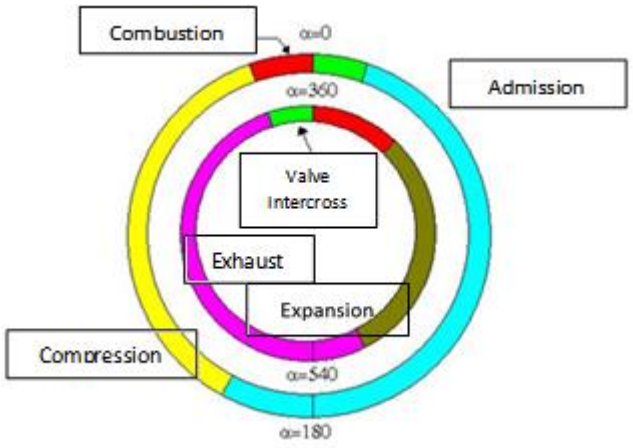


**Fig. 1.**Complete cycle of a four-stroke engine

The advance and delay time of a CIE are the following[7,8,9]:

- Intake: The intake valve opens before the piston starts to move from the BTC to the TDC, it opens while the piston rises and the exhaust valve remains open, cleaning the combustion chamber of the already burned gases and obtaining that the air is moving inside the combustion chamber during the displacement of the BTC to the TDC.
- Compression: The piston rises and the intake and exhaust valves are closed, decreasing the remaining volume and increasing the pressure and temperature, where the high pressure values will favor a good performance, without being excessive and avoiding the detonation of the mixture that would cause considerable damage to the engine by causing a force contrary to the piston's ascent.
- Explosion: It starts with the jump of the spark of the spark plug and the explosion of the mixture, a moment that does not coincide with the BTC, because it is made before, since if it were realized in the BTC when the mixture explodes, already would have crossed part of the down stroke of the piston, wasting the force provided by the explosion.
- Exhaust: The ignition advance plays a very important role with which it is obtained that the pressure exerted in the piston is maximum, in fact, the power of the engine will depend on the average pressure in the piston and the revolutions to which it rotates. In the lowering phase of the piston the intake and exhaust valves are closed; before the TDC is reached, the exhaust valve opens so that exhaust gas evacuation is started as soon as possible. The exhaust valve will not close until the BDC is exceeded, being in the intake phase again. The exhaust gases continue to have inertia within the combustion chamber, so if delaying the closing angle of the exhaust valve is prolonged, it is possible to maximize the evacuation of the already burnt gases and, having the intake valve open, it will contribute to the new inlet mixture by the intake valve pushing the gases.

## 2. Materials and Methods

The calculations were based on the VW Pointer City SA, BHG 67kW (90HP) 1.80 Lt 4 08 / 02-08 / 05 POINTER "MEX", with the following characteristics: BHG = EOBD (European On-Board Diagnostics); Indirect injection; simultaneous ignition; ball type injection system.

### *2.1. Conduit flow – inlet admission valve*

When the velocity of the flow through the vent reaches the local sound velocity, the pressure changes downstream of the vent will no longer propagate upstream of the vent. This is because the pressure wave moves at the speed of sound and the incoming flow, in the opposite direction of the pressure wave, travels at the same speed. Thus, the flow is called stagnant, and the mass flow cannot be increased above this point.

The Mach number $M$ is defined as the relation between the instantaneous velocity ($V$) of the flow and the speed of the local sound ($a$).

In the case where $M = 1$, the flow is stagnant and cannot be increased. The stagnation of the flow through the intake valve (that is, when it reaches the speed of sound) is one of the most serious limitations of engine performance.

The design of the duct assembly and intake valve is largely directed to avoid stagnant flow in the desired performance range.To control the engine speed at which the flow reaches the stagnant condition, the designer must control the number, size and height of the intake valves, as well as the influence of these three parameters on the combustion chamber.

### *2.2. Intake Valve Flow*

The nature of the flow through the intake valve can be examined for three valve risers: low, medium and high. We refer to a valve with sharp edges, which are typical in series production motors.Intake Valve Flow:

- At the lowest elevation, the flow separates from the inside edges of both the seat and the valve, and re-contacts the outer edges of the seat and valve.
- For the middle elevation, the flow separates from the inside edges of both the seat and the valve, re-contacts the outer edge of the seat, but detachment is maintained at the outer edges of the valve.
- When reaching the highest elevation, the flow separates into the inner edges of the seat and valve, thus remaining as it discharges into a conical path.
- Separation occurs in many practical streams of interest. Most of the time it occurs in sharp edges, where the inertia of the flow does not allow it to follow the contours. It is important to note that reaching a certain point, increasing the height of the valve does not increase the mass flow through it, because it does not fully occupy the area available for it. On the other hand, for very high elevations, the limiting area is that of the valve seat.

### *2.3. Discharge Coefficient*

There are many ways in which stationary flow through the valve (or any other vent) can be evaluated. One of the most direct is the discharge coefficient. It consists of measuring the flow rate for a given valve lift (fixed), considering that the load loss is constant.

The compressible isentropic flow theory is used to calculate the mass flow through an ideal frictionless vent, with the same area as the effective area of passage of the valve and subjected to the same pressure difference.The discharge coefficient $CD$ is defined as the ratio of the effective flow area to the geometric flow area through the valve lift.

The isentropic flow through a vent is obtained with the following equation:

$$\dot{m}_i = A\left\{2p_0\rho_0\left[(p/p_0)^{2/\gamma}\cdot\left(1-(p/p_0)^{\frac{\gamma-1}{\gamma}}\right)\right]\right\}^{1/2} \quad (1)$$

Where:$p_0$ and $\rho_0$ are the stagnation pressure and the stagnation density respectively;$\gamma$ is the specific weight ($\gamma = 1.4$ for air);$A$ is the reference area.

The actual flow rate can be expressed by introducing the discharge coefficient ($CD$), with the expression:

$$\dot{m}_{real} = CD \cdot \dot{m}_i \quad (2)$$

If the flow is incompressible the equation (1) is as follows:

$$\dot{m}_i = A \cdot [2\rho(p^0 - p)]^{1/2} \quad (3)$$

The pressure $p$ relative to atmospheric pressure ($p_0 = atm$) is measured above the admission duct, at a distance approximately equal to two cylinder diameters above the engine. The discharge coefficient can be expressed as:

$$CD = \dot{m}_{real}/\dot{m}_i \quad (4)$$

For incompressible flow:

$$CD = \dot{m}_{real}/A \cdot [2\rho(p_0 - p)]^{1/2} \quad (5)$$

The reference area can be considered in two different ways: the minimum geometric area based on the valve seat and lift geometry. The minimum geometric flow area can be divided into three ranges, according to the dimensions indicated in Fig. 2.

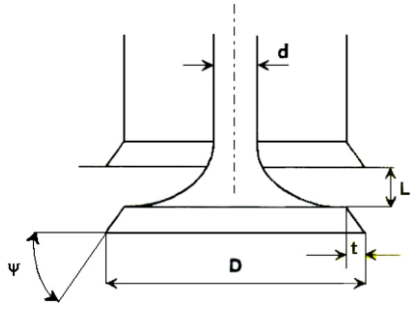


**Fig. 2.**Valve Dimensions Nomenclature

*Rang 1*is fulfilledwhen $[0 < L \leq (2t/\mathrm{Sin}\, 2\Psi)]$. The area of minimum geometric flow corresponds to the lateral area of a sector of cone with height perpendicular to the seat of the valve, and is expressed as:

$$A = \pi L \cdot Cos\,\Psi\,[D - 2t + (L/2)\,Sin\,\Psi] \quad (6)$$

*Rang 2* occurs when $(2t/Sin2\Psi) < L \leq \left(t\,Tan\,\Psi + \sqrt{\{[(D-2t)^2 - D^2]/[4(D-t)]\}^2 - t^2}\right)$. The minimum geometric flow area corresponds to the lateral area of a cone trunk with height perpendicular to the valve seat, and is expressed as:

$$A = \pi(D-t)\cdot\sqrt{(L - t\,Tan\,\Psi)^2 + t^2} \quad (7)$$

*Rang 3* is for $\left(t\,Tan\,\Psi + \sqrt{\{[(D-2t)^2 - D^2]/[4(D-t)]\}^2 - t^2}\right) < L$. The minimum geometric flow area corresponds to the passage area of the intake manifold:

$$A = \frac{\pi}{4}[(D-2t)^2 - d^2] \quad (8)$$

For incompressible flow and low load losses in the valve, the discharge coefficient is calculated using the peripheral curtain area, which is defined as:

$$A = \pi D_v L \quad (9)$$

Where $D_v$ is the internal diameter of the valve seat.The discharge coefficient can be calculated with the expression:

$$CD = \dot{m}/\left(\pi D_v L\sqrt{2\rho 2\Delta p}\right) \quad (10)$$

For practical purposes, the value of the discharge coefficient for a (fixed) valve lift is constant if the Reynolds number is sufficiently high. The results are plotted as a ratio between the flow rate and the dimensionless valve lift, for a given load loss.

It is possible to increase the values of the discharge coefficient by modifying the flow area in the vicinity of the intake valve, rounding the sharp edges for example. It is also possible to perform smoothing and changing the shape of the intake ducts.

### *2.4. Mach number*

The evaluation of the number of Mach, as defined above, has the disadvantage of depending on the velocity of the instantaneous flow $V$, which varies over the cycle. For the purposes of the design, it would be more convenient to have an average expression, which allows to evaluate the flow throughout the interval that the intake valve is open.

If the velocity of the ideal gas (invisible and incompressible) at the opening of the valve for the area of the valve ($A_v = \pi D^2/4$), the instantaneous velocity ($V$) and area of the piston ($A_p = \pi d_p^2/4$) and the actual flow area through the valve ($A_f$), then:

$$V \cdot A_f = V_p \cdot A_p \quad (11)$$

Considering the real flow velocity ($V_r$) through the valve:

$$V_r = V_p\left(d_p/D\right)^2 \cdot \left(A_v/A_f\right) \quad (12)$$

The actual flow area through the valves can be calculated as the area of the intake duct. In turn, the ratio between the actual flow area $A_f$ and the area of the valve $A_v$ is known as the flow coefficient:

$$C_v = A_f / A_v \quad (13)$$

These expressions only serve for instant heats, at some point in the cycle. The importance of having an average expressionallows to evaluate the entire opening interval of the intake valve. First, the coefficient of flow is averaged:

$$\dot{C}_v = \frac{1}{\emptyset_2 - \emptyset_1} \int_{\emptyset_1}^{\emptyset_2} C_v * d\emptyset \quad (14)$$

Where:$\emptyset_1$– angle when the intake valve opens;$\emptyset_2$– angle when it closes. The average velocity of the piston is calculated as $V_p = 2NC$, where $½N$ is the time elapsed for one rotation of the crankshaft and $C$is the stroke of the piston. The average speed of the actual flow will be:

$$\tilde{V}_r = \tilde{V}_p \left(d_p / D\right)^2 \cdot C_v^{-1} \quad (15)$$

If the "Mach index" $I_m$ is defined as the ratio between the average velocity of the actual flow and the velocity of isentropic sound, then:

$$I_m = \left(V_p / a\right) \cdot \left(d_p / D\right)^2 \cdot C_v^{-1} \quad (16)$$

For $n$ number of valves, assuming that all are open at the same time, there is $n$ times the flow area, therefore:

$$I_{m_n} = (1/n) \cdot \left(V_p / a\right) \cdot \left(d_p / D\right)^2 \cdot C_v^{-1} \quad (17)$$

Experience shows that the Mach index is the only relevant parameter to evaluate engine efficiency for different elevations and different valve diameters. Graphs of the Mach index versus some property of the engine (ex. volumetric efficiency) show that from a given value of $I_m$ the volumetric efficiency starts to fall suddenly. It is expected that in such a value of $I_m$ the Mach number reachesto$M = 1$.

## 3. Results and Discussion

To determine the type and moment of injection and the timing advance and delays of both admission and exhaust valves for the injection of the mixture Hydrogen-Gasoline, it was analyzed the injection of gasoline, as well as the injection of Hydrogen.

Calculations made demonstrated that to use the mixture Hydrogen-Gasoline it is necessary to adequate the engine for it. Instead, using only Hydrogen, it is no required any significant engine changes. For this reason, are presented calculations for 2004 VW Pointer 1.8 engine using Hydrogen.

Complete cycle of a four-stroke engine at 2004 VW Pointer 1.8using Hydrogen was determined (Fig. 3).

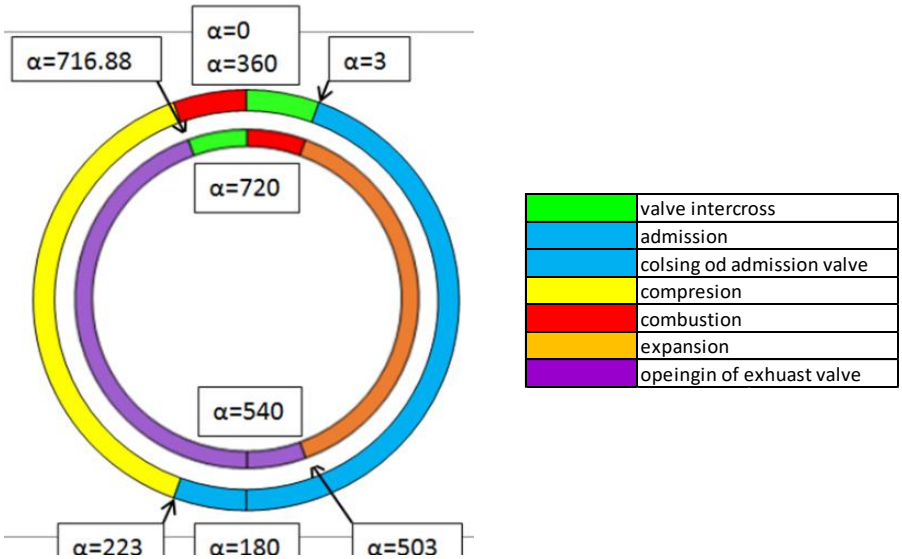


**Figure 3.** Complete cycle of a four-stroke in the 2004 VW Pointer 1.8engineusing Hydrogen

In Table 1 are presented the characteristic angles in the 2004 VW Pointer 1.8engineusing Hydrogen, as well as the angle of rotation of the crankshaft for admissions and exhaust points.

**Table 1.** Admission and exhaust points in 2004 VW Pointer 1.8using Hydrogen

| 2004 VW Pointer 1.8 | | | |
|---|---|---|---|
| Admission | Open | AFTDC | 3˚ |
| | close | ABDC | 43.12˚ |
| Exhuast | Open | BBDC | 37˚ |
| | close | BTDC | 3.12˚ |

In addition, obtained results of Delay and Time Advancement in the 2004 VW Pointer 1.8engineusing Hydrogen are shown in Fig. 4.

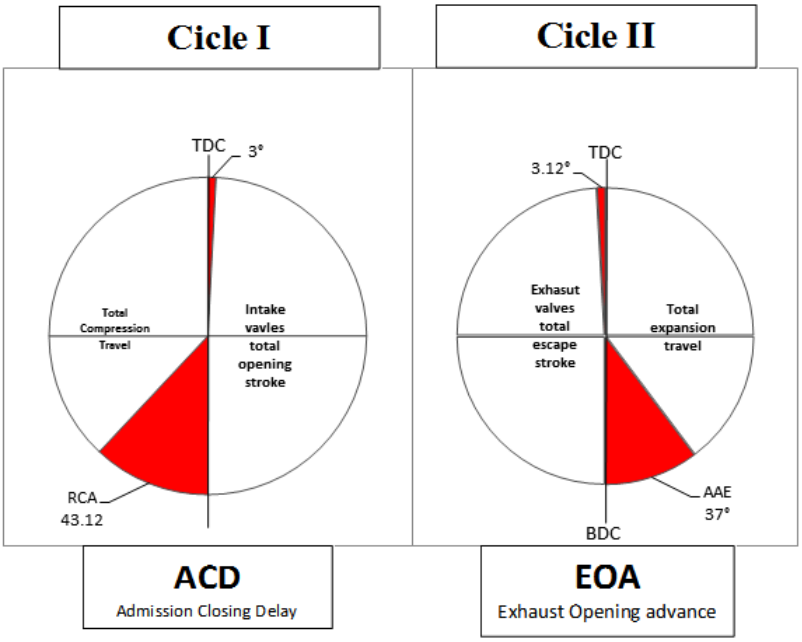


**Figure 4.** Delay and Time Advancement in the 2004 VW Pointer 1.8 engine using Hydrogen

The Mach number $M$ obtainedis $M = 0.0745$.The incompressible flow hypothesis allows to calculate the discharge coefficient with a very small error. If the load loss is $(p_0 - p) = 2\ kPa$, the error committed is approximately $1.2\%$.

Dimensions valve were:$D = 38\ mm.$, $d = 0.7955\ mm.$, $t = 0.15\ mm.$ and $\Psi = 45°$.The minimum geometric flow area can be divided into three ranges: for Rang 1, $A = 788.0574\ mm^2$; for 2, $A = 1016.8308\ mm^2$; and for Rang 3, $A = 1115.7815\ mm^2$.The need to use three equations to determine the minimum flow area, depending on a range of elevations, has drawbacks in practical use.

In Table 2 are shown significate results in 2004 VW Pointer 1.8 using Hydrogen.

**Table 2.** Significateresults in 2004 VW Pointer 1.8using Hydrogen

| ***Concept*** | **Value** |
|---|---|
| *Velocity of the piston ($V_p$)* | $1728\ m/s$ |
| *Area of the piston ($A_p$)* | $5184.2169\ mm^2$ |

| | |
|---|---|
| *Velocity of the instantaneous flow ($V$)* | $15.88\ m/s$ |
| *Area of the valve ($A_v$)* | $1134.1149 mm^2$ |
| *Flow area through the valve ($A_f$)* | $564.1043\ mm^2$ |
| *Flow coefficient ($C_v$)* | $0.4973$ |
| *Real flow velocity ($V_r$)* | $15.88\ m/s$ |
| *Averaged velocity of the piston ($\tilde{V}_p$)* | $25.92\ mm/s$ |
| *Average speed of the flow($\tilde{V}_r$)* | $3.6095\ mm/s$ |
| *Mach index ($I_m$)* | $1.69x10^{-5}$ |

## 4. Conclusion

Comparison for the use of gasoline, of a mixture of Hydrogen-Gasoline and of Hydrogen to determine the type and moment of injection, also for timing advance and delays of both admission and exhaust valves,shows that the Hydrogen use do not require any significant engine changes. Consequently, all calculationspresented were for a 2004 VW Pointer 1.8 engine using Hydrogen.

## Acknowledgements

The authors thank the “Programa para el Desarrollo Profesional Docente, para el Tipo Superior (PRODEP)” for the financial support granted for the realization of this project. As well as the Mexican Hydrogen Society for the scholarships granted to the students participating in the research.

## References

[1] Hiticas I., Marin D., Mihon L.(2013). Modelling and operational testing of pulse-width modulation at injection time for a spark-ignition engine / Tehnički vjesnik 20, 1, 147-153.

[2]Reif K. (Ed.). (2014). Gasoline Engine Management: Systems and Components. Bosch Professional Automotive Information. Springer.

[3] Kegl B., Kegl M., Pehan S. (2013). Green diesel engines. Biodiesel usage in diesel engines. Springer.

[4] Antunes J.M.G. (2010). The use of hydrogen as a fuel forcompression ignition engines. PhD. Thesis. Newcastle University.

[5] Qihui Yu, Yan Shi, and Maolin Cai (2014). Working Characteristics of Variable Intake Valve in Compressed Air Engine / The Scientific World Journal, Volume 2014.

[6] Ohm I.Y. (2013). Effects of intake valve angle on combustion characteristic in an SI engine / International Journal of Automotive Technology. August 2013, Volume 14, Issue 4, pp 529–537.

[7] Effects of injection timing, before and after top dead center on the propulsion and power in a diesel engine. NaderRaeie, SajjadEmami, OmidKarimi Sadaghiyania. Propulsion and Power Research. Volume 3, Issue 2, June 2014, Pages 59-67.

[8] Lino Guzzella and Christopher H. Onder.(2010). Introduction to Modeling and Control of InternalCombustion Engine Systems. Springer-Verlag Berlin Heidelberg.

[9] Sellnau M., Foster M., Hoyer K., Moore W., Sinnamon J., Husted H. (2014). Development of a Gasoline Direct Injection Compression Ignition(GDCI) Engine / SAE Int. J. Engines / Volume 7, Issue 2 (July 2014).

# 1.26 Theoretical development of the hydrogen-gasoline feed of an internal combustion engine

P.T. Cruz Callejo, J.A. Vargas Solorio, D. Alemán Meza, G.A. Radovich Quiroz

[1]Department of Mechanical & Automotive Engineering, Universidad Politécnica de Chihuahua, Av. Téofilo Borunda No. 13200 Col. Labor de Terrazas, Chihuahua, Chih., 31220, México

* Corresponding author: +52 (614) 2142424, dania.aleman@gmail.com

## ABSTRACT

The purpose of the present investigation is to determine the exact quantity of hydrogen to be mixed with gasoline to fuel an Internal Combustion Engine (ICE), maintaining a suitable pressure and temperature while avoiding wear of the main engine components. The work was calculated using Ottos cycle with a mixture of air-hydrogen-gasoline, as well as Hydrogen. Having as starting data, the environmental temperature, the atmospheres pressure and the cylinders capacity at its bottom dead center point to obtain the power indicated. Being that it is necessary to have a hydrogen cell, a neodimo nucleus generator system has been developed, evaluating the magnetic field causes the generator to protect the sensors and other important components vulnerable to a magnetic field.

***Keywords:*** Hydrogen-gasoline; ICE; Otto cycle; neodimo

## 1. Introduction

The use of fossil fuels in the industrial area and transport have generated an enormous damage to the ecosystem, therefore environmental groups and organizations have taken the task to know and foment the use of alternative fuels.

It is engineering's job to make the most of these energy sources for a better tomorrow by developing environmentally friendly technology. Focusing on private automobiles, we

can note that the most common emissions are Nox, Carbon Monoxide, Carbon Dioxide, and Sulfur Dioxide.

According to the World Health Organization [1], the cities in Mexico that present the highest amount of harmful particles are Monterrey, Toluca and the Federal District with 36, 33 and 25 micrograms of $PM_{2.5}$ $m^3$, respectively. Although such levels of the mixture of organic and inorganic substances there are inhaled can reach the bronchial tubes, are far from reaching the level of the most polluted city in the world, New Delhi with 153 micrograms of $PM_{2.5}$ $m^3$ providing an alert of consideration of the latent environmental problem existing in the country.

As a result of various investigations, alternative fuels have been developed (biodiesel, bioethanol, hydrogen and electricity), which offer the opportunity to help the ecological impact without relying on a source of fuel that is not going to run out, reducing at the same time, the harmful damages that the emission gases cause our health [2,3]. Hence, it's the importance of developing a vehicle that takes advantage of the properties of such alternative fuels.

The present article shows the development of the modification of a vehicle to work with the alternative fuel "Hydrogen", explaining its properties and disadvantages in a system developed for gasoline changed to Hydrogen, analyzing the thermodynamic and energy processes that were carried out to arrive at the optimum mixtures for the correct operation of the internal combustion engine; however, since hydrogen gas is so light, it rises to the atmosphere, therefore, it's rarely found in it's pure form, $H_2$, so that new technologies must be used in relation to the hydrogen producing cells, in order to save on fuel [4].

## 2. Materials and Methods

### *2.1. Fuel Properties*

Table 1 shows the comparative table of hydrogen and gasoline properties.

**Table 1.**Hydrogen and gasoline properties comparative

| Properties | HYdrogen | Gasoline |
|---|---|---|
| Density at 1 atm y 300K, [kg/$m^3$] | 0.082 | 5.11 |
| Fraction of stoichiometric volumen with air, [vol%] | 29.53 | 1.65 |
| Minimumignitionenergy, [mJ] | 0.02 | 0.25 |
| Auto IgnitionTemperature, [K] | 858 | 500-750 |
| AdiabaticFlameTemperature, [K] | 2318 | 2470 |
| Flammability limit in air, [vol%] | 4 - 75 | 1.2 – 6.0 |
| Minimum heating value, [MJ/kg] | 119.2 | 44.79 |
| Maximum heating value, [MJ/kg] | 141.7 | 48.29 |
| Specific heat at constant volume, [J/kg*K] | 14267 | 2220 |

### *2.2. Combustion and thermodynamic analysis of the Otto cycle*

The calculations are based on the comparison of the engine with the power curve having as parameter the average power indicated$W_1$:

$$W_1 = (\pi * D)\ /4 * (C * Pmi) \quad (1)$$

Where: $D$ – Cylinder's diameter (manufacturer specific data); $C$ – Piston Stroke (manufacturer specific data); $Pmi = W_n/(V_1 - V_2)$– Average pressure indicated; $W_n$ – Net work.

For the indicated mean pressure formula, it is necessary to know the volume ratio, both at the top dead center and the bottom dead center, taking the displacement as an initial value.

Initially, the work done by the Otto cycle with the air-hydrogen-gasoline mixture is calculated, taking as initial data the ambient temperature, atmospheric pressure and displacement as the bottom dead volume. For the adiabatic process,Gay-Lussac Law is considered,expressions (1) and (2) are fulfilled and shown in Fig. 1

$$P_1/T_1 = P_2/T_2 \quad (2)$$

$$P_A \cdot {V_A}^r = P_B \cdot {V_B}^r \quad (3)$$

Where: $P_1, P_2$ – Pressure at the intake points ($P_1$) and compression points ($P_2$); $T_1, T_2$ – Temperature in the previous points; $V_A, V_B$ – Volume in admission and compression.

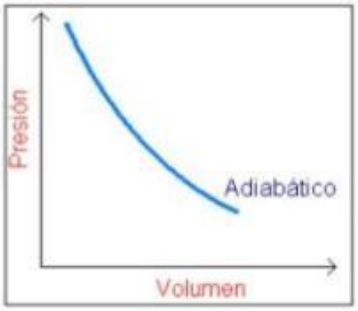


**Fig. 1.** Adiabatic Process

Heat was used for the isochoric process, empirically calculating thevalues of the specific heat and of the heat yield to the system; a percentage ratio was used that occupied in the mixture each of the elements and using its specific heat obtained from thermodynamic tables. The stoichiometric mixture 14: 1 was taken as the reference, considering the mass entering the cylinder.

Obtaining the Heat capacity at constant volume ($C_v$), heat of input and output is calculated ($Q$).

$$Q = mC_v\,(T_B - T_A) \tag{4}$$

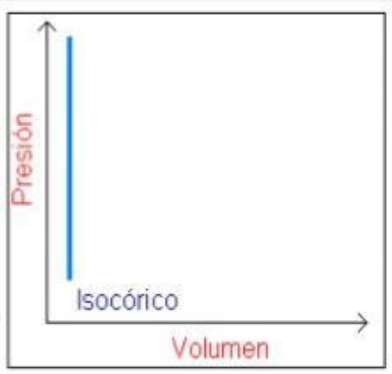


**Fig. 2.** Isochoric Process

To obtain the cycle work (Fig. 3), the following expression is used with the Input and Output Heat ($QH, QS$):

$$Wn = QH + QS \tag{5}$$

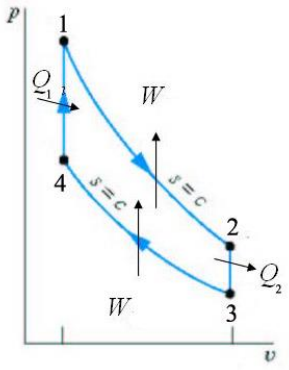


**Fig. 3.** Ideal Otto Cycle

In addition, the maximum temperature and the maximum pressures values reached the cycle were taken to consideration the actual engine limits.

### *2.3. Power indication in relation to the mixture of air-gasoline-hydrogen*

To calculate the indicated powers it is necessary to have in consideration the different $C_v$ to determine the proportions:$C_{vair} = 1012\ J/Kg \cdot k$; $C_{vgasoline} = 22200\ J/Kg \cdot k$; $C_{vHydrogen} = 14267\ J/Kg \cdot k$, [5].

The formula for determining the $C_v$ of the mixture (6) is used to calculate the work and the indicated mean pressure ($pmi$) to obtain the indicated power:

$$C_{vmixture} = (C_{vair})(\%_{air} inmixture) + (C_{vgasoline})(\%_{gasoline} inmixture) + (C_{vHydrogen})(\%_{Hydrogen} inmixture) \quad (6)$$

### *2.4. Magnetic fuel of the neodymium core generator*

Since the hydrogen cell will have the peculiarity of having its own power system in order to avoid severe wear on the battery, a neodymium core generator system was developed.

By reason of magnetism affects the vehicle sensors, it was necessary to evaluate the magnetic field of the generator for system protection.

The magnetic field generated by the toroid ($\beta$) is calculated by:

$$\beta = (\mu NI)/2\pi r \quad (7)$$

Where: $\mu$ – Permeability; $N$ – # of turns; $I$ – current intensity; $R$ – toroid radius.

In addition, the magnetic force between conductors at the time of wiring for the generator ($F$) were considered:

$$F = [(\mu_o * I_1 * I_2)/(2\pi\alpha)] \cdot \lambda \quad (8)$$

Where: $\mu_o$ – Free bond permeability; $I$ – current intensity; $\alpha$ – Distance between conductor; $\lambda$ – cable length.

## 3. Results and Discussions

After the elaboration of the thermodynamic calculations, the following results are presented based on each one of the scenarios that were planted en the use of the different fuels and changing their presence in the compositions, for which it varied due to the percentage that occupies the mixture.

### *3.1. Gasoline*

The first scenario compares the engine without modification, that is to say using gasoline, which will be useful to compare when fuel is replaced in the system for it's advantage.

The highlighted and underlined data, case 8, represent the ideal behavior know as a stoichiometric mixture (14:1).

**Table 2.** Results table with use of Gasoline

| | Work, [J] | Mean pressure indicated (*Pmi*), [Pa] | Powerindicated,[W] | %Air | % Gasoline |
|---|---|---|---|---|---|
| 1 | 245,319.25 | 153,209,626.50 | 69,085.30 | 100% | 0.00% |
| 2 | 248,247.57 | 155,038,452.90 | 69,909.96 | 99.00% | 1.00% |
| 3 | 251,175.89 | 156,867,279.20 | 70,734.61 | 98.00% | 2.00% |
| 4 | 254,104.20 | 158,696,105.60 | 71,559.27 | 97.00% | 3.00% |
| 5 | 257,032.52 | 160,524,932.00 | 72,383.92 | 96.00% | 4.00% |
| 6 | 259,960.84 | 162,353,758.40 | 73,208.58 | 95.00% | 5.00% |
| 7 | 262,889.15 | 164,182,584.70 | 74,033.23 | 94.00% | 6.00% |
| **8** | **264,797.31** | **165,374,289.20** | **74,570.60** | **93.33%** | **6.66%** |
| 9 | 265,817.47 | 166,011,411.10 | 74,857.89 | 93.00% | 7.00% |
| 10 | 268,745.79 | 167,840,237.50 | 75,682.54 | 92.00% | 8.00% |
| 11 | 271,674.11 | 169,669,063.90 | 76,507.20 | 91.00% | 9.00% |
| 12 | 274,602.42 | 171,497,890.20 | 77,331.85 | 90.00% | 10.00% |
| 13 | 303,885.59 | 189,786,153.90 | 85,578.40 | 80.00% | 20.00% |
| 14 | 333,168.76 | 208,074,417.70 | 93,824.94 | 70.00% | 30.00% |

### *3.2. Hydrogen*

Subsequently, the mixture was changed with hydrogen, replacing in its entirely the gasoline, allowing a more accurate understanding of the behavior that the fluid will develop in the engine, were the increase of specific heat and work become noticeable.

**Table 3.** Results table with use of Gasoline

| | Cycle work, [J] | Mean pressure indicated (*Pmi*), [Pa] | Powerindicated, [W] | % Hydrogen | % Air |
|---|---|---|---|---|---|
| 1 | 245,319.25 | 153,209,626.5 | 69,085.30 | 0.00% | 100% |
| **2** | **277,450.74** | **173,276,756.9** | **78,133.98** | **1.00%** | **99%** |

| | | | | | |
|---|---|---|---|---|---|
| 3 | 309,582.23 | 193,343,887.4 | 87,182.65 | 2.00% | 98% |
| 4 | 341,713.72 | 213,411,017.8 | 96,231.32 | 3.00% | 97% |
| 5 | 373,845.21 | 233,478,148.2 | 105,280.00 | 4.00% | 96% |
| 6 | 405,976.70 | 253,545,278.6 | 114,328.67 | 5.00% | 95% |
| 7 | 438,108.19 | 273,612,409.1 | 123,377.34 | 6.00% | 94% |
| 8 | 459,290.44 | 286,841,394.2 | 129,342.56 | 6.66% | 93.33% |
| 9 | 470,239.68 | 293,679,539.5 | 132,426.02 | 7.00% | 93% |
| 10 | 502,371.17 | 313,746,669.9 | 141,474.69 | 8.00% | 92% |
| 11 | 534,502.66 | 333,813,800.4 | 150,523.36 | 9.00% | 91% |
| 12 | 566,634.15 | 353,880,930.8 | 159,572.04 | 10.00% | 90% |
| 13 | 887,949.04 | 554,552,235.1 | 250,058.77 | 20.00% | 80% |
| 14 | 1,209,263.93 | 755,223,539.3 | 340,545.50 | 30.00% | 70% |

Case 2 shows the values at which the engine could ideally work, or stoichiometric mixture, by the percentage of Hydrogen in relation to air (1:99).

### *3.3.Hydrogen – gasoline Mixture*

Table 4 shows the results of the use of Gasoline-hydrogen-air mixture.

**Table 4.**Table of results use of mixture Gasoline-Hydrogen-Air

| | PowerIndicated, [W] | Work, [J] | Mean Presure Indicated (*Pmi*), [Pa] | %Hydrogen | %Gasoline |
|---|---|---|---|---|---|
| 1 | 79,783.75 | 283,309.03 | 176,935,439.10 | 0.00% | 12.99% |
| **2** | **88,279.91** | **313,478.54** | **195,777,255.90** | **1.00%** | **12.32%** |
| 3 | 96,503.92 | 342,681.71 | 214,015,560.00 | 2.00% | 11.32% |
| 4 | 104,727.94 | 371,884.89 | 232,253,864.00 | 3.00% | 10.32% |
| 5 | 112,951.96 | 401,088.06 | 250,492,168.10 | 4.00% | 9.32% |
| 6 | 121,175.98 | 430,291.23 | 268,730,472.10 | 5.00% | 8.32% |
| 7 | 129,400.00 | 459,494.40 | 286,9687,76.20 | 6.00% | 7.32% |
| 8 | 137,624.01 | 488,697.58 | 305,207,080.20 | 7.00% | 6.32% |
| 9 | 145,848.03 | 517,900.75 | 323,445,384.30 | 8.00% | 5.32% |
| 10 | 154,072.05 | 547,103.92 | 341,683,688.40 | 9.00% | 4.32% |
| 11 | 162,296.07 | 576,307.09 | 359,921,992.40 | 10.00% | 3.32% |

| | | | | | |
|---|---|---|---|---|---|
| 12 | 170,520.09 | 605,510.27 | 378,160,296.50 | 11.00% | 2.32% |
| 13 | 178,744.11 | 634,713.44 | 396,398,600.50 | 12.00% | 1.32% |
| 14 | 186,968.13 | 663,916.61 | 414,636,904.60 | 13.00% | 0.32% |

### *3.4. Delimitation of mixtures*

Based on tables 1,2 and 3, it is shown that it's possible to use the three options presented in an internal combustion engine: Gasoline, Hydrogen-Air and Gasoline-hydrogen-air. However, fuels with relations and results that clearly leave the use of gasoline far below, given the development of work that generates pear to the better appreciated the blending of the mixtures analyzed the following graphs:

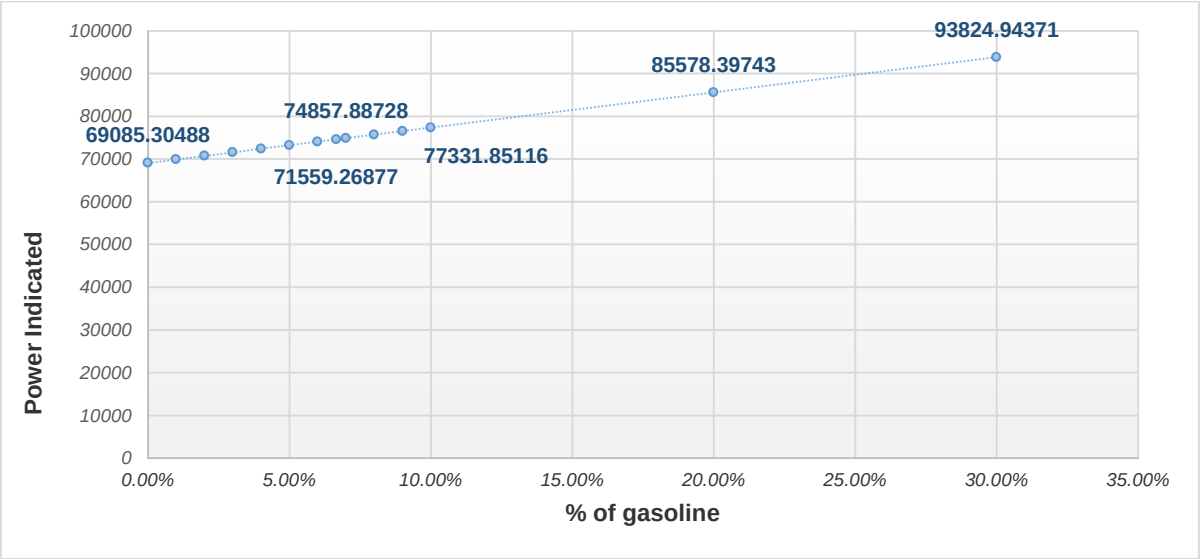


**Fig. 4.** Power indicated with the use of gasoline

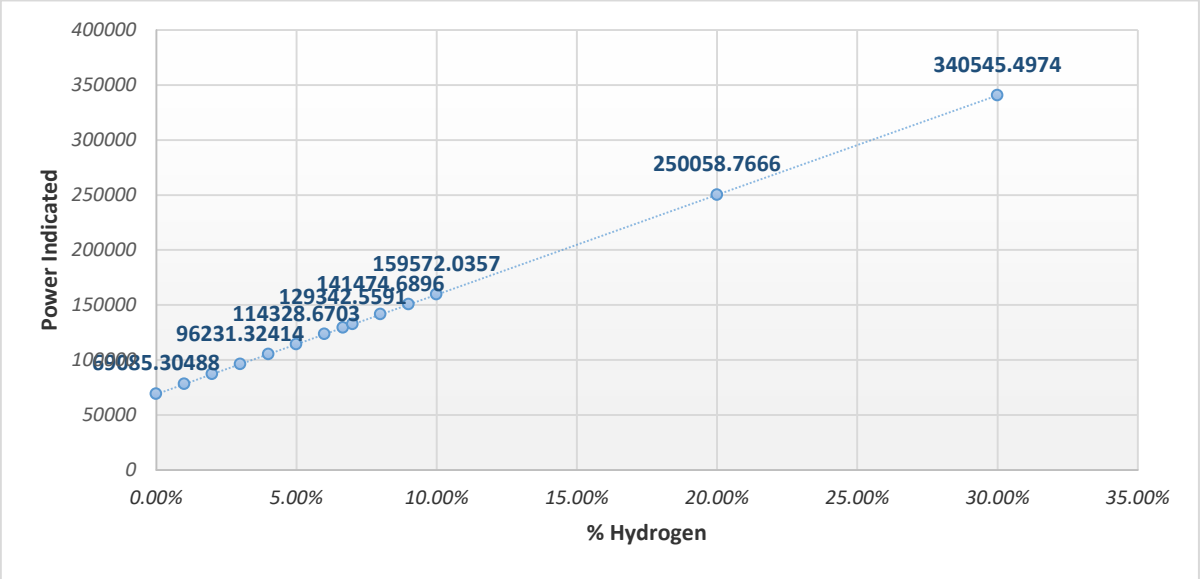


**Fig. 5.**Power indicated with use of Hydrogen

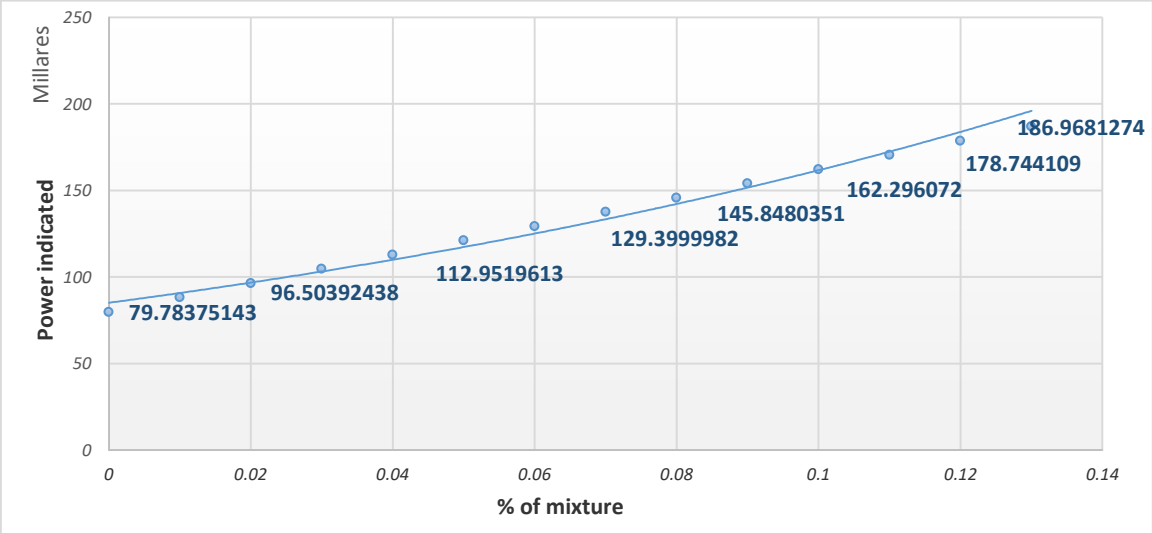


**Fig. 6.**Power indicated with use of Gasoline-hydrogen-air

As it can be seen in the graphs the power developed by the gasoline in relation to the stoichiometric mixture percentage, which are as follows.

**Table 5.** List of ideal mixtures

| Fuel | Powerindicated, [Pa] | Power, [HP] |
|---|---|---|
| Gasoline | 74,570.60 | 100.00 |
| Hydrogen-Air | 78,133.98 | 106.23 |
| Gasoline-Hydrogen-Air | 88,279.91 | 118.38 |

Taking into account the economic investment to be made in the ICE when feeding the engine with a fuel, it was considered to make the slightest modifications to the vehicle, therefore it was taken as the base standard of stoichiometric mixture at 100HP, avoiding to

modify the systems of sensor of the car, with the exception of Hydrogen injectors and adaptations for fuel cells (lines, regulators and safety devices).

In addition, we take into account the changes involved in modifying the fuel in the car, based on the graphs and power tables, the following is concluded for the ideal mixture:

- Hydrogen: 1% / 17.81cm$^3$of Hydrogen and 99% / 1763.19cm$^3$ of Air.
- Mixture Hydrogen – Gasoline: 1% / 17.81cm$^3$ of Hydrogen, 12.32% / 219.41cm$^3$ of Gasoline and 86.68% / 1543.77cm$^3$

## 4. Conclusion

With the above results it is concluded the ideal is the use of pure Hydrogen given the advantages of the fuel compared to the mixture Gasoline-Hydrogen:

a. *The indicated power development.*It is observed in the graphs the power that develops the engine is of 100HPs when modifying the fuel to Hydrogen and gasoline in its minimum mixture generates 118 HPs which already involves the modification of piston rods, rings and valves, since the increase of 18HPs is equivalent to placing a turbo charger in the car, in relation to the economic sense increases the cost of the change, in addition to considering a dual infection system (Hydrogen and gasoline separately) having to modify the injection times.

b. *Fuel cells.*When using a double fuel system, the number of lines increase and safety systems in case of an accident avoid a fire or explosion of the vehicle, as well the use of dual fuel regulation systems, gas tank and Hydrogen cell, which complicate the assembly of the same, increases the control that must have the same temperatures.

c. *Risk of auto – ignition*.An important point to be addressed are the temperatures of the auto ignition given to both fuels are different, they have individual properties which leads us to control the auto ignitions to get the maximum heat benefit should be prevented.

Doing so in a double mixture should be controlled at the same time and this does not affect each element separately if a hydrogen only system is used then is prevented with the car cooling system and the correct spraying (atomized) of the injector.

It is concluded that the use of a mixture is unnecessary for the vehicle, since it is possible to generate better results using only Hydrogen-air as fuel, instead of Gasoline or Gasoline-Hydrogen.

## Acknowledgements

The authors thank the “Programa para el DesarrolloProfesionalDocente, para el Tipo Superior (PRODEP)” for the financial support granted for the realization of this project. As well as the Mexican Hydrogen Society for the scholarships granted to the students participating in the research.

## References

[1] WHO. (2016 de September). *Calidad del aire ambiente (exterior) y salud*. Obtenido de Organización Mundial de la Salud: http://www.who.int/mediacentre/factsheets/fs313/es/

[2] Lee, Sunggyu; Speight, James G. ; Loyalk, Sudarshan K. ;. (2014). *Handbook of Alternative Fuel Technologies* (Second ed.). (C. Press, Ed.)

[3] Plan Nacional de Difusión y Divulgación de la Ciencia y la Tecnología, 2003 del Ministerio de Ciencia y Tecnología. (2003). *energia sostenible.net*. Obtenido de http://www.energiasostenible.net/fundamentos_hidrogeno.htm

[4] Busby, J., & Altork, L. (2010). Hydrogen Fuel Cells: Part of the Solution. *Technology and Engineering Teacher, 70*(2), 22-27.

[5] Kyle, B. G. (1992). *Chemical and process thermodynamics* (2nd. ed.). New Jersey: Prentice Hall.

# 1.27 Ecological motorcycle with dual gasoline-hydrogen fuel

José Javier Jiménez García, Jorge Medina Rodríguez, Marisol Rico Cortez, Alfonso Campos Vázquez, Juan Manuel Sandoval Pineda, Rosa de Guadalupe González Huerta

[1]Instituto Politécnico Nacional-ESIME-Azc, SEPI, Av. De las Granjas, No. 682, Azcapotzalco, CP 02250, México, CDMX
[2]Instituto Politécnico Nacional -ESIQIE, Laboratorio de Electroquímica y Corrosión, UPALM, CP 07738, México, CDMX
[3]Instituto Politécnico Nacional-UPIITA, Mecatrónica, Av. IPN 2580, CP 07340, México, CDMX

## ABSTRACT

Internal combustion engine (ICE) vehicles are an important source of pollution gases; therefore, several research groups are implementing systems to reduce hydrocarbon emissions. Gasoline enrichment with alternative fuels such as ethanol, hydrogen, and others has been considered to generate dual fuel system. A water alkaline electrolyzer (WAE) was chosen as the oxyhydrogen gas generator because the alkaline water electrolysis is one of the easiest way for hydrogen production, offering the advantage of simplicity and lower costs. The electrolyser was designed following the APQP methodology, the system was composed by 4 mono-cells connected in serie, a supply current from 10 A at 12 V. Cathodes were of stainless steel and nickel with matte finish was deposited on stainless steel surfaces to conformed anodes, it improve its resistance to corrosion and wear. Electrolyte was an alkaline solution (NaOH 5% w).

Oxyhydrogen system was adapted on gasoline motorcycle (Honda CG 125 Tool: 9.7 Hp@8500 rpm; displacement: 124.1 cc; torque: 8.8 Nm@7500 rpm; and compression ratio 9). The engine was working at a speed range from 2000 to 5000 rpm. The experimental work consisted of two main stages: In the first, the engine was tested only with gasoline, and in the second one, an oxyhydrogen gas volume was injected. The total oxyhydrogen gas real intake in air flow was 400 smL min−1. Finally, the oxyhydrogen gas mixture allowed the reduction of 8% gasoline consumption and contributed to a decrease in CO2 emissions. The challenges to widespread use of alkaline water electrolysis are to reduce energy consumption, cost, and maintenance and to increase reliability, durability, and safety.

***Keywords:*** Alkaline electrolyzer, oxyhydrogen, dual fuel system: gasoline-hydrogen, Internal combustion enginee.

# 1.28 Hydrogen generation by aluminum alloy corrosion in aqueous acid solutions promoted by nanometal: kinetics study

A. L. Martínez-Salazar, J. A. Melo-Banda, M. A. Coronel-García, C. H. Treviño-Sandoval, J. J. González-Barbosa, J. M. Domínguez-Esquivel

[1]Tecnológico Nacional de México, Instituto Tecnológico de Ciudad Madero, Centro de Investigación en Petroquímica, Prol. Bahía del Aldair, Av. de las Bahías. Parque Industrial Tecnia, Altamira, Tamaulipas, México, 89608.

[2]Instituto Mexicano del Petróleo, Eje Central Lázaro Cárdenas 152, San Bartolo Atepehuacan, Gustavo A. Madero, Ciudad de México, Distrito Federal, México, 07730.

* Corresponding author: (833)1212100, analidiams@gmail.com

## ABSTRACT

Hydrogen has attracted much attention as an environmentally friendly fuel with high calorific value. However, most of $H_2$ consumed worldwide nowadays is produced by using fossil fuels with the corresponding generation of $CO_2$. In addition, conventional methods for $H_2$ production are not profitable due to the high energy requirements. This scenario encourages the research focused in new, sustainable and economical ways to produce $H_2$.

Hydrogen production based in the corrosion of light metals in water solutions can be considered as an alternative route. Among all of them, Al is probably the most adequate metal for energetic purposes due to its high electron density and oxidation potential.

The open literature concerning the kinetics study of aluminum corrosion in aqueous acid solutions reaction is very poor. In this research, catalytic properties of HCl and sodium molybdate nanoparticles in the production of hydrogen by aluminum alloy corrosion in aqueous acid solutions were analyzed. Catalytic evaluations were carried out at pilot level using a stainless steel batch reactor, varying the amount of HCl (0.5 to 1.75 M) at 313 K.

Models for non-homogeneous reactions has been used to analyze kinetics behavior. Model discrimination has been performed and the kinetic parameters calculated.

***Keywords:*** hydrogen production; corrosion; kinetics

# 1.29 Synthesis of spinel-type ferrites by the Oil-in-Water microemulsion reaction method and its evaluation for photocatalytic water-splitting

Arturo A. Rodríguez Rodríguez, Miguel J. Meléndez Zaragoza, Alejandro López Ortiz, Virginia Collins Martínez, Eduardo Martínez Guerra, Margarita Sánchez Domínguez

[1] Centro de Investigación en Materiales Avanzados S. C. (CIMAV), Unidad Monterrey, Alianza Norte 202, Parque de Investigación e Innovación Tecnológica, 66600 Apodaca, México.

[2] CIMAV Unidad Chihuahua, Av. Miguel de Cervantes Saavedra 120, Complejo Industrial Chihuahua, 31136 Chihuahua, Chih. México.

* Corresponding author: tel. 8448073209, e-mail: arturo.rodriguez@cimav.edu.mx

## ABSTRACT

Spinel-type ferrites have the molecular formula $MFe_2O_4$, where M represents a divalent metallic cation, such as $Co^{2+}$, $Ni^{2+}$ and $Zn^{2+}$ for $CoFe_2O_4$, $NiFe_2O_4$ and $ZnFe_2O_4$, respectively.As photocatalyst, spinel-type ferrites have shown an efficient visible light absorption, high sorption ability, thermal stability, and low toxicity. Moreover the magnetic response of $MFe_2O_4$ allows their easy recovery from the liquid reaction media. Thanks to these features, $MFe_2O_4$ compounds are a promising option for the photocatalytic water-splitting, a clean and simple technology to obtain $H_2$. In regard to the light driven production of hydrogen, the capacity of these oxides has not been fully explored, especially $MFe_2O_4$ nanoparticles synthesized by microemulsion. Based on this, we synthesized cobalt, niquel and zinc spinel-type ferrites employing the oil-in-water microemulsion reaction method and explored its $H_2$ evolution. In order to perform the photocatalytic experiments, a dispersion of nanoparticles in water (with 2% of MeOH) was prepared inside a quartz tube reactor; this system was sealed, and then illuminated with a 250 W mercurial lamp. $H_2$ production was monitored by gas chromatography. Prior to photocatalytic evaluation, as-synthesized nanomaterials were thermally treated and characterized. Obtained results evinced nanoparticles with a spinel-type crystalline structure and a semi-globular morphology. Furthermore, $MFe_2O_4$ materials exhibited an adequate surface area, visible light absorption, and a soft magnetic behavior. In the evaluation of the photoactivity, $ZnFe_2O_4$ yielded a higher amount of hydrogen (354 $\mu molH_2g^{-1}$) compared with Co and Ni ferrites in an 8 h experiment. Broadly, this work represents a novel contribution to the studies of spinel-type ferrites for the photocatalytic production of $H_2$.

***Keywords:*** spinel-type ferrites; microemulsion; hydrogen production; photocatalytic water-splitting.

# 1.30 Review of the global delivery pathways of hydrogen fueling stations for fuel cell electric vehicles and their potential application in México

Salvador Vidal, Félix Loyola, Ulises Cano

[1]Instituto Nacional de Electricidad y Energías Limpias, Gerencia de Energías Renovables. Reforma 113, Col. Palmira, 62490, Cuernavaca, Morelos, México.

[2]Instituto de Energías Renovables. Privada Xochicalco S/N, Temixco, Morelos, México. C.P. 62580

* Corresponding author: +52 (777) 3623811 (Ext. 7140), felix.loyola@iie.org.mx

## ABSTRACT

In this work, the delivery pathways of Hydrogen Fueling Stations (HFSs) for Fuel Cell Electric Vehicles (FCEVs) in the world are reviewed. The main objective is to identify the global trend or technology availability and their potential application in Mexico in the near term. The key activity is the integration of the information related with the HFSs summarized in the international government energy agencies or research centers official reports. According to the results, 372 HFSs with 36 defined delivery pathway are identified. The compressed hydrogen, off-site system, liquid hydrogen and on-site electrolysis are the more common representing 75 % of the total HFSs with a defined delivery pathway. North America prefers the compressed hydrogen delivery pathway with 40 HFSs followed by on-site electrolysis with 13 stations, and finally liquid hydrogen with 11. Europe shows almost equal delivery pathways selection between compressed hydrogen and on-site electrolysis with 33 and 30 HFSs, respectively, followed by only 8 stations with liquid hydrogen delivery pathway. On the other hand, Asia prefers off-site systems with 35 hydrogen stations along with 10 compressed hydrogen delivery pathway. At present, Japan is the country with the highest quantity of HFSs with a total of 92 active and 3 planned units. In contrast, Mexico and South American countries, with the exception of Argentina, Brazil, and Costa Rica, have none active or planned HFS for FCEVs. It is important to note that 134 HFSs detected through the sources consulted do not have a defined delivery pathway; all of them located principally in Europe and Asia. According to this, the amount of compressed hydrogen delivery pathway is higher than the on-site electrolysis followed by the offsite system and liquid hydrogen delivery. It is important to say that the compressed hydrogen, offsite system, and liquid hydrogen delivery pathways do not have a defined process for hydrogen production, but certainly it is produced in a centralized process in contrast to the on-site electrolysis pathway. On the basis of the above discussion and the natural resources available, it can be concluded that Mexico has a high potential to initiate the installation of HFSs for FCEVs using the compressed and on-site electrolysis delivery pathways supported by the emerging renewable energy market.

***Keywords:*** Hydrogen; Delivery pathways, Hydrogen fueling stations, FCEV.

# 1.31 Design and integration of a hybrid electric power plant for a scooter

Carlos A. Reynoso, Iván A. Prado, Manuel de J. López, Félix Loyola, Ulises Cano

[1]Instituto Nacional de Electricidad y Energías Limpias, Gerencia de Energías Renovables. Reforma 113, Col. Palmira, 62490, Cuernavaca, Morelos, México.

* Corresponding author: +52 (777) 3623811 (Ext. 7140), felix.loyola@iie.org.mx

## ABSTRACT

In this paper the design and integration of a Hybrid Power Plant (HPP) based on Proton Exchange Membrane Fuel Cells (PEMFC) for a low scale electric power traction system (scooter) is presented. The HPP consists of an in house made PEMFC stack (as the main source), a commercial battery pack and the auxiliary components that integrate the Balance of Plant (BoP), as well as the electronic control system. The BoP components include pneumatic, electronic and power electronics parts. In the control system, the electronic circuits for different functions like measurements (voltage, electrical current, PEMFC temperature, and hydrogen gas pressure), drive actuators (electro-valves and fans) and electric power conditioning were developed. The control system supervises the PEMFC general function, and it is allowed to manage the energy from PEMFC and batteries. The control system limits the PEMFC polarization to avoid stress and starvation condition. Additionally, if the electrical current demand is higher than maximum PEMFC current capacity, the batteries adds current to complete the demand. On the other hand, if the demand is lower, the PEMFC sends energy to batteries to charge it. This power source configuration and operating strategy increases the autonomy of the scooter compared with the only batteries configuration. The design proposed in this work is possible to extrapolate to a higher power traction system as an electric vehicle.

***Keywords:*** Fuel cells; Balance of plant; Scooter.

# 1.32 $Cu_2O/TiO_2$ nanostructures for hydrogen production from methanol photoreforming

O.F. Plascencia-Hernández, G. Valverde-Aguilar, M. A. Valenzuela-Zapata

[1]Centro de Investigación en Ciencia Aplicada y Tecnología Avanzada Unidad Legaria del Instituto Politécnico Nacional,Legaria No. 694, Col. Irrigación, Delegación Miguel Hidalgo, 11500 Ciudad de México, México.

[2]Lab. Catálisis y Materiales. Escuela Superior de Ingeniería Química e Industrias Extractivas, Instituto Politécnico Nacional,Av. Instituto Politécnico Nacional No. 1936, Unidad Profesional "Adolfo López Mateos" Zacatenco C.P. 07738, Col. Lindavista, Delegación Gustavo A. Madero, 07738 Ciudad de México, México

* Corresponding author: 57296000 ext. 67763 fernandoplascenciah@gmail.com

## ABSTRACT

The search of clean and energy resources is one of the main tasks in which the scientific community has paid great attention in the last decade. In such a way, the conversion of solar energy into chemical energy, especially in the formation of products such as hydrogen, hydrocarbons, alcohols, an so on, from cheap and abundant raw materials (e.g., water, carbon dioxide, glycerol, etc), is a highly desirable approach for a sustainable development. Heterogeneous photocatalysis is considered as one of the most recognized alternative to convert solar energy into useful chemicals due its the accumulated experience in environmental purification and water splitting for $H_2/O_2$ formation.

Photoreforming is reasonably easier than water spitting to produce hydrogen, and its use in biomass-derived substrates performing can simultaneously produce hydrogen and clean wastes. For this reason, the present investigation was focused on methanol photoreforming as viable option to pure hydrogen production.Within the wide range of photocatalysts that have been studied, $TiO_2$ together with $Cu_2O$ are promising candidates for this reaction. Thus, in this work a series of $Cu_2O/TiO_2$ nanostructures was synthesized by chemical reduction and mixed with $TiO_2$ P25 at room temperature. The obtained materials were characterized by difuse reflectance spectroscopy (DRS), scanning electron microscopy (SEM) and X-ray photoelectron spectroscopy (XPS). According to our results, $Cu_2O$ spheres with an average size of 180 nm were homogeneously dispersed on $TiO_2$ and the best hydrogen production rate was obtained with a 0.06:1 $Cu_2O$:$TiO_2$ molar ratio after 8 h of irradiation using simulated solar light. An explanation for this surprising behavior was made in terms of a weak interaction between the two oxides.

***Keywords:*** $Cu_2O/TiO_2$; hydrogen; methanol photoreforming

## 1. Introduction

In the last decade, heterogeneous photocatalysis has shown great advances in aspects related to the environment and energy, among others [1]. For instance, the efficient hydrogen production from water splitting in the presence of a suitable semiconductor and sunlight is emerging as an attractive option to solve simultaneously real problems to the impending energy crisis and environment pollution [2]. However, the task is not easy, there must be a material capable of performing a coupled strong water oxidation and reduction, besides of showing a high stability and low cost. Tiatanium dioxide ($TiO_2$, n-type semiconductor) has been the most studied material for this reaction, although due to the high value of its band gap ($E_g$= 3.2 eV) demands UV-light for its activation, which is only available in 3-4% in the whole radiant solar energy [3,4]. On the other hand, another of the disadvantages of $TiO_2$ is its fast recombination of photogenerated electron–hole pairs, during hydrogen evolution reaction [5].

For this reason, several options have been conserted to improve the photocatalytic activity of $TiO_2$ under visible light, among which it can be mentioned: (i) surface modification via organic materials, (ii) band gap modification by nonmetals, (iii) metals doping and (iv) semiconductor coupling [6]. Particularly, combining a n-type semiconductor with a p-type semiconductor (e.g. $Cu_2O$), to form a heterojunction, is an efficient method to separate the photoinduced electrons and holes due to the effect of the inner electric field [7]. $Cu_2O$ with a direct-band of 2.0 eV, with virtual non-toxicity and natural abundance, has been widely explored by several research groups on applications for water splitting, solar cell, gas sensor, and so on [8]. Furthermore, the $Cu_2O/TiO_2$ system has been studied showing promising photocatalytic results in many reactions [7,8], which has been explained in terms of an enhanced charge separation due to the photogenerated electrons from $Cu_2O$ conduction band can transfer to the conduction band of $TiO_2$, and the holes can migrated from valence band of $TiO_2$ to the valence band of $Cu_2O$.

The goal of this research was to synthesize $Cu_2O/TiO_2$ nanostructures at room temperature in two steps. In the first stage, $Cu_2O$ uniform polyhedra were obtained by chemical reduction process; after that, $TiO_2$ P25 was added over the $Cu_2O$ polyhedra, controlling the ethanol/water relationship. Under this procedure, it was synthesized four materials, varying the $Cu_2O/TiO_2$ molar ratio. Difuse reflectance spectroscopy (DRS), scanning electron microscopy (SEM) and X-ray photoelectron spectroscopy were the main characterization techniques employed. The photocatalytic activity of the prepared materials was tested in the methanol photoreforming reaction using a solar simulator as the radiation source.

## 2. Materials and Methods

*2.1 Materials*

Copper (II) chloride ($CuCl_2$; 97%), sodium hydroxide (NaOH; 98.2%), L-ascorbic acid (99.5%), Polivinilpilorridone (PVP; $M_W$ 55,000), titanium dioxide P25 Degussa ($TiO_2$ P25; 99.5%) were purchased from Aldrich and used without further purification. Aqueous solutions were prepared using deionized water (Milli-Q with 18.6 MΩ) and ethanol reagent grade (denatured).

*2.2 Synthesis of $Cu_2O$ polyhedral*

$Cu_2O$ polyhedral particles were synthesized at room temperature by the chemical reduction route. Sodium hydroxide solution (1M, 40 mL) was prepared and stirred vigorously and then, a copper chloride solution (0.15 M, 40 mL) was added drop by drop and stirred for 15 minutes. After that, a 60 mL of PVP:L-ascorbic acid solution (1.42 weight ratio) was added fast and the final solution was stirred for 30 minutes. The resultant $Cu_2O$ polyhedral particles were washed three times with a 1:1 water:ethanol solution, and dry under air atmosphere for storage.

*2.3 Synthesis of $Cu_2O/TiO_2$ composite*

$Cu_2O$ polyhedral particles were dissolved in a water:ethanol (1.25 volume ratio) solution. At the same time, titanium dioxide P25 was dissolved in a water:ethanol solution (1.5 volume ratio) an added to a 100 mL $Cu_2O$ solution and stirred for 30 minutes. Following the same procedure, four composites with a molar ratio ($Cu_2O$:$TiO_2$): A=0.6:1, B=0.3:1, C=0.06:1 and D=0.03:1, were synthesized.

*2.4 Characterization*

UV–vis diffuse reflectance spectra (DRS) were obtained in a GBC Cintra 20 spectrometer on the range of 200-800 nm. Scanning electron microscopy (SEM) analysis was carried out on a JEOL 7800F microscope. XPS analyses were performed using a ThermoFisher Scientific K-Alpha X-ray photoelectron spectrometer with a monochromatized AlKα X-ray source (1487 eV).

*2.5 Photocatalytic evaluation*

The $Cu_2O/TiO_2$ composites were evaluated in hydrogen production by means of methanol photoreforming. An Hg-Xe lamp (200 W) was used as irradiation source without any type

of filter. Initially, it was prepared a methanol:water solution (1:5 volume ratio) and the photocatalyst was dissolved maintaining a concentration of 1 mg/mL. The resulted solution was stirred in the dark for 30 min to perform the adsorption process. After that, the reactor was placed in front to the light source, and irradiated for 8 h. The gas effluent from the reactor was analyzed every hour by gas chromatography.$Cu_2O$ polyhedral particles and $TiO_2$ P25 were also evaluated separately at the same reaction conditions.

## 3. Results and Discussion

### 3.1 Scanning electron microscopy

Figure 1a) shows $Cu_2O$ polyhedral particles with average size of 196 nm. The facets of the structure clearly are appreciated, but is not possible determine exactly their number. Some agglomeration zones can be observed. The commercial $TiO_2$ P25 is presented Fig.1b), without a clear shape or structure, only agglomerates of nanoparticles. Figures 1c) to 1f) correspond to the $Cu_2O/TiO_2$ composites. The identification of the $Cu_2O$ polyhedral particles is more difficult when the molar ratio decreases. Composite A (0.6:1) is showed in Fig. 1c). The $Cu_2O$ polyhedral particles are close to P25 nanoparticles, probably by an electrostatic interaction. Figure 1d) shows composite B (0.3:1), where the $Cu_2O$ polyhedral particles are more surrounded by P25 particles and still it is possible to identify them. The composite C (0.06:1) and D (0.03:1) are showed in Figures 1e) and 1f). $Cu_2O$ polyhedral particles were not identified, only P25 nanoparticles, because the molar ratio was very low.

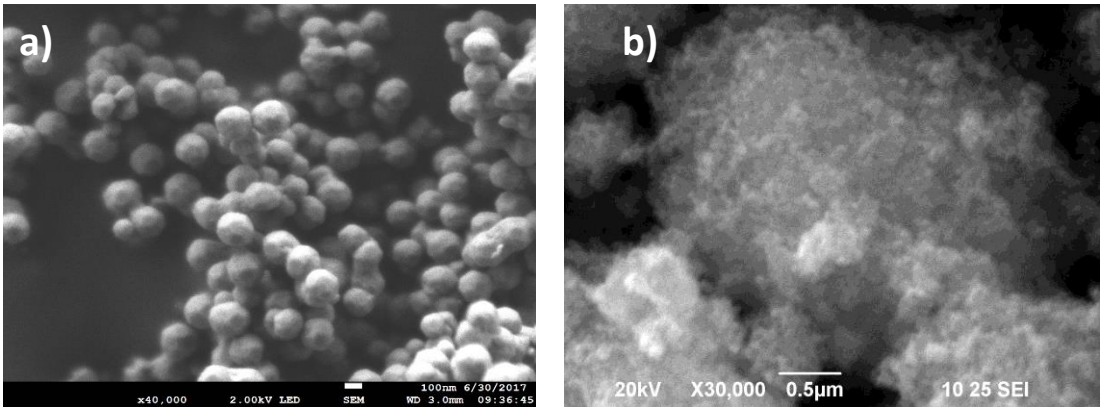

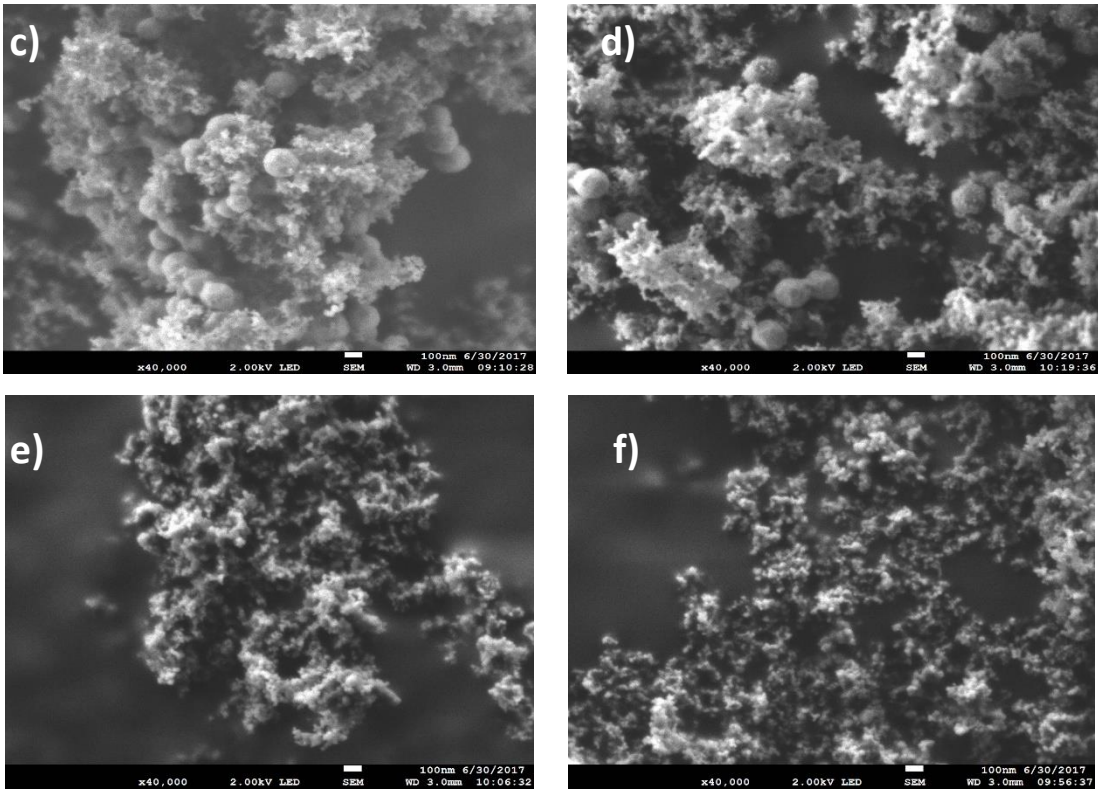


**Fig. 1.** SEM analyses of synthesized structures ofa) $Cu_2O$ polyhedral particles, b) commercial $TiO_2$ P25, composites ($Cu_2O/TiO_2$ ): c) A (0.6:1), d) B (0.3:1), e) C (0.06:1), f) D (0.03:1)

3.2 Diffuse Reflectance Spectroscopy

Absorption spectra of the $Cu_2O$ polyhedral particles, P25 and $Cu_2O/TiO_2$ composites are presented in Fig. 2a). As can be seen, the $Cu_2O$ particles showed a clear photon absorption in the visible range and P25 only in the UV region. The $Cu_2O/TiO_2$ composites presented two strong adsorption peaks on the visible and UV regions that was interpreted as separate contribution of each compound to the global spectrum shown in Fig. 2a). Figure 2b) shows a plot of hv vs $(\alpha hv)^2$ and the band gap energy of $Cu_2O$ polyhedral particles were determined as an average value of 2.18 eV, and for commercial P25 was 3.3 eV, which were similar to those reported in the literature [4].

**a)** **b)**

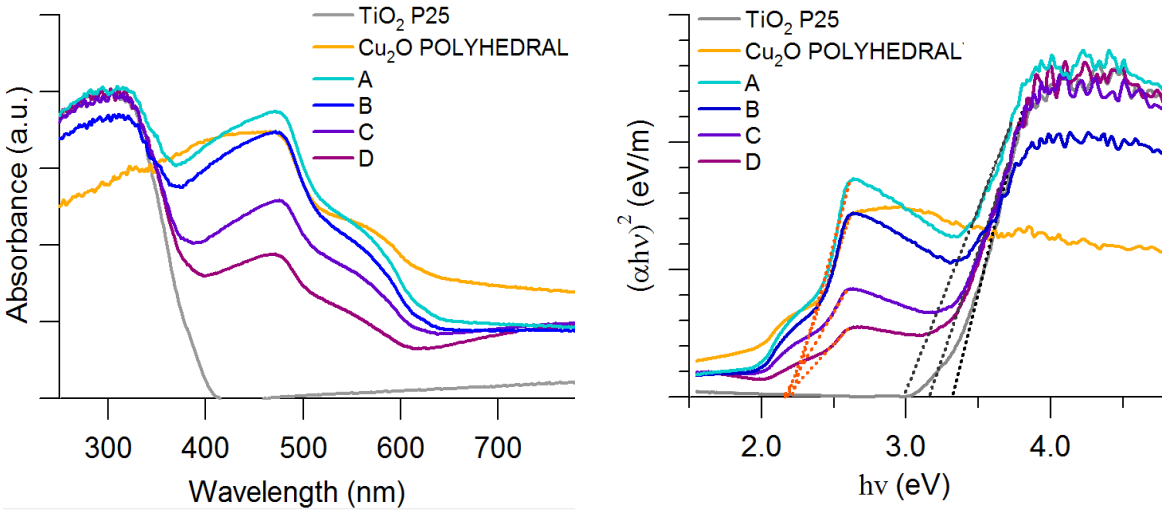


**Fig. 2.** a) Absorption spectra of composites, $Cu_2O$ polyhedra and the commercial P25, b) Plot of hv vs $(\alpha hv)^2$

3.3 XPS

XPS spectra of photocatalyst C, fresh and spent after 8 h irradiation time are shown in Fig.3. Cupprous oxide characteristic peaks at 932.48 eV and 952.28 eV binding energies correspond to Cu2p3/2 and Cu2p1/2 of cuprous oxide,Fig 3a. After irradiation, a slight decrease in the signals of $Cu_2O$ was detected. Figure 3b) shows two peaks at 458.28 eV and 464.08 eV, correspond to Ti2p3/2 and Ti2p 1/2, respectively. Finally, one peak was at 529.58 eV corresponding to oxygen 1s was localizated.These results revealed the presence of cuprous oxide species which showed photocatalytic stability after 8 h of irradiation time without any interaction with $TiO_2$. It seems that both oxides were mixed but each one maintaining their original properties.

3.3 Photocatalytic activity

The results for hydrogen production by methanol photoreforming are shown in Fig. 3. $Cu_2O$ polyhedral particles did not show photocatalytic activity under the reaction conditions. The commercial P25 has a slightly hydrogen production. All $Cu_2O/TiO_2$ composites showed a higher photocatalytic activity than that presented by each oxide separately. The maximum hydrogen production was reached by the composites C and D, with the less molar ratio of $Cu_2O$ polyhedral particles, with a value around 136 μmol/gr.

**a)** **b)**

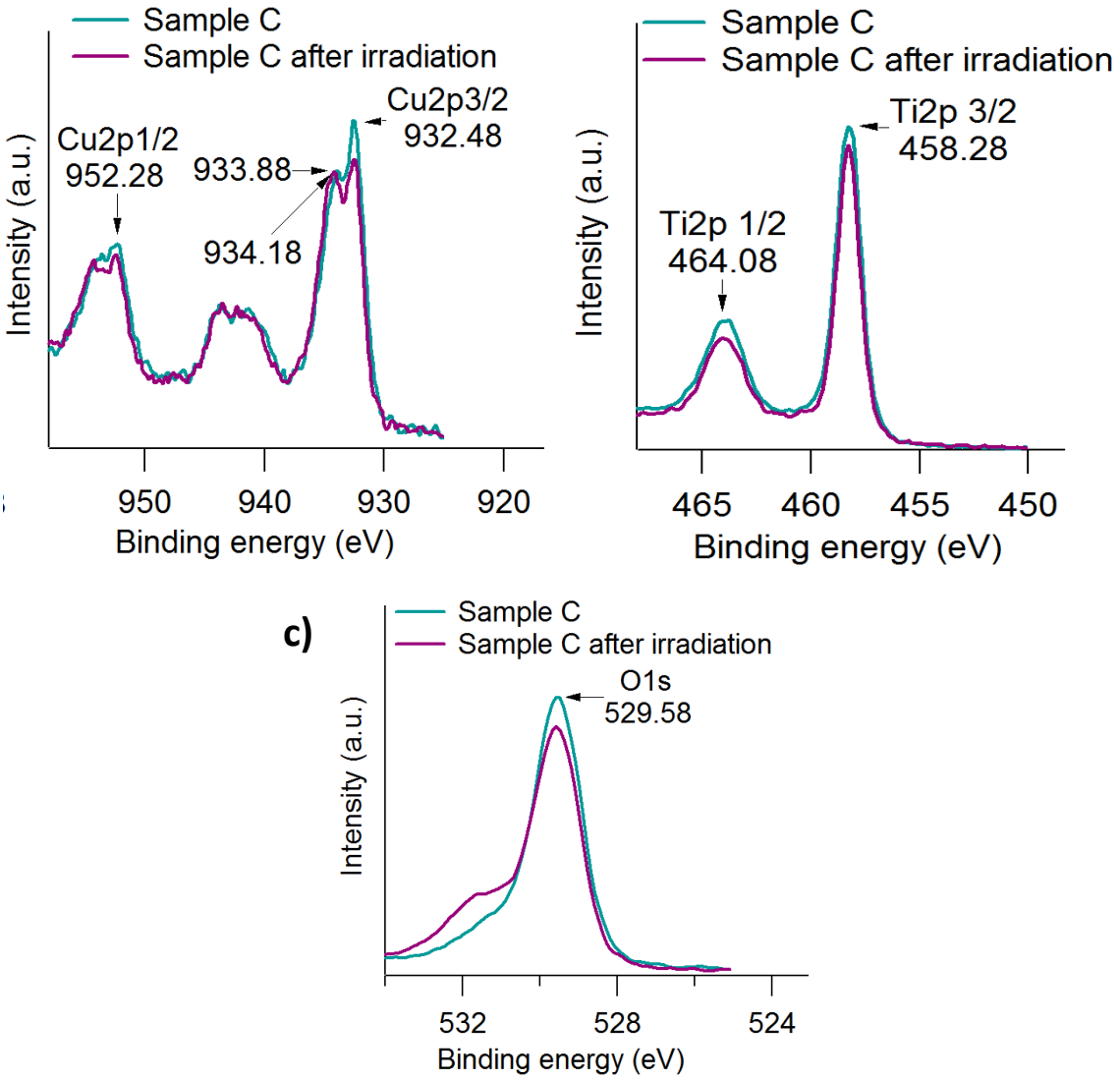


**Fig. 3.** a) Peaks of copper b) Peaks of titanium,c) Peaks of oxygen d) New peaks after irradiation

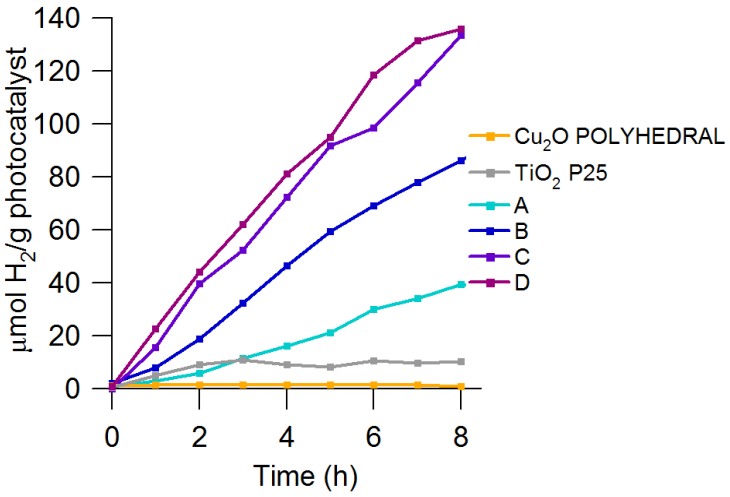


**Fig. 4.** Hydrogen production by methanol photoreforming under solar simulator.

## 4. Conclusion

$Cu_2O$ polyhedral particles were synthesized successfully at room temperature.The $Cu_2O/TiO_2$ composites conserved their specific band structure with a minimal interaction. The closeness of the two oxides was enough for improving the charge separation in the photocatalytic system and the highest hydrogen production compared to each oxide.

## Acknowledgements

The authors acknowledge the financial supports of SIP 20170002 and SIP 20171127. FPH is grateful for CONACyT and BEIFI fellowships.

## References

[1] Li Y, Wang B, Liu S, Duan X, Hu Z. Synthesis and characterization of Cu2O/TiO2 photocatalysts for H2 evolution from aqueous solution with different scavengers. Appl Surf Sci 2015;324:736–44. doi:10.1016/j.apsusc.2014.11.027.

[2] Rahman MM. H2 production from aqueous-phase reforming of glycerol over Cu-Ni bimetallic catalysts supported on carbon nanotubes. Int J Hydrogen Energy 2015;40:14833–44. doi:10.1016/j.ijhydene.2015.09.015.

[3] Jung M, Hart JN, Boensch D, Scott J, Ng YH, Amal R. Hydrogen evolution via glycerol photoreforming over Cu-Pt nanoalloys on TiO2. Appl Catal A Gen

2016;518:221–30. doi:10.1016/j.apcata.2015.10.040.

[4] Huang L, Peng F, Wang H, Yu H, Li Z. Preparation and characterization of Cu2O/TiO2 nano-nano heterostructure photocatalysts. Catal Commun 2009;10:1839–43. doi:10.1016/j.catcom.2009.06.011.

[5] Han T, Zhou D, Wang H, Zheng X. The study on preparation and photocatalytic activities of Cu2O/TiO2 nanoparticles. J Environ Chem Eng 2015;3:2453–62. doi:10.1016/j.jece.2015.09.020.

[6] Falah M, MacKenzie KJD. Synthesis and properties of novel photoactive composites of P25 titanium dioxide and copper (I) oxide with inorganic polymers. Ceram Int 2015;41:13702–8. doi:10.1016/j.ceramint.2015.07.198.

[7] Liu L, Yang W, Sun W, Li Q, Shang JK. Creation of Cu2O@TiO2 composite photocatalysts with p - N heterojunctions formed on exposed Cu2O facets, their energy band alignment study, and their enhanced photocatalytic activity under illumination with visible light. ACS Appl Mater Interfaces 2015;7:1465–76. doi:10.1021/am505861c.

[8] Geng Z, Zhang Y, Yuan X, Huo M, Zhao Y, Lu Y, et al. Incorporation of Cu2O nanocrystals into TiO2 photonic crystal for enhanced UV–visible light driven photocatalysis. J Alloys Compd 2015;644:734–41. doi:10.1016/j.jallcom.2015.05.075.

# 1.33 Enhanced Photocatalytic Activity for $H_2$ Production by RGO/P25 Composite through UV Assisted Anchoring

B. C. Hernández-Majalca, M.J. Melendez-Zaragoza, J.M. Salinas-Gutiérrez, A. López-Ortiz, V. Collins-Martínez

Laboratorio Nacional de Nanotecnología Centro de Investigación en Materiales Avanzados, S. C. Chihuahua, Chih., México
* Corresponding author: virginia.collins@cimav.edu.mx

## ABSTRACT

In this work, graphene oxide (GO) was prepared by the Tour method from graphite powder employing a microwave pre-treatment, which was used to modify $TiO_2$ (P25). A composite of reduced graphene oxide (RGO) and P25 was prepared (RGO/P25) by UV assisted anchoring of P25 on RGO. The structure, morphology, textural and optical properties were studied by XRD, SEM, BET and UV-Vis techniques, respectively. Water splitting photocatalytic evaluation used an aqueous methanol solution of the suspended composite material and a 250 W mercury lamp as light irradiation source. Results indicate a bandgap value of 2.57 eV for the RGO/P25 composite, while this material exhibited a $H_2$ production rate greater than either P25 or graphene oxide alone. A significant enhancement in the hydrogen production rate was achieved by RGO/P25 as photocatalyst obtaining ~400 µmol $H_2$/gh. This can be presumably attributed to graphene oxide acting as an electron collector and transporter in the RGO/P25 composite.

***Keywords:*** graphene oxide, anchorage UV-assisted, Photocatalysis, hydrogen production.

## Introduction

Globally, the demand for energy in the coming years will considerably increase. An ideal alternative, already considered, is solar energy becoming the most powerful, accessible as far as "cost" is concerned, as well as the richest source of renewable and sustainable energy [1].

Furthermore, hydrogen has a high specific energy density and its combustion generates only water as a by-product, which makes $H_2$ an attractive carbon free fuel. Despite the fact that hydrogen in its elemental form is not very abundant in the environment, this is offset by its abundant natural source (water molecule) the obtaining of this fuel and the combination of the use of solar technologies, makes it possible to cover the global demand for energy in an environmentally friendly manner.

Nowadays, there is a variety of methods used to produce hydrogen by water splitting using solar radiation [2], [3]; photovoltaic electrolysis of water by proton exchange membranes [4] and alkaline electrolytes [5], which is costly, the thermochemical method that needs

very high temperatures 700-1000°C [6] and the photo-electrochemical process, which is very interesting due to its simplicity and potential for development in the future [7].

Since water splitting by photo-electrochemical processes with a $TiO_2$ electrode was reported[2] photocatalytic production of $H_2$ has been of great interest. A wide variety of semiconductor materials with photocatalytic properties have been studied, for example: $C_3N_4$ [3], $TiO_2$ [10, 11], $BiVO_4$[6], CdS[7], $WO_3$[8]and ZnO [15, 16]. Not to mentionthe use of the Pt as dopantforthesematerials, itisworthmentioningthat Pt ishighcostelement and thisrepresentsa greatdisadvantageas a massivetechnologyforhydrogenproduction.

The tendency to use semiconductor nanomaterials for the development of photon energy storage technologies, has paved the way for novel techniques to use renewable resources. All this as a consequence of their large surface areas and different morphologies [11]. In order to solve the different issues arising in $TiO_2$ lack of photoactivity under visible light irradiation, several proposals have been implemented as doping with metal ions [12], carbon or nitrogen [13], as well as addition of sacrifice elements, as either electron donors or holes scavengers [14].

Among the range of materials that can be selected to synthetize composites with $TiO_2$ and improve its photocatalytic efficiency is the introduction of nanostructured carbon materials (carbon nanotubes, fullerenes, graphene single layers) [21-23], which offer unique benefits, such as chemical stability in both basic and acidic environments and flexible textural properties. Recently, these materials and, in particular, graphene have awaken great interest in this context because of its unusual structural and electronic properties [18].

RGO/$TiO_2$ as photocatalyst

$$TiO_2 + h\nu \rightarrow TiO_2(h + e) \xrightarrow{C_2H_5OH} TiO_2(e) + C_2H_4OH + H^+ \quad (1)$$

$$TiO_2(e) + GO \rightarrow TiO_2 + RGO \quad (2)$$

RGO/$TiO_2$ composites have achieved great popularity because of their complementary properties, and can be synthesized by different techniques. One of them is by photo-assistedreduction, which consist in the use of the photocatalytic nature of $TiO_2$. Through the use of reducing agents such as hydrazine, glucose andseveral solvents including water [19]. Using mixing or sonication, which is the most simple method, however the interaction between the two materials is weak because a chemical bond is expected [20]. Another popular technique is by Sol-gel, that is the most used to obtain a chemical interaction between the GO and the $TiO_2$, generally the GO layers are available to interact with the precursors of the $TiO_2$ due to the solubility of the GO, however,GO in aqueous solutions are not adequate for the reason that induces the precipitation of $TiO_2$, therefore, the use of ethanol[21]. Other techniques include hydrothermal and solvothermal methods that involve controlled pressure and temperature during its synthesis, however, these are not highly recommended because the $TiO_2$crystalline phase may change and sometimes the reduction of graphene oxide is not adequate[18].

The first researchperformed about RGO/$TiO_2$ synthesisby UV-assisted photo reduction was reported by Williams et al, where GO was reduced by accepting electrons generated from $TiO_2$ at the time of being irradiated. The following reaction equations describe thismechanism[22].

## Methodology

### Oxidation of graphite

Graphite oxide was synthesized from graphite powder using a modification of Hummers method [30, 31]. 1 g of graphite was subjected to a microwave pretreatment [25] during 15s, immediately after the sample was added to a concentrated solution of $H_2SO_4$ /$H_3PO_4$ with 9:1 ratio (43.2 mL and 4.8 mL, respectively), this mixture is kept under magnetic stirringin an ice bath (4°C) for 3 h. After this time 6 g of $KMnO_4$ were added by shaking for 2 h, finally a solution of $H_2O_2$ (12 mL) and HCl 10% (13 mL) was added by drip irrigation keeping the mixture with stirring for 0.5 h; even in ice due to the exothermic nature of the reaction [26]; Next step was washing and filtering with trice distillated water, assisted by a vacuum pump until the remains of acid and potassium permanganate present in the mixture are removed, once completed this step GO is taken to dryness in a muffle furnace at 65°C.

### Composite of $TiO_2$ anchored in reduced graphene oxide

For this study a commercial titanium dioxide Evonik P25was utilized. To synthesize the compositeof reduced graphene oxide/titanium dioxide (RGO/ $TiO_2$) a certain amount of microwaved graphene oxide (MWGO) and $TiO_2$(as required to obtain 10 % by weight of graphene oxide) was suspended in an aqueous solution at 30% ethanolusing an ultrasonic bath (Branson 2510) at a frequency of 40 kHz for 15 min, separately. Additionally, the GO to the P25 is also subjected to ultrasound to obtain a homogeneous suspension. After 15 min, the MWGO suspension is poured into the suspension of $TiO_2$, continuing exposure to sonication until 40 min. The sample is then placed within a photoreaction systemunder visible radiation of a mercurial lamp (250 W) and stirring continues for 24 h, the resulting solution was dried on a hot plate at 80°C for 12h.

### Characterization

### X-ray diffraction

Crystalline phases present in each of the synthesized materials in this study were determined by the x-ray diffraction technique by making use of a Phillips Xpert Pro diffractometer, which used a copper Cu kα radiation (λ = 1.54056 Å). Diffraction patterns were obtained with a 2θ sweep angleof 5° to 90°, with a step of 0.05.

### Diffuse reflectance spectroscopy

Absorption and diffuse reflectance spectra of the synthesized samples were analyzed in a UV-Visible Evolution 220 Thermo UV spectrophotometer equipped with integration sphere, the range used in this technique were visible and near UV (adjacent to and part of the near IR) 190-1100 nm wavelengths, the band gap values can be estimated using the Tauc technique by plotting KubelkaMunk units against energy in electron volts (eV) considering the following equation:

$$\alpha_b = \frac{B(hv - E_g)\hat{}n}{hv} \quad (3)$$

where $\alpha_b$ is the absorption coefficient, hν is the absorbed energy, B is the absorption constant and n takes values of ½ or 2 if director indirect transition occur, respectively.

In order to determine the band gap energy value of the samples the Kubelka-Munk approach was used, which estimates this value by extrapolation where $\alpha = 0$ [27].

### Field emission scanning electron microscopy

Synthesized sample was analyzed by field emission scanning electronic microscopy(FESEM) in aJEM-2200FS Field Emission Transmission Electron Microscope, where the sample will be exposed to a beam of electrons generated from a tungsten filament, to minimize energy losses or deviations of the beam, the column must operate under a ultra-high vacuum of $10^{-8}$ Torr[28].

### Photocatalytic Evaluation

The photocatalytic activity was evaluated based on the performance of the material towards the production of hydrogen for the dissociation of the water molecule, using a

250W mercurial lamp as a source of energy, 2% methanol aqueous solution as ansacrificeagent. Monitoring of the reaction was followed by gas chromatography using a gas chromatograph Perking Elmer Clarus 580, taking aliquots at 1h time intervals with 8 repetitions.

## Results and discussion

### X-ray diffraction

Phase and crystalline structure of the samples were analyzed by X-ray diffraction.

Fig. 1 shows the diffraction pattern of graphite (GR), as well as MWGO, P25 and RGO/P25samples. GR shows the major intensity peak stake at an angle 2θ= 28°≅3.18Å, which belongs to typical graphite. The diffraction pattern of MWGO presents a signal at 2θ=17°≅ 5.02 Å, corresponding to graphene oxide, the peak in 2θ= 44° which is associated with RGO forming a crystal block according to Hontoria et al. [29] may be a highly oriented graphene oxide. However, an increase in the amorphous phase is observed, which is mainly associated with the partial decomposition of the oxygenated groups of graphene oxide, while the increase in the width of the peak is attributed to the generation of a more separated laminar structure, which allows physical and chemical intercalation [30].

P25 diffraction pattern denotes the presence of Anatase and Rutile crystalline phases. From the Rietveld plot of the composite, it can be clearly seen a fading signal attributed to graphene oxide showing mainly the characteristic P25peaks, while maintaining the amorphous phase associated with graphene oxide.

This behavior can be mainly attributed to two processes; reduction of graphene oxide by $TiO_2$ photo anchorage and to the exfoliation of graphene oxide during sonication.

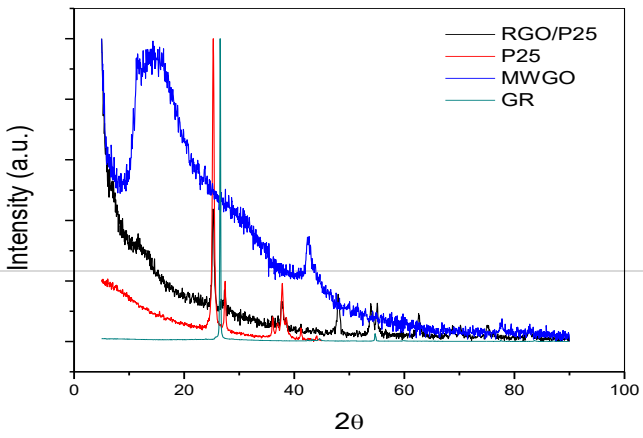

**Fig. 1 Rietveld plot belonging to Graphite (GR) $TiO_2$ (P25), MWGO and RGO/P25 10% wt.**

UV-Vis Spectroscopy diffuse reflectance

Fig. 2 a) shows the plot of the percentage of absorption of GRO/P25 obtained using the diffuse reflectance in a wavelength range from 190 to 1100 nm, showing the limit of its range of absorption at 460nm, which means a maximum absorbance in the visible range [27]. In order to estimate the band gap value of the sample a Tauc graph was generated by plotting the Kubelka-Munk function against the light energy, which produced an estimated value of the indirect band gap of 2.57 e.V.

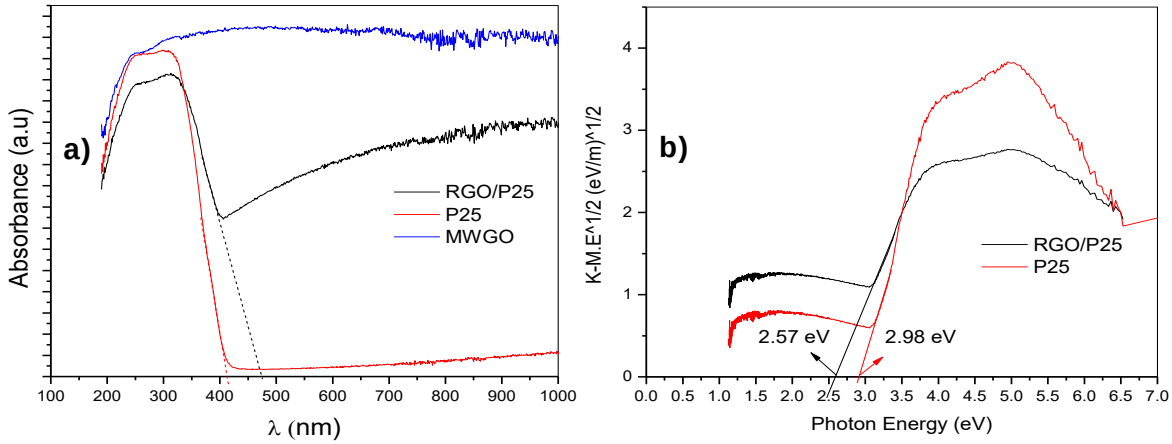


**Fig. 2 a) UV-Vis spectrometry to determinate the band gap using the absorbance pattern of the RGO/P25 sample. b) Estimation of the indirect band gap by the Tauc plot through the approximation of the Kubelka-Munk coefficient (Comparison Chart).**

Fig. 2 b) shows a comparison betweenRGO/P25 and P25 behavior, where RGO/P25 presentsits maximum absorption shifted to a visible range. These results are consistent

whitobservations by Cheng et al., in addition to being similar to the values achieved when P25 is doped with carbon[31] with values reported in the literature ranging from 2.66 eV to 3.18 eV.

This decrease in band gap energy can be attributed to the change in the bands structure, which is widely associated with the improvement ofP25interaction with RGO [20].

Scanning electron microscopy (SEM)

Morphology of the RGO/P25 was investigated through scanning electron microscopy, as revealed in the micrograph of Fig. 3. In this Figure, it can be seen that P25 is supported in the leaves of RGO, and that the length of the RGO is in the order of microns. This is morphology is associated with the microwave pretreatment during the synthesis of graphene oxide [25]. This unique morphology allows a greater amount of P25 particles to be physisorbedby RGO, which may lead to small agglomerates, it is difficult to assess groups of less than 5 sheets of RGO or a monolayer of RGO, because they are often confused with the membrane of the grid used for the analysis. However, in the MWGO image a) it can be seen that exfoliation is poor. The images (b) and (c) confirms the existence of fixed single layers along with P25. Images (d) and (e) are groups of less than 5 sheets of RGO andin image f) it can be observed that P25 nanoparticles arealternately anchored on the layers of RGO, such as in sandwich structure [32], [33], which shows a

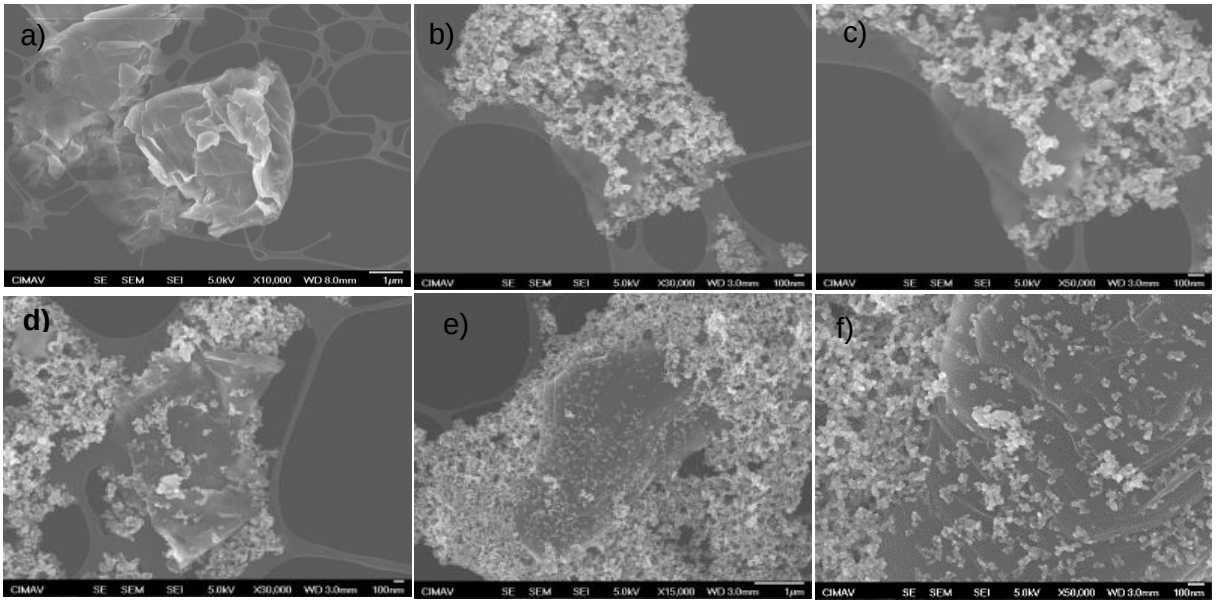


**Fig. 3 a) MWGO, b) and c) RGO/P25 monolayer, d) and e) RGO/P25 < 5 layers, f) RGO/P25 type sandwich.**

successful RGO exfoliation by sonication, as well as the P25 photo anchorage.

Photocatalytic Evaluation

Incorporation of RGO to P25 has unique advantages;**¡Error! No se encuentra el origen de la referencia.** shows the hydrogen evolution produced by P25, MWGO, RGO/P25materials, which were evaluated as photocatalysts under the standards for hydrogen generation with a production of 187,150 and 400μmol/gh, respectively. From these results it can be concluded that the RGO/P25 exhibits an enhanced performance than their precursors, since it is evident that the photocatalytic properties of P25 were improved. This improvement is related to the RGO electrical properties as electrons collector and to its great charge mobility, a feature that is attributed to its two-dimensional structure [30]. In addition to this the unpaired πelectrons of RGO, make the surface interaction of P25 with the RGO to extend the range of absorption of P25. Even though there was not a significant change in the specific area of 60 $m^2/g$ for the P25 and 52$m^2/g$ for RGO [34]. This change in $TiO_2$ photocatalytic activity cannot be attributed to the specific surface area enhancement. Otherwise, this effect can be ascribedto the increase in charge transfer triggered by RGO, due to its two-dimensional structure and the conjugation of the pi bond [35], which makes to extend the absorption of light, so the electrons in the P25 are transferred to the RGO, thus allowing a reduction in the recombination time of charges.

Conclusions

Microwavepretreatment of the Graphite favors the intercalation of the oxygenated functional groups and its sonic exfoliation.

These oxygenated functional groups facilitatethe photo anchoring of the $TiO_2$P25 and the formation of sandwich-type structures.

The shifting of the band gap value toward the visible spectrum of the P25 is associated to the addition of small amounts of RGO.

Improvement of the P25 photocatalytic activity for hydrogen production under visible light can be attributed to reduction of its band gap energy value by doping with RGO.

**Acknowledgements**

The authors acknowledge M.Sc. Ernesto Guerrero Lestarjette, M. Sc. Karla Campos Venegas, Eng. Wilber Antunez Flores, and Eng. Luis de la Torre Saenz for their contributions to the XRD, SEM, BET, results. Special thanks are given to Laboratorio Nacional de Nanotecnología in Centro de InvestigaciónenMaterialesAvanzados, S. C., for their support in the use of the facilities.

## References


[1] A. Paracchino, V. Laporte, K. Sivula, M. Grätzel, and E. Thimsen, "Highly active oxide photocathode for photoelectrochemical water reduction," *Nat. Mater.*, vol. 10, no. 6, pp. 456–461, Jun. 2011.

[2] A. Fujishima and K. Honda, "Electrochemical photolysis of water at a semiconductor electrode.," *Nature*, vol. 238, no. 5358, pp. 37–8, Jul. 1972.

[3] X. Wang *et al.*, "A metal-free polymeric photocatalyst for hydrogen production from water under visible light," *Nat. Mater.*, vol. 8, no. 1, pp. 76–80, Jan. 2009.

[4] S. Li, D. Chen, F. Zheng, H. Zhou, S. Jiang, and Y. Wu, "Water-Soluble and Lowly Toxic Sulphur Quantum Dots," *Adv. Funct. Mater.*, vol. 24, no. 45, p. n/a-n/a, Sep. 2014.

[5] F. Zuo *et al.*, "Active Facets on Titanium(III)-Doped $TiO_2$: An Effective Strategy to Improve the Visible-Light Photocatalytic Activity," *Angew. Chemie Int. Ed.*, vol. 51, no. 25, pp. 6223–6226, 2012.

[6] Q. Jia, K. Iwashina, and A. Kudo, "Facile fabrication of an efficient $BiVO_4$ thin film electrode for water splitting under visible light irradiation.," *Proc. Natl. Acad. Sci. U. S. A.*, vol. 109, no. 29, pp. 11564–9, Jul. 2012.

[7] Y. Li, Y. Hu, S. Peng, G. Lu, and S. Li, "Synthesis of CdS Nanorods by an Ethylenediamine Assisted Hydrothermal Method for Photocatalytic Hydrogen Evolution," *J. Phys. Chem. C*, vol. 113, no. 21, pp. 9352–9358, May 2009.

[8] M. Higashi, R. Abe, T. Takata, and K. Domen, "Photocatalytic Overall Water Splitting under Visible Light Using $ATaO_2$ N (A = Ca, Sr, Ba) and $WO_3$ in a $IO_3^-$ /$I^-$ Shuttle Redox Mediated System," *Chem. Mater.*, vol. 21, no. 8, pp. 1543–1549, Apr. 2009.

[9] X. Lu *et al.*, "Efficient photocatalytic hydrogen evolution over hydrogenated ZnO nanorod arrays," *Chem. Commun.*, vol. 48, no. 62, p. 7717, 2012.

[10] P. Gao, Z. Liu, and D. D. Sun, "The synergetic effect of sulfonated graphene and silver as co-catalysts for highly efficient photocatalytic hydrogen production of ZnO nanorods," *J. Mater. Chem. A*, vol. 1, no. 45, p. 14262, 2013.

[11] A. Fujishima, X. Zhang, and D. A. Tryk, "Heterogeneous photocatalysis: From water photolysis to applications in environmental cleanup," *Int. J. Hydrogen Energy*, vol. 32, pp. 2664–2672, 2007.

[12] M. Amir, U. Kurtan, and A. Baykal, "Rapid color degradation of organic dyes by $Fe_3O_4$@His@Ag recyclable magnetic nanocatalyst," *J. Ind. Eng. Chem.*, vol. 27, pp. 347–353, Jul. 2015.

[13] R. Asahi, T. Morikawa, T. Ohwaki, K. Aoki, and Y. Taga, "Visible-Light Photocatalysis in Nitrogen-Doped Titanium Oxides," *Science (80-. ).*, vol. 293, no. 5528, pp. 269–271, Jul. 2001.

[14] Q. Xiang, J. Yu, and M. Jaroniec, "Enhanced photocatalytic H2-production activity of graphene-modified titania nanosheets," *Nanoscale*, vol. 3, no. 9, p. 3670, Sep. 2011.

[15] M. J. Sampaio, C. G. Silva, R. R. N. Marques, A. M. T. Silva, and J. L. Faria, "Carbon nanotube–$TiO_2$ thin films for photocatalytic applications," *Catal. Today*, vol. 161, no. 1, pp. 91–96, Mar. 2011.

[16] J. Yu, T. Ma, G. Liu, and B. Cheng, "Enhanced photocatalytic activity of bimodal mesoporous titania powders by C60 modification," *Dalt. Trans.*, vol. 40, no. 25, p. 6635, 2011.

[17] F. Wang and K. Zhang, "Physicochemical and photocatalytic activities of self-assembling $TiO_2$ nanoparticles on nanocarbons surface," *Curr. Appl. Phys.*, vol. 12, no. 1, pp. 346–352, Jan. 2012.

[18] S. Li, X. Pan, L. K. Wallis, Z. Fan, Z. Chen, and S. A. Diamond, "Comparison of $TiO_2$ nanoparticle and graphene–$TiO_2$ nanoparticle composite phototoxicity to Daphnia magna and Oryzias latipes," *Chemosphere*, vol. 112, pp. 62–69, 2014.

[19] D. R. Dreyer *et al.*, "The chemistry of graphene oxide," *Chem. Soc. Rev.*, vol. 39, no. 1, pp. 228–240, 2010.

[20] S. Morales-Torres, L. M. Pastrana-Martínez, J. L. Figueiredo, J. L. Faria, and A. M. T. Silva, "Design of graphene-based $TiO_2$ photocatalysts—a review," *Environ. Sci. Pollut. Res.*, vol. 19, no. 9, pp. 3676–3687, Nov. 2012.

[21] X.-Y. Zhang, H.-P. Li, X.-L. Cui, and Y. Lin, "Graphene/$TiO_2$ nanocomposites: synthesis, characterization and application in hydrogen evolution from water photocatalytic splitting," 2010.

[22] G. Williams, B. Seger, and P. V. Kamt, "$TiO_2$-graphene nanocomposites. UV-assisted photocatalytic reduction of graphene oxide," *ACS Nano*, vol. 2, no. 7, pp. 1487–1491, Jul. 2008.

[23] W. S. Hummers and R. E. Offeman, "Preparation of Graphitic Oxide," *J. Am. Chem. Soc.*, vol. 80, no. 6, pp. 1339–1339, 1958.

[24] J. M. Tour *et al.*, "Improved synthesis of graphene oxide," *ACS Nano*, vol. 4, no. 8, pp. 4806–4814, 2010.

[25] X. Liu *et al.*, "Microwave-assisted production of giant graphene sheets for high performance energy storage applications," *J. Mater. Chem. A*, vol. 2, no. 31, pp. 12166–12170, 2014.

[26] B. Dehghanzad, M. K. Razavi Aghjeh, O. Rafeie, A. Tavakoli, and A. Jameie Oskooie, "Synthesis and characterization of graphene and functionalized graphene via chemical and thermal treatment methods," *RSC Adv.*, vol. 6, no. 5, pp. 3578–3585, 2016.

[27] P. Cheng *et al.*, "$TiO_2$-graphene nanocomposites for photocatalytic hydrogen production from splitting water," *Int. J. Hydrogen Energy*, vol. 37, no. 3, pp. 2224–2230, 2012.

[28] J. I. Goldstein and H. Yakowitz, *Practical Scanning Electron Microscopy : Electron and Ion Microprobe Analysis*. Springer US, 1975.

[29] C. Hontoria-Lucas, A. J. López-Peinado, J. de D. López-González, M. L. Rojas-Cervantes, and R. M. Martín-Aranda, "Study of oxygen-containing groups in a series of graphite oxides: Physical and chemical characterization," *Carbon N. Y.*, vol. 33, no. 11, pp. 1585–1592, 1995.

[30] W. Gao, *Graphene Oxide*. Cham: Springer International Publishing, 2015.

[31] L. Shen, X. Zhang, H. Li, C. Yuan, and G. Cao, "Design and tailoring of a three-dimensional $TiO_2$-graphene-carbon nanotube nanocomposite for fast lithium storage," *J. Phys. Chem. Lett.*, vol. 2, no. 24, pp. 3096–3101, 2011.

[32] X. Zhang *et al.*, "Electrospun $TiO_2$ –Graphene Composite Nanofibers as a Highly Durable Insertion Anode for Lithium Ion Batteries," *J. Phys. Chem. C*, vol. 116, no. 28, pp. 14780–14788, 2012.

[33] X. Rong, F. Qiu, C. Zhang, L. Fu, Y. Wang, and D. Yang, "Preparation, characterization and photocatalytic application of $TiO_2$-graphene photocatalyst under visible light irradiation," *Ceram. Int.*, vol. 41, no. 2, pp. 2502–2511, 2015.

[34] Y. Zhang, Z. R. Tang, X. Fu, and Y. J. Xu, "Engineering the unique 2D mat of graphene to achieve graphene-$TiO_2$ nanocomposite for photocatalytic selective transformation: What advantage does graphene have over its forebear carbon nanotube?," *ACS Nano*, vol. 5, no. 9, pp. 7426–7435, 2011.

[35] M. J. Allen, V. C. Tung, and R. B. Kaner, "Honeycomb carbon: A review of graphene," *Chem. Rev.*, vol. 110, no. 1, pp. 132–145, 2010.

# 1.34 Determination of local volumetric rate of photon absorption of $NiFe_2O_4$ photocatalyst in aqueous suspensions under visible light

Jorge Domínguez-Arvizu, Alejandro López Ortiz, J. M. Salinas-Gutierrez, M. J. Meléndez-Zaragoza, Virginia Collins-Martínez

[1]Centro de Investigación en Materiales Avanzados S. C., Miguel de Cervantes 120, CP. 31136, Chihuahua, México

* Corresponding author: virginia.collins@cimav.edu.mx, jorge.dominguez@cimav.edu.mx

## ABSTRACT

In the present work the absorption ($\kappa$) and scattering ($\sigma$) coefficients were determined for $NiFe_2O_4$ nanoparticles in aqueous suspensions. The photocatalyst was previously synthetized by a modified Pechini method, measurements were carried out through UV/Visible spectroscopy, and experimental data were fitted with a new proposed model called 3-dim-3-dir. The resultant coefficients were used to solve the radiative transfer equation (RTE) using a discrete ordinated method (DOM) in order to determine the local volumetric rate of photon absorption (LVRPA) in a proposed reactor design model employing $NiFe_2O_4$ as photocatalyst.

***Keywords:*** Visible light photocatalyst; LVRPA; Radiative transfer equation; absorption and scattering coefficients

## 1. Introduction

Nowadays, fossil fuels supply about 90% of energy in transportation and industrial sectors. In 2013 energy consumption reached approximately 17 TW and according to the U.S. EIA (Energy information administration) a 56% increment is expected for 2040 where the fossil fuels will comprise the 78%. Massive utilization of fossil fuels has been responsible for climate change due to greenhouse gases generation and pollutant emissions, besides to produce other harmful effects such as acid rain, increasing ozone concentration in urban zones and particle emissions affecting the environment. For those reasons, global interests have been oriented towards developing new energy systems capable of balancing energy supplies and current demands, protecting the environment, and ensuring reliable energy power sources as well as economic viability [1-4].

Within proposed alternatives, hydrogen as energy carrier is considered advantageous with respect to fossil fuels as numerous studies suggest hydrogen would be a more economic and cleaner energy source. Furthermore, this fuel has 2.75 times higher energy yield (122 kJ/g) than typical fossil fuels. To be economically sustainable hydrogen must be obtained from a renewable source e.g. solar energy. While, photocatalysis is one of the most promising technologies for this purpose, since $H_2$ and $O_2$ molecules can be directly obtained from a water splitting process through light irradiation of semiconductor materials. Among main features of these photocatalyst must present: a high efficiency and photocorrosion stability, not be harmful to the environment and to be active under visible light [5, 6].

At this moment, $TiO_2$ is the most common and widely studied photocatalyst, this is due to its high stability and photocorrosion resistance. There is a considerable number of publications where reactor modeling and design have been carried out for hydrogen production [7, 8] and water/air purification [9, 10] with this material. Nevertheless, $TiO_2$ efficiency is very low under visible light, since this process is limited to UV light sources, which unfortunately comprises 4% of solar light irradiation. It is in this sense, that the search of a highly efficient active material under visible light (which comprises the 43% of the solar energy) has become one of the most important challenges in today's photoreactor design [11, 12].

As an alternative, transition metals ferrites have in general a low cost, high photocorrosion resistance and activity under visible light. Selection of these materials is based on their redox activity and specifically on their ability to store oxygen in its crystalline lattice. This phenomena are due to the tendency of these materials to form oxygen vacancies when they are synthetized by methods that generate reducing atmospheres while increasing its photocatalytic activity [11].

However, at the present, there are no publications related to photoreactor designs that comprise these materials. Therefore, it is necessary to determine their optical properties in aqueous suspensions, i.e. the absorption coefficient ($\kappa$), scattering coefficient (σ) and the phase function p (Ω´→Ω), which only have been determined for $TiO_2$ at the present using methodologies involving UV/visible spectroscopy and a mathematical model called 1-dim-1dir [13, 14].

These optical properties play an important role in determining the radiation distribution of heterogeneous photoreactors, since those are required to solve the radiative transfer equation (RTE) [15]:

$$\frac{dI_\lambda(s,\Omega)}{ds} = -\kappa_\lambda I_\lambda(s,\Omega) - \sigma_\lambda I_\lambda(s,\Omega) + \frac{1}{4\pi}\sigma_\lambda \int_0^{4\pi} p(\Omega' \rightarrow \Omega)\, I(s,\Omega')d\Omega' \qquad \textbf{(2)}$$

RTE solution will provide the radiation intensity distribution in the reactor, and with this information it is possible to calculate the local volumetric rate of photon absorption (LVRPA), a parameter directly related to the photochemical reaction kinetics [12, 16].

This work is aimed to determine the absorption and scattering coefficients of $NiFe_2O_4$ aqueous suspensions previously synthetized by a modified Pechini's method in order to calculate the LVRPA in a proposed design of an aqueous photoreactor by means of the RTE solution. All of this, aiming to take advantage of $NiFe_2O_4$ as a potential photocatalytic material for hydrogen production under visible light.

## 2. Materials and Methods

### *2.1 The phase function*

The phase function describes the directional distribution of scattered radiation. In order to choose the appropriate mathematical expression for it, there is a size parameter (ξ) related to the wavelength $\lambda$ of the radiation inside the reactor and the particle spherical size $d_p$ that needs to be determined through the equation 2.

In order to measure $d_p$ of the particle agglomerates, SEM images were taken in a field emission microscope JEM-2200-FS. Samples were prepared over a carbon coated copper grid by dispersing 1 mg of the material in 1mL of distilled water and sonicating for 20 minutes.

$$\xi = \left[\frac{\pi d_p}{\lambda}\right]_{min} \quad \textbf{(3)}$$

Later, a drop of suspension was applied over the grid and it was exposed to a lamp to evaporate the water. Figure 1 shows an image of $NiFe_2O_4$ nanoparticle agglomerates.

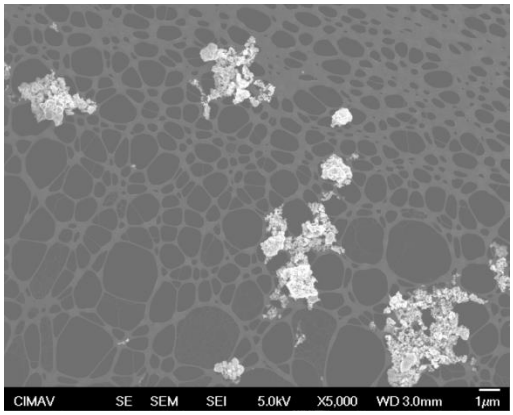


**Fig 1. $NiFe_2O_4$ nanoparticles agglomerates formed in aqueous suspensions**

An estimate of the size parameter ξ, was obtained by measuring the shortest distance of the agglomerates in various sample zones, where the minimum value of $d_p$ was set to 100 nm, and using the maximum wavelength in the experiments (800 nm), thus obtaining a value equal to 0.4.

According to the assumption that the agglomerates are of spherical shape, the adequate phase function to be used is the following [12]:

$$p(\theta) = 1 + A\cos(\theta) \quad \textbf{(4)}$$

With A= 1, 0, -1 for forward, isotropic and backward scattering, respectively.

### *2.2 Extinction coefficient*

In radiation transport theory, the sum of the scattering and absorption contribution represents the extinction coefficient ($\beta = \sigma + \kappa$). Through absorbance measurements in a heterogeneous medium, the obtained data will provide the "lost" radiation by absorption and light scattering (Figure 2). Thus, the "extinctance" will be obtained through UV/Vis measurements [13].

For the extinction coefficient determination, $NiFe_2O_4$ suspensions were prepared in 100 mL volumetric flasks at 0.13, 0.26, 0.35 y 0.48 g/L with distilled water, which were exposed under sonication during the whole experiment. Quartz cells with 10 mm path length were used and the measurements were carried out in a Perkin Elmer Lambda 35 UV/Vis spectrometer using distilled water as a blank reference.

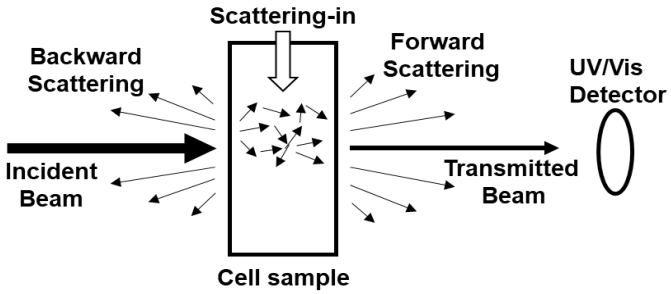


**Fig 2. Optical phenomena involved in the determination of the extinction coefficient**

With the objective of avoiding an eventual settling of coarser aggregates, readings were punctually carried out from 300 to 800 nm in 100 nm intervals by replacing the suspension every time a measurement was performed.

The extinction coefficient was calculated through the following equation:

$$\beta_\lambda = \frac{2.303 EXT_\lambda}{L} \quad \textbf{(5)}$$

Where *L* is the path length of the quartz cell and $EXT_\lambda$ denotes the extintance.

Later, a specific extinction coefficient per unit mass was obtained ($\beta^*_\lambda = \beta_\lambda/C_m$) [$m^2/g$] by calculating the slope of the curve through a linear regression of the $\beta_\lambda$ vs $C_m$ data that showed a linear relationship.

### *2.3 Absorption coefficient*

By means of transmittance measurements with an integrating sphere model RSA-PE-20 Labsphere, the front scattered and transmitted rays were detected by positioning the quartz cell in front of the sphere. To collect the whole rays mentioned before, a blank with a ~1 reflectance made of Spectralon® material was positioned behind the sphere. The whole system configuration used is shown in Figure 3.

Same conditions as in the extinction coefficient were performed during sample preparation corresponding to 0.10, 0.22, 0.31 and 0.37 g/L concentrations and the absorption coefficient ($\kappa_\lambda$) was obtained through the following equation:

$$\kappa_\lambda = \frac{2.303}{L}\log\frac{1}{T_\lambda} \qquad (6)$$

Where *L* is the path length of the quartz cell and transmittance is $T_\lambda$.

A linear regression from $C_m$ vs $\kappa_\lambda$ plots (resulting in a linear trend) was carried out in order to obtain a specific absorption coefficient $\kappa^*_\lambda$ through the slope of this data. Finally the scattering coefficient $\sigma^*_\lambda$ was obtained from the difference $\beta^*_\lambda - \kappa^*_\lambda$.

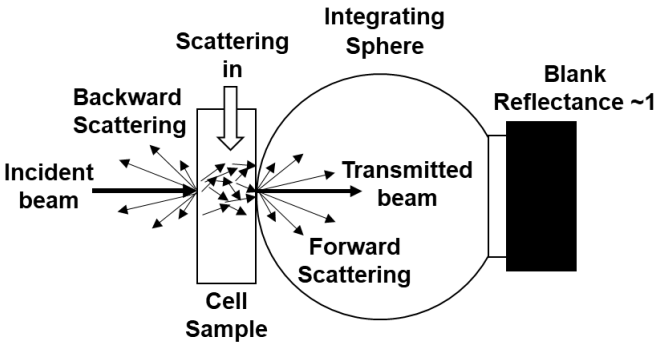


**Fig. 3. Scheme configuration to evaluate absorption coefficients in $NiFe_2O_4$ aqueous suspensions**

### *2.4 3-dim-3dir methodology*

To adjust the $\kappa^*_\lambda$ and $\sigma^*_\lambda$ coefficients obtained experimentally, the radiation distribution in the quartz cells was simulated by solving the RTE equation in three dimensions and thee directions with a discrete ordinate method (DOM) in ANSYS FLUENT 17.0.

First, the collimated incident beam was measured in order to introduce its dimensions as a boundary condition (1 mm x 8 mm) with a user defined function (UDF) in ANSYS FLUENT. Only the quartz cell volume that was exposed in the sample cell holder was considered in the model (Figure 4a and 4b), using the refractive index of water of 1.33. The number of volume elements on the mesh was 47424 with 51480 nodes (Figure 4c).

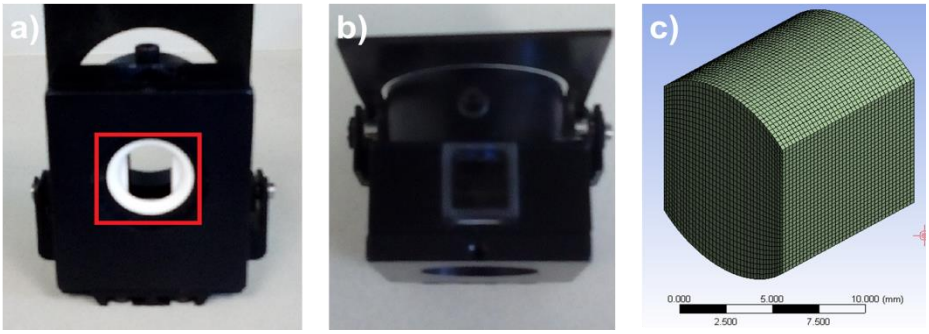


**Fig 4. Cell sample zones where physical phenomena was studied, a) and b): two perspectives of the cell sample holder, c): meshing involved in the simulation**

The transmittance values were obtained by calculating the ratio between the radiation power in the whole face oriented to the integrating sphere and the collimated beam power using the $\kappa_\lambda$ and $\sigma_\lambda$ values determined in the transmittance measurements as well as the linear anisotropic phase function with A=1. The values were varied by a trial and error procedure until obtaining the highest coincidence of the experimental with respect to the calculated transmittance. By this procedure, the fitted $\kappa^*_\lambda$ and $\sigma^*_\lambda$ values were obtained.

### *2.5 LVRPA determination*

#### *2.5.1 Specifications, reactor and lamp dimensions*

Reactor dimensions are based on a design reported by Pareek et al. (2004) [16], while lamp specifications were obtained from a GE ARC-SREAM double ended spec sheet: 150 W ($1.08 \times 10^{-3}$ Einsteins/s) power from 300 to 800 nm (Figure 5b). The reactor and lamp dimensions as well as configuration are shown in Figure 5a.

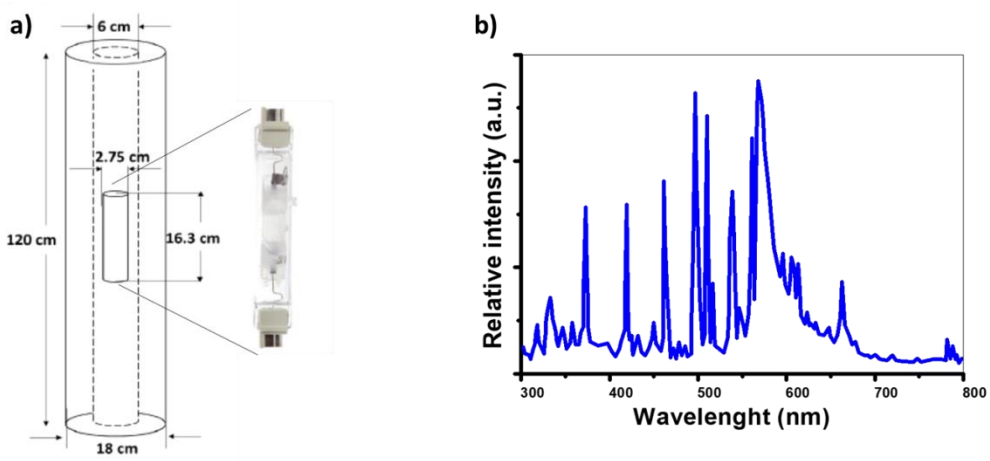


**Fig 5. a) Photoreactor system configuration, b) Lamp spectra obtained from 300 to 800 nm**

### *2.5.2 Boundary conditions*

In order to compute the radiation intensity at the inner wall of the reactor, the volume source model was used (VSM) [12]:

$$G_v = \frac{K_{v3}}{4\pi} \int_{h=-L}^{h=L} \int_{\eta=0}^{\eta=R} \int_{\phi=-\pi}^{\phi=\pi} \frac{\eta d\phi d\eta dh}{[(rcos\theta - \eta cos\phi)^2 + (rsen\theta - \eta sen\phi)^2 + (z-h)^2]} \quad \textbf{( 6)}$$

Where $G_v$ is the radiation intensity at point $Q(r, \theta, z)$ in the reactor wall, $L$ and $R$ the semilenght and lamp radius respectively and $K_{v3}$ the lamp emission power per unit volume.

The VSM equation was introduced as a boundary condition in a semi-transparent wall as a used defined function assuming specular emission. The external walls were considered as an opaque medium with an absorptivity equal to 1 and the meshing consisted of 16040 cylindrical volume elements with 19064 nodes (Figure 8).

Once the radiation distribution on the inner wall was determined, the RTE was solved over the whole reactor space, thus obtaining the radiation intensity value at any point in the reactor, then the LVRPA was calculated by means of the following equation:

$$LVRPA = \langle \kappa^* \rangle I\,(s, \Omega) \quad \textbf{( 7)}$$

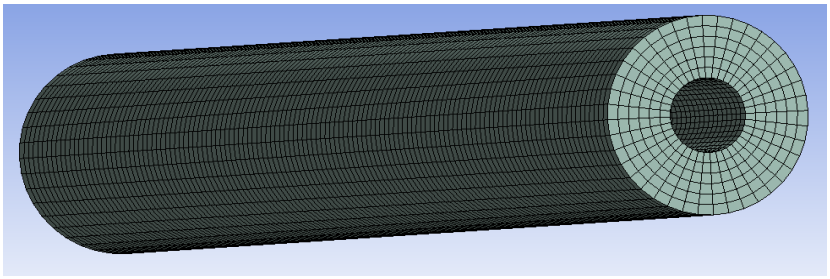

**Fig 6. Meshing for the solution of the RTE in the $NiFe_2O_4$ photoreactor**

### *2.5.3 Solver parameters*

FLUENT's segregate solver was used to perform the simulations in the photoreactor with a unity relaxation factors for energy and radiation intensity to achieve a faster convergence. To avoid control angle overhanging, a pixilation of 3 x 5 was used. The iterations were performed until residuals were less or equal than 1 x $10^{-6}$, a typical convergence history required about 100 – 150 iterations being dependent on the values of σ and $\kappa$.

## 3. Results and Discussion

### *3.1 Scattering and absorption coefficients*

Plots of experimental and fitted specific coefficients are shown in Figure 7. It is possible to observe that obtained values for the extinction coefficient decreased with respect to the experimental ones. This is because possibly not all transmitted radiation was detected in the UV/Vis due to the refractive index of the samples. For example, some of the transmitted beams did not reach the detector. In addition, the corrected values for the absorption coefficient are smaller than the experimental ones too. This is due to the fact that front scattered rays could not be detected by the integrating sphere, thus increasing the "radiation losses" and consequently the computed absorbance in the experiment.

In order to prove the validity of the obtained data, a comparison between experimental and calculated transmittance through the fitted coefficients for 300, 500 and 800 nm (Figure 8) was performed.

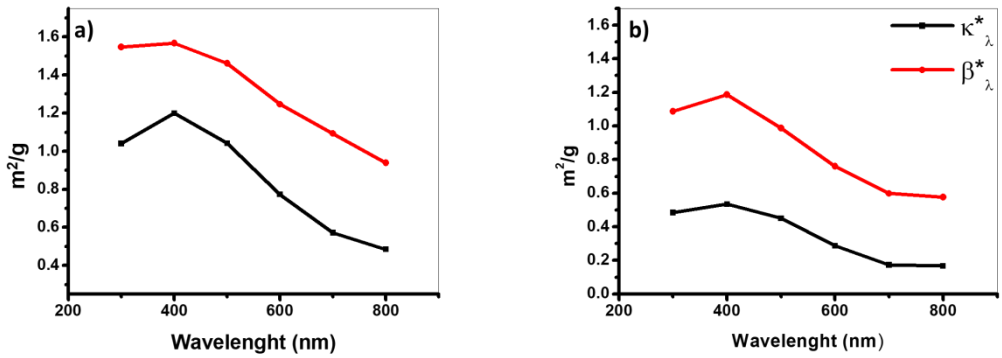


**Fig 7. a) Experimental readings of extinction and absorption coefficients, b) Fitted values of extinction and absorption coefficients from 3-dim-3-dir methodology**

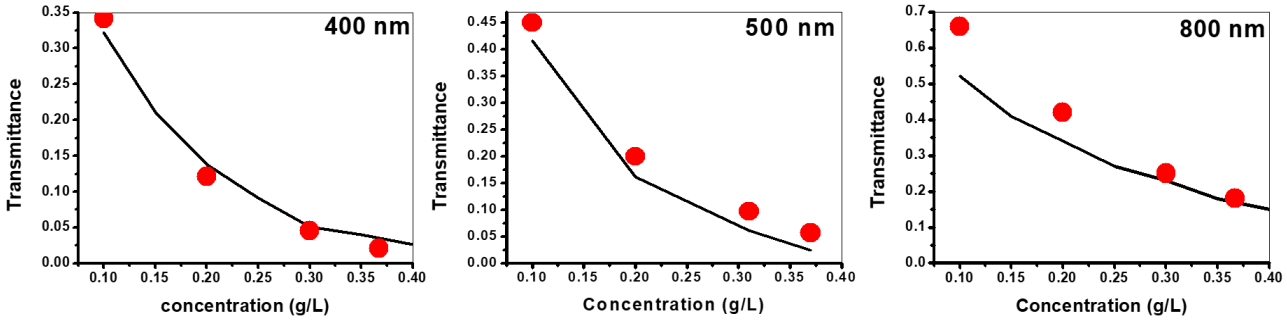


**Fig 8. Experimental transmittance values vs calculated at 300, 800 and 500 nm**

It can be seen that there exists a good agreement between experimental and the theoretical model despite the refractive index of suspensions was considered the same as water (1.33).

Since calculations of LVRPA in the reactor could be intensive considering the scattering and absorption coefficients wavelength dependence, a wavelength-averaged coefficients were obtained by the following integrations:

$$\langle \kappa^* \rangle = \frac{\int_{300\ nm}^{800\ nm} \kappa_\lambda^* d\lambda}{\langle \lambda \rangle} = 0.35\ m^2/g \quad \textbf{(8)}$$

$$\langle \sigma^* \rangle = \frac{\int_{300\ nm}^{800\ nm} \sigma_\lambda^* d\lambda}{\langle \lambda \rangle} = 0.52\ m^2/g \quad \textbf{(9)}$$

### *3.2 LVRPA determination*

Figure 9 shows results of contour plots for the $NiFe_2O_4$ suspension at 0.1 g/L in radial and three dimensions-axial perspective. As expected, the LVRPA decreases as the radial and axial distance increases. This is because rays during the path between the inner wall and the outer walls are absorbed by the solid photocatalyst, thus suggesting that an optimal distance can be fixed in order to improve the reactor efficiency, which will eventually be translated in a reduction of reactor dimensions. However, kinetic parameters must be obtained in order to obtain more accurate predictions. In order to have a more detailed perspective, LVRPA was calculated and plotted in the two perspectives mentioned before (Figure 10), the range of LVRPA obtained was between $2.22x10^{-4}$ and 1.57 Einstenis/$m^3$s.

It is important to notice a decrease at 0.1 m in the axial coordinate, having a LVRPA of 0.2 Einstein/$m^3$s. Therefore, it can be relevant to reduce the reactor length, whereas the decrease of LVRPA in radial distance is not as significant as in the axial coordinate.

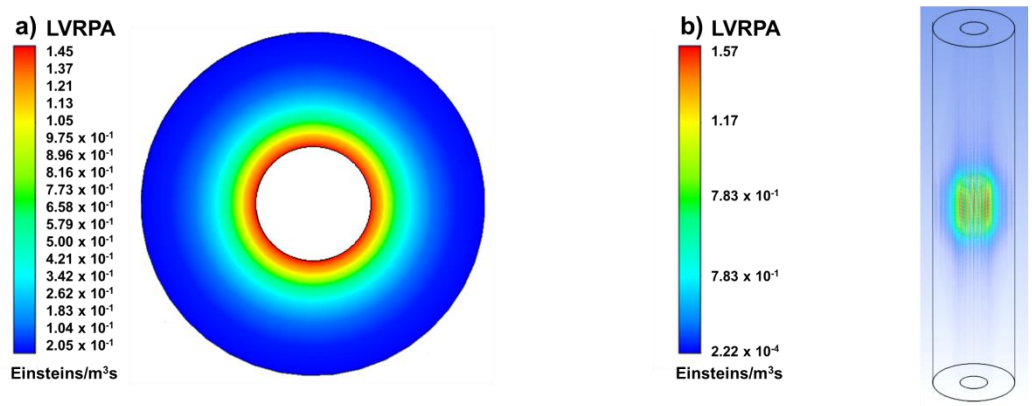


**Fig 5. Contours of LVRPA values for the $NiFe_2O_4$ at 0.1 g/L: a) Radial coordinate, b) Axial coordinate**

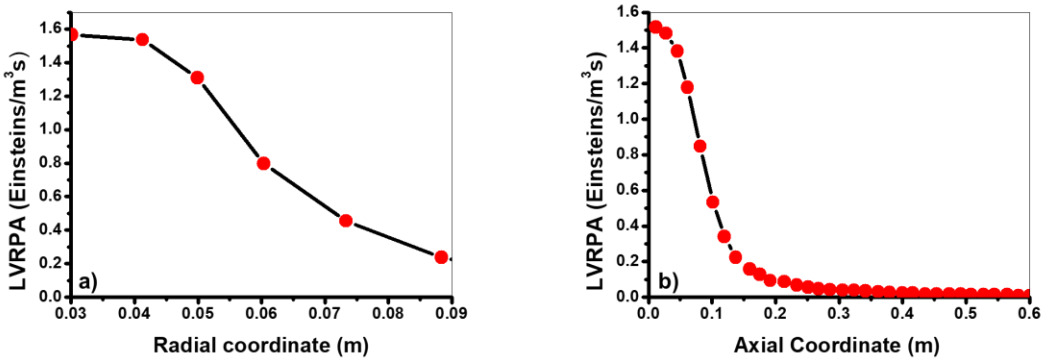


**Fig 6. Values of LVRPA at 0.1 g/L at: a) Radial coordinate, b) Axial coordinate**

## 4. Conclusions

A new methodology called 3-dim-3-dir was developed and this showed a good agreement with experimental and theoretical data. Absorption and scattering coefficients of $NiFe_2O_4$ nanoparticles were determined, which values corresponded to 0.354 $m^2/g$ and 0.519 $m^2/g$ respectively. These results can be more accurate if the refractive index of the suspensions is considered. Finally the LVRPA was calculated in the photocatalytic reactor with values between $2.22x10^{-4}$ and 1.57 Einsteins/$m^3$s.

**Aknowledgments**

The authors acknowledge M.Sc. Ernesto Guerrero Lestarjette, M. Sc. Karla Campos Venegas, Eng. Wilber Antunez Flores, and Eng. Luis de la Torre Saenz for their contributions to the XRD, SEM, BET, results. Special thanks are given to Laboratorio Nacional de Nanotecnologia in Centro de Investigacion en Materiales Avanzados, S. C., for their support in the use of the facilities.

## References

[1] Jafari, T., Moharreri, E., Amin, A. S., Miao, R., Song, W., & Suib, S. L. (2016). Photocatalytic Water Splitting—The Untamed Dream: A Review of Recent Advances. Molecules, 21(7), 900.

[2] Suleman, F., Dincer, I., & Agelin-Chaab, M. (2015). Environmental impact assessment and comparison of some hydrogen production options. International journal of hydrogen energy, 40(21), 6976-6987.

[3] Michaelides, E. E. S. (2012). Alternative energy sources. Springer Science & Business Media.

[4] Won, W., Kwon, H., Han, J. H., & Kim, J. (2017). Design and operation of renewable energy sources based hydrogen supply system: Technology integration and optimization. Renewable Energy, 103, 226-238.

[5] Hosseini, S. E., & Wahid, M. A. (2016). Hydrogen production from renewable and sustainable energy resources: Promising green energy carrier for clean development. Renewable and Sustainable Energy Reviews, 57, 850-866.

[6] Ortiz, A. L., Zaragoza, M. M., & Collins-Martínez, V. (2016). Hydrogen production research in Mexico: A review. International Journal of Hydrogen Energy, 41(48), 23363-23379.

[7] Castedo, A., Uriz, I., Soler, L., Gandía, L. M., & Llorca, J. (2017). Kinetic analysis and CFD simulations of the photocatalytic production of hydrogen in silicone microreactors from water-ethanol mixtures. Applied Catalysis B: Environmental, 203, 210-217.

[8] Salas, S. E. (2013). Photocatalytic Water Splitting Using a Modified $PtTiO_2$. Kinetic Modeling and Hydrogen Production Efficiency (Doctoral dissertation, Ph. D. Thesis, The University of Western Ontario, London, ON, Canada).

[9] Alfano, O.M., Vicente, M., Esplugas, S., Cassano, A.E., 1990. Radiation field inside a tubular multilamp reactor for water and waste water treatment. Ind. Eng. Chem. Res. 29, 1270–1278.

[10] Castrillon, S.R.V., de Lasa, H.I., 2007. Performance evaluation of photocatalytic reactors for air purification using computational fluid dynamics (CFD).Ind. Eng. Chem. Res.46, 5867–5880.

[11] López, Y. O., Vázquez, H. M., Gutiérrez, J. S., Velderrain, V. G., Ortiz, A. L., & Martínez, V. C. (2015). Synthesis method effect of CoFe2O4 on its photocatalytic properties for H 2 production from water and visible light. Journal of Nanomaterials, 16(1), 76.

[12] Boyjoo, Y., Ang, M., & Pareek, V. (2013). Some aspects of photocatalytic reactor modeling using computational fluid dynamics. Chemical Engineering Science, 101, 764-784.

[13] Cabrera, M. I., Alfano, O. M., & Cassano, A. E. (1996). Absorption and scattering coefficients of titanium dioxide particulate suspensions in water. The Journal of Physical Chemistry, 100 (51), 20043-20050.

[14] Satuf, M. L., Brandi, R. J., Cassano, A. E., & Alfano, O. M. (2005). Experimental method to evaluate the optical properties of aqueous titanium dioxide suspensions. Industrial & engineering chemistry research, 44(17), 6643-6649.

[15] Pareek, V., Chong, S., Tadé, M., & Adesina, A. A. (2008). Light intensity distribution in heterogenous photocatalytic reactors. Asia-Pacific Journal of Chemical Engineering, 3(2), 171-201.

[16] Pareek, V. K., & Adesina, A. A. (2004). Light intensity distribution in a photocatalytic reactor using finite volume. AIChE journal, 50(6), 1273-1288.

# CHAPTER 2
# Direct Oxidation Fuel Cells

# 2.1 Methanol oxidation reaction of Pd-Co, Pd-Ni and Pd-Au catalysts obtained by mechanical alloying

M. Landa Castro, A. Ezeta Mejía, M.G. Montes de Oca Yemha, E.M. Arce Estrada, M. A. Romero Romo, M. E. Palomar Pardavé

[1]Universidad Autónoma Metropolitana-Azcapotzalco, Departamento de Materiales. Av. San Pablo Xalpa 180. Colonia Reynosa Tamaulipas, Azcapotzalco. C.P. 02200. Ciudad de México, CDMX, México.

[2]Instituto Politécnico Nacional. Escuela Superior de Ingeniería Química e Industrias Extractivas. Departamento de Metalurgia y Materiales. UPALM. Edif. 7 C.P. 07830. Ciudad de México, CDMX, México.

*Corresponding author: 525553189472, mepp@correo.azc.uam.mx

## ABSTRACT

Polymeric Exchange Membrane Fuel cells (PEMFCs) represents an important development in the green energy generation;however, a majorinconvenientarises with generating, storing and distributing hydrogen as a fuel, which have led to an intensive search for alternative fuels that are easy to use, like alcohols, that also arouse great interest. Direct methanol fuel cells (DMFCs) are highly promising, because methanol is a fuel with a higher energy density than hydrogen, easy to transport and store, it can be used with existing infrastructure and it iselectrochemically active.The oxidation reactions carried out at the fuel cell anode must be catalyzed to increase their reaction rate. A synthesis method little used, that allows obtainingnanometric size electrocatalysts with good performance and efficiency is the mechanical alloying method, that is based on the fusión-fracture phenomenon of metallic solid particles during high energy milling. In this work Pd-Co, Pd-Ni and Pd-Au 2:1nanostructured electrocatalystswere synthesized by mechanical alloying at 30 hours milling time. The materials were synthesized in a high energy Spex mill 8000. The bimetallic materials were characterized by X-Ray Diffraction (XRD), Scanning Electron Microscopy (SEM) and Transmission Electron Microscopy (TEM). Electrocatalytic evaluation of the methanol oxidation was carried out using Cyclic Voltammetry (CV) and Chronoamperometry (CA) to obtain the steady stateanodic current density ($j_{ss}$). The electro-active area was determined by the CO adsorption stripping technique. According to the results obtained, the best methanol oxidation electrocatalystmust be based on the highest$j_{ss}$, which was Pd-Ni, followed Pd-Co and finally Pd-Au.

***Keywords:*** DMFC***;*** methanol oxidation; mechanical alloying; nanometricelectrocatalysts.

# 2.2 Synthesis and functionalization of nanostructured carbons with Ru organometallic compounds: application as supports for Pt fuel cell electrocatalysts

J.C. Martínez-Loyola, C. Cabello-Alvarado, A.A. Siller-Ceniceros, A. Hernández-Ramírez, E. Candia-García, I.L. Alonso-Lemus, M.E. Sánchez-Castro, F.J. Rodríguez-Varela

[1]Universidad Tecnológica de Coahuila, Av. Industria Metalúrgica # 2001, Parque Industrial Ramos Arizpe, Coahuila.
[2]Nanociencias y Nanotecnología, Cinvestav Unidad Saltillo, Av. Industria Metalúrgica 1062, Parque Industrial Ramos Arizpe, Ramos Arizpe, C.P 25900, Coahuila, México.
[3]Instituto Tecnológico de Saltillo, 25280-Saltillo, Coahuila, México
[4]Sustentabilidad de los Recursos Naturales y Energía, Cinvestav Unidad Saltillo.
[5]Cátedra CONACyT, Cinvestav Unidad Saltillo
*javier.varela@cinvestav.edu.mx

## ABSTRACT

Functionalization of carbon supports with ruthenium organometallic compounds is of high interest on account of its surface modification, which promote the efficient anchorage of Pt nanoparticles due to the presence of functional groups. Moreover, the formation of Ru metallic sites proceeding from the complex modifies the electronic and geometrical structure of Pt, leading to the development of alloyed Pt-Ru phases on the catalyst. It has been shown that a Pt catalyst supported on Vulcan functionalized with Ru organometallic complex ($Pt/C_{Ru\text{-}dim}$) is more active for the Methanol Oxidation Reaction (MOR) that conventional Pt/C (Applied Catalysis B: Environmental 209 (2017) 455–467). Following with our previous studies on this subject, in this work several carbons (Vulcan XC-72, Graphene and biocarbon AB7) are functionalized with the $[(\eta^6\text{-}C_6H_5OCH_2CH_2OH)RuCl_2]_2$(**Ru-dim**) and $[(\eta^6\text{-}C_6H_4(CHMe_2)Me)RuCl_2]_2$ (**Ru-cym**)organometallic compounds synthesized in our lab using the Schlenk technique. From that procedure, supports (for example: $C_{Ru\text{-}dim}$) are obtained. Afterwards, Pt nanoparticles are dispersed on the functionalized carbon supports by the microwave-assisted polyol method, giving as a result the $Pt/C_{\mathbf{Ru\text{-}dim}}$, $Pt/C_{\mathbf{Ru\text{-}cym}}$, $Pt/G_{\mathbf{Ru\text{-}dim}}$, $Pt/G_{\mathbf{Ru\text{-}cym}}$, $Pt/AB7_{\mathbf{Ru\text{-}dim}}$ and $Pt/AB7_{\mathbf{Ru\text{-}cym}}$ catalysts. **Ru-dim** and **Ru-cym** have been characterized by NMR, while the chemical composition of the functionalized carbons has been determined by SEM-EDS. The catalytic activity of the nanostructured Pt catalysts for the oxidation of ethanol, ethylene glycol and formic acid has been evaluated in acid media.

**Keywords:**Ruthenium organometallic compounds, carbon surface functionalization, Pt-based catalysts, oxidation of organic molecules, fuel cells.

# 2.3Synthesis and evaluation of Pt anode electrocatalysts supported on carbon structures functionalized with Ru organometallic compounds

E. Candia-García, J.A. Díaz-Guillén, J.C. Martínez-Loyola, A.A. Siller-Ceniceros, M.E. Sánchez-Castro, Samuel Dessources, I.L. Alonso-Lemus, F.J. Rodríguez-Varela.

[1]Instituto Tecnológico de Saltillo, 25280-Saltillo, Coahuila, México

[2]Universidad Tecnológica de Coahuila, Av. Industria Metalúrgica 2001, Ramos Arizpe, Coahuila

[3]Nanociencias y Nanotecnología, Cinvestav Unidad Saltillo, Av. Industria Metalúrgica 1062, Ramos Arizpe, Coahuila, C.P. 25900, México

[4]Sustentabilidad de los Recursos Naturales y Energía, Cinvestav Unidad Saltillo.

*javier.varela@cinvestav.edu.mx

## ABSTRACT

For the electrooxidation reaction of methanol, ethanol and ethylene glycol, 6, 12 and 10 electrons respectively should theoretically be transferred on the anode electrode and transported to the cathode one. Even though these are thermodynamically favorable processes, their kinetics has to be improved to produce high current densities at low overpotentials. In order to enhance the kinetics and also to improve the Pt stability, its combination with a co-catalyst (such as transition metals: Sn, Ru, etc.) and the use of novel methodologies for high dispersion of nanoparticles can be of great importance. A good dispersion of Pt nanoparticles can be achieved on large surface area carbon supports (Vulcan, Carbon Nanotubes, Graphene Oxide etc.), displaying a high number of anchoring sites. Further efficiency of Pt dispersion can be obtained by surface functionalization of the supports with organometallic compounds. Here in this work, the effects of functionalizing carbon supports with Ru complexes on the performance of Pt electrocatalysts is studied. A series of carbon materials (Vulcan XC-72, Graphene and Biomass-based) have been functionalized with organometallic compounds like $[(\eta^6\text{-}C_6H_5OCH_2CH_2OH)RuCl_2]_2$**(Ru-dim)** and $[(\eta^6\text{-}MeC_6H_4{}^iPr)RuCl_2]_2$**(Ru-cym)**. The modified carbons have been used as supports to synthesize nanostructured Pt anode electrocatalysts by the polyol method (labeled as $Pt/C_{Ru\text{-}dim}$, $Pt/C_{Ru\text{-}cym}$, $Pt/G_{Ru\text{-}dim}$, $Pt/G_{Ru\text{-}cym}$, $Pt/AB7_{Ru\text{-}dim}$, $Pt/AB7_{Ru\text{-}cym}$, for Vulcan, Graphene and Biomass-based, respectively). Their catalytic activity for the electrooxidation of methanol, ethanol and ethylene glycol in alkaline media is evaluated compared to that of a conventional Pt/C anode.

This type of organometallic functionalized supports are an attractive alternative to increase the catalytic activity, stability and tolerance to CO groups of nanostructured Pt. Under such approach, the performance of Direct Alcohol Fuel Cells can be improved.

**Keywords**: Ru organometallic compounds, carbon surface functionalization, oxidation of organic molecules, Direct Alcohol Fuel Cells

# 2.4 Development of high performance Sn@Pt/C core-shell electro-catalysts for the Ethanol Oxidaton Reaction (EOR)

Samuel Dessources, I.L. Alonso-Lemus, F.J. Rodríguez-Varela

[1]Sustentabilidad de los Recursos Naturales y Energía, Cinvestav Unidad Saltillo, Av. Industria Metalúrgica 1062, Ramos Arizpe, Coahuila, C.P. 25900, México

[2]Programa de Nanociencias y Nanotecnología, Cinvestav Unidad Saltillo.

*samuel.dessources@univ-poitiers.fr

## ABSTRACT

Pt/C is often used as anode material for the EOR, but platinum itself is known to be rapidly poisoned by strongly adsorbed species coming from the dissociative adsorption of ethanol. Efforts to reduce the poisoning of Pt have been concentrated on the addition of co-catalysts. Few metals are used as co-catalysts of Pt for the EOR. The more extensively investigated anode materials for the reaction are the binary Pt–Ru and Pt–Sn. However, Ru is an expensive noble metal, while Sn is a less expensive transition metal. It is known that the synthesis method may influence the size, the dispersion and the crystallinity of the nanoparticles of a catalyst. It is also known that these features influence the electro-catalyst activity. Our objectives are to prepare carbon supported Sn@Pt core-shell catalysts with small particles size and good dispersion, in order to improve the activity of these anodes for the EOR and mitigate the poisoning of Pt with $CO_{ads}$ groups.

Here in this study, well dispersed Sn@Pt/C core-shell nanostructured materials have been obtained by two different methods (polyol and Bromide Anion Exchange). The physico-chemical characterization shows that the crystallinity and particle size differ according to the synthesis method. The electrochemical measurements of the different prepared materials show that the presence of Sn as core in the Sn@Pt/C core-shell highly improves the catalytic activity in comparison to that of Pt/C. CO-stripping has been performed on these materials. The result displays an oxidation peak of CO at lower potential for the Sn@Pt/C than that of Pt/C.

The synthesis methods used to prepare the Sn@Pt/C catalysts show different particle size, but all improve the catalytic activity for the EOR and allow to Pt to be more tolerant to $CO_{ads}$.

**Keywords** : Ethanol Oxidation Reaction, Direct Alcohol fuel cell, core-shell nanoparticles.

# 2.5 Methanol oxidation in presence of acid-Y zeolite

Miguel Villicaña Aguilera, Adriana Medina Ramírez, Beatriz Ruíz Camacho

[1]Universidad de Guanajuato, Campus Guanajuato, División de Ciencias Naturales y Exactas, Noria Alta S/N, Col Noria Alta, Guanajuato, Gto, 36050, México.

* Corresponding author: m.villicana1103@gmail.com tel:473-117-68-46

## ABSTRACT

Currently around the world efforts to improve the efficiency of the methanol oxidation in Direct Methanol Fuel Cell (DMFC) are being performed. In this work we prepared zeolite type Y in acid form as Pt support. The zeolite was synthesized by hydrothermal method in two different Si/Al ratio, then it was submitted to ionic exchange with NH4Cl, and subsequently it was heating treated at 300°C for 2 h. On a second part, the Pt metallic compound was incorporated (10%wt) on the zeolite support. Finally two different electrocatalysts of Pt/Y-H and Pt/Y-75-H were obtained. The materials synthesized were characterized by SEM and XRD to analyze its morphology and crystalline structure. The electrochemical activity of the materials synthesized was evaluated as electrocatalysts for methanol oxidation reaction (MOR) in acid media using cyclic voltammetry and choronoamperometry. According to SEM analysis the zeolites exhibited morphology of octahedral. By XRD was observed that the Y-75-H presented a higher structural stability than Y-H zeolite. The information obtained in two characterizations, allowed determinate the principals reasons because Pt/Y-H and Pt/Y-75-H presence exhibit good behavior and current densities for MOR. In addition we compared our materials with the conventional catalyst commonly used in fuel cells DMFC: Pt- Vulcan coal. Zeolite Y can be considerate as support of platinum as electrocatalyst applications.

***Keywords:*** Acid Zeolite; Electrochemistry; Methanol Oxidation; medium acid;

## 1. Introduction

Actually the zeolites are chemical compounds very important, because they have many applications in some research fields, for example: separation principles, catalysis, and recently in electrochemistry in specific fuel cell of hydrogen or alhohols.[1].

Zeolites have many industrial applications, for example: separation and purify of gaseous compounds, petrochemical cracking, also enviroment applications for example:

Bioremediation of soils and aquifers contaminated with heavy metals such as chromium, cadmium, lead. These materials with a correct synthesis conditions can easily be produced. Actually researches are enfocated to improve their electrochemical, physic and mechanic properties. The modifications most common are: a) ion exchange, b) heteroatomic substitution in the crystalline structure and c) post-synthesis treatment with a purpose to promote mesoporosity, laminar structures and bi or three dimensional.

Superficial area and high porosity is two important characteristics, reason because some scientists are working in design and produce new electrodes for DMFC applications. A fuel cell is electrochemistry equipment so permit to convert fuel energy in electricity, then this is storage in non conventioal batteries. The efficiency of those cells are very high. The next step this energy can be employee in electronic equipments, vehicles, all about those allow have a important solution for a climate change.

One of the most important problems with the cell DMFC is associated with slow oxidation reaction kinetic and high anodic overpotentials. Other bad aspect is related with the crossover of alcohol, that produce a mixed potential decreasing the oxygen reduction reaction (ORR) activity. For the above mentioned is important to produce new supports of electrocatalysts that can be accelerate methanol oxidation reaction to operate a fuel cel in optimal conditions.

Actually all research efforts are specified in synthesis new electrocatalysts, using new materials, for example taking in count the zeolites properties, that permit produce composites with platinum.

## 2. Materials and Methods

2.1 Preparation of acid zeolites: Y-H and Y-75

The zeolites was obtained and based in an investigation before [Medina A et al., 2010]. A kinds of zeolite: Y-H and Y-75-H was synthesized with a high purity materials. The reaction begin with 1 g of Y-NH4 , Y75-NH4 , then was put in a crucible and subject a treatment thermal (300°C/2h).

We need wait to sample have 50°C and finally the products were stored for the next step that will be electrochemical and physical characterizations.

The equipment used to obtain acid zeolites of their ammoniacal form was electric oven Ney VULCAN 3-130.

2.2 Incorporation of platinum to Zeolite Support

In a Volumetric flask (100 ml) was preparated a solution a H2PtCl6 (1x10-3M), next, it was poured 50 ml into a Erlenmeyer flask. Later it was added 60 ml of isopropyl alcohol (98%).Then was covered with a cork and put in a ultrasonic for 2 h. For incorporation nano-particles to platinum was used an ultrasonic bath Elmasonic P 60 H. When it ends ultrasonic's time, the liquid in an flask was added on a 250 ml glass of precipitate, then was heated in a electric grill for 130 °C/4h, because the target was evaporate all liquid and permit separate desired product. Once dry, then it was weighed and calculates the weigh electrocatalyst Pt-Y-H and Pt-Y-75-H weight (view Table 2.1); the aspect of material was non-fine powder, very bulky and dispersed.

**Table 2.1** Product recovered and details of zeolite-carbon synthesis.

| Composite | Zeolite | Volume H2PtCl6 (ml) | Volume Isopropyl alcohol (ml) | Product recovered (g) |
|---|---|---|---|---|
| Y-carbon-H | Y-H | 50 | 60 | 0.0825 |
| Y-75-carbon-H | Y75-H | 50 | 60 | 0.0790 |

2.3 Physical Characterization

The catalysts synthesized have a general form Pt/zeolite-C were characterized with X-ray diffraction (XRD), for identify all kind of phases in each material was using diffractometer model D8 ADVANCE (zeolites acids), likewise the electrocatalysts were analyzed with a diffractometer PANalytical model Epyrean. For the DRX characterization was utilizate an electrocatalyst representative sample, they were packed in an refractories round aluminum.

For determinate pore's kind and size of each one of supports and electrocatalysts was use nitrogen physisorption using a Micromeritics equipment model ASAP 2010. The specific superficial area was calculated with BET method while the size and pore distribution was detected with BJH method.

The morfology was analized with an equipment JEOL® model JSV-6610LV equipped with system of microanalysis EDS OXFORD®, model XMAX, using high vacuum secondary electrons (SEI). For meet distribution of platinum above zeolite, was used an

Electronic Transmission Microscope JEOL®, model JEM-1010 coupled a digital camera, model ORIUS de Gatan.

It was preparate a solution with 0.5 mg of electrocatalyst with isoprophyl alcohol, then it was sonicated for 2 h, an 1 µL aliquot was taken and finally it was placed in a commercial glass cell and puting on a TEM.

2.4 Electrochemical Characterization

The reagents used to preparated the catalytic inks were next: zeolite Y-H and Y-75-H, distilled water, isopropyl alcohol (98%), Liquid Nafion, H2S04 (98%) and Methanol (99%).

In a vial was put 250 µL of isopropyl alcohol, 25 µl de Nafión and 3 mg of catalyst, The ink was put for 2 h in an ultrasonic bath Elmasonic..

The Electrochemical activity of the electrocatalysts was evaluated with cyclic voltammetry, lineal voltammetry and chronoamperometry. We use two different kinds of alcohols: methanol and ethanol to investigated the alcohol oxidation reaction using cyclic voltammetry.

All electrochemical tests were used equipment: Potentiostat/Galvanostat ZRA, model INTERFACE 1000 T GAMRY®. Likewise with assistance of software Gamry Framework.

Before to doing every electrochemical test such as: cyclic voltammetry (CV) and chronoamperometry (CA), is necessary to do activation of electrode surface with a cyclic voltammetry, this step is really apply 20 cicles to scanning oxidation-reduction, the purpose is eliminate all impurities that was absorbed in a material surface, in this technical was used nitrogen, the scanning rate was 50 mV/s.

For the electrode activation was used a ($H_2SO_4$ 0.5 M) solution, when this electrode was activated, this solution was changed to ($H_2SO_4$ 0.5 M + $CH_3OH$ 0.5 M). The CV was carried in N2 atmosphere at 50 mV s-1 at room temperature during 20 cycles.

The CV curves were measured at a scanning rate of 50 mV $s^{-1}$ in nitrogen atmosphere; the potential applied was between 0.05 and 1.2 V/NHE; 20 cycles were necessary to

stabilize the system. The CA test was carried out under constant potentials of 0.79 V/NHE during 3000 s. All measured potential values in this work are given relative to the normal hydrogen electrode (NHE).

## 3. Results and Discussion

### 3.1 X-ray diffraction results of supports

The crystallinity and particle size of those electrocatalyst are important factors that permit maxim exposed area and active sites density per mass unit, these factors has a positive effect in material catalytic activity. Figure 3.1 presents the XRD results of composites Y-H, Y-75-H. We can observe to the effect of thermal treatment to which they were subjected to produce a zeolite form acid, decrease its cristallinity, this theory is sustained in a reduction of intensity of peaks in each one supports.

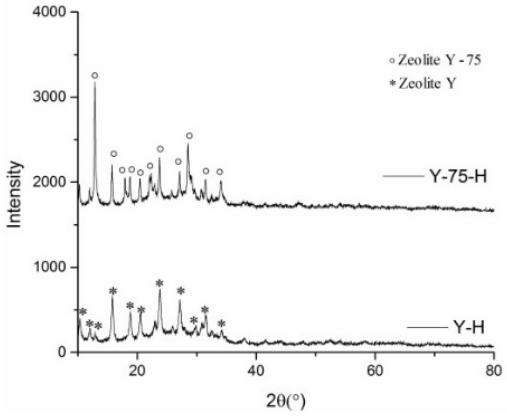


**Fig. 3.1** Supports Y-H, P-H, Y-75-H analyzed with DRX.

### 3.2 Scanning electron microscopy (SEM) of supports

Figure 3.2 shows a SEM images of supports synthesized Y-H and Y-75-H with this picture we can know geometry and kind of crystallographic structure. This two supports are a genre of Faujacite, both materials present the same crystal structure, based in a silicon oxide tetrahedron, inside the structure is an atom distribution in crystal network.

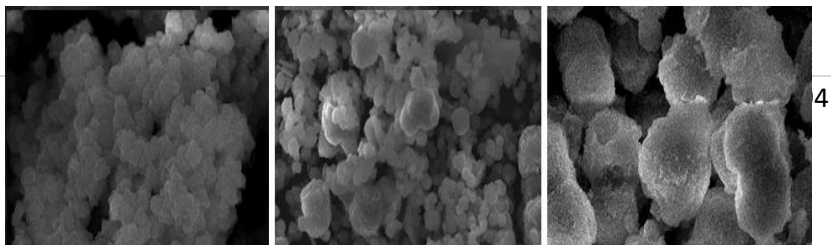

**Fig. 3.2** Scanning electron microscopy (SEM) of supports A) Y-H, B) Y-75-H.

## 3.3 XRD results of Pt-Y-H and Pt-Y-75-H Composites

Figure 3.3 shows the XRD results of electrocatalyst Pt-Y-H and Pt-Y-75-H.materials presents the zeolite and Pt difraction peaks. These last peaks are observed around 39.76°, 46.24° y 67.45° de 2-tetha. It´s important mention the platinum peaks appear in the same position 2-tetha for both electrocatalyst, however the intensity and widening of peaks is more full-scale for Pt-Y-H and then Pt-Y-75-H.

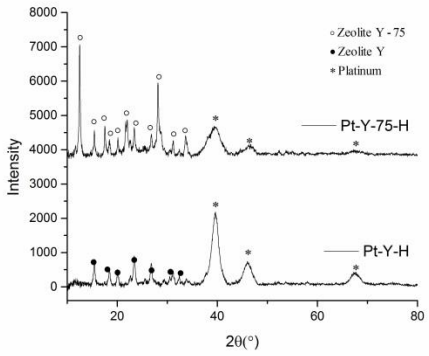


**Fig. 3.3** Electrocatalyst Pt-Y-H and Pt-Y-75-H analyzed with DRX.

## 3.4 Transmission electron microscopy (TEM) of electrocatalyst

Figure 3.4 shows the TEM images of of electrocatalyst Pt-Y-H and Pt-Y-75-H. An agglomeration of Pt was found. In addition a spherical morphology with platinum



nanoparticles on zeolitic crystals are saturated. For the Pt-Y-H electrocatalyst (Fig.3.4 A) was observed an octahedron morphology, with a homogeneous dispersion of platinum nanoparticles.

**Fig. 3.4** Transmmision electron microscopy (TEM) of Electrocatalyst A) Pt-Y-H, B) Pt-Y-75-H.

## 3.5 Electrochemical characterization results

The cyclic voltammograms in presence of methanol for Pt/C commercial sample and the electrocatalyst synthesized: Pt-Y-H and Pt-Y-75-H can be observed in Fig.3.5. Two peaks were obtained the first peak corresponds to organic species electro-oxidation and second correspond to methanol oxidation. The materials synthesized exhibit similar current density, which is lower compared to commercial sample.

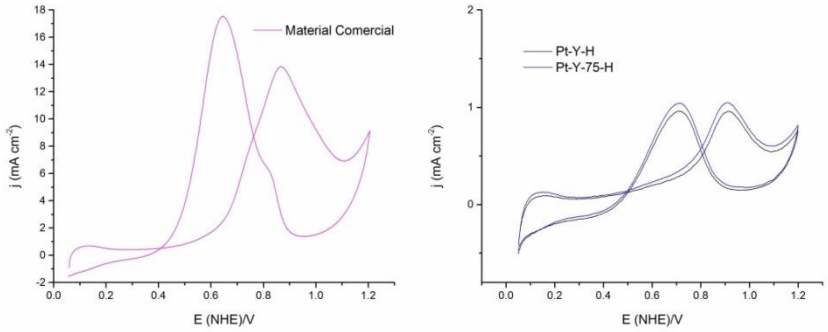


**Fig. 3.5** Cyclic Voltametry for methanol electro-oxidation and commercial material using to reference in an solution H2SO4 0.5 M.

Fig. 3.6 exhibit the cyclic voltammetry in absence of methanol, for both electrocatalysts synthesized Pt-Y-H and Pt-Y-75-H. The current density for materials synthesized is really low compared with Pt commercial sample. However it was found both electrocatalyst have a great potential methanol oxidation reaction.

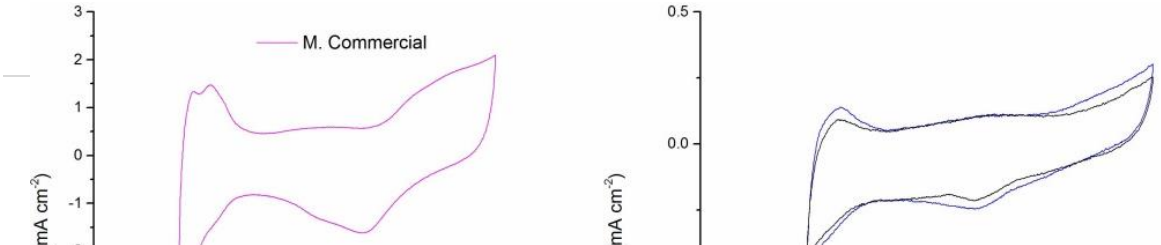

**Fig. 3.6** Cyclic Voltametry for methanol electro-oxidation and commercial material using to reference in an solution $H_2SO_4$ 0.5 M + $CH_3OH$ 0.5 M.

In figure 3.6 was observed that electrocatalyst Pt-Y-75-H, the electro-oxidation intermediates absorbed at Pt peak (cathodic) are bigger that methanol oxidation (anodic), this is consequence to increase of CO adhered to Pt. However for Pt-Y-H both peaks are at the same current density, this indicates that the material have the same capacity for oxidize methanol or oxidize organic species, as well as good CO tolerance. All peaks ends to oxidize in 1 V (ENH). The electrocatalyst Pt-Y-75-H have a great capacity for oxidize the methanol and this is a reason because this material is the best candidate for use in anode within a DMFC, also present a maximum current density 1 (mA cm-2).

## 3.6 Methanol Oxidation Chronoamperometry Study

With this technical is possible know how it is stability of each electrocatalyst in function of time in electro-oxidation of methanol. Then present results of CA for Pt-Y-H, Pt-Y-75-H and commercial material (90 % Pt/C), using a solution H2SO4 0.5 M + 0.5 M de CH3OH. Fig 3.7.

**Fig. 3.7** Comparation for electrocatalyst: Pt-Y-H, Pt-Y-75-H and commercial material using to reference in a solution H2SO4 0.5 M + CH3OH 0.5 M.

With At first it is observated a current peak, this is generate for accumulation of species in the vicinity of the electrode, when it impose a potential pulse of 0.5 V, all species are electro-oxidized and permit a increase in current density. Then in 500 s was observed a fast decay due the decrease in the concentration of species present on the surface, however, the new species reach the nucleus of the solution to the electrode, thanks to mass transport by diffusion.

Due to above we expect that will be constat current density, however it is not posible, conversely a loss of catalytic activity is still perceived over time [Shukla et al., 2010]. At 1750 s it is noted a activity stabilization of the activity is achieved for Pt-Y75-H and Pt-Y-H is: 0.09 y 0.24 mA cm-2 .The above indicate this electrocatalyst have a great potential in methanol oxidation and good stability respect with reaction time.

## 4. Conclusion

We synthesized two new electrocatalysts using zeolite-carbon materials as support of Pt with electrochemical activity for methanol oxidation reaction. The preliminary results of physical characterization indicated the crystallinity of Pt/zeolite-carbon material depends of the thermal treatment. The Pt nanoparticles were synthesized by ultrasound and incorporated to composite supports. The TEM images indicated a poor distribution of Pt onto the composites substrates. These materials exhibit electrochemical activity for MOR however these preliminary results could be improved changing the synthesized method of Pt nanoparticles.

## Acknowledgements

The autor are grateful to the University of Guanajuato (UG) for the financial support of this work under project PROMEP No.103.15/15/7007. Also thanks to University

National Autonomus of Mexico (UNAM) campus juriquilla and the Microscopy unity with support technical for doing study of TEM that was presented here, in specific to Academic technician Ma.Lourdes Palma Tirado. Finally a sincere thank you from the SMH and XVII International Congress of the Mexican Hydrogen Society.

## References

[1] J.D. Kistler., N. Chotigkrai., P. Xu., B. Enderle., P. Praserthdam., C.Y. Chen., N.D. Browning., B.C. Gates.,(2014). A Single-Site Platinum CO Oxidation Catalyst in Zeolite KLTL: Microscopic and Spectroscopic Determination of the Locations of the Platinum Atoms. Angew Chem Int. (53) 8904 –8907.

[2] Medina A., Gamero P., Almanza J.M., Vargas A., Montoya A., Vargas G., Izquierdo M., (2010). Fly ash from a Mexican mineral coal. II. Source of Wzeolite and its effectiveness in arsenic (V) adsorption. Journal of Hazardous Materials. (181) 91-104.

[3] Shukla, A. K., Tintula, K.K., Pitchumani. S., Sridhar. P., (2010). A solid-polymer-electrolyte direct methanol fuel cell (DMFC) with Pt-Ru nanoparticles supported onto poly (3,4-etylenedioxythiophene) and polystyrene sulphonic acid polymer composite as anode. J. Chem. Sci. (122) 381-389.

[4] Lo A.Y., Hung C.T., Yu N., Kuo C.T., Liu S.B., (2012). Syntheses of carbon porous materials with varied pore sizes and their performances as catalyst supports during methanol oxidation reaction. Applied Energy. (100) 66–74.

[5] Lo A.Y., Liu S.H., Huang S.J., Kuo C.T., Liu SB., (2008). Hollowed carbon capsule based Pt-Fe/carbon electrodecatalysts prepared by chemical vapor infiltration method. Diam Relat Mater (2008). (17) 1541-1550.

# 2.6 N-doped Carbon Nanofibers as Oxygen reduction electrocatalysts in alkaline media

R. Ojeda-López; G. Ramos-Sanchez; J. M. Esparza-Schulz; I. J. Pérez-Hermosillo; A. Domínguez-Ortiz; I. González.

[1]Departamento de Química. Universidad Autónoma Metropolitana–Iztapalapa. Avenida San Rafael Atlixco 186, Leyes de Reforma 1ra Sección, 09310 Iztapalapa, CDMX.

[2]Cátedras CONACYT comisionado a Universidad Autónoma Metropolitana.

*G. Ramos-Sánchez, +52 55 5804 4600 ext 4396, gramossa@conacyt.mx

## ABSTRACT

Carbon nanofibers (CNFs) are carbon allotropes with interesting properties which can be applied in electrochemical technologies such as polymer electrolyte membrane fuel cells (PMFC). CNFs can be modified by nitrogen doping, the dopant allows the formation of specific sites on the nanofibers surface which, when used as support, lead to controlled size and dispersion of the active material; moreover, the presence of nitrogen atoms as dopants, modifies the electronic density close to the doping site, leading to the formation of sites capable to catalyze the fuel cell reactions.

In this work, we propose the production of CNFs with intrinsic formation of nitrogen doping sites. N-doped carbon nanofibers were synthetized by electrospinning of polyacrylonitrile (PAN), these materials were carbonized at different temperatures (873, 973, 1073, 1173 and 1273 K) under inert atmosphere in order to obtain materials with different quantity and species of nitrogen (corroborated through X-ray Photoelectron spectroscopy). In general, the increasing in carbonization temperature decreases the nitrogen content; however, this process also modifies the type of nitrogen species. For carbonization temperatures of 873 and 973 K, nitrogen species were mainly found in N-6 form (piridinic) with a small amount of nitrile groups. On the other hand, for materials calcined above 1073 K, the N-Q (quaternary or graphitic nitrogen) became the most abundant nitrogen species, indicating that at higher temperatures the formed of N-Q was more stable than N-6. The obtained CNFs were evaluated as electrocatalysts for the oxygen reduction reaction (ORR) in alkaline conditions. The preliminary results show that increasing the quantity of N-Q augments the catalytic activity, i.e. the onset potential for oxygen reduction increases.

***Keywords:*** Catalyst support, Fuel cells, N-doped CNFs.

# 2.7 Synthesis and characterization of Pd electrocatalysts supported on carbon xerogels for the oxidation reaction of ethanol in alkaline media

F. J. Galván-Cabrera.,R. Carrera-Cerritos., I. R. Galindo-Esquivel., R. Fuentes-Ramírez

[1]Universidad de Guanajuato, División de Ciencias Naturales y Exactas, Departamento de Ingeniería Química, Noria Alta S/N, Guanajuato, Gto., México. Postal address: 36050.

[2]Instituto Politécnico Nacional, Unidad Profesional Interdiciplinaria de Ingeniería Campus Guanajuato (IPN-UPIIG), Departamento de Formación Profesional Genérica, Av. Mineral de Valenciana No. 200 Fracc. Industrial Puerto Interior, Silao de la Victoria, México. Postal Address: 36275.

* Corresponding author: 044 (473) 1219730 fgalvan_iq@hotmail.com

## ABSTRACT

In the present study, carbon xerogels were synthetized by resorcinol polycondensation with formaldehyde in aqueous media, using $Na_2CO_3$ as polymerization catalyst. The aging conditions in order to understand its effect on xerogel structure. Finally, the gel was dried, thermally treated and characterized by $N_2$ adsorption-desorption, transmission electron microscopy (TEM). Carbon Xerogels-supported Pd Catalysts for the ethanol oxidation reaction in alkaline media are successfully synthesized by the incipient wet impregnation. X-ray diffraction characterization confirms the formation of the face-centered cubic crystalline on the carbon xerogel for the Pd/CX catalysts. The cyclic voltammetry tests showed the activity for the ethanol oxidation reaction in the alkaline medium for all the synthesized catalysts. Carbon xerogels may be a new class of materials that replace the use de carbon blacks such Vulcan XC-72 as supports because of their high specific area and ability to control pore size during the process of synthesis.

***Keywords:*** Carbon xerogel, aging conditions, palladium catalyst

## 1. Introduction

Environmental problems and increased global demand for energy have mobilized the scientific community in search for clean and renewable energy sources. Direct ethanol fuel cells (DEFCs) have attracted much attention recently in the development for alternative energy sources. As an emerging technology, DEFCs have many challenges that need to be addressed. For instance, it is necessary to improve the catalytic activity of the anode to oxidize the ethanol. Palladium-based catalysts are receiving great attention because of their abundance and unique properties in the alcohol electro-catalytic oxidation in alkaline media.

Generally, the catalytic properties dependence of heterogeneous metal catalyst depends several factors such the support type and texture, particle size and alloy formation is well known. The catalyst support material plays the main role in determining the performance and durability of electrocatalysts. Carbon Xerogels (CXs) are relatively a new class of material that has attracted great attention recently for the use as catalyst supports, adsorbents and electrodes for supercapacitors or batteries, due to the high surface area, pore size manipulation, and uniform metal distribution. Despite these properties, the studies of carbon-xerogels as support in DEFC is still scasead.

Direct ethanol fuel cells (DEFCs) have been projected to be strong candidates to compete with advanced batteries for powering mobile and portable electronic devices owing to their uniquely high specific energy. The use of ethanol is attractive because of its low toxicity. Moreover, ethanol can be produced in large quantities from agricultural products or biomass. For these reasons, DEFCs have recently been receiving increased attention[1,2]. A significant challenge in the development of DEFC technology is the need highly active catalysts for the ethanol oxidation reaction (EOR) that takes place at the negative electrode (anode). One of the routes pursued is the development of new carbon supports of high electric conductivity, high surface area (mesoporosity) and adjustable surface chemistry [3], such as carbon nanofibres [4], carbon nanotubes [5–7], carbon xerogels and aerogels [8–10], among others. Since their introduction by Pekala in 1989 [11], resorcinol-formaldehyde aqueous gels have been extensively studied. The reason why these materials have attracted an enormous attention is due to the possibility of fine-tuning their textural properties during sol-gel method employed for their preparation. One may change the ratio of micro-, meso-, and macro-pores and accordingly their specific surface areas over a wide range. In the present work, two carbon xerogels were synthesized; the aging time was studied to understand its effect on the xerogel structure, as well as the effect on the activity of Pd catalysts in the ethanol oxidation reaction.

## 2. Materials and methods

### *2.1 Carbon xerogels synthesis*

Resorcinol (1-3-Benzenediol)-formaldehyde organic gels were synthesized by the sol-gel method introduced by Pekala et al. [11]. The synthesis conditions in the present work are shown below R/F=1/2, R/C=100, where R/f stands for molar resorcinol to formaldehyde, R/C for molar ratios resorcinol to sodium carbonate (catalyst). Gelation was performed at 85 $^{O}$C, and the aging period at the same temperature for 24 h. A second aging stage was carried out where the carbon xerogels were treated in a system under temperature and constant pressure 85 $^{O}$C and 1 kg/cm$^2$ respectively, the aging time studied was 1 and 6 days of aging.

Finally, pyrolysis of the organic gels was performed in a tubular furnace at 900 $^{O}$C for 2 h under $N_2$ flow of 100 mL/min.

*2.2 Catalysts preparation*

Pd was deposited on the synthesized carbon xerogels by incipient wet impregnation. The amount of metallic precursor $Pd(OAc)_2$ was calculated to obtain a metal loading of 20% w/w. Precursor was dissolved in acetonitrile, then the resulting solution was added dropwise onto the carbon supports. The resulting product was dried at room temperature for 8 h, and activated for 2 h to reduce the precursor Pd in mixture of 8% $H_2$ -Ar at 350 $^{O}$C (flow rate 60 mL/min).

*2.3 Physico-chemical and electrochemical characterization*

The textural and morphological features of the different carbon supports were determined by means of nitrogen physisorption at -196 $^{O}$C (TriStar II Plus 3030 Micromeritics), transmission electron microcopy (JEOL-100S). Textural properties such as specific surface area, pore volume and pore size distribution were calculated form each corresponding nitrogen adsorption-desorption isotherms applying the Brunauer-Emmet-Teller (BET) and t-plot methods. Catalysts were as well characterized by X-Ray Diffraction (XRD), using a Miniflex of Rigaku diffractometer, using Cu-Kα radiation.

Catalysts electrochemical activity towards the oxidation of ethanol was studied by cyclic voltammetry (CV) and chronoamperometry (CP) at room temperature. Both CV and CP were carried out with a potentiostat (Gamry Instruments, model 1000T) in a conventional three-electrode cell, in which a glass carbon electrode (GCE) with area of 0.0706 $cm^2$ was used as the underlying support for the working electrode, a platinum foil as the counter electrode, and Ag/AgCl/NaCl (3.5 $molL^{-1}$) as the reference electrode. The GCE was modified by depositing a catalyst layer on it and served as the working electrode. The catalysts ink was prepared by ultrasonically dispersing 1 mg of 20wt.% Pd/CX1 or Pd/CX6 in 76 µL isopropyl alcohol, to which 10 µL Nafion (Sigma Aldrich). After 20 min, a homogeneous solution was obtained and 2 µL of the ink was pipetted on top of the GCE and dried in air to yield a Pd loading. All the CV and CP experiments were performed at room temperature and in a 1.0 M KOH solution containing 1.0 M ethanol. The CV tests were performed between the potential range of -1.0 to 0.274 V at a scan rate of 50 mV $s^{-1}$ and CP test were conducted at a potential of 0.3 V for 50 min. All potentials in this work all refer to the Ag/AgCl/NaCl (3.5 mol $L^{-1}$), and the current densities were calculated according to the geometric area of the GCE (0.0706 $cm^2$).

## 3. Results and Discussion

*3.1 Textural characterization of the carbon supports*

Table 1 shows the textural parameters determined by means of $N_2$ adsorption, for the synthesized carbon xerogels, CX1 and CX6. Carbon xerogels show high values of BET surface area, higher than the reported for Vulcan carbon black (250 $m^2/g$). In fact, these materials possess an extensively developed porous structure, with an important contribution of micropores, but can be mainly considered as mesoporous carbons.

Table 1. Surface area, average pore size for the synthesized carbon xerogels.

| Carbon support | Aging time (days) | $S_{BET}$ ($m^2/g$) | $V_p$ ($cm^3/g$) | Average pore size (nm) |
|---|---|---|---|---|
| XC1 | 1 | 537 | 0.173 | 5.78 |
| XC6 | 6 | 494 | 0.196 | 5.72 |

*3.2 XRD and TEM characterizations of Pd/XC1 and Pd/XC6 catalysts.*

Bulk structural information for the Pd/XC1 and Pd/XC6 catalysts was obtained by XRD and is show in Fig. 1. It can be seen that there are three common peaks for both the samples. Located at the 2θ value of about 40.119°, 46.659 °, and 68.121 ° are assigned to the (1 1 1), (2 0 0), and (2 2 0) facets of the face-centered cubic (fcc) crystalline Pd (JCPDS 46-1043), respectively.

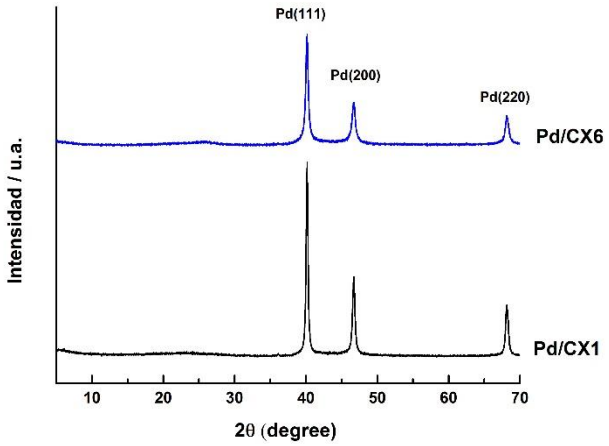


Fig. 1. XRD patterns of Pd/XC1 and Pd/XC6.

The average size of the metal particles is calculated based on the broadening of the (1 1 1) diffraction peaks according to Scherrer´s equation[12]:

$$d = \frac{0.9\lambda}{B_{2\theta}\cos\theta_{max}} \quad (1)$$

Where λ represents the wavelength of the X-ray, $\theta$ is the angle of the maximum peak, and $B_{2\theta}$ is the width of the peak at half height. The average size of Pd particles is 27.3 nm in Pd/CX1 and 20.6 nm in Pd/CX6.

Fig. 2a and b shows typical TEM images for the Pd/XC1 and Pd/XC6. The metal particles of both catalysts exhibit particles of different shapes and sizes. It is possible to observe the formation of agglomerates on the surface of the carbon xerogels.

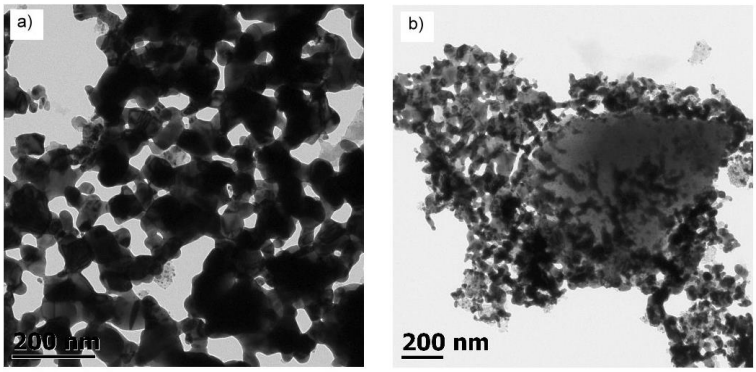


Fig. 2 TEM micrographs for the electrocatalysts: a) Pd/XC1; and b) Pd/XC6.

*3.3 Electrochemical characterization*

Pd-catalysts supported on carbon xerogels were characterized by cyclic voltammetry (CV). Fig. 3 compares typical CV curves of EOR on Pd/XC1 and PdXC6 catalysts measured in 1.0 M KOH solution in the potential range from -1.0 to 0.274 V in presence of ethanol 1.0 mol $L^{-1}$.

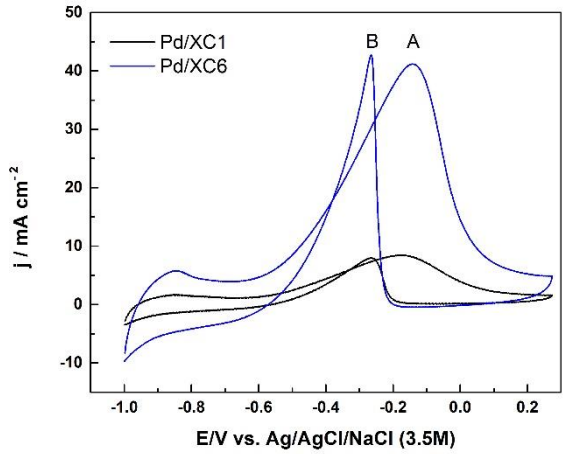


Fig. 3. CV curves of EOR on Pd/XC1 and Pd/XC6.

The hydrogen desorption/adsorption region (<-0.7) is significantly suppressed in the presence of ethanol in the solution. The ethanol oxidation reaction starts at -0.7 V and current peak (designated as Peak A) centered at -0.20 V is observed during the forward scan, In the reverse scan, another current Peak B is sound centered at about -0.27 V, In the hydrogen region, the suppression of the peak can be attributed to the dissociative adsorption of ethanol in the low-potential region, i.e.:

$$Pd + CH_3CH_2OH \leftrightarrow Pd - (CH_3CH_2OH)_{ads} \quad (2)$$

$$Pd - (CH_3CH_2OH)_{ads} + 3OH^- \rightarrow Pd(CH_3)_{ads} + 3H_2O + 3e^- \quad (3)$$

The voltammograms were analyzed in terms of the peak potentials and the current densities shown in Table 2, it is possible to observe that catalysts have catalytic activity in the presence of ethanol. The highest peak current densities were registered for the catalysts Pd/XC6 41.18 mA/cm$^2$and peak potential around of -0.14 V.

Table 2. Peaks potentials and the current densities Pd/XC1 and Pd/XC6.

| Catalysts | $i_{Peak\ A}$ [mA cm$^{-2}$] | $E_{Peak\ A}$ [V] |
|---|---|---|

| | | |
|---|---|---|
| **Pd/XC1** | 8.42 | -0.18 |
| **Pd/XC6** | 41.18 | -0.14 |

The results of chronoamperometric curves towards ethanol oxidation are shown in Fig. 4.The measurement were preformed for 50 min. Catalysts stability and evaluation of their activity over prolonged periods of time will be subject of future studies. Pd / XC proved to be the most stable catalyst.

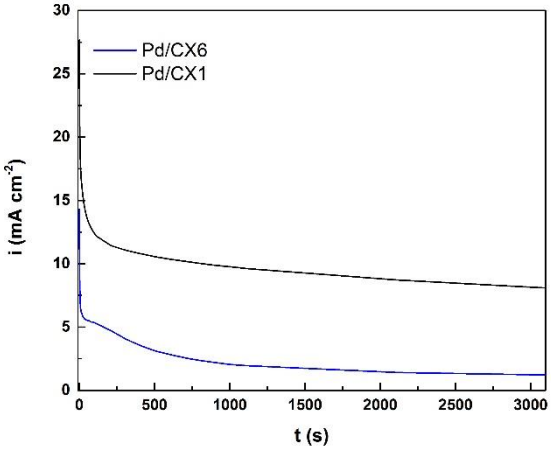


Fig. 4. CV curves of EOR on Pd/XC1 and Pd/XC6.

## 4. Conclusions

Two carbon xerogels were synthesized, were used as supports in the preparation of Pd-catalysts which were characterized and tested for the ethanol oxidation reaction via cyclic voltammetry and chronoamperometry. Pd/XC6 showed to be the most active catalyst, according to the results obtained in TEM and XRD both catalysts have Pd agglomerates, the difference in catalytic activity may be related to the pore volume of the synthesized supports a higher volume may favor the transport of reagents.

## 5. Acknowledgements

I. B. Q. Lourdes Palma for their support in the physicochemical characterization by means of Transmission electron microscopy at the Institute of Neurobiology of the University Autonomous University of Mexico, Campus Juriquilla, Querétaro.

Dr. Marina Vega for her support in the physicochemical characterization by means of X-ray diffraction at the Institute of Geosciences of the Autonomous University of Mexico, Campus Juriquilla, Querétaro.

## 6. References


[1] Antolini E, Gonzalez ER. Alkaline direct alcohol fuel cells. J Power Sources 2010;195:3431–50. doi:10.1016/j.jpowsour.2009.11.145.

[2] Rousseau S, Coutanceau C, Lamy C, Léger JM. Direct ethanol fuel cell (DEFC): Electrical performances and reaction products distribution under operating conditions with different platinum-based anodes. J Power Sources 2006;158:18–24. doi:10.1016/j.jpowsour.2005.08.027.

[3] Zainoodin AM, Kamarudin SK, Daud WRW. Electrode in direct methanol fuel cells. Int J Hydrogen Energy 2010;35:4606–21. doi:10.1016/j.ijhydene.2010.02.036.

[4] Sebastián D, Calderón JC, González-Expósito JA, Pastor E, Martínez-Huerta M V., Suelves I, et al. Influence of carbon nanofiber properties as electrocatalyst support on the electrochemical performance for PEM fuel cells. Int J Hydrogen Energy 2010;35:9934–42. doi:10.1016/j.ijhydene.2009.12.004.

[5] Hiltrop D, Masa J, Maljusch A, Xia W, Schuhmann W, Muhler M. Pd deposited on functionalized carbon nanotubes for the electrooxidation of ethanol in alkaline media. Electrochem Commun 2016;63:30–3. doi:10.1016/j.elecom.2015.11.010.

[6] Wang MY, Chen JH, Fan Z, Tang H, Deng GH, He DL, et al. Ethanol electro-oxidation with Pt and Pt-Ru catalysts supported on carbon nanotubes. Carbon N Y 2004;42:3257–60. doi:10.1016/j.carbon.2004.07.018.

[7] Chetty R, Kundu S, Xia W, Bron M, Schuhmann W, Chirila V, et al. PtRu nanoparticles supported on nitrogen-doped multiwalled carbon nanotubes as catalyst for methanol electrooxidation. Electrochim Acta 2009;54:4208–15. doi:10.1016/j.electacta.2009.02.073.

[8] Job N, Pereira MFR, Lambert S, Cabiac A, Delahay G, Colomer JF, et al. Highly dispersed platinum catalysts prepared by impregnation of texture-tailored carbon xerogels. J Catal 2006;240:160–71. doi:10.1016/j.jcat.2006.03.016.

[9] Kim H-J, Kim W-I, Park T-J, Park H-S, Suh DJ. Highly dispersed platinum–carbon aerogel catalyst for polymer electrolyte membrane fuel cells. Carbon N Y 2008;46:1393–400. doi:10.1016/j.carbon.2008.05.022.

[10] Smirnova A, Dong X, Hara H, Vasiliev A, Sammes N. Novel carbon aerogel-supported catalysts for PEM fuel cell application. Int J Hydrogen Energy 2005;30:149–58. doi:10.1016/j.ijhydene.2004.04.014.

[11] Pekala RW. Organic aerogels from the polycondensation of resorcinol with formaldehyde. J Mater Sci 1989;24:3221–7. doi:10.1007/BF01139044.

[12] Shen SY, Zhao TS, Xu JB, Li YS. Synthesis of PdNi catalysts for the oxidation of ethanol in alkaline direct ethanol fuel cells. J Power Sources 2010;195:1001–6. doi:10.1016/j.jpowsour.2009.08.079.

# 2.8 Evaluation of PtRu/C Type Electrocatalysts Prepared by Different Methods for Application in PEM Unit Fuel Cell

Marcos M.S. Paula, Elson A. de Souza, Vanessa M.F. de Araújo, Paulo R.C. Couceiro, Roberto Benavides, Leandro A. Pocrifka, Raimundo R. Passos

[1]Instituto de Ciências Exatas e Tecnologia/ICET - UFAM, Rua Nossa Senhora do Rosário, 3863 - Tiradentes. 69103-128 - Itacoatiara, AM - Brasil.
[2]Laboratório de Eletroquímica e Energia – LEEN, Departamento de Química, Universidade Federal do Amazonas, Av. Gal. Rodrigo Octávio, 6200, 69077-000, Manaus-AM, Brazil
[3]Laboratório de Físico-Química, Departamento de Química, Universidade Federal do Amazonas, Av. Gal. Rodrigo Octávio, 6200, 69077-000, Manaus-AM, Brazil
[4]Centro de Investigación en Química Aplicada (CIQA), Blvd. Enrique Reyna 140, 25294 Saltillo, Coahuila, México

*Corresponding author: +55 (92)3305-2817 rdopassos@gmail.com or rrpassos@ufam.edu.br

---

## ABSTRACT

Direct Alcohol Fuel Cells (DAFC) are considered a promising alternative for the conversion of energy, especially because the fuel is directly oxidized under conditions of ambient temperature and pressure. In general, such cells use Pt as a catalyst. However, it has been observed that the use of binary electrocatalysts can improve the oxidation process of methanol, making the conversion process more efficient. The use of ruthenium as a second metal has been shown to be efficient because when associated with platinum, a CO-tolerant PtRu catalyst is formed. In this work, we present a comparative study of the oxidation reaction of methanol using PtRu/C prepared by three different reducing agents, namely formic acid, methanol, and ethylene glycol. The synthesis of the electrocatalysts was made by the reduction of the metals from the precursors $H_2PtCl_6.xH_2O$ and $RuCl_3.xH_2O$ and later impregnation on carbon. The catalytic systems prepared were characterized by X-Ray Fluorescence (EDX) and X-Ray Diffraction (XRD). The electrochemical characterization was performed by voltammetry, chronoamperometry, and polarization curve. The results showed that the three methods of synthesis were efficient in the preparation of these electrocatalysts. Studies conducted in a commercial unit cell, operating with direct methanol were carried out by varying the temperature in the range of 70 $^oC$ to 90 $^oC$ and at different pressures of $O_2$. The best electrochemical performance was observed for the catalytic system using ethylene glycol as a reducing agent. For this electrocatalyst, a maximum power of 74.88 mW $cm^{-2}$ was obtained at 90 °C and with a partial oxygen pressure of 3.0 atm.

***Keywords:*** direct alcohol fuel cells; electrocatalysts; methanol; PtRu/C

# 2.9 Electrochemical Oxidation of Methanol On Layered Double Hydroxides

M. Oliver-Tolentino, A. Guzmán-Vargas, G. Ramos Sánchez, A. Manzo-Robledo, R.G. González-Huerta.

[1]Instituto Politécnico Nacional, Centro de Investigación en Ciencia Aplicada y Tecnología Avanzada, Calzada Legaria 694, Col. Irrigación, México D.F. 11500, Mexico.

[2]Instituto Politécnico Nacional, ESIQIE-Departamento de Ingeniería Química, Laboratorio de Investigación en Materiales Porosos, Catálisis Ambiental y Química Fina, UPALM Edif. 7 P.B. Zacatenco, GAM, México, DF 07738, Mexico

[3]CONACYT comisionado a Universidad Autónoma Metropolitana-Iztapalapa, Departamento de Química, Av. San Rafael Atlixco 186. Col. Vicentina, 09340, México, DF, Mexico.

[4]ESIQIE-Departamento de Ingeniería Química, Laboratorio de Electroquímica y Corrosión, Instituto Politécnico Nacional, Edif. Z-5 3er piso, UPALM, Zacatenco, GAM, México, DF 07738, Mexico

* Corresponding author: otma_iq@hotmail.com

---

## ABSTRACT

The methanol oxidation (MOR) in alkaline media over Nickel hydroxides has been studied for some years, with the aim to use these materials in direct methanol fuel cell, however the Nickel hydroxides exhibited a catalytic deactivation due to the strong adsorption of methanol over catalytic site. So in this work was evaluated the Layered Double Hydroxides NiAl and NiMn for MOR, the materials were synthetized by co-precipitation method, the samples was characterized by XRD and IR spectroscopy; The electronic properties of LDHs were proved by UV-Vis and EPR spectroscopy, by UV-Vis was observed the Jahn-Teller distortions of $Mn^{3+}$, whereas for EPR is observed a strong dipolar interaction among the spins of Ni and Mn atoms and resulting a ferromagnetic response (F) in the system. On the other hand, the *g* value is indicating a highly distorted octahedral system. The electrochemical results reveal a better electrochemical reversibility in NiMn sample, whereas the electrocatalytic behavior showed a high activity for MOR, in situ differential electrochemical mass spectroscopy (DEMS) technique, exhibited that NiAl material produced $O_2$ and $CO_2$ in same proportion and NiMn produces preferably carbon dioxide.

***Keywords:*** MOR; Layered Double Hydroxides; Jahn Teller; Catalytic Activity.

# CHAPTER 3
# Fuel Cells Components and Stacks

# 3.1 Effect of $LnPO_4$ incorporation on the electrical properties of $Ln_2Zr_2O_7$ (Ln = Gd and Sm) solid electrolytes

M. Salazar-Zertuche, J.A. Díaz-Guillén, C.A. Durón-Sifuentes, N.M. Cepeda-Sanchez,M.E. Bazaldúa-Medellín and A.F. Fuentes,

[1] División de Estudios de Posgrado e Investigación, Instituto Tecnológico de Saltillo, 25280-Saltillo, Coahuila México.

[2] Cinvestav Saltillo, Apartado Postal 663, 25000-Saltillo, Coahuila, México.

* Corresponding author: (+52) 844 4389500, email. jadiaz@itsaltillo.edu.mx

## ABSTRACT

This research reports the synthesis and analysis of the electrical properties of a new group of composites with general formula $Ln_2Zr_2O_7/LnPO_4$ (weight ratios 100-0 and 50-50. Ln = Sm) on views to be applied as solid electrolytes in Solid Oxide Fuel Cells (SOFC). Each composite was synthesized (phosphate and zirconate in the same process) by the molten salt method, preceded by a metathesis reaction induced by mechanical milling, by using a planetary mill with $ZrO_2$ mortars and balls as grinding media, and starting from nitrates of involved elements, $Na_2HPO_4$ and NaOH. Synthesized powders were characterized by different techniques, including XRD and thermal analysis, among others. Ionic conductivity and activation energies for oxygen ion diffusion were determined in uniaxially pressed and sintered samples (1500°C) by impedance spectroscopy, as a function of temperature and frequency. Morphology of sintered samples was analyzed by SEM. Results show that these materials can be successfully obtained after one hour of milling the starting reactants, followed by a molten salt process at 500°C during 3 hours and three cycles of washing with distilled water. Thermal treatments of the synthesized products generate an increasing of their crystallinity, giving place to ordered phases. Morphology of sintered samples reveals that $Sm_2Zr_2O_7$ shows well defined grains with some remnant porosity, while $SmPO_4$ is composed by plates distributed along the zirconate grains. Analysis of electrical properties reveals that these materials show interesting electrical properties, similar to those obtained for good ionic conductors. Ionic conductivity was found in the range of 2.8-3.5 S/cm at 700°C.

***Keywords:*** solid electrolytes; SOFC; molten salt method; composite ceramics; zirconates; phosphates

## 1. Introduction

Solid Oxide Fuel Cells (SOFC) consist in electrochemical reactors that generate electrical energy from a controlled reaction between hydrogen and oxygen, generating only clean water as byproduct [1]. This technology usually works at high temperatures (700-1000°C) which after certain periods of operation generate an interfacial diffusion between the electrolyte and the electrodes, limiting their use. The electrolyte is the fundamental part of SOFC and is currently composed by an yttrium stabilized zirconia (YSZ) ionic conductor. Anode and cathode are composed by Ni-YSZ cermet and $LaSrMnO_3$, respectively.A possibility to overcome the mentioned problem is replacing the electrolyte by a different and stable ionic conductor, such as a lanthanide zirconate $Ln_2Zr_2O_7$. These zirconates present high ionic conductivity and can be thermally stable at temperatures at high as 1500°C, which make them an interesting group of materials to be applied in SOFC. [2-4]. With a general formula $Ln_2Zr_2O_7$, these lanthanide zirconates (Ln = La, Nd, Gd, Sm, Dy, Ho, Eu, Yb, Y, among many others) belong to a family of $A_2B_2O_7$ oxides which can show two different cubic structural arrangements, pyrochlore and anion deficient fluorite. Fundamental difference between these structures lies in the distribution of vacancies in the anion lattice. In the pyrochlore-type structure, vacancies are ordered in one given direction, while in the fluorite are randomly distributed along the anion sublattice. Additionally, in fluorites, ions A and B are found randomly distributed in a single available crystallographic position. [5,6]

Diverse reports of lanthanide circonates involve synthesis by different methods, characterization and analysis of electrical and thermal properties. In most cases, interesting properties have been obtained, mainly on views to apply these materials in SOFC or TBC (Thermal Barriers Coatings) technologies. [7-11]

This work reports the synthesis of a composite $Sm_2Zr_2O_7$ by the molten salt method, which is an environmentally friendly and sustainable chemical process, with low energy consumption compared to other conventional methods (such as solid state synthesis), and which allows the production of single phase ceramic powders at low temperatures, short reaction times and with just a few residual impurities. In this research, method is assisted by mechanical milling, in a metathesis reaction prior to the molten salt process. (12-15)

Additionally we obtain a composite $Sm_2Zr_2O_7/SmPO_4$ in a 50%/50% weight ratio by the same technique, on views to study the effect of combination of these materials on their electrical properties. These rare earth orthophosphates LnPO4 (Ln = La, Nd, Gd, Sm, Ce and Eu) also represent an interesting group of ceramics with good properties to different uses, being the lanthanum orthophosphate $LaPO_4$ the most studied [16].

These materials usually have a monazite structure at high temperatures. Hydrated phases, such as $LaPO_4$. 0.5 $H_2O$, Known as rapdophane can be also present at low temperatures. Monazite structural arrangement is based on a Ln cation coordinated with nine oxygen atoms forming an equatorial polyhedron ($LnO_9$), surrounded by seven $PO_4$ tetrahedra. See full description of the monazite structure in [17].

Lanthanide phosphates can be used in many technologies, including as proton conductors for SOFC or gas sensors [18,19], or combined with a refractory oxide ($Al_2O_3$ or $ZrO_2$) as

ceramic high temperature composites, easier to machine than the corresponding simple oxides [20].They have also been proposed as a thermal barrier coatings to protect metal parts of turbines and diesel engines [21].

Both synthesized samples were then characterized, uniaxally pressed and sintered at 1500°C and their morphologies and electrical properties were studied.

## 2. Materials and Methods

Two different compositions, $Sm_2Zr_2O_7$ and 50%$Sm_2Zr_2O_7$/50%$SmPO_4$ (weight ratio) were synthesized by the molten salt method, starting from the raw materials which consisted in powders of high purity of $Sm(NO_3)_3{\cdot}6H_2O$, $Na_2HPO_4$, $ZrO(NO_3)_2{\cdot}6H_2O$ and NaOH, weighed out as required by stoichiometry, according with equations 1 ($Sm_2Zr_2O_7$) and 2 (50%$Sm_2Zr_2O_7$/50%$SmPO_4$)

$$20[Sm(NO_3)_3{\cdot}6H_2O] + 20[ZrO(NO_3)_2{\cdot}6H_2O] + 100[NaOH] \rightarrow 10[Sm_2Zr_2O_7] + 100[NaNO_3] + 290[H_2O] \quad (1)$$

$$22[Sm(NO_3)_3{\cdot}6H_2O] + 12[Na_2HPO_4] + 10[ZrO(NO_3)_2{\cdot}6H_2O] + 62[NaOH] \rightarrow 12[SmPO_4] + 5[Sm_2Zr_2O_7] + 86[NaNO_3] + 229[H_2O] \quad (2)$$

and milled together during 1 hour in a planetary ball mill (RETSCH PM 100) using $ZrO_2$ containers and balls as grinding media. The resulting activated precursor material was dried 2 h at 120 °C to reduce moisture and minimize violent gas evolution on melting. Dry powders were then loaded into alumina crucibles for the molten salt process, which consisted in firing the powders in air during 3 hours at 500°C (in order to melt the $NaNO_3$ formed as byproduct during mechanical milling process) using a heating and cooling rate of 5°C/min. The obtained material was manually milled and subjected to 3 washes in distilled water to remove the soluble $NaNO_3$ and then dried for 1 h at 120°C to remove moisture. Phase identification at different stages of the process was carried out by X-ray powder diffraction (XRD) in a Philips X'Pert diffractometer, using a Ni-filtered and Cu k(alpha) radiation (λ = 1.5418 Å). To analyze the melting process of the $NaNO_3$ during the molten salt process, just milled samples were analyzed by a thermogravimetric and differential thermal analysis (TGA/DTA) in a Perkin-Elmer Inc. Pyris Diamond TG/DTA model using a heating/cooling rate of 5°C/min. Washed samples were then fired at 1000, 1200 and 1500°C, in order to analyze by XRD the structural evolution of all compositions with temperature. Washed samples were also uniaxially pressed and sintered at 1500°C, to increase their mechanical strength and obtain dense pellets. Morphology of these pellets was analyzed by scanning electron microscopy (SEM) in a JEOL JSM-6610LV SEM microscope equipped with an EDAX Inc. energy-dispersive X-ray detector for

microanalysis. Electrical properties were measured as a function of temperature and frequency, by Impedance Spectroscopy, using a Solartron 1260 Frequency Response Analyzer over the 100 Hz–1 MHz frequency range. Blocking electrodes were made by coating both sides of the pellets with a conductive platinum paint and firing them at 900°C during 3 h to eliminate organic components and harden the Pt coating.

## 3. Results and discussions

### 3.1. Synthesis and characterization

For the $Sm_2Zr_2O_7$ zirconate and $SmPO_4$:$Sm_2Zr_2O_7$ composite, the synthesis process started with a metathesis reaction between starting reagents, promoted by mechanical milling. It consists in an interchange reaction to give place to a precursor of the zirconate (or the composite) plus $NaNO_3$ and water as byproducts of reaction. This behavior is revealed in Figure 1(a), which shows a comparison of XRD patterns of different samples during the molten salt process, corresponding to the system 50$SmPO_4$:50$Sm_2Zr_2O_7$, as representative of both systems. Part (b) and (c) from the same figure show the XRD reported for both $SmPO_4$ and $Sm_2Zr_2O_7$ respectively, form ICDD (international Centre for Diffraction Data).
Pattern corresponding to the sample milled during one hour shows the characteristic reflections of the $NaNO_3$, corroborating the metathesis reaction during mechanical milling. The presence of very low reflections of $Sm(OH)_3$ y $Sm(OH)_2NO_3$ is also detected. These last reflections disappear after the molten salt process at 500°C while $NaNO_3$ prevails.

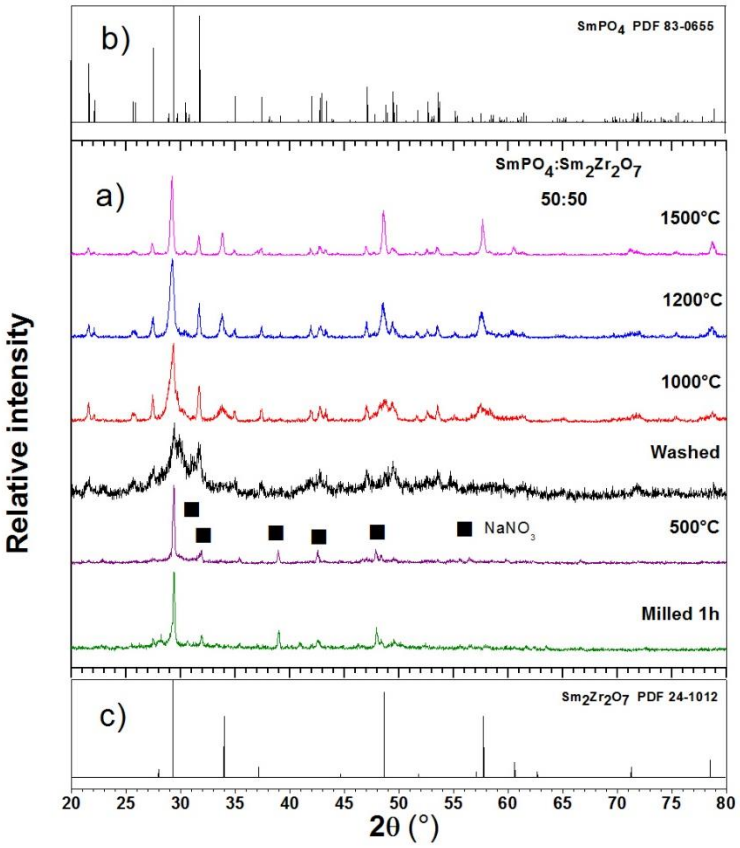


**Fig. 1.** (a) Evolution of the system $50SmPO_4$:$50Sm_2Zr_2O_7$ during the process of molten salt synthesis by XRD. For comparison, ICDD reported XRD patterns for $SmPO_4$ (b) and $Sm_2Zr_2O_7$ (c)

The main aim to the molten salt synthesis is to melt a salt (formed during metathesis reaction), $NaNO_3$ in this case, which is mixed with the precursor, consisting in a mixture of amorphous materials, which will form the final composite. This melt acts as a catalyst, which will help to give place to the crystallization of the composite and most be eliminated by washing after the melting process. The selected temperature for the treatment was 500°C, considering that volatilization of melted $NaNO_3$ occurs at 550°C.

After washing the samples to eliminate $NaNO_3$, XRD pattern shows some low intensity reflections, similar to the $SmPO_4$ and $Sm_2Zr_2O_7$, which corroborates the viability of this method to obtain the composite proposed. Increasing of Intensity and decreasing of width of reflections at higher temperatures is a probe to a major crystallinity in these materials. These patterns reveal that, as was expected, $SmPO_4$ has a monazite-type structure, while pyrochlore-type phase is present for $Sm_2Zr_2O_7$.

Figure 2(a) shows a comparison of both samples studied in this research, treated at 1500°C after the molten salt synthesis. It is clear that for the $Sm_2Zr_2O_7$ sample,

reflections correspond only to the pyrochlore-type structure of this samarium zirconate, while pattern of the composite shows reflections of both monazite and pyrochlore. Reflections of $NaNO_3$ or other byproducts are absent, so the reactions were considered as successfully completed.

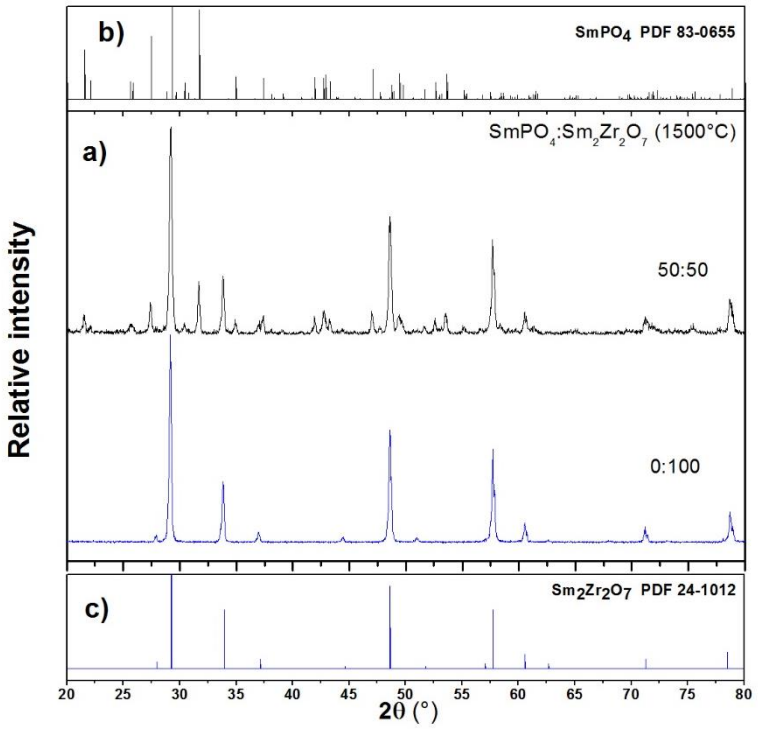


**Fig. 2.** (a) XRD patterns of the composite 50%$SmPO_4$:50%$Sm_2Zr_2O_7$ and $Sm_2Zr_2O_7$ (0:100) after be fired at 1500°C. For comparison, ICDD reported XRD patterns for $SmPO_4$ (b) and $Sm_2Zr_2O_7$ (c)

Figure 3 shows the morphology of sintered samples at 1500°C, obtained by SEM. Figure 3(a) y (b) correspond to the $Sm_2Zr_2O_7$ at 1500 and 5000Xrespectively. This microstructure is composed by well-defined grains with clean borders and some remnant porosity, indicating that higher temperatures are necessary to totally densify this material. Grain size in this sample is less than 2 µm. Figure 3 (c) corresponds to the composite $SmPO_4$:$Sm_2Zr_2O_7$. A notorious difference in morphologies of both oxides is observed since $Sm_2Zr_2O_7$ shows its same morphology, but the composite presents a similar microstructure to plates, located in groups along a matrix of $Sm_2Zr_2O_7$. This morphology has not been reported until now and requires future investigations to be analyzed.

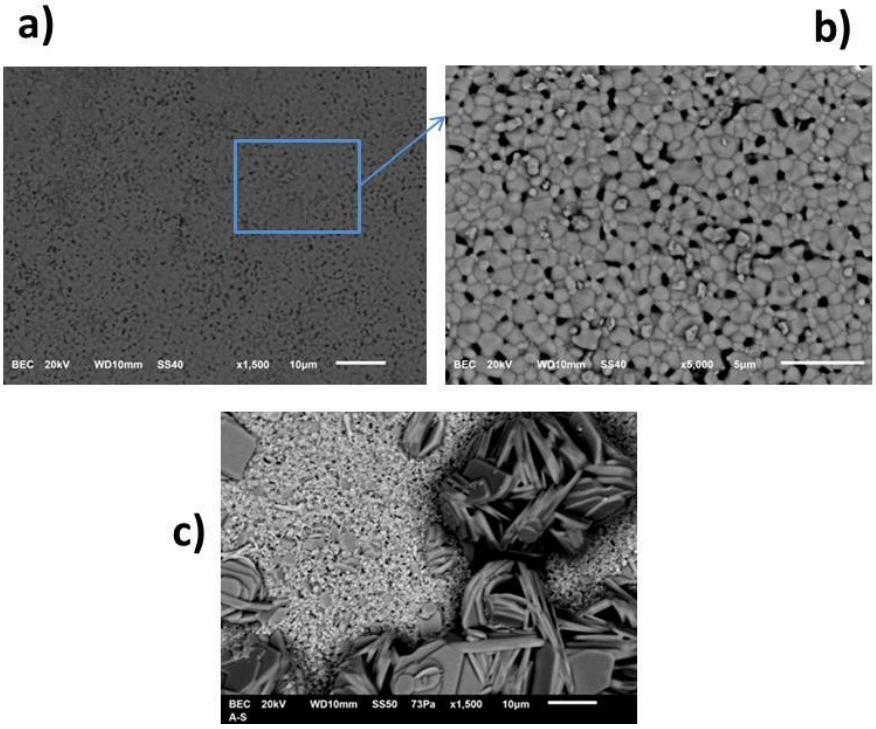


**Fig. 3.** SEM images of the morphology of sintered $Sm_2Zr_2O_7$ at 1500 (a) and 5000 magnifications (b), and the composite50%$SmPO_4$:50%$Sm_2Zr_2O_7$ at 1500 magnifications(c).

## 3.2. Electrical properties

Figure 4(a) shows the behavior of the ionic conductivity σ as a function of the frequency and temperature in double-logarithmic scale and in a range from 100Hz to 1MHz for the composite 50%$SmPO_4$:50%$Sm_2Zr_2O_7$ uniaxially pressed and sintered at 1500°C. In ionic conductors, it is possible to appreciate in this type of representations some potential dependences of the conductivity with frequency (increasing of ionic conductivity at high frequencies) at low temperatures and high frequencies. This behavior was reported by A. K. Jonscher, and is known as Dynamic Universal Response [18]. In this type of representation the value of the conductivity dc (bulk conductivity or conductivity of the material) at each temperature is manifested as a plateau in which the value of the conductivity is independent of frequency. This plateau is marked with blue arrows in figure 4(a). Same figure corroborates that the process of ionic conduction is thermally activated, since conductivity increases with temperature, obtaining a highest value at 700°C. Same behavior was obtained for the $Sm_2Zr_2O_7$ system.

Figure 4(b) shows he dependence of the dc conductivity with temperature for the same composition, analyzed using an Arrhenius type representation of the form:

$$\sigma_{dc}\, T = (\sigma^{0})\, exp(-E_{dc}/k_B T) \qquad (3)$$

where $\sigma^0$ is the pre-exponential factor, related to the number of mobile ions, oxygen in this case, $E_{dc}$ corresponds to the activation energy for the oxygen diffusion, or energy required by an $O^{2-}$ ion to jump from its position and contribute to the conductivity. This energy also includes the interaction between the given ion with others during diffusion process. The dc conductivity values used for this representation were obtained directly from the plot of conductivity versus frequency (plateau) for each composition (Figure 4(a)). The linear fit of the experimental data in these processes for ionic conductors generates straight lines whose slope is proportional to the activation energy ($E_{dc}$) making it possible to determine the activation energy values for each analyzed composition. Figure 4(b) shows such representation for the same composite.

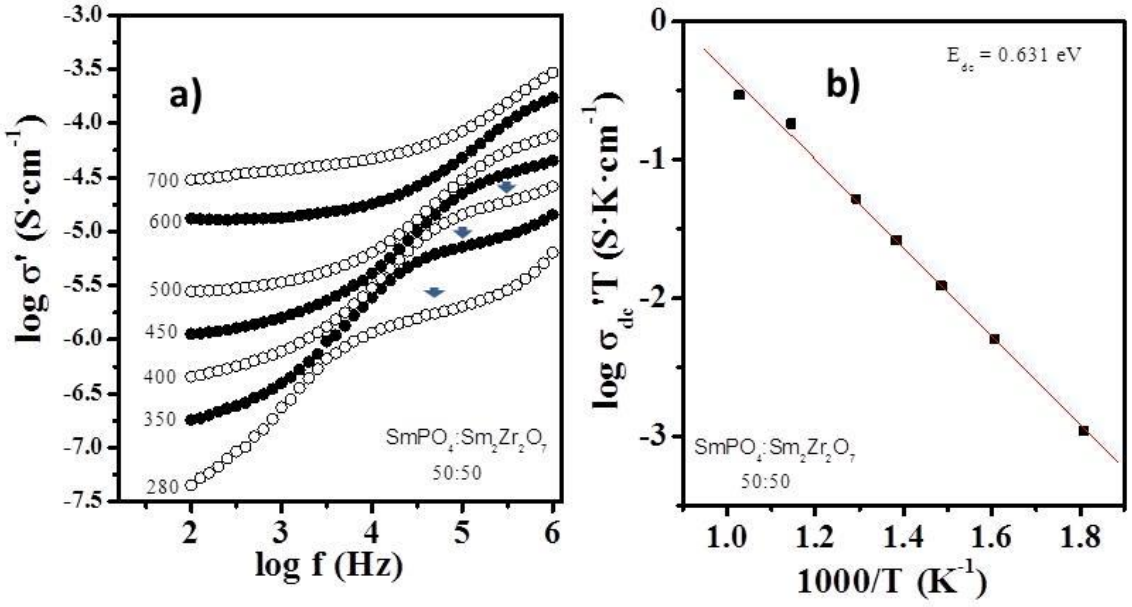


**Fig. 4.** Conductivity vs. frequency for the composite $SmPO_4$:$Sm_2Zr_2O_7$ in a double logarithmic scale as representative of both systems (a). Arrhenius graphic representation of the dc conductivity for the same composition (b).

These $E_{dc}$ activation energies together with the conductivity $\sigma_{dc}$ are ploted for both samples, $SmPO_4$:$Sm_2Zr_2O_7$ and $Sm_2Zr_2O_7$ in Figure 5.

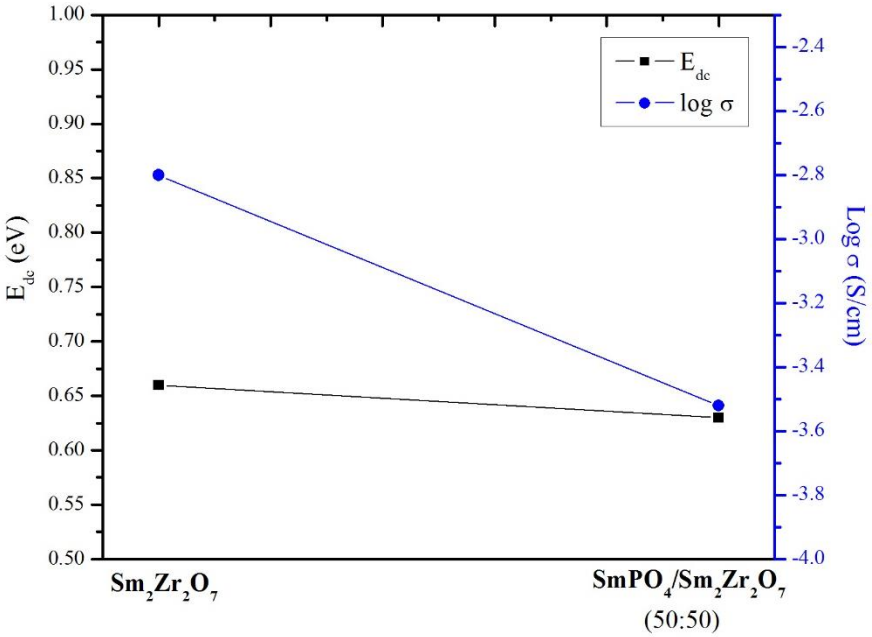


**Fig. 5.** Activation energies $E_{dc}$ and dc conductivity $\sigma_{dc}$ at 700°C for both analyzed systems. Straight lines only represent the trends of experimental data.

These results reveal that both compositions show good electrical properties, similar to those in ionic conductors. Ionic conductivity for both systems is in the range of $10^{-2.8}$-$10^{-3.5}$ S/cm at 700°C. Activation energies are similar for both samples and are found in the range of 0.63 to 0.66 eV. These values of $E_{dc}$ are considered lower than such of similar materials synthesized by different methods and should be traduced in higher ionic conductivities, since lower energy is required by the charge carriers to contribute to the conduction process.

Dc conductivity $\sigma_{dc}$ decreases for the composite. This behavior can be explained if we consider that $LaPO_4$ is known as a protonic conductor, which has an important application in a different type of Fuel Cell. However ionic conductivity in both systems is considered good enough to apply these materials in the SOFC technology.

## 4. Conclusion

In this research, molten salt method is successfully used to obtain $SmPO_4$:$Sm_2Zr_2O_7$ and $Sm_2Zr_2O_7$ at low temperatures on views to their application as solid electrolytes in SOFCs. The mechanical milling process generates a metathesis reaction between starting reactants, giving place to NaNo3 and a set of precursors of the desired compositions. The molten salt process allows generating disordered phases of $SmPO_4$:$Sm_2Zr_2O_7$ and $Sm_2Zr_2O_7$. These phases increase in crystallinity with increasing of temperature, showing

the $SmPO_4$ a monazite-type structure and the $Sm_2Zr_2O_7$ a pyrochlore-type arrangement. None intermediate phases are found in the composite $SmPO_4$:$Sm_2Zr_2O_7$, indicating that this system is stable enough even at 1500°C.

Morphology of the $Sm_2Zr_2O_7$ as pure material and into the composite shows well defined grains with clean borders and some remnant porosity. $SmPO_4$ in the composite has morphology in form of groups of plates located in a matrix of grains of $Sm_2Zr_2O_7$.

Ionic conductivity values for all compositions are found in the range of $10^{-2.8}$-$10^{-3.5}$ S/cm at 700°C. Higher ionic conductivities were obtained for $Sm_2Zr_2O_7$ due mainly to his nature as ionic conductor. These results demonstrate that these oxides can be considered as important candidates to be applied as solid electrolytes in SOFC.

## Acknowledgements

This work was financially supported by CONACYT (grants CB-2011-01-166 995 and CB2013-221 701-Y) and TecNM (grant 5747.16-P)

## References

[1] Hwang CS, Tsai CH, Chang CL, Chuang M, Shie ZYC, Cheng SW, Wu SH. Plasma sprayed metal-supported solid oxide fuel cell and stack with nanostructured anodes and diffusion barrier layer. Thin Solid Films 2014; 570: 183-8.

[2] Yang F, Wang Y, Zhao X, Xiao P. Enhanced ionic conductivity in pyrochlore and fluorite mixed phase yttrium-doped lanthanum zirconate. J. Power Sources 2015; 273: 290-7.

[3] Harley G, Yu R, Jonghe LCD. Proton transport paths in lanthanum phosphate electrolytes. Solid State Ionics 2007; 178: 769-73.

[4] Mahato N, Banerjee A, Gupta A, Omar S, Balani K. Progress in Material Selection for Solid Oxide Fuel Cell Technology: A Review. Prog. Mater. Sci. 2015; 72: 1-9.

[5] Michel D, Perez M, Collongues JR. Etude de la transformation ordre-désordre de la structure fluorite à la structure pyrochlore pour des phases (1-x) $ZrO_2$ – x $Ln_2O_3$. Mater. Res. Bull. 1974; 9: 1457-68.

[6] Hatnean MC, Lees MR, Balakrishnan G. Growth of single-crystals of rare-earth zirconate pyrochlores, $Ln_2Zr_2O_7$ (with Ln=La, Nd, Sm, and Gd) by the floating zone technique. J. Cryst. Growth 2015; 418: 1-6.

[7] López-Cota FA, Cepeda-Sánchez NM, Díaz-Guillén JA, Dura OJ, López de la Torre MA, Maczka M, Ptak M, Fuentes AF. Electrical and thermophysical properties of mechanochemically obtained lanthanide hafnates. J Am Ceram Soc. 2017;100:1994–04.

[8] Cepeda-Sánchez NM, Díaz-Guillén JA, Maczka M, Amador U, Fuentes AF. Mechanochemical synthesis, crystal structure and ion conduction in the $Gd_2Hf_{2-x}Ti_xO_7$ system. J Mater Sci 2017;1-14.

[9] Díaz-Guillén JA, Díaz-Guillén MR, Almanza JM, Fuentes AF, Santamaría J, León C. Effect of La substitution for Gd in the ionic conductivity and oxygen dynamics of fluorite-type $Gd_2Zr_2O_7$ J Phys-Condens Mat 2007;19 35: 356212.

[10] Díaz-Guillén JA, Fuentes AF, Díaz-Guillén MR, Almanza JM, Santamaría J, León C. The effect of homovalent A-site substitutions on the ionic conductivity of pyrochlore-type $Gd_2Zr_2O_7$. J Power Sources 2009; 186: 349-52.

[11] Shlyaktina AV, Shcherbakova LG. New solid electrolytes of the pyrochlore family. Russ J Electrochem 2012; 48:1–25.

[12] Mendoza-Mendoza E, Karinjilottu P, Martínez-Montemayor S, Fuentes AF. Molten salts synthesis and electrical properties of Sr-and/or Mg-doped perovskite-type $LaAlO_3$ powders", Springer Science Business Media 2012; 1-10.

[13] Rastogi R, Singh N, Shukla S. Synthesis of NiO nano crystals through nitrate eutectic melt", Indian J. Mar. Sci. 2010; 17: 477-80.

[14] Mendoza-Mendoza E, Martínez-Montemayor S, Maczkac M, Marciniakc Ł, Fuentes AF. A facile and "green-chemistry" method to synthesize pure and Nd-doped $Y_3Al_5O_{12}$ nanopowders at low-temperatures. Ceram. Inter. 2013; 39: 9405-14.

[15] Hernández AR, Martínez AL, Fuentes AF, Nelson AGD, Ewing RC, Martínez-Montemayor S. Molten salts activated by high-energy milling: A useful, low-temperature route for the synthesis of multiferroic compounds. J. Alloys Compd. 2014; 584: 93-00.

[16] Hikichi Y, Nomura T. Melting Temperatures of Monazite and Xenotime. J. Am. Ceram. Soc. 1987; 70: 252-3.

[17] Clavier N, Podor R, Dacheux N. Crystal chemistry of the monazite structure. J. Eur. Ceram. Soc. 2011; 31: 941-76.

[18] Norby T, Christiansen N. Proton conduction in Ca- and Sr-substituted $LaPO_4$. Solid State Ionics 1995; 77: 240-3.

[19] Amezawa K, Maekawa H, Tomii Y, Yamamoto N. High temperature protonic conduction in aragonite-type $NdBO_3$. Solid State Ionics 2001; 145: 233-40.

[20] Davis JB, Marshall DB, Housley RM, Morgan PED. Machinable ceramics containing rare-earth phosphates. J. Am. Ceram. Soc. 1998; 81: 2169-75.

[21] Levi CG. Emerging materials and processes for thermal barrier systems. Solid State Mater. Sci. 2004; 8: 77-91.

[22] Jonscher AK. Dielectric relaxation in solids. Chelsea Dielectrics Press Ltd.; 1983.

# 3.2 Novel materials for substitutes of platinum and Nafion in microbial fuel cells

E. A. Enciso Hernández, S. Kumar Kamaraj, Sergio Durón Torres, Veronica Avila Vazquez

[1] Instituto Politécnico Nacional, Unidad Profesional Interdisciplinaria de Ingeniería campus Zacatecas, Blvd. El Bote s/n Cerro del Gato, Ejido La Escondida, Col. Cd Administrativa C.P. 98160, Zacatecas, Zac. México.
[2] Universidad Politécnica de Aguascalientes, Paseo San Gerardo 207 C.P. 20342. Aguascalientes Ags. México.
[3]Universidad Autónoma de Zacatecas, Área de Ciencias Químicas, Carretera Zacatecas-Guadalajara km 6, Ejido "La Escondida", Edificio 6, C.P. 98160, Zacatecas, Zac. México.
*vav_taba@hotmail.com.

## ABSTRACT

The principal limitation for the escalation of microbial fuel cells is the highest cost that represent platinum and Nafion® use. This work show the physicochemical and electrochemical characterization of microbial fuel cells (MFC) based on novel materials, like clay as substitute of Nafion in proton exchange membranes (PEM), and a mixture of carbons as substitute of platinum as catalyst in the oxygen reduction reaction (ORR) in the MFC for the degradation of glycerin.

The MFC consisted in a vertical single chamber, with soil like inoculum and a solution of glycerin 2g $L^{-1}$ and 150g$L^{-1}$and phosphate buffer inside. The cells were operated in batch cycles of 20 to 30 days. The MFC show a $V_{OCmax}$1.05V, $i_{max}$759mA$m^{-2}$ and $P_{max}$ 100.37 mW$m^{-2}$ with alternative materials and a $V_{OCmax}$1.4V, $i_{max}$1391 mA$m^{-2}$ and $P_{max}$ 230.46mW$m^{-2}$ with platinum as cathode. A COD removal efficiency superior to 90% was obtained in both systems after 23 days in operating.

The novel materials evaluated show a similar behavior in both MFC, this represent a reduction in the system cost and a development in the energy production.

***Keywords:*** carbon, clay, substitutes, low cost

## 1. Introduction

Biodiesel is a biofuel resulting from the reaction of transesterification in vegetable oils and animal fats [1], it had become very important internationally for its low emissions of greenhouse gases, this had been reflected in the growth that this industry had in the last years[2], however, the increase in the production of biodiesel had also brought a

considerable increase in the production of glycerin, which had begun to accumulate due to the absence of methods of treatment that cover the large volume of current production[3].

The transesterification reaction had as products to biodiesel and glycerin, producing 1L of glycerinper 10 L of biodiesel produced [4]. This glycerin was previously sold as raw glycerin or high purity glycerin [5] for the pharmaceutical and cosmetic industry [6], however in the last few years the residual glycerin production of biodiesel had exceeded the global demand for glycerin [5,7], this had brought a number of consequences such as the fall in glycerin prices 8], this proves that the sale of glycerin is no longer profitable, so it is now tried as an industrial waste plus [9], causing unanticipated costs for the biodiesel industry and consequently an increase in the biodiesel prices [8].

The industry had begun to adopt new methods to dispose of residual glycerin, such as reusing it as a lubricant or incorporating it into fermentation processes [9]for obtaining other products such as: n-butanol[10], 1,3 propanediol [11,12], ethanol [13,14], lactic acid [15], propionic acid [16], hydrogen [4,9,17] and electric energy through MFC [4,18,19].

The MFCs show a great potential as an alternative method for the treatment of residues, besides treating them, they allow having an energetic gain. For this, it had begun to investigate their application in the treatment of the residual glycerin coming from biodiesel production.

Teera Chookaew in 2014[18] used a two-stage system for the treatment of crude glycerin. In the first stage, it was able to produce 332 $mLL^{-1}$ of $H_2$ with a rate of 0.55 $molH_2mol^{-1}$ glycerin, with a COD removal of 20%, after the fermentation, the mixture was transferred to a MFC with carbon brush anodes and carbon cloth as cathode and stainless steel with an organic load of 7620 $mgL^{-1}$, obtaining 92 $mWm^{-2}$, removing up to 50% of COD.

Yujie Feng in 2010 [19] and co-workers obtained 487 ± 28 $mWm^{-2}$ with a phosphate buffer solution of 50mM, then the maximum power of the MFC was increased to 778 ± 67 $mWm^{-2}$ with a carbon brush cathode, and finally to 1310 ± 15 $mWm^{-2}$ with carbon cloth as cathode, subsequently the concentration of the buffer solution was increased to 200mM, to finally obtain a power of 2110 ± 68$mWm^{-2}$.

Yogesh Sharma in 2010 [4] evaluated a continuous feed two-chamber MFC with an anode made from graphite fibers (Panex 35, Gordon Brushes, CA) and a carbon brush anode with 0.35 $mgcm^{-2}$ of platinum, obtaining a maximum power of 4579 $mWm^{-3}$, when glucose was added as co-substratum in a concentration of $2gL^{-1}$.

Queiroz Guimarães in 2014 [20] evaluated a double chamber cell with a platinum cathode supported on a carbon brush with aeration, as anode had a carbon brush and a Nafion® membrane PEM, she evaluated the effect of using different concentrations of glycerin (160, 240,320, 640, 1800 and 2160$mgL^{-1}$), obtaining a maximum power of 28.1 $mAm^{-2}$ with the concentration of 1080 $mgL^{-1}$ and a COD removal of 92%. Ghadge in 2015 [21]developed an MFC with a capacity of 26L using clay containers with a wal l width of 8mm as base of MFC and cathodes that consisted of conductive carbon ink prepared fromVulcan XC-72R carbon powder with $MnO_2$, achieving 2800 $mAm^{-3}$ and 780 $mWm^{-3}$.

This study focuses on the use of alternative materials to platinum and Nafion® as catalysts and PEM membranes in MFC for the treatment of residual glycerin from biodiesel, introducing a mixture of coals as a new catalyst and orange clay cylinders as support for MFC and membrane PEM. The hypothesis of the project assumes that the mixture of coals maintains a symbiotic relationship with each other, being able to behave as a medium-range catalyst (compared to platinum) in the oxygen reduction reaction, while the ceramic base of the MFCs will allow the exchange of protons by proton hopping (Grotthus mechanism) to moisten, being a low cost alternative compared to MFC based on the use of platinum and Nafion®.

## 2. Materials and Methods

### 2.1 Obtaining glycerin

The glycerin used in this study was obtained by a transesterification reaction in the laboratory. This reaction consisted in mixture 17 mL of methanol with 0.5 g of potassium hydroxide (KOH) per each 50 mL of used vegetable oil at 60 °C with vigorous stirring for 2 hours. Then it could stand for 24h and finally the glycerin was separated of the biodiesel by decantation [22,23].

### 2.2 Manufacturing of MFC

The MFC had based on jars of orange clay of 70ml, its was sanded and apply a thin layer of acrylic enamel, later a mesh of stainless steel wasfixed with wires, the ink CAC is a mixture of carbons and ethyl alcohol, the ink was applied on the mesh of stainless steel with a brush.

### 2.3 Preparationof inoculum

The preparation of the inoculum was made in anoxic conditions with chicken skin and native soil in a bottle, the bottle was closed and placed in an incubator at 36 °C for one week until the MFCs were started.

### 2.4 Operating Conditions

The MFC were operated under anoxic conditions in batch cycles, using as anode and support for the bacteria a carbon felt, a suspensions of $2gL^{-1}$and 150 g $L^{-1}$of residual glycerin in aphosphate buffer solution (8.6g of $KH_2PO4$, 1.2g NaOH, dissolved in one liter of distilled water[24])was prepared for the treatment, the suspension was inoculated with 10 g of soil per liter of glycerin suspension, then 50 mL of the solution was poured into the jars or until the carbon felt was covered with the solution, finally a special rubber cap was placed through which it is possible to introduce a cable that functions as an electron

collector. The MFC were operated 28 ºC and neutral pH, operating until the voltage of the MFC decayed showing the depletion of the glycerin, in this point the solution was withdrawn and glycerin solution was added again.

### 2.5 Electrochemical characterization

The electrochemical characterization start with the record of the Open Circuit Voltage (OCV) the MFC, when the value of the OCV becomestable the rest of the analyses were performed, the polarization curves was built by a LinearSweep Voltamperometri (LSV) with a sweep speed of 0.1mV$s^{-1}$, finishing the sweep in 50mV as a safety measure, the impedance tests were performed with a scan of 1X$10^{5}$ Hz at 1X$10^{-2}$ Hz, finally the chronoamperometric was realized fixing a voltage of 350mV during 18000s.

## 3. Resultsand Discussion

In the Fig 1, show the record of OCV of MFCs with two different concentration of glycerin, the Fig 1 a) 150 g$L^{-1}$and the Fig1 b) 2 g$L^{-1}$, , the first part of both curves correspond to the bacterial growth conditioning stage, in the Fig 1 a) this stage had a duration of 200 h, while in de Fig 1 b) this stage had a reduction its duration at 120 h, flowed of a stationary phade of 480 h, with a $V_{max}$ of 1400 mV for Pt_2 g and 1000 mV for CAC_2 g, since in the Fig b) show an stationary phade with a duration of more of 700 h and $V_{max}$ of 550 mV for Pt_150 gand 480 mV for CAC_150g, this show that the bacteria had a better response and adapted easily to low concentration of glycerin, this is reflected in a shorter degradation time of glycerin and higher OCV[25].

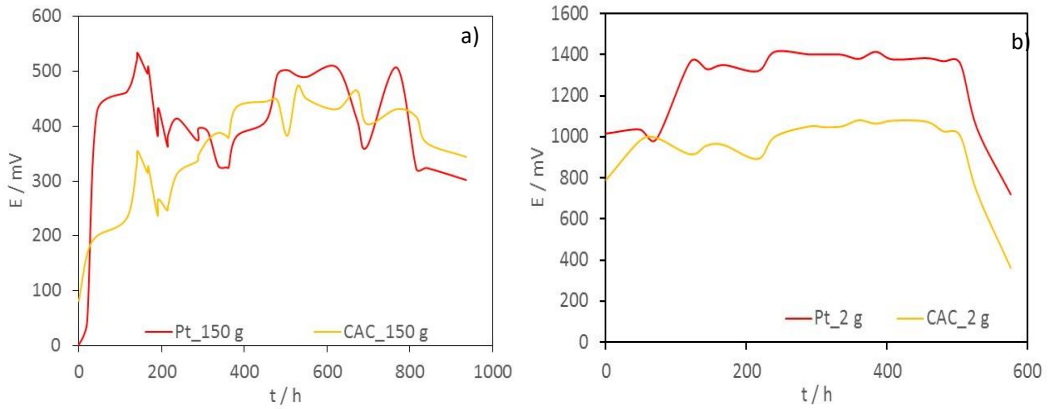


**Fig 1.**OCV record of MFC a) 150 g of glycerin and b) 2 g of glycerin with Pt and CAC cathodes.

Once the system achieved the stationary conditions in terms of OCV, these was characterized with polarization curves, impedance curves and stabilization curves. The Fig 2shows the polarization curves for the MFCs evaluated,in the Fig 2 a) the curves of MCF CAC_150 g and Pt_150 g shows a less electrochemical activity compared with MFC CAC_2g and Pt_2 g in the Fig 2 b), can be observed that the MFC CAC_2 g achieve an $i_{max}$of 759 mA$m^{-2}$and a $P_{max}$of 100.37 mW$m^{-2}$, since the MFC CAC_150 g achieve an $i_{max}$ of

0.5 $mAm^{-2}$ and a $P_{max}$of 0.07 $mWm^{-2}$showing be the most resistive MFC given the marked slope in its voltage-current line, this can be confirmed with its impedance curve in Fig 3 a), since the MFC Pt_2 g achieve an $i_{max}$ of 1391$mAm^{-2}$ and a $P_{max}$ of 230.46 $mWm^{-2}$ doubling the values achieved of MFC CAC_2 g and far exceeding the results obtained for the MFC Pt_150 g that only achievedi$_{max}$ of 2 $mAm^{-2}$ and a $P_{max}$ of 0.35 $mWm^{-2}$.The MFC operated with a low concentration of glycerin presented a best behavior that the MFC that operated with a high concentration of glycerin, a possible explain for this is the invitation of electrogenic activity of bacteria for an excess of substrate and an accumulation of aqueous products in the anode [4,20].Compared with others studies the MFC the power output obtained is higher that reported by Teera, Yogesh and Queiroz [4,18, 20].

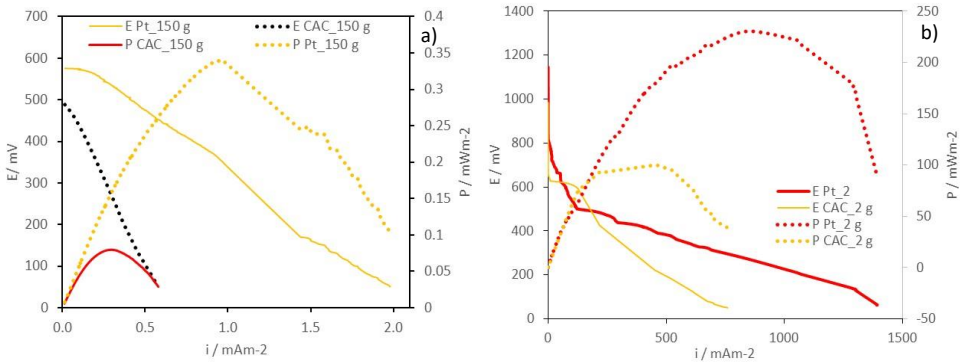


**Fig 2.** Polarization curves, a) MFC with150 g and b) MFC with 2 g of glycerin use CAC and Pt cathodes.

The Fig 3 show the impedance curves of the MFC evaluated, in the Fig 3 a) the curve CAC_150 gis very large reaching more of 3 kΩ, the most resistive MFC that explain its low current output, the insert correspond the Pt_150 .The MFC operated with 2 g $L^{-1}$ a little resistance and big activity consistent with the results showed before.

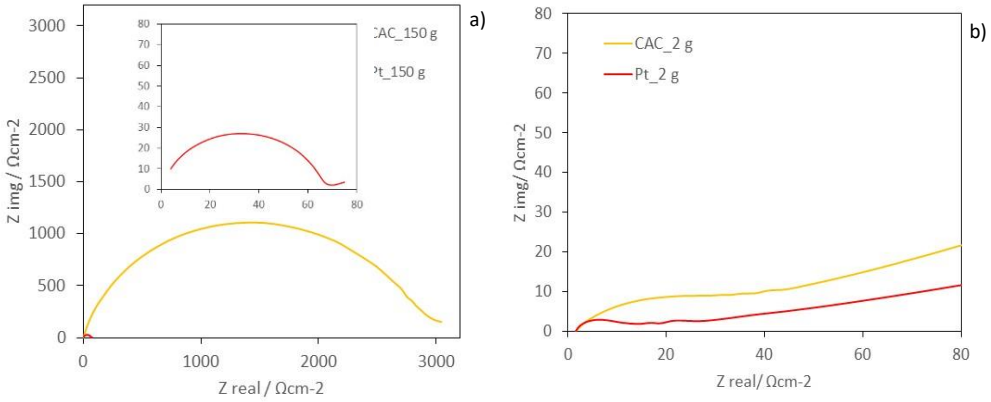


**Fig 3.** a) EIS curve of 150g of glycerin, b) EIS curves of 2g of glycerin use CAC and Pt cathodes.

The stability curves were evaluates with chronoamperometry at 350mV, Fig 4 a) shows the stability curves of the cells with 150 g of glycerin, where it can be observed that Pt_150 g initially offers a current output of 65 µA and down to 20 µA in 10 000 seconds, after that down again for 8 000 seconds to 18 µA, since the cell CAC_150 g start at 10 µA

and down to 4.5 µA after 5500 seconds and stay stable this current to the end of the test. The Fig 4 b) shows the stability curves of the cells with 2 g of glycerin, for this concentration show greater stabilility and current in the test. the results of the test showthat the cell CAC are a fairly stable cathode, and with a significantly lower initial degradation to the platinum cathode.

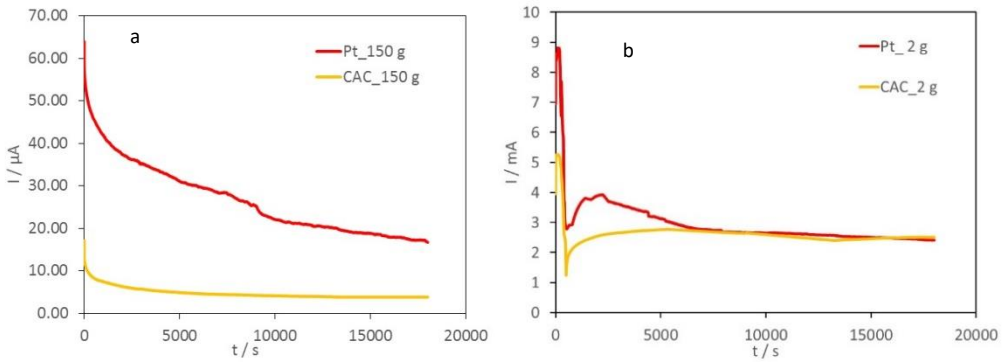


**Fig 4.** Stability curves 150g of glycerin, b) 2g of glycerin use CAC and Pt cathodes.

## 4. Conclusion

The excess of substrate and the accumulation of aqueous compounds in anode inhibited the electrogenic activity of the bacteria reducing its power output, making necessary a conditioning stage through consecutive culture increasing the concentration in each culture so that the bacteria can adapt to such high concentrations.

The MFCs with platinum cathode show a lower charge transferresistance, as well as a higher output of current and power, whereas the CAC cathode have shown to have a similar performance although in a lower average, obtaining power outputs 28% lower in lows concentration of glycerin, however the CAC cathode show a more uniform behavior among them, as well as being more stable over time, achieving a current output of 2.5 mA in a shorter time and without a degradation rate as long as the platinum cathodes

Given their stability the MFCs with CAC cathode are presented as a feasible alternative to CCM platinum cathodes in the treatment of glycerin coming from biodiesel waste by MFC, which together with its low cost of manufacture make them he most reliable option when wanting to climb

## Acknowledgements

Special thanks to the Unidad Académica de CienciasQuímicas of the Universidad Autónoma de Zacatecas for giving all facilities for the realization of this project.

## References

[1]Inter-American Institute for Cooperation on Agriculture. Atlas of agroenergy and biofuels in the Americas II. http://unpan1.un.org/intradoc/groups/public/documents/icap/unpan045305.pdf; 2010 [accessed 20.08.16].

[2] Biodiésel.org. Production Statistics, http://Biodiésel.org/production/production-statistics: 2016 [accessed 20.08.16].

[3] Fan, X. Burton, R., Zhou, Y.Glycerol (byproduct of biodiesel production) as a source for fuels and chemicals – mini review. Open Fuels Energy Sci. J.,2010:3:17-22.

[4] Sharma, Y., Parnas, R., Li, B. Bioenergy production from glycerol in hydrogen producing bioreactors (HPBs) and microbial fuel cells (MFCs). Int. J. Hydrogen ,2011:36:3853-3861.

[5] Pérez, L., Redondo, R.USP Glycerin production. http://www.edutecne.utn.edu.ar/PPI-CAI/ppi2014trabajo.pdf/2014 [accessed 22.08.16].

[6]Johnson, D., Taconi, K. The glycerin glut: Options for the value-added conversion of crude glycerol resulting from biodiesel production. EnvironProgSustain Energy, 2007:26:338-348.

[7]Infinita, Biodieselinform2015, http://www.infinita.eu/download.php?file=Informe%20Biodiésel%20UE_abril2015_AC_65.pdf/ 2015 [accessed 22.08.16].

[8]Da Silva, G., Mack, M., Contiero, J. Glycerol: a promising and abundant carbon source for industrial microbiology. Biotechnol. Adv. 2009:27:30-39.

[9] Suehara, K., Kawamoto, Y., Fujii, E., Kohda, J., Nakano, Y., Yano, T. Biological treatment of wastewater discharged from biodiesel fuel production plant with alkali-catalyzed transesterification. J. Biosci. Bioeng.2005:100:437-442.

[10] Wilkens, E., Ringel, AK., Hortig, D., Willke, T., Vorlop, KD. High-level production of 1,3-propanediol from crude glycerol by *Clostridium butyricum*AKR$_{102a}$.Appl. Microbiol. Biotechnol.2012:93:1057-1063.

[11] González, M., Meynial, I., Mendes, F., Andrade, J., Vasconcelos, I., Soucaille, P. Metabolic engineering of *Clostridium acetobutylicum* for the industrial production of 1,3-propanediol from glycerol. Metab. Eng. 2005:7:329-336.

[12] Jensen, T., Kvist, T., Mikkelsen, M., Christensen, P., Westermann, P. Fermentation of crude glycerol from biodiesel production by *Clostridium pasteurianum*.J IndMicrobiolBiotechnol 2012:39:709–717.

[13] Hong, A., Cheng, K., Peng, F., Zhou, S., Sun, Y., Liu, C., Liu, D.Strain isolation and optimization of process parameters for bioconversion of glycerol to lactic acid. J. Chem. Technol. Biotechnol. 2009:84:1576-1581.

[14] Zhao, F., Slade, R., Varcoe, J. Techniques for the study and development of microbial fuel cells: an electrochemical perspective. ChemSoc Rev.2009:38:1926-1939.

[15] Zhang, X., Shanmugam, T., Ingram, L. Fermentation of glycerol to succinate by metabolically engineered strains of*Escherichia coli*.Appl. Environ. Microbiol.2010:76:2397-2401.

[16]Ruhal, R., Choudhury, B. Improved trehalose production from biodiesel waste using parent and osmotically sensitive mutant of *Propionibacterium freudenreichii subsp. shermanii* under aerobic conditions. J IndMicrobiolBiotechnol 2012:39:1153-1160.

[17] Yang, C., Jiang, P., Xiao, S., Zhang, C., Lou, K., Xing, X.Fed-batch fermentation of recombinant *Citrobacter freundii* with expression of a violacein-synthesizing gene cluster for efficient violacein production from glycerol.BiochemEng J.2011:57:55–62.

[18]Chookaew, T., Prasertsan, P., Ren, Z. Two-stage conversion of crude glycerol to energy using dark fermentation linked with microbial fuel cell or microbial electrolysis cell.N Biotechnol. 2014:3:179-184.

[19] Feng, Y., Yang, Q., Wang, X., Liu, Y., Lee, H., Ren, N. Treatment of biodiesel production wastes with simultaneous electricity generation using a single-chamber microbial fuel cell.BioresourTechnol.2011:102:411-415.

[20] Queiroz, A., Linares, J.Glycerol Utilization in Microbial Fuel Cells: Conditioning Stage and Influence of the Glycerol Concentration. J. Electrochem. Soc. 2012:161:125-132.

[21] Ghadge, A., Ghangrekar, M.Performance of low cost scalable air–cathode microbial fuel cell made from clayware separator using multiple electrodes.BioresourTechnol.2015:182:373-377.

[22] Food and Agriculture Organization of the United Nations. “Fats and oils in human nutrition” .http://www.fao.org/home/en/ 1997 [accessed 23.08.16].

[23]Sánchez, I., Huertas, K.Obtention and characterization of biodiesel from oil seed of Ricinuscommunis (Higuerilla) genetically modified and cultivated in the coffee axis. Technological University of Pereira. 2012

[24]Karthikeyan, R., Sathish-Kumar, K., Murugesan, M., Berchmans, S., Yegnaraman, V.Bioelectrocatalysis of *Acetobacter aceti* and *Gluconobacterroseus* for Current Generation.Environ. Sci. Technol.2009:43:8684-8689.

[25]Min, B., Kim, J., Oh, S., Regan, J., Logan, B. Electricity generation from swine wastewater using microbial fuel cells. Water Res. 2005:39:4961-4968.

# 3.3 Roughness analysis in different kind or machining for the collector plates of PEM fuel Cells

Hector Morano, David Huerfano, Dulce Viridiana Melo

[1]School of Design, Engineering and Architecture ITESM, Campus Estado de México

[2]School of Engineering and Science ITESM, Campus Estado de México

[3]School of Design, Engineering and Architecture ITESM, Campus Estado de México

* 5543656240, dhuerfanoiq@hotmail.com

---

## ABSTRACT

This paper shows the experimental determination of the roughness factor presented in different machining methods for the current collector plates of the protonic membrane exchange (PEM) fuel cells. Two machining methods was implemented in the graphite plates: CNC and laser micromachining. This plates was subject of analysis with profilometer and an experimental test of the friction loss. Additionally, an optic analysis using the scanning electron microscope (SEM) was implemented, to show then characteristic of the machining.

***Keywords:*** PEM fuell cells; machining, CNC, laser, roughness.

# 3.4 Design, manufacture and experimental validation of a millimeter PEMFC

C. Pacheco, B. Escobar, R. Barbosa, J. Sierra

[1] Centro de Investigación Científica de Yucatán, A.C. Carretera Sierra Papacal Chuburna Puerto Km 5, C.P. 97302, Sierra Papacal, Yucatán, México.

[2] Universidad de Quintana Roo, Boulevard Bahía s/n, C.P 77019, Chetumal, Q. Roo, México.

[3] Universidad Autónoma del Carmen, Calle 56 No. 4 Esq. Avenida Concordia, Col. Benito Juárez. C.P. 24180, Cd. del Carmen, Campeche, México

* Tel: +52 9831566032; e-mail: romelix1@gmail.com

* Tel: +52 9999300205; e-mail: beatriz.escobar@cicy.mx

## ABSTRACT

One of the most promising applications on renewable energy are the fuel cells, which are devices that convert chemical energy into electrical energy. Specifically, Proton Exchange Membrane Fuel Cell (PEMFC) is the most versatile of all types for its light weight and easy transport. The present work focuses on the design, manufacture and validation of an air breathing PEMFC (AB-PEMFC) of millimetric size with a different design from conventional fuel cells, as well as the construction of a stack. The design was carried out using computational fluid dynamics (CFD) techniques to find the correct position of the current collector. The manufacturing process of the milli AB-PEMFC consisted of the depositions of the components in layers: 1) end plate composed of a flat polymer, 2) fuel flow channel with gas diffusion layer, 3) silicone seal with micro platinum wires embedded, 4) membrane electrode assembly with high platinum load, 5) gas diffusion layer with micro platinum wires. Performance tests were done on a single AB-PEMFC and the configuration in stack of two mono cells under different flow conditions. In addition, a wing design is implemented for the cathode gas diffusion layer, as the air intake contributes significantly in the cell performance. The results of the CFD study helped to determine the best position for the current collector, which is between the catalytic layer (CL) and the gas diffusion layer. In this work, the performance results showed current a density of 30 mA $cm^{-2}$ for a single cell and 32 mA $cm^{-2}$ for the stack.

***Keywords:*** Fuel cell; air-breathing; portable applications; CFD.

## 1. Introduction

The energy plays an important paper for global development in various aspects such as social, technological and economic. In the last years the consumption of fossil fuels has been increasing due to the industrialization of developing countries, which has brought an increase in global pollution [1]. It is necessary and urgent to accelerate the development of new technologies to guarantee the demand for electric energy that society requires. In the last years, significant efforts have been made in the search for alternatives to make energy generation more friendly with the environment [2]. Another important aspect to consider is the increase in the market and the complexity of portable electronic devices. Some research shows that traditional ways like nickel and lithium batteries in rechargeable presentations, they will not be able to satisfy the demand required by the portable devices, mainly due to its limited energy density. A feasible alternative to provide electric power in a feasible and effective to portable systems, are the fuel cells (FC´s) [3, 4]. FC´s convert the chemical energy of a fuel into electrical energy, in a single stage of conversion. It is an electrochemical process, that involving an oxidation-reduction pair and has a higher efficiency compared to a thermo-mechanical process inside and internal combustion engine [5-9]. The theoretical efficiency of a FC is 80% and the efficiency in operation is around 50% [10]. There are several types of FC´s, the most important of which are the proton exchange membrane (PEM) which have gained the most attention due to their light weight and easy transport. Among the applications of PEMFC´s, millimeter-size designs with self-breathing open cathode(AB) are the best for portable applications [11].

There are numerous investigations on FC´s, in the literature there is a great variety of references destined to its description [12]. In our work group, research has been carried out for the improvement of the catalytic layer, made synthesis of new and better materials [13-16] and numerical simulation for the determination of effective transport coefficients [17-19]. Also, application solutions and control systems have been proposed [3, 4, 20, 21].

The use of numerical methods of computational fluid dynamics (CFD) in the design phase of FC´s allows the study of the electrochemical phenomena that occur inside the cell, such as transport of mass, heat an energy, kinetics of the electrode and electrical response of the cell, without having to construct the structure and eliminating the costs of manufacture [22, 23]. It allows the possibility of reconstruction of a curve of the overall electric behavior of the cell.

In this paper, we present the electrical and simulated response through CFD techniques of an AB-PEMFC, which has an unconventional design to replace the graphite-based bipolar plate, by the use of polymer plates in conjunction with a micro-wire. The manufacturing process comprising the assembly of the components by layers. The

numerical simulation, using Ansys-Fluent software, which studies the behavior of the electric current inside the cell. The electrical response is validated experimentally by polarization curves.

## 2. Description of the computational model

The schematic configuration of the model is shown in Fig.1, the mesh is made in the Gambit modeling software and its simulated in Ansys-Fluent.

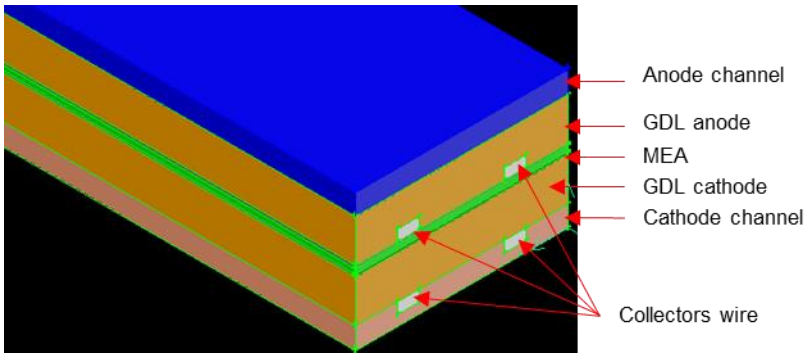


**Fig. 4**Proposed PEMFC geometric model

A single channel of rectangular shape is used for the anode side and the open cathode is represented in the same way by a rectangular channel for the computational model. The geometry contemplates the gas diffusion layers, the platinum micro-wires used as collectors and the electrode-membrane-electrode assembly (MEA). The main characteristics of the components are presented in table 1.

**Table 3**.- Dimensions of the model components

| Parameter | Dimensions (mm) |
|---|---|
| Channel width | 2 |
| Channel heigth | 0.2 |
| Channel length | 100 |
| Thickness of GDL | 0.315 |
| Thickness of CL | 0.02 |
| Thickness membrane | 0.05 |
| Diameter Pt wire | 0.1 |

The PEMFC geometry includes the MEA, GDL, flow channels and current collectors. The mesh of volumes is of hexaedral type, with an amount of 632,000 elements. The defined boundary conditions are: mass flow inlet and pressure outlet for the anode and cathode zones. The anode and cathode current collectors are wall-like surfaces. Between each component of the MEA and the gas diffusion layers, the boundary condition is defined which allows unaltered continuation of the phenomena (interior). The phenomena that occur inside the cell are modeled by the governing equations of conservation of mass, momentum, energy, species and cargo transport; these equations are presented in table 2.

**Table 4.** Governing equations of the fuel cell model

| Governing equiations | Mathematical expressions | |
|---|---|---|
| Continuity | $\frac{\partial(\rho\vec{u})}{\partial x}+\frac{\partial(\rho\vec{v})}{\partial y}+\frac{\partial(\rho\vec{w})}{\partial z}$ | (1) |
| Momentum transport | $u\frac{\partial(\rho\vec{u})}{\partial x}+v\frac{\partial(\rho\vec{u})}{\partial y}+w\frac{\partial(\rho\vec{u})}{\partial z}=-\frac{\partial P}{\partial x}+\frac{\partial}{\partial x}\left(\mu\frac{\partial\vec{u}}{\partial x}\right)+\frac{\partial}{\partial y}\left(\mu\frac{\partial\vec{u}}{\partial y}\right)+\frac{\partial}{\partial z}\left(\mu\frac{\partial\vec{u}}{\partial z}\right)+S_{px}$ | (2) |
| | $u\frac{\partial(\rho\vec{v})}{\partial x}+v\frac{\partial(\rho\vec{v})}{\partial y}+w\frac{\partial(\rho\vec{v})}{\partial z}=-\frac{\partial P}{\partial y}+\frac{\partial}{\partial x}\left(\mu\frac{\partial\vec{v}}{\partial x}\right)+\frac{\partial}{\partial y}\left(\mu\frac{\partial\vec{v}}{\partial y}\right)+\frac{\partial}{\partial z}\left(\mu\frac{\partial\vec{v}}{\partial z}\right)+S_{py}$ | |
| | $u\frac{\partial(\rho\vec{w})}{\partial x}+v\frac{\partial(\rho\vec{w})}{\partial y}+w\frac{\partial(\rho\vec{w})}{\partial z}=-\frac{\partial P}{\partial z}+\frac{\partial}{\partial x}\left(\mu\frac{\partial\vec{w}}{\partial x}\right)+\frac{\partial}{\partial y}\left(\mu\frac{\partial\vec{w}}{\partial y}\right)+\frac{\partial}{\partial z}\left(\mu\frac{\partial\vec{w}}{\partial z}\right)+S_{pw}$ | |
| Energy | $\frac{\partial(\rho CT)}{\partial x}+v\frac{\partial(\rho CT)}{\partial y}+w\frac{\partial(\rho CT)}{\partial z}=\frac{\partial}{\partial x}\left(k\frac{\partial T}{\partial x}\right)+\frac{\partial}{\partial y}\left(k\frac{\partial T}{\partial y}\right)+\frac{\partial}{\partial z}\left(k\frac{\partial T}{\partial y}\right)+S_h$ | (3) |
| Hydrogen transport (anode) | $\vec{u}\frac{\partial(\rho y_{H_2})}{\partial x}+\vec{v}\frac{\partial(\rho y_{H_2})}{\partial y}+w\frac{\partial(\rho y_{H_2})}{\partial z}=\frac{\partial(\vec{J}_{x,H_2})}{\partial x}+\frac{\partial(\vec{J}_{y,H_2})}{\partial y}+\frac{\partial(\vec{J}_{z,H_2})}{\partial z}+S_{H_2}$ | (4) |
| Water transport (anode) | $\vec{u}\frac{\partial(\rho y_{aW})}{\partial x}+\vec{v}\frac{\partial(\rho y_{aW})}{\partial y}+w\frac{\partial(\rho y_{aW})}{\partial z}=\frac{\partial(\vec{J}_{x,aW})}{\partial x}+\frac{\partial(\vec{J}_{y,aW})}{\partial y}+\frac{\partial(\vec{J}_{z,aW})}{\partial z}+S_{aW}$ | (5) |
| Oxygen transport (chatode) | $\vec{u}\frac{\partial(\rho y_{O_2})}{\partial x}+\vec{v}\frac{\partial(\rho y_{O_2})}{\partial y}+w\frac{\partial(\rho y_{O_2})}{\partial z}=\frac{\partial(\vec{J}_{x,O_2})}{\partial x}+\frac{\partial(\vec{J}_{y,O_2})}{\partial y}+\frac{\partial(\vec{J}_{z,O_2})}{\partial z}+S_{O_2}$ | (6) |
| Water transport (chatode) | $\vec{u}\frac{\partial(\rho y_{cW})}{\partial x}+\vec{v}\frac{\partial(\rho y_{cW})}{\partial y}+w\frac{\partial(\rho y_{cW})}{\partial z}=\frac{\partial(\vec{J}_{x,cW})}{\partial x}+\frac{\partial(\vec{J}_{y,cW})}{\partial y}+\frac{\partial(\vec{J}_{z,cW})}{\partial z}+S_{cW}$ | (7) |

Source terms

$$S_m = S_{H_2} + S_{aW} S_m = S_{O_2} + S_{cW} \quad (8)$$

$$S_{px} = -\frac{\mu \vec{u}}{k} S_{py} = -\frac{\mu \vec{v}}{k} S_{pz} = -\frac{\mu \vec{w}}{k} \quad (9)$$

$$\vec{J}_i = -\rho D_i \nabla y_i \quad (10)$$

$$S_h = h_{reac} - R_{an,ca} \eta_{an,ca} + I^2 R_{ohm} \quad (11)$$

$$S_{H_2} = -\frac{M_{H_2}}{2\mathrm{F}} R_{an} \quad (12)$$

$$S_{aw} = -\frac{M_{H_2O}}{\mathrm{F}} R_{an} \quad (13)$$

$$S_{O_2} = -\frac{M_{O_2}}{4\mathrm{F}} R_{ca} \quad (14)$$

$$S_{ac} = -\frac{M_{H_2O}}{2\mathrm{F}} R_{Ca} \quad (15)$$

Charge transport

$$\nabla \cdot (\sigma_{sol} \nabla \phi_{sol}) + R_{sol} \quad (16)$$

$$\nabla \cdot (\sigma_{mem} \nabla \phi_{mem}) + R_{mem} \quad (17)$$

For the particular PEMFC´s, in addition to the governing equations, the electrochemical equations are coupled by the source terms. The model that describes the transfer of current in an electrochemical reaction of a PEMFC is characterized by the Butler-Volmer equation. Table 3 presents the electrochemical parameters used in this work, which correspond to the experimental conditions.

**Table 5.** Electrochemical parameters of the model

| Parameter | Symbol | Units | Value |
|---|---|---|---|
| **Anode pressure** | $P_{an}$ | atm | 1 |
| **Cathode pressure** | $P_{ca}$ | atm | 1 |

| | | | |
|---|---|---|---|
| **Temperature of the cell** | $T_C$ | K | 300 |
| **Temperature of the fuel and oxidant ($H_2$,$O_2$)** | $T_i$ | K | 300 |
| **Density of exchange current at the anode** | $j_{an}^{ref}$ | $A/m^2$ | 2000 |
| **Density of exchange current at the cathode** | $j_{ca}^{ref}$ | $A/m^2$ | 20 |
| **Exponent of concentration (anode)** | $\gamma_{an}$ | - | 0.5 |
| **Exponent of concentration (cathode)** | $\gamma_{ca}$ | - | 1 |

The main suppositions considered for the modeling of this work are: 1) laminar flow and steady-state conditions, 2) the membrane is impermeable to gases, 3) the porous media is isotropic, 4) the proton flow is uni- Dimensional, 5) the distribution of the catalyst is uniform, 6) the transport of species occurs without phase change. The operating conditions used in the model and the experimental tests are as follows: a) Input volumetric flow 0.03 and 0.0012 (Lt / min) for the anode and cathode respectively; B) 1 V open circuit voltage for the anode and cathode; C) the solid phase potential (USD-0) varied between 0 and 0.94 at the cathode; C) the coefficient of exchange was fixed at 2 for the anode and cathode.

The simulation was performed on a laptop with Intel Core i7 processor at 3.20 GHz and 16 GB of RAM. Each simulation converged at approximately 150-200 iterations and took about 2 hours for each case.

## 3. Manufacturing and characterization of the PEMFC

The manufacturing process is done by stacking the components previously manufactured and cut to size. The method consists in positioning each of the layers one on top of the other, in the following order: a) End plate (mechanical support); B) GORE-TEX® anode end seal; C) flat polymer plate; D) anode elastomer seal with current collectors; E) flat polymer anode flow channel; f) GDL-anode; G) MEA assembly; H) GDL-cathode; I) cathode current collectors; J) final cathode seal; K) flat polymer end plate.

The materials used to manufacture the PEMFC were selected in order to obtain a light and relatively small prototype for application in devices that require mobility and versatility. In this prototype the membrane used is of the brand Dupont®, Nafion NR212, with a

thickness of 0.05 mm. The catalytic layer used was manufactured in our laboratory, was deposited by airbrushing on the membrane with platinum as electro catalyst and dispersed electrolyte Nafion® in 5% solution diluted in aliphatic alcohols. Alfa-Aesar brand platinum wires with 99.95% purity, 0.025 mm diameter were used. The diffusion layers are of the brand SIGRACET 34BC, of 0.315 mm of thickness, machined with different geometric design in the anode and cathode. In fig. 2 shows the prototype of the PEMFC.

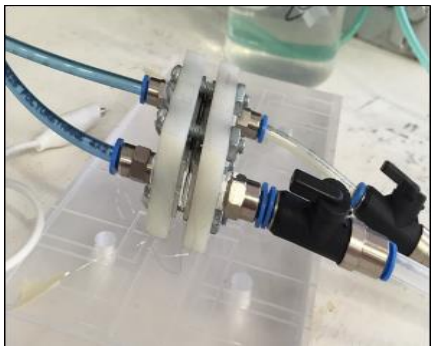

**Fig. 5**Prototype of the PEMFC.

The PEMFC is characterized to know the electric response, that is through the polarization curves [10], Which are potential curves (V) against current density (A $cm^{-2}$). In the simulation, the mathematical model allows to determine the electric current generated as a function of the potential imposed as a boundary condition at the terminals of the cell. The polarization curve is obtained by varying the potential in a parametric sequence that simulates the actual imposition of the potentiostat.

## 4. Results and Discussion

Figure 3 presents the experimental electrical response of a single-cell, using two hydrogen flows. In the result a maximum current density of 32 mA $cm^{-2}$ and a maximum power density of 11 mW cm-2 with the flow of 0.03 L $min^{-1}$ is observed. Both curves are under natural convection conditions at the cathode.

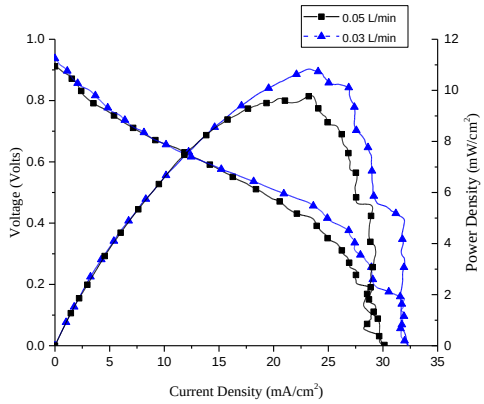


**Fig. 6**Polarization curves for two different volumetric flows of hydrogen in the PEMFC.

One of the reasons why this is getting better performance at a flow of 0.03 L min$^{-1}$ compared to the flow of 0.05 L min$^{-1}$, may be due to having a higher speed gives less time to hydrogen to be Diffuses between the flow channel and the gas diffuser, otherwise with a lower velocity, which gives the fuel more time to diffuse towards the gas diffuser layer.

The experimental polarization curve allows us to validate the simulation performed on the proposed design. Figure 4 presents the comparison of the experimental polarization curve and the resultant of the data collected by the simulation. The volumetric flow rate of the gases and the electrochemical parameters have already been described in Table 3 and in the previous section.

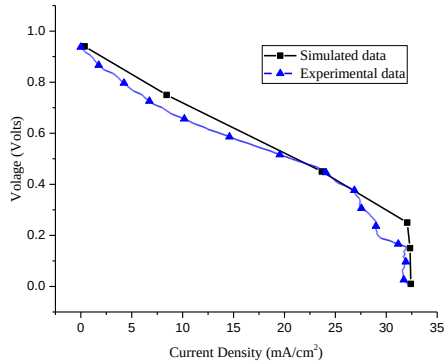


**Fig. 7**Validation of the model by comparing the experimental and simulated polarization curve

It is observed that the simulated polarization curve follows the experimental trend. The points have an average standard deviation of 0.11 mA cm$^{-2}$. This standard deviation allows us to validate the modeling. However, there are limitations that allow us to obtain an extensive validation in function to the changes of operation, among which we highlight: 1) experimentally, being the self-breathing cathode cell, it is complicated to characterize the volumetric flow that enters the cathode. 2) As

for the numerical simulation, the current model does not contemplate the phase change, so in this model it is not possible to study the change of resistance to the transport of protonic charge.

Figure 5 presents the chronoamperometric measurement performed at the PEMFC with a mass flow of fuel of 0.05 L/minute to natural convection. A stable behavior of the fuel cell can be seen throughout almost all the time that the test was performed, however it presents a series of elevations that can be product of the presence of greater oxygen, because the air flows of random manner in the environment.

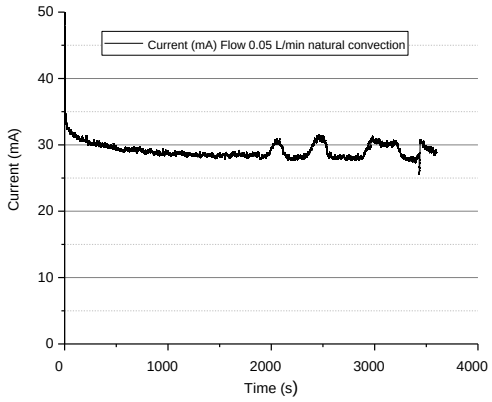


**Fig. 8**Behavior of the current at a volumetric flow of 0.05 L/minute of hydrogen over time.

Although the tests carried out in the cell were carried out in a controlled environment, in the figure above we can see that there are oxygen currents which generate the effect of the peaks in the chronoamperometry.

## 5. Conclusion

From this research it was demonstrated that the use of CFD techniques can be easily used as a design and analysis tool for mili-PEMFC. These techniques allow to determine optimum conditions of operation, to make modifications to different parameters or changes to the geometry of the cell without having to resort to experimental tests, the latter can be slow and expensive. The proposed mill-PEMFC design, in rectangular configuration without graphite bipolar plates as well as the replacement of the materials of the components that make up the cell, provide better electrical performance and smaller cell and stack dimensions. This gives a more compact device with a lighter weight than those using bipolar graphite plates. It is confirmed that manufacturing techniques and methods impact significantly on the performance and performance of the mill-PEMFC, as well as on the stack.

It was verified that the proposed design for the PEMFC shows promising results, since it reached a performance of 32.31 mA $cm^{-2}$ in an active area of 1.8 $cm^2$, also

it was confirmed that the mono cell presents electrical stability which was verified by the chronoamperometry where the prototype showed that it is able to maintain a continuous production of current. This model and design of the PEMFC represents an important step for future developments of PEM fuel cell mili-cells.

## Acknowledgements

The authors are grateful for the SEP-CONACYT funding made through project CB-2013/221988 and PRODEP support through the Mexican Renewable Energies Network of the Yucatan peninsula.

## References

1. Panwar, N. L.; Kaushik, S. C.; Kothari, S., Role of renewable energy sources in environmental protection: A review, *Renewable and Sustainable Energy Reviews***15**(3), 1513-1524, 2011
2. Wang, Y.; Chen, K. S.; Mishler, J.; Cho, S. C.; Adroher, X. C., A review of polymer electrolyte membrane fuel cells: Technology, applications, and needs on fundamental research, *Applied Energy***88**(4), 981-1007, 2011
3. Barbosa, R.; Escobar, B.; Sanchez, V. M.; Hernandez, J.; Acosta, R.; Verde, Y., Sizing of a solar/hydrogen system for high altitude long endurance aircrafts, *International Journal of Hydrogen Energy***39**(29), 16637-16645, 2014
4. Barbosa, R.; Sanchez, V. M.; Escobar, B.; Cruz, J. C.; Toral-Cruz, H., Sizing of a solar-hydrogen power source for a portable emergency communication system: Case study of hurricanes in Cancun, Mexico, *International Journal of Hydrogen Energy***40**(48), 17361-17370, 2015
5. Aguilar, C.; Vazquez, A.; Canales, F.; Gordillo, J., Integrated DC‐AC Converter as Power Conditioner for Fuel Cell Based System, *IEEE Latin America Transactions***14**(5), 2107-2113, 2016
6. Colson, C.; Nehrir, M., Evaluating the benefits of a hybrid solid oxide fuel cell combined heat and power plant for energy sustainability and emissions avoidance, *IEEE Transactions on energy conversion***26**(1), 140-148, 2011
7. Torres, S. O. A.; de Mesquita, A. C.; de Miranda, P. E. V., Control Strategy for Balance of Plant in Solid Oxide Fuel Cell, *IEEE Latin America Transactions***11**(2), 726-736, 2013
8. Kelouwani, S.; Adegnon, K.; Agbossou, K.; Dube, Y., Online system identification and adaptive control for PEM fuel cell maximum efficiency tracking, *IEEE Transactions on Energy Conversion***27**(3), 580-592, 2012
9. Silva, S.; Severino, M.; de Oliveira, M., Sizing and optimization of hybrid photovoltaic, fuel cell and battery system, *IEEE Latin America Transactions***9**(1), 817-822, 2011
10. EG&G Technical Services, I., *Fuel Cell Handbook*, U. S. D. o. Energy, Editor. 2004: USA. p. 427.

11. Weiland, M.; Wagner, S.; Hahn, R.; Reichl, H., Design and evaluation of a passive self-breathing micro fuel cell for autonomous portable applications, *International Journal of Hydrogen Energy***38**(1), 440-446, 2013
12. Varela, F. J. R.; Feria, O. S.; Pacheco, E. H., *Celdas de combustible*, Canada, 2010,
13. Rosado, G.; Verde, Y.; Valenzuela-Muñiz, A. M.; Barbosa, R.; Miki Yoshida, M.; Escobar, B., Catalytic activity of Pt-Ni nanoparticles supported on multi-walled carbon nanotubes for the oxygen reduction reaction, *International Journal of Hydrogen Energy***41**(48), 23260-23271, 2016
14. Ordóñez, L. C.; Escobar, B.; Barbosa, R.; Verde-Gómez, Y., Enhanced performance of direct ethanol fuel cell using Pt/MWCNTs as anodic electrocatalyst, *Journal of Applied Electrochemistry***45**(11), 1205-1210, 2015
15. Escobar, B.; Barbosa, R.; Miki Yoshida, M.; Verde Gomez, Y., Carbon nanotubes as support of well dispersed platinum nanoparticles via colloidal synthesis, *Journal of Power Sources***243**88-94, 2013
16. Ledesma-García, J.; Barbosa, R.; Chapman, T. W.; Arriaga, L. G.; Godínez, L. A., Evaluation of assemblies based on carbon materials modified with dendrimers containing platinum nanoparticles for PEM-fuel cells, *International Journal of Hydrogen Energy***34**(4), 2008-2014, 2009
17. Barbosa, R.; Escobar, B.; Cano, U.; Ortegon, J.; Sanchez, V. M., Multiscale relationship of electronic and ionic conduction efficiency in a PEMFC catalyst layer, *International Journal of Hydrogen Energy***41**(42), 19399-19407, 2016
18. Cano-Castillo, U.; Barbosa-Pool, R., *Chapter 2 : Reconstruction of PEM fuel cell electrodes with micro- and nano-structures*, in *Micro & Nano-Engineering of Fuel Cells*, D. C. Leung; J. Xuan, Editors. 2015: London, UK.
19. Barbosa, R.; Andaverde, J.; Escobar, B.; Cano, U., Stochastic reconstruction and a scaling method to determine effective transport coefficients of a proton exchange membrane fuel cell catalyst layer, *Journal of Power Sources***196**(3), 1248-1257, 2011
20. Rosas-Caro, J. C.; Sanchez, V. M.; Vazquez-Bautista, R. F.; Morales-Mendoza, L. J.; Mayo-Maldonado, J. C.; Garcia-Vite, P. M.; Barbosa, R., A novel DC-DC multilevel SEPIC converter for PEMFC systems, *International Journal of Hydrogen Energy***41**(48), 23401-23408, 2016
21. Sanchez, V. M.; Barbosa, R.; Arriaga, L. G.; Ramirez, J. M., Real time control of air feed system in a PEM fuel cell by means of an adaptive neural-network, *International Journal of Hydrogen Energy***39**(29), 16750-16762, 2014
22. Rezakazemi, M.; Niazi, Z.; Mirfendereski, M.; Shirazian, S.; Mohammadi, T.; Pak, A., CFD simulation of natural gas sweetening in a gas–liquid hollow-fiber membrane contactor, *Chemical engineering journal***168**(3), 1217-1226, 2011
23. Jeon, D.; Greenway, S.; Shimpalee, S.; Van Zee, J., The effect of serpentine flow-field designs on PEM fuel cell performance, *International journal of hydrogen energy***33**(3), 1052-1066, 2008

# 3.5 Advances in the knowledge of phase transformation of perovskite $La_xSr_{1-x}Cr_yMn_{1-y}O_{3-\delta}$ structure with potential application in SOFC cells

José Juan Alvarado Flores, Jaime Espino valencia, Jorge Víctor Alcaraz Vera, María Liliana Ávalos Rodríguez

[1]Facultad de Ingeniería en Tecnología de la Madera, Universidad Michoacana de San Nicolás de Hidalgo, Francisco J. Mújica S/N, Col. Felicitas del Rio, C.P. 58040, Morelia, Michoacán, México.

[2] Facultad de Ingeniería Química, Universidad Michoacana de San Nicolás de Hidalgo, Francisco J. Mújica S/N, Col. Felicitas del Rio, C.P. 58040, Morelia, Michoacán, México.

3 Instituto de Investigaciones Económicas y Empresariales, Universidad Michoacana de San Nicolás de Hidalgo, Francisco J. Mújica S/N, Col. Felicitas del Rio, C.P. 58040, Morelia, Michoacán, México.

* Corresponding author: doctor.ambientalista@gmail.com

## ABSTRACT

The main features of the Solid oxide fuel cells (SOFC) are all solid-state construction and high-temperature operation. The combination of these features leads to several unique advantages for this type of fuel cell, including flexibility in cell and stack designs, manufacturing processes, and power plant sizes. SOFC cells are systems that have potential application to anticipate high energy demands at industrial and residential levels. Applications have recently been found in transport for trucks with high load capacity. This type of cells does not require pure hydrogen, because SOFCs can oxidize methane, CO besides hydrogen, so they are also interested because of the flexibility of the fuel. Currently, great efforts have been made to improve its performance, focusing its development on new anode materials of perovskite structure type $La_xSr_{1-x}Cr_yMn_{1-y}O_{3-\delta}$ (LSCM). Today, the large number of publications describing thermochemical stability under reducing conditions is quite limited and rarely demonstrate the mechanism, kinetics of reduction, as well as phase transformation of the perovskites at high and intermediate temperature. Thus, to allow optimum performance, it is very important to know the possible phase transitions in the perovskite LSCM at high temperatures and how important properties such as the electronic conductivity and final power density of the cell are affected in reducing atmosphere. In this sense, and from various analyzes by XRD-Rietveld, it has been determined that the perovskite LSCM presents different transformations when there is a change of temperature. This study examines some of the transformations observed on such perovskite when transition metals have been added.

***Keywords:*** SOFC cells; perovskite; anode; phase transformation

## 1. Introduction

Today, energy is the most valuable resource for human activity and the basis for all human progress. Oil, which is the main source of energy worldwide, is of a limited and non-renewable nature, which will lead to serious energy crises, in addition to associated environmental problems such as high pollution. In the future, modern societies will face the depletion of fossil fuels, while demand for energy increases as more and more countries move towards a higher level of industrialization and as the world population increases [1]. Standard technologies based on the combustion of fossil fuels cannot meet the growing demand for energy. In this sense, there have already been proposed technological alternatives derived from wind (wind energy), sun, biomass, as well as fuel cells that can replace conventional methods of energy production. Fuel cells are considered a promising technology because they are devices that convert chemical energy into electrical energy with high efficiency. Such technology can be produced in a variety of different types, from the low temperature polymer exchange membrane (PEMFC), to high temperature (1000°C) ceramic electrolyte cells, such as solid oxide fuel cells) [2]. Due to the high operating temperature in the SOFC cells, a range of hydrocarbon fuels such as gasoline, diesel, natural gas and methane (biomass) can be used in addition to hydrogen. However, the high temperature can greatly impair the components in the cell reducing their durability and increasing the problems associated with thermal cycles, as well as degradation of performance due to the interdiffusion or reaction of each component (anode-electrolyte-cathode) Of the cell.

In this sense, and with the aim of reducing costs, the development of SOFC cells has focused on the research of new materials that operate at lower temperature (500-1000°C). Given that in the foreseeable future most of the hydrogen will come from the reform of natural gas, liquid hydrocarbons or coal gasification, direct use in SOFC cells has a significant advantage in terms of efficiency, although Introduces additional requirements on the anode material [3]. In recent research attention, has been focused on electro-oxidation with methane using anodes including Cu, Ni, Co-$CeO_2$, Ni/$Ce_{1-x}Gd_xO_{2-\delta}$, Ni-Co/YSZ, Ni-Cu/YSZ, Cu/YSZ [4] and perovskite type materials ($ABO_3$) with Ni [5]. The perovskite $La_xSr_{1-x}Cr_yMn_{1-y}O_{3-\delta}$ (LSCM) is considered one of the most promising anodes for SOFC cells operating below 1000°C [6,7]. The LSCM material is a p-type semiconductor with an approximate conductivity of 38 S $cm^{-1}$ in air and 1.5 S $cm^{-1}$ in 5%$H_2$/Ar at 900°C, with a similar performance in methane [8]. This perovskite has demonstrated high resistance to coal from hydrocarbons. However, the structure of the perovskite can be very complicated due to the inclination of the octahedrons and to the ordering of the elements at site A and B [9]. Perovskite oxides can undergo several phase transitions at high temperatures, as observed with the material $Pr_{1-x}Sr_xMnO_3$ [10]. In a perovskite, first and second order transitions may occur. Knowledge of possible phase transitions in LSCM at elevated temperature is crucial to enable an optimal electrolyte-anode interface in a SOFC cell at the operating temperature to be achieved. In this study a review is made on phase transformations of perovskite LSCM.

## 2. Materials and Methods

For the present study, the analysis of the phase transformation of the perovskite $La_{0.7}Sr_{0.3}Cr_{0.4}Mn_{0.6}O_{2.85}$ with additions of nickel (Ni) has been considered. The oxides were prepared from the sol-gel method. After drying, the powders were pressed and sintered at 1200°C. The structural composites were X-ray diffraction analysis, as well as an analysis by the Rietveld method to verify their crystallinity and to evaluate the phase transformations of each compound. The data of the microstructural evolution of the anodes were obtained with a scanning electron microscope JEOL-5600 to which it is attached to an EDAX equipment.

## 3. Results and Discussion

### 3.1. Phase transformation of perovskite $La_{0.7}Sr_{0.3}Cr_{0.4}Mn_{0.6}O_{2.85}$

According to the figure 1, after the first cycle of the reduction process at 800°C in a 10%$H_2N_2$ atmosphere; the rhombohedral phase of perovskite type $La_{0.7}Sr_{0.3}Cr_{0.4}Mn_{0.6}O_{2.85}$ (R3c) and the absence of NiO crystals are clearly confirmed. However, in figure 2, it is observed that when the anodes are treated in a second reduction cycle at 1050°C, the crystal structure of the perovskite undergoes a clear phase transformation of $ABO_3$ (R3c) to a structure of type $A_2BO_4$ (I4/Mmm) [11]. At 800°C, the perovskite phase is hexagonal and the unit cell consists of six molecules. However, at 1050°C it only consists of two molecules per cell. This leads to a reduction in oxygen content from 0.58% to 0.56%, leads to phase alteration, which is also caused by the amount of Ni. This phase transformation can be caused by the inclination of adjacent layers of the $BO_6$ type octahedron near the axes of rotation of the hexagonal perovskite [12,13]. To date, the exact ratio for such a phase transformation (R3c → Pm3m) is not well known yet, but can be explained using the tolerance factor of the perovskite [14]. The phase transformation in the perovskite, has also been verified by other authors, where it was also observed the perovskite phase undergoes a R3c→Pm3m, rhombohedral to cubic phase transition over the temperature range from 500 to over 1100°C using in situ high-temperature neutron powder diffraction. The fraction of the cubic phase increases with increasing temperature and reaches 85% at 1000°C. The phase transition is gradual; therefore, any sudden volume change due to a phase transition would be minimized, allowing a good electrolyte/anode interface on thermal cycling, it is interesting that the two-phase coexistence spans a temperature range of about 600°C [15]. In other investigations, another phase transformation has been confirmed in the perovskite $La_{0.75}Sr_{0.25}Cr_{0.4}Mn_{0.6}O_{2.85}$, where the crystal structure changes from hexagonal in air to orthorhombic in $H_2$ for all LSCM compositions. This transformation is accompanied by only a 1% volume change, indicating very good structural stability under redox conditions [16].

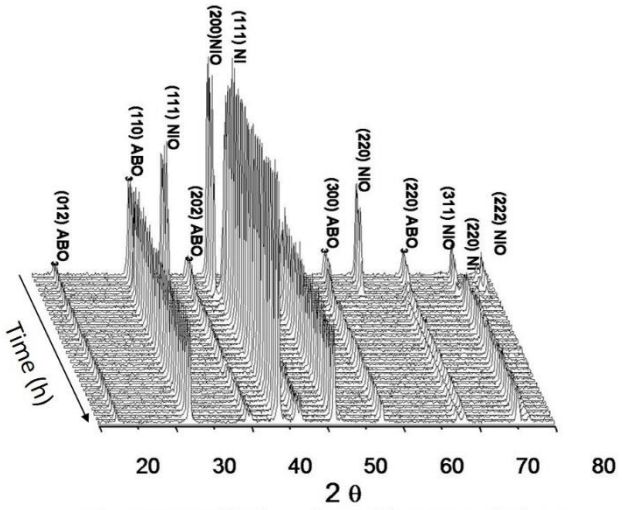


Fig. 1. XRD, stable phase of perovskite $ABO_3$; reduction to 800°C in atmosphere $N_2$-10% $H_2$.

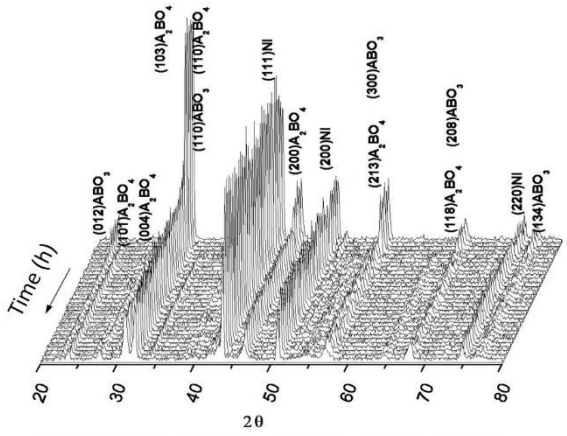


Fig. 2. XRD, phase transformation $ABO_3 \rightarrow A_2BO_4$ at 1050°C as a function of time with atmosphere $N_2$-10%$H_2$.

## 3.2. Morphological analysis of perovskite $La_{0.7}Sr_{0.3}Cr_{0.4}Mn_{0.6}O_{2.85}$

The SEM microstructure of the perovskite $La_{0.7}Sr_{0.3}Cr_{0.4}Mn_{0.6}O_{2.85}$ with 25% by weight of nickel after of the reduction process (10% $H_2$-$N_2$). The analysis showed that the ceramics have the same morphology and a perovskite with average particle size of 0.5 µm. Particles with perovskite structure were observed around the NiO particles. These NiO particles vary in size from 1 to 2 µm. The observations agree with the behavior of the phase transformation, because they obstruct the perovskite particles.

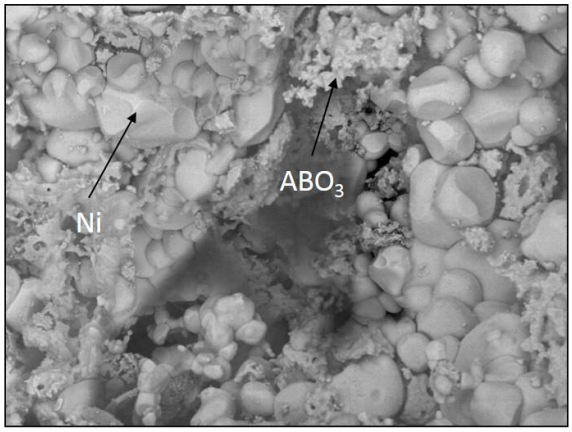


Fig. 3. SEM perovskite $La_{0.7}Sr_{0.3}Cr_{0.4}Mn_{0.6}O_{2.85}$ + Ni

## 4. Conclusion

Perovskite type compounds with Ni additions were synthesized through the sol-gel method. The reduction of $La_{0.7}Sr_{0.3}Cr_{0.4}Mn_{0.6}O_{2.85}$ - NiO → $La_{0.7}Sr_{0.3}Cr_{0.4}Mn_{0.6}O_{2.85}$ - Ni was obtained at 800ºC without evidence of intermediate crystalline structures. It was found that there is a diffusion problem. The perovskite phase undergoes a R3c to Pm3m, rhombohedral to cubic phase transition. This phase transformation in the perovskite can be produced due to the introduction of $Ni^{2+}$ cations into the solid solution and reduction in oxygen content, when the temperature increases to 1050°C.

## References

[1] Boudghene A, Traversa E. Fuel cells, an alternative to standard sources of energy. Adv Mater Res-Switz 2002; 6 (3): 295-304.

[2] Cowin P, Petit C, Lan R, Irvine J, Tao S. Recent progress in the development of anode materials for solid oxide fuel cells. Adv Energ Mater 2011; 1 (3): 314-332.

[3] Jacobson, A. Materials for solid oxide fuel cells. Chem Mater 2009; 22(3): 660-674.

[4] Yongxin L, Yuhua, G, Bing X. Catalytic combustion of methane over M (Ni, Co, Cu) supported on ceria–magnesia. Fuel Process Technol 2009; 90 (5): 652-656.

[5] Lo Faro M, La Rosa D, Isabella N, Vincenzo A, Salvatore A. Electrochemical investigation of a propane-fed solid oxide fuel cell based on a composite Ni–perovskite anode catalyst. Appl Catal B – Environ 2009; 89 (1): 49-57.

[6] Tao SW, Irvine JTS. A redox-stable efficient anode for solido xide fuel cells. Nat Mater 2003; 2 (5): 320-323.

[7] Peña J, Marrero D, Pérez D, Ruiz J, Nuñez P. Performance of XSCoF (X= Ba, La and Sm) and LSCrX′ (X′= Mn, Fe and Al) perovskite-structure materials on LSGM electrolyte for IT-SOFC. Electrochim Acta 2007; 52(9): 2950-2958.

[8] Tao S, Irvine J. Synthesis and characterization of $(La_{0.75}Sr_{0.25})Cr_{0.5}Mn_{0.5}O_{3-\delta}$, a redox-stable, efficient perovskite anode for SOFCs. J. Electrochem Soc 2004; 151 (2): A252–A259.

[9] Tao S, Canales J, Irvine J. Structural and electrical properties of the perovskite oxide $Sr_2FeNbO_6$. Chem Mater 2004; 16 (11): 2309–2316.

[10] Knížek K, Hejtmanek J, Jirak Z, Martin C, Hervieu M, Raveau B, Andre´ G, Bouree F. Structure, Magnetism, and Transport Properties of $Pr_{1-x}Sr_xMnO_3$ (x= 0.45− 0.75) up to 1200 K. Chem Mater 2004, 16 (6): 1104-1110.

[11] Inorganic Crystal Structure Database ICSD (atomic positions) version 2009-1.

[12] Glazer A. The classification of tilted octahedra in perovskites. Acta Crystall B-Stru 1972; 28 (11): 3384-3392.

[13] Dove M. Theory of displacive phase transitions in minerals. Am Mineral 1997; 82 (3-4): 213-244.

[14] Flores J. Análisis de la estructura perovskita $La_xSr_{1-x}Cr_yMn_{1-y}O_{3-\delta}$ con potencial aplicación como ánodo para celdas de combustible de óxido sólido. Bol Soc Esp Ceram V 2017; 56 (2): 73-82.

[15] Tao S, Irvine J. Phase transition in perovskite oxide $La_{0.75}Sr_{0.25}Cr_{0.5}Mn_{0.5}O_{3-\delta}$ observed by in situ high-temperature neutron powder diffraction. Chem Mater 2006; 18 (23): 5453-5460.

[16] Zha S, Tsang P, Cheng Z, Liu M. Electrical properties and sulfur tolerance of $La_{0.75}Sr_{0.25}Cr_{1-x}Mn_xO_3$ under anodic conditions. J Solid State Chem 2005; 178 (6): 1844-1850.

# 3.6 Synthesis and characterization of $Ln_4Zr_3O_{12}$ solid electrolytes for their use in SOFC

J.A. Díaz-Guillén, J.O. Acosta-García, N.M. Cepeda-Sanchez, J.C. Díaz-Guillén, M. Salazar-Zertuche, O. Burciaga-Díaz, M.E. Bazaldúa-Medellín, A.F. Fuentes

[1]División de Estudios de Posgrado e Investigación, Instituto Tecnológico de Saltillo, 25280-Saltillo, Coahuila México.

[2]Cinvestav Saltillo, Apartado Postal 663, 25000-Saltillo, Coahuila, México.

[3]CONACYT-Corporación Mexicana de Investigación en Materiales. Saltillo, Coahuila México. C.P 25290

* Corresponding author: (+52) 844 4389500, email. jadiaz@itsaltillo.edu.mx

## ABSTRACT

We show results of characterization and electrical properties of zirconates with general formula $Ln_4Zr_3O_{12}$ (Ln = Y, Ho, Er and Yb), obtained by mechanical milling and on views to be used as solid electrolytes in Solid Oxide Fuel Cells (SOFC). All compositions were obtained by mechanical milling, by using a planetary mill and zirconia containers and balls, and starting from stoichiometric mixtures of high purity oxides. Milling time needed to achieve single phase products was determined by examining the XRD patterns of samples at different time intervals; reactions were considered completed when no traces of the starting reagents were evident by this technique. Synthesized powders were also analyzed by thermal analysis and scanning electron microscopy, among others. Results show that Y, Ho and Er zirconates can be synthesized after 30 hours of milling, whereas 40 hours are needed to synthesize Y zirconate. Results also show that as-prepared powder samples show XRD patterns similar to the fluorite-like materials, which persist after post-milling treatments at high temperatures (800, 1200 and 1500°C). Morphologies of sintered (1500°C) samples consisted in well-defined grains with clean grain limits. Remnant porosity in samples revealed that higher sintering temperatures are necessary to totally densify these zirconates. Ionic conductivity and activation energies for oxygen ion diffusion were determined by impedance spectroscopy in pressed and sintered (1500°C) pellets. Ionic conductivity values for all compositions were found in the range of $10^{-3.82}$ to $10^{-6.13}$ S/cm at 700°C, and values of activation energies for the conduction process were in the range of 1.20-1.30 eV, similar to some ionic conductors. These results corroborate the possibility of application of these ionic conductors as solid electrolytes in the SOFC technology.

***Keywords*:** solid electrolytes; zirconates; SOFC; mechanical milling

## 1. Introduction

Solid Oxide Fuell Cells (SOFC) represent an interesting and promissory technology with a large quantity of potential applications. SOFC function consists in generate electrical energy from a clean reaction between oxygen (from air) and hydrogen, generating only pure water as reaction product. These electrochemical devices are usually composed by three active elements, a solid electrolyte, the cell heart, composed by $ZrO_2$ stabilized with 8% $Y_2O_3$ (YSZ, Yttria Stabilized Zirconia), an anode made with a cermet (YSZ-Ni) and a cathode composed by a perovskite type ceramic, with general formula $LaSrMnO_3$ (LSM). [1-3]

In operation, hydrogen is fed in the anode and under an oxidation reaction releases electrons to the external circuit. The oxidant is fed into the cathode and accepts the electrons from the external circuit by a reduction reaction. The electrons flow directly from the anode to the cathode through the external circuit, producing electric power. These electrochemical reactions take place at 700-1000°C, common range of operation temperatures of SOFC. [3]

These high operations temperatures make necessary to consider some issues. it has been reported that during sintering stages at temperatures higher than 1200°C and after several cycles of operation of the SOFC at 900-1000° C, solid state reactions at the cathode / electrolyte interface are present (between YSZ and LSM), leading to the presence of insulating phases, such as $La_2Zr_2O_7$, which notably affect the performance of the electrolyte and the efficiency and useful life of the fuel cell. [4-6]

Looking to solve this and others problems in this technology, scientist have proposed alternatives ceramics with good properties to replace the YSZ as solid electrolyte in SOFC, with high thermal and chemical stability, to avoid chemical reactions with LSM (cathode), and good electrical properties, mainly ionic conductivity. In this context, different lanthanide zirconates and hafnates with pyrochlore or fluorite-type cubic structure and with general formula $A_2B_2O_7$ have been reported, showing good electrical properties, due mainly to the presence of intrinsic anion vacancies in their structure and the different degrees of structural disorder, both having an interesting effect on their electrical and even thermal properties. [7-13]

A different group of circonates and hafnates have been less studied. These consist in $A_4B_3O_{12}$ phases, where A element can be a lanthanide (Y, Er, Ho and Yb) and B element Zr or Hf. These ceramics are commonly known as δ-phases and their synthesis, characterization and electrical properties have been barely studied. The proposed crystalline arrangement for a delta phase is not fully described until now, but researchers consider it as a rhombohedral symmetry, corresponding to the space group R3, derived from a fluorite-type structure. [14-15]

Looking to increase the knowledge about delta phase circonates and to corroborate their viability to be used as solid electrolytes in SOFC, this paper reports studies of synthesis, characterization and analysis of electrical properties of circonates of general formula $Ln_4Zr_3O_{12}$ (ln = Y, Er, Ho and Yb), by using a mechanical milling as the synthesis method,

which allows the generation at low temperatures of highly disordered materials. This method allows the preparation of metastable phases of multicomponent oxides, from ionic conductors to dielectric ceramics and low thermal conductivity materials. [7-9,16]

## 2. Materials and Methods

The synthesis by mechanical milling started with manual mixing of the raw materials, which consisted in powders of high purity of $Ho_2O_3$, $Y_2O_3$, $Er_2O_3$, $Yb_2O_3$ and $ZrO_2$, weighed in the appropriate stoichiometric proportions to give place to each studied composition, $Y_4Zr_3O_{12}$, $Er_4Zr_3O_{12}$, $Ho_4Zr_3O_{12}$ and $Yb_4Zr_3O_{12}$. All samples were then milled during different times by using a planetary mill (RETSCH PM 100) and $ZrO_2$ containers and balls as grinding media. Evolution of samples with milling time was followed by X-ray powder diffraction (XRD), by using a Philips X 'Pert 3040 diffractometer at a scan rate of 0.03 ° / sec over a range of 2θ from 10 to 75°. Reactions were considered completed when no traces of starting reagents were identified by this method. Just milled samples were then fired at 800, 1200 and 1500°C in order to analyze by XRD the structural evolution of all compositions with temperature.

Milled powders were also uniaxially pressed and sintered at 1500°C with a heating and cooling rate of 2 °C/min, during 6 hours, in order to densify and to increase mechanical strength of pellets. Morphology of these pellets was analyzed by Field Emission Scanning Electronic Microscopy (FE-SEM) using a TESCAN MIRA 3 Microscope. Analysis of electrical properties was carried out in air, as a function of temperature and frequency, by Impedance Spectroscopy, using a Solartron 1260 Frequency Response Analyzer over the 100 Hz–1 MHz frequency range. Electrodes were made by coating both sides of the pellets with a conductive platinum paint and firing them at 700°C to eliminate organic components and harden the Pt coating.

## 3. Results and Discussion

### 3.1. Synthesis and characterization

Figure 1(a) shows the XRD patterns corresponding to the evolution of composition $Y_4Zr_3O_{12}$ (system$Y_2O_3$ +$ZrO_2$) with milling time (at 1, 3, 6, 9, 20, 30 and 40 hours). From this figure, the sample milled during 1 hour shows a pattern containing reflections corresponding to the starting reagents,$Y_2O_3$ and $ZrO_2$. These reflections decrease in intensity and increases in width as milling time increases. This behavior is due to a considerable increasing of structural defects and decreasing of the particle size.

After 20 hours of milling, this composition shows a pattern where the main reflections of the cubic anion deficient fluorite (e.g. Miller indexes (100), (200), (220) and (311), at 29.5, 34, 49 and 58.5° (2θ) respectively) can be appreciated. As the pattern of sample milled during 30 h shows, further milling produces light increasing in intensity. Nevertheless at this milling time there is still reflection of the $ZrO_2$ at 31.5° (2θ), so 10 more hours of milling were necessary to consider the reaction as completed. After 40 hours, no additional phases seem to be present in the powder so reactions were considered as finished. For

the rest of studied compositions, 30 hours of milling were necessary to complete reactions. As table 1 shows, this behavior can be related to the size of the lanthanide used to form each composition, since Y is the larger element of all used lanthanides an the difficulty of being incorporated to the $ZrO_2$ lattices is higher, so more energy is necessary to complete the reaction and thus more time of milling. Figure 1(b) shows a comparison of XRD patterns of the same composition $Y_4Zr_3O_{12}$, milled during 40 hours and after be fired at 800, 1200 y 1500°C. Thermal treatments in the samples generate an increasing of intensity and decreasing of width of reflections.

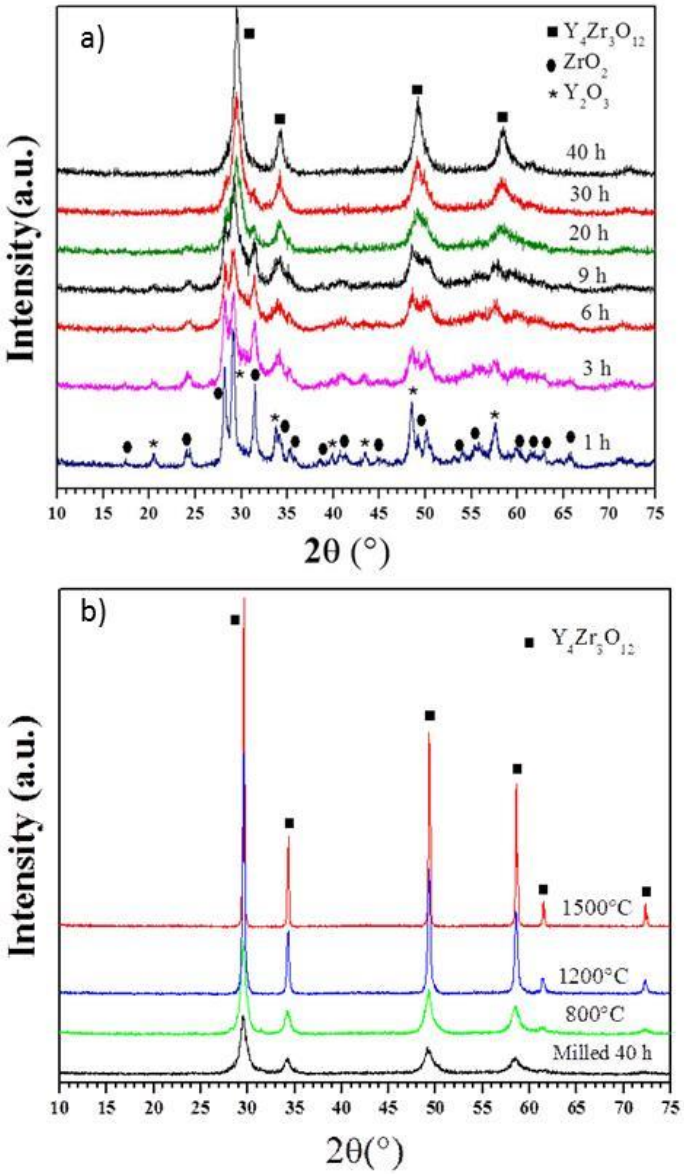


**Fig. 1.** (a) Evolution of the system $Y_2O_3$ + $ZrO_2$ ($Y_4Zr_3O_{12}$) with milling time by XRD. (b) Effect of firing temperature on the present phases for the same composition.

These patterns reflect the presence of materials with higher crystallite size and crystallinity. Fluorite-type prevails for al studied compositions, which show XRD pattern similar to $Y_4Zr_3O_{12}$. These obtained results corroborate the viability of mechanical milling to obtain lanthanide zirconates with δ phase-type at low temperature.

**Table 1**. Times of milling required to obtain all compositions in this research. Ionic radii obtained from [17]

| $Ln_4Zr_3O_{12}$ | Ln element | Ionic radii (Å) | Required milling time (h) |
|---|---|---|---|
| $Yb_4Zr_3O_{12}$ | Yb | 0.985 | 30 |
| $Er_4Zr_3O_{12}$ | Er | 1.004 | 30 |
| $Ho_4Zr_3O_{12}$ | Ho | 1.015 | 30 |
| $Y_4Zr_3O_{12}$ | Y | 1.019 | 40 |

Figure 2 represents the XRD patterns corresponding to the compositions $Er_4Zr_3O_{12}$, $Ho_4Zr_3O_{12}$ and$Y_4Zr_3O_{12}$ synthesized by mechanical milling and fired at 1500°C during 6 hours. All samples fired present the reflections characterizing the fluorite crystal structure and no additional reflections belonging to other phases are observed. The presence of reflections shift towards low angles (2δ) is evident in the left part of figure 2, due mainly to an increasing of the unit cell for samples containing bigger lanthanides, such as yttrium (ionic radii = 1.019 Å).

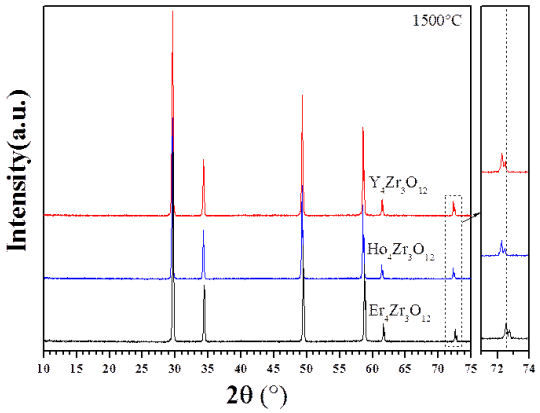


**Fig. 2.** XRD patterns of the compositions $Er_4Zr_3O_{12}$, $Ho_4Zr_3O_{12}$ and $Y_4Zr_3O_{12}$ synthesized by mechanical milling and fired at 1500°C.

Prior the analysis of electrical properties, morphology of all studied compositions was analyzed by FE-SEM. These typical morphologies of the unpolished $Ln_4Zr_3O_{12}$ samples, milled during 30 h (40 h for $Y_4Zr_3O_{12}$) and sintered during 6 h at 1500°C are presented in Figure 3, at 30K and 50K magnifications. A microstructure with inhomogeneous grains and irregular surface is clearly seen for al compositions, with a general grain size below 2 micrometer. Grain boundaries seem clean and no other phases are found at interfaces. Some remnant porosity is still present in some samples. Grain size of $Yb_4Zr_3O_{12}$ composition is clearly smaller than other compositions, which can be attributed to the lower diffusion coefficient of this sample.

## 3.2. Electrical properties

Figure 4(a) presents a representation in double-logarithmic scale of the dependence of the ionic conductivity as a function of frequency (in a range from 100Hz to 1MHz) and measurement temperature (300-700°C) for the $Er_4Zr_3O_{12}$ composition sintered at 1500°C and prepared as described in experimental section. In this type of representations, there is a potential dependence of the conductivity with frequency (increasing of ionic conductivity) at low temperatures and high frequencies. This behavior was reported by A. K. Jonscher, and was called as Dynamic Universal Response [18]. In this type of representation the value of the conductivity dc (bulk conductivity or conductivity of the material) at each temperature is manifested as a plateau in which the value of the conductivity is independent of frequency. In ionic conductors, it is known that conductivity is a thermally activated process and this is clearly seen in figure 4(a), since higher values of conductivity dc (bulk) were obtained for higher temperatures. Similar conductivity plots were obtained for all samples analyzed in this work.

The dependence of the dc conductivity with temperature for all four compositions was analyzed using an Arrhenius type representation of the form:

$$\sigma_{dc}\, T = (\sigma^0)\, exp(-E_{dc}/k_B T) \qquad (1)$$

where $\sigma^0$ is the pre-exponential factor, related to the effective number of mobile oxygen ions and $E_{dc}$ denotes the activation energy for the oxygen ion conduction process, which involves the energy that an ion requires to leave its potential hole and to contribute to the conductivity. The dc conductivity values used for this representation were obtained directly from the plot of conductivity versus frequency for each composition (Figure 4(a)). The fit of the experimental data in thermally activated processes usually generates straight lines whose slope is proportional to the activation energy ($E_{dc}$) making it possible to determine the activation energy values for each analyzed composition. Figure 4(b) shows such representation for the same selected and representative composition ($Er_4Zr_3O_{12}$). The straight line is the best linear fit to an Arrhenius law, confirming that ionic diffusion in the series is thermally activated.

Figure 5 represents the activation energy $E_{dc}$ and the dc conductivity $\sigma_{dc}$ measured at 700°C as a function of the lanthanide (Ln) used in $Ln_4Zr_3O_{12}$. Ionic size of the lanthanide element increases from left to right in the figure. Ionic conductivity values for all compositions are found in the range of $10^{-3.82}$ to $10^{-6.13}$ S/cm at 700°C, and activation energies $E_{dc}$ for the conduction process were found in the range from 1.20 to 1.30 eV, similar to some good ionic conductors [10]. A decreasing of $E_{dc}$ is evident with increasing the ionic size of the lanthanide, having consequently a positive effect on the ionic conductivity.

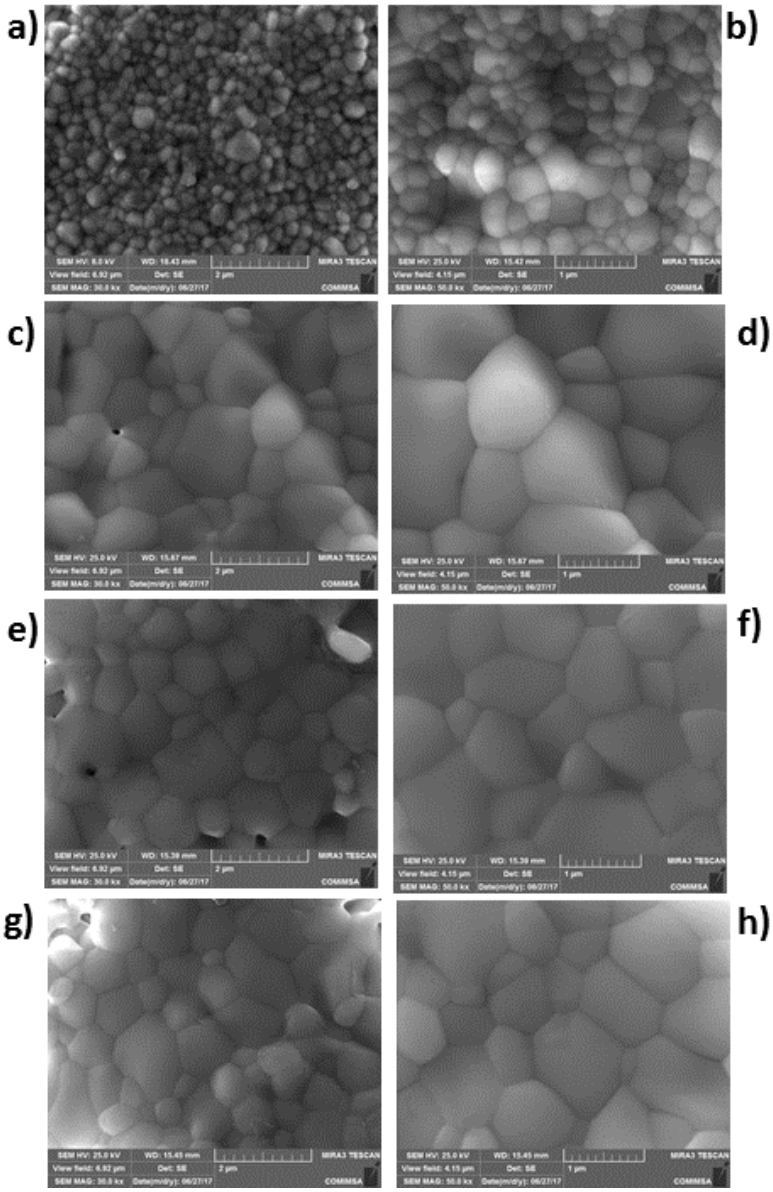


**Fig. 3.** EF-SEM images of the morphology of $Yb_4Zr_3O_{12}$ (a and b), $Er_4Zr_3O_{12}$ (c and d), $Ho_4Zr_3O_{12}$ (e and f) and $Y_4Zr_3O_{12}$ (g and h) sintered at 1500°C. 30K (left) and 40K (right) magnifications.

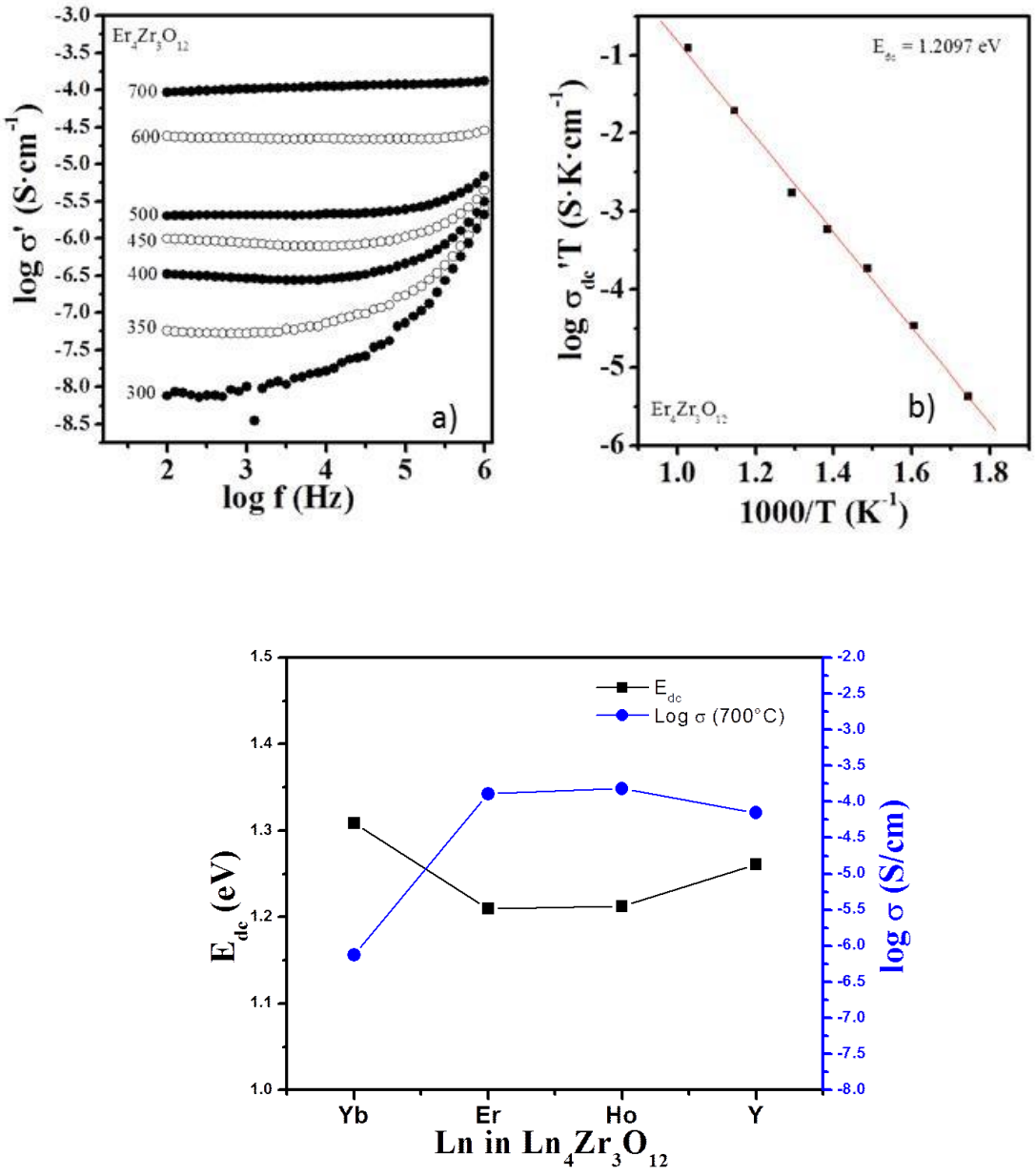


**Fig. 5.** Activation energy $E_{dc}$ and dc conductivity $\sigma_{dc}$ at 700°C for all studied compositions of the system $Ln_4Zr_3O_{12}$. Straight lines only represent the trends of experimental data.

## 4. Conclusion

This work demonstrates the viability of a mechanochemical process to obtain $Ln_4Zr_3O_{12}$ (Ln = Y, Ho, Er and Yb) materials, on views to their application as solid electrolytes in SOFCs. The just milled powders (30-40 hours of milling) in all cases consist in fluorite-type materials. This structure prevails even after thermal treatments at 1500°C.

Ionic conductivity values for all compositions are found in the range of $10^{-3.82}$ to $10^{-6.13}$ S/cm at 700°C, and activation energies $E_{dc}$ for the conduction process were found in the range from 1.20 to 1.30 eV. Higher ionic conductivities were obtained for Er, Ho and Y zirconates, as a result of lower activation energies. Results of electrical properties demonstrate that these oxides represent an interesting group of advanced materials with high ionic conductivity and good properties to be considered important candidates to be applied as solid electrolytes in SOFC.

## Acknowledgements

This work was financially supported by CONACYT (grants CB-2011-01-166 995, CB2013-221 701-Y and CB2015-257 705) and TecNM (grant 5747.16-P)

## References

[1] Stambouli AB, Traversa E. Solid oxide fuel cells (SOFCs): a review of an environmentally clean and efficient source of energy. Renew Sust Energ Rev 2002; 6: 433–55.

[2] Mahato N, Banerjee A, Gupta A, Omar S, Balani K. Progress in material selection for solid oxide fuel cell technology: A review. Prog Mater Sci 2015; 72:141-337

[3] Minh NQ, Solid oxide fuel cell technology—features and applications, Solid State Ionics 2004; 174 1:271-7.

[4] Labrincha JA, Frade JR, Marques FM. $La_2Zr_2O_7$ formed at ceramic electrode / YSZ contacts. J Mater Sci 1993; 28: 3809-15.

[5] Mitterdorfer A, Gauckler LJ. $La_2Zr_2O_7$ formation between yttria stabilized zirconia and $La_{0.85}Sr_{0.15}MnO_3$ at 1773 K. J Solid State Chem Inog Mat 1997; 453: 425-30.

[6] Yokokawa H, Sakai N, Kawada T, Dokiya M. Thermodynamic analysis of reaction profiles between $LaMO_3$ ( M = Ni , Co , Mn ) and $ZrO_2$. J Electrochem Soc 1991; 138: 2719-27.

[7] López-Cota FA, Cepeda-Sánchez NM, Díaz-Guillén JA, Dura OJ, López de la Torre MA, Maczka M, Ptak M, Fuentes AF. Electrical and thermophysical properties of mechanochemically obtained lanthanide hafnates. J Am Ceram Soc. 2017;100:1994–2004.

[8] Cepeda-Sánchez NM, Díaz-Guillén JA, Maczka M, Amador U, Fuentes AF. Mechanochemical synthesis, crystal structure and ion conduction in the $Gd_2Hf_{2-x}Ti_xO_7$ system. J Mater Sci 2017;1-14.

[9] Díaz-Guillén JA, Díaz-Guillén MR, Almanza JM, Fuentes AF, Santamaría J, León C. Effect of La substitution for Gd in the ionic conductivity and oxygen dynamics of fluorite-type $Gd_2Zr_2O_7$ J Phys-Condens Mat 2007;19 35: 356212.

[10] Díaz-Guillén JA, Fuentes AF, Díaz-Guillén MR, Almanza JM, Santamaría J, León C. The effect of homovalent A-site substitutions on the ionic conductivity of pyrochlore-type $Gd_2Zr_2O_7$. J Power Sources 2009; 186: 349-52.

[11] Shlyaktina AV, Shcherbakova LG. New solid electrolytes of the pyrochlore family. Russ J Electrochem 2012; 48:1–25.

[12] Kumar S, Gupta HC. First principles study of dielectric and vibrational properties of pyrochlore hafnates. Solid State Sci 2010; 14:1405–11.

[13] Xia XL, Ouyang JH, Liu ZG. Electrical properties of gadolinium-europium zirconate ceramics. J Am Ceram Soc 2010; 93:1074–80.

[14] Stanek CR, Jiang C, Uberuaga BP, Sickafus KE. Predicted structure and stability of $A_4B_3O_{12}$ -phase compositions. Phys Rev 2009; 80:174101.

[15] Zhang J, Wang YQ, Valdez JA, Tang M, Sickafus KE. Irradiation induced order-disorder phase transformation in $A_4Zr_3O_{12}$ (A = Sc, Lu and Dy)" J Nucl Mater 2011; 419: 386-91.

[16] Díaz-Guillén JA, Durá OJ, Díaz-Guillén MR, Bauer E, López de la Torre MA, Fuentes AF. Thermophysical properties of $Gd_2Zr_2O_7$ powders prepared by mechanical milling: Effect of homovalent Gd substitution. J Alloy Compd 2015; 649:1145-50.

[17] Shannon RD, Revised effective ionic radii and systematic studies of interatomic distances in halides and chalcogenides. Acta Crystalogr 1976; A32: 751-767.

[18] Jonscher AK, Dielectric relaxation in solids, Chelsea Dielectric London; 1983.

# 3.7 Electrical and Dielectric Properties of Calcia Doped Ceria Solid Electrolyte System

K.P. Padmasree, A.F. Fuentes

Cinvestav-Saltillo, Avenue Industria Metalurgica 1062, Parque Industrial, Ramos Arizpe 25900, Coahuila, México

* Corresponding author: phone number: 8444389600, e-mail: padmasree@cinvestav.edu.mx

## ABSTRACT

The solid solution of 10 mol% of calcia doped ceria electrolyte was prepared by mechanical milling technique. The electric and dielectric relaxation technique were applied to the sample $Ce_{0.9}Ca_{0.1}O_{1.95}$ to investigate the ionic transport process in the frequency range 100Hz to 1MHz and in the temperature range 200 to 800 °C. The frequency dependence of ac conductivity of this oxide ion conductor showed an unusual behavior compared to that of the cations. Ac conductivity spectra was found to obey the universal dielectric response at low temperatures and at high temperatures, the low frequency plateau is influenced by the space charge polarization at grain boundaries and high frequency plateau agreed with the bulk conductivity. Tan δ spectra at low temperatures shows that the relaxation peak is due to bulk conduction and the high temperature measurement shows the relaxation peak is due to grain boundary conduction.

***Keywords:*** SOFC; solid electrolyte; ionic conductivity; dielectricrelaxation

## 1. Introduction

Solid Oxide Fuel Cells (SOFCs) represents the cleanest, most efficient and versatile technologies for chemical-to-electrical energy conversion [1-2]. It consist of a solid electrolyte separated by two porous electrodes on either sides. The solid electrolytes with high oxygen ionic conductivity have been attracting a great interest because for SOFC application the transport of oxygen ions plays a significant role. Current SOFC technology is based on a combination of a Sr-doped $LaMnO_3$ (LSM) cathode, the conventional 8YSZ solid electrolyte (yttria-stabilized zirconia with 8 mol% $Y_2O_3$) and a Ni-YSZ cermet anode. The SOFCs based on YSZ will be operated at high temperatures near 1000$^{o}$C, and different cell materials will be exposed to either oxidising or reducing atmosphere over a long time. Problems associated with such high temperatures include thermal stresses at electrode-electrolyte interface, inter-diffusion between cell components, and degradation in cell performance. The replacement of YSZ with an ionic conductor having abundant

conductivity at low temperatures can improve the cell stability over prolonged operation. This lead to the search of alternative electrolytes which can be used at intermediate temperature range (500-800°C) of SOFC operation [3,4].

Ionic conductivity in ceria system is closely related to formation and migration of oxygen vacancies. Ceria is a fluorite structured ceramic material (space group Fm3m) that can be readily doped with a variety of aliovalent (alkaline earth or rare earth) cations to form solid solutions. Oxygen vacancies are generated to compensate the lower charge of the dopant cations. Ionic conductivity of ceria resulting from oxygen vacancies depends on the nature and amount of the dopant [5, 6]. Pure ceria is basically a poor oxide ion conductor ($\sigma \sim 10^{-5}$ S $cm^{-1}$ at 600 °C) [7]. Ionic conductivity is significantly increased when ceria is substituted with bivalent or trivalent cations which increase the concentration of oxygen vacancies. Compared to the widely used yttria-stabilized zirconia (YSZ) electrolyte, gadolinia doped ceria (CGO) or samaria-doped ceria (SDC) shows much higher ionic conductivity in the intermediate temperature range. However, from the viewpoint of material expenses, both Gd and Sm are very costly. Hence, there is an increasing interest to identify and develop new ceria based oxides using cost-effective dopants for technological applications [7]. The cost effective calcia oxide, when doped properly has shown competitive conductivity compared to rare earth doped ceria [8]. In this work, we studied the electrical and dielectric properties of the calcia doped ceria in order to understand the ionic transport mechanism. The dielectric measurements directly provide the knowledge of relaxation process due to ionic displacement induced by the migration of $O^{2-}$ ions.

## 2. Materials and Methods

The solid solution of $Ce_{0.9}Ca_{0.1}O_{1.95}$ was synthesized by mechanical milling, using high purity (Aldrich, >99+%) $CeO_2$, CaO as starting materials. Stoichiometric mixtures of the above chemicals were placed in zirconia containers together with 20 mm diameter zirconia balls as grinding media (balls to powder mass ratio = 10:1). Dry mechanical milling was carried out in air in a planetary ball mill for 18 h by using a rotating disc speed of 350 rpm. Phase evolution on milling of the powdered sample was analyzed by using X-ray powder diffraction in Philips X'pert Diffractometer using Ni-filtered $CuK_\alpha$ radiation (λ=1.5418Å) in the range of 2θ =10-80°. The morphological features of the particle were observed using a scanning electron microscope (SEM) Philips XL 30ESEM. The relative density of the sintered samples was calculated from the ratio of the measured density by the Archimedes method and that of the theoretical density.

Specimens for electrical property measurements were pellets obtained by pressing the sample powder in a hydraulic press at a pressure of 5MPa and sintered at 1500°C for 2 h, with a diameter of 10 mm diameter and ~ 1 mm thickness. The two electrodes were formed by applying platinum paste to either surface of the pellets and then heat treated at 600°C for two hours before the measurement to burn out the binder of the platinum paste and to ensure good contact of the electrodes with the pellet. The transport properties of the sintered pellets were examined by ac impedance spectroscopy using Solartron 1260 Frequency Response Analyzer. Temperature and frequency dependence of electrical

properties were studied in the frequency range 100 Hz to 1MHz and temperature range 200-800°C.

## 3. Results and Discussion

The powder X-ray diffraction pattern of $Ce_{0.9}Ca_{0.1}O_{1.95}$ is shown in Fig. 1 after (a) 1 h, (b) 9 h, (c) 18 h of milling at room temperature and (d) sintered at 1500°C. A single phase fluorite type structure is observed in the XRD pattern; as it exactly matches with the reported XRD pattern of cubic fluorite $CeO_2$ (PDF-ICDD 34-0394). This may suggest that the dopants are dissolved into ceria. Any additional phase corresponding to the dopants is not observed. As the milling time increases from 1h to 18 h, there is considerable decrease in intensity and broadening of the characteristic diffraction peaks as a result of the decrease in crystallite size and increase in lattice strain taking place during milling. Also, the number and intensity of the characteristic reflections of fluorite phase remains the same with no additional peaks present. Fig. 1(d) shows the XRD pattern of $Ce_{0.9}Ca_{0.1}O_{1.95}$ sample after sintered at 1500°C. XRD pattern of the sintered sample are same as that of green sample except the XRD peaks are more intense in the case of sintered sample. This suggests that the sintering process helps to increase the crystal size and the increase of pellet compaction.

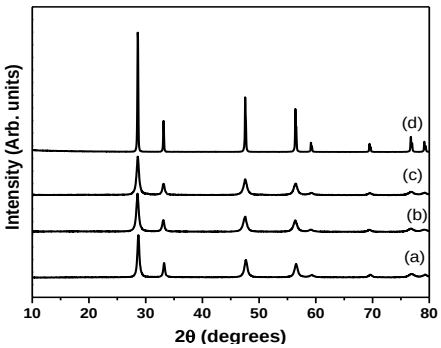


**Fig. 1.** XRD patterns of $Ce_{0.9}Ca_{0.1}O_{1.95}$ sample milled after (a) 1 h (b) 9 h (c) 18 h (d) sintered at 1500°C

The relative density of the pellet of $Ce_{0.9}Ca_{0.1}O_{1.95}$ sample milled for 18 h and after sintered at 1500°C measured by Archimedes method shows 96%, and it indicate that highly sinterable samples were synthesized by mechanical milling. The scanning electron micrograph of the sample sintered at 1500°C is shown in Fig.2. The figure shows a dense structure as well as grains exhibited non-uniform size and shapes.

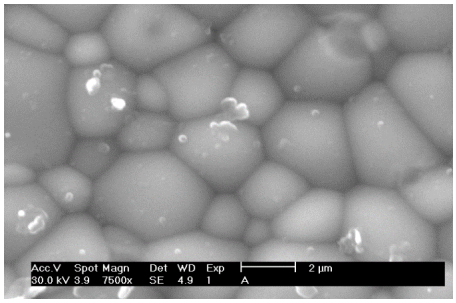


**Fig. 2.** SEM micrograph of $Ce_{0.9}Ca_{0.1}O_{1.95}$ sample sintered at 1500°C.

Impedance spectroscopy is a well-developed tool to separate out the bulk and grain boundary contribution to the total conductivity [9]. The impedance spectrum is usually represented as the negative of imaginary component of impedance $(-Z'')$ versus real component of impedance $(Z')$, which is referred as the Nyquist plot. In an impedance spectra frequency increases from right to left across the plot. In an ideal case, ac impedance of an ionic conductor contains contributions from the bulk, grain boundaries and electrode-electrolyte interfaces, which can be reflected in a complex plane by three successive semi-circles, representing different relaxation process. The intercept of the high frequency semicircle at real axis represents the bulk resistance ($R_b$), low frequency intercept point of the intermediate semicircle represents the grain boundary resistance ($R_{gb}$) and intercept of the low frequency semicircle corresponds to the electrode polarization resistance. The resistance value at different temperatures can be obtained and then converted to bulk conductivity ($\sigma_b$) and grain boundary conductivity ($\sigma_{gb}$) using the relation $\sigma = l/AR$, where $l$ and $A$ represent the sample thickness and electrode area of the sample surface, $R = R_b + R_{gb}$ is resistance obtained from the impedance plot respectively.

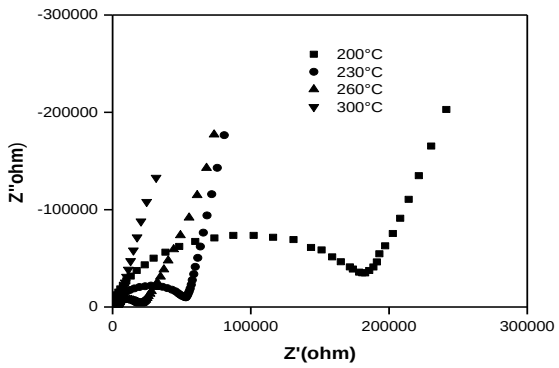


**Fig. 3.** Complex impedance plot obtained for the sample at different temperatures.

Fig. 3 shows the impedance spectra of $Ce_{0.9}Ca_{0.1}O_{1.95}$ conducted at different temperatures. Figure shows an incomplete depressed arc at high frequency and a part of the second arc at low frequency. The high frequency arc is due to resistive and capacitive effects of the bulk whereas the low frequency arc is related to the blocking of charge carriers at grain to grain interfaces. As the temperature increases, both bulk and grain boundary resistance decreases indicating an increase in both the bulk and grain boundary conductivities which results in an increase in the total ionic conductivity of the material. Since the electrical conduction in these materials are thermally activated, this type of behavior can be analyzed by the Arrhenius equation:

$$\sigma = \sigma_0 \exp\left(-\frac{E_a}{kT}\right) \quad (1)$$

where $\sigma_0$ is the pre-exponential factor being a constant in certain temperature range, $k$ is the Boltzmann constant, $T$ is the absolute temperature and $E_a$ is the activation energy for ion

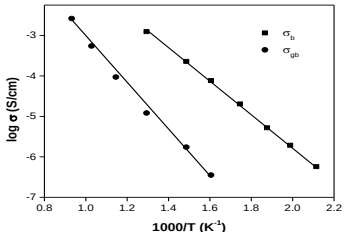


**Fig. 4.** Arrhenius plot for bulk and grain boundary conductivity

migration. Fig.4 shows the plot of log $\sigma$ vs 1000/T for the bulk and grain boundary conductivity of $Ce_{0.9}Ca_{0.1}O_{1.95}$ sample. The ionic conductivity increases as the temperature increases, whereas the difference in bulk ionic conductivity decreases with the increase of temperature [10]. The difference in bulk conductivity decreases with the increase of temperature is due to the increase in the concentration of charge carriers arising from the aliovalent doping. In the low temperature range, the concentration of charge carriers is determined by the thermodynamic equilibrium between the free defects and defect association pairs [11]. The linear behavior of the Arrhenius plot over a wide temperature range indicate the presence of only one type of ion conduction in these electrolyte systems. The activation energy is calculated from the Arrhenius plot and values of bulk and grain boundary are 0.82 and 1.1 eV.

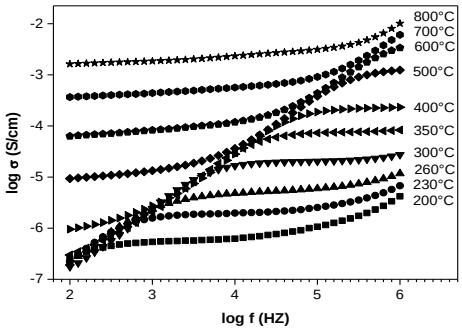


**Fig. 5.** Conductivity spectra at different temperatures

The real part of ac conductivity as a function of log f at various temperatures for the sample $Ce_{0.9}Ca_{0.1}O_{1.95}$ is shown in Fig.5. The conductivity plots strongly depend on the measuring temperatures. In the temperature range below 350°C, there is only one plateau region associated with the dc conductivity $\sigma_{dc}$ and a high frequency dispersion following the power law behavior and is referred as Jonscher's 'Universal Dielectric Response' [6]. The overall response can be given by $\sigma_\omega = \sigma_0 + A\omega^n$, it explains ac conductivity is frequency independent at low frequencies but increases with increase in frequencies following the power law behavior, $\sigma_\omega \alpha \omega^n$. This behavior has been linked with the existence of cooperative effects in the dynamics of

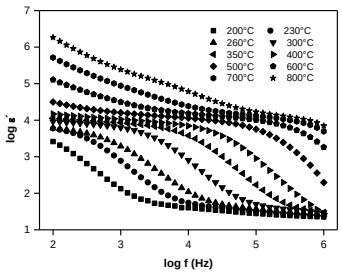


**Fig. 6.** Dielectric spectra at different temperatures

hopping ions. The temperature above 350 °C shows the presence of two plateaus. The appearance of low frequency plateau is due to the blocking effect of grain boundaries which show prominent effect at low frequencies. The frequency dispersions both at low and high frequencies shift to still higher frequencies with increase of temperature. In the high temperature range, for example at 500°C, the conductivity value (1.2 X $10^{-5}$ S/cm) estimated from the low frequency plateau did not agree with that of bulk conductivity, but agreed with the conductivity (1.3 X $10^{-5}$ S/cm) estimated from grain boundary of the

impedance spectra. This means that power law behavior could not always be suitable for oxide ion conductors because one part of the mobile oxide-ions contributes to oxide ion conduction and the other part does to the polarization at the grain boundary barrier as the space charge [12]. The charge can follow no longer with the frequency in the high frequency range, therefore the plateau at the high frequency corresponds to bulk conductivity.

The dielectric relaxation study provides the dissipation of electrical energy in the material with the ac field or the tangent of the loss angle (tan δ) due to the electric field induced reorientation of defects, where tan δ ($=\varepsilon''/\varepsilon'$) corresponds to the dissipation factor and the angle δ is the phase difference between the applied field and the induced current, $\varepsilon'$ and $\varepsilon''$ are the dielectric constant and dielectric loss [14]. The dielectric constant of oxide ion conductors was composed of both Debye type polarization and electrode-electrolyte interface polarization which depend on the inverse of frequency [15]. The dielectric constant and dielectric loss can be obtained from the impedance data by the relation

$$\varepsilon' = \frac{-Z''}{\omega C_0 (Z'^2 + Z''^2)}, \varepsilon'' = \frac{Z'}{\omega C_0 (Z'^2 + Z''^2)} \qquad (2)$$

where $C_0$ is the vacuum capacitance, $Z'$ and $Z''$ are the real and imaginary part of the impedance respectively. Fig.6. shows the frequency dependence of dielectric constant at different temperatures. At 200°C, the value of dielectric decreases with frequency and became constant at high frequencies. From 230°C to 400°C shows a plateau at low frequencies and then decreases with frequencies and became constant at high frequencies. From 500°C onwards an increase in dielectric is seen in the low frequency region and is attributed to the polarization of oxygen ions at the electrode–electrolyte interface. This behavior is quite common for the dielectric spectra of complex ionic conductors [16,17].

In the low frequency region, the ions jump in the field direction and pile up at sites with high free energy barrier resulting in an increase of capacitance in the field direction after successfully hopping through sites with low free energy barrier. At high frequencies, the periodic reversal of the field takes place so rapidly that there are no excess ion jumps in the field direction. The capacitive effect at high free energy barrier sites disappears, which reduces the contribution of charge carriers to the dielectric constant and is seen as a decrease in $\varepsilon'$ with increase in frequency finally it saturates at higher frequencies giving rise to $\varepsilon_\infty$[18-20]. As the temperature increases the values of dielectric constant $\varepsilon'$ increases and the dispersion at $\varepsilon'$ is moving towards higher frequencies when the temperature increases. Figure shows from 230°C a plateau region starts appearing in the low frequency region and the plateau region increases as the temperature increases. This plateau region seen at the intermediate region is attributed to grain-boundary relaxation. Such dispersion at intermediate frequencies was also observed in yttria doped $ZrO_2$ electrolyte [21]. It indicates that there exists a change in the lattice at grain boundaries, when the oxygen ion migrates through it [22].

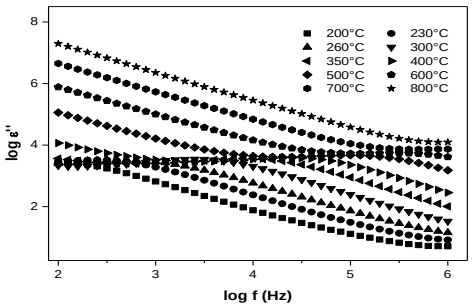


**Fig. 7.** Dielectric spectra at different temperatures

The frequency dependence of dielectric loss ε´´at different temperature is shown in Fig. 7. The figure indicates that loss in dielectric is very high at low frequency region. This part comes from the free charges contributing to dc conduction and the bound charges which oscillate 90° out of phase with the applied time varying electric field [23]. According to dielectric theory, the activation energy of a dielectric relaxation process could be estimated from the dielectric loss factor ε´´. However, in the present oxide system, the loss factor did not give any dielectric relaxation process like many other oxide systems [24]. In such a case, the activation energy for the relaxation process is usually estimated by the approximation that the loss factor ε´´ is proportional to the dielectric loss tangent tan δ [25].

Fig. 8 (a) and (b) shows the frequency dependence of dielectric loss tangent, tan δ at different temperatures from 200 to 800°C. The tan δ exhibit the presence of relaxation peaks at resonant frequencies. The relaxation peaks shift to higher frequency region with increase in temperature, and an increase in the peak intensity at the same time. For the present oxide system, within the measurement limit, relaxation peak due to bulk conduction shows only up to 350°C (Fig. 8(a)), higher temperatures indicate that there is also grain boundary relaxation, though the full relaxation peak is not visible in the measurement range (Fig.8 (b)). The fact that this spectrum contains two relaxation peaks is an important evidence for the relaxation due to the bulk and the grain boundary ionic transport process [26].

The fluorite structured ceria when doped with divalent cation $Ca^{2+}$, oxygen vacancies are formed for charge neutrality and these oxygen vacancies are responsible for the ionic conduction. Each hop of an oxygen vacancy from one site to another lead to the orientation of dipole. When an electric field is applied, a portion of these dipoles become oriented in the field direction with a certain time delay, thus creating the frequency dependent polarization conductivity. The polarization conductivity is attributed to the dielectric relaxation, i.e., the non-cooperative or short range (localized) hopping motion of a charge carrier, such as an oxygen vacancy. This is different from the dc conductivity

which involves frequency independent cooperative hopping motion. Usually, these oxygen vacancies will be associated with the dopant ions and in the conduction process the oxygen vacancies dissociate from the pairs and assist the migration of oxygen ions. The relaxation process resulting from the $O^{2-}$ migration appears in the dielectric properties and their intensities are proportional to the number of migrating $O^{2-}$ ions or the density of oxygen vacancies.

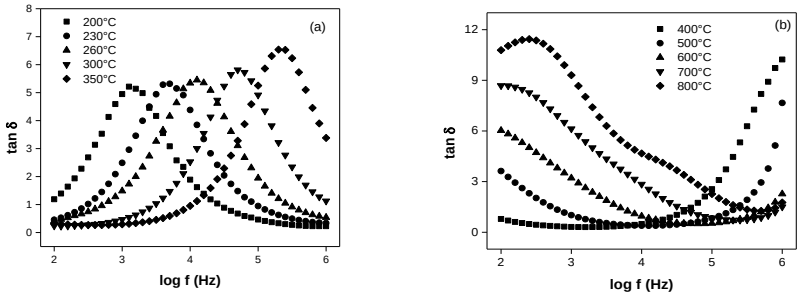


**Fig. 8 (a) and (b).** Tan δ spectra at different temperatures

For oxide electrolytes which contain excess oxygen vacancies, the oxygen vacancies get associated to the dopant ions at low temperatures and some energy is required to create a mobile vacancy. This is $E_o$, the dissociation energy of an oxygen vacancy from the restrained state. The activation energy for the dielectric relaxation process is the migration energy $E_M$ associated with the jump of an $O^{2-}$ ion, which requires ionic displacement around a saddle point in a diffusion path. The activation energy, $E_a$ for oxygen ionic conduction is the sum of $E_o$ and the migration energy $E_M$ [27]. The dielectric relaxation process in the ceria doped electrolyte did not show the loss factor ε´´, in that case the activation energy is estimated by employing the approximation that the loss tangent is proportional to the loss factor, i.e., tan δαε´´, then the maximum loss tangent can be written as

$$(tan\delta)_{max} \alpha \frac{\varepsilon_0 - \varepsilon_\infty}{2} \qquad (3)$$

where $\varepsilon_0$ and $\varepsilon_\infty$ are the static and high frequency dielectric constants. Since $(\varepsilon_0 - \varepsilon_\infty)T$ is proportional to the amount of migrating oxygen ions at T, i.e., the density of the free single oxygen vacancies at T, then the above equation can be written as:

$$(tan\delta)\max \propto N \propto \left(\frac{\exp\left(-\frac{E_0}{k_B T}\right)}{T}\right. \qquad (4)$$

Therefore, the maximum value of the relaxation peak yields the energy required for the creation of oxygen vacancy assisting $O^{2-}$ migration, $E_{o.}$

$$T(tan\delta)_{max} \propto \exp(\frac{-E_0}{k_B T}) \quad (5)$$

The temperature dependence of the resonance frequency in tan δ gives the activation energy for the dielectric relaxation process and is equal to the migration energy per oxide ion, $E_M$ [28].

$$f_{tan\delta} \propto \exp(\frac{-E_M}{k_B T}) \quad (6)$$

The binding energy or the association energy of the oxygen vacancies can be obtained from the plot of log ($T\tan\delta_{max}$) versus 1/T plot. In the same way migration energy ($E_M$) associated with the jump of oxygen vacancies can be obtained from the plot of log ($f_{tan\delta}$) versus 1/T plot. Fig. 9 shows the log($f_{tan\delta}$) versus 1/T and log $[T(tan\delta)_{max}$ versus 1/T for the peak present in the tan δ plot. The $E_M$ and $E_O$ value obtained from the high frequency peak of bulk conduction are 0.84 eV and 0.08 eV respectively. The sum of these energies does not differ from the activation energy obtained from the bulk conductivity 0.82 eV. There is however a difference of around 0.1 eV, which may be due to the reason that in the present study it is difficult to distinguish the bulk and grain boundary conduction [9,25,29]. This fact suggests a high possibility that the dielectric relaxation process governs the electrical conduction.

## 4. Conclusion

In this work the solid solutions of $Ce_{1.9}Ca_{0.1}O_{1.95}$ have been successfully prepared at room temperature via mechanochemical synthesis. The X-ray diffraction pattern confirms the cubic fluorite structure. At high temperatures, ac conductivity in the low frequency range was strongly influenced by space charge polarization at grain boundary and the high frequency plateau agreed with the bulk conductivity of the system. The dielectric relaxation process obtained from the ac conductivity studies provide detailed information of the bulk and grain boundary contributions. The migration energy and dissociation energy obtained from the temperature dependent resonance frequency and the maximum relaxation peak value is equal to the activation energy obtained from the conductivity plot.

## Acknowledgements

The work was supported by Conacyt, Mexico under the project (Grant SEP-2007-CB-84267).

## References

[1] Kharton VV, Marques FMB, Atkinson A. Transport properties of solid oxide electrolyte ceramics: a brief review. Solid State Ionics 2004;174:135–149.

[2] Anderson RG, Nowick A.S. Ionic conductivity of CeO2 with trivalent dopants of different ionic radii. Solid State Ionics 1981;5:547–550.

[3] Etsell TH, Flengas SN. Electrical properties of solid oxide electrolytes. Chem. Rev. 1970;70:339–376.

[4] Kurumada M, Hara H, Iguchi E. Oxygen vacancies contributing to intragranular electrical conduction of yttria-stabilized zirconia (YSZ) ceramics. Acta Mater. 2005;53:4839–4846.

[5] Da Yu Wang, Park DS, Griffith J, Nowick AS. Oxygen-ion conductivity and defect interactions in yttria doped ceria. Solid State Ionics 1981;2:95–105.

[6] Jonscher AK. Analysis of the alternating current properties of ionic conductors. J. Mater. Sci.978;13:553–562.

[7] Montalvo-Lozano RA, Montemayor SM, Padmasree KP, Fuentes AF. Effect of $Ca^{2+}$ or $Mg^{2+}$ additions on the electrical properties of yttria doped ceria electrolyte system. J Alloys and Compounds 2012;525:184–190.

[8] Yan M, Mori T, Zou J, Drennan J. Grain growth condition affected densification behavior and conductivity property of Ca-doped CeO2 as electrolyte material for IT-SOFC. J. Am. Ceram. Soc. 2009;92:2745–2750.

[9] Iguchi E, Nakayama S, Munakata F, Kurumada M, Y.Fujie. Ionic conduction due to oxygen diffusion in $La_{0.8}Sr_{0.2}GaO_{3-\delta}$ electrolyte. J. Appl. Phys. 2003;93:3662–3664.

[10] Yamamura H, Yagi Y, Kakinuma K. Dielectric relaxations of Y-doped ZrO2 single crystal. J. Ceram. Soc. Jpn. 2007;115:546–550.

[11] Iguchi E, Mochizuki S, Electric conduction and dieletric relaxation processes in solid oxide fuel cell electrolyte. J. Appl. Phys. 2004;96:3889–3895.

[12] Komine S. Anisotropic dielectric properties in $Y_2O_3$-stabilized $ZrO_2$. Solid State Ionics 2007;178:315–318.

[13] Yamamura H, Takeda S, Kakinuma K. Relationship between oxide-ion conductivity and dielectric relaxation in Sm-doped CeO2. Solid State Ionics 2007;178:889–893.

[14] Iguchi E, Hashimoto T, Yokoyama S. Electrical transport and stability of small polarons of O2p holes in $Li_xCo_{1-x}O$. J. Phys. Soc. Jpn. 1996;65:221–229.

[15] Yamamura H, Nishino H, Kakinuma K. Ac conductivity for Eu2Zr2O7 and La2Ce2O7 with pyrochlore-type composition. J. Ceram. Soc. Jpn. 2004;112:553–558.

[16] Iguchi E, Ueda K, Jung WH. Conduction in LaCoO3 by small-polaron hopping below room temperature. Phys. Rev. B 1996;54:17431–17437.

[17] Pimenov A, Ullrich J, Lunkenheimer P, Loidl A, Ruscher CH. Ionic conductivity and relaxations in ZrO2-Y2O3 solid solutions. Solid State Ionics 1998;109:111–118.

[18] Komine S, Munukata F. Dielectric relaxation analysis for 8 mol% YSZ single crystal. J. Mater. Sci. 2005;40:3887–3890.

[19] Li J, Ikegami T, Wang Y, Mori T. Nanocrystalline $Ce_{1-x}Y_xO_{2-x/2}$ ($0 \le x \le 0.35$) oxides via carbonate precipitation: Synthesis and characterization. J. Solid State Chem. 2002;168:52– 59.

[20] Iguchi E, Akashi K. Dielectric relaxations and electrical transport due to nanadiabatic small polarons in p-type NiO doped with Li. J. Phys. Soc. Jpn. 1992;61:3385–3393.
[21] Liu Yi. Dielectric and electrical properties of gadolina doped ceria. J. Alloys Compd. 2009;479:769–771.
[22] Baral AK, Sankaranarayanan V. Electrical study and dielectric relaxation behavior in nanocrystalline Ce0.85Gd0.15O2-d material at intermediate temperatures. Appl. Phys A 2010;98:367–373.
[23] Sarkar P, Nicholson PS. ac Conductivity and conductivity relaxation studies in the CeO2-Y2O3 system. Solid State Ionics 1986;21:49–53.
[24] Yamamura H, Satake J, Saito M, Kakinuma K. Dielectric relaxations in the $Ce_{1-x}Yb_xO_{2-d}$ system. Jpn. J. Appl. Phys. 2008;47:212–216.
[25] Padmasree KP, Montalvo-Lozano RA, Montemayor SM, Fuentes AF. Electrical conduction and dielectric relaxation process in $Ce_{0.8}Y_{0.2}O_{1.9}$ electrolyte system. J. Alloys Compounds 2011;509:8584–8589.
[26] Komine S. Dielectric relaxation study on $Ce_{0.9}Gd_{0.1}O_{1.95}$ ceramics, Physica B 2007;392:348–352.
[27] Kurumada M, Hara H, Munakata F, Iguchi E. Electric conductions in La0.9Sr0.1Ga3-d and La0.9Sr0.1Ga0.9Mg0.1O3-d. Solid State Ionics 2005;176:245–251.
[28] Frohlich H, Theory of Dielectrics Dielectric Constant and Dielectric Loss, Clarendon: Oxford; 1958.
[29] Iguchi EW, Jung H, Electrical transports of $LaFe_{1-x}Ti_xO_3$ (x≤0.10). J. Phys. Soc. Jpn. 1994;63:3078–3086.

# 3.9 Synthesis and characterization of NiCu nanoparticles decorated whit Pt for ORR

M.A. Padilla-Islas,M. M. Tellez-Cruz, O. Solorza-Feria

[1]Departamento de Química, CINVESTAV, Av. Instituto Politécnico Nacional 2508, Cuidad de México, C.P. 07360, México

* Corresponding author: 57473800, adrianmapi@gmail.com

## ABSTRACT

Controllable synthesis of non-noble alloys remains a significant challenge. Among core-shell nanoparticles of various combinations, those made of an inexpensive metal core and a noble metal shell has received particular attention.

The cores obtained with phases (111) which facilitate coverage at the same stage by the platinum which greatly favors the oxygen reduction reaction.

Nano-catalyst of NiCu is synthesized by two steps; reduction of non-noble metals as nuclei and decoration of platinum (shell) by galvanic displacement. New synthesis of catalysts for the reduction reaction of oxygen by the adequate amount of oleylamine and oleic acid and precursor salts of non-noble metals, Cu (acac)2 and Ni(acac)2 , and using morpholine borane as a reducing agent is present. The prepared NiCu@Pt octahedral core-shell were characterized by TEM, octahedral nanoparticles have narrow size distribution, with a measured average edge length of 30 ±5 nm. The EDX analysis by elemental mapping show that three elements were found homogeneously distributed throughout nanoparticles. The XRD pattern shows characteristic peaks, it suggests that CuNi is decorated whit Pt. The metallic core inherits the crystal structure of its composing elements, i.e., the face-centered-cubic (FCC) structure. The diffraction peaks at can be assigned to (1 1 1), (2 0 0), (2 2 0) and (311) crystallographic planes, respectively, which correspond to FCC phase. The electrochemical performance of NiCu decorate with Pt/C was evaluated by cyclic voltammetry, CO stripping and rotating disk electrode in HClO4 as electrolyte. NiCu@Pt/C shows better catalytic activity in terms of mass activity 311mA/cm2 and specific activity, which is 246 mA/cm2 , respect to commercially available 20-wt% Pt/C-Etek® with mass activity of 105 mA/cm2 and specific activity of 184 mA/cm2 . Therefore, this finding suggests a methodology for producing a carbon supported octahedral nanocatalyst, which could be used as a cathode electrode in a PEM fuel cell.

***Keywords:*** NiCu alloy; octapods, octahedral nanoparticles; ORR catalyst; fuel cells.

# 3.10 Effect of Er and Dy doping on the electrical properties of yttria partially stabilized zirconia solid electrolytes

C.A. Durón-Sifuentes, J.A. Díaz-Guillén, M. Salazar-Zertuche, O. Burciaga-Diaz, and A.F. Fuentes,

[1] División de Estudios de Posgrado e Investigación, Instituto Tecnológico de Saltillo, 25280-Saltillo, Coahuila México.

[2] Cinvestav Saltillo, Apartado Postal 663, 25000-Saltillo, Coahuila, México.

* Corresponding author: (+52) 844 4389500, email. jadiaz@itsaltillo.edu.mx

---

## ABSTRACT

This work reports results of electrical properties of yttria partially stabilized zirconia (YPSZ) solid electrolytes doped with two different lanthanides, Er and Dy, and synthesized by mechanical milling. Phases with general formula $Ln_xY_{0.04}Zr_{0.96-x}O_{2-\delta}$ (Ln = Er and Dy, x = 0.02, 0.05 and 0.1) were synthesized by using a planetary mill and zirconia containers and balls, and starting from mixtures of corresponding oxides. Evolution of samples with milling time was followed by XRD at different time intervals. Reactions were considered completed when no traces of the starting reagents were evident by this technique. Synthesized powders were also characterized by SEM and thermal analysis, among others. Ionic conductivity and activation energies for oxygen ion diffusion were determined by impedance spectroscopy. Results show that these materials can be successfully obtained after 20 hours of milling, and after be fired at 1500°C, show good electrical properties, similar to those obtained for ionic conductors. According with these results, these materials can be considered as interesting candidates to be used as solid electrolytes in Solid Oxide Fuel Cell (SOFC) technology.

***Keywords:*** solid electrolytes; SOFC; YPSZ; doping

# 3.11 Microstructure and functional properties of polymer nanocomposites filled with carbon nanotubes and carbon nanofibers for applications in bipolar plates

C. A. Ramírez-Herrera, J. Pérez-González, A. Flores-Vela, O. Solorza-Feria, N. Romero-Partida, J. G. Cabañas-Moreno

[a]Programa de Doctorado en Nanociencias y Nanotecnología, CINVESTAV, Av. Instituto Politécnico Nacional 2508, Cd. de México, C.P. 07360, México.

[b]Departamento de Física, Escuela Superior de Física y Matemáticas, Instituto Politécnico Nacional, Av. Instituto Politécnico Nacional s/n, Cd. de México, C.P. 07738, México.

[c]Centro Mexicano para la Producción más Limpia, Instituto Politécnico Nacional, Av. Acueducto s/n, Cd. de México, C.P. 07340, México.

[d]Departamento de Química, CINVESTAV, Av. Instituto Politécnico Nacional 2508, Cd. de México, C.P. 07360, México.

[e]Industrias Romfer S.A. de C.V., Sierravista 298, Cd. de México, C.P. 07300, México.

* Corresponding author: 0458331289066, caramirezh@cinvestav.mx

---

## ABSTRACT

Fuel cells are considered as a new power sources to reduce the dependence on fossil fuels and ameliorate the effects of global warming. Among the fuel cell systems available, proton exchange membrane fuel cells (PEMFCs) have received special attention to replace internal combustion engines in transportation applications due to its fast start-up and response time, low operating temperature and high power density. However, the manufacturing costs of fuel cell stacks are relatively high and limit their current commercial viability. Bipolar plates are a key component of PEMFCs in terms of cost and weight; therefore, one of the major challenges in the production of economical PEMFCs is the development of advanced materials for bipolar plates which can be readily manufactured, are highly electrically and thermally conductive and have adequate mechanical strength. Polymer nanocomposites filled with carbon-based nanofillers have demonstrated great potential as suitable material for bipolar plates by combining the good processability and the excellent mechanical properties of polymers with the electrical and other functional properties of carbon nanofillers. A preferential distribution of well dispersed and highly connected nanofillers forming conductive 3D networks is required to exploit their potential as reinforcing materials. In this work, polypropylene-multiwalled carbon nanotubes-carbon nanofibers (PP-MWCNT-CNF) nanocomposites have been prepared by melt-blending using different amounts of each type of nanofiller. The microstructure and properties of

these nanocomposites have been evaluated in samples molded by compression into plates of 1.5 mm thickness. The state of dispersion of the nanofillers in the polymer matrix was investigated by SEM and laser confocal optical microscopy. Electrical and mechanical properties of the nanocomposites have been measured to evaluate their performance. The maximum value obtained of electrical conductivity was 4.63 S/cm for the PP/21.5% MWCNT nanocomposite and 0.75 S/cm for the PP/15% MWCNT/15% CNF.

***Keywords:*** carbon nanotubes; carbon nanofibers; polymer nanocomposites

# 3.12 Performance of Microtubular Solid Oxide Fuel Cell Prototypes at Intermediate Temperatures

C. I. Ramos Villegas, H. J. Ávila Paredes

[1]Departamento de Ingeniería de Procesos e Hidráulica, Universidad Autónoma Metropolitana, Unidad Iztapalapa, Av. San Rafael Atlixco186, Col. Vicentina, C.P. 09340, Ciudad de México, México.

*(52) 55 5804 4600, ext. 1243; hjap@xanum.uam.mx

## ABSTRACT

Solid oxide fuel cells (SOFCs) are made up of two electrodes (anode and cathode) and one electrolyte that forms an ionic bridge between them. Traditionally they operate at high temperatures (800-1000 °C). In recent years intermediate temperature SOFCs (500 - 700 °C; IT-SOFCs) have been developed in order to reduce the operating costs of this type of devices. However, the electrochemical mechanisms that dictate the output power of the IT-SOFCs are thermally activated processes, so that decreasing the operating temperature leads to a drastic decrease in performance. New materials need to be developed for the components of IT-SOFCs. A cathodic material that has been proposed is $La_{0.8}Sr_{0.2}Co_{0.2}Fe_{0.8}O_3$ (LSCF), with a perovskite crystalline structure, and compatible with Gd-doped ceria electrolytes (e.g. $Ce_{0.8}Gd_{0.2}O_{2-x}$, GDC). Therefore, in the present work the performance of IT-SOFC prototypes, with a microtubular architecture and LSCF as cathodes, was evaluated. Prototypes (Ni-GDC/GDC/LSCF) were fabricated based on a dip coating technique. The electrical characterization was carried out by linear sweep voltammetry and impedance spectroscopy at 500 °C, with hydrogen as fuel. The evaluation of the performance of the prototypes was performed based on the polarization curves obtained from the linear voltammetry measurements.

***Keywords:*** power generation; fuel cells; dip coating.

## 1. Introduction

Among the different types of fuel cells, one of the best candidates for stationary applications is solid oxide fuel cells. These devices have efficiencies close to 60 % (and 85

% in cogeneration) [1]. SOFCs traditionally operate at high temperatures (800 - 1000 °C) [2,3], however, at these temperatures there are some issues related to the degradation of the cell components and the restriction of the type of materials to be used as interconnectors and supports (i.e. it is only possible to use ceramics), which increases the cost of these devices. Therefore, SOFCs operating at the so-called intermediate temperature (IT) range (500 - 700 °C) have been developed, in order to reduce manufacturing costs while maintaining their high efficiency. At the IT the charge transfer at the cathode-electrolyte interface restricts the cell performance and oxygen must be catalytically reduced to oxygen ions at the cathode (equation 1) [4,5]. The kinetics of this process depends mainly on the oxygen partial pressure, temperature and active material.

$$\frac{1}{2}O_2 + 2e^- \rightarrow O^{2-} \quad \text{.... (1)}$$

The most frequently used cathodic material for conventional SOFCs is $La_{1-x}Sr_xMnO_{3-\delta}$ (LSM), which has high electric conductivity (~ 300 S/cm at 900 °C) and high catalytic activity for the reduction of oxygen at elevated temperatures [6,7]. In addition, LSM has a thermal expansion coefficient close to that of yttria stabilized zirconia (YSZ), the most commonly used electrolyte for SOFCs at high temperatures. However, at IT the catalytic activity of LSM decreases (~180 S/cm at 500 °C), and no longer provides adequate oxygen reduction when integrated in IT-SOFCs with $Ce_{0.8}Gd_{0.2}O_{2-\delta}$ (GDC) as the electrolyte. Currently, one of the cathodic materials that provides the highest performance in IT-SOFCs is $La_{0.8}Sr_{0.2}Co_{0.2}Fe_{0.8}O_3$ (LSCF), due to its high conductivity (250 S/cm at 500 °C), stability and compatibility with GDC [7].

As already mentioned, traditional SOFC applications are in stationary power generation systems, but research is underway to develop micro-cells for portable applications. Cells with flat and tubular geometry are the most studied by the scientific community. However, micro-tubular SOFCs (with length < 10 cm and diameter < 5 mm) have recently attracted great attention because of their lower operating temperature, higher tolerance to thermal cycling, faster start-up capacity and higher volumetric power density compared to conventional tubular SOFCs [8,9]. In the present work LSCF was integrated as a cathode in some μSOFC prototypes (Ni-GDC/GDC/LSCF) that were fabricated based on a dip coating technique and their performance was evaluated in terms of the electric power densities and the impedance.

## 2. Materials and Methods

The fabrication of μSOFCs was based on a dip coating process. The composition of the anodic suspension was 25 wt % GDC (fuelcellmaterials, 6.0 $m^2/g$), 25 wt % NiO (fuelcellmaterials, 3.6 $m^2/g$), 12 wt % polymethylmethacrylate (PMMA TechPolymer, 99 %), 0.5 wt % ethyl-cellulose (Sigma Aldrich, 99 %), 16 wt % ink vehicle (fuelcellmaterials), 5 wt % bis-(2-ethylhexyl)phthalate (Alfa Aesar, 98 %) and 15.5 wt % 2-butanone (Alfa Aesar, 99 %). The composition of the electrolytic suspension was 20 wt % GDC (fuelcellmaterials, 36.0 $m^2/g$) and 80 wt % ink vehicle (fuelcellmaterials). The cathodic suspension had a composition of 41 wt % LSCF (LSCF-P, fuelcellmaterials), 5 wt % PMMA (TechPolymer, 99 %), 30 wt % ink vehicle (fuelcellmaterials) and 23 wt % 2-butanone. Each suspension was homogenized by ball milling with spheres of yttria stabilized zirconia for 24 h. PMMA bars (~1.10 mm diameter, Goodfellow) were dip coated (ND-DC Nadetech Innovations dip-coater) in the anodic suspension up to having a dried coating thickness close to 0.5 mm. Subsequently the electrolytic coatings were applied by dip coating. Afterwards, the half-cell (anode-electrolyte) was brought to a sintering process at 1420 °C for 8 h under air in a Thermolyne model 46100 furnace. The cathodic suspension was brushed on the sintered electrolyte. The cell was brought to a sintering process at 1150 °C for 2 h under air. Current collectors were fabricated with silver wires and silver paint. The characterization of the cells was performed by Scanning Electron Microscopy (SEM), Linear Sweep Voltammetry (LSV) and Electrochemical Impedance Spectroscopy (EIS). Before the electrical measurements, the anode reduction was carried out under a flow of 5 mL/min $H_2$ (3 % $H_2O$) at 500 °C for 2 h. Electrochemical measurements were performed with a PARSTAT Model 2273 potentiostat at 500 °C and a flow rate of 5 mL/ min $H_2$ (3 % $H_2O$). Characterization by LSV was performed from the open circuit potential down to 0 V. EIS measurements were performed in the frequency range of 0.008 Hz - 1 MHz and an amplitude of 10 mV. Figure 1 shows the schematic representation of a μSOFC prototype assembly for the electrochemical characterization.

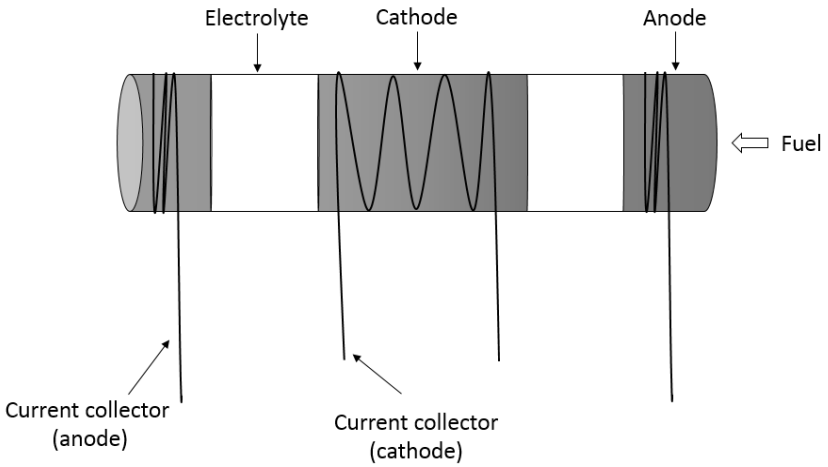


**Fig. 1.** Schematic representation of the μSOFC in the experimental setup for electrical measurements.

## 3. Results and Discussion

Figure 2a shows a scanning electron microscopy image, at 55X, of the cross-sectional surface of a microtubular cell manufactured in the present project. Dimensions of the μSOFC prototypes are: length ~ 2 cm and outer diameter ~1.5 mm. Figure 2b presents a micrograph at 1000X of the cross section of a prototype; the anodic, electrolytic and cathodic layers could be identified. No open porosity within the electrolyte is observed, which is a requirement to avoid direct contact of the gases supplied to the anodic and cathodic chambers. In contrast, open porosity of the anodic and cathodic sections is also clearly observed. Based on SEM images, the estimated thickness of the anode is ~ 350 μm, while the thickness of the electrolyte and cathode was 15 μm and 40 μm, respectively. Figure 2c shows a prototype, in which the cathodic layer is visualized in black, the anode in light green and the electrolytic layer is almost transparent white.

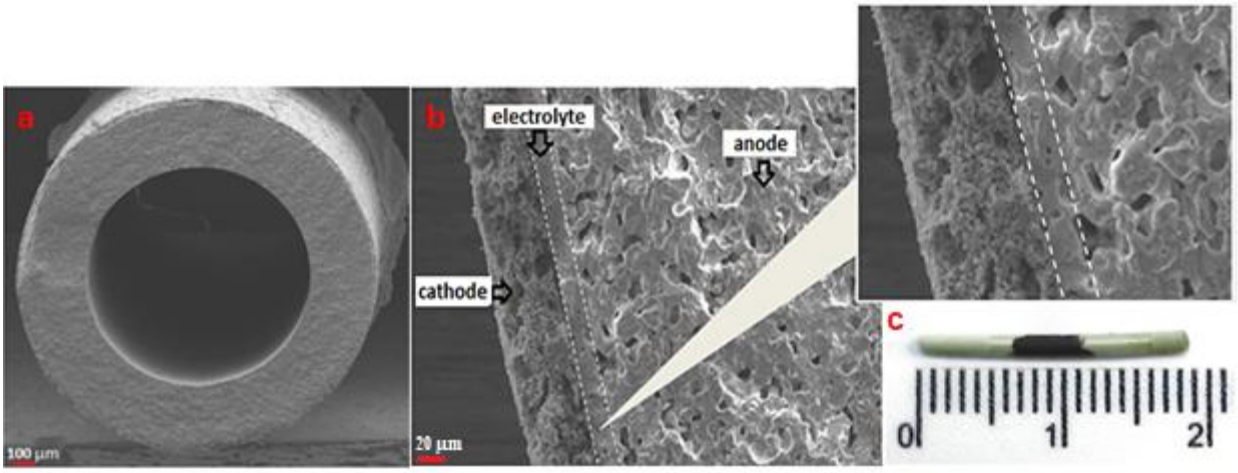


**Fig. 2.** (a) SEM image of a cross section of a μSOFC prepared in this project and; (b)SEM image of a anodic, electrolytic and cathodic layers of a μSOFC; (c) photograph of a μSOFC prototype.

Based on the characterization by LSV, the polarization curves were obtained (Fig. 3). The open circuit potential was ~ 1 V. In the I-V polarization curve as the current density increases, the potential decreases; this behavior is typical of this type of systems. The maximum power density was 420 mW/cm$^2$at a current density of 1200 mA/cm$^2$ and a cell potential of 0.35 V.This power density is similar to that reported by T. Susuki et al., for a μSOFC prototype (Ni-GDC/GDC/LSCF) of 1 cm in length and an external diameter of 1.6 mm; they reported a maximum power density of 400 mW/cm$^2$ at a current density of 1250 mA/cm$^2$ at 500 °C [10].On the other hand, Liu et al.studied the effect of the length of μSOFCs (Ni-GDC/GDC/60 % vol LSCF- 40 % vol GDC) in the power density. The power density of cells with lengths of 1.5 and 2 cm was determined. A decrease in the value of the maximum power density was observed with the increase of the length. The maximum power density at 500 °C was 110 mW/cm$^2$for the cell of 1.5 cm in length and 30 mW/cm$^2$for the cell of 2 cm in length [11]. These results clearly indicate that the performance of the cells is strongly limited by their length. Compared with these reported values, the device manufactured in this project has a length of ~ 2 cm and the power density obtained is greater than that reported by Liu et al, so that there is still a chance for optimization of the fabrication conditions that could enhance the performance of the cells.

The total resistance of the cell obtained by LSV was 831 Ω, while the total resistance evaluated by EIS in the used frequency range was ~ 275 Ω (Fig. 4). Unfortunately it was not possible to obtain measurements at lower frequency values due to equipment limitations, nor at higher temperatures due to cell degradation, which resulted in fractures occurring in the prototype.

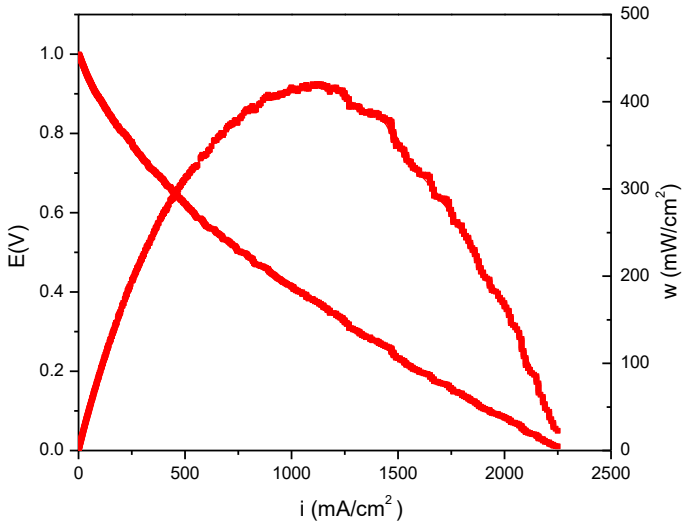


**Fig. 3.** Polarization curves of a μSOFC at 500 °C.

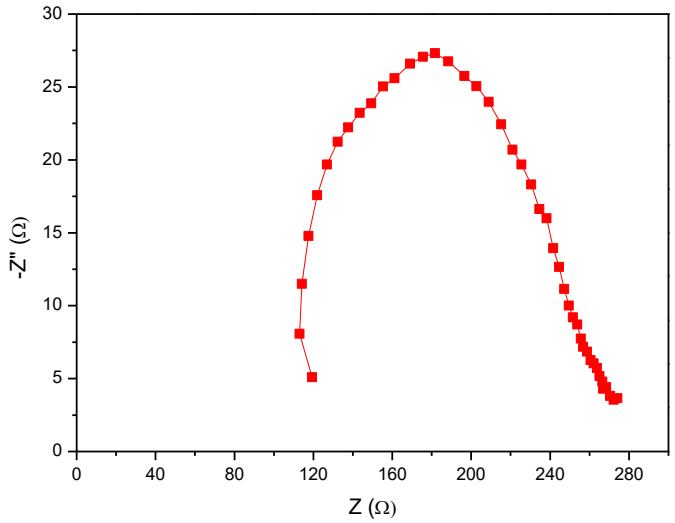


**Fig. 4.** Nyquist plot of a μSOFC at 500 °C.

## 4. Conclusion

It was possible to construct μSOFC prototypes of using a dip coating technique. The obtained prototypes present a null open porosity in the electrolyte, but the electrodes have adequate porosities. The μSOFC had an open circuit potential of ~ 1V and a power density of 420 $mW/cm^2$ at 500 °C with hydrogen as fuel. The results show to be promising, since the fabrication process could be further optimized.

## Acknowledgements

Funding for this research was provided by Ministery of Science, Technology and Innovation of Mexico City (Secretaría de Ciencia, Tecnología e Innovación del Distrito Federal, SECITI-DF; project PICSO 12-060). C.I. Ramos Villegas is thankful to Consejo Nacional de Ciencia y Tecnología for the scholarship received to pursue his graduate (M.S. and currently, Ph.D.) studies.

## References

[1] Wincewicz KC, Cooper JS, Journal of Power Sources 2005: 140:280-296.
[2] Miriam K, Riess I, Tannhauser DS, Langpape R, Rohr FJ, Journal of Solid State

Chemistry 1982: 42: 125-129.

[3] Flores JA, Rodríguez LA, Materiales para ánodos, cátodos y electrolitos utilizados en celdas de combustible de óxido sólido, Revista Mexicana de Física 2013: 59: 66-87.

[4] Minh NQ, “Ceramic Fuel Cells”, Journal of the American Ceramic Society 1993:76-3: 63-588.

[5] Kilius LB, Krstic V, Journal of Power Sources 2009: 194: 690-696.

[6] Mc Evoy AJ, Journal of Materials Science 2001: 36: 1087-1091.

[7]Alvarado-Flores J, Espino-Valencia J, Ávalos-Rodríguez LA, Análisis de materiales catódicos de estructura Perovskita para celdas de combustible de óxido sólido, SOFC´s, Revista Mexicana de Física 2015: 61: 32-57.
[8] Yang C, Jin C, Chen F, “Micro-tubular solid oxide fuel cells fabricated by phase-inversion method”, Electrochemistry Communications 2010: 12: 657–660.

[9] Yamaguchi T, Galloway KV, Yoon J, Sammes NM, “Electrochemical characterizations of microtubular solid oxide fuel cells under a long-term testing at intermediate temperature operation”, Journal of Power Sources 2011: 196: 2627–2630.

[10] Susuki T, Funahashi Y, Yamaguchi T, Fujishiro Y, Awano M, Fabrication and characterization of micro tubular SOFCs for advanced ceramic reactors. Journal of Alloys and Compounds 2008: 451: 632-635.

[11] Liu Y, Hashimoto SI, Nishino H, Takei K, Mori M, Suzuki T, Funahashi Y, Fabrication and characterization of micro-tubular cathode-supported SOFC for intermediate temperature operation, Journal of Power Sources 2007: 174: 95-102.

# 3.13 Effect of gamma irradiation on sulfonated polystyrene-co-acrylic acid membranes to use for fuel cells

R. Benavides, R. Urbano, D. Morales-Acosta, M.E. Martínez-Pardo, H. Carrasco.

[1]Centro de Investigación en Química Aplicada, Blvd. Enrique Reyna H. 140, 25294 Saltillo, Coah., México.

[2]Instituto Nacional de Investigaciones Nucleares, Carretera México-Toluca s/n, La Marquesa Ocoyoacac, Méx.,52750

* Corresponding author: +52(844) 438 9830, mail: roberto.benavides@ciqa.edu.mx

## ABSTRACT

Copolymers of styrene-co-acrylic acid were synthesized by radical bulk copolymerization and sulfonated during 3 different periods of time (1, 2 or 3 hours). Sulfonation reactions were carried out with sulfuric acid catalyzed with silver sulfate, at a level of 170% of benzene rings theoretically present in the copolymer. Membranes of the sulfonated copolymers were prepared by casting from their THF solutions and then subjected to gamma irradiation treatment at several doses (50, 75 and 100 kGy) in an industrial irradiator. Irradiation effect on sulfonated membranes was evaluated following Tg by DSC, thermal stability by TGA, water retention capacity by WU and their ionic properties by IEC measurements. Sulfonation reduce Tg transition of the copolymer (already reported), but irradiation partially recover such Tg value; particularly for the less sulfonated material (1 h). Level of sulfonation reduces thermal stability as well (already reported) and irradiation recovers someway such lost stability, particularly in the region of 200-300ºC, where sulfonated groups start to decompose. Water uptake (WU) is higher for more sulfonated membranes; such values are also reduced along irradiation dose, ending in almost half their WU value at 100 kGy, comparing with their corresponding non-irradiated sulfonated membranes. IEC values are also higher for more sulfonated copolymers and after irradiation suffer an approximate 50% reduction; however, IEC value for 100 kGy irradiated for the copolymer sulfonated during 3 h is of 0.15 meq/g, and the one treated at only 50kGy has 0.25 meq/g. While sulfonation reduces thermal and mechanical properties, irradiation treatment tends to recover them. On the other hand, WU and IEC are greatly enhanced with sulfonation, but irradiation treatment partially reduces their values. The general view is that gamma irradiation crosslinking give benefits for mechanical and thermal stability, but ion exchange properties are affected when sulfonic groups are used to crosslink the copolymer matrix.

***Keywords:*** fuel cells; membranes; crosslinking; gamma irradiation

## 1. Introduction

A great impact in economy is expected for those countries not taking care of new energy production development [1], considering the worldwide reduced oil stocks. In addition, there is also a general trend to use ecologic energy production technologies, since climate change is a reality with devastating effects in our environment [2].

Fuel cells are one of the most growing alternative technologies for clean energy production, basically due to their high conversion efficiency [3]. There are various types of cells, however, the ones containing a polymeric electrolyte (PEMFC) are some of the most studied in recent years. Such PEMFC have a polymeric membrane in charge of proton transportation and evaluated by their polyelectrolyte yield [4]. Main components of a PEMFC are the bipolar plates and the membrane-electrode assembly (MEA), which consists of two electrodes containing the catalyzer and the membrane in the center; MEA is specific of each constructor [5].

Commercial membranes are based on perfluorocarbonated ionomers (teflon with sulfonic groups) and Dupont, Dow Chemicals and Asahi are the most known private companies selling them [6]. Proton conductivity is provided by sulfonic groups, then they must be always hydrated and over 80 ºC conductivity is reduced, it means that are highly dependant on water management; furthermore, over 100 ºC sulfonic groups decompose and membrane stability is at risk. Alternative membranes have been studied, involving sulfonated copolymers of styrene/acrylonitrile or metacrylonitrile [7], styrene crosslinked with ultrahigh molecular weight polyethylene sulfonated with chlorosulfonic acid [8], polybenzimidazole composites [9], crosslinked poly(aryletherketone) sulfonated [10], etc.. Polymeric materials loaded with inorganic materials, known as hybrid membranes, is an effective way of improvement.

One of the main problems found on alternative non-teflon based membranes is tunning mechanical properties maintaining ion conduction. Crosslinking with ionizing radiation (gamma or accelerated electrons) is a safe, clean and easy method to enhance mechanical properties; moreover, the crosslinking reaction is carried out for already formed membranes, eliminating the need of processing reticulated materials. Many polymeric materials have been irradiated before, some of them need the presence of a crosslinking agent to enhance reaction yield [11], but many does not need it. Tha latter is a consequence of two competing reactions during irradiation: crosslinking and degradation [12].

This work is related with the sinthesis of a copolymer based on styrene and acrylic acid, further sulfonated and then irradiated at several doses with gamma radiation. Previous results have indicated that such copolymer have enough crosslinking yield to avoid the need of a crosslinking agent [13] and in this case, results of characterization for the sulfonated copolymer is shown.

## 2. Materials and Methods

2.1.- Membranes preparation

Synthesis of poly(styrene-co-acrylic acid) copolymer was carried out by a free radical method and has been described previously [14]. The material was sulfonated with sulfuric acid catalyzed with silver sulfate and the reaction let to proceed during 1, 2 and 3 hours; details has also been reported previously [14]. Such materials were dissolved in tetrahydrofuran (Aldrich analytical grade) and films (membranes) prepared by casting.

2.2.- Dosimetry

Dosimetric studies were carried out for the industrial irradiator used to treat copolymers, necessary to assure the needed time to apply the proposed doses. Two methods were applied: one is by calculation under a computing program, which uses irradiator activity, its caracteristics and Co-60 pencils distribution, to give the dose rate at a specific point of the irradiator. The second method corresponds to an experimental evaluation using dosimeters red acrylic type L8-C1, which are placed aside samples and suffer color changes with irradiation and are measured in a specific dosimeter reader AECL BC-2 (see Figure 1).

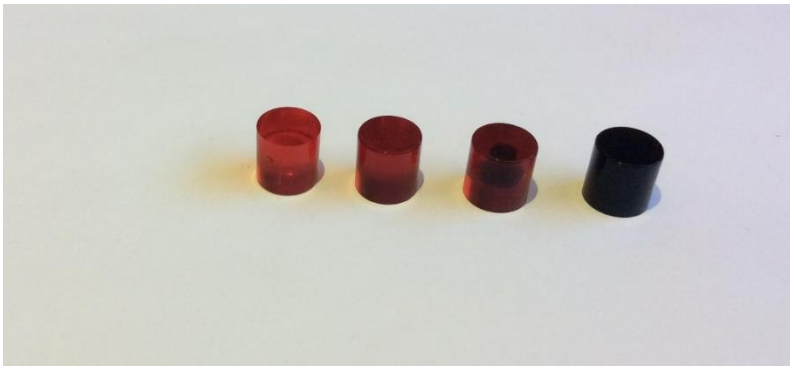

Figure 1.- Color changes observed for red acrylic dosimeters subjected to gamma irradiation

2.3.- Membrane Irradiation

Sulfonated and non sulfonated membranes were irradiated in an industrial irradiator JS-6500, placed in a sample holder and then taken to a specific position into the irradiation chamber, were dosimetric studies were carried out. The irradiation rate of the equipment was 15.42 kGy/h from the Co-60 gamma source. Doses were applied at 10,30,50,75 and 100 kGy.

2.4.- Characterization

Thermal transitions of irradiated membranes were evaluated by differential scanning calorimetry (DSC), the calorimeter used corresponds to TA Instruments MDSC 2920 in the conventional mode. The second heating was recorded in the interval of -30 to 160 ºC, at a 10 ºC/min heating ramp.

Thermogravimetric analyses were also carried out in order to evaluate the behaviour and thermal stability. A Dupont 951 instrument was used from ambient temperature until 700 ºC, with a heating ramp of 10 ºC/min.

Water retention capacity (WU) was calculated for the membranes, since it is an important parameter related with proton difusion into the membrane. Dry samples of 1 x 2 cm were immersed during 24 h in distilled water, then wiped with an absorbent paper and taken to weight. Calculus involve the sample weigth in both dry and wet weight taken to percentage.

Ion exchange capacity was also evaluated for membranes. First membranes were immersed in a 1 M Hcl solution during 24 h, for protonation; then were rinsed with distilled water to eliminate excess of the acid. Rinsing water was continuously monitored to measure the proper elimination. Protonized membranes were immersed in a 1 M NaCl during 24 h, to exchange protns for sodium ions. Finally, the proton solution was titrated with a 0.01 M NaOH solution using a color change indicator. IEC was calculated through the following formula [15]:

$$IEC = (V \times M) / W$$

Where V is the volume of titration solution at the equilibrium, M is titration solution concentration and W is the dry sample weight.

## 3. Results and Discussion

Vitreous transition (Tg) is an important parameter to evaluate, since it defines when membranes loss some mechanical properties. Table 1 show Tg values for membranes sulfonated at the 3 time periods and irradiated at the 3 doses. Curves of base materials has been shown previously [14].

Table 1.- Tg Transition for membranes sulfonated and gamma irradiated

| Membrane | Vitreous Transition Tg (ºC) | | | |
|---|---|---|---|---|
| | No irradiated | Gamma 50 kGy | Gamma 75 kGy | Gamma 100 kGy |
| PS/AA | 118 | 125 | 127 | 135 |
| PS/AA 1h s. | 105 | - | - | 112 |
| PS/AA 2h s | 103 | - | - | 108 |
| PS/AA 3h s | 98 | - | - | 102 |

The neat copolymer reduces its Tg values when is sulfonated, apparently due to its hydrophilicity enhanced with the sulfonic groups in the molecular structure. However, when copolymer by itself is irradiated, it suffers an increment in Tg values along irradiation dose, as a result of its crosslinked structure. Even for sulfonated copolymers, gamma radiation give the benefit of enhancing Tg values, recovering to some extent the property lost during sulfonation. Sulfonated membranes were only irradiated at 100 kGy.

TGA analyses indicate some light differences among copolymers before and after sulfonation and after irradiation. Figure 2 show mass loss for no sulfonated membranes after irradiation, where the loss starting before 200 ºC is always higher along the irradiation dose. Such decomposition has been attributed to low molecular weight components, including aromatics, formed during irradiation [16] or to several species formed during oxidative degradation [17]. The next big mass loss (400 ºC) corresponds to the main copolymer structure decomposition, which is similar for all membranes. Sulfonated membranes does not show important differences with previous materials after irradiation; the main difference is observed around 100 ºC, as a consequence of hydrophilicity of sulfonated; however, other decompositions occur in a similar way.

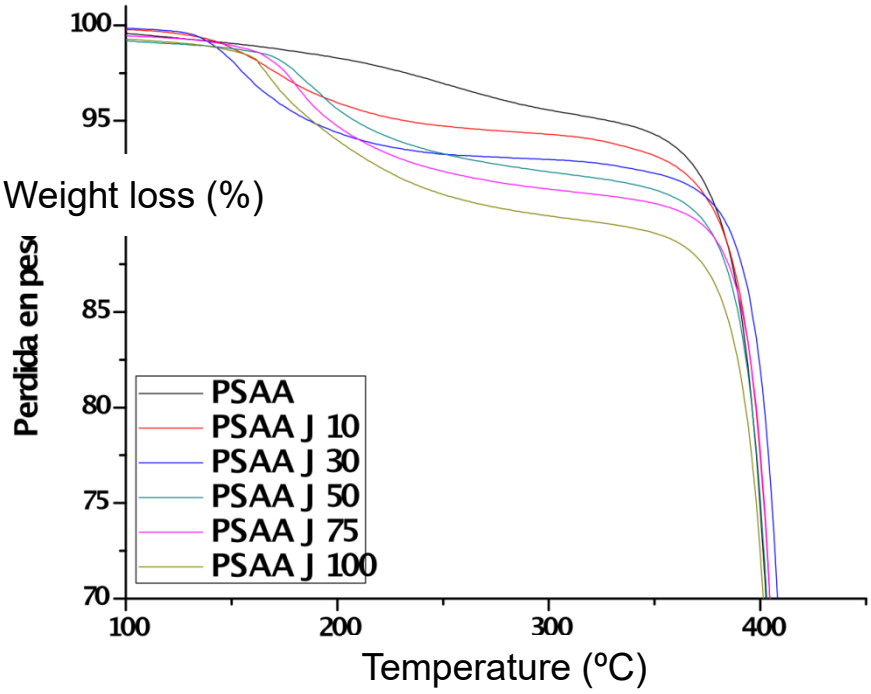


Figure 2.- TGA curves for non sulfonated copolymer after irradiation

Water absorption or water uptake (WU) is a very important condition for membranes, and this property is affected during sulfonation and gamma irradiation. Table 2 concentrate WU results obtained for our membranes.

Table 2.- Water uptake for sulfonated and irradiated membranes

| **Membrane** | **Water Uptake (%)** | | | |
|---|---|---|---|---|
| | **No irradiated** | **Gamma 50 kGy** | **Gamma 75 kGy** | **Gamma 100 kGy** |
| PS/AA 1h s. | 21.3 | 16.2 | 13.4 | 9.6 |
| PS/AA 2h s | 28.7 | 22.1 | 18.3 | 13.1 |
| PS/AA 3h s | 35.7 | 29.4 | 24.4 | 17.5 |

It is clear that sulfonation time, involving sulfonation level, enhance the amount of water inside the membrane, however gamma irradiation reduce considerably such ability for the copolymers, and such reduction is basically the same independently of the sulfonation level in the membrane. In this way, a treatment with 100 kGy for a 3 h

sulfonated material reduces WU values to a membrane only sulfonated during less than 1h.

Similarly, same membranes were evaluated in their capacity to exchange ions (IEC) and results are shown in Table 3.

Table 3.- Ion exchange capacity for sulfonated and irradiated membranes

| **Membrane** | **Ion exchange capacity (meq/g)** | | | |
|---|---|---|---|---|
| | **No irradiated** | **Gamma 50 kGy** | **Gamma 75 kGy** | **Gamma 100 kGy** |
| PS/AA 1h s. | 0.190 | 0.161 | 0.128 | 0.102 |
| PS/AA 2h s | 0.246 | 0.214 | 0.167 | 0.132 |
| PS/AA 3h s | 0.299 | 0.252 | 0.196 | 0.151 |

The capacity to exchange ions is clearly enhanced along sulfonation level, since sulfonic groups promote water absorption and the ion exchange sites are more exposed; however, gamma irradiation generate changes ending in IEC values reduction. The latter is a consequence of the use of sulfonic groups for the crosslinking reactions.

## 4. Conclusion

The sulfonation of copolymers of styrene-co-acrylic acid reduces thermal properties as Tg and decomposition temperature; however greatly enhance the water uptake and IEC values. Gamma irradiation recover thermal properties: increase Tg values and thermal stability, but it also reduce the water absorption and IEC values, due to the loss of sulfonic groups to obtain crosslinking.

## Acknowledgements

Thanks are given to CONACyT for the MC scholarship given to R.U.

**References**

[1] Giddey S. A comprehensive review of direct carbon fuel cell technology. Progress in Energy and Combustion Science 2011; 38:360-399.

[2] Andújar J.M., Segura F. Fuel cells: History and updating. A walk along two centuries., Renewable and Sustainable Energy Reviews 2009,13:2309–2322

[3] Banerjeea S., Curtin E.D. Nafion perfluorinated membranes in fuel cells, Journal of Fluorine Chemistry 2004, 125:1211–1216

[4] ZaidiS.M.J., Matsuura T. Polymer Membranes for Fuel Cells. Germany: Springer; 2009

[5] Hakenjos A. A PEM fuel cell for combined measurement of current and temperature distribution and flow field flooding. Journal of Power Sources 2004,131:213–216

[6] Rajalakshmi N., Raja M., Dhathathreyan K.S. Evaluation of current distribution in a proton exchange. Journal of Power Sources 2002,112:331–336

[7] Jetsrisuparb K., Ben-Youcef H., Wokaun A., Gubler L. Radiation grafted membranes for fuel cells containing styrene sulfonic acid and nitrile comonomers. Membrane Science 2013,28-37.

[8] Sherazi, T.A., Guiver M.D., Kingston D., Ahmad S., Kasmiri M.A., Xue X. Radiation-grafted membranes based in polyethylene for direct metanol fuel cells, Journal of Power Sources, 2010, 195:21-29

[9] Suryani-Chang Y.N., Lai J.Y., Liu Y.L. Polybenzimidazole (PBI)- functionalized silica nanoparticles modified PBI nanocomposite membranes for proton exchange membranes fuel cells. Membrane Science 2012, 403-404:1-7.

[10] Park J.Y., Kim T.H., Kim H.J., Choi J.H., Hong Y. Crosslinked sulfonated poly (arylene ether sulfone) membranes for fuel cell application. Hydrogen Energy 2012, 37:2603-2623

[11] Bowmer T.N., Davis D.D., Kwei T.K., Vroom W.I. Journal of applied polymer Science 2002, 26:3669-3688

[12] Woods R.J., Pikaev A.K. Applied Radiation, Chemistry-Radiation Processing. Canada: Wiley Interscience; 1994

[13] Urbano R., Irradiación gamma de de membranas de poliestireno-co ácido acrílico para su uso en celdas de combustible, MSc Thesis, Centro de Investigación en Química Aplicada, Saltillo, Coah. México 2016

[14] Benavides R., Urbano R., Morales-Acosta D., Martinez-Pardo M.E., Carrasco H. Gamma irradiation of polystyrene-co-acrylic acid copolymers to use them as membranes for fuel cells. International Journal of Hydrogen Energy 2017, in reviewing.

[15] Wang L., Li K., Zhu G., Li J. Preparation and properties of highly branched sulfonated poly(ether ether ketone)s doped with antioxidant 1010 as proton exchange membranes. Journal of Membrane Science 2011, 379:440 – 448

[16] Hui Liu , Zhengping Fang , Mao Peng, Lie Shen , Yongchang Wang. The effects of irradiation cross-linking on the thermal degradation and flame-retardant properties of the HDPE/EVA/magnesium hydroxide composites. Radiation Physics and Chemistry 2009, 78:922–926

[17] Kudoh, H, Sasuga, T, Seguchi T.High-Energy Ion Irradiation Effects onPolymer Materials. Irradiation of Polymers.American Chemical Society Symposium Series 1996, 620:2-10

# 3.14 Electrochemical study corrosion of a gas diffusion layer based Ti / $IrO_2$ for URFC

E. Zapata Tun, J.C. Cruz, D.L. Trejo Arroyo, G. Rodriguez-May, B. Escobar, A. M. Valenzuela Muñiz

[1]Instituto Tecnológico de Chetumal, Av. Insurgentes s/n, 77013,Chetumal, Quintana Roo, México

[2]Centro de Investigación Científica de Yucatán, A.C., Calle 43 No. 130 Colonia Chuburná de Hidalgo, Mérida, Yucatán 97200, México

[3] Instituto Tecnológico de Cancun, Avenida Kabah, Km. 3, Centro, 77515 Cancún, Q.R. México

* Corresponding author: 442 32 90 609, jcruz@itchetumal.edu.mx

---

## ABSTRACT

The Unitized Regenerative Fuel Cell (URFC) constitute renewable energy sources that work in a dual way, both for electrolyzer to generate hydrogen as well as fuel cell to accomplish electric power generation. Since some of its main components are GDLs, attendanting reactants distribution, its physical, chemical and electrical conditions variate. Carbon paper is used as GDLs on both electrodes; in a URFC testing, carbon material is unsuitable because of the anodic potentials both for electrode and the GDL itself when is doing its electrolyzer function, hence Ti/$IrO_2$ is proposed as corrosion resistant material, because it endures the environmental conditions better through the electrolysis process and increases both its efficiency and lifetime. In order to obtain the mentioned material, five Ti meshes patterns were trimmed in 2.5x 2.5cm, and this patterns were submitted to a porosity treatment in $C_2H_2O_4$ to 0.5 M at 80°C during 3 hours each one, acquiring a microstructural surface for the Ir deposit, when 7% equivalent to mesh weight was used. The $IrCl_3$ is dissolved inside Butanol, waving it along the mesh in order to get Butanol completely evaporated. At last, the mesh is dried at 100°C during 24 hours, for later being calcined at 400°C for an hour. It was distinguished by means of cyclic voltammetry, linear voltammetry, spectroscopy of electrochemical impedance and corrosion curves, where this last ones exposed that carbon paper through multicycle techniques presents instability from 500 cycles onwards, displaying corrosion products, whereas that Ti/$IrO_2$ featured stings from cycles 1000 onwards, superior in stability compared with carbon paper.

***Keywords:*** URFC, Gas diffusion layer, Ti/IrO2

# 3.15 A Proposal based on quantum phenomena for the ORR mechanism on Nitrogen-doped Carbon-based electrocatalysts. A DFT study

A. Legarreta-Mendoza, N.Flores-Holguín, V.Collins-Martínez, D. Lardizabal-Gutiérrez*

Centro de Investigación en Materiales Avanzados, S.C., Miguel de Cervantes 120, Complejo Industrial Chihuahua, 31136, Chihuahua, Chih. México.

* 52(614) 439 1100, daniel.lardizabal@cimav.edu.mx

## ABSTRACT

Several theories attempt to explain how nitrogen-doped carbon-based electrocatalysts work during the oxygen reduction reaction (ORR). However, no consensus has been reached on which of the proposedmechanisms is the most accurate. The present work aims to establish a hypothesis of this mechanism, based on the hybridization change of graphene lattice carbons, from $sp^2$ to $sp^3$. As shown in several studies, carbons with $sp^3$ hybridization are able to store electrons (i.e. work as capacitors), this phenomenon, along with nitrogen inversion, due tolattice defects, presumably allows nitrogen to work as a switch, by letting pass or stopping the flow of electrons, thus generating active sites to enhance the ORR. Computational chemistry has been propose to prove this hypothesis. Ninety-two doped and undopedgraphene atomswere constructed using the Gaussian View 5.0® program and geometries optimized by applying the DFT in Gaussian 09® program, to compare lattice changes in bond angles and lengths. The obtained results did not present significant changes to help demonstrating the hypothesis. The understanding of this phenomenon will allow to evaluatethe feasibility of continuing the study and development of these type of materials or if they have reached their limit as low-cost electrocatalysts.

***Keywords:*** ORR,Carbon-based electrocatalysts, nitrogen inversion, DFT.

## 1. Introduction

One of the main processes during the operation of fuel cells is the oxygen reduction reaction (ORR). The rate at which this reaction takes place is slow in comparison to hydrogen oxidation, which limits the performance of fuel cells. For this reason, the development of electrocatalysts has been studiedin the last decades. According to diverse investigations, metal-free carbon compounds present adequate electrocatalytic activity, making them one of the most promising options as low-cost electrocatalytic materials.

Among carbon compounds recently studied are those doped using heteroatoms[i,ii,iii],mainly nitrogen [iv](N), which significantly improves the reaction rate.

There is no clear understanding of the effect of these atoms within the carbon lattice, so the scientific community has the task of explaining this phenomenon, since these materials prove to be more economical and chemically stable.

The inclusion of heteroatoms (N, S, P) and the generation of defects in carbon compounds such as graphite, graphene and carbon nanotubes, from pyrolytic processes, modify their atomic and electronic structure, resulting in a wide range of new materials with outstanding properties, thus providing a broad outlook for research into the development of electrocatalysts, supercapacitors and batteries.

Remarkable researches related to the mechanism of heteroatom-doped carbon-based electrocatalysts in ORR areZahoor*et al.*who explain the effect in carbon-based materials with $sp^2$ electron configuration (graphite, graphene and carbon nanotube), which have abundant pi (π) electrons. These electrons are transferred without resistance due to the type of their hybridization. This electron flow makes these materials potential catalysts for reactions in need of electrons like the ORR. However, these electrons are not enough reactive to be used directly for this purpose. It is then considered that π electrons can be activated by bonding with the solitary electron pairs of N, so that $O_2$ molecules are reduced in the positively charged carbons by the effect of neighboring nitrogen atoms[v].

Li Ting *et al*. explain that the factors contributing to the electrocatalytic activity of heteroatom-doped graphene in the ORR are the microstructure and high spin density or charge density on adjacent carbon atoms. Edge plane sites or defects in graphene are the primary source of their electrochemical activity, the addition of impurities alter the basal surface and create defects or sites in the edge of the plane, which are responsible for controlling the catalytic activity[vi].

Somesimulation aided researches: Wang *et al*. examined three BCN graphenemodels using DFT models. In thesemodels, B and N atoms were distributedeither randomly or without any BN bonds. The spin density, charge density andenergy gap models were

calculated and compared.The authors observed that highly doped graphene has no spin density and possesses higher energy gap than pure grapheneand the other models[vii]. Yu *et al*. using a DFT studyrevealedthat the possibility of doping two or more nitrogen atoms intwo neighboring defect sites is quite low by examining the interaction energy between the two nitrogen atoms[viii]. Okamoto *et al.*using the Atom TEchnology (STATE) simulation tool calculated the atomic geometry and electronic structure according with their DFT results to investigate oxygen reduction reactions (ORRs) on N-doped carbon. Graphene sheets having one to four N impurities in the substitutional site of C around a C=C bond were examined as a model structure. They found that the binding interaction between graphene and $O_2$ becomes stronger as the number of N bonding atoms with the C=C increases[ix].

These studies provide a preliminary understanding of the ORR, but until today, a thorough explanation of why different compounds derived from carbon doped with heteroatoms achieve good performance as electrocatalysts is missing.

This work is the first part of several calculations that will be performed in an attempt to explain the nitrogen-doping graphene lattice mechanism in ORR electrocatalysts. It differs from othermechanisms based on platinum, as it presents the possible interaction of nitrogen atoms in the graphene lattice and the electron flow necessary for ORR at a stage prior to oxygen adsorption on the electrocatalyst. The theoretical studies are based on phenomena of quantum nature, the tunnel effect and nitrogen inversion. Computational chemistry has been proposed to prove the theory by working with Gaussian 09 ® and Gaussian View 5.0 ®.

**Quantum tunnel effect.**

The quantum tunnel effect occurs when a particle is able to penetrate a potential or impedance barrier greater than the kinetic energy of the particle. According to theory, even though the particle does not have sufficient energy to penetrate this barrier, it passes through it energetically, because at the quantum level it exhibits a wave behavior that is possible to describe as a wave function, where there is a possibility that this particle is displaced through the structure[x].

**Nitrogen inversion**

A type of quantum tunnel is the phenomenon called nitrogen inversion, which is the translation of the pair of lone nitrogen electrons through the nitrogen nucleus and their

reappearance on the opposite side. This effect has an intermediate state with the appearance of *p*orbitals with a trigonal structure. The structure goes from hybrid $sp^3$ orbitals to $sp^2$to later stabilize in the $sp^3$ form of its optical isomer. Nitrogen must have three different groups and a pair of lone electrons. Theoretically many molecules are capable of this inversion, but laboratory measurements show that only in nitrogen the inversion barrier is low enough for this phenomenon to occur constantly[xi].

**Nitrogen inversion in the graphitic lattice**

As mentioned previously in a graphene lattice, carbon is present in $sp^2$ hybridization, causing resonance with adjacent carbon atoms, producing an electron flow throughout the graphene lattice. It would behave as an excellent electrical conductor with a gap close to 0 with a metallic character, like other graphene compounds such as carbon nanotubes (NTC).

The ORR is favored in a graphene lattice environment with multiple defects, as evidenced by various studies that relate electrocatalytic activity to Raman spectrometry analysis. These topological defects can be produced by heteroatom (nitrogen) insertions, by various chemical processes or by mechanical ball-milling, producing $sp^3$ hybridizations with tetrahedral structures, different from $sp^2$ bonds that have a flat trigonal structure. Additionally, this distortion of the graphene lattice produces a variation in the measurement of angles of carbons attached to the nitrogen atom.This could cause those adjacent carbons to function with the nitrogen atom as if they were different radicals (even though they are the same carbon) achieving nitrogen inversion, causing the electron pair to travel across the nitrogen nucleus causing hybrid states $sp^2$ - $sp^3$ and vice versa continuously at a very high speed. This phenomenon may result in nitrogen to behave mainly as an on-off switch. As it switches back, nitrogen inversion produces its change to $sp^3$ hybridization interrupting resonance and electron flow, thus causing nitrogen to take the function of a diode where current follows a single direction. Then, these electrons are the able to interact with the oxygen and achieve the overpotential required for the ORR.
Another factor that could favor this reaction is that carbon structure in $sp^3$ hybridization may retain electrostatic charges, since its behavior is that of an electrical insulator as several studies claim[xii,xiii] thatthis would work as a capacitor with charge-discharge interactions, during the nitrogen inversion, helping with the concentration of electrons that can be use in ORR.

## 2. Computational details

## 2.1 Molecular construction

Using a graphene lattice model comprised by 25 hexagonal carbon rings with resonance, with 92 atoms.Two different lattices were constructedusing Gaussian View 5.0®, one graphene lattice with 70 carbons $sp^2$ hybridization and 22 hydrogen atoms, with the second one using the first one as a base, with the difference of just a central $sp^2$ carbon being replaced by a nitrogen atom.

### 2.2 Geometry optimization and frequency

The lattices were optimized and frequencies were calculated to verify the geometry in the minimum energy state, using density functional theory (DFT). All calculation were developed with Gaussian 09 ® program. The employed calculation methodology has been widely used by NANOCOSMOS group at CIMAV and is the combination of the hybrid functional Lee, Yang and Parr (B3LYP) and 6-31G basis set[xiv,xv,xvi]. All calculations were performed in gas phase.

## 3. Results and Discussion

The graphene latticestructure is planar, with an average length bond of 1.42Å and the measure of its angles is 120°[xvii]. A variation in bond length and/or opening of angles between atoms where carbon was replaced by a nitrogen atom were expected. The graphene lattice before and after the optimization presented a planar structure without deformations (F*igure 1*).*Table 1* shows bond length and angle measurements for the optimized lattice. The values are according with experimental measurements[17]. The nitrogen-doped graphene lattice before the optimization show a small deformation (*Figure 2 (A)*), after optimization the lattices present aplanar structure (*Figure 2 (B)*). *Table 2* shows bond lengths and angles being present in the doped lattice after optimization.

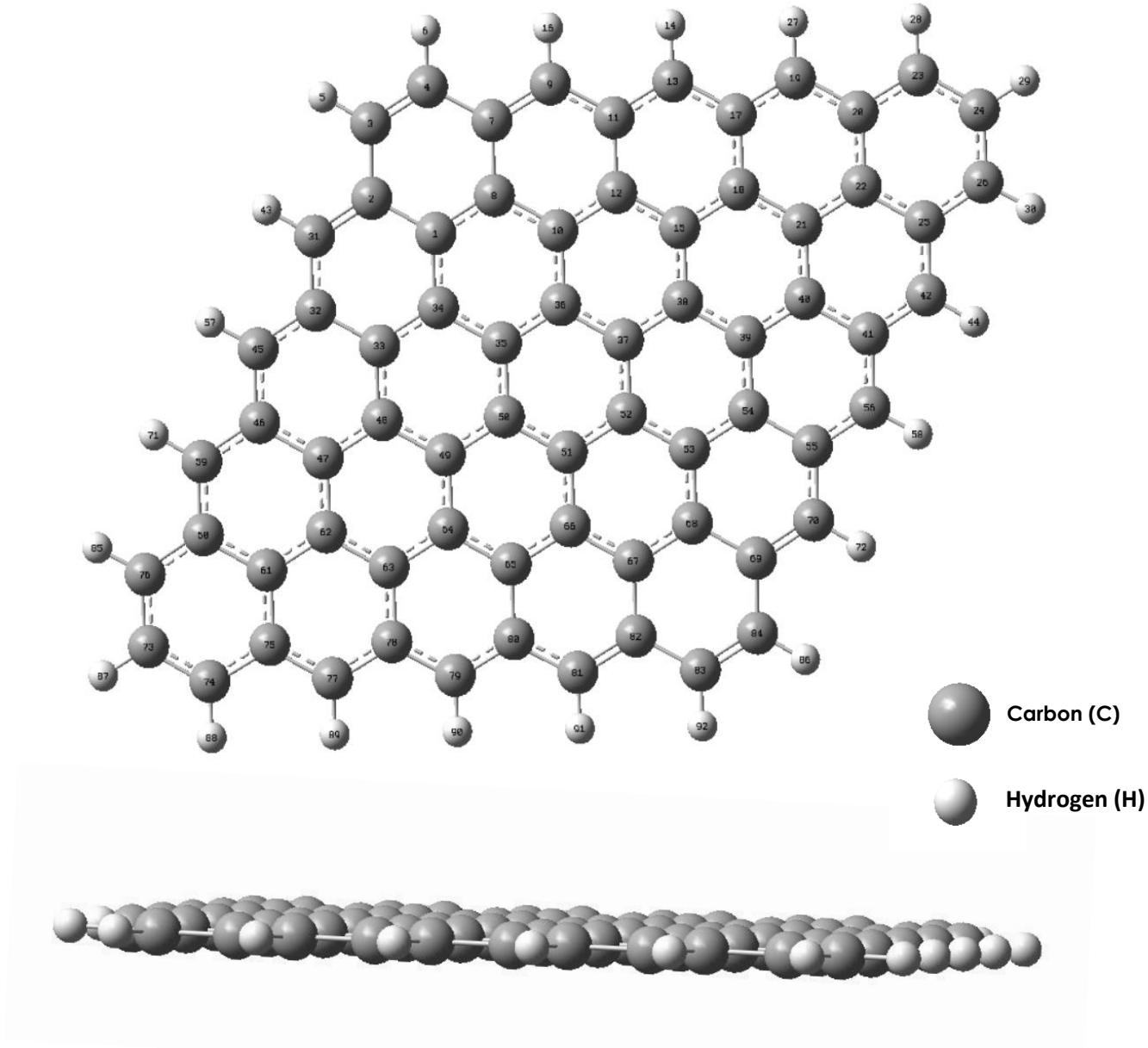


***Fig 1***. Graphitic lattice optimized by DFT.

***Table 1***. Bond lengths and angle measurements in the graphene lattice.

| OPTIMIZED GRAPHENE B3LYP | |
|---|---|
| **Bond** | **Length (Å)** |
| $C_3$-$H_5$ | 1.08611 |
| $C_{24}$-$H_{29}$ | 1.08539 |

| | |
|---|---|
| $C_{84}$-$H_{86}$ | 1.0811 |
| $C_{73}$-$H_{87}$ | 1.08539 |
| $C_3$-$C_4$ | 1.35913 |
| $C_4$-$C_7$ | 1.4491 |
| $C_7$-$C_9$ | 1.38072 |
| $C_3$-$C_2$ | 1.4491 |
| $C_{24}$-$C_{26}$ | 1.3959 |
| $C_{24}$-$C_{23}$ | 1.3959 |
| $C_{70}$-$C_{69}$ | 1.38072 |
| $C_{69}$-$C_{84}$ | 1.4491 |
| $C_{84}$-$C_{83}$ | 1.35913 |
| $C_{73}$-$C_{74}$ | 1.3959 |
| $C_{73}$-$C_{76}$ | 1.3959 |
| $C_{18}$-$C_{21}$ | 1.42863 |
| $C_{54}$-$C_{55}$ | 1.44776 |
| $C_{65}$-$C_{66}$ | 1.41178 |
| $C_{47}$-$C_{62}$ | 1.42863 |
| **Atoms** | **Angle (°)** |
| $C_3$-$C_4$-$C_7$ | 121.608 |
| $C_4$-$C_7$-$C_8$ | 117.872 |
| $C_{20}$-$C_{23}$-$C_{24}$ | 120.907 |
| $C_{23}$-$C_{24}$-$C_{26}$ | 120.907 |
| $C_{82}$-$C_{83}$-$C_{84}$ | 121.608 |
| $C_{83}$-$C_{84}$-$C_{69}$ | 121.608 |
| $C_{76}$-$C_{73}$-$C_{74}$ | 120.907 |
| $C_{73}$-$C_{74}$-$C_{75}$ | 120.827 |

| OPTIMIZED GRAPHENE B3LYP | |
|---|---|
| **Bond** | **Length (Å)** |
| $C_{35}$-$C_{36}$ | 1.41601 |
| $C_{35}$-$C_{34}$ | 1.43262 |
| $C_{35}$-$C_{50}$ | 1.42971 |
| $C_{36}$-$C_{37}$ | 1.42971 |
| $C_{34}$-$C_{33}$ | 1.41177 |
| $C_{36}$-$C_{10}$ | 1.43262 |
| $C_{50}$-$C_{51}$ | 1.42972 |
| $C_{34}$-$C_{1}$ | 1.43949 |
| $C_{10}$-$C_{12}$ | 1.41177 |
| **Atoms** | **Angle (°)** |
| $C_{34}$-$C_{35}$-$C_{36}$ | 120.111 |
| $C_{34}$-$C_{35}$-$C_{50}$ | 119.842 |
| $C_{50}$-$C_{35}$-$C_{36}$ | 120.047 |
| $C_{35}$-$C_{50}$-$C_{51}$ | 119.905 |
| $C_{35}$-$C_{50}$-$C_{49}$ | 120.047 |
| $C_{35}$-$C_{34}$-$C_{1}$ | 119.555 |
| $C_{35}$-$C_{34}$-$C_{33}$ | 120.034 |
| $C_{35}$-$C_{36}$-$C_{10}$ | 120.111 |

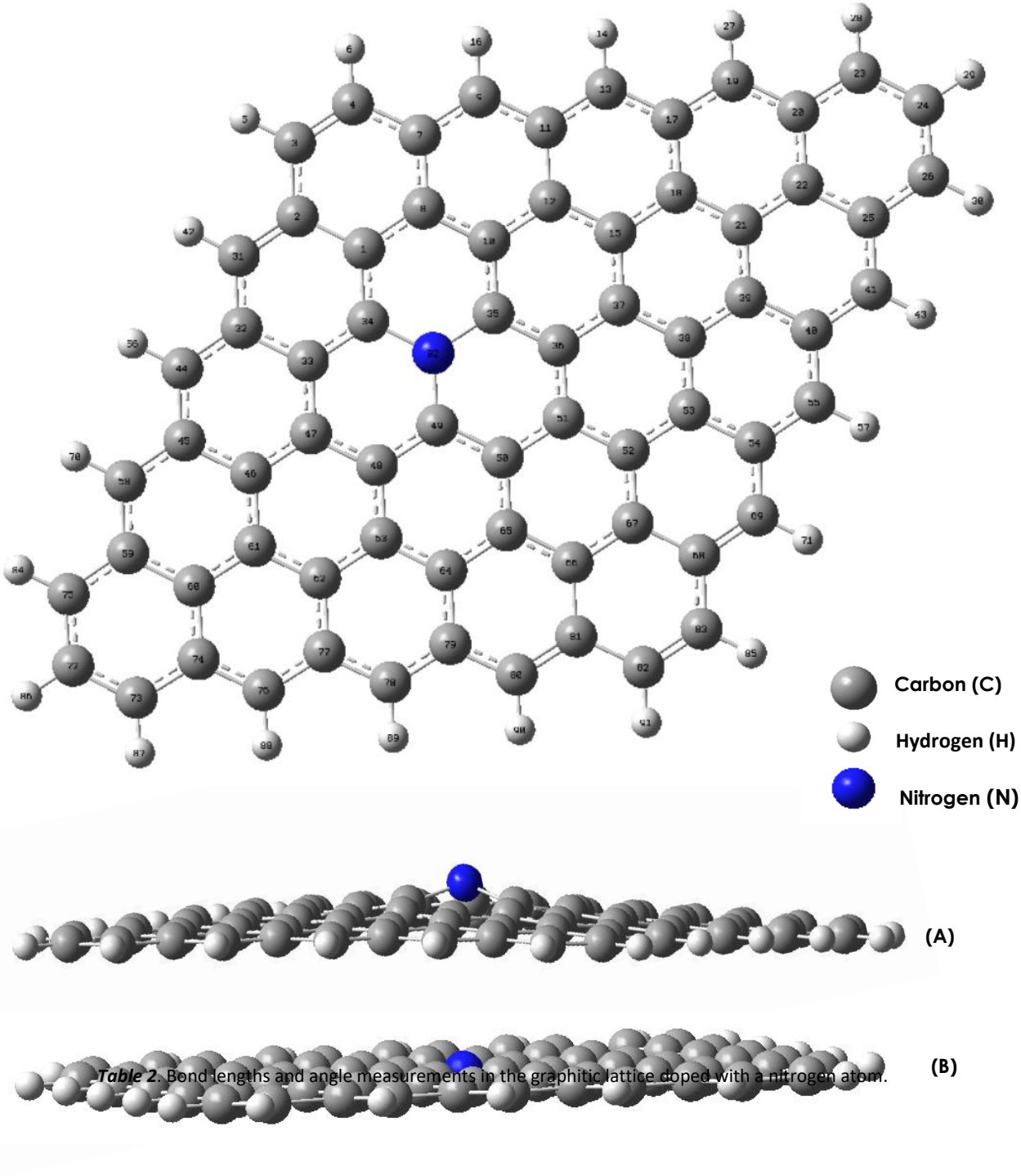


***Table 2***. Bond lengths and angle measurements in the graphitic lattice doped with a nitrogen atom.

***Fig 2***. Graphene lattice with one nitrogen optimized by DFT, using the B3LYP functional. (A) Graphene lattice before the optimization shows deformation. (B) Graphene lattice after optimization, with a plannarestructure.

| OPTIMIZED GRAPHENE WITH NITROGEN B3LYP | |
|---|---|
| **Bond** | **Length (Å)** |
| $C_3$-$H_5$ | 1.08561 |
| $C_{24}$-$H_{29}$ | 1.08572 |
| $C_{84}$-$H_{86}$ | 1.08597 |
| $C_{73}$-$H_{87}$ | 1.08573 |
| $C_3$-$C_4$ | 1.35993 |
| $C_4$-$C_7$ | 1.44411 |
| $C_7$-$C_9$ | 1.38877 |
| $C_3$-$C_2$ | 1.44429 |
| $C_{24}$-$C_{26}$ | 1.39821 |
| $C_{24}$-$C_{23}$ | 1.39294 |
| $C_{70}$-$C_{69}$ | 1.38244 |
| $C_{69}$-$C_{84}$ | 1.44747 |
| $C_{84}$-$C_{83}$ | 1.3593 |
| $C_{73}$-$C_{74}$ | 1.38936 |
| $C_{73}$-$C_{76}$ | 1.40234 |
| $C_{18}$-$C_{21}$ | 1.42414 |
| $C_{54}$-$C_{55}$ | 1.43819 |
| $C_{65}$-$C_{66}$ | 1.41381 |
| $C_{47}$-$C_{62}$ | 1.43322 |
| **Atoms** | **Angle (°)** |
| $C_3$-$C_4$-$C_7$ | 121.326 |
| $C_4$-$C_7$-$C_8$ | 118.047 |
| $C_{20}$-$C_{23}$-$C_{24}$ | 120.802 |
| $C_{23}$-$C_{24}$-$C_{26}$ | 121.082 |
| $C_{82}$-$C_{83}$-$C_{84}$ | 121.677 |

| | |
|---|---|
| $C_{83}$-$C_{84}$-$C_{69}$ | 121.507 |
| $C_{76}$-$C_{73}$-$C_{74}$ | 121.098 |
| $C_{73}$-$C_{74}$-$C_{75}$ | 120.88 |

| OPTIMIZED GRAPHENE WITH NITROGEN B3LYP | |
|---|---|
| **Bond** | **Length (Å)** |
| $N_{92}$-$C_{35}$ | 1.4107 |
| $N_{92}$-$C_{34}$ | 1.4227 |
| $N_{92}$-$C_{49}$ | 1.41979 |
| $C_{35}$-$C_{36}$ | 1.41968 |
| $C_{34}$-$C_{33}$ | 1.40679 |
| $C_{35}$-$C_{10}$ | 1.42263 |
| $C_{49}$-$C_{50}$ | 1.42415 |
| $C_{34}$-$C_{1}$ | 1.42583 |
| $C_{10}$-$C_{12}$ | 1.41806 |
| **Atoms** | **Angle (°)** |
| $C_{34}$-$N_{92}$-$C_{35}$ | 120.165 |
| $C_{34}$-$N_{92}$-$C_{49}$ | 119.547 |
| $C_{49}$-$N_{92}$-$C_{35}$ | 120.289 |
| $N_{92}$-$C_{49}$-$C_{50}$ | 119.637 |
| $N_{92}$-$C_{48}$-$C_{49}$ | 120.263 |
| $N_{92}$-$C_{34}$-$C_{1}$ | 119.47 |
| $N_{92}$-$C_{35}$-$C_{10}$ | 120.112 |
| $N_{92}$-$C_{34}$-$C_{33}$ | 120.122 |

## 4. Conclusion

Comparison of measurements obtained from bond lengths and angles between the nitrogen-doped and undoped graphene lattice, do not show a significant difference. It is necessary to continue this work byincludingmore parameters (e.g. electron density) to see if it is possible to observe an effect that will provide enough information to prove or disapprove our hypothesis, whichis based on the nitrogen inversion and $sp^3$carbon

influence on the activity enhancement of nitrogen-doped carbon electrocatalysts towards the ORR.

## Acknowledgment

The authors thank NANOCOSMOS for the computing time to carry out this work.

## References

[1]Sun, Y., Wu,
J., Tian, J., Jin, C., & Yang, R. (2015). Sulfur-doped carbon spheres as efficient metal-free electrocatalysts for oxygen reduction reaction. *ElectrochimicaActa*, *178*, 806-812.

[1]Wang, S., Zhang, L., Xia, Z., Roy, A., Chang, D. W., Baek, J. B., & Dai, L. (2012). BCN graphene as efficient metal-free electrocatalyst for the oxygen reduction reaction. *AngewandteChemie International Edition*, *51*(17), 4209-4212.

[1]Shui, J., Wang, M., Du, F., & Dai, L. (2015). N-doped carbon nanomaterials are durable catalysts for oxygen reduction reaction in acidic fuel cells. *Science advances*, *1*(1), e1400129.

[1]Wang, S., Dai, C., Li, J., Zhao, L., Ren, Z., Ren, Y., Qui, Y.& Yu, J. (2015). The effect of different nitrogen sources on the electrocatalytic properties of nitrogen-doped electrospun carbon nanofibers for the oxygen reduction reaction. *International Journal of Hydrogen Energy*, *40*(13), 4673-4682.

[1]Zahoor, A., Christy, M., Hwang, Y. J., Lim, Y. R., Kim, P., &Nahm, K. S. (2014). Improved electrocatalytic activity of carbon materials by nitrogen doping. *Applied Catalysis B: Environmental*, *147*, 633-641.

[1]Soo, L. T., Loh, K. S., Mohamad, A. B., Daud, W. R. W., & Wong, W. Y. (2015). An overview of the electrochemical performance of modified graphene used as an electrocatalyst and as a catalyst support in fuel cells. *Applied Catalysis A: General*, *497*, 198-210.

[1] Wang, S., Zhang, L., Xia, Z., Roy, A., Chang, D. W., Baek, J. B., & Dai, L. (2012). BCN graphene as efficient metal-free electrocatalyst for the oxygen reduction reaction. AngewandteChemie International Edition, 51(17), 4209-4212.

[1]Yu, L., Pan, X., Cao, X., Hu, P., &Bao, X. (2011). Oxygen reduction reaction mechanism on nitrogen-doped graphene: A density functional theory study. *Journal of catalysis*, *282*(1), 183-190.

[1]Okamoto, Y. (2009). First-principles molecular dynamics simulation of O 2 reduction on nitrogen-doped carbon. Applied Surface Science, 256(1), 335-341.

[1]Bell, R. P. (2013). The tunnel effect in chemistry. Springer.

[1]Aquino, N., Campoy, G., &Yee-Madeira, H. (1998). The inversion potential for NH 3 using a DFT approach. *Chemical physics letters*, *296*(1), 111-116.

[1]Miyasato, T., Kawakami, Y., Kawano, T., &Hiraki, A. (1984). Preparation of sp3-rich amorphous carbon film by hydrogen gas reactive RF-sputtering of graphite, and its properties. Japanese Journal of Applied Physics, 23(4A), L234.

[1]Li, Y., Zhang, S., Song, H., Chen, X., Zhou, J., & Hong, S. (2015). New insight into the heteroatom-doped carbon as the electrode material for supercapacitors. *ElectrochimicaActa*, *180*, 879-886.

[1]Sanchez-Bojorge, N. A., Rodriguez-Valdez, L. M., Glossman-Mitnik, D., & Flores-Holguin, N. (2015). Theoretical calculation of the maximum absorption wavelength for Cyanidin molecules with several methodologies. *Computational and Theoretical Chemistry*, *1067*, 129-134.

[1]Hernández-Paredes, J., Glossman-Mitnik, D., Duarte-Moller, A., & Flores-Holguín, N. (2009). Theoretical calculations of molecular dipole moment, polarizability, and first hyperpolarizability of glycine–sodium nitrate. *Journal of Molecular Structure: THEOCHEM*, *905*(1), 76-80.

[1]Cervantes-Navarro, F., &Glossman-Mitnik, D. (2013). Density functional theory study of indigo and its derivatives as photosensitizers for dye-sensitized solar cells. *Journal of Photochemistry and Photobiology A: Chemistry*, *255*, 24-26.

[1]Ioniţă, M., Vlăsceanu, G. M., Watzlawek, A. A., Voicu, S. I., Burns, J. S., &Iovu, H. (2017). Graphene and functionalized graphene: Extraordinary prospects for nanobiocomposite materials. *Composites Part B: Engineering*.

# CHAPTER 4
# Modelling and Design

## 4.1 Numerical Modeling of the Cathode Catalytic Layer for Polymeric Membrane Fuel Cell

Juan Guzman, Ivan Bustamante, Roberto Hernandez, Rafael Escarela, Julio Valle, Brenda Martinez

[1]Universidad Politécnica Metropolitana de Hidaldo, Boulevard Acceso a Tolcayuca # 1009 Ex Hacienda de San Javier, C.P. 43860, Tolcayuca, Hidalgo, México

[2]Departamento de Energía, Universidad Autónoma Metropolitana-Azcapotzalco, Av. San Pablo 180 Col. Reynosa Tamaulipas, México, D.F., 02200, México.

[3] Universidad Autonoma del Estado de Hidalgo, Escuela Superior de Apan

* Corresponding author: tel: +52 743 741-10-15, maestro_juan_rafael@hotmail.com

## ABSTRACT

This work presents the theoretical basic models that describe the numerical modeling of the dynamic of the cathode catalytic layer for a polymeric membrane fuel cell (PEM cell). The catalytic layer consists of a carbon film with platinum impurities. In this catalytic layer occur the oxygen-hydrogen reactions. It is calculated numerically the space distribution of the oxygen concentration and the overpotential. It is proposed a methodology that simplifies the numerical calculation using the fact that the space distribution of the overpotential can be approximated by a linear function. In contrast, other models require the space discretization of the overpotential. The proposed equation that describes the space distribution of the oxygen is solved using the finite element method and a iterative scheme. This iterative scheme finds, also, the total current as a function of the overpotential in the cathode. The slope of the space distribution of overpotential is a increasing function of the current; while, the oxygen tend to form a ultra-thin film at high currents. The solution is compared with experimental results available in literature.

***Keywords:*** PEM cell, modeling, numerical, layer, catalytic, cathode

# 4.2 Design of a Novel Electrochemical Membrane Reactor for Hydrogen Production Via the S-NH3 Cycle

R. Márquez-Montes; R. Orozco-Mena; V. Collins-Martínez; E. Herrera-Peraza, D. Chávez-Flores, V. H. Ramos-Sánchez

[1]Facultad de Ciencias Químicas, Universidad Autónoma de Chihuahua, Nuevo Campus Universitario, Circuito Universitario, Chihuahua, Chih., México. C.P. 31125

[2]Centro de Investigación en Materiales Avanzados, S.C., Miguel de Cervantes #120, Complejo Industrial Chihuahua, Chihuahua, Chih., México. C.P. 31109.

* Corresponding author: vramos@uach.mx, (614) 183 1068

## ABSTRACT

The solar-driven hybrid sulfur-ammonia (S-$NH_3$) water splitting cycle is a novel approach to produce hydrogen through a large-scale design. This cycle involves the photochemical oxidation of ammonium sulfite as a solar-photocatalytic hydrogen production step, followed by a high-temperature solar thermochemical oxygen evolution step. This process has many advantages like high-purity hydrogen production at ambient temperature; generation of value-added by-products such as ammonium sulfate; exploitation of the entire solar spectrum and consumption of greenhouse gases (*i.e*. sulfur dioxide). However, there is a lack of information on aspects which have strong impact on hydrogen production rates like pH, kinetic parameters, and/or efficient reactor design. Moreover, an electrochemical hydrogen production step has been proposed to enhance the large-scale viability of the S-$NH_3$ cycle instead the photocatalytic step. This electrochemical approach still makes use of solar energy resources, but *via* thermodynamic cycles which take advantage of the high temperature gases during the oxygen evolution step to produce electricity. In this work, we propose a novel electrochemical reactor for the hydrogen production step in the S-$NH_3$ cycle, which uses an ion-exchange membrane to achieve pH control. The reactor is designed in such a way that allows a suitable and dynamic analysis of hydrogen production at laboratory-scale. A preliminary pH-control analysis was carried out, in which the best reaction rates were achieved using an Anion Exchange Membrane (AEM). Hence, a two-chamber electrochemical membrane reactor separated with an AEM was developed to allow the hydrogen production analysis. The reactor performance was later analyzed using a design of experiments approach to establish optimal operating conditions of voltage and concentration, being 350 mV (*vs* Ag/AgCl) and 55 mM of ammonium sulfite the suggested values. Finally, hydrogen production rate was verified at optimal operating conditions and at 800 mV / 50 mM as well. The electrochemical hydrogen production was proven at room temperature. Currently, kinetic and mass transport studies are being carried out to discuss a better reaction design for this electrochemical approach.

***Keywords:*** Solar Hydrogen; Sulfur-Ammonia; Electrochemical Reactor; Hybrid Cycle.

# 4.3 Design of Production System for the OXHiDROG® System

Maricruz Olalde, Marisol Rico, Ricardo Rodríguez, Juan Manuel Sandoval, Rosa González

[1]Instituto Politécnico Nacional, ESIME-SEPI Unidad Azcapotzalco, Av. de Las Granjas 682, Santa Catarina Azcapotzalco, CP 02250, Mexico City.

2Instituto Politécnico Nacional, ESIME-SEPI Unidad Profesional "Adolfo López Mateos", San Pedro Zacatenco Gustavo A. Madero, CP 07738, Mexico City.

3Instituto Politécnico Nacional, ESIQIE Laboratorio de Foto-Electro catálisis Unidad Profesional "Adolfo López Mateos", Lindavista Gustavo A. Madero, CP 07738, Mexico City.

* 5518201760, molaldep29@mail.com

## ABSTRACT

With the objective of promoting the use of hydrogen as an energy vector, the concept of producing oxyhydrogen gas-generating devices capable of feeding an internal combustion engine was planted, in order to reduce the use of fossil fuels. In this research work the design of the production process of the OXHiDROG® Fuel Saver System is presented, which was designed to be installed in marine vessels. Based on the third and fourth stage of the Advanced Product Quality Planning (APQP) methodology, the production system was established for a run of 90 daily reaction units, in order to satisfy the market demand of the main coastal zones of the country. As a result, the validation of the manufacturing system through the simulation in Flexsim® software is presented.

***Keywords:*** Production system, oxhydrogen, Flexim®, APQP

## 1. Introduction

Hydrogen has the highest energy content per unit mass and the lowest explosive energy per unit of stored energy, which makes it the safest fuel, in addition it has the highest calorific value of all fuels, almost three times higher than gasoline Veziroglu [1].

One way of hydrogen production is the electrolysis, which consists of dissociating the water molecule using electrical energy Sastre [2]. Although it requires a secondary energy, is one of the cleanest procedures besides obtaining a hydrogen of great purity.

Using hydrogen as fuel is an inspiring challenge, which is achieving by designing electrolytic cells. Such is the case of Model ECS-002, which is an oxyhydrogen gas reactor designed to create the fuel saver system called OXHiDROG®, which will be installed in marine vessels to reduce the fuel consumption and to lessen the production of polluting gases.

Hence the need to develop a production system for the OXHiDROG® fuel saver system, and to boost the use of hydrogen as fuel through the diffusion of this technology one hundred percent Mexican.

## 2. Background

The creation of electrolytic cells is not something new. In Mexico the generation of hydrogen is a little developed practice, however in the market already exist devices capable of generating hydrogen. This situation is not entirely good since there are no clear guidelines to guarantee the safety and operation of these reactors; so it is vital to develop safe devices, based on quality standards to ensure their correct operation.

Instituto Politécnico Nacional (IPN), through the electrochemical laboratory of Escuela Superior de Ingeniería Química e Industrias Extractivas (ESIQIE), has contributed to the design and manufacture of electrolytic cells, obtaining oxyhydrogen gas reactors with excellent performance indexes. This is the case of the prototype Model ECS-002 **Fig.1**, which is the fourth prototype of dry cell created, and is capable of producing 1.32 l / min. oxyhydrogen gas with an expenditure of 40 amperes. The estimated cost of each reactor is approximately $ 2,945.00.

The goal is the creation of the OXHiDROG® fuel saver system, which is made up of 6 Model ECS-002 oxyhydrogen reactors and a control unit.

Taking advantage of the geographical situation of our country is intended to direct the supply of the OXHiDROG® fuel saving system to marine vessels; Due to the number of vessels that are registered in each port and terminal.

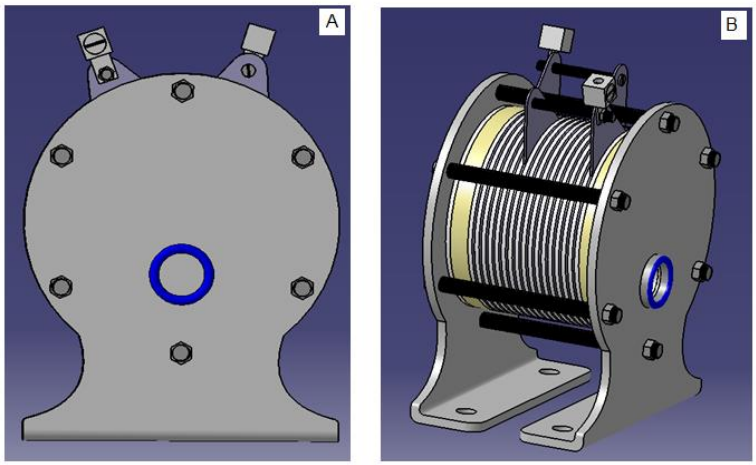


**Fig. 1.**Model ECS-002 Oxyhydrogen Reactor Model ECS-002. (a) Front view; (b) Isometric view.

## 3. Development

### 3.1 Methodology

Advanced Product Quality Planning (APQP) methodology Chrysler [3] was selected to meet the quality assurance requirements of ISO 9001-2008.

The design of the production system for the OXHiDROG® fuel saver system is based on the third and fourth stage of this methodology, due to the need to design and develop the product process **Fig. 2**.

This work is focused solely on the development of the manufacturing system and the control plans that make it possible to move from prototype to a product.

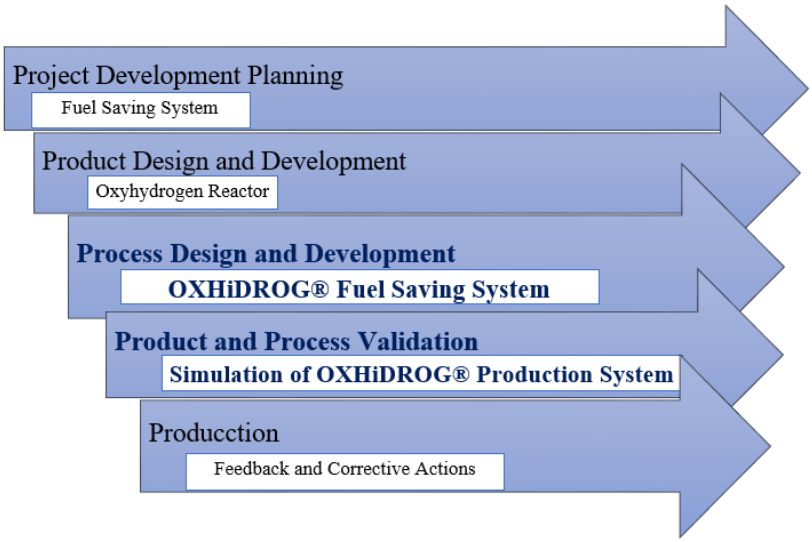


**Fig. 2.** Product Process Design and Develop

## 3.2 Market

The OXHiDROG® fuel saver system is designed to overfeed a Diesel cycle internal combustion engine from 350 to 550 hp, which means that the system is functional only for boats that have a propulsion system within this power range.

According to the National Fleet Statistics of 2014, carried out by Secretaría de Comunicaciones y Tranposrtes (SCT) [4], total number of vessels registered is 172, 265; Of which 169 695 have a TRB <100, that means that they are within the power range.

Based on this number, the production lot size was determined.

### 3.2.1 Production Lot

To supply to total of the national fleet, the Pareto Principle is applied which states the following: “80% of the consequences are derived from 20% of the causes" Verdoy [5]; that is, the production lot size corresponds to 80% of the sales coming from 20% of the demand. In other words the level of production corresponds to 80% of the 20% of the total existing demand.

So, the production lot for OXHiDROG® fuel saver systems should be calculated for 27,151 boats. This means that to achieve production in 5 years, 15 OXHiDROG® systems must be produced daily.

Due to each system has 6 reactors, daily production of Model ECS-002 oxyhydrogen reactors must be 90 **Table 1**.

**Table 1.** Production Detail.

| | |
|---|---|
| Total Marine vessels | 27,151 |
| Total Time in years | 5 |
| Total OXHiDROG® System per year | 5,400 |
| Total OXHiDROG® System per month | 450 |
| Total oxyhydrogen Reactors per month | 2,700 |
| Total OXHiDROG® System per day | 15 |
| Total oxyhydrogen Reactors per day | 90 |

## 3.3 Model ECS-002 Oxyhydrogen Reactor

The Modelo ECS-002 is composed of the parts described in **Fig. 3**. The production line to be focused on the manufacture of the Model ECC-02 Oxyhydrogen Reactor and on the auxiliary systems, which are shown in **Table 2**.

| Components | Figure |
|---|---|
| **Covers** |  |
| **Electrodes** |  |
| **Seals and tanks** |  |

**Fig. 3.** Components ofModel ECC-02 Oxyhydrogen Reactor

**Table 2.** Auxiliary systems

| System | Description |
|---|---|
| Circulation System | Electrolyte flow, between the container and the electrolytic cell. |
| Structural System | It is the whole system casing. |
| Control System | Controls the injection of Oxyhydrogen gas into the engine |

## 3.4 Production System

The production process consists of 6 phases, which are Input, Forming, Conditioning, Assembly, Testing and Output. Determining the phases is vital to know the minimum number of workstations, the flow direction and also to identify the type of plant distribution.

The type of plant distribution will be structured by manufacturing cells, because of the production line is focused on both the process and the product. Next the block diagram of the industrial building is show in **Fig. 4.**

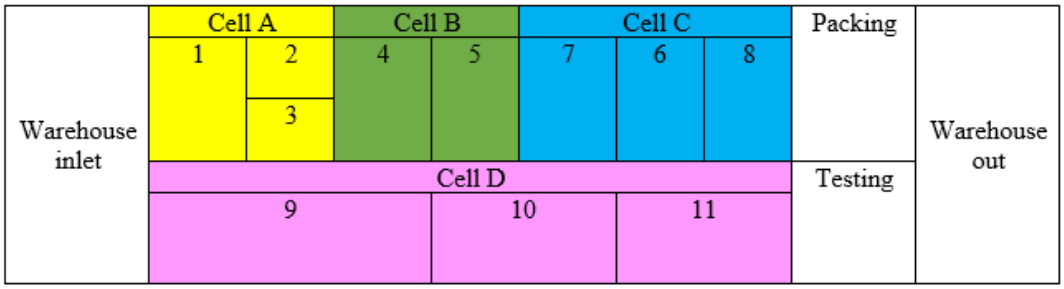


**Fig. 4.** Block Diagram of Plant Layout

The manufacturing process of the OXHiDROG® Fuel Saver System begins with the entry of stainless steel, nylamid and teflon.

The first process is the cutting of the electrodes, the next process is the drilling and then the electrodes are nickel plated. In parallel, the cut of the covers is done, then they are folden.

For the manufacture of seals and tanks, the geometries are cut and passed through a finishing process. The following consists of the assembly of the oxyhydrogen reactors. In parallel, the assembly of the circulation system, the structural system and the control system are carried out.

Finally, the final assemblies corresponding to the block of 6 oxyhydrogen reactors are realized with each of the auxiliary systems.

Finally, the entire device is analyzed at the test station and sent to the packing station for its exit to the finished product warehouse.

## 3.5 Simulation

The simulation of the production system is done using the software Flexim [6], which allows real-time knowledge of the behavior of a process through statistical control, and also predicts results that allow optimizing the entire production system.

The top view of the simulation of the production process for the OXHiDROG fuel saver system is shown in **Fig. 5.** Having this configuration allows you to save space, speed up the movement of materials, use an operator in various tasks and easily locate the state of the process at any time


**Fig. 5.** Simulation of the production process for the OXHiDROG fuel saver system

## 4. Results

Through the statistical study, it was known that achieving the goal of daily production is possible through the implementation of double processes.

The production behavior per hour is observed in **Fig. 6.**

Producing 15 OXHiDROG Fuel Saver Systems per day is achieved in less than 21 hours, which means setting 3 production shifts.

At least 7 workers are required per shift and it is possible because of the pace of production that an operator performs several processes.

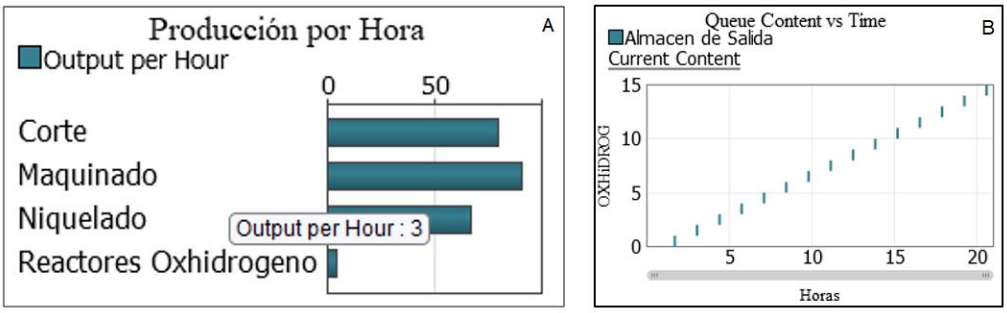


**Fig. 6.** Graphic Production Behavior. (a) Production per hour; (b) OXHiDROG Production

## 5. Conclusion

The use of software, such as the FlexSim®, is a reliable tool that helps to obtain simulations to plan and modify the selection of processes to reach the optimum. At the beginning of this study, it was considered the use of dies for the manufacture of circular geometries in stainless steel, however, according to the results obtained, the finish results out of tolerance and it is necessary to add a finishing process, this means greater Time of production that prevents reaching the desired level of production, so a viable solution is to obtain all the geometries by means of Computer Numerical Control (CNC).

As for the optimization of plant distribution, the software proposes some changes in the organization of the processes with the objective of avoiding long shifts in the flow of material and operators.

## Acknowledgements

To: 1. Government of México, 2. Instituto Politécnico Nacional (IPN), 3. Escuela Superior de Ingeniería Mecánica y Eléctrica (ESIME), 4. Escuela Superior de Ingeniería Química e Industrias Extractivas (ESIQIE), 5. Consejo Nacional de Ciencia y Tecnología (CONACYT), 6. Authors, and 7. The organizers of the event by its attentive invitation.

## References

[1] Veziroglu, T. (2002). Current Status of Hydrogen Energy. Renewable and Sustainable, 6, 141-179.

[2] Sastre Soriano, “Aplicación de la energía eólica para la producción de hidrógeno mediante electrólisis”, Escola Universitaria d'Enginyeria Técnica Industrial de Barcelona, Universidad Politécnica de Catalunya, 2010.

[3] Chrysler Corporation, F. M. (Julio de 2008). Advanced Product Quality Planning and Control Plan. Estados Unidos de Norteamerica.

[4] Secretaría de Comunicaciones y Transportes. Obtenido de http://www.sct.gob.mx/puertos-y-marina/puertos-de-mexico/

[5] Verdoy, Juan Pablo, Mahiques Mateu, Jorge, Segasta Pellicer, Santiago, Sirvent Prades, Raúl, “Manual de Control Estadístico de Calidad: teoría y aplicaciones”, Publicacions de la Universitat Jaume, I.D.L., 2006

[6] FlexSim Obtenido de https://www.flexsim.com/es/

# 4.4 Statistical analysis for the electrochemical performance of a 3D reconstructed catalytic layer

Romeli Barbosa

[1]Universidad de Quintana Roo, Boulevard Bahía s/n, Chetumal, Q. Roo, México, 77019

* Corresponding author: +52 983 1566032; romelix1@gmail.com

## ABSTRACT

The structure of a catalyst layer (CL) in a proton exchange membrane fuel cell (PEMFC) varies according with the deposition technique and the chemical composition that build it up. Then, the electrical, ionic and catalytic properties depend on the final structure. These characteristics have also an impact on the overall response of the PEMFC. In this work, stochastic reconstruction of the microstructure of a PEMFC CL and a scaling method are used to determine the effective transport coefficients and a statistical electrochemical surface area of platinum associated with the active sites. The case study contains three stages: 1) the charge transport continuity equation is used to determine conduction efficiency. 2) The platinum surface is determined by a statistical algorithm that considers the percolation and the three-phase union condition. 3) Finally, an analytical model for electrochemical behavior is applied. These numerical and analytical models are applied to hypothetical microstructures of the carbon support, ionomer electrode load and platinum to carbon weight ratio.

***Keywords:*** Stochastic simulation; Scaling method; PEMFC catalyst layer.

# 4.5 Adsorption and dissociation of $O_2$ on pure Pd, Ni-doped Pd and NiPd alloy clusters

Luis López-Sosa, Heriberto Cruz-Martínez, Patrizia Calaminici, Omar Solorza-Feria

[1]Departamento de Química, CINVESTAV, Av. Instituto Politécnico Nacional 2508, CP: 07360, Ciudad de México, Mexico.

[2]Programa de Doctorado en Nanociencias y Nanotecnología, CINVESTAV, Av. Instituto Politécnico Nacional 2508, AP: 14-740, 07000 Ciudad de México, Mexico

*Corresponding author: Tel.: +52 (55) 5747 3800, ext. 4473, e-mail: hcruzm@cinvestav.mx

## ABSTRACT

Activation energies and the adsorption-dissociation pathways of molecular oxygen on the ground state structures of the pure $Pd_n$, Ni-doped $Pd_{n-1}$ and $Pd_{n/2}Ni_{n/2}$ alloy (n=4, 6, 8 and 10) clusters were studied. All calculations were carried with the auxiliary density functional theory as implemented in the deMon2k program. The calculations were performed using the functional PBE98-PBE96 in combination with the DZVP-GGA basis sets for the Ni and O atoms whereas palladium atoms are described using an 18 electron quasi-relativistic effective core potential. The restricted open-shell Kohn–Sham methodology was employed to avoid spin contamination. For each cluster size, several molecular oxygen adsorption sites were studied to determine the more favored adsorption site on the structures. The transition state search of the molecular oxygen dissociation on the clusters were performed using a hierarchical transition state search algorithm, it combines the so-called double-ended interpolation method with the uphill trust region method. For the Ni-doped $Pd_{n-1}$ and $Pd_{n/2}Ni_{n/2}$ (n=4, 6, 8 and 10) clusters the molecular oxygen adsorption on the Ni atoms is favored. Ni atoms modify the reactivity of the Ni-doped $Pd_{n-1}$ and $Pd_{n/2}Ni_{n/2}$ (n=4, 6, 8 and 10) clusters towards the adsorption and dissociation of molecular oxygen.

***Keywords:*** Transition state; Activation energy; Auxiliary density functional theory; Bimetallic clusters

# 4.6 Thermodynamic Evaluation during the Reduction of MWO4 (M = Fe, Mn, Zn) with Methane for the Production of Hydrogen-Syngas

V. Collins-Martínez, M. J. Meléndez-Zaragoza, A. López-Ortiz

Departamento de Ingeniería y Química de Materiales, Centro de Investigación en Materiales Avanzados, S.C., Miguel de Cervantes 120, Chihuahua, Chih., México, 31136, México.

**ABSTRACT**

Different types of $MWO_4$ (M = Fe, Mn, Ni) were evaluated through thermodynamic analysis and process simulation for the production of hydrogen-synthesis gas (syngas). The partial oxidation (POX) of methane is a more efficient reaction than steam reforming (SMR). However, currently the dominant technology in hydrogen production is through SMR. To overcome one of the most important disadvantages of POX reaction, which deals with the use of pure oxygen as a gas feed, a mixed metal oxide ($MWO_4$, M = Fe, Mn, Ni) is proposed as an oxygen carrier (POX-MeO). The aim of the present study is to evaluate the feasibility of these tungstate metal oxides through the use of thermodynamic analyses and process simulations of an arrangement of two reactors. In the first reactor POX-MeO reactions ($CH_4 + MWO_4 = H_2 + CO + M + W$; $CH_4 + MWO_4 = H_2 + CO_2 + M + W$) and the undesirable coal formation ($CH_4 = C + 2H_2$) are carried out. While in the second reactor, solid products of the first reactor are combined with steam to gasify the previously deposited coal ($C + H_2O = H_2 + CO$; $C + 2H_2O = 2H_2 + CO_2$) and simultaneously regenerate the metal oxide to produce syngas ($M + W + H_2O = MWO_4 + H_2$). Then, the regenerated oxide is recycled back to the first reactor to make a continuous process. Results of simulation of this process with the different $MWO_4$ oxides are presented using Aspen Plus.

***Keywords:***Thermodynamicanalysis, chemical looping, tungstate oxides, hydrogen production, syngas.

## 1. Introduction

Despite the current weakness of world energy markets and the sluggish Chinese growth, demand for energy will continue to grow over the next 20 years and even later as

the world economy expands and more energy is needed to push for greater industrial activity. According to the 2016 BP World Energy Outlook [1], global energy demand is expected to increase by 34% between 2014 and 2035, at an average of 1.4% per year. This growth in demand generally includes significant changes in the composition of the energy mix, with faster growth of low-carbon fuels than those with higher emissions as the planet begins the transition to a future with lower carbon emissions.

Even though the fast growth in other energy sources, it is predicted that fossil fuels will continue to be the predominant form of energy by 2035, accounting for 60% of the expected increase in demand and almost 80% of the world's total energy supply by 2035.Natural gas will be the fastest growing fossil fuel, with an annual increase of 1.8%, and oil will grow at a constant rate of 0.9% per year, although its share in the energy mix will continue to decline. Coal growth is expected to decline dramatically, so that by 2035 its share of the energy mix will be the lowest ever, being replaced by gas as the second largest source of fuel. Furthermore, natural gas supply is growing strongly thanks to a large increase in the production of shale gas worldwide, which is expected to grow by 5.6% annually. The share of shale gas in total gas production will increase from 10% in 2014 to almost 25% in 2035 [1].

Moreover, hydrogen has been employed as a common raw material for a wide variety of processes, for example, in ammonia synthesis, pharmaceuticals, hydrogen peroxide generation,electronics and petrochemical industries [2, 3]. Nowadays, hydrogen has been considered as aclean, renewable and efficient fuel since, when used in combination with fuel cells, hydrogen can produce heat and electricity with the only waste being pure water. The fact that hydrogen is not a primary energy source like most common fossil fuels (coal or natural gas) makes it an energy vector that can be produced from many traditional energy systems (most hydrogen today is produced from natural gas). However, in order for hydrogen to be considered as a clean fuel this must come from renewable energy sources.

Furthermore, of comparable importance to hydrogen, the mixture of hydrogen and carbon monoxide ($H_2$ + CO), commonly called synthesis gas or syngas [4-6] is a valuable raw material for various industrial applications.Technically, syngas can be generated from any hydrocarbon feedstock [7]. However, in most applications, natural gas is the predominant raw material [4].

Steam reforming of natural gas (mainly methane, SMR, reaction 1) is the main process for the production of syngas [7-10]. However, partial oxidation of methane (POX, reaction 2) for the production of syngas has been reported to present higher efficiencies than SMR [11]. Furthermore, POX exhibits other benefits such as: less investment required to produce a syngas at a molar ratio of $H_2/CO = 2$, an inherent exothermic reaction of this process, thus inferring substantial energy savings, fast kinetics derive in the useof small

reactors and high methane conversions (≈90%) with elevatedselectivity towards hydrogen (94 ~ 99%). However, this process also presents some disadvantages such as high operating temperatures (900 ~ 1000°C), and the need for an oxygen plant, which makes this a highlycost process [11].

$$CH_{4(g)} + H_2O_{(g)} = 3H_{2(g)} + CO_{(g)} \quad (1)$$

$$2CH_{4(g)} + O_{2(g)} = 4H_{2(g)} + 2CO_{(g)} \quad (2)$$

In an attempt to solve these disadvantages research has been conducted in order to reduce production costs of syngas through POX and to lower operating temperatures. A proposed strategy is the elimination of the oxygen plant, which represents about half of the investment [12]. An example of such achievements is the use of metal oxides as oxygen carriers, based on a variation of the partial oxidation of methane to produce syngas and/or hydrogen involving two steps: first, the necessary oxygen for partial oxidation is provided by a metal oxide (MeO) containing oxygen, which is released under a reducing atmosphere to produce syngas and the reduced metal (Me) (Reaction 3); while in the second, the reduced metal is reoxidized with steam to produce hydrogen and the MeO (Reaction 4).

$$CH_{4(g)} + MeO = 2H_{2(g)} + CO_{(g)} + Me \quad (3)$$

$$H_2O_{(g)} + Me = MeO + H_{2(g)} \quad (4)$$

The MeO is then used again in reaction (3) to complete a full cycle, this process is called POX-MeO or chemical looping partial oxidation (CLPO) [5, 11]. It is important to notice that the overall reaction of this process is comparatively equal to the SMR [12]. TheCLPO system composed of two reactors.In the first reactor, called the fuel reactor, reaction (3) takes place, where a fuel such as methane is fed together with a fresh metal oxide (MeO). The gaseous products from the fuel reactor may include $H_2$, CO, $CO_2$ and $H_2O$, while the reduced oxygen carrier (Me) is the only solid product, which is sent to a second oxidation reactor where a gaseous oxidant (steam) reacts with the reduced metal through reaction (4) producing $H_2$ and the oxidized oxygen (OC) carrier (MeO), which is sent back to the fuel reactor to complete one full cycle of the OC. Partial oxidation of methane under this concept was first proposed by Ryden and Lyngfelt [13] and followed by Mattisson and Lyngfelt [14, 15]. Chemical looping partial oxidation (CLPO) allows for partial oxidation of the fuel using the metal oxide concept. In contrast, in a conventional partial oxidation only pure oxygen is used, while autothermal reforming uses both steam and oxygen.The reactions used in CLPO (reactions 3 and 4) are similar to conventional reforming and partial oxidation, except the metal oxide provides oxygen to the fuel. From reaction (4) only

a limited number of metals can be oxidized by steam, such as Fe, Co, Mn, Zn, Mo and W among others [16].

Processes that make use of this CLPO concept include the syngas chemical looping (SCL) process developed by Tong et al. [17] the iron-based IGCC process proposed by Cormos [18], the one-step decarbonization process envisioned by Mizia et al. [19] and the three-reactor scheme projected by Kang et al. [20]. Hydrogen production using steam to oxidize reduced iron employing solar energy to reduce this metal has also been reported by Nakamura [21]. Specifically, for the chemical looping process towards the production of syngas (CLPO), the main metal oxides studied have been Ce, Fe, and Ni.

Because of the many limitations (thermodynamics and kinetics) of single metal oxides, binary metal oxides have been proposed to enhance the selectivity of the oxygen carrier for syngas production. An example of these materials are mixed oxides with spinel structure, perovskite-type mixed oxides composed of transition metals that function not only as lattice oxygen carriers but also as catalysts for $CH_4$ activation as reported by Ryden et al. [22]. Mihai et al. [23] indicate that ceramic materials such as perovskite-type complex oxides ($ABO_3$)offer a well-defined structure and high thermal stability as oxygen carriers for CLPO applications and have been widely studied in some important areas of solid state chemistry, catalysis, advanced materials and physics. These researchers claim that the cation A is responsible for the high thermal resistance, while the high valence cations at the B site provide the catalytic activity. Therefore, both A and B cations can influence the stability of the perovskite structure as well as the reactivity and selectivity of lattice oxygen during the oxidation of $CH_4$. Examples of these perovskite materials include $LaFeO_3$, and $La_{0.7}Sr_{0.3}FeO_3$.

Furthermore, some researchers have centered their efforts in the synthesis of oxygen carrier materials for syngas production based in the so called concept of “solid diffusional reactive barrier” in order to avoid sintering effects in the material. This concept consists in a well-defined crystalline structure of a mixed-metal oxide that when exposed to a reducing environment such as $CH_4$, this changes to reduced metallic species. Then, when these reduced metallic mixture is reoxidized using, steam, these come back to its original crystalline structure. The reconstitution of the original crystalline structure is thought to be responsible for the high thermal stability of these materials avoiding sintering effects, responsible for the reduction of activity when oxygen carriers are exposed to several reduction-oxidation cycles. Examples of these type of materials include iron-titanium metal oxide ($Fe_2TiO_5$) proposed by Luo et al. [24] for the oxidation of methane under a CLPO scheme. Thermodynamic simulations and experimental results have confirmed that the CLPO chemical looping process using the $Fe_2TiO_5$ oxygen carrier is capable of producing >90% purity syngas at nearly a 2:1$H_2$:CO ratio. Furthermore, De los Rios et. al [2, 11, 25] proposed cobalt tungstate ($CoWO_4$) together with a nickel catalyst as an oxygen carrier for

CLPO to produce high purity syngas and found that this material is very stable to cyclic tests subjected to partial oxidation of methane to syngas production.

Between these two materials $CoWO_4$ is a very remarkable material, since the reduced form of $Fe_2TiO_5$ with methane is reported to lead to a mixture of Fe and $FeTiO_3/Fe_2TiO_4$ [24]. Whereas, the reduction of $CoWO_4$ produces only Co and W metallic species and these when reoxidized with steam generate $CoWO_4$ again.

Following this innovative concept, a number of other possible tungstate species are feasible to be considered under these moieties. For example, tungstate species having the structure $MWO_4$are expected to produce syngas during the reduction step with $CH_4$ and be reoxidized back again with steam according to the following reactions:

$$4CH_{4(g)} + MWO_4 \rightarrow 8H_{2(g)} + 4CO_{(g)} + M + W \quad (5)$$

$$CH_{4(g)} + MWO_4 \rightarrow 2H_2O_{(g)} + CO_{2(g)} + M + W \quad (6)$$

$$CH_{4(g)} \rightarrow C + 2H_{2(g)} \quad (7a)$$

$$2CO_{(g)} \rightarrow C + CO_{2(g)} \quad (7b)$$

$$4H_2O_{(g)} + M + W \rightarrow MWO_4 + 4H_{2(g)} \quad (8)$$

$$C + H_2O_{(g)} \rightarrow H_{2(g)} + CO_{(g)} \quad (9a)$$

$$C + 2H_2O_{(g)} \rightarrow 2H_{2(g)} + CO_{2(g)} \quad (9b)$$

Where M = Fe, Mn or Ni. The POX-MeO-1 reaction (5) produces syngas (CO + $H_2$) together with M and W reduced metallic species, while POX-MeO-2 reaction (6) describes the possible complete oxidation of methane to produce $CO_2$ and $H_2O$. Under these oxygen starving conditions, other reactions may arise such as coal formation reactions 7(a) and 7(b), which correspond to the methane decomposition and Boudard reactions, respectively. The reoxidation of the metallic Co and W species with steam is described by reaction (8) to produce the $MWO_4$ oxygen carrier and $H_2$, while if some carbon may have formed according to previous reactions 7(a) and 7(b), coal gasification reactions (9a) and (9b) may occur during the reoxidation stage leading to further hydrogen production and carbon oxide species (CO and $CO_2$).

Due to the remarkable reaction behavior of the $CoWO_4$ oxygen carrier towards the production of syngas from methane and the reoxidation of its reduced species (Co and W)

with steam to further produce $H_2$, makes this reaction concept very attractive to be evaluated using other metallic tungstates such as $FeWO_4$, $MnWO_4$ and $NiWO_4$under a CLPO reaction scheme. Therefore, the aim of the present study is to evaluate the feasibility of these tungstate metal oxides through the use of thermodynamic analyses performed by process simulations to evaluate the feasibility of these tungstate oxides to be used under a chemical looping partial oxidation (CLPO) reaction scheme for the production of hydrogen and/or syngas.

## 2. Methodology

Process Simulation

Concentration at equilibrium calculations in the CLPO for the $MWO_4$ oxygen carriers will be performed using the RGIBBS reactor model from Aspen Plus© process simulation software. This reactor model has been successfully employed in the simulation of several chemical looping reaction systems [26, 27, 28 and 29]. Thisreactor model is able to determine the equilibrium amount of all different possible product species as well as their phases (gas, solid and liquid). For the methane partial oxidation (fuel reactor) and $H_2$ production (steam oxidation reactor) systems the gaseous species included were: $CH_4$, CO, $CO_2$, $H_2$, and $H_2O$, while solid species included: C, $NiWO_4$, $MnWO_4$, $FeWO_4$, Ni, Fe, Mn, W, $WO_2$ and $WO_3$. The RGIBBS module is based on the Gibbs free energy minimization technique (also called the nonstoichiometric method), details of this method can be found elsewhere [30, 31].

Process simulations using Aspen Plus© will concentrate in determining process material and energy balances, as well as optimal operating conditions in both reactors and in the entire process [1, 31].During the thermodynamic simulation work, process simulation variables studied were: fuel reactor temperature, which varied from 100-1000 °C at 1 atm, $MWO_4$ molar feed, which varied from 1 to 3 kmol/h, while fixing 4 kmol/h of $CH_4$. Whereas, in the oxidation reactor $H_2O$ molar feed rate was varied from 3 to 9 kmol/h, in a temperature range of 200-700 °C. Other simulation conditions employed include: the use of a thermodynamic system based on the Redlich-Kwong-Aspen equation of state (EOS) to calculate the physical properties of the chemical species employed, which is an adequate EOS in processes involving hydrocarbons and their mixtures with polar components, and combinations of small and large molecules or hydrogen-rich systems at medium and high pressures [32]. Also, the calculation basis for $CH_4$ feed to the fuel reactor was fixed at 4 kmol/h, while calculations in the fuel reactor aimed for conditions where no carbon formation was allowed. It is important to state that all the present simulation calculations are based on theoretical thermodynamic considerations and these are to be taken as a guide to further experimental evaluation of the reaction CLPO process, since no

heat and mass diffusional limitations as well as kinetics effects were taken into account for the conformation of the present thermodynamic and process analysis.

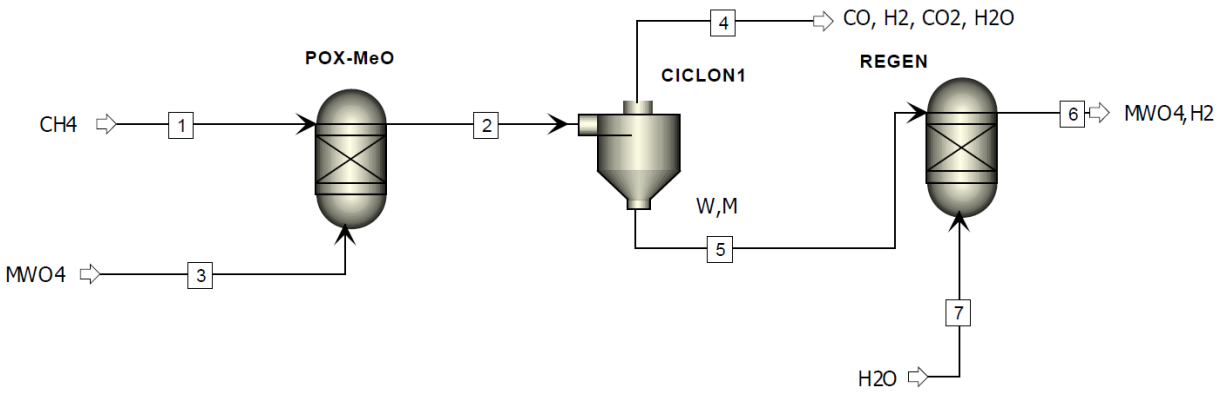


Figure 1. Process simulation flowsheet

The CLPO process for $MWO_4$(M = Fe, Ni) OC scheme is shown in Figure 1. Here, the reactors used (POX-MeO and REGEN) used the RGIBBS model. In the first fuel (POX-MeO), the oxidation of methane in the presence of the tungstate oxide ($MWO_4$) takes place, while in the second (REGEN reactor) tungsten and the reduced metal reoxidation reactions occur in the presence of steam, thus regenerating the tungstate oxide and producing hydrogen, as well as the removal of any carbon deposits on the oxygen carrier. A cyclone at the outlet of the first reactor (CICLON1)is used to separate the solid and gaseous products resulting from this reactor. In the case of the first separation, the expected resulting solids from the POX-MEO reactor (M, tungsten, and a possible small fraction of deposited carbon) are carried out as reagents for the second reactor (REGEN) and the separated gas (stream 4) constitutes the syngas. In the REGEN reactor, according to reactions (8), (9a) and (9b), the solid products andthe tungstate oxide (stream 6) constitute a hydrogen-rich product.

In order to find optimal variables of the CLPO process, several sensitivity analyzes will be performed and these are aimed to obtain the highest yield towards syngas (CO + $H_2$) in the fuel reactor, while avoiding carbon formation and to produce a rich hydrogen gaseous stream in the oxidation reactor. The first sensitivity analysis is performed in the fuel reactor aiming to find the molar feed of $MWO_4$ to react with 4 kmol/hr of $CH_4$ to produce the maximum amount of syngas (CO + $H_2$), while avoiding carbon formation. Also, in the same sensitivity analysis the temperature of this operation is varied to determine the optimal temperature to obtain the highest yield towards syngas production. The second sensitivity analysis is to be carried out in the steam oxidation reactor by studying the variation of the operating temperature and the molar flow of steam feed to achieve complete regeneration

of $MWO_4$ from the solid reaction products comingfrom the fuel reactor (M and W species) with steam to produce a rich hydrogen gaseous stream. Once the optimal operating variables of the simulation are determined, the resulting mass and energy balances of the process are established.

## 3. Results and Discussion

Thermodynamic Analysis

Figure 2 presents results from a thermodynamic analysis consistingin the calculation of the equilibrium amounts within the POX-MEO reactor using the RGIBBS model using a $CH_4$molar feed of 4 kmol/h.

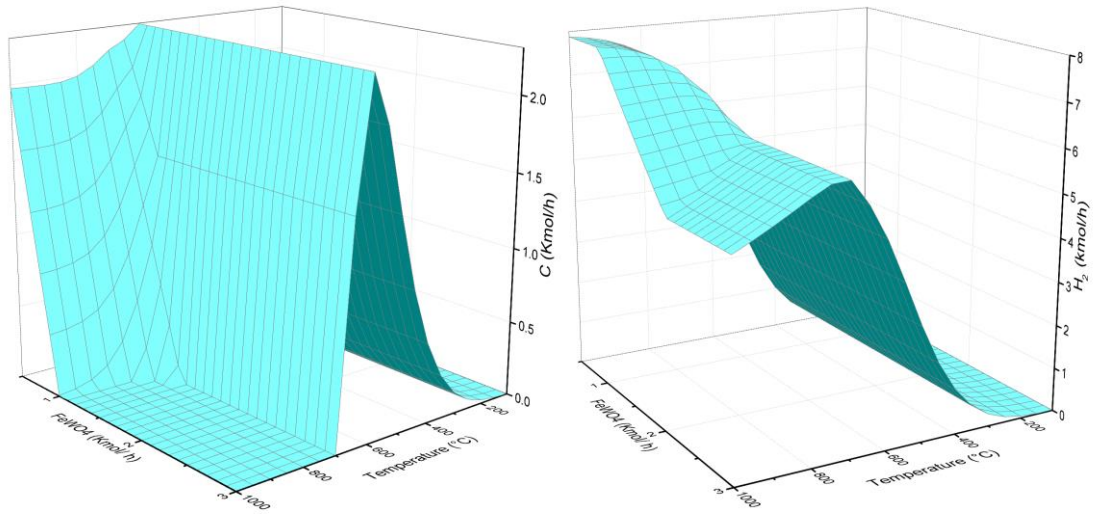


Figure 2. Thermodynamic analysis of the POX-MEO reactor with $FeWO_4$, C (left) and $H_2$ (right)).

In Figure 2 the carbon formation C (kmol/h) is plotted as a function of the $FeWO_4$ feed (kmol/h) and temperature (°C). In this Figure it is evident that the null generation of deposited carbon in the reaction products from the POX-MEO reactoris comprised in a region from 700 °C and 1.4-3 kmol/h of $FeWO_4$ and 1000 °C and 1.2 kmol/h of $FeWO_4$. Within this region according to Figure 2 the maximum hydrogen production that can be achieved is 6.51 kmol/h of $H_2$ at 750 °C and 1.5 kmol/h of $FeWO_4$.

Otherwise, Figure 3 shows results from the thermodynamic analysis of the $MnWO_4$ oxygen carrier in the POX-MeO reactor. Again, in this Figure the generation of deposited carbon

and the hydrogen production is plotted as a function of $MnWO_4$ feed in kmol/h and temperature (°C).

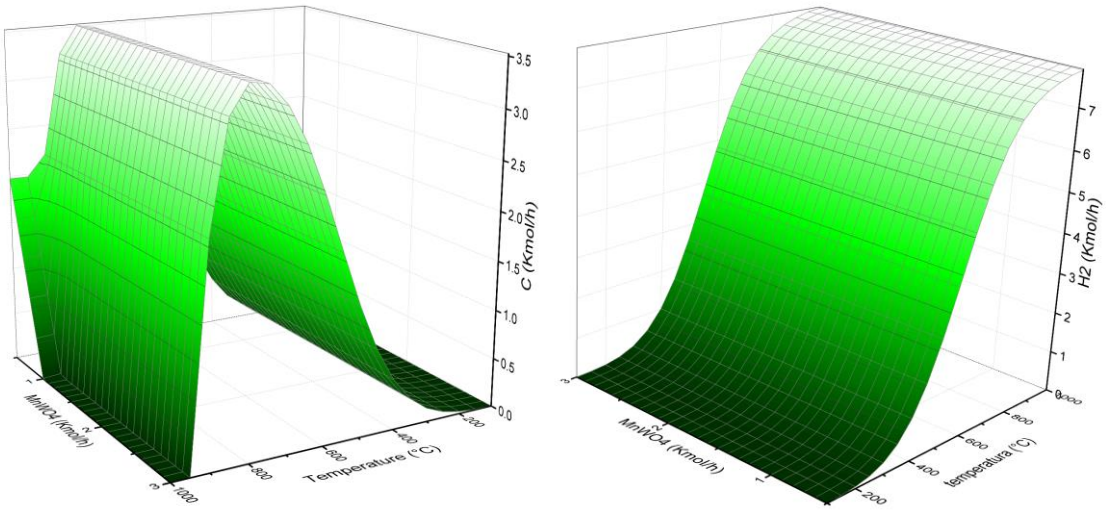


Figure 3. Thermodynamic analysis of the POX-MEO reactor with $MnWO_4$, C (left) and $H_2$ (right)).

In this Figure it is apparent that no carbon formation within the reaction products from the POX-MEO reactor is generated in a square small region formed at 950-1000 °C and 1.1-3 kmol/h of $MnWO_4$. While, maximum hydrogen production within this small region is of 7.83 kmol/h of $H_2$ at 950 °C and 1.1 kmol/h of $MnWO_4$.

Moreover, Figure 4 shows results from the thermodynamic analysis of the $NiWO_4$ oxygen carrier in the POX-MeO reactor. In this Figure the formation of deposited carbon and the hydrogen production is plotted as a function of $NiWO_4$ feed in kmol/h and temperature

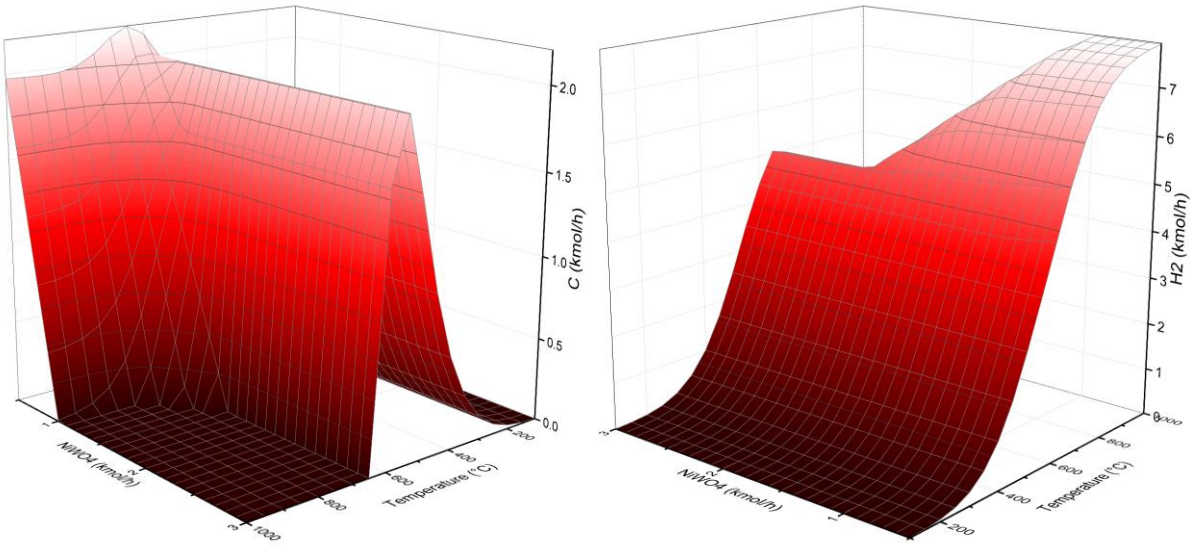

(°C).

Figure 4. Thermodynamic analysis of the POX-MEO reactor with $NiWO_4$, C (left) and $H_2$ (right)).

In Figure 4 the carbon formation C (kmol/h) is plotted as a function of the $NiWO_4$ feed (kmol/h) and temperature (°C). In this Figure it is evident that no generation of deposited carbon in the reaction products from the POX-MEO reactor is included in a region from 700°C @ 3 kmol/h of $FeWO_4$ and 650 °C@ 3 kmol/h of $NiWO_4$. Within this region according to Figure 4 the maximum hydrogen production that can be achieved between 700°C @ 1.5 kmol/h $NiWO_4$and650°C@ 3kmol/h $NiWO_4$, where the H2 production varies from 5.98 to 6.62 kmol/h of $H_2$, respectively.

According to results from Figures 2-4 maximum free-carbon hydrogen production can be achieved by either $FeWO_4$or $NiWO_4$ oxygen carriers. It is important to note that even though both oxygen carriers produce an important amount of $H_2$ within the no carbon formation region, $NiWO_4$ presents a wider range of operation for the production of hydrogen. Furthermore, reduced Ni according to POX reaction (5) will produce metallic Ni, which is a very well-known active metal catalyst for the dry as well as for the steam reforming of methane.

Therefore, due to these previous results and convenient features, it was concluded that $NiWO_4$ is the best oxygen carrier among the studied tungstate materials for the production of $H_2$ and/or syngas based on theoretical thermodynamics point of view.

Figure 5 and 6 present other the production of CO, $CO_2$andW and Ni, respectively based on $NiWO_4$ as oxygen carrier for the POX-MeO reactor.

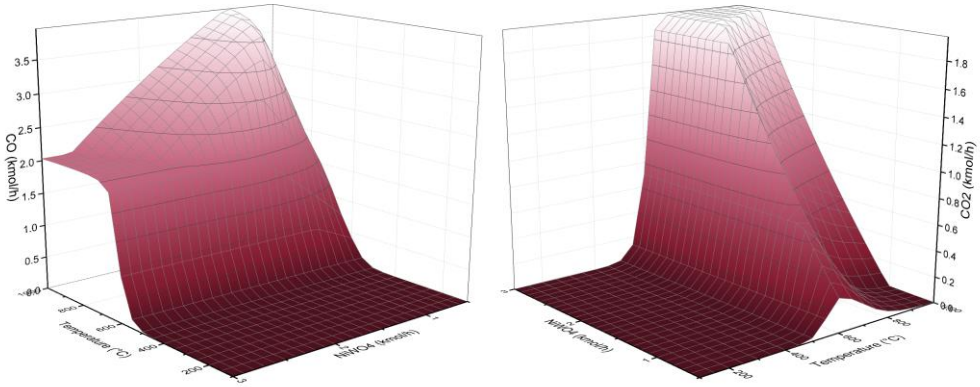


Figure 5. Thermodynamic analysis of the POX-MEO reactor with $NiWO_4$, CO (left) and $CO_2$ (right)).

Results of Figure 4and 5 show that a maximum of 6.8 kmol/h of hydrogen can be obtained and combined with 2.6 kmol/h of CO at a temperature of 700 ° C and a production of 1.7 kmol/h of W and also of Ni, thus avoiding carbon generation. These results can also be observed in Figure 6 where the production of Ni and Win the reduction reactor is shown.

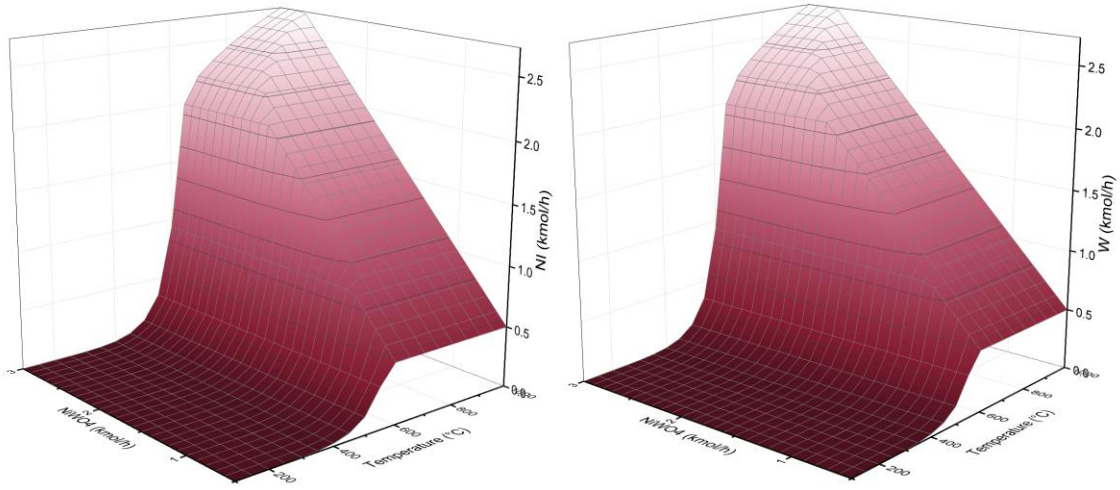


Figure 6. Thermodynamic analysis of the POX-MEO reactor with $NiWO_4$, Ni (left) and W (right)).

Results of this analysis reveal that high temperatures promote syngas production ($H_2$ + CO) in the product gas, while keeping the $H_2$/CO molar ratio equal or greater than 2 as shown in Figures 4 and 5. This is expected since at high temperatures the partial oxidation of methane by $NiWO_4$ is an endothermic reaction, which implies that this reaction (5) governs the thermodynamic system of gaseous species within the fuel reactor. On the other hand, solid products from this fuel reactor as a function of temperature as shown in Figure 6. Here, it is possible to observe that in order to avoid carbon formation, it is necessary to raise the temperature to more than 650 ° C. Also, in Figure 6 it can be seen that greater temperatures than 400 °C will lead to formation of Ni and W, while greater temperatures than 675 °C will

produce greater amounts of these reduced metallic species (Ni and W).

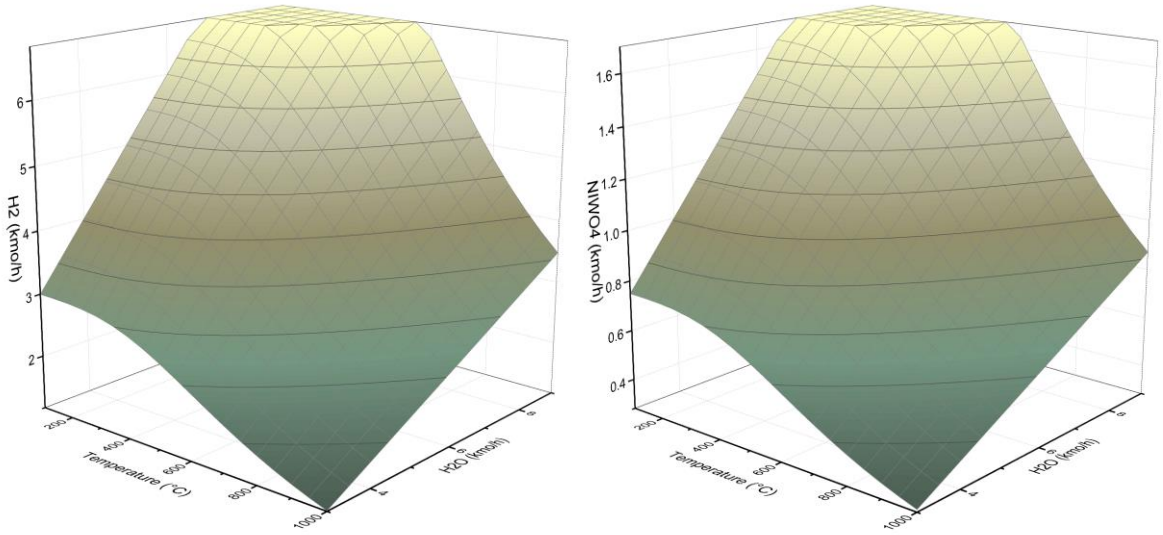


Figure 7. Thermodynamic analysis of the REGEN reactor with $NiWO_4$, $H_2$ (left) and $NiWO_4$ (right)

Figures 7 presentsresults from a thermodynamic analysis consisting in the calculation of the equilibrium amounts within the REGEN reactor using the RGIBBS model using $H_2O$ (steam) as molar feed. In this Figure the production of $H_2$ and $NiWO_4$is plotted as a function of a range oftemperature of 100-1000 °C and a steam feed of 2-9 kmol/h.In this reactor the solid products from thereduction reactor consisting of 1.7 kmol/h of both W and Ni were also fed.

From this Figure it can be seen that oxidation of the reduced metals (Ni and W) to form$NiWO_4$ is feasible at relatively low temperatures (even below 300 °C) and at a maximum $H_2$ generation of 6.8kmol/h at 7 kmol/h of $H_2O$ feed. However, in order to favor the reaction kinetics of reaction (8), it is convenient to use temperatures above 500 °C. This condition allows a reasonable small temperature gradient between the two reactors.

According to the results shown in figure 7 it was observed that the most suitable operating temperature for the regeneration reactor is in the range of 100-550 °C and more specifically at 500 °C since inthis range the nickel tungstate generation is stable with a production of 1.7 kmol/h,while a maximum production of $H_2$ of 6.8 kmol/h is obtained at a feed of 8.5 kmol/h of water vapor. Thus, the optimum operating conditions selected for the second reactor is 500 °C, which according to Figure 7 corresponds to a molar steam feed flow of 6.5 kmol/hr and producing 1.7 kmol/h of $NiWO_4$ and 6.8 kmol/h of $H_2$.

Therefore, it can be concluded thatin the reduction reactor (POX-MeO) for the synthesis gas production optimal operating conditions of this reactor are as follows: a temperature of 700°C and a feed of 4 kmol/h of $CH_4$ and 1.7 kmol/h of $NiWO_4$.The established operating temperature of 700 °C in the first reactor, where the partial oxidation of methane occurs, is relatively lower than those reported with other oxygen carrier materials and this represents potential energy savings. Meanwhile in the regeneration reactor (REGEN)optimum operating conditions are 500 °C anda feed of 1.7 kmol/h of Ni, 1.7 kmol/h of W and 8.5 kmol/h of steam to produce 1.7 kmol/h of $NiWO_4$and 6.8 kmol/h of $H_2$.

Within the simulation, once the appropriate parameters for the entire process were established through the sensitivity analyzes, it was possible to obtain the results shown in Table 1.

**Table 1**. Simulation results according to Figure 1.

| Stream | 1 | 2 | 3 | 4 | 5 | 6 | 7 |
|---|---|---|---|---|---|---|---|
| Temperature, °C | 25 | 750 | 0 | 750 | 0 | 500 | 25 |
| Pressure, bars | 2.026 | 2.026 | 2.026 | 1.013 | 1.013 | 2.026 | 2.026 |
| Vapor Fraction | 1 | 364.81 | 459.806 | 1 | 363.81 | 451.516 | 0 |
| Molar Flow, kmol/hr | 4 | 11.803 | 0 | 11.803 | 0 | 6.5 | 6.5 |
| Mass Flow, kg/hr | 64.171 | 160.167 | 0 | 160.167 | 0 | 30.393 | 117.099 |
| Volume Flow, $m^3$/hr | 97.692 | 991.167 | 0.045 | 991.143 | 0.024 | 412.518 | 0.118 |
| Enthalpy Gcal/hr | -0.071 | -0.168 | 0 | -0.168 | 0 | -0.04 | -0.449 |
| molar Flow kmol/hr | 0 | 3 | 1.5 | 0 | 3 | 1.645 | 0 |
| $H_2$ | 0 | 6.513 | 0 | 6.513 | 0 | 5.419 | 0 |
| CO | 0 | 3.092 | 0 | 3.092 | 0 | 0 | 0 |
| $CO_2$ | 0 | 0.809 | 0 | 0.809 | 0 | 0 | 0 |

| | | | | | | | |
|---|---|---|---|---|---|---|---|
| $H_2O$ | 0 | 1.289 | 0 | 1.289 | 0 | 1.081 | 6.5 |
| W | 0 | 1.5 | 0 | 0 | 1.5 | 0.145 | 0 |
| C | 0 | 0 | 0 | 0 | 0 | 0 | 0 |
| $CH_4$ | 4 | 0.099 | 0 | 0.099 | 0 | 0 | 0 |
| $NIWO_4$ | 0 | 0 | 1.5 | 0 | 0 | 1.355 | 0 |
| NI | 0 | 1.5 | 0 | 0 | 1.5 | 0.145 | 0 |
| Mass Flow, kg/hr | 64.171 | 523.977 | 459.806 | 160.167 | 363.81 | 480.909 | 117.099 |
| Enthalpy, Gcal/hr | -0.071 | 0.0019 | -0.808 | -0.168 | 0.034 | -0.728 | -0.449 |

These results show the production of synthesis gas in the first reactor of reduction of $NiWO_4$, whereas in the regeneration reactor a production of hydrogen results from the oxidation of the previously reduced metals.

## 4. Conclusions

Different types of $MWO_4$ (M = Fe, Mn, Ni) were evaluated through thermodynamic analysis and process simulation for the production of hydrogen-synthesis gas (syngas) using Aspen Plus. According to the thermodynamic analysis results, it is concluded that $NiWO_4$ is the best oxygen carrier among the studied tungstate materials for the production of $H_2$ and/or syngas. Simulation results found at the exit of the reduction reactor a free carbon deposition window located between a feed range of 1.6-3 kmol/h of $NiWO_4$ and a temperature range of 100-1000 °C. While the working window in which no coal is produced is at a temperature range of 700-1000 °C at a feed range of 1.7-3 kmol/h of $NiWO_4$. Within the reduction reactor the $H_2$/CO molar ratio of the synthesis gas is from 2.5-2.7 kmol/h and producing from 1.6-2 kmol/h of W, with a maximum of 1.7 kmol/h at a temperature of 700 °C. While in regeneration reactor there is a reduced range of temperatures, consisting of 100-550 °C at a feed of 6-9 kmol/h of steam and more specifically at 500 °C with a feed of steam of 8.5 kmol/h. Finally, it is concluded that relatively moderate temperatures such as 700 °C and a $NiWO_4$ feed of 1.6-3 kmol/h are needed to generate carbon-free synthesis gas. While in the regenerator 1.7 kmol/h of $NiWO_4$ is obtained at a temperature of 500 °C, while producing 6.8 kmol/h of $H_2$.

## References


[1] BP Energy Outlook 2035, available at: http://www.bp.com/es_es/spain/conozca-bp/informes-y-publicaciones/bp-energy-outlook.html

[2] Sunny A., Solomon P.A., Aparna K., Syngas production from regasified liquefied natural gasand its simulation using Aspen HYSYS. J. Nat. Gas Sci. Eng. 2016. 30: p. 176-181.

[3] De Los Ríos T., Delgado Vigil M.D., Collins-Martinez V., Lopez Ortiz A., Synthesis,characterization and stability performance of CoWO4 as an oxygen carrier under redox cyclestowards syngas production. Int. J. Chem. Reactor Eng. 2007. 5(1): p. 1-12.

[4] Wilhelm DJ., Simbeck D.R., Karp AD., Dickenson RL., Syngas production for gas-to-liquidsapplications: technologies, issues and outlook. Fuel Process. Technol. 2001. 71(1–3): p. 139-148.

[5] Vázquez Sosa MI., Delgado Vigil MD., Salinas Gutiérrez J., Collins-Martínez V., LópezOrtiz A., Synthesis gas productionthroughredoxcycles of bimetallic oxides and methane. J.New Mater. Electrochem. Syst. 2009. 12: p. 029-034.

[6] Haarlemmer G., Bensabath T., Comprehensive Fischer–Tropsch reactor model with non-idealplug flow and detailed reaction kinetics. Comput. Chem. Eng. 2016. 84: p. 281-289.

[7] Dincer I., Acar C., Review and evaluation of hydrogen production methods for bettersustainability. Int. J. Hydrogen Energy. 2015. 40(34): p. 11094-11111.

[8] Jansen D., Gazzani M., Manzolini G., Carbo MC., Pre-combustion CO2 capture. Int. J. Greenhouse Gas Control. 2015. 40: p. 167-187.

[9] Makarshin LL., Sadykov VA., Andreev DV., Gribovskii AG., Privezentsev VV., Parmon VN. Syngas production by partial oxidation of methane in a microchannel reactor over a Ni–Pt/La0.2Zr0.4Ce0.4Ox catalyst. Fuel Process. Technol. 2015. 131: p. 21-28.

[10] Voldsund M., Jordal K., Anantharaman R. Hydrogen production with $CO_2$ capture. Int. J. Hydrogen Energy. 2016. 41(9): p. 4969-4992.

[11] De los Ríos Castillo T., Salinas Gutiérrez J., López Ortiz A., Collins-Martínez V. Global kinetic evaluation during the reduction of $CoWO_4$ with methane for the production of hydrogen. Int. J. Hydrogen Energy. 2013. 38(28): p. 12519-12526.

[12] Protasova L., Snijkers F. Recent developments in oxygen carrier materials for hydrogen production via chemical looping processes. Fuel, 2016. 181: p. 75-93.

[13] Rydén M., Lyngfelt A. Using steam reforming to produce hydrogen with carbon dioxide capture by chemical-looping combustion. Int. J. Hydrogen Energy. 2006, 31: p.1271–1283.

[14] LyngfeltA,.Mattisson T. Trestegsf¨orbr¨anningf¨oravskiljningavkoldioxid. Patent-ochregistreringsverket, Sweden, 2005.

[15] Mattisson T., Lyngfelt A., Leion H. Chemical-looping with oxygen uncoupling for combustion of solid fuels. Int. J. Greenhouse Gas Control. 2009, 3: p. 11–19.

[16] Svoboda K., Siewiorek A., Baxter D., Rogut J., Pohorely M. Thermodynamic possibilities and constraints for pure hydrogen production by a nickel and cobalt-based chemical looping process at lower temperatures. Energy Convers Mgmt 2008, 49: p. 221–231.

[17] Tong A., Sridhar D., Sun Z., Kim HR., Zeng L., Wang F., Wang D., Kathe MV., Luo S., Sun Y. Continuous high purity hydrogen generation from a syngas chemical looping 25kWth sub-pilot unit with 100% carbon capture. Fuel 2013, 103: p. 495–505.

[18] Cormos CC. Hydrogen production from fossil fuels with carbon capture and storage based on chemical looping systems. Int. J. Hydrogen Energy 2011, 36: p. 5960–5971.

[19] Mizia F., Rossini S., Cozzolino M., Cornaro U., Tlatlik S., Kaus I., Bakken E., Larring Y. One step decarbonization. In: Eide LI, ed. Carbon Dioxide Capture for Storage in Deep Geologic Formations, vol. 3. Berkshire: CPL Press; 2009.

[20] Kang K-S., Kim C-H., Bae K-K., Cho W-C., Jeong S-U., Lee Y-J., Park C-S. Reduction and oxidation properties of $Fe_2O_3/ZrO_2$ oxygen carrier for hydrogen production. Chem. Eng. Res. Des. 2014, 92(11): p. 2584–2597.

[21] Nakamura MT. Hydrogen production from water utilizing solar heat at high temperatures. Solar Energy 1977, 19: p. 467–475.

[22] Rydén M., Leion H., Mattisson T., Lyngfelt A. Combined oxides as oxygen-carrier material for chemical-looping with oxygen uncoupling. Appl. Energy 2014;113: p. 1924–32.

[23] Mihai O.., Chen D., Holmen A. Catalytic consequence of oxygen of lanthanum ferrite perovskite in chemical looping reforming of methane. Ind. Eng. Chem. Res. 2011;50: p. 2613–21.

[24] Luo S., Zeng L., Xu D., Kathe M., Chung E., Deshpande N., Qin L., Majumder A., Hsieh T-L, Tong A. Shale gas-to-syngas chemical looping process for stable shale gas conversion to high purity syngas with a $H_2$:CO ratio of 2:1. Energy Environ. Sci. 2014, 7: p. 4104–4117.

[25] De Los Ríos-Castillo, T., Cortez Palacios L., De los Ríos SA., Delgado Vigil D., Salinas Gutiérrez J., López Ortiz A., Collins-Martínez V. Study of $CoWO_4$ as anOxygenCarrierfortheProduction of HydrogenfromMethane. J. New Mater. Electrochem. Sys. 2009. 12(1): p. 55-61.

[26] Mehrpooya, M., Sharifzadeh MMM., Rajabi M., Aghbashlo M., Tabatabai M., Hosseinpour S., Ramakrishna S. Design of an integrated process for simultaneous

chemical looping hydrogen production and electricity generation with $CO_2$ capture. Int. J. Hydrogen Energy, 2017. 42(12): p. 8486-8496.

[27] Antzara, A., Heracleous E., Bukur DB., Lemonidou AA. Thermodynamic analysis of hydrogen production via chemical looping steam methane reforming coupled with in situ $CO_2$ capture. Int. J. Greenhouse Gas Control, 2015. 32: p. 115-128.

[28] Meng, W.X., Banerjee S., Zhang X., Agarwal RK. Process simulation of multi-stage chemical-looping combustion using Aspen Plus. Energy, 2015. 90: p. 1869-1877.

[29] Zhou L., Zhang Z., Agarwal RK. Simulation and validation of chemical-looping combustion using ASPEN plus. Int. J. Energy Environ, 2014. 5(1): p. 53-59.

[30] Collins-Martínez V., Escobedo Bretado M., Meléndez Zaragoza M., Salinas Gutiéerrez J., López Ortiz A. Absorption enhanced reforming of light alcohols (methanol and ethanol) for the production of hydrogen: thermodynamic modeling. Int. J. Hydrogen Energy 2013. 28: p. 12539-53.

[31] Sandler SI., Using Aspen Plus in thermodynamics instruction: a step-by-step guide. 2015: John Wiley & Sons.

[32] Mathias PM. A versatile phase equilibrium equation of state. Ind. Eng. Chem. Process Des. Dev., 1983. 22(3): p. 385-391.

# 4.7 Validation of a novel kinetic model for fed-batch hydrogen production process using a microalgae consortium isolated from wastewater

Dulce J. Hernández Melchor, B. Ruiz Camacho, B. Camacho Pérez, David Meneses González, Pablo A. López Pérez

[1]Universidad Tecnológica de Tecámac, A5 Químico-Biológicas, Carretera Federal México - Pachuca Km 37.5, C.P. 55740, Col. Sierra Hermosa, Tecámac, Estado de México

[2]Universidad de Guanajuato, División de Ciencias Naturales y Exactas, noria alta s/n, Col. Noria alta, Guanajuato, Guanajuato México

[3]UAEH-ICBI-AACyE, Carr. a Tulancingo Km. 4.5Cd. Universitaria, C.P. 42184, Pachuca, Hgo. México

[4]Escuela Superior de Apan, Carretera Apan-Calpulalpan, Km 8, Chimalpa Tlalayote s/n, Colonia Chimalpa, Apan, Hgo., México. C.P. 43900.

* Corresponding author: save1991@yahoo.com.mx

Tel (771) 7172000. Ext 5809

## ABSTRACT

This research explores the photo-fermentation of acetate to hydrogen by a microalgae consortium isolated from wastewater, with the objective to maximize hydrogen production in batch operation using as reducing agent the cysteine. Moreover, an alternative phenomenological model of the main state variables of the process was formulated, with the optimum condition of hydrogen production considering an unstructured kinetic approach based on substrate inhibition model; this kinetic model was experimentally validated in batch operation. The advantages of the proposed model are: incorporates two substrates and the effect of the initial concentration of cysteine. The parameters of the model are optimized by using the Levenberg–Marquardt approach. The performance of technique is evaluated using a numerical simulation. The maximum hydrogen concentration was about 10.6 mg/L to 36 h in batch operation. These results showed that intermittent addition of cysteine (time: 36 h, cysteine 480 mg/L) in a repeated fed-batch mode, can improve the production compared to the addition of an equal amount once at the beginning of a batch. The model can then be applied as the connection to transfer hydrogen production from laboratory scale, optimization and control purposes into semi-pilot scale.

***Keywords:*** Feed-batch; cysteine; Consortia; Kinetic modelling

## 1. Introduction

Nowadays, there are two major problems that the world faces in the energy sector, the decline in oil reserves and the pollution caused by burning fossil fuels, coupled with this the thermoelectric plants (coal, natural gas, oil and nuclear) are responsible for about 80% of world electricity production, which through its process generates large amounts of $CO_2$, contributing to global warming. For this, arise the need to find new sources of renewable energy that can generate electrical energy friendly to the environment [1]. No longer is organic matter simply burned to produce heat and light, as advanced technologies now convert raw biomass into more useful forms of energy that are easy to use and transport. Alternatively, hydrogen is a clean energy carrier, producing water as it's only by product when it burns. The development of hydrogen biotechnology is advancing rapidly as hydrogen as a fuel of increasing importance, in parallel to the demise of fossil fuels [2].

A promising option to generate electricity is using photosynthetic microorganisms that convert solar energy into chemical energy, which can be used to produce $H_2$ through its metabolism, as in the case of algae that use specific enzymes called hydrogenases [3]. Hydrogen is generated by biochemical reactions, mainly in anaerobic fermentation processes: Biophotolysis of water using green algae and blue-green algae (cyanobacteria) [4], direct biophotolysis and indirect biophotolysis photofermentation dark fermentation [5], hybrid systems using dark fermentative and photofermentative bioreactors (semiconductor photocataliyst) [6], using bioelectrochemically assisted microbial bioreactors [6], therefore, hydrogen yields by pure or mixed cultures have been reported maximum average hydrogen production rate (212.2 mL/(L•h)), but also had stable hydrogen production under continuous culture conditions, which was 1.968 mol $H_2$/mol glucose [7].

Considering the high theoretical yields, several researchers have begun exploring approaches to increase hydrogen production [8]. Mathematical modeling approaches could contribute to large-scale $H_2$ production as various microorganisms can produce $H_2$ under moderate conditions from readily available, renewable substrates, making operation strategies potentially competitive [8]. However, few published works have reported the mathematical modeling of hydrogen production [9,10]. Several mathematical models have been developed for natural systems, some include affinity models such as the Monod-type, others are based on product or substrate inhibition, such as those developed by Haldane, Andrew's, Luong's, Han-Levenspiel, Boulton, Moser and Aiba [8-10]. Nevertheless, the above mentioned models are complicated because 1) the models are a higher order and some of them are described by partial differential equations; 2) there are too many parameters and these parameters cannot be uniquely determined. Therefore, for industrial application, it is necessary to develop models with the following characteristics: few parameters, easy determination of the values of these parameters, they are easily mastered by process engineers, strong potential in on-line estimation and control of bioprocesse and these parameters must have physical-biological meaning rather than empirical.

The aim of this project was the optimization and kinetic modeling of a bubble column photobioreactor to produce hydrogen from a microalgae consortium isolated from wastewater. A mathematical model was developed to describe the kinetics of hydrogen production in a batch operation. The performance of the proposed mathematical model were statistically evaluated using the dimensionless coefficient of efficiency (Π) and correlation coefficients ($R^2$>0.96).

## 2. Materials and Methods

### 2.1 Microbial growth kinetics

The inoculum was isolated from the wastewater treatment plant "Sierra Hermosa" Organismo Descentralizado de Agua Potable, Alcantarillado y Saneamiento (ODAPAS) of Tecámac México. $BG_{11}$ medium was used as for the enrichment of algal strains in wastewater prior to isolate them in different colonies. For strains enrichment, 50 mL of $BG_{11}$ media were taken into 250 mL flask in different flasks [11]. The kinetics of microbial growth was carried out in bubble column photobioreactors of 250 mL in batch culture with hydraulic residence time of 5 days.The batch operation was performed under conditions at 37°C for 120 hours. An aliquot was taken every 12 hours, for analyses of; acetate, $N_2$, biomass, and $H_2$ concentrations. Experimental designs $3^2$ were proposed; the factors were: air, carbon source (acetate) and reducing agent (cysteine: 498.0 mg/L and 700 mg/L). Experiments were performed per duplicate. In this experiment biomass production was evaluated spectrophotometrically at 750 nm (Perkin Elmer UV/Vis spectrometer Lambda XLS+). The operating conditions of the photobioreactor were: air flow 0.5 vvm, light 80 µmol /$m^2$ s photon flux density and photoperiod light: dark 12: 12.Then, acetate concentrations was measured using an HPLC equipment (Shimadzu LC10Ai) connected to a UV detector (k=210 nm) and a BioRad HPLC Organic Acid Analysis Column, using a flow rate of 0.700 mL/min and a sulfuric acid/water (0.33/0.067) mobile phase anhydride sodium acetate(HPLC grade, SIGMA®) was used as standards

### 2.2 Hydrogen production

From the previous step, were selected the combinations in which were obtained the best results biomass production to use as inoculum in the hydrogen production. For this, experimental designs $2^2$ were proposed (air and medium composition). The hydrogen was determined by gas chromatography in a Gow-Mac chromatograph model 350 fitted with a thermal conductivity detector and Molecular Sieve 5A packed column; Argon was the carrier gas [12].

### 1.3 Kinetic modeling

#### 2.3.1. Model development

The bioprocess advancement is determined by the living cells capabilities and characteristics, the bioreactor performance as well as by the cultivation media composition and the main parameters evolution. The high metabolic network complexity inside the cells often determine very sophisticated, non-linear growth and product formation kinetics, with further consequences on the bioprocess behavior, but at the same time on the product quality and yield. In order to improve process understanding or performance, different tools can be considered, as simulators able to reproduce system behaviours, software sensors, virtual sensors, observer state which allow obtaining an estimation of an unmeasured signal to maintain optimal conditions. All these tools rely on a representation of the considered system, which is generally a mathematical model of the process [7, 8].
Consider a biological system described by a set of state variables, i.e. the concentrations of substrates, metabolic products and biomass in the extracellular solution. In a batch bioreactor, the process dynamics can be described by the following model [13]:

$$\frac{dx}{dt} = K\zeta(x) \qquad (1)$$

Where

$x \in \Re_+^n$ is the vector of concentration

$K \in \Re_+^{n\,x\,m}$ are the corresponding stoichiometric coefficients matrix (m < n),

$\zeta_i \in \Re_+^n$ is the vector of reaction rates kinetic term

$t \in \Re_+$ Time

$$\zeta(x) = \mu(x) \qquad \ldots\ldots\ldots \qquad (2)$$

Here $\mu(t)$ is the specific growth rate, which is a function of the concentrations ; acetate, $N_2$, biomass, and $H_2$. Such reaction rates vary with time and are usually influenced by many physicochemical and biological environmental factors like substrate, biomass and product concentrations as well as pH, temperature, dissolved oxygen concentration or various microbial growth inhibitors.

These kinetic structures are able to reproduce different behaviors like component limitations

$$lim_{x\to 0}\,\zeta(x(t)) = 0 \qquad (3)$$

Inhibitions

$$lim_{x\to \infty}(x(t)) = 0 \qquad (4)$$

Saturations

$$lim_{x\to \infty}\,\zeta(x(t)) = constant \qquad (5)$$

**Model equations**

The Droop model is very common for the simulation of microorganism fermentation [14]. In the Droop model, the growth rate of microorganism is not only affected by the concentration of limiting nutrients, but also decided by the intracellular concentration of the limiting nutrient, which is usually termed as nutrient quota (mg nutrient/g biomass) [14]. Monod kinetic model, Logistic equation, and Haldane model are most commonly used non-structured models for describing microbial growth during the complex dark

fermentation process. However, the unstructured kinetic models are frequently employed for modeling simulation of microbial growth, substrate consumption and product formation, Monod, Gompertz, logistic, and Luedeking-Piret models have been used to determine the kinetic parameters for $H_2$ production [15,16]. Some investigators developed mathematical models that included the enzyme deactivation, these models are complex whose solutions cannot be solved analytically [17]. Furthermore, it has been shown that that not always the use of complex models is the best way to obtain a good process representation for monitoring and control purposes [18]. Based on the dynamic model developed, the current research also explores the effects of operating conditions such as starting nutrient concentrations, carbon source conversion efficiency and fermentation operating time on hydrogen production.

**Model proposed assumptions and limitations**

Assumptions of the model were as follows:

1) The photobioreactor is completely mixed;
2) The specific growth rate of algae is related to the nitrogen, cysteine and acetate;
4) The concentration of phosphorus well as light intensity remains constant;
5) A light limited continuous flow culture was assumed for writing the energy balance;

Where all incident photosynthetically available radiance is absorbed;

6) Although the size of gas bubbles are not constant inside the bioreactor and the gas liquid mass transfer rate changes continuously, it is assumed that the bubbles size remains almost constant due to the short length of the reactor;
8) Temperature and pH are constant in the culture;
9) Yield coefficients are constants and the same as their theoretical values.

Limitations to the model are listed as follows:

1) Kinetic parameters were obtained from initial conditions;
2) Nutrient inhibition is considered in the proposed expression for the specific growth rate;
3) Since the proposed model was derived on the basis of the Monod and Luong model, it will have the same limitations of the unstructured-type.

The advantages of the proposed model are:

1) Incorporates two substrates;
2) Effect of the initial concentration of cysteine and air flow;

Kinetic term:

$$\varphi_1 = \left(1 - \frac{X}{k_{X_1}}\right)^{\alpha} \left[\frac{N_2}{k_S + N_2}\right]\left[\frac{H_2}{k_{H_2} + H_2}\right] \tag{6}$$

Hydrogen production kinetic:

$$\varphi_2 = \left(1 - \frac{X}{k_{X_2}}\right)^{\beta} \left[\frac{N_2}{k_S + N_2}\right]\left[\frac{A}{k_A + A}\right] \tag{7}$$

Equations:

Acetate mass balance (*A*):

$$\frac{dA}{dt} = -\frac{\mu_{max}}{Y}\varphi_1 A \tag{8}$$

Nitrogen mass balance ($N_2$):

$$\frac{dN_2}{dt} = -\frac{\mu_{\max}}{Y}\varphi_1 N_2 \quad (9)$$

Biomass Balance ($X$):

$$\frac{dX}{dt} = \mu_{max}\varphi_1 A - k_d\ X \quad (10)$$

Hydrogen mass balance ($H_2$):

$$\frac{dH_2}{dt} = \frac{\mu_{max_{H2}}}{Y_P}\varphi_2 H_2 - k_{H_{2(cys)}} H_2 \quad (11)$$

Here $\mu_{max,\ j}$ = maximum specific rate for $j$ concentrations, $Y$ = yield constant, $Y_P$= product yield constant, $k_s$ = Monod saturation constant for Nitrogen, $k_{x1}$ = inhibition constant for Biomass, $\alpha$ and $\beta$ = Exponential term for Luong model, $k_{H_{2(cys)}} = e^{\left(-\left(\left(\frac{Cys_0}{t}\right)*\chi + Q_{air}*\delta\right)\right)}$, $t$= *time*, $Cys_0$ = initial concentration of cysteine, $\chi, \delta$ = parameters adjustment, $Q_{air}$ = 0.125 L/min, air flow and $Q_{air}$ = 0.0 L/min "anaerobic conditions".

### 2.3.2. Determination of kinetic parameters

Levenberg–Marquardt optimization approach

Biological systems have been traditionally fit using graphical-based techniques, in which parameter estimation is converted to a linear regression problem [19]. However, the applicability of this approach is related to the functionality of the model. Furthermore, graphical methods have been shown to produce inferior parameter estimates than those generated using nonlinear regression techniques. Nonlinear regression was used based on the Levenberg-Marquardt least squares minimization algorithm, which is a hybrid of the Gauss- Newton and the steepest descent methods [19, 20].

Equations (6)-(11), were used for the parameter fitting with the following initial conditions: A0 = 364 mg/L; N2, 0 = 206 mg/L, X0: = 42 mg/L, H2,0 = 5 mL. The Model-Maker® software (based on Levenberg–Marquardt optimization approach) was used for the non-linear fitting data. The performance of the proposed mathematical model was statistically evaluated using the dimensionless coefficient of efficiency ($\Pi$).

$$\Pi = 1 - \frac{\sum_{i=1}^{N}\left[\left|Y - Y^*\right|\right]}{\sum_{i=1}^{N}\left|Y^* - \bar{Y}\right|} \quad (12)$$

Where $Y$ is the simulated value of the variable at time $t_i$, $Y^*$ is the observed value of the same variable at time, and $\bar{Y}$ is the mean value of the observed variable. $\Pi$ varies between (-∞, 1]. A positive value of $\Pi$ represents an acceptable simulation whereas $\Pi$ > 0.5 represents a good simulation

## 3. Results and Discussion

### 3.1. Effect on microalgae consortium growth and hydrogen production.

Figure 1 show the biomass growth of microalgae consortium to different treatments. The maximum microalgae biomass production was obtained with the medium $BG_{11}$ containing acetate and cysteine with and without air. The acetate helps to grow microalgae consortium because together $CO_2$ of air supply a carbon source. According to previous results, the experimental design for evaluation of hydrogen production was $2^2$, where we evaluated air and medium composition. It is observed that the best conditions for growth were: acetate + cysteine with air and acetate + cysteine without air. Effect of air and medium composition on hydrogen production is shown in Figure 2. It is shown that the effect of air concentration and cysteine is important in the production of hydrogen. Moreover, the maximum total $H_2$ production was determined about 10.6 mg/L in 36 for a cysteine concentration 498 mg/L, but decreased with further increasing the cysteine concentrations from 498 to 700 mg /L (maximum $H_2$ production was determined about 5.6 mg/L in 36 hours (data not shown)). For this reason the cysteine concentration of 498 mg /L is used for the development of the proposed model, in addition, at 498 mg/L of cysteine, hydrogen production started rapidly with the lag phase of about 4 h, reaching the maximum production rate of 36 ml/ l/h (see figure 2). The microalgae consortium showed a maximum hydrogen production of 18% using cysteine as reducing agent without air. The results indicated that a concentration of cysteine without air increase hydrogen production, while cysteine with air depressed the hydrogen production. In general, maximum total $H_2$ production was determined about 10.6 mg/L in 24 hours. Marquez-Reyes et al. [3] studied experimental conditions similar to this study, using cysteine to reduce the photosintetic oxygen produced by *Chlamydomonas gloeopara* and *Scenedesmus obliquus* getting better hydrogen production. Therefore, in this study the alternative of producing $H_2$ by a microalgae consortium arises being that handling and scaling is more feasible compared to pure cultures (see, table 1). Addition, cysteine, as a reducing agent, has the ability to reduce the Oxidation-Reduction Potential (ORP) value in the fermentation system, which enhances the growth of some hydrogen producing bacteria, thus considerably increasing the cumulative hydrogen production [21] it is verified in the above results (see figure 1 and 2). Many studies have shown the effects of concentrations of soluble starch, ferrous iron and cysteine on hydrogen productivity based on the “one-variable-at-a-time” approach. However, these just carried out on individual factor but not mutual factors. So those results could not explain the mutual interactions among the independent variables and guarantee the determination of optimal conditions [22]. These reasons explained that three selected factors (nitrogen, cysteine and air) were necessary and all have significant effect to hydrogen production by in our study.

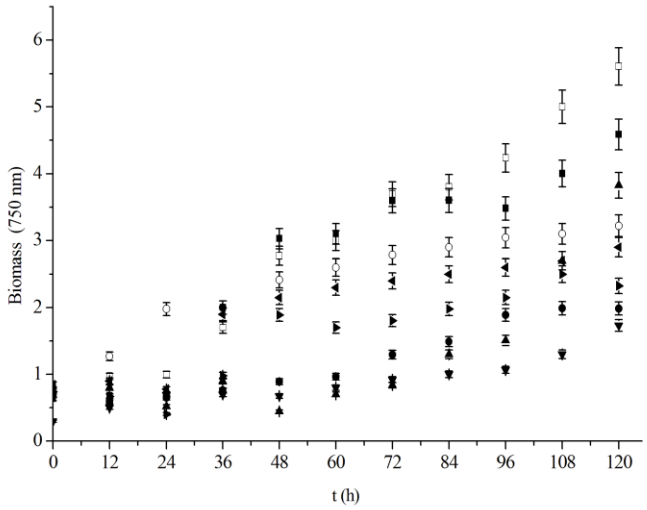


**Fig. 1** Maximum microalgae biomass production : cysteine without air ( ●) cysteine with air (○),acetate + cysteine with air (□),acetate + cysteine without air (■), BG11 with air (▲), BG11 without air (▼), acetate without air (◄) and acetate with air (►).

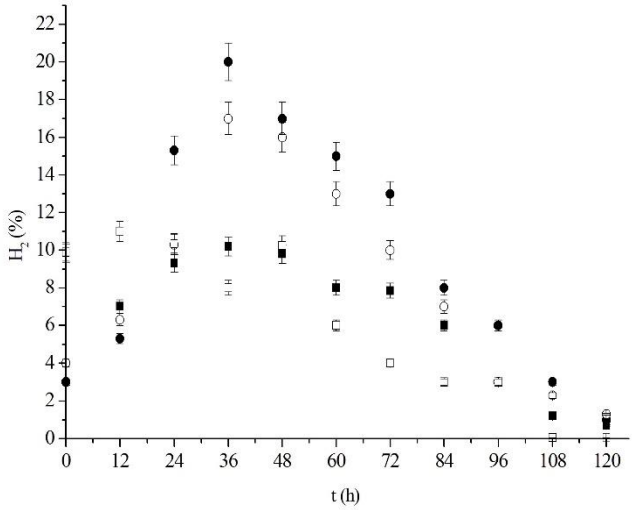


**Fig. 2** Maximum hydrogen production: cysteine without air (●) cysteine with air (○), acetate + cysteine with air (□), acetate + cysteine without air (■).

**Table 1.** Summary of hydrogen production with different microorganisms

| Inoculum | Experimental conditions | $H_2$ production | Reference |
|---|---|---|---|
| *C. gloeopara* and *S. obliquus* | - Bioreactors: Serological bottles (120 mL of culture medium)<br>- Inoculum: 1.3 x $10^6$ cells/mL of *C. gloeopara* and 3.3 x $10^6$ cells/mL of *S. obliquus*<br>- Temperature: 28°C | 23. 4 pmol | [3] |
| Consortium | - Bioreactors: 230 ml<br>- Inoculum: 8 g<br>- Substrate: 32 g (70% of sugarcane bagasse, 15% of waste activated sludge)<br>- Temperature: 35°C | 3 mmol $H_2$/gds | [23] |
| Consortium | - Substrate: local dining hall dried food wastes and waste office paper at 60:40 ratio<br>- pH : 6.2 - 6.8 | 200 NmL $H_2$ $(kg_{wmr}\ d)^{-1}$ | [24] |
| *Chlamydomonas reinhardti* | - Photobioreactor: acrylic tubes with operation volumes of 3L.<br>- Biomass concentration: 350 mg/L | 200 mV/L | [25] |
| *Enterobacter aerogenes* (Facultative anaerobic) | - Dark fermentation<br>- Substrate: Microalgae biomass, *Scenedesmus obliquus* (2.5 g/L)<br>- Inoculum: 10% v/v (corresponding to 0.1 g dry weight biomass/L culture media)<br>- Temperature: 30°C | 56.8 mL $H_2$/gvs | [26] |
| Microalgae consortium | - Substrate: Acetate<br>- Reducing agent: Cysteine<br>- Without air<br>- batch operation<br>- Temperature: environmental | 10.6 mg/L to 36 h<br><br>18% $H_2$ | This study |

### 3.2. Effect on microalgae consortium growth and hydrogen production

Considering the effect of air and cysteine kinetic growth of the consortium and the production of hydrogen in the presence of air and without air were developed, to propose a kinetic model in a batch regime that has the capacity to predict the concentration of acetate, nitrogen, biomass and finely hydrogen and establish batch-fed operation conditions. Numerical simulations were carried out using MATLABTM library 23 ODE. The parameter values were determined by non-linear regression employing the Model maker $^{TM}$ software. It is recommended therefore use (Π) in lieu of correlation-based measures to provide a relative assessment of model performance. This statistics used absolute values rather than squared differences (as in their originally specified counterparts). Interpretation of correlation-based measures 0.982 indicates that the model explains 98.2% of the variability in the observed data (see, table 2). With the indices of agreement, any value (accepting 0.0 and 1.0) is difficult to interpret because of its physical meaning.

**Table 2.** Correlation coefficients and model efficiency

| Variable | $R^2$ | | Model Efficiency(Π) | |
|---|---|---|---|---|
| | cysteine without air | cysteine with air | cysteine without air | cysteine with air |

| | | | | |
|---|---|---|---|---|
| Acetate | 0.986 | 0.971 | 0.972 | 0.972 |
| Nitrogen | 0.987 | 0.965 | 0.982 | 0.962 |
| Biomass | 0.989 | 0.945 | 0.978 | 0.958 |
| Hydrogen | 0.996 | 0.975 | 0.995 | 0.95 |
| Global | 0.989 | 0.964 | 0.982 | 0.960 |

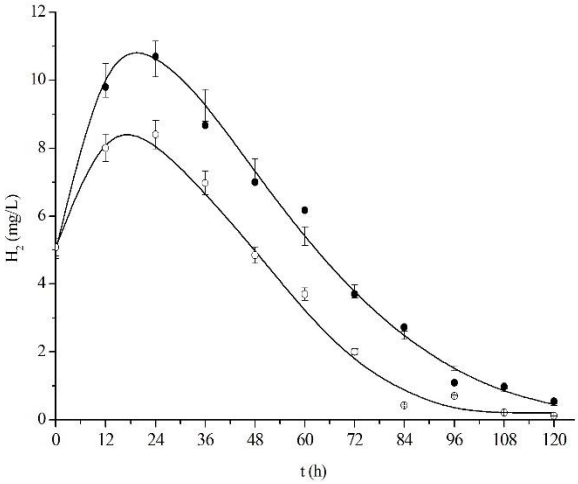


**Fig. 3** Temporal evolution of the hydrogen concentration: cysteine without air (●) cysteine with air (○) and (▬▬) proposed model.

The value of $\mu_{max}$ was calculated with the experimental data for two conditions were: $\mu_{umax}$: 0.041 1/h and $\mu_{umax}$: 0.056 1/h cysteine without air and cysteine with air respectively, $\mu_{umaxH2}$: 0.06 1/h and $\mu_{umaxH2}$: 0.04 1/h cysteine without air and cysteine with air respectively. The proposed model fits both cases to increase the production of hydrogen: cysteine without air and cysteine with air.
These results showed that intermittent addition of cysteine (time: 36 h, cysteine 480 mg/L) in a repeated fed-batch mode, can improve the production compared to the addition of an equal amount once at the beginning of a batch (Fig. 3).

## 4. Conclusion

This study focused on the optimization of the key factors for enhancement the bio-hydrogen production. Experimental results showed that three independent variables (air, carbon source (acetate) and reducing agent (cysteine)) and interaction between them had significant influences on the hydrogen production potential. The optimum conditions for fermentation hydrogen were $BG_{11}$-medium with 3645 mg/L acetate; 206 mg/L $N_2$; 1000 mg/L cysteine; 498 mg /L without air. In this optimum condition, maximum $H_2$ gas obtained 10.6 mg/L to 36h. The obtained results showed that the proposed mathematical model can

be useful to optimize the hydrogen production process and to improve the hydrogen production potential by inoculum isolated in México. The model can then be applied as the connection to transfer hydrogen production from laboratory scale, optimization and control purposes into semi-pilot scale.

## Acknowledgements

PALP is grateful with supported by the Red Temática de Bioenergía del CONACYT, López-Pérez, P.A. is grateful for the support of “Apoyo a la Incorporación de Nuevos PTC 2015, F-PROMEP-39/Rev-04, DSA/103.5/15/7001”1, DSA/103.5/15/7001, Universidad Tecnológica de Tecámac, planta “Sierra Hermosa” Organismo Descentralizado de Agua Potable, Alcantarillado y Saneamiento (ODAPAS) of Tecámac México.

## References

[1]. Ribeiro LA, Silva PP, Mata TM, Martins AA. Prospects of using microalgae for biofuels production: Results of a Delphi study. Renew Energ 2015;75:799-804.
[2]. Schügerl K. Progress in monitoring, modeling and control of bioprocesses during the last 20 years. J Biotechnol 2001;85:149–173.
[3]. Marquez-Reyes LA, Sanchez-Saavedra MP, Valdez-Vazquez I. Improvement of hydrogen production by reduction of the photosynthetic oxygen in microalgae cultures of Chlamydomonas gloeopara and Scenedesmus obliquus. Int J Hydrogen Energy 2015;40:7291-7300.
[4]. Tao Y, Chen Y, Wu Y, He Y, Zhou Z. High hydrogen yield from a two-step process of dark- and photo-fermentation of sucrose. Int J Hydrogen Energy 2007;33: 200-206.
[5]. Akkerman I, Janssen M, Rocha J, Wijffels HR. Photobiological hydrogen production: photochemical efficiency and bioreactor design. Int J Hydrogen Energy 2002;27:1195- 1208.
[6]. Chun-xiang Q, Lu-yuan C, Hui R, Xiao-ming Y. Hydrogen production by mixed culture of several facultative bacteria and anaerobic bacteria. Prog Nat Sci 2011;21:506–511.
[7]. López Pérez PA, Aguilar-López R, Neria González MI. Increasing the Bio-hydrogen production in a continuous bioreactor via nonlinear feedback controller. Int J Hydrogen Energy 2015;40: 1-7.
[8]. Hafez NHH, El Naggar MH, Nakh LG. (2013) Application of artificial neural networks for modeling of biohydrogen production. Int J Hydrogen Energy 38: 3189-3195.
[9]. Zhang D, Dechatiwongse P, del Rio-Chanona EA, Maitland GC, Hellgardt K, Vassiliadis VS. Modelling of light and temperature influences on cyanobacterial growth and biohydrogen production. Algal Research 2015;9: 263–274.
[10]. Gadhe A, Sonawane SS, Varma MNL. Kinetic analysis of biohydrogen production from complex dairy wastewater under optimized condition. Int J Hydrogen Energy 2014; 39:1306-1314.

[11]. Rippka R, Deruelles J, Waterbury JB, Herdman M, Stanier RY. Generic assignments, strain histories and properties of pure cultures of cyanobacteria. J Gen Microbiol 1979;111: 1-61.
[12]. Garibay-Orijel C, Rios-Leal E, Garcia-Mena J, Poggi-Varaldo HM. 2, 4, 6-Trichlorophenol and phenol removal in methanogenic and partially-aerated methanogenic conditions in a fluidized bed bioreactor. J Chem Technol Biotechnol 2005; 80 (10): 1180-1187.
[13]. Dochain D. State and parameter estimation in chemical and biochemical processes: a tutorial. J Process Contr 2003;13: 801–818.
[14]. Vatcheva I, de Jong H, Bernard O, Mars NJI. Experiments election for the discrimination of semi-quantitative models of dynamical systems. Artif Intell 2006;170: 472–506.
[15]. Luedeking R, Piret EL. A kinetic study of the lactic acid fermentation. J Biochem Microbiol Technol Eng 1959;1:393-412.
[16]. Koku H, Eroglu I, Gunduz U, ucel MY, Turker L. Kinetics of biological hydrogen production by the photosynthetic bacterium Rhodobacter sphaeroides O.U. 001 Int J Hydrogen Energy 2003;8:381–388
[17]. Dahl C, Rákhely G, Pott-Sperling AS, Fodor B, Takács M, Tóth A, Kraeling M Győrfi K, Kovács Á, Tusz J, Kovács KL. Genes involved in hydrogen and sulfur metabolism in phototrophic sulfur bacteria. FEMS Microbiol Lett 1999;180(2):317 – 24
[18]. Jung KW, Kim DH, Kim SH, Shin HS. Bioreactor design for continuous dark fermentative hydrogen production. Bioresour Technol 2011;102(18): 8612-20.
[19]. Vasanth Kumar K. Linear and non-linear regression analysis for the sorption kinetics of methylene blue onto activated carbon. J Hazard Mater 2006;137: 1538–1544.
[20]. López-Pérez PA, Puebla H, Velázquez Sánchez HI, Aguilar-López R. Comparison Tools for Parametric Identification of Kinetic Model for Ethanol Production using Evolutionary Optimization Approach Int J Chem React Eng 2016;14(6):1201-1209.
[21]. Bao MD, Su HJ, Tan TW. Dark fermentative bio-hydrogen production: Effects of substrate pre-treatment and addition of metal ions or L-cysteine. Fuel 2013;112: 38-44
[22]. Taherdanak M, Zilouei H, Karimi K. Investigating the effects of iron and nickel nanoparticles on dark hydrogen fermentation from starch using central composite design. Int J Hydrogen Energy 2015;40:12956-12963.
[23]. Robledo-Narváez PN, Muñoz-Páez KM, Poggi-Varaldo HM, Ríos-Leal E, Calva-Calva G, Ortega-Clemente LA, Rinderknecht-Seijas N, Estrada-Vázquez C, Ponce-Noyola MT, Salazar-Montoya JA. The influence of total solids content and initial pH on batch biohydrogen production by solid substrate fermentation of agroindustrial wastes. J Environ Manage 2015;128:126–137
[24]. Escamilla-Alvarado C, Poggi-Varaldo HM, Ponce-Noyola T, Ríos-Leal E, Robles-Gonzalez I, Rinderknecht-Seijas N. Saccharification of fermented residues as integral part in a conceptual hydrogen-producing biorefinery. Int J Hydrogen Energy 2015;40: 17200-17211.
[25]. Martín del Campo JS, Escalante R, Robledo D, Patiño, R. Hydrogen production by Chlamydomonas reinhardtii under light-driven and sulfur-deprived conditions: Using biomass grown in outdoor photobioreactors at the Yucatan Peninsula. Int J Hydrogen Energy 2014;39: 20950-20957.

[26]. Batista AP, Ambrosano L, Graça S, Sousa C, Marques PASS, Ribeiro B, Botrel EP, Neto PC, Gouveia L. Combining urban wastewater treatment with biohydrogen production – An integrated microalgae-based approach. Bioresour Technol 2015;184: 230–235.

# 4.8 Design of a low-power solar-hydrogen system with smart energy management

Jorge Olmedo González, Rosa de Guadalupe González Huerta, Miguel Tufiño Velázquez, Luis Armando Loera Cervantes

[1]ESIQIE-IPN, Laboratorio de Electroquímica y Corrosión, UPALM, CP 07738, Ciudad de México

[2]ESFM-IPN, Laboratorio de Física Avanzada, UPALM, CP 07738, Ciudad de México

[3]CECyT 3-IPN, Laboratorio de Maquinas Eléctricas, CP 55119, México, Edo.Mex

## ABSTRACT

At the present time hydrocarbons are the principal way to produce energy (International energy agency). However, they have not been good for the environment and we have to considerate that the demand of energy has been growing in the last decades. For these reasons, it is so important developing new ways to produce energy. Renewable energy sources such as solar or wind energy are cleaner than hydrocarbons and they could satisfy the demand of energy, when the energy is administered in a correct way. One of the problems of these primary sources are their natural intermittence and hydrogen could be a good solution for this problem.

In this work is proposed a solar-hydrogen system with a smart energy management, in the hybrid system solar panels are used to provide energy for a PEM electrolyser which produces hydrogen and oxygen gases through the water electrolysis, gases are stored in a variable volume tanks (atmospheric tanks), so they are supplied into a PEM fuel cell to generate electrical energy. The design was developed to produce enough hydrogen for the two requirements, illumination or for analyses of low power PEM fuel cells. It was considered the period of time for illumination and the flow rate of hydrogen and oxygen that the PEM fuel cells could require. The analysis of the system was developed studying each part of this and developing the material and energy balance. It shows the period of time for gases production and it allows to understand their efficiency and efficacy of the system. It was found that the system has a good behaviour when it is designed in order to be a flexible system, it improve the use of energy produced increasing its efficacy. Storing part is efficient because it is not necessary auxiliary energy to store gases. However, it is suitable for low power systems.

Developing a smart energy management is really important when the energy system is limitative. It allows to administrate solar energy and produce hydrogen in the best moment and still using solar energy when it is not necessary to produce hydrogen. The strategy

permits to save 5 times more energy and optimise the use of hydrogen and the photovoltaic system.

***Keywords:*** Solar-hydrogen system; PEM fuel cell applications; Management energy

## 1. Introduction

We live in a world where technology is growing rapidly and society increasingly depends on this, it is very important to innovate in sustainable energy sources in order to satisfy the energy demand, therefore it permits to reduce carbon emissions that create environmental problems such as global warming and climate change.

We have the challenge to develop efficient processes to produce electrical energy from primary renewable energy sources such as wind and solar energy, which due to its natural intermittency is necessary to develop ways to correct this problem, in relation with a constant demand of electricity by society. The solution is store energy in different ways and on of this is hydrogen, shown in the technology road map of energy storage and the technology road map of hydrogen and fuel cells by the International energy agency (IEA).

Storing the electrical energy produced by a photovoltaic system (PS) is a good solution to solve its intermittence. It is possible to store this energy as a hydrogen (H2) using, in this case, a PEM electrolyser (PEME) which produces hydrogen and oxygen (O2 and H2) of high purity from water electrolysis. In order to have a feasible process at least H2 and in some cases like this, O2 have to be stored safely and efficiently under the predetermined conditions of use by the storage system, which in this work H2 an O2 are stored in an atmospheric tank at Mexico City conditions (T & P).

The main goal of store energy as H2 is generate electrical energy with PEM fuel cells (PEMFC) when the primary source is not able to produce enough energy due to two principal factors. One, when energy produced by the primary source system (PSS) is lesser than the estimated electrical energy consumption by the system. It is too common because renewable energies have a natural intermittence and their behaviour could be highly random. For the example, solar energy has variations due to the weather and the position of the sun. Two, when energy consumption exceeds the maximum energy that the PSS can produce. It happens when not planned charges are connect in the system.

H2 also can be used as a backup system. In this case H2 is not used as a regulation system, it is used when PSS is not available, for example solar energy at night, or when their intensity is not enough to charge PS batteries and this energy could be endangered.

It is very important to mention that H2 storage is not an option to electrical conditioning produced by de the primary sources in comparison with batteries that is an excellent option. PEMFC's have a complex behaviour and it is recommended a continual use, so PEMFC should not be used for too short periods or transitional periods, for example, when PS energy decrease due to cloudiness.

The proposed project is a backup system in the electrochemistry & corrosion lab at Higher School of Chemical Engineering & Extractive Industries (ESIQIE-IPN) where H2 is used in periods where solar energy is not available or its intensity is too low, for example in the early morning or at night. In this case H2 is used in a PEMFC of 50W which is used to power two led laps of 25W each one. H2 is also used in different PEMFC's evaluations, in order to have a flexible system where the use of H2 is maximized therefore efficacy increase.

Hybrid systems require a methodology of energy management where is very important to know its limitations and understand that its efficiency and efficacy is variable and it does not totally depend of the equipment efficiency. So, having a good methodology of energy management is decisive in an energy system or in smart grids.

Energy management consist in different techniques to make the system more efficient and improve the use of the energy resources. The major issue in energy management is to meet the energy needs of the load efficiently, promoting renewable sources and optimizing cost. Several studies have been made to overcome these problems by adjusting the size of the system or the degrees of implications of different sources. There are several studies in the literature for energy management. They have a common goal: continually meet the needs of the installation, ensure maximum use of the energy produced by renewable sources, minimizing the cost of the energy produced by sources and minimize additional cycles of charging and discharging of the battery and superconducting if they exist [3].

## 2. Materials and Methods

### 2.1 System design

The system design is explained in five main stages. The first step is the generation of electricity by a PS. The primary source is the sun and it is used a PS, which was designed

based on the study of the energy required by the PEME and the behaviour of sunlight in Mexico City, where the average peak sunlight is 5 hours (figure 1a) [1] and the average irradiance is 900W $m^{-2}$ (figure 1b).

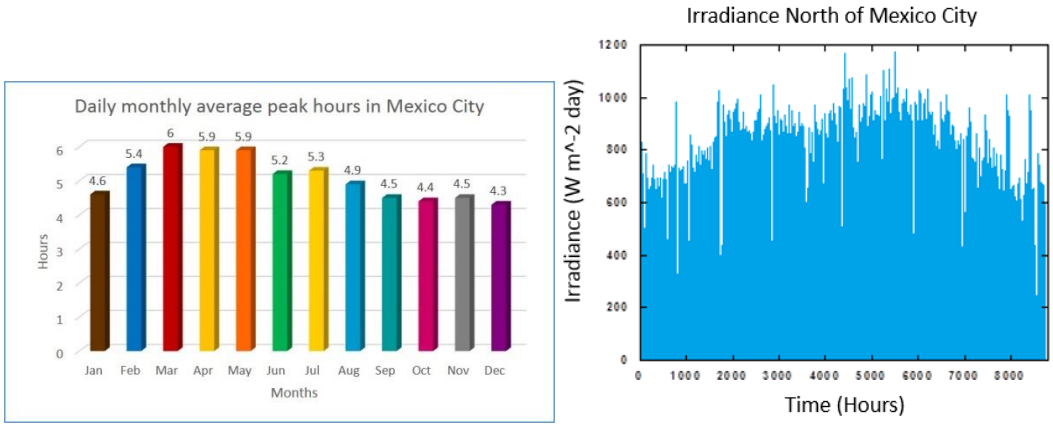


**Fig. 1.** a)Daily monthly average peak hours and b) Irradiance in north of Mexico City

Mexico City has an acceptable geographic position to capture sunlight, one of these reasons is that it is near of the equator, where daylight hours are relatively constant in all seasons and months therefore peak hours of sunlight either do it, which it allows a stable PS. This information permits to understand the maximum and minimum PS energy can produce during the year.

PS consists in 6 modules of polycrystalline silicon (rigid panels) of 85 W each one, these modules are connected in a series-parallel arrangement to produce 510 W at optimum sunlight and it can generate 2.55 kWh / day when the irradiance is 1000W $m^{-2}$ in March and 1.535 kWh / day when the irradiance is 700W $m^{-2}$ in December.

The PS is a type island or stand alone, which is independent of the grid, it requires a DC/DC regulator, an inverter and batteries to regulate the electricity produced and store the minimum energy required for H2 production. The electrical specifications of the solar panels, DC/DC controller and inverter are presented in Table 1.

**Table 1**. Electrical Specifications of PS

| **Solar Panel** | | **DC/DC Regulator** | |
|---|---|---|---|
| Maximum Power | 87W (+10%/ -5%) | Nominal Voltage | 12/24V |
| Maximum Power | 17.4V | Maximum Current | 20A |

| | | | |
|---|---|---|---|
| Voltage | | | |
| Maximum Power Current | 5.02A | **Inverter** | |
| Open Circuit Voltage | 21.7 | Output Voltage | 120VAC |
| Short Circuit Current | 5.34A | Output Frequency | 60Hz |
| *STC: Irradiance 1000W/m$^2$ AM1.5 Spectrum, module temperature 25°C | | | |

The second step is the generation of H2 and O2, which are produced with a commercial PEME (Peak Scientific PH300), this device produces $H_2$ in a range of 30 to 300ml min-1 at pressures from 7 kPa to 827 kPa, with consumption of 340W, alternating current (AC).

The proper analysis of the internal elements, especially the electrolytic cell (EC) is essential to understand the behaviour of the PEME that works with AC in order to adapt it in a correct way, therefore create a correct energy management. EC behaviour was analysed, obtaining performance curve current vs voltage (VvsI) at different pressures, it was also analysed the quantity of $H_2$ produced as a function of the current applied into the EC (Flow vs. current) at different pressures., which was evaluated with the Michael Faraday law, equation 1.

$$m = ItEe \quad (1)$$

for this case of study *m* is the mass of H2 produced, *I* is the applied current *t* is the time *Ee* is the electrochemical equivalent.

The third stage is the storage of $H_2$ and $O_2$. The storage system (SS) was designed in relation with the demand of the PEMFC, it is worth noting that the $H_2$ has the highest energy content per unit of weight, but not per unit volume. This relatively low volumetric energy content is an important scientific and technological challenge for store $H_2$.

$H_2$ storage system stationary may occupy a relatively large volume and it is able to operate at lower temperatures and pressures where the refuelling time can be large, in the right conditions.

The SS was designed in order to save energy, storage systems such as pressurized tanks at high pressures requires a compressor to store the gases entails to increased energy consumption, likewise hydride systems for storing $H_2$ are really efficient however, these systems are often expensive and require significant care, these are the reasons that it was designed a variable volume system at Mexico City conditions (25 ° C, 585mmHg).

The SS illustrated in Figure 2 is composed of a main acrylic manufactured container which contains water, within these two floating capsules are of the same material, where $H_2$ and $O_2$ are stored in each one of these. System capacity is 15 l of $O_2$ and 30l of $H_2$. The system was designed in order to be safe as the water protects gases to escape through the bottom of the container. Connections were designed especially for the safe handling of $H_2$, based on the Hydrogen Technologies Code NFPA standard.

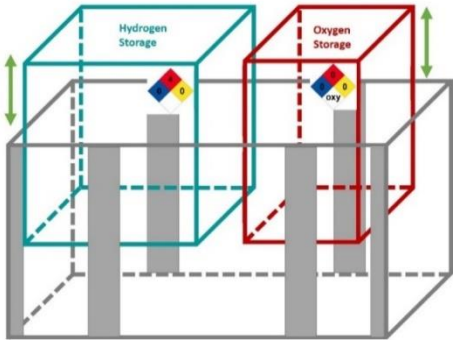


**Fig 2.** Storage System

The residence time or duration of the gases in the SS according to consumption was analysed, allowing to understand the operating time of the PEMFC proposed to lighting and the time available for analysis of different PEMFC's according to the consumption of these in the analyses tests. The power available by the $H_2$ stored in the SS according with the environmental conditions was analysed.

The fourth step is the generation of electricity by the PEMFC's, the system was designed to operate a PEMFC which was designed at the CINVESTAV-IPN Zacatenco by a group of experts in the area. The PEMFC designed for this project (Figure 3) contains 20 individual cells, each with an active area of 0.0035m2. The cells are stacked in a series configuration with current collectors placed in the anode and cathode sides. The components considered in the volume size restriction are: end plates, current collectors, bipolar plates, all seal materials and MEAs. The dimensions of the PEMFC are 0.13mx 0.075 m 0.140 m when it is fully assembled, its weight is 1.6 kg.

PEMFC is expected to consume 800 ml min-1 of H2 and 400ml min-1 O2 at a pressure of 1.2 bar to generate 50W of power. It was designed an automatic regulation system of

gases in to the PEMFC, which enables different PEMFC's for future experiments having a constant and controlled feed.

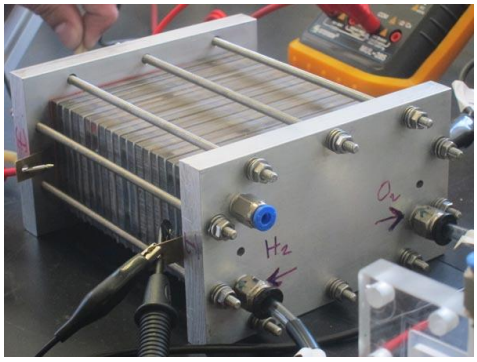


**Fig 3.** PEM Fuel Cell

The fifth step consists in the electrical charges energized by the PEMFC which in this case is two LED lamps of 25W each one with a predetermined time interval work. Power consumption LED lamps was analysed in relation to the amount of energy that the PEMFC can provide. It permits to determine the adjustments required by the system for proper operation.

The five principal steps of the global system are showed in the schematic diagram, figure 7, and described in table 3 where the different connections and lines have been detailed that de global system requires for a correct and safe operation.

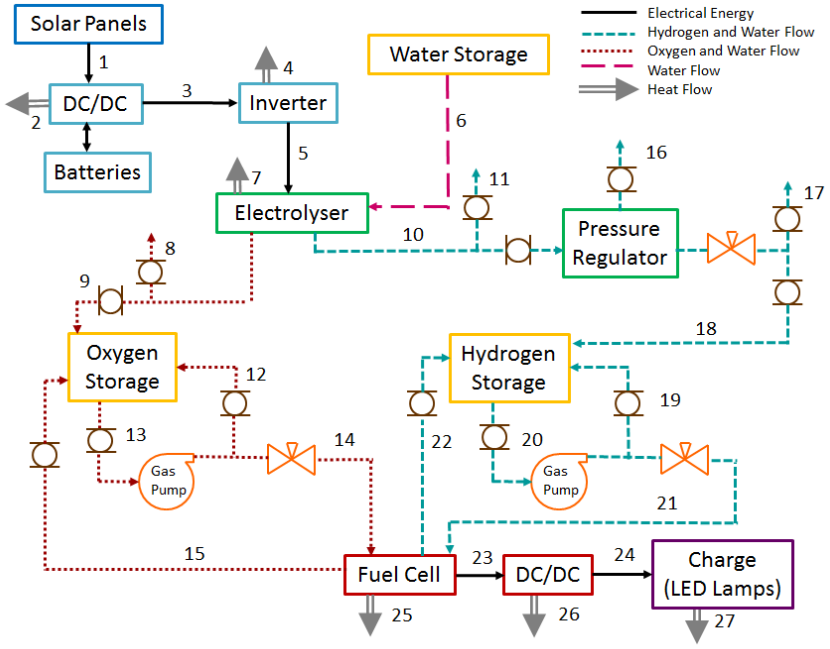


**Fig 4.** Photovoltaic-hydrogen system schematic diagram

**Table 2.** Information of photovoltaic-hydrogen system schematic diagram

| Flow | Typology | Flow | Typology | Flow | Typology |
|---|---|---|---|---|---|
| 1 | Electrical Energy | 10 | $H_2$ | 19 | $H_2$ Recirculation |
| 2 | Heat Flow | 11 | Purge | 20 | $H_2$ |
| 3 | Electrical Energy | 12 | $O_2$ Recirculation | 21 | $H_2$ Regulated |
| 4 | Heat Flow | 13 | $O_2$ | 22 | $H_2$ + $H_2O$ Recirculation |
| 5 | Electrical Energy | 14 | $O_2$ Regulated | 23 | Electrical Energy |
| 6 | $H_2O$ | 15 | $O_2$ + $H_2O$ Recirculation | 24 | Electrical Energy |
| 7 | Heat Flow | 16 | Purge | 25 | Heat Flow |
| 8 | Purge | 17 | Purge | 26 | Heat Flow |
| 9 | $O_2$ | 18 | $H_2$ | 27 | Heat Flow |

In colour blue is showed the first step PS, in colour green the second step the PEME, in colour yellow the third step SS, in colour red the fourth step PEMFC and the fifth step in colour purple the charges.

## 2.2 Energy management strategy (EMS)

It exists different types of strategies of energy management. Most of them included computational programming that include a linear programming approach, artificial intelligence approach with a fuzzy logic controller, these strategies include standalone hybrid renewable energy systems and grid-connected hybrid renewable systems [4]. For this work, we developed an energy management strategy where the user takes decisions according with an algorithm and it is no used a computational strategy. Obviously computational strategy has several advantages than a manual strategy, one of this is an autonomous management.

A manual strategy allows to understand how human decisions could affect the efficiency and efficacy of the system and it shows the importance of the planning the use of the primary source that is PS and the secondary source the H2. Especially when the system has important limitations for example the quantity stored of H2 that is the case. In figure 5 is shown the general strategy for the system focused in H2 system. Strategy is based on using the PS before using H2 system.

It is very important to understand that to increase the efficiency and efficacy of the system, it is necessary to make use of particular methodologies for each section of the global system. For example, H2 production requires alternating current, so it is a priority that it always operates at its maximum capacity of hydrogen production with the lowest possible energy consumption.

The EMS also has to take in consideration the time of the day in order to take the best decision, for example, if it is early morning, proximately 7am or if it is starting to dusk, proximately 7pm, the PS will not able to produce enough energy to starts PEME. So, we have to create a time map where shows the best periods to make the activities and it inform us about what are the repercussions of decisions taken, for example if we use H2 during the evening or at night, in the early morning next day will cannot use it again, we will have to wait until PS and PEME can produce H2.

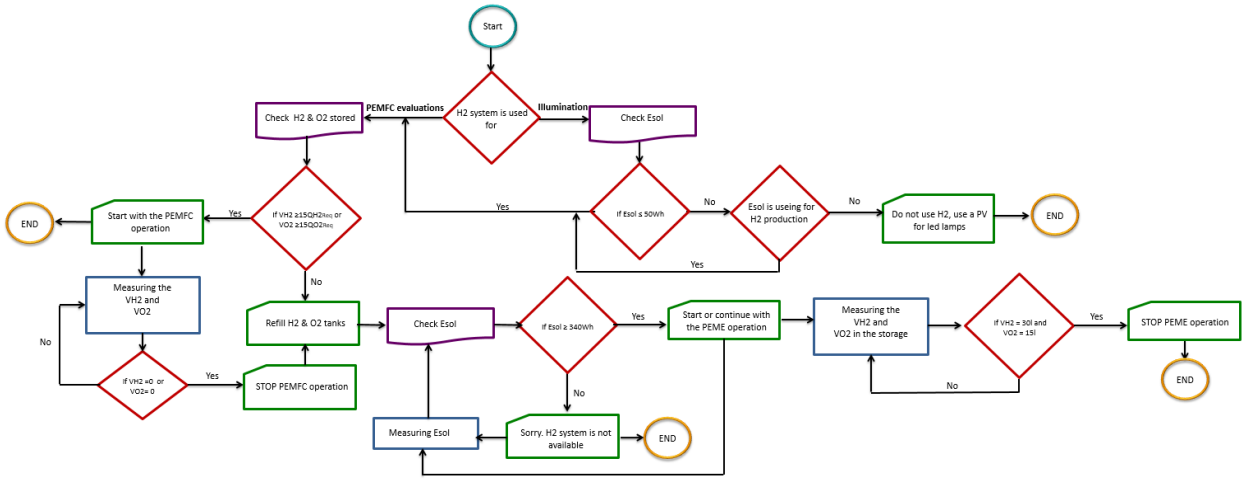


**Fig 5.** Proposed energy management strategy

It is studied this algorithm and it is expected to obtain the best periods to do the different activities, H2 production, illumination with H2, illumination with PS, PEMFC's evaluations.

## 3. Results and Discussion

It was studied PEME energy consumption (figure 6). We can observe the energy consumed by the PEME only for $H_2$ production compared to the charge of the auxiliary energy conversion from AC to DC and the control system.

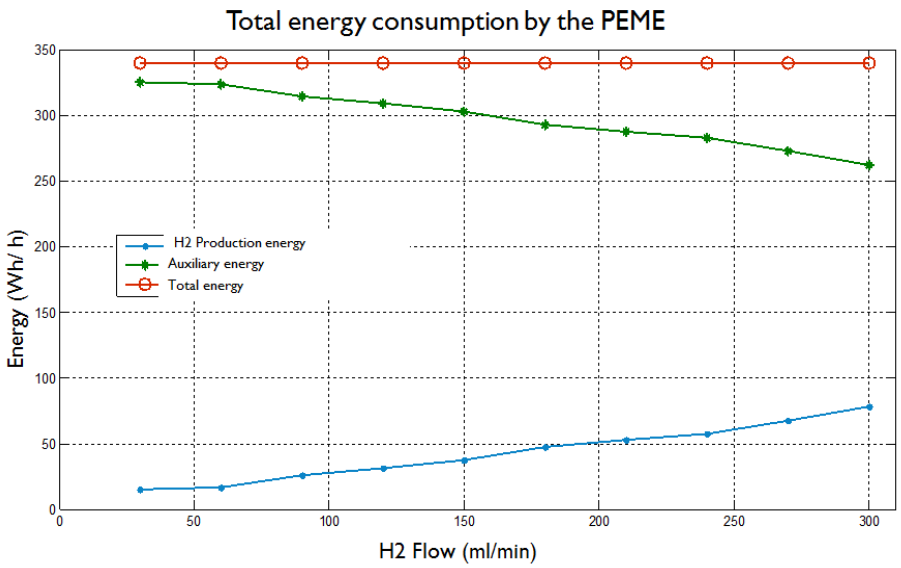

**Fig 6.** Total energy consumption by the PEME

Figure 6 allows to understand that if we operate the PEME at maximum capacity the efficiency production of H2 will be higher due to the energy consumption for different flow rate H2 production is the same. The energy required to produce 30l at 60 ml $min^{-1}$ H2 production is 2.833kWh and for 300ml ml $min^{-1}$ is 566.67Wh. At low capacity, it is required five times more energy than at maximum capacity. This information shows the importance to implement PEME with a DC power electronics. Where the energy consumption can depend of the H2 produced.

The energy balance (figure 7 and table 3) permits to understand the system requires a lot of energy for the electrolysis process due it is used a AC PEME. The most important thing in this system is the flexibility of energy, where it is possible to use $H_2$ energy when it was required.

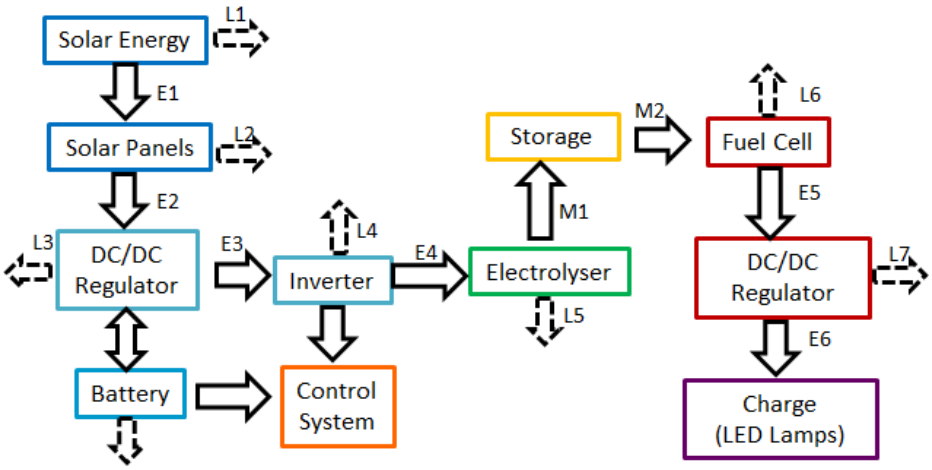


**Fig 7.** Energy flows in the system

**Table 3.** Energy flows in the system

| Flows | Energy | Flows | Energy |
|---|---|---|---|
| E1 | 1336 Wh/$m^2$ | M1 | 76.29 Wh |
| E2 | 697.39 Wh | M2 | 64.66 Wh |
| E3 | 627.653 Wh | E5 | 50Wh |
| E4 | 566.67 Wh | E6 | 50Wh |

| | **Activity** | **Best time to do** |
|---|---|---|

| | | |
|---|---|---|
| 1 | PS not for H2 production | When storage is full and it is not required illumination |
| 2 | PS for H2 production | Between 11am to 4pm |
| 3 | Illumination with PS | When storage is full or PS has an energy surplus |
| 4 | Illumination with H2 | Between 7am to 11am and 4pm to 9pm or when PS is no available |
| 5 | PEMFC's evaluations | Between 11am to 4pm. |

## 4. Conclusion

1. The design of a solar-hydrogen hybrid system is of great current importance, allowing to understand and solve the challenges of sizing for optimal and safe use.

2. The optimum hydrogen production and safe storage is very important in a power generation system based on hydrogen, therefore it is possible to determine with the analysis that the adaptation of a commercial PEM electrolyser is feasible for this purpose.

3. The development of a variable volume storage reduces energy consumption to only require the pressure of H2 and O2 production electrolyser avoiding auxiliary systems to perform this task. However, for systems that require greater amount of H2 it is impractical a system of this type in relation to size, increasing the risk of storage.

4.It is very important to implement an energy management strategy in order to get a better efficiently and effectively of the hybrid system.

5. The strategy implemented allows to understand that the PEME should be used at maximum capacity because its energy consumption is constant.

6. H2 as a gas test in PEMFC evaluations increases its usefulness sand its efficacy.

7. Strategy will allow to have available the energy of the PS and H2 as much time as possible.

## Acknowledgements

We tank to IPN multidisciplinary project SIP-1820 (2017-2018) and to CONACYT project of CEMIE-Océano 249795: Transverse Line I-LT1 "*Technologies and strategies of electrical interconnection of ocean energies for the Mexican Territorial sea*"

## References

[1]Geophysics Institute, Radiación Solar Promedio Disponible en la Ciudad de México, UNAM., Mexico., 2005.

[2]Fernández JM. Compendio de Energía Solar, Fotovoltaica, Térmica y Termoeléctrica. 1st ed. Madrid: Mundi-Prensa AMV Ediciones; 2010.

[3] PH User Manual, PEAK Scientific, Scotland., 2011.

[4] Mompin P. Energía Solar Fotovoltaica. 2nd ed. Barcelona: Marcocombo; 1985.

[5] Aguer M , Miranda A. El Hidrógeno, Fundamento de un futuro equilibrado. 1st ed. España: Ediciones Díaz de Santos; 2005.

[6] Hoogers G. Fuell Cell Techonology, Handbook. 1st ed. USA: CRC Press LLC; 2003.

[7] Barbir F. PEM Fuel Cells, Theory and Practice. 2nd ed. USA: Elsevier, Inc; 2013.

[8] Corbo P, Migliardini F, Veneri O. Hydrogen Fuel Cell for Road Vehicles. 1st ed. London: Springer-Verlag; 2011.

[10] Smith JM, Van Ness HC, Abbott MM. Introducción a la termodinámica en Ingeniería Química. 7th ed. Mexico: Mc Graw Hill; 2007.

[11] A. Rabhi, J. Bosch, A. Elhajjaji, Energy Management for an Autonomous Renewable Energy System, Energy Procedia, Volume 83, 2015, Pages 299-309, ISSN 1876-6102, http://dx.doi.org/10.1016/j.egypro.2015.12.184.

[12] Lanre Olatomiwa, Saad Mekhilef, M.S. Ismail, M. Moghavvemi, Energy management strategies in hybrid renewable energy systems: A review, Renewable and Sustainable Energy Reviews, Volume 62, 2016, Pages 821-835, ISSN 1364-0321, http://dx.doi.org/10.1016/j.rser.2016.05.040.

[13] IEA (2014a). Technology Roadmap Energy storage. OECD/IEA, France

[14]IEA (2015c). Technology Roadmap Hydrogen and Fuel Cells. OECD/IEA, France

# CHAPTER 5
# Renewable Energy Systems

# 5.1 Ultrasonic synthesis of acanthite silver sulfide nanoparticles for solar energy harvesting

Joselyne Soria, Ma. Concepción Arenas-Arrocena

[1]Laboratorio de Investigación Interdisciplinaria, Área de Nanoestructuras y Biomateriales, Escuela Nacional de Estudios Superiores Unidad León, Universidad Nacional Autónoma de México, León, Guanajuato 37684, México

* Corresponding author: 477 194 08 00 ext 43418, carenas@enes.unam.mx; mcaa05@gmail.com

## ABSTRACT

Introduction: Silver sulfide ($Ag_2S$) is a non-toxic semiconductor with a narrow band gap about 1.0 eV and a high optical absorption ($10^4$ $cm^{-1}$). It is a good option as energy harvesting for solar cells applications. The size and morphology depend on the reaction conditions and the synthesis method.

Objective: To synthesize silver sulfide nanoparticles by using ultrasonic waves as a function on the time.

Methodology: The ultrasonic synthesis was carried out at 42 kHz for 1, 2 or 3 h. Briefly; solutions of sodium citrate ($9.9x10^{-3}$ M), silver nitrate ($5x10^{-2}$ M) and sodium sulfide ($2x10^{-2}$ M) were mixed and subsequently an excedent solution of sodium sulfide ($2x10^{-4}$ M) was added, the mixture was kept under ultrasonic stirring (1, 2 or 3h). The dark product was washed several times with water by using centrifugation.

Results: Nanoparticles presented acanthite phase (PDF#014-0072) according with the X ray results: the crystallinity increased as a function on the ultrasonic time without any phase change. The size of nanoparticles was 9.44 nm ± 1.56 nm at 1 h, 9.12 nm ± 1.23 nm at 2 h and 14.14 nm ± 3.30 nm at 3 h. The maximum optical absorption of the silver sulfide was in the range 382 nm to 461 nm and the band gap was from 1.04 to 1.32 eV.

Conclusion: The ultrasonic synthesis was an effective to obtain regular silver sulfide nanoparticles, which could be used to for solar energy harvesting accoriding to the optical properties.

Acknowledges: Thanks to SENER-CONACyT for its financial support through project no. 207450 (CEMIE-Sol/27) and CONACyT México (CB176450).

***Keywords:*** nanoparticles; metallic sulfides, photovoltaic effect, morphology.

# 5.2 Reducing sugar recovery by acid hydrolysis of corn stover for biohydrogen production

J. C. Gómora-Hernández, M. C. Hernández-Berriel, S. M. Fernández-Valverde

[1]Depto. de Química, ININ, A.P. 18-1027, México D.F. C.P.11801, Mexico. Tel. 5553297200 ext 12277

[2]ITT, Avenida Tecnológico s/n, Fracc. La Virgen, Metepec, Edo Mex., México. C.P. 52149. Tel. 7222087200

* Corresponding author: 5553297200 ext. 12277, suilma.fernandez@inin.gob.mx

## ABSTRACT

Corn in Mexico is one of the most important agricultural crops, residues generated after harvesting are burned contributing in this way to environmental deterioration due to greenhouse gasses emissions or they are disposed in open dumps provoking soil erosion, as a result of biological decomposition. Corn stover is comprised mainly by cellulose and hemicellulose, for this fact stover has been considered as a promising source for value-add product production if this residue is treated and properly hydrolyzed into its monomeric sugars. In recent years corn stover use for energy purposes has been studied extensively, however, in order to increase the performance of sugar recovery and biohydrogen production more researches are needed. The aim of the present work was to evaluate the sugars production from corn stover by acid hydrolysis as well as to estimate biohydrogen production from these sugars. The experiments were carried out in 5 g of dried material in 75 mL of two different phosphoric acid solutions (3 or 7%v) heated at two temperatures 100ºC or 130ºC during 2 h, after hydrolysis solid and aqueous phase were separated. The amount of sugars in liquid phase was determined by dinitrosalicylic acid method, while holocellulose content and hydrolyzed mass yield were calculated in solid phase. The maximum sugar production yield was 30.42 g of sugars / 100 g of corn stover obtained with 7%v phosphoric acid solution heated at 130ºC for 2 hours; this value corresponds to a holocellulose-sugar conversion of 47.39%. At this hydrolysis conditions, the maximum hydrolyzed corn stover yield and the minimum holocellulose mass were 58.51% and 1.36 g respectively. According to IR spectroscopy of solid phase, vibrational bands of hemicellulose located at 1732 and 1238 $cm^{-1}$ corresponding to C-O linkage diminished its intensity after hydrolysis. The estimation of biohydrogen production by dark fermentation employing reducing sugars present in corn stover hydrolysates is also discussed.

***Keywords:*** Agricultural wastes, dark fermentation, hydrolysis, phosphoric acid, saccharides.

## 1. Introduction

Lignocelluloses are the most abundant biomasses around the world; their annual production exceeds 220 billion tons worldwide and covers some biomaterials such as hardwood, softwood, grasses, agricultural wastes and forestry residues. Lignocellulose is mainly composed by cellulose, hemicellulose and lignin. Both cellulose and hemicellulose are comprised by pentoses and hexoses which can be used for microorganisms in biotechnological processes to produce chemicals, fuels, drugs and energy [1]. Lignin is formed by three cross-linked phenyl propane units and is the most recalcitrance compound of lignocellulose. This carbohydrate represents the physical barrier of cell wall plants and confers rigid, impermeability and resistance to microbial attack and to oxidative stress [2].

Pretreatment technologies have the aim of remove partially amount of lignin, disrupt physicochemical structure of lignocellulose, reduce the degree of polymerization and cristalinity of cellulose, increase surface area and even produce monomeric sugars from hemicellulose and cellulose [3]. There is a wide variety of pretreatment methods, the most important technologies can be categorized into physical (steam explosion, liquid hot water), chemical (acid, alkali, ionic liquids) and biological (enzymes). Among all chemical pretreatments, acid hydrolysis has been reported as a very effective and fast way to remove lignin and to produce monomeric sugars mainly from hemicellulose [4]. Sulfuric acid has been the most employed acid due to its high catabolic activity, however, other acids such as phosphoric and hydrochloric has some advantages over sulfuric acid like being less corrosive, less toxic, contributes to reducing the construction and operational costs as well as phosphorus can be served as a nutrient for the microorganisms employed in the subsequent fermentation process [5, 6].

Corn stover is one of the most abundant agricultural residues around the world. In USA the amount of this waste is approximately 3 MT $ha^{-1}$ $year^{-1}$ and about 20% is attributed to cobs [7], moreover, in agreement with Cao *et al.* [8], China produces 1.2 billion dry tons per year of corn stover. This agricultural waste in addition to be abundant has the potential to be used for biofuels production. In recent years some countries such as China and Brazil have developed biorefinery processes for bioethanol production [9]; however, studies related for biohydrogen production from lignocelluloses are still few. The aim of the present work was used dilute phosphoric acid to obtain the maximum amount of reducing sugars from corn stover. Temperature, acid concentration and reaction time were considered as variables, while sugar production, combined severity factor and holocellulose fraction were the responses. Biohydrogen production from sugars obtained by acid hydrolysis was estimated employing empirical yields.

## 2. Materials and Methods

### *2.1 Raw material*

Corn stover was collected from a local crop located in Mexico State, Mexico. This waste was air-dried at room temperature, milled using an agricultural mill and then separated to recovery particles with a size under 250 µm. Dried particles were stored at room temperature until further use. The amount of ashes and volatile total solids (VTS) were quantified according to Standard Methods [10]. The content of holocellulose and lignin present in raw corn stover was respectively determined using chlorite method [11] and the ASTM D1106-56 technique reported by Colín-Urieta [12].

### *2.2 Acid hydrolysis of corn stover*

Acid hydrolysis was carried out at 100ºC and 130ºC and at initial phosphoric acid concentration of 3%v and 7%v. Operational conditions were selected according with previous works [5,8,13]. 5 g of milled and dried raw corn stover was mixed with 75 mL of phosphoric acid solution into a 150 mL glass flasks and the mixture was slowly homogenized.

The glass flasks were heated until desired temperature and after 15, 30, 60, 90 and 120 minutes every glass flask was cooled at room temperature for 30 minutes. The solid and liquid phases were separated by filtration. The amount of reducing sugars and pH were determined in hydrolysate (liquid phase). Combined severity factor (CSF) was calculated to integrate the combined effect of temperature, reaction time and pH into a single factor and in agreement with Pappas *et al.* [14] it can be defined as follows.

$$CSF = \log[t \cdot exp\left(\frac{T_H - T_r}{14.75}\right) - pH] \quad (1)$$

Where $t$ is the reaction time in minutes, $T_H$the reaction temperature in ºC, $T_r$ the reference temperature most often 100ºC and $pH$ is the acidity of the aqueous solution at the end of the hydrolysis.

The remainder solid phase was washed with hot water until pH 7 and then it was dried overnight at 50ºC. The content of holocellulose was determined [11] in the solid phase, and a Fourier Transform Infrared Spectroscopy (FTIR) analysis was performed in order to examine the structural changes on corn stover attributed to acid hydrolysis.

### *2.3 Quantification of reducing sugars*

The total amount of reducing sugars was quantified by dinitrosalicylic acid (DNS) method [15]. 300 µL of each hydrolysate was diluted with deionized water until 3 mL of final volume and were mixed with sodium hydroxide until reach pH 8, then they were centrifuged at 10,000 rpm for 5 minutes and 500 µL of liquid phase was taken and mixed with 500 µL of DNS reagent in a 12 mL test tube, which were subsequently placed in a water bath at 92ºC for 5 minutes. Tubes were cooled at room temperature and 10 mL of

deionized water was added. Absorbance was read at 540 nm. Calibration curve was made using xylose as reference sugar; a prior analysis of corn cob hydrolysate showed the presence of this sugar as the main product.

### *2.4 FTIR analysis of raw and hydrolyzed corn stover*

FTIR was used to analyze the main functional groups as well as to determine the structural changes attributed to acid hydrolysis. Raw and hydrolyzed corn stover was analyzed in a *"Varian 640"* spectrometer employing a spectral range of 400 to 4000 $cm^{-1}$ with a resolution of 4 $cm^{-1}$ in 16 scans.

### *2.5 Estimation of biohydrogen production from reducing sugars*

Hydrogen production yields from hydrolysates of corn cob and faba bean stem obtained in the same experimental conditions used in this research were considered to estimate, the maximum amount of hydrogen production from the corn stover hydrolysates obtained in this work. The results were referred to hydrogen produced with a consortium of mesophilic bacteria.

## 3. Results and Discussion

### *3.1 Composition of corn stover*

VTS is defined as a measured of organic load that can be consumed by microorganisms. The content of VTS present in raw corn stover was 87.25% ± 0.47%, thus, the percentage of ashes calculated was 12.85%. The amount of holocellulose (sum of cellulose and hemicellulose) and lignin present in corn stover was respectively 64.17% ± 0.66% and 16.33% ±0.11%. The composition of raw material resulted similar to that reported previously by Avci *et al.* [6], and Cao *et al.* [8] who determined a holocellulose percentage of 63.3% and 61.1% respectively.

### *3.2 Reducing sugar production by acid hydrolysis*

The sugar production units in the present work were g sugar / 5 g corn stover. As can be seen in **Fig. 1** with exception of the experiment carried out at 130ºC and 3%v $H_3PO_4$ the rest of experiments showed the maximum production yield after 120 minutes, one possible explanation to this fact is that sugar production at 130ºC and 3%v $H_3PO_4$ reached the maximum yield at 90 minutes and after this time the velocity of sugars decomposition to furfural and hidroximetil furfural (inhibitory compounds) was higher in comparison with the velocity of sugars production [13].

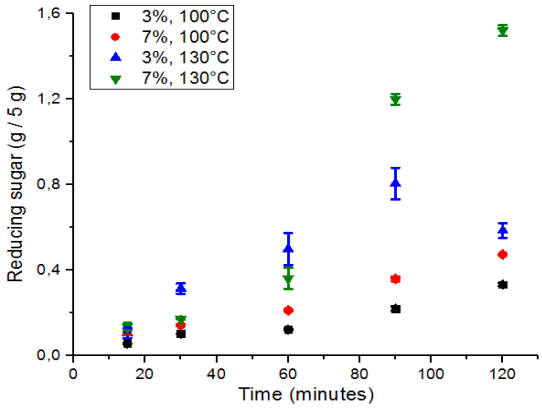


**Fig. 1** Production of reducing sugars at different hydrolysis conditions from corn stover

The minimum sugar production was obtained with 3%v $H_3PO_4$ and 100°C. The maximum sugar production was observed at 130ºC, 7%v $H_3PO_4$ and 120 minutes reaching a yield of 1.52 g / 5 g corn stover.

The conversion efficiency of holocellulosic fraction to reducing sugar was done with the total mass of holocellulose present in 5 g of corn stover (3.209 g). The maximum holocellulose-sugar conversion was 47.39%, obtained at 130°C, 7%v $H_3PO_4$ and 120 minutes reaction time. The amount of hydrolyzed biomass with $H_3PO_4$ followed the same trend at the same experimental conditions, reaching the maximum mass degradation of 58.51%. For each experiment and after 120 minutes reaction time, it was detected the lowest mass of corn stover residue, the minimum mass of holocellulose, the highest value of CSF and with exception of the experiment carried out at 130°C and 3%v $H_3PO_4$ the maximum sugar production yield. **Table 1** summarizes the data obtained after 120 minutes time hydrolysis.

**Table 1.** Data obtained after 120 minutes hydrolysis time for each experiment

| Factor | 3%v and 100ºC | 7%v and 100ºC | 3%v and 130ºC | 7%v and 130ºC |
|---|---|---|---|---|
| Sugar (g / 5 g) | 0.33 | 0.47 | 0.58 | 1.52 |
| Conversion (%) | 10.40 | 14.77 | 18.25 | 47.39 |
| Mass hydrolyzed (%) | 33.11 | 39.42 | 46.49 | 58.51 |
| Final Holocellulose mass (g) | 1.75 | 1.75 | 1.53 | 1.36 |
| CSF | 0.634 | 0.969 | 1.580 | 1.847 |

According to **Table 1,** the maximum sugar production yield is correlated with the highest value of CSF. An increase in hydrolysis temperature and acid concentration generates a gain in CSF value and a subsequent increase of sugar production yield. **Fig. 2** shows a

logarithmic increase of CSF as a function of reaction time, moreover, reducing sugars production can be correlated with CSF in an exponential function.

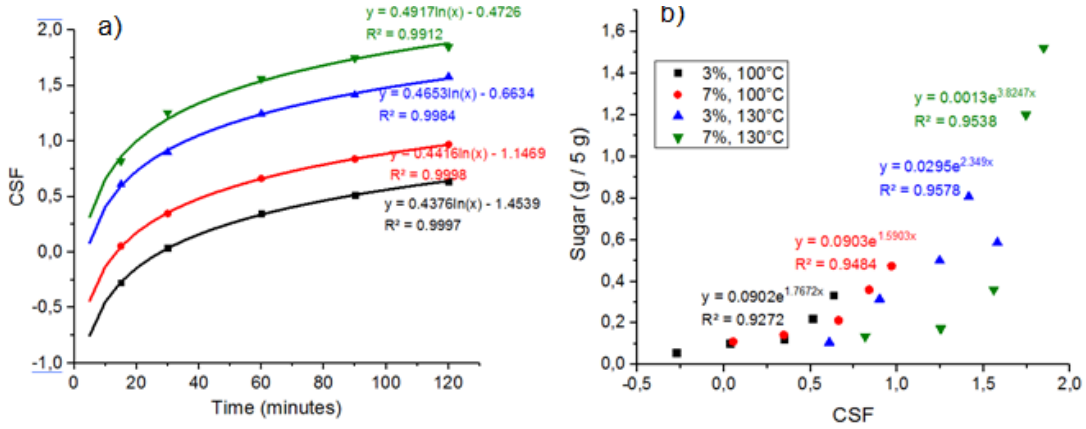


**Fig. 2** Correlation between a) CSF and reaction time and b) sugar production and CSF

Pappas *et al.* [14], studied the behavior between sugar production and CSF, the maximum production of reducing sugar reported by them was 26.1 g / 100 g raw material with CSF = 0.93, both sugar yield and CSF resulted lower in comparison to that obtained in the present work (30.4 g / 100 g corn stover at CSF = 1.85).These differences can be attributed to the hydrolysis conditions as well as the nature of raw material.

In order to compare the sugar production yield obtained in present work with data reported in literature, the sugar production yield was calculated per 100 g of raw material, the maximum value of sugar production was 30.4 g sugar / 100 g of corn stover obtained at 130°C, 7%v $H_3PO_4$ and 120 minutes. As can be seen in **Table 2**, this yield was higher in comparison with that obtained previously by Cao *et al.* [8], Guerra-Rodríguez [13], Pappas *et al*. [14] and Lloyd *et al.* [16]. The differences in sugar yields can be attributed to feedstock nature and hydrolysis conditions.

**Table 2.** Sugar production yields reported in literature

| Raw material | Hydrolysis conditions | CSF | Sugar yield (g / 100 g) | Reference |
|---|---|---|---|---|
| Corn stover | 7%v $H_3PO_4$, 130°C, 120 min, solid-liquid ratio 1:15. | 1.85 | 30.4 | Present work |
| Corn stover | 2.13%v $H_2SO_4$, 121°C, 105 min, solid-liquid ratio 1:10 | - | 12.23 | [8] |
| Wheat straw | 0.55%v $H_2SO_4$, 130°C, 180 min, solid-liquid ratio 1:12 | - | 26.8 | [13] |
| *Phalaris aquatica L* | 2%w $H_2SO_4$, 130°C, 30 min, solid-liquid ratio 1:10<br><br>Enzymatic hydrolysis: 50°C, 150 rpm and 24 hours. | 0.93 | 26.1<br><br>58.5 | [14] |
| Corn stover | $H_2SO_4$ at pH1.24, 160°C, 5 min | 1.22 | 8.79 | [16] |
| Stem of faba bean | 7%v $H_3PO_4$, 130°C, 120 min, solid-liquid ratio 1:15. | 1.83 | 16.57 | [17] |
| Corn cob | 7%v $H_3PO_4$, 130°C, 120 min, solid-liquid ratio 1:15. | 1.84 | 42.72 | [17] |

### *3.3 FTIR analysis of raw and hydrolyzed corn stover*

**Fig. 3** shows the FTIR spectra of raw and hydrolyzed corn stover at 130°C, 7%v $H_3PO_4$ and after 60 and 120 minutes. The acronyms C, H and L corresponds to cellulose, hemicellulose and lignin respectively, β is representative of beta 1-4 glycosidic bond, own of cellulose and hemicellulose. All spectra were normalized. In agreement with Li *et al.* [9] and Hsu *et al.* [18] between 1200 and 1000 $cm^{-1}$ characteristic vibrational bands of cellulose appears. Hemicellulose showed its main vibrational bands at 1240 cm-$^{1}$ and 1732 $cm^{-1}$. This last vibration has been attributed to the ester linkage C=O of acetyl group as well as to covalent bond between hemicellulose and lignin. β glycosidic bond was detected in all spectra at 897 $cm^{-1}$, while the main vibrational bands of aromatic skeletal of lignin was observed at 833, 1422, and 1511 $cm^{-1}$. After dilute acid hydrolysis, adsorption bands of lignin increased their intensity and amplitude. In opposite case, the main vibrational bands of cellulose and hemicellulose diminished as a function of reaction time. This fact suggests that monomeric sugars present in hydrolysate were formed by depolymerization of cellulosic and mainly hemicellulosic fraction. The O-H bond located at 1645 $cm^{-1}$ is attributed to residual moisture, however, at 1200 $cm^{-1}$ this linkage was only detected after hydrolysis and is associated to hidroxi functional group of cellulose and hemicellulose. H-C-H bonds observed at 1310 $cm^{-1}$ is also related to these polysaccharides.

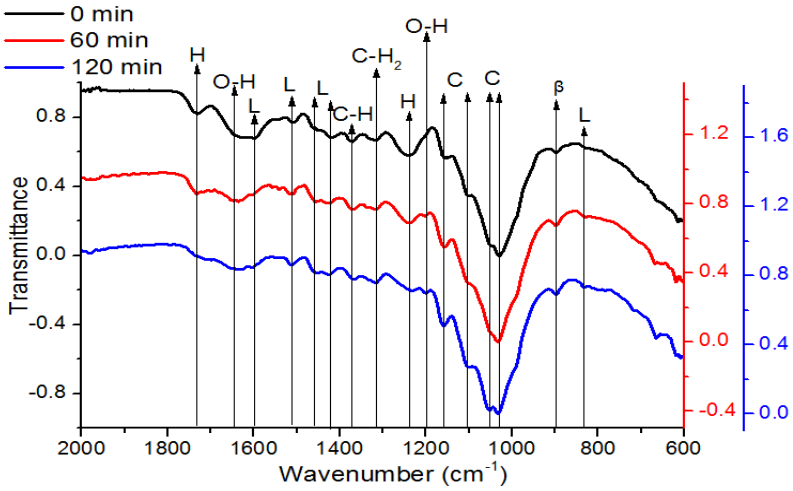


**Fig. 3** FTIR spectra of corn stover before and after acid hydrolysis at 130°C and 7%v $H_3PO_4$

### *3.4 Estimation of biohydrogen production from reducing sugars*

The maximum sugar production yield was 30.4 g of sugar / 100 g of corn stover obtained in the experiment carried out at 130°C, 7%v $H_3PO_4$ and 120 minutes hydrolysis time. This value was used to estimate biohydrogen production by dark fermentation. Taking into account the maximum hydrogen yields obtained in previous work with *Clostridium butyricum* and *Enterobacter cloacae*; mol $H_2$ / mol hexose 0.52 for corn cob and 0.33 for stem of faba bean hydrolysates [17]. The maximum hydrogen production volume is 1.96 and 1.25 liters respectively.

Lo *et al.* [19] studied biohydrogen production from glucose obtained by acid and enzymatic hydrolysis of microcrystalline cellulose employing *Clostridium butyricum* as fermentative microorganism. 1.58 mol $H_2$ / mol hexose was the maximum hydrogen production yield, thus, the hydrogen production volume expected with this yield is 5.98 liters. The difference between this yield and that obtained in the present work can be due to that: enzymatic hydrolysis not produces inhibitor compounds which negatively affect bacteria metabolism.

As can be seen in **Table 3**, approximately 2 liters of biohydrogen can be produced assuming an experimental yield of 0.52 mol $H_2$ / mol hexose from 75 g of raw corn stover, and with the highest yield (1.73 mol $H_2$ / mol hexose) 6.54 liters could be obtained [20]. These values show the potential of corn stover acid hydrolysates for its application in biohydrogen production.

In order to increase biohydrogen production from corn stover hydrolysates two ways are possible: thermophilic fermentation or microbial electrolysis cell which has a maximum theoretical hydrogen production yield of 4 [22] and 12 mol $H_2$ / mol hexose [23]

respectively. Considering these hypothetical yields the maximum volume of hydrogen expected from reducing sugars recovered by acid hydrolysis at 130ºC and 7%v $H_3PO_4$ are 15.14 and 45.43 liters for dark fermentation and microbial electrolysis cell respectively.

**Table 3.** Estimation of biohydrogen production from reducing sugars

| Raw material | Hydrolysis conditions | Bacteria | mol $H_2$ / mol hexose | Hydrogen expected (L) | Reference |
|---|---|---|---|---|---|
| Stem of faba bean | 7%v $H_3PO_4$, 130°C, 2 hrs. | *Clostridium butyricum* and *Enterobacter cloacae* | 0.33 | 1.25 | [17] |
| Corn cob | 7%v $H_3PO_4$, 130°C, 2 hrs | *Clostridium butyricum* and *Enterobacter cloacae* | 0.52 | 1.96 | [17] |
| Microcrystalline cellulose | 83%v $H_3PO_4$, 50°C, 30 min. Enzymes | *Clostridium butyricum* | 1.58 | 5.98 | [19] |
| Sugarcane bagasse | 0.5 %v $H_2SO_4$, 60 min, 121°C. | *Clostridium butyricum* | 1.73 | 6.54 | [20] |
| Rice straw | 55%v $H_2SO_4$, 40°C y 20 min. | Mesophilic anaerobic sludge | 0.44 | 1.66 | [21] |

## 4. Conclusion

Acid hydrolysis with $H_3PO_4$ is an efficient method to obtain high amount of reducing sugars from holocellulosic fraction of corn stover. The sugar yield can be improved increasing acid concentration and reaction time. The reducing sugars obtained in acid hydrolysis were mainly produced from hemicellulosic fraction present in corn stover.

Reducing sugars seems to have the potential to produce biohydrogen, however, is necessary to obtain experimental data of hydrogen production with corn stover hydrolysates. Biohydrogen production could be increased by using thermofilic bacteria or a microbial electrolysis.

**Acknowledgements**
Julio César Gómora Hernández thanks CONACYT for his Doctorate scholarship. ITT and ININ sponsored this work.

**References**

[1] Kumar G., Bakonyi P., Periyasamy S., Kim S. H., Nemestóthy N., Bélafi-Bakó K. Lignocellulose biohydrogen: Practical challenges and recent progress. *Renewable and Sustainable Energy Reviews*. 2015; 44: 728-737.

[2] Singh R., Shukla A., Tiwain S., Srivastava M. A review on delignification of lignocellulosic biomass for enhancement of ethanol production potential. *Renewable and Sustainable Energy Reviews*. 2014; 32: 713-728.

[3] Behera S., Arora R., Nandhagopal N., Kumar S. Importance of chemical pretreatment for bioconversion of lignocellulosic biomass. *Renewable and Sustainable Energy Reviews*. 2014; 36: 91-106.

[4] Camesasca L., Ramírez M. B., Guigou M., Ferrari M. D., Lareo C. Evaluation of dilute acid and alkaline pretreatments, enzymatic hydrolysis and fermentation of napiergrass for fuel ethanol production. *Biomass & Bioenergy.* 2015; 74: 193-201.

[5] López-Linares J. C., Cara C., Moya M., Ruiz E., Castro E., Romero I. Fermentable sugar production from rapeseed straw by dilute acid phosphoric acid pretreatment. *Industrial Crops and Products.* 2013; 50: 525-531.

[6] Avci A., Saha B. C., Dien B. S., Kennedy G. J., Cotta M. A. Response surface optimization of corn stover pretreatment using dilute phosphoric acid for enzymatic hydrolysis and ethanol production. *Bioresource Technology.* 2013; 130: 603-612.

[7] Eylen D. V., Dongen F. V., Kabel M., Bont J. Corn fibers, cobs and stover: Enzyme-aided saccharification and co-fermentation after dilute acid pretreatment. *Bioresource Technology.* 2011; 102: 5995-6004.

[8] Cao G., Ren N., Wang A., Lee D. J., Guo W., Liu B., Feng Y., Zhao Q. Acid hydrolysis of corn stover for biohydrogen production using *Thermoanaerobacterium thermosaccharolyticum* W16. *International Journal of Hydrogen Energy.* 2009; 34: 7182-7188.

[9] Li P., Cai D., Luo Z., Qin P., Chen C., Wang Y., Zhang C., Wang Z., Tan T. Effect of acid pretreatment on different parts of corn stalk for second generation ethanol production. *Bioresource Technology.* 2016; 206: 86-92.

[10] APHA. 2005. Standard Methods for Water and Wastewater Examination, 21 st ed. American Public Health Association-American Water Works Association, *Water Environment Federation Publication*, Washington, DC. USA.

[11] Wise L. E., Murphy M., D'Adieco A. Chlorite holocellulose, its fractionation and beating on summative wood analysis and on studies on the hemicelluloses. PaperTradeJournal 1946; 122:35-45.

[12] Colín-Urieta S., Ma. A. Carcía C., López A P., Rutiaga Q. J. G. Análisis preliminar de la composición química de la madera de *Cordiaeleagnoides* DC. *4to. Congreso*

*Forestal, IV Simposio Internacional sobre técnicas agroforestales, III Congreso Internacional de Jóvenes Investigadores DEFORS 2007.* La Habana, Cuba. p. 223.

[13] Guerra-Rodríguez E., Portilla-Rivera O. M., Jarquín-Enríquez L., Ramírez J. A., Vázquez M. Acid hydrolysis of wheat straw: A kinetic study. *Biomass & Bioenergy*. 2012; 36: 346-355.

[14] Pappas I. A., Koukoura Z., Tananaki C., Goulas C. Effect of dilute acid pretreatment severity on the bioconversion efficiency of *Phalaris aquatica L*: Lignocellulosic biomass into fermentable sugars. *Bioresource Technology.* 2014; 166: 305-402.

[15] M. G. Lorenz. Use of dinitrosalicylic acid reagent for determination of reducing sugars. *Analytical Chemistry.* 1959; 31: 426-428.

[16] Lloyd T. A., Wyman C. E. Combined sugar yields for dilute sulfuric acid pretreatment of corn stover followed by Enzymatic hydrolysis of the remaining solids. *Bioresource Technology.* 2005; 96: 1967-1977.

[17] Gómora-Hernández J. C., Alcántara-Díaz D., Fernández-Valverde S. M., Hernández-Berriel M. C. Biohydrogen production by anaerobic digestion of corn cob and stem of faba bean hydrolysates. *2016 XVI International Congress of the Mexican Hydrogen Society.* 2017:1-6.doi: 10.1109/CSMH.2016.7947659.

[18] Hsu T. C., Guo G. L., Chen W. H., Hwang W. S. Effect of dilute acid pretreatment of rice straw on structural properties and enzymatic hydrolysis. *Bioresource Technology.* 2010; 101: 4907-4913.

[19] Lo. Y. C., Su Y. C., Cheng C. L., Chang J. S. Biohydrogen production from pure and natural lignocellulosic feedstock with Chemical pretreatment and bacterial hydrolysis. *International Journal of Hydrogen Energy.* 2011; 36: 13955-13963.

[20] Pattra S., Sangyoka S., Boonmee M., Reungsang A. Biohydrogen production from the fermentation of sugarcane bagasse hydrolysate by *Clostridium butyricum*. *International Journal of Hydrogen Energy.* 2008; 33: 5256-5265.

[21] Liu C. M., Chu C. Y., Lee W. Y., Li Y. C., Wu S. Y., Chou Y. P. Biohydrogen production evaluation from rice straw hydrolysate by concentrated acid pre-treatment in both batch and continuous systems. *International Journal of Hydrogen Energy.* 2013; 38: 15823-15829.

[22] Ivanova G., Rákhely G., Kovács K. L. Thermophilic biohydrogen production from energy plants by *Caldicellulosiruptor saccharolyticus* and comparison with related studies. *International Journal of Hydrogen Energy.* 2009; 34: 3659-3670.

[23] Ghimire A., Frunzo L., Pirozzi F., Trably E., Escudie R., Lens P. N. L., Esposito G. A review on dark fermentative biohydrogen production from organic biomass: Process parameters and use of by-products. *Applied Energy.* 2015; 144: 73-95.

# 5.3 Activated metal-free electrocatalyst from *Sargassum spp.* for the oxygen reduction reaction

K. Perez-Salcedo, I. Lemus, D. Pacheco, R. Barbosa, B. Escobar

[1]Centro de Investigación Científica de Yucatán, Carretera Sierra Papacal– Chuburná Puerto, Km. 5, Sierra Papacal, Mérida, 97302, México.
[2]Cinvestav Unidad-Saltillo, Saltillo, 25900 México
[3]Universidad de Quintana Roo, Boulevard Bahía s/n, Chetumal, Q. Roo 77019, México

## ABSTRACT

Large surface area of biomass-derived carbons plays a vital role for the synthesis of high-quality metal-free electrocatalysts (MFE) for oxygen reduction reaction (ORR). The use of sargassum as a source for the biological synthesis of MFE is a feasible alternative since lately its overproductionhas become a problem as this waste must be constantly removed from the affected tourist areas.In this work, a new synthesis method is proposed in order to increase MFE surface area. The pristine sample was collected from Mar Caribe and washed with distilled water. Then, the sample was ground well with KOH (1: 2, 1:3 and 1:4 ratio).A pyrolytic treatment was performed in a tube furnace at 700°C under nitrogen atmosphere for 2 hours at 10°C·min$^{-1}$ heating rate. The resulted sample was washed with 2M HCl solution. The increased area was confirmed by BET. Also, CHONS, SEM, BET, FT-IR, DRX and XPS characterization was performed. ORRelectrocatalytic activity measurements were performed by the rotating disk electrode (RDE) technique at different rotation speeds (200, 400, 800, 1200, 1600 and 2000 rpm). A 0.5M KOH solution was used as electrolyte.The results showed best performance for 1:2 ratio KOH activated samples,increase in area from 59 $m^2 g^{-1}$to 1948 $m^2 g^{-1}$after acid treatment and improvement in electrochemical properties.

*Keywords:*ORR; *sargassum spp.*; KOH activation

# 5.5 Photocatalytic Studies of Calcium Doped Intergrowth Oxides $Sr_{3.2-x}Ca_xLa_{0.8}Fe_{1.5}Co_{1.5}O_{10-\delta}$

J. Oliva, C.R. Garcia, E. Verduzco, A. Martinez, A. Manthiram, and K. P. Padmasree

[1 a] Cinvestav Unidad Saltillo, Parque Industrial, Ramos Arizpe, Coahuila, 25900, Mexico

[b] CONACYT-Facultad de Ciencias Químicas, Universidad Autónoma de Coahuila, 25000, Saltillo, México

[c] Facultad de Ciencias Físico-Matemáticas, Universidad Autónoma de Coahuila, 25000, Saltillo, México

[d] Materials Science and Engineering Program & Texas Materials Institute, The University of Texas at Austin, TX 78712, USA

* Corresponding author: phone number: 8444389600, e-mail: padmasree@cinvestav.edu.mx

## ABSTRACT

The photocatalytic properties of the intergrowth oxides $Sr_{3.2-x}Ca_xLa_{0.8}Fe_{1.5}Co_{1.5}O_{10-\delta}$ (SCLFCO), with x = 0, 0.2, 0.4, and 0.8 has been studied by monitoring the degradation of methylene blue (MB) dyein water solution under solar irradiation. The SCLFCO samples were synthesized by a conventional solid-state reaction. XRD patterns show the presence of tetragonal phase for undoped and Ca doped SCLFCO samples. Scanning electron microscopic image of SCLFCO samples showed a mixture of small and large irregular grains and the grain size decreases with the increase in calcium concentration. Furthermore, an enhancement of the absorption band in the UV-VIS-NIR range occurred as the amount of calcium dopant increases, which is beneficial for the photocatalytic process because the degradation of MB dye was possible under solar irradiation. The SCLFCO sample doped with x = 0.8 produced a total degradation of MB (100%) after 150 min at a pH = 6.0, whereas the undoped sample showed only a maximum degradation percentage of 27 % after 300 min. Hence, our results suggest that Ca doping with x = 0.8 in the SCLFCO sample could be useful for the degradation of dyes under solar exposure in water treatment plants.

***Keywords:*** intergrowth oxides; methylene blue; solar photocatalysis; Ruddlesden–Popper phase

## 1. Introduction

Since the development of $TiO_2$-based semiconductive photocatalysts for the photoelectric conversion of water into hydrogen, various photocatalytic semiconducting materials

received much attention [1]. In recent years, perovskite-related intergrowth oxides or layered perovskites have attracted considerable attention because of their interesting properties including colossal magnetoresistance, superconductivity, ferroelectricity, photocatalysis, ionic conductivity, ion-exchange, ion intercalation [2,3]. Therefore, there is an active research to develop new layered perovskites. Recently, the layered perovskites belonging to Ruddlesden-Popper (R–P) family of general formula $A_{n+1}B_nO_{3n+1}$ (A = alkali, alkaline earth or rare earth; B = transition metal) have investigated widely because of their electrical and electrochemical properties, and photocatalytic activities [4,5]. The crystal structure of the R–P phase is closely related to that of the perovskite phase, in which *n* is the number of $ABO_3$ perovskite blocks having corner-shared $BO_6$ octahedra alternating with AO rock-salt layers along the c-axis. As the number of perovskite layers increases from *n* = 1 to ∞, the R–P phases gradually lose the two-dimensional feature of the *n* = 1 phases, reaching the three-dimensional limit for the perovskite (n = ∞) [6]. The R–P phases show higher photocatalytic activity compared to that of the simple oxides such as $TiO_2$ and ZnO, and this can be attributed to the layered structure of R–P phases [7]. The R–P structure uses its interlayer space as reaction sites where the electron-hole recombination process could be retarded by physical separation of the electron-hole pairs generated by photo-absorption [8].

The semiconducting properties of these intergrowth oxides, i.e., their electronic conductivity and energy band gap at room temperature suggest that they can be efficient for the degradation of dyes, since these materials can conduct photogenerated electrons to the water for the generation of $OH^-$ radicals, which in turn will decompose the dye. Methylene blue (MB), a well-known dye, is highly used in textile industry [9] and it is normally degraded using materials such as sulfides, non-semiconducting oxides, and persistent phosphors [10-11], and the total degradation time reported for the MB is in the range of 100 − 200 min. In fact, the highest degradation rates of MB have been observed with $TiO_2$, but this material is hard to remove from water after the photocatalytic treatment and it is toxic for the environment [12,13]. Most of the materials mentioned above have a weak absorbance in the visible (VIS) region, so materials with a stronger absorbance in the VIS-NIR region are required for their use under solar photocatalysis.

The perovskite based on lanthanum strontium cobalt ferrite, $La_{1-x}Sr_xCo_{1-y}Fe_yO_{3-\delta}$, is the most studied cathode material for solid oxide fuel cells (SOFC) and its photocatalytic activity for the degradation of Rhodamine-B has also been reported. [14]. The three-layer R–P phase of the composition $Sr_3Ln(Fe,Co)_3O_{10-\delta}$ has been studied widely due to its mixed oxide-ion and electronic conducting properties; this material can be used as a cathode material for SOFC and as an oxygen permeation membrane [15-18]. Similarly, the calcium-doped three layer R–P phases, $(Sr,Ca)_3Ln(Fe,Co)_3O_{10-\delta}$ have also been reported with enhanced electrochemical performance [6,19]. Although the thermal, electrical, and the electrochemical properties of the above-mentioned R–P phases have been reported for SOFC applications, there is no studies on the photocatalytic properties of this type of intergrowth oxides. Therefore, the photocatalytic properties of SCLFCO materials with different Ca contents are presented in this work by monitoring the degradation of the MB dye under solar exposure.

## 2. Materials and Methods

### 2.1 Synthesis of the Intergrowth oxides

All the chemicals were acquired from Sigma Aldrich and used without further treatment. The intergrowth oxides of the composition $Sr_{3.2-x}Ca_xLa_{0.8}Fe_{1.5}Co_{1.5}O_{10-\delta}$ were synthesized by conventional solid-state reaction. In this procedure, stoichiometric amounts of $SrCO_3$, CaO, $La_2O_3$, $Fe_2O_3$, and $Co_3O_4$ were weighed and thoroughly mixed with ethanol with an agate mortar and pestle. Subsequently, the mixed powder was calcined in air at 1000 °C for 12 h. The calcined powders were then ground and pressed to form pellets. After this, the pellets were sintered in air at 1200 °C for 24 h. Four $Sr_{3.2-x}Ca_xLa_{0.8}Fe_{1.5}Co_{1.5}O_{10-\delta}$ samples were synthesized with different Ca contents: SCLFCO0 (x = 0), SCLFCO2 (x = 0.2), SCLFCO4 (x = 0.4), and SCLFCO8 (x = 0.8).

### 2.2 Structural, Morphological, and optical Characterizations

The powder samples were characterized with a Rigaku Miniflex 600 X-ray diffractometer (Cu-Kα, λ= 1.5406 Å) in the range 10°< 2θ< 80° with steps of 0.02°. The morphology of the sample powder was analyzed by scanning electron microscopy (SEM) with a Philips XL30 ESEM microscope equipped with an EDAX Inc. energy dispersive X-ray detector for microanalysis at room temperature. The absorbance spectra of the powders were acquired with a Perkin-Elmer Lambda 365 spectrophotometer with an integrating sphere of Spectralon in the range of 200 nm-1100 nm. Specific surface area and pore size measurements were carried out by using the BET method (Quantachrome model AS-1CT-8 apparatus).

### 2.3 Photocatalytic measurements

The photocatalytic activity of the SCLFCO powders in aqueous methylene blue (from Sigma Aldrich) solution was carried out under the following conditions. The photocatalytic reactor consisted of a 200 mL Pyrex glass beaker filled with 100 mL of aqueous solutions of MB (25 ppm). The samples for the photocatalytic study were prepared by mixing 30 mg of SCLFCO powder with the MB solution. These solutions were stirred in darkness for 1 h to adsorb the MB molecules on the surface of the SCLFCO powder. Later, the beakers with the solutions and the photocatalysts were directly exposed to sunlight irradiation up to 250 min in a sunny day (10 am to 2 pm). During the solar irradiation, 200 µL of the MB solution was regularly extracted and the photocatalyst was separated from the liquid by centrifugation at 6000 rpm for 20 min. Subsequently, the absorbance of each sample was measured to observe a decrease in the intensity of the main absorption band of the methylene blue centered at 665 nm. The absorbance spectrum of the liquid was achieved with a UV-Vis UNICO SQ-4802 spectrophotometer in the range of 300 nm – 800 nm. The solar irradiance was monitored with a photodiode detector (CCD Davis solar radiation detector) every 30 min and the average irradiance value during the experiment was: 642 ± 40 $W/m^2$. The photodiode detector is part of the meteorological station in the Astronomical Observatory of the University of Coahuila, Mexico.

## 3. Results and Discussion

### 3.1 Structure and Morphology

The XRD pattern of the SCLFCO4 sample is shown in Fig. 1. All the synthesized SCLFCO powders doped with different calcium contents correspond to the tetragonal *I/4mmm* space group [6,19]. The main observed planes were (107), (110), (118), (200), (217) and (220), and the X-ray diffraction peaks shifted towards higher angles with the increase in Ca content on the Sr site, indicating a decrease in the lattice parameters. The lattice parameters *a* and *b* decrease from 3.844 Å to 3.834 Å and the lattice parameter *c* decreases from 27.877 Å to 27.782 Å as the Ca content increases from the sample SCLFCO0 to SCLFCO8. Similarly, the volume diminished from 411.92 $Å^3$ in SCLFCO0 to 408.51 $Å^3$ in SCLFCO8. These observations are consistent with a smaller ionic radius of $Ca^{2+}$ (1.12 Å) compared to that of $Sr^{2+}$ (1.26 Å).

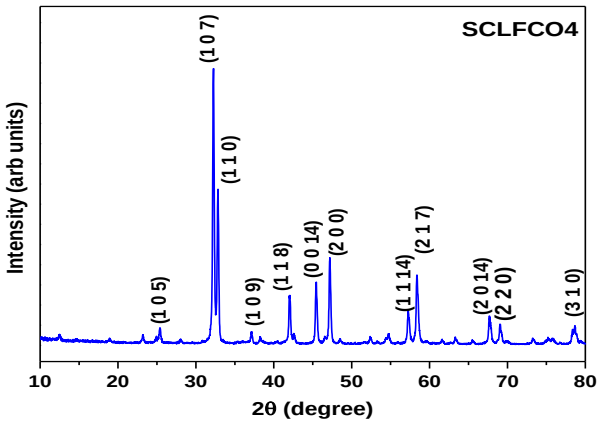


**Fig. 1**. The X-ray diffraction pattern of SCLFCO4 sample

SEM images of SCLFCO samples with different Ca contents are shown in Fig. 2. The SCLFCO samples exhibit a mixture of small and large grains of irregular size in the range of 0.1 − 8 µm. The microparticles are highly agglomerated for samples with calcium contents from x = 0 to 0.4. When the amount of Ca dopant is x = 0.8, the microparticles are smaller and more dispersed. The percentages of microparticles with sizes in the range of 0.1 − 2 µm were 56%, 63%, 67% and 70%, respectively, for x = 0, 0.2, 0.4 and 0.8.Furthermore, the percentages of microparticles with sizes in the range of 4 − 8 µm were 44%, 37%, 33% and 30%. These values indicate that smaller microparticles are produced as the Ca content increases.

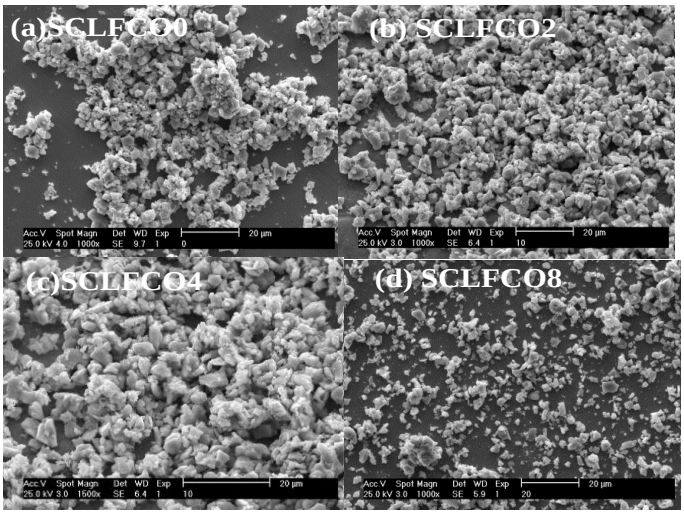


**Fig. 2**. SEM images of SCLFCO powders: (a) x = 0, (b) x = 0.2, (c) x= 0.4 and (d) x = 0.8

### 3.2 Optical Properties

Fig. 3 shows the absorbance spectra in the range of 350 − 1100 nm for the SCLFCO samples. It shows that the absorption band in the near UV range (350 − 400 nm) and VIS-NIR region is enhanced as the Ca content increases. The absorbance spectra in the range of 350 − 800 nm is beneficial for the photocatalytic process since the photocatalysts could be efficiently activated with natural sunlight. In fact, most of the popular photocatalytic materials present a strong absorbance only in the UV region [20,21] and some of them have enhanced VIS-NIR region after doping with Bi or Gd, but the absorbance in the NIR region is still weak [22,23].

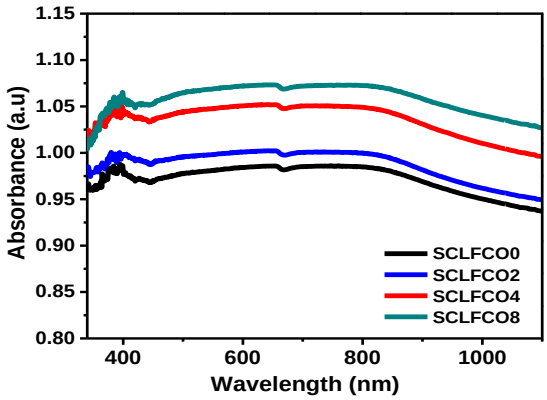


**Fig. 3**. Absorbance spectra of the undoped and Ca doped SCLFCO samples.

In contrast, the absorbance of all the intergrowth oxides studied in this work is extended from 400 nm to 1100 nm, covering the VIS-NIR region. Moreover, the absorbance is enhanced

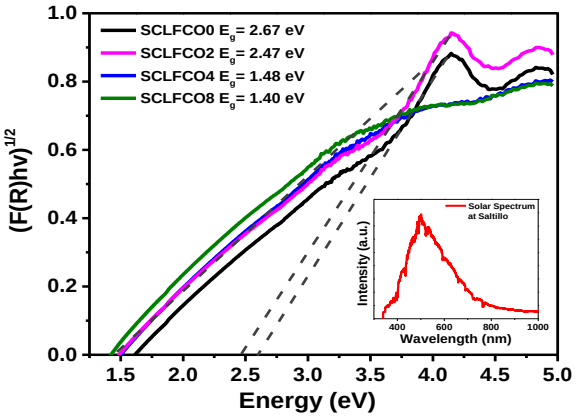


**Fig. 4**. Kubelka-Munk plots for the SCLFCO samples. Inset shows the distribution of solar irradiance in Saltillo city.

progressively as the Ca content increases. This increase in absorbance is probably due to the creation of defects such as atomic dislocations induced by the replacement of Sr by Ca. Therefore, Ca substitution not only alter the unit cell parameters, but also creates defects since the ionic radius of $Ca^{2+}$ differs from that of $Sr^{2+}$. The formation of defects such as oxygen vacancies or trapping centers are normally suitable for photocatalysis because these oxygen vacancies or traps may help to reduce the time of recombination rate of electrons and holes [24].

Another effect of doping with Ca is the decrease in the band gap ($E_g$) as the Ca content increases, as shown in Fig. 4. The optical band gap ($E_g$) of the intergrowth oxides was obtained for each sample by plotting the function $[F(R)h\nu]^2$ versus photon energy ($h\nu$). Fig. 4 shows the diffuse reflectance spectra of the SCLFCO samples after the Kubelka-Munk treatment. The inset shows the distribution of solar irradiance in Saltillo city, Mexico. The intersection between the linear fit and the photon energy axis gives the value of band gap, $E_g$. The optical band gap $E_g$ obtained from the plot for the host sample SCLFCO0 is 2.67 eV. When calcium is introduced in the SCLFCO samples, the band gap reduced to 1.40 eV for the SCLFCO8 sample.

3.3 Photocatalysis under Solar irradiation

Fig. 5 shows the degradation percentage of MB as a function of time for a blank solution as well as for the SCLFCO samples. The blank solution without the photocatalyst (prepared by dissolving MB in water) shows a pH of 8.3 and 8.6 at t = 0 and t = 300 min respectively. In the case of MB solutions with photocatalysts, average pH values of the solutions at the beginning (t = 0) and at the end (t = 300 min) of the photocatalytic process were 10.4 and 11.5. This increase in pH suggests the generation of $OH^-$ radicals during the photocatalytic process. In addition, a comparison of the pH value in the blank solution (8.3) at t = 0 with that for the MB solution + SCLFCO powder (10.4), indicates an increase of ~ 23%. This shows that the SCLFCO powder could produce alkaline conditions even in darkness by the generation of $OH^-$ radicals.

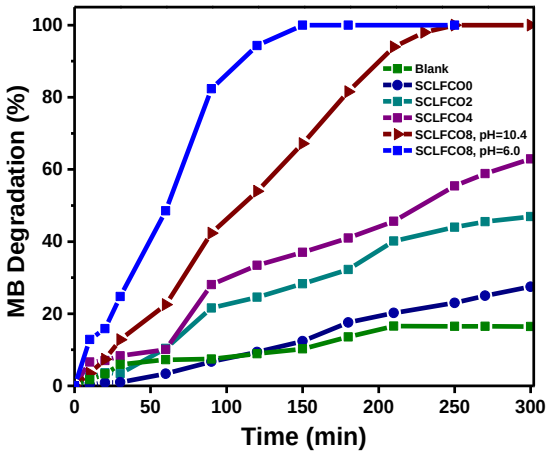


**Fig. 5.** Degradation percentage of MB as a function of time for the SCLFCO samples.

The MB is a cationic dye highly soluble in water and its characteristic absorbance peak is located at 665 nm. The intensity of the main absorption band corresponding to MB was monitored as a function of time, and a diminution of that characteristic band suggests the degradation of such dye. The blank sample shows a maximum degradation percentage of 16 % after 300 min and a low degradation average rate. In contrast, all the intergrowth oxides have a faster MB degradation rate during the first 210 minutes, because a quasi-linear behavior is observed. Total degradation of MB dye was observed for the SCLFCO8 sample after 250 min, but only a maximum degradation of 27% was shown by the SCLFCO0 sample. The samples SCLFCO2 and SCLFCO4 have higher maximum degradation percentages of only 47% and 63% of MB after 300 min. In order to understand how the pH condition affect the performance of the best photocatalytic powder (SCLFCO8), an additional experiment was carried out at a constant pH = 6.0. To keep this pH constant during all the time for photocatalytic degradation, few micro-liters of an aqueous solution of nitric acid (0.1M) was added to the MB solution approximately every 15 min. As observed in Fig. 5, the performance for the photocatalytic degradation was enhanced by the decrease of pH from 10.4 to 6.0, since total degradation was reached

after 150 min. This time is ≈ 67% lower than that obtained for SCLFCO8 at a pH = 10.4. Moreover, the average degradation rate at pH = 6.0 was ≈ 24% higher with respect to that obtained at a pH = 10.4. The photocatalytic degradation was favored at acidic conditions because water photo-oxidation is favored and this promotes the generation of $OH^-$ radicals [25].

It has been reported that SCLFCO oxides have an intrinsic electronic conduction at room temperature, as the content of oxygen vacancies increases the electrical conductivity decreases, therefore, a higher content of oxygen in intergrowth oxides promotes their electronic conductivity [17]. According to EDS measurements (spectra not shown here) the oxygen contents were 15.85 wt.%, 13.61 wt. %, 15.07 wt. % and 16.18 wt. % for x = 0, 0.2, 0.4 and 0.8 samples respectively. Those values indicate that as the calcium concentration increases, there is an increase in oxygen content. The electronic conductivity and photocatalytic degradation should be enhanced in those samples with high Ca content. The increase of oxygen content with the concentration of Ca dopant is in agreement with the increase of the degradation rates for MB.

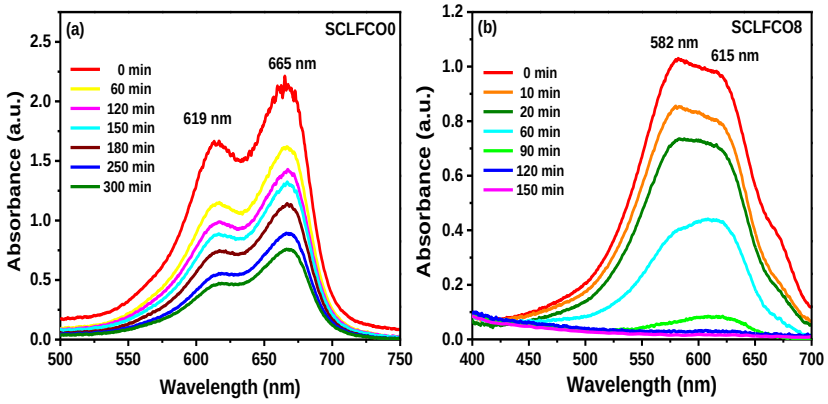


**Fig. 6.** Absorbance spectra of the MB solution with the SCLFCO samples of different Ca contents under solar irradiation at different times: (a) x = 0 and (b) x = 0.8.

The higher content of Ca increases the amount of oxygen in the samples, in consequence, the electronic conductivity is raised and the probability of electron-hole recombination is reduced. As a result, the maximum degradation percentage reached after 300 min is also incremented, see Fig. 5. Thus, a faster conduction of electrons and holes produced by the introduction of calcium promotes a more effective generation of $O^{2-}$ and $OH^-$ radicals. Consequently, the degradation of MB dye is faster under solar irradiation.

The degradation mechanism can be supported by comparing the shape of the absorbance at t = 0 (absorbance of MB obtained before solar irradiation) for the samples SCLFCO0 and SCLFCO8 (obtained at an initial pH = 10.4) in Figs. 6a and 6b. As observed, the

absorption band of MB was broader for the SCLFCO8 sample in comparison with SCLFCO0 and the two typical peaks of MB located at 619 nm and at 665 nm (corresponding to the transition $n \rightarrow \pi*$ [26]) are not present in SCLFCO8 sample. Similarly, the absorbance band at t = 0 for the SCLFCO8 sample is centered at 600 nm instead of 665 nm. The broadening and shifting towards lower wavelength of the absorbance band in the SCLFCO8 sample with respect to the SCLFCO0 sample at t = 0, as well as the lower initial value of absorbance in the SCLFCO8 sample with respect to SCLFCO0 suggest not only a partial degradation of MB before solar irradiation but also a modification of the MB molecule due to the presence of calcium.

The SCLFCO samples were added to the MB solution and kept in darkness for 1 h; probably during this time, the calcium interacted electrostatically with $Cl^-$ in the MB molecule as suggested above and provoked a partial degradation. Moreover, the structure of the MB molecule can be modified due to the formation of dimers (*i.e.*, two MB molecules overlapping and coexisting together), which is probably caused by the high content of Ca in the SCLFCO8 powders and by the high value of pH (11.5) in the MB solution during the photocatalytic degradation. A high value of pH (above 8.8) in the MB solution could favor the adsorption of MB molecule on the photocatalyst, as observed by Tayade et al. [27]. Similarly, the low degree of agglomeration of the particles in the SCLFCO8 sample, as shown in the SEM images could facilitate the adsorption of MB molecules on it. Therefore, a change in the shape of the absorbance spectra was observed at t = 0 in the SCLFCO8 sample, whereas the rest of the samples presented the typical bands of MB at 619 nm and 665 nm at t = 0 as depicted in Fig. 6a. Therefore, our results indicate that only the sample with a high content of calcium, x = 0.8 could produce a previous degradation and modification of MB molecule before starting solar photocatalysis.

The SCLFCO8 sample has a higher MB degradation percentage than that of the samples SCLFCO4, SCLFCO2 and SCLFCO0. This may be due to the fact that the absorbance was higher for SCLFCO8 and also the energy band gap of SCLFCO8 was lower than that of the other samples. Accordingly, as the Ca content increases, a higher degradation rate for MB dye is observed. The enhanced photocatalytic performance of SCLFCO8 sample can also be explained by the degree of agglomeration and size of SCLFCO powders. SCLFCO8 sample presented the lowest particle size and the lowest degree of agglomeration of microparticles in comparison with therest of samples (see Fig. 2). This means that its enhanced photocatalytic activity with respect to the other samples should be associated exclusively to the effects produced by calcium, that is, lowest band gap and highest electronic conduction.

## 4. Conclusions

The effect of Ca doping on the photocatalytic activity of the intergrowth oxides $Sr_{3.2-x}Ca_xLa_{0.8}Fe_{1.5}Co_{1.5}O_{10-\delta}$ has been investigated. Doping SCLFCO samples with Ca not only enhanced the absorption in the UV-VIS-NIR range. Similarly, the introduction of Ca decreases the band gap values and increased the oxygen content in SCLFCO samples. Both the enhancement of absorption and the increase of electronic conduction were beneficial for the photocatalytic process. Total degradation of MB dissolved in water was observed after 150 min and 250 min at an initial pH = 6.0 and 10.4 for the SCLFCO8 sample. The presence of calcium caused a faster degradation of the MB dye due to a possible unbalance of charge produced by $Ca^{2+}$ ions and the $Cl^-$ ions located in the MB

molecule. Furthermore, the formation of MB dimers, small particle size and low degree of agglomeration in the SCLFCO8 sample could help a faster degradation of MB. The calcium-doped intergrowth oxides can be considered as good candidates for the elimination of dyes in water treatment plants due to their enhanced solar photocatalytic properties.

**Acknowledgements**

The author K.P. Padmasree thanks CONACYT, Mexico, for the grant C/2607/15/261205. The work at University of Texas at Austin was supported by the Welch Foundation grant F-1254.

**References**

[1] Fujishima A, Honda K. Electrochemical photolysis of water at a semiconductor electrode. Nature 1972;238:37–38.
[2] Rodionov A, Zvereva A. Photocatalytic activity of layered perovskite-like oxides in practically valuable chemical reactions. Russ. Chem. Rev. 2016;85:248-279.
[3] Bhuvanesh NSP, Crosnier-Lopez MP, Duroy H and Fourquet JL. Synthesis and structure of novel layered perovskite oxides: $Li_2La_{1.78}Nb_{0.66}Ti_{2.34}O_{10}$, and a new family, $Li_2[A_{0.5n}B_nO_{3n+1}]$. J. Mater. Chem. 1999;9:3093-3100.
[4] Ruddlesden SN and Popper P. The compound $Sr_3Ti_2O_7$ and its structure,Acta Crystallogr. 1958;11:54-55.
[5]Armstrong T,Prado F, Manthiram A. Synthesis, crystal chemistry, and oxygen permeation properties of $LaSr_3Fe_3$-$xCoxO_{10}$ (0≤x≤1.5).Solid State Ionics 2001;140:89–96.
[6] Kim JH, Lee KT, Kim YN, Manthiram A. Crystal chemistry and electrochemical properties of $Ln(Sr,Ca)_3(Fe,Co)_3O_{10}$ intergrowth oxide cathodes for solid oxide fuel cells. J. Mater. Chem. 2011;21:2482-2488.
[7] Huang Y, Wei Y, Cheng S, Fan, Li L, Lin J, Wu J.Photocatalytic property of nitrogen-doped layered perovskite $K_2La_2Ti_3O_{10}$, Sol. Energy Mater. Sol. Cells. 2010;94:761–766.
[8] Shimizu K, Tsuji Y, Hatamachi T, Toda K,Kodama T, Sato M, Kitayama Y. Photocatalytic water splitting on hydrated layered perovskite tantalate $A_2SrTa2O_7 \cdot nH_2O$ (A=H, K, and Rb).Phys. Chem. Chem. Phys. 2004;6:1064–1069.
[9] Sahoo C, Gupta AK, Pillai MS, Photocatalytic degradation of methylene blue dye from aqueous solution using silver ion-doped $TiO_2$and its application to the degradation of real textilewastewater, J. Environ. Sci. Health., Part A 2012;47:1428–1438.
[10] Ma H, Zhuo Q, Wang B, Electro-catalytic degradation of methylene blue wastewater assisted by $Fe_2O_3$-modified kaolin.Chem. Eng. J. 2009;155:248–253.
[11] Chauhan R, Kumar A, Chaudhary RP. Visible-light photocatalytic degradation of methyleneblue with Fe doped CdS nanoparticles. Appl. Surf. Sci. 2013;270:655–660.
[12] García CR, Diaz-Torres LA, Oliva J, Romero MT, Hirata GA. Effect of $Eu^{3+}$ concentration on the photocatalytic activity of $LaSr_2$ $AlO_5$ powders. Inorg. Chem. Commun. 2015;59:63 –67.

[13] García CR, Diaz-Torres LA, Oliva J, Romero T, Salas P. Photocatalytic Activity and Optical Properties of Blue Persistent Phosphors under UV and Solar Irradiation. Int. J. Photoenergy. 2016;1303247:1–8.

[14] J. Šíma, P. Hasal. Photocatalytic Degradation of Textile Dyes in a$TiO_2$/UV System. Chem. Eng. Trans. 2013;32:79–84.

[15] Zhu X, Zhou J, Cai Z. $TiO_2$ Nanoparticles in the Marine Environment: Impact on the Toxicity
of Tributyltin to Abalone (Haliotis diversicolor supertexta) Embryos,Environ. Sci. Technol. 2011;4:3753–3758.

[16] García-López E, Marcì G, Puleo F, La Parola V, Liotta LF, $La_{1-x}Sr_xCo_{1-y}Fe_yO_{3-\delta}$ perovskites: Preparation, characterization and solar photocatalytic activity. Appl. Catal. B: Environ. 2015;178:218–225.

[17] Lee KT, Manthiram A, $LaSr_3Fe_{3-y}Co_yO_{10-\delta}$ ($0 \le y \le 1.5$) Intergrowth Oxide Cathodes for Intermediate Temperature Solid Oxide Fuel Cells.Chem. Mater. 2006;18:1621–1626.

[18] Prado F, Gurunathan K, Manthiram A,Synthesis, crystal chemistry, and electrical, oxygen permeation, and magnetic properties of $LaSr_3GaFe_{2-x}Co_xO_{10-\delta}$($0 \le x \le 2$ and $0 \le \delta \le 2$).J. Mater. Chem. 2002;12:2390–2395.

[19] Kim YN, Manthiram A, Electrochemical Properties of $Ln(Sr,Ca)_3(Fe,Co)_3O_{10} + Gd_{0.2}Ce_{0.8}O_{1.9}$ Composite Cathodes for Solid Oxide Fuel Cells. J. Electrochem. Soc. 2011;158:1206–1210.

[20] Hashimoto K, Irie H, Fujishima A, $TiO_2$ Photocatalysis: A Historical Overview and Future Prospects. Jpn. J. Appl. Phys.2005;44:8269–8285

[21] Wu J, Fang T, Cai R, Li S, Wang Y, Zhao C, Fabrication of an Ag/$Fe_2O_3$/ZnO ternary composite with enhanced photocatalytic performance, RSC Adv. 2016;6:4145–4150.

[22] García CR, Oliva J, Romero MT, Diaz-Torres LA, Enhancing the photocatalytic activity of $Sr_4Al_{14}O_{25}$: Eu, Dy persistent phosphors by codoping with Bi ions. J. Photochem. Photobiol. 2016;92:231–237.

[23] Zhang N, Chen D, Niu F, Wang S, Qin L, Huang Y. Enhanced visible light photocatalytic activity of Gd doped $BiFeO_3$ nanoparticles and mechanism insight, Sci. Rep. 2016;1:1–11.

[24] Zhang M, Wu J, Lu D, Yang J. Enhanced Visible Light Photocatalytic Activity for $TiO_2$ Nanotube Array Films by Codoping with Tungsten and Nitrogen. Inter. J. Photoenergy. 2013; 471674:1−8.

[25] Nakabayashi Y, Nosaka Y. The pH dependence of OH radical formation in photo-electrochemical water oxidation with rutile $TiO_2$ single crystals. Phys.Chem.Chem.Phys. 2015;17:30570-30576.

[26] Sun J, Dong S, Feng J, Jing X. Enhanced sunlight photocatalytic performance of Sn-doped ZnO for Methylene Blue degradation. J. Mol. Catal. A: Chem. 2011;335:145–150.

[27] Tayade R, Natarajan TS, Bajaj H, Photocatalytic Degradation of Methylene Blue Dye Using Ultraviolet Light Emitting Diodes. Ind. Eng. Chem. Res. 2009;48:10262 – 10267.

# 5.6 Integration of a flexible solar power generation system

Sánchez-Rodríguez O.A, Pérez-Hernández G. A., López-Hernández J. A.[1], Hernández-Hernández E. M., Cortés-Escobedo C.A

[1]Centro de Investigación e Innovación Tecnológica, Cda. Cecati S/N Col. Santa Catarina, Azcapotzalco, México, 02250.

* Corresponding author: +525535031484 gastromar.1202@gmail.com

## ABSTRACT

The photovoltaic energy system turn the luminous energy from the sun into electrical energy. To achieve this there are used the solar panels formed by photovoltaic cells, constituted of material semiconductors. These cells connected in series or parallel they form a solar panel entrusted to give the current that fits to the demand that is needed. The photovoltaic systems need from other components to be able to use and to control the electrical energy without affecting the electrical devices. This work arises due to the requirement of night lighting and electrical energy in the field of the roof at the Centro de Investigación e Innovación Tecnológica, in which there are realized investigation works related to the photobiological hydrogen production. Considering such, were implemented a solar system to produce electrical energy for the functioning of a lamp led and a bomb of ventilation, which works as a source of secondary light for a system of production of biological hydrogen. During the process of carrying the characterization of the bomb of required ventilation and the used lamp, this way estimate the characteristics of the cell, once the solar flexible cells were had to use, they were characterized and connected to a manager of potency, a battery of deep load, a regulator with his respective protections and to the source of load. Finally, we were obtained a functional system that operates to support the lamp led lit during the night and the air bomb 24 hours.

***Keywords***: solar energy; hydrogen; sustainable; hybrids

# 5.7 Application of Electrophoretic Deposition Process to Improve the Anode Efficiency in Dye Sensitized Solar Cell Technology

J. R. Zapata-Cruz, W. J. Pech-Rodríguez, C. E. Velázquez-González, C. Álvarez-de los Reyes, C. A. Calles-Arriaga, J. A. Rodríguez García, E. Rocha-Rangel

[1]Universidad Politécnica de Victoria, Av. Nuevas Tecnologías 5902, Parque Científico y Tecnológico de Tamaulipas, Ciudad Victoria, Tamaulipas, C.P. 87138, México

*Phone number: (834)1711100 ext; 2315 e-mail: wpechr@upv.edu.mx

---

## ABSTRACT

This work presents the obtained results from the fabricated anodes for dye sensitized solar cell (DSSC). The developed anodes have been based on homogeneous thin film of titanium dioxide ($TiO_2$) deposited on conductive glass substrate, by using an electrophoretic deposition (EPD) method. The effect of different parameters e.g., time of deposition, voltage magnitude and waveform have been studied. A Taguchi orthogonal array design was performed to investigate the optimal operation parameters. The efficiency of the electrode and the fabricated DSSC was investigated by photovoltaic performance test and electrochemical characterization. The result clearly shows that waveform has a predominant effect on the total photovoltaic conversion efficiency. Therefore, EPD is a promising method to develop anode a very large scale resulting in low price and high efficiency.

***Keywords:*** Dye sensitized solar cell, electrophoretic deposition, $TiO_2$.

# 5.7 Potential of biohydrogen production from paper industry wastes by SSF:A Study of the influence of temperature

I. Moreno-Dávila, E. Herrera-Ramírez, M. Rodríguez-Garza, L. Ríos González, Y. Garza-García.

[1]Departament of Biotechnology, Facultad de Ciencias Químicas, Universidad Autónoma de Coahuila.

Boulevard V. Carranza y José Cárdenas Valdez, col. Republica Oriente. C.P.25280. Saltillo, Coahuila, México.

Tel: +52 844 4155752, ext. 5. Fax: +52 844 4159234

* contact email: imayelamorenod@uadec.edu.mx

## ABSTRACT

This study evaluated the potential for bioconversion of paper industry wastes by simultaneous saccharification and fermentation (SSF) into hydrogen through the dark fermentation process, by applying anaerobic biofilms developed in fiber ixtle. The inoculum used for biofilms was previously pretreated. The evaluation of the process of SSF was performed with paper industry wastes (PIW) subjected to chemical pretreatment with $H_2SO_4$ 1.5% Anaerobic batch reactors were operated in triplicate. The key process parameters: pH (5), and enzyme loading of Celluclast enzyme (10, 40 and 70 UPF) and three different temperatures (35, 45, 55° C) were optimized by the response surface methodology (RSM) based on a two factor-three level central composite design (CCD), respectively. The results showed optimal working conditions, to maximize the production of hydrogen by the SSF process, at a pH of 5.and an enzyme load of 70 FPU, the maximum expected value of hydrogen yield was 60.75 mmol /h*gSV and there was no methane generation.

***Keywords:*** Biohydrogen; paper industry wastes; anaerobic digestion; response surface methodology

## 1. Introduction

Hydrogen is recognized as a potential energy substitute for fossil fuels due to its clean, renewable and high electrical-conversion efficiency, which plays an important role in future [1]. However,current hydrogen is mainly produced from fossil fuels, which causes environment pollution. In contrast, bio-hydrogen production is one of the potential solution because of its low cost, environmentally friendly, and sufficient supply [2] Biological

hydrogen production, with its mild processing conditions, abundant raw material sources, and low energy consumption, has attracted the attention of various researchers [3].Among the various biological hydrogen production processes dark anaerobic fermentation is an interesting alternative method for producing biohydrogen ($H_2$) as a renewable fuel because of its low cost and various usable organic substrates. Paper industry wastes containing plentiful cellulosic substrate could be feasibly utilized for $H_2$ production by dark fermentation.

Although starchy and sugar based biomass and wastes are readily fermentable by microorganisms for hydrogen generation, lignocellulosic biomass needs to be pretreated so as to be exploitable. Pretreatment is commonly accepted to be an essential prerequisite to make lignocellulosic biomass accessible to enzymatic attack (either by microorganisms or enzymes), by breaking the lignin seal, removing hemicellulose, or disrupting the crystalline structure of cellulose [4]. During physicochemical pretreatment, lignocellulosic biomass is exposed to acidic, alkaline or oxidative conditions, at ambient or elevated temperature. The use of high temperatures without the addition of some chemical agent can also be effectuated, leading to a process simply called thermal pretreatment. For acid pretreatment of lignocellulosic biomass, either dilute or concentrated acids, such as H2SO4 and HCl, can be used. The main reaction that occurs during acid pretreatment is the hydrolysis of hemicellulose, especially xylan, since glucomannan is more stable. Current strategies to produce hydrogen from lignocellulose, as the paper wastes is the Simultaneous saccharification and fermentation (SSF).SSF can not only predigest the technological process, shorten the operation time, reduce the equipment cost [5], but also improve hydrogen yield by eliminating end-product inhibition during cellulose hydrolysis [6].

## 2. Materials and Methods

### 2.1 Raw Material

The paper industry solid wastes were collected from a paper processing industry located in the state of Coahuila, Mexico. The residue was crushed into powder, and screened with 25-mesh sieve. The composition of the processed sample is as follows in table 1.

**Table 1. Proximate analysis of paper industry wastes**

| Composition | Wt% |
|---|---|
| Protein | 0 |
| Extractives | 0.836 ± 0.02 |
| Moisture | 2.00 ± 0.03 |
| Ash (600°C) | 50.98 ± 0.12 |
| Cellulose, | 16.16 ± 0.25 |
| Hemicellulose | 19.40 ± 0.34 |
| Lignine | 10.44 ± 0.29 |
| Total | 99.81 |

Values are mean ± SD (n = 3).

Pretreatment of paper industry wastes was conducted by placing 5 g with 50 mL of 2.5% sulfuric acid, autoclaving for 30 minutes at 120 ° C, then filtering the supernatant and drying the residue at 100 ° C.

2.2 Preparation and conditioning support.

Solid plastic spheres with a diameter of approximately 25.5 ± 0.04 mm were used and were coated with 2.20 mt ± 0.02 of ixtle fiber cord. Two beads per reactor were used and each sphere had 2.23 g ± 0.02 of adhered biofilm.

2.3 Microorganisms and enzyme.

Mixed anaerobic microbial consortium was obtained from a UASB reactor, from brewing industry located in Zacatecas, Mexico. 0.5 L of granular sludge were macerated and subsequently were pretreated by combining two pretreatments described by Chen et al. [7] and modified by Moreno-Davila et al. [8]. For heat pretreatment, the anaerobic sludge was placed in a water bath at least 90 ° C temperature for a minimum period of 30 min with vigorous stirring during this time and finally subjecting it to thermal shock in ice water.

Subsequently, the consortium at room temperature, was subjected to acid pretreatment, in which the pH was lowered to 3.0 with 3N HCl solution for a period of 24 h and was finally readjusted pH to 7.0 with 3N NaOH solution.

The enzyme employed was cellulase *(Trichoderma reesei*ATCC 26921), with an cellulase activity of 74 FPU/mL and ß-glucosidase activity was of 1200 U/g.

2.4 Immobilization process and maturation of the biofilm in a UASB reactor using as substrate synthetic medium

In an UASB reactor of 5 L capacity and a working volume of 4 L, they were placed 0.4 L (10% by volume) mixed anaerobic sludge pretreated, plus 60 coated spheres ixtle, and a synthetic medium was used for growth cell and hydrogen production. The culture medium contained (mg L-1): glucose as the sole carbon source, 20.000; $NH_4Cl$, 2,000; $NaHCO_3$, 6,720; $K_2HPO_4$, 125; $MgCl_2 \cdot 6H_2O$, 100; $MnSO_4 \cdot 6H_2O$, 15; $FeSO_4 \cdot 7H_2O$, 25; $CuSO_4 \cdot 5H_2O$, 5; $CoCl_2 \cdot 5H_2O$, 0.125 (4); at pH 5.0. The reactor was operated three TRH's: 6, 3 and 1 h, using a peristaltic pump (Manostat-division of Branant Compay, Simon varistaltic pump, USA) for the recirculation of the medium. The amount of hydrogen and methane produced were determined at regular time intervals during 90 days for develop the biofilm, using a gas chromatograph equipped with a thermal conductivity detector (GC-TCD). The operational temperatures of the injector, detector and column were 200, 200 and 50 °C, respectively.

2.5 Design of the experiment $2^3$.

A central composite design with two factors and three levels each factor was used for biohydrogen production, generated from industry paper wastes with/without chemical pretreatment by anaerobic biofilms.

In each experimental design independent variables were: initial pH and enzyme concentration. The conditions that were tested are listed in Table 2.

**Table 2 - Factors and levels in the experiment design of CCD**

| Independent Variables | Symbol | Range and levels | | |
|---|---|---|---|---|
| | | **- 1** | **0** | **+ 1** |
| Temperature | $X_1$ | 35 | 45 | 55 |
| FPU | $X_2$ | 10 | 40 | 70 |

2.6 Simultaneous saccharification and fermentation process.

Each experimental unit was performed in a glass reactor with a capacity of 0.25 L, with two rubber plugs which functioned as sampling ports; the workload of the reactor was 0.140 L. In each reactor were placed: 7 g (dry weight) of waste paper, ground and sieved, two spheres with immobilized biofilm (number of spheres considered to be placed in the batch reactor due to their size), cellulase enzyme loadings 10, 40 or 70 mL $FPU^{-1}$ (Celluclast®, Novozymes, Denmark) in citrate buffer 0.05 M to complete the workload. The pH of the buffer was adjusted to the 5, adjusting the pH with NaOH 3.0 N and HCl 3.0 N. The reactors were hermetically sealed, to which were shifted oxygen using argon gas for 20 min with an efflux 10 $mL/min^{-1}$, to create anaerobic conditions. The incubation temperatures and stirring rate were controlled to 35, 45 and 55 ± 0.1 ° C and at 100 rpm respectively, in an orbital shaker (IRO Lumistell 70). At each time interval, the total gas volume was measured (hydrogen and methane) using a gas chromatograph equipped with a thermal conductivity detector (GC-TCD). pH was also determined with a potentiometer (HI 2550, HANNA instruments). A central composite design, with two variables, was used to determine the optimum simultaneous saccharification and fermentation conditions based on the maximum hydrogen yield with/without pretreatment residue. The effect of the independent variables $X_1$ (pH), $X_2$ (enzyme concentration) at three variation levels (Table 1). Three replicates at the centre of the design were used to allow for estimation of a pure error sum of squares. Experiments were randomized in order to maximize the effects of unexplained variability in the observed responses due to extraneous factors. The minitab software were used for the further regression and graphical analyses of the experimental data. The optimum values of selected variables were obtained by solving the regression equation and by the analysis of the response surface contour plots.

2.7 Analysis methods

Cellulose, hemicelluloses and lignine in the dry paper industry wastes in total, determined using [9], protein was determinated by Kjeldahl method, extractives, humidity, ashes and pH were determinate by standard methods [10], ß-glucosidase activity and filter paper activity were measured the method described by Ghose [11]. The concentration of $H_2$ and $CH_4$ were measured by Gas Cromatography (GC-TCD) Varian 3400. The temperature of the injection port, the detector, and the oven were 200ºC, 200 ºC and 50°C. Argon was the gas carrier at a flow rate of 8 mL/min.

## 3. Results and Discussion

3.1 Evaluation of simultaneous saccharification and fermentation process (SSF) from paper industry wastes without chemical pretreatment using batch reactors with anaerobic biofilms developed ixtle fiber.

The analysis of the results of simultaneous saccharification and fermentation process, with a factorial arrangement $2^3$ at pH 5.0 was carried out with the MINITAB program where different concentrations of enzyme and temperatures were established, which they were used to establish a factorial design shown in Table 3, and was obtained as response variable, hydrogen accumulated for each experiment, a fermentation time of 288 hours.

**Table 3**. **Evaluation of SSF of waste from the paper industry with chemical pretreatment**

| FPU | pH | Temperatura °C | $H_2$ (mmol /h*g SV) |
|---|---|---|---|
| **10** | 5 | 35 | 41.97 |
| **10** | 5 | 45 | 43.90 |
| **10** | 5 | 55 | 20.17 |
| **40** | 5 | 35 | 43.50 |
| **40** | 5 | 45 | 44.83 |
| **40** | 5 | 55 | 28.36 |
| **70** | 5 | 35 | 45.96 |
| **70** | 5 | 45 | 60.75 |
| **70** | 5 | 55 | 29.66 |

The analysis of variance obtained from the statistical program MINITAB (GRAPH) with respect to the two variables studied: temperature and concentration of enzyme (FPU) during the simultaneous saccharification and fermentation of waste acid pre-treatment, showed significance for both variable. In the interaction between variables enzyme-temperature significance was detected (Fig. 1)

The hydrogen production due to temperature was statistically significant (P> 0.05) in their interaction with the enzyme concentration, indicating that the temperature and the enzyme loading in the process had relevant effect. However, to obtain optimum values of hydrogen production, the initial pH should be settled to 5.

Enzyme concentrations used in the experiment were 10, 40 and 70 FPU, this factor showing a strong influence on the production of hydrogen, which enzyme concentration increased hydrogen production (Fig. 2).The high cost of cellulases is one of the major bottlenecks for the economic features of lignocellulosic biohydrogen production [12],special attention should be devoted to improve the ratio between the amount of sugar generated and the enzymatic activity required for this purpose[13].In this research the optimum enzyme loading was investigated,. Fig. 1 showed that by increasing the initial enzyme loading from 10 to 70 FPU, an 39% increase in hydrogen yield was observed. This result indicated that an increase in enzyme loading resulted in an improvement in the substrate conversion efficiency and hydrogen yield, which is in good accordance with Liu et al. (2010).

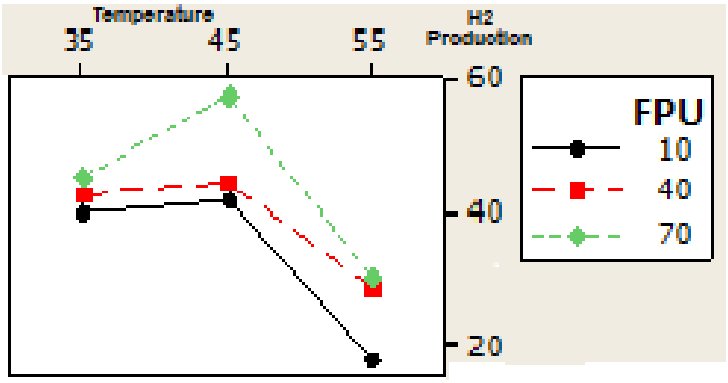


**Fig. 1**. Interaction of factors (concentration of enzyme-temp) on the accumulated $H_2$ production of the SSF process from PIW with chemical pretreatment.

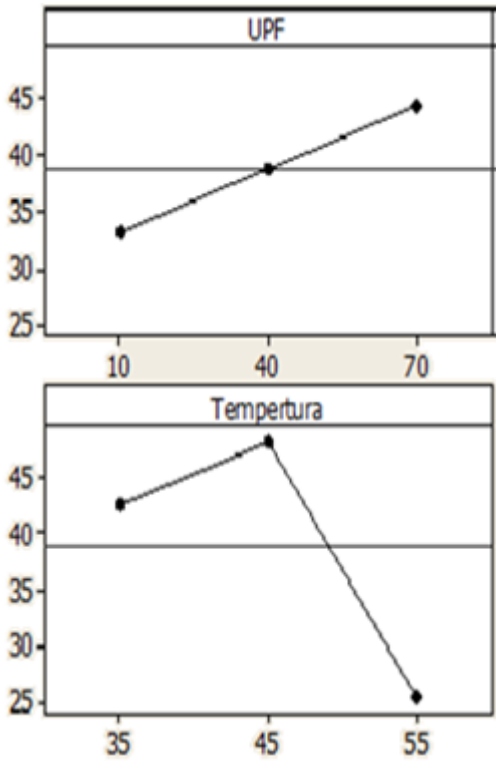


**Fig, 2**. Main effects for hydrogen production from SSF from paper waste without chemical pretreatment.

3.2 Graphic surface interactions.

Stability of hydrogen production, with respect to temperature range evaluated (Fig. 3) as well as the effect of the increase in enzyme concentration is observed, shows a positive effect on hydrogen production. Therefore, increased hydrogen production was obtained pH 5.0, with a FPU enzyme loading of 70 to 45 ° C.

Figure 3 shows the graphical representation of response surface and contour corresponding graph based on the equation 1 with a variable that remains constant at its optimal level (pH=5) and varying the other two variables within the experimental range. As seen in Figure 2 the response surface of the hydrogen production showed a clear increase, indicating that the optimum conditions were also within the experimental design. Hydrogen production increased with increasing enzyme loading (70 UPF).

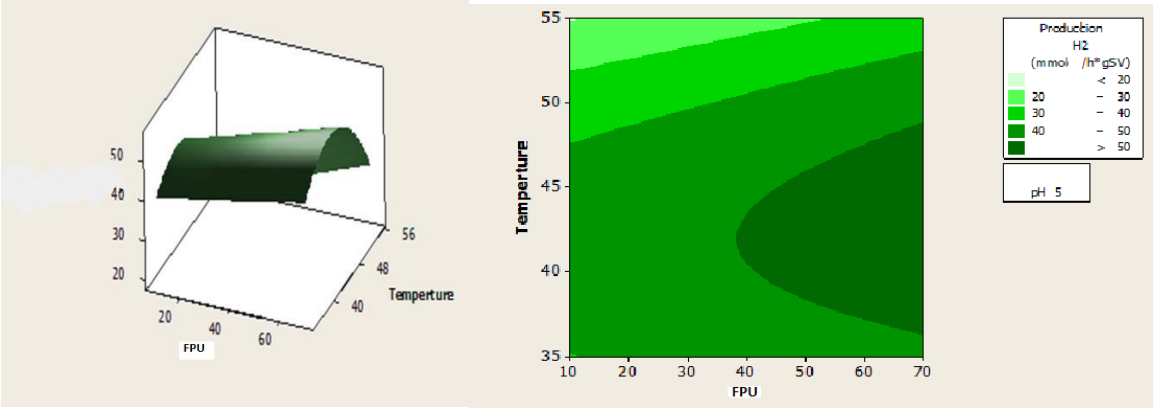


**Fig. 3.**The response surface plots and corresponding contour plots of $H_2$ yield from wastes without pre-treatment: temperature versus enzyme concentration.

3.3 Optimization of production process of hydrogen by the SSF process from RIP with chemical pretreatment.

Analysis of variance was performed to test the importance of the polynomial equation of second order for the hydrogen yield as shown in Table 2. The F-value represents the probability that two groups are statistically different, which was 95%, which implies that the model was significant because the value 'Prob> f ¨ was less than 0.05 so it was considered significant. Besides the models showed no lack of adjustment and presented a high coefficient of determination ($R^2$ = 0.95) accounting for 95.0% of the variability in responses. Therefore, Eq. 1 adequately describes the hydrogen yield in this study.

Equation 1:

Production $H_2$ = 60263.12-1168.87 * 43.93 * x-y + 5.69 * x ^ 2 to 0.2685 * 6.874 * x + y ^ 2 (1)

Consequently, we can have the maximum point of the model, which optimum working conditions to maximize hydrogen production by SSF process was at a pH of 5.0, an enzyme load of 70 FPU and temperature of 45 ºC. The maximum expected value of hydrogen yield obtained was 60.75 mmol / h * gSV. (Figure 3).

## 4. Conclusion

From the results obtained, the evaluation of the process of SSF was performed with paper industry wastes subjected to chemical pretreatment with $H_2SO_4$ 2.5% The results showed the optimum working conditions to maximize hydrogen production by SSF process: pH (5), an enzyme load of 70 FPU and temperature 45ºC, the maximum value of hydrogen yield was 60.75 mmol / h * gSV.

The key process parameters were optimized by the response surface methodology (RSM) based on a two factor-three level central composite design (CCD), using as variables: temperature (35,45 and 55°C), enzyme loading of Celluclast® (10,40 and 70 UPF) and pH= 5, analysis of variance was performed to test the importance of the polynomial equation of second order, so both equations describe the hydrogen yield in this study, Pretreatment of paper industry wastes with diluted acid was a most effective method for hydrogen production by SSF using biolfilms developed of ixtle fiber cord. This suggested a potential of hydrogen production from cellulosic wastes.

## Acknowledgements

The authors would like to thank the National Science Council of México, for financially supporting this research.

## References

[1] Li Y, Zhang L.Y., Zhu S., Zhang H., Zhang Y., Zhang T., & Zhang, Q. Comparison of bio-hydrogen production yield capacity between asynchronous and simultaneous saccharification and fermentation processes from agricultural residue by mixed anaerobic cultures. Bioresource Technology 2017

[2] Wong, Y. M., Wu, T. Y., & Juan, J. C. (2014). A review of sustainable hydrogen production using seed sludge via dark fermentation. Renewable and Sustainable Energy Reviews, 34, 471-482.

[3] Singh, L., & Wahid, Z. A. (2015). Enhancement of hydrogen production from palm oil mill effluent via cell immobilisation technique. International Journal of Energy Research, 39(2), 215-222.

[4] Cheng, J., Su, H., Zhou, J., Song, W., & Cen, K. (2011). Microwave-assisted alkali pretreatment of rice straw to promote enzymatic hydrolysis and hydrogen production in dark-and photo-fermentation. International Journal of Hydrogen Energy, 36(3), 2093-2101.

[5] Lo, Y.C., Lu, W.C., Chen, C.Y., Chang, J.S., 2010. Dark fermentative hydrogen production from enzymatic hydrolysate of xylan and pretreated rice straw by Clostridium butyricum CGS5. Bioresour. Technol. 101, 5885–5891.

[6] Saha, B.C., Nichols, N.N., Qureshi, Nasib., Cotta, M.A., 2011. Comparison of separate hydrolysis and fermentation and simultaneous saccharification and fermentation processes for ethanol production from wheat straw by recombinant Escherichia coli strain FBR5. Appl. Microbiol. Biotechnol. 92, 865– 874.

[7] Chen S., Hu B. “Pretreatment of methanogenic granules for immobilized hydrogen fermentation”, Int J Hydrogen Energ. vol. 32 (15), pp. 3266-3273, 2007.

[8] I.M.M. Moreno-Dávila, L.J. Ríuos González, J.G. Gaona-Lozano, Y. Garza García, J.A. Rodríguez-de la Garza and J. Rodríguez Martínez “Biohydrogen Production by Anaerobic Biofilms from a Pretreated Mixed Microflora” Research Journal of Applied

Sciences, vol. 5, pp. 376-382, 2010.

[9] P.J. Van Soest,. “Use of detergents in the analysis of fibrous feeds. I Preparation of fiber residues of low nitrogen content”. Journal of the Association of Official Analytical Chemistry. vol. 46, pp. 825-829, 1963a.

[10] APHA, AWWA, WEF, “Standard Methods for the Examination of Water and Wastewater, 20th edn, American Public Health Association, Washington, D.C, USA, 1998..

[11] T.K. Ghose, “Ensayo con papel filtro para sacarificación por celulasa (FPU Assay)”, Pure & App. Chem., vol. 59(2), pp. 257-268, 1987.

[12] Lin, Y., Tanaka, S., 2006.Ethanol fermentation from biomass resources: current state and prospects.Appl-Microbiol. Biotechnol. 69, 627-642.

[13] John, R.P., Anisha, G.S., Nampoothiri, K.M., Pandey, A., 2009. Direct lactic acid fermentation: focus on simultaneous saccharification and lactic acid production.Biotechnol.Adv. 27, 145-152.

[14] Liu, Q., Cheng, K.K., Zhang, J.A., Li, J.P., Wang, G.H., 2010.Statistical optimization of recycled-paper enzymatic hydrolysis for simultaneous saccharification and fermentation via central composite design. Appl. Biochem.Biotechnol. 160, 604-612.

# CHAPTER 6
# Control and Power Conditioning

# CHAPTER 7
# Policies, Economy and Market Strategies

# 7.1 Market study for the marketing of oxyhydrogen reactors *OXHiDROG®*

Marisol Rico, Juan Manuel Sandoval, Eduardo Oliva, Rosa González

[1] Instituto Politécnico Nacional, ESIME-SEPI Unidad Profesional “Adolfo López Mateos”, San Pedro Zacatenco Gustavo A. Madero, CP 07738, México City.

2 Instituto Politécnico Nacional, ESIME-SEPI Unidad Azcapotzalco, Av. de Las Granjas 682, Santa Catarina Azcapotzalco, CP 02250, México City.

3Instituto Politécnico Nacional, ESIQIE Laboratorio de Foto-Electro catálisis Unidad Profesional “Adolfo López Mateos”, Lindavista Gustavo A. Madero, CP 07738, México City.

* 5518201760, molaldep29mail.com

## ABSTRACT

In this research, an analysis of the market is presented in order to know the feasibility for the commercialization of Oxyhydrogen Reactors in México. To determine the beginnings of this analysis it has been necessary to identify the potential market, through a broad review of scientific literature and the development of surveys as primary sources of research.

On the other hand, although some consumption projections were revised in countries such as Brazil, Argentina and Australia, this information is insufficient to make a projection of the supply and demand of the use of hydrogen in our country. So detecting one or several market niches is critical to the marketing of ROH2. As a result of this study it was found that the demand for alternative energies, such as the use of hydrogen, continues to increase due to the detection of the potential market and the society's need to use alternative renewable energies in order to reduce the emission of pollutants to the environment. According to the results obtained from the surveys, 93% of the people answered that they could buy the product, which means a great acceptance of the product of society. On the other hand, it is detected the need to obtain more financing in order to conclude with the stage of testing and adaptation of the product to accelerate the insertion of this technology to the market. Research on the use of hydrogen energy is widespread, however, in Mexico, its share in the current energy system remains low relative to other similar sources of renewable energy. According to the information obtained, on the supply and demand of hydrogen, its presence is significant in some countries of the European Union, the United States and Japan. Therefore, detecting a niche market in Mexico is essential to create a business model appropriate to the Company.

***Keywords:*** Hydrogen, Oxhydrogen Gas, Marketing, Business Model, Oxhidrog®

## 1. Introduction

The demand for fossil fuels is increasing every day around the world, as a consequence has generated its exhaustion. This is one of the reasons why scientific research and technological development of alternative energies that can be used as complementary energy systems is important. Among a variety of resources, hydrogen is one of the most promising options to be used as an energy vector, in addition to its physical and chemical properties [1]

Despite its unique characteristics, the use of hydrogen as a fuel has not been promoted, especially in developing countries. In contrast, in some countries in Europe, in addition to the United States, a large infrastructure and projects on this technology [2]. On the other hand, in countries like Brazil, Argentina and Australia, they have published long-term projections on economic benefits, through the use of hydrogen as fuel. According to these projections, a rapid introduction of Hydrogen would accelerate the creation of a Hydrogen economy. As a result, this article highlights the strong need to implement and extend the use of H2 in Mexico, with the purpose of generating economic progress both in society as well as in the scientific community.There are different ways to promote the use of hydrogen, such as the internet and the mass media, but first, the development of an Oxyhydrogen reactor as a functional product is necessary for the generation and use of H2. This product should be affordable and long lasting. In addition, they have to be carefully tested to ensure they can work under safe conditions, be competitive and represent a real alternative to reduce gasoline use and CO2 emissions. The introduction of a quality Oxyhydrogen reactor could be the key to opening up a new and unexplored market that could generate substantial benefits [3-6]. For this reason, a multidisciplinary group made up of students of manufacturing engineering and automotive engineering in collaboration with the Escuela Superior de Ingeniería Química e Industrias Extractivas y la Escuela Superior de Ingeniería Mecánica y Eléctrica Unidad Azcapotzalco del Instituto Politécnico Nacional in Mexico are developing a system which, through alkaline electrolysis, generates a mixture of hydrogen and oxygen (namely: Oxyhydrogen Gas), which is added at the entrance of the air of an internal combustion engine, with the intention of enriching the mixture Air-gasoline up to 15%. This is not the first attempt to achieve this goal [6-8]. This indicates that it is very important to introduce this product in the Mexican market. To achieve this objective, as a first step the market, the quantity of products to be supplied and the demand for the product [9] should be investigated. In that sense the preliminary results of hydrogen demand and supply in Mexico indicate that there is a great opportunity to commercialize hydrogen energy, at low cost. Meanwhile, the scientific community involved in this topic, should promote the use of hydrogen as a source of energy.

## 2. Development of market research

Figure 1 shows the steps of the methodology suggested by Baca [9], which is used to elaborate the market study.

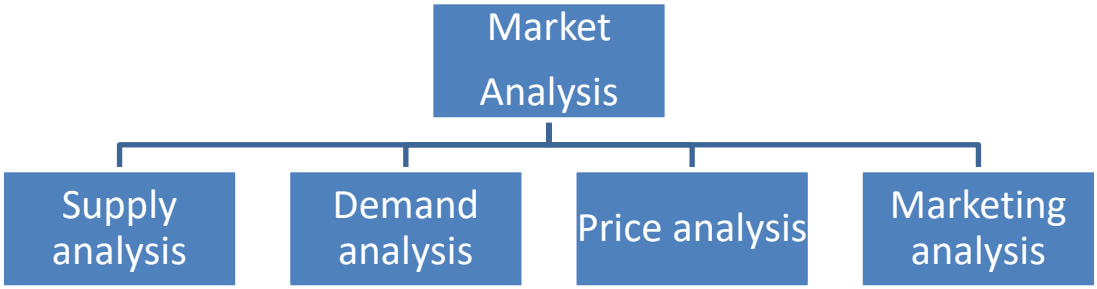


**Fig. 1.** Methodology for market research [9]

The present investigation begins by collecting all the information available in secondary sources related to the historical data of the supply as well as the demand in Mexico. Although there is not enough information on this topic. Consequently it was necessary to design a survey to know the opinion of potential customers.

## 3. Results

108 people were consulted, of the total sample, 62% were men and 38 were women. The question was asked about the gasoline expense that the potential customer makes weekly. Trends are depicted in Figure 2.The amount of money that 65% of respondents pay weekly for gasoline is between $ 300 and $ 500. So users can safely infer that an electrolysis system that generates more hydrogen is necessary and the return on investment happens quickly. Another question was about the number of cylinders of the car engine, to calculate the average possible size and cost of the alkaline electrolyzer. Most respondents responded that they have their own four-cylinder car.

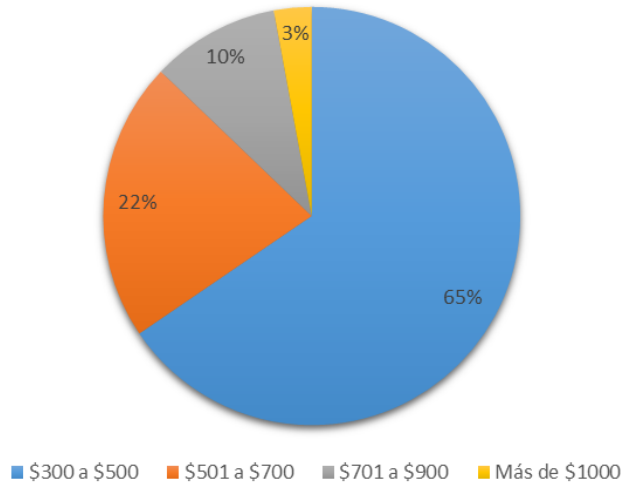


**Fig. 2.** Weekly Gasoline Spending

The fourth question is about the perception of hydrogen as fuel and testing fuel economy with hydrogen under safe and environmentally friendly conditions. Figure 3 shows how interesting this idea seems to people.

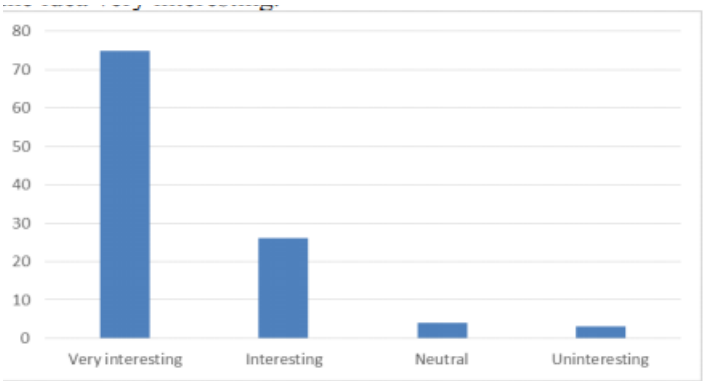


**Fig.1.** Perception of the use of hydrogen mixed with fuel under safe and environmentally friendly conditions

The fifth question is very important, since it allows us to know about; Yes or no, people would invest in an electrolysis system. The responses were very satisfactory stating that 89% of people could probably invest in an electrolysis system, as long as they can save up to 11% gas, as shown in Figure 4.

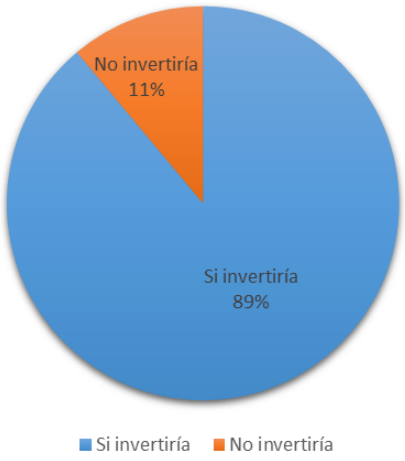


**Fig. 4.** Probability of investment in an electrolysis system

Question number six was designed to determine which aspects are most important when purchasing this type of product, the most important factors being the price and percentage of gasoline saved. Other factors that people consider important to acquire this device is the cost-benefit ratio.

The possibility of using hydrogen energy for economic and environmental benefits should be widely disseminated. In the seventh questionnaire question, people were asked how they would prefer to receive information about an Oxyhydrogen generator. The answers are clearly shown in Figure 5, where it is easy to see that the internet is the preferred way to receive this type of information. In this question the respondents could also choose more than one reference, with the intention of knowing the best way to know about the reactors Oxyhydrogen.

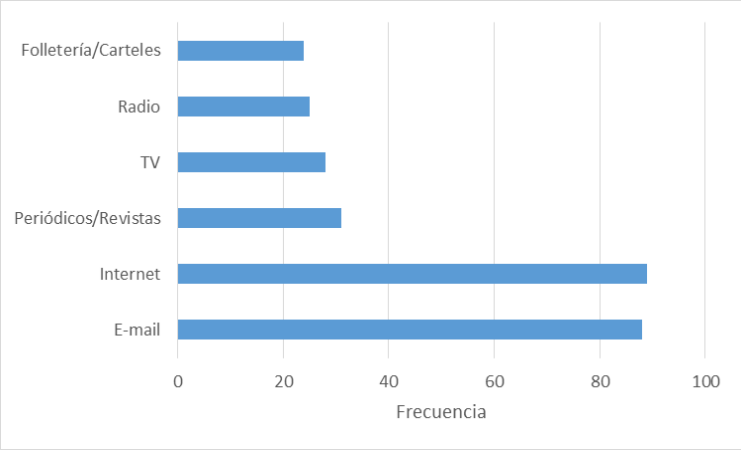


**Fig. 5.** Preferred media for receiving information on hydrogen and electrolysis systems

The eighth question showed, as shown in Figure 6, the price that people are willing to pay for the product mentioned. Most of them could pay on average $ 8000.00 for it, which shows the importance of optimizing the model to lower the price of the electrolysis system, without sacrificing quality and benefits for developers. Price ranges were calculated based on the functional prototype developed.

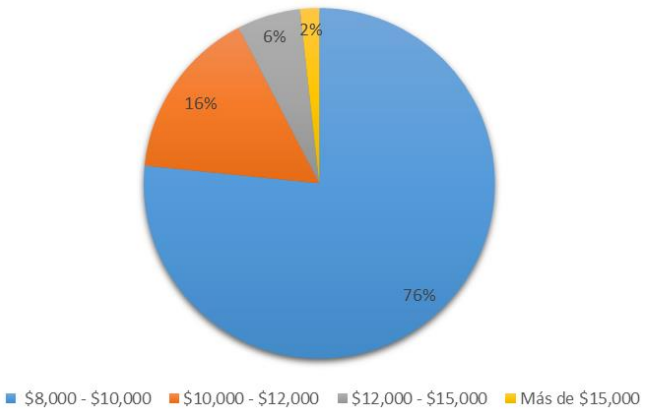


**Fig. 6.** Price that the consumer could afford to pay for an Oxyhydrogen reactor

Finally, question 9 aims to know directly whether or not the consumer would buy the product. This question has only three options: yes, immediately, yes, after a while, and no, I might not buy it. Fortunately, 93% of people answered that they could buy the product, but 73% would expect it to be introduced to the market. As a consequence, it is essential to ensure the reliability of this technological product and as mentioned, to widely and actively disseminate the great advantage of the use of hydrogen to bring about a rapid introduction in the market.

## 4. Conclusion

Derived from the results obtained, the introduction of hydrogen in the market could be accepted by the company. This is the reason for the strong need to extend the use of hydrogen as a safe or complementary fuel. The first approach to people's preferences, allows us to know the main characteristics that a product should possess to succeed in the market: price and percentage of gasoline saved, but also, that the product is friendly to the environment and easy to use.This study also shows that the best way to advertise is online, in contrast to the preconceived idea that the best medium is television. As is well known, it is much cheaper to start with an internet advertising campaign instead of radio or television. As the surveys show, the optimization of the Oxyhydrogen system is crucial to reduce the sale price, due to all those involved in innovation processes (researchers, state and society [5]) that could have benefits of hydrogen energy. In sum, there is considerable market potential for Oxyhydrogen reactors in Mexico, and the scientific community has to develop products that are competitively priced and work under high safety standards.

## Acknowledgements

To: 1. Government of México, 2. Instituto Politécnico Nacional, 3. Escuela Superior de Ingeniería Mecánica y Eléctrica (ESIME), 4. Escuela Superior de Ingeniería Química e Industrias Extractivas (ESIQIE), 5. AL Consejo Nacional de Ciencia y Tecnología (CONACyT). Project SIP 20170047 and the organizers of XVII International Congress of the Mexican Hydrogen Society.

## References

[1] Gutiérrez Jodra, L. El hidrógeno, combustible del futuro. Rev. R. Academia de Ciencias Exactas, Físicas y Naturales, 2005; 99: 49-67.

[2] Bennaceur K., Clark B., M. Orr F., Ramakrishnan T.S., Roulet C., Stout E. El Hidrógeno: ¿Un futuro portador energético? Oilfield Review. Schlumberger 2005; 34-47.

[3] Do Sacramento, E.M., Carvalho, P. C. M., De Lima, L. C. & Veziroglu, T.N. Feasibility study for the transition towards a hydrogen economy: A case study in Brazil. Energy Policy 2013; 62: 3-9.

[4] K. biswas W., Thompson C. B., Islam N. M. environmental life cycle feasibility ssessment of hydrogen as an automotive fuel in Wenstern Australia. 2013; 38: 246-254.

[5] Bozeman B., Rimes H., Youtie J. The evolving state-ofthe-art in technology transfer research: Revising the contingent effectiveness model. Research Policy 2015; 44: 34-49.

[6] Ciniviz M., Köse H. Hydrogen use in internal combustion engine: a review. Academic Paper 2012; 1: 1-15.

[7] White C.M., Steeper R.R., Lutz A.E. The hydrogen- fueled internal combustion engine: a technical review. International Journal of Hydrogen Energy 2006; 31: 1292-1305.

[8] Das L.M. Near-term introduction of hydrogen engines for automotive and agricultural application. International Journal of Hydrogen Energy 2002; 27: 479-487.

[9] Baca U. G. Evaluación de Proyectos

# 7.2 The legal regulation of the $H_2$ as a strategy for public policy Mexico from the consolidation of a Nacional Council of the hydrogen

María Liliana Ávalos Rodríguez, Jorge Víctor Alcaraz Vera , José Juan Alvarado Flores , Jaime Espino Valencia

[1]Instituto de Investigaciones Económicas y Empresariales, Universidad Michoacana de San Nicolás de Hidalgo, Francisco J. Mújica S/N, Col. Felicitas del Rio, C.P. 58040, Morelia, Michoacán, México.

[2]Facultad de Ingeniería en Tecnología de la Madera, Universidad Michoacana de San Nicolás de Hidalgo, Francisco J. Mújica S/N, Col. Felicitas del Rio, C.P. 58040, Morelia, Michoacán, México.

[3] Facultad de Ingeniería Química, Universidad Michoacana de San Nicolás de Hidalgo, Francisco J. Mújica S/N, Col. Felicitas del Rio, C.P. 58040, Morelia, Michoacán, México.

* Corresponding author: 4434 09 59 44, lic.ambientalista@gmial.com

## ABSTRACT

The recognition of the potential energy of the $H_2$ is prominent and accepted in the scientific community, however, few efforts have been made to translate the theoretical contributions in to precise public policy schemes, which seek to address a social problem, through strategies, mechanisms and mechanisms. Tools that link the academic, social, institutional and economic sector in an environmental framework that promotes improvements in living conditions. This problem is reflected in the lack of effective public policies in Mexico, which despite the efforts to be placed in the boom of the hydrogen economy, continues to present legal biases and little social recognition that limits any possibility of sustainable development in the field energetic. For this reason, the main objective of the research was to analyze the Mexican legal framework on $H_2$ regulation and Mexican public policies that consider $H_2$ as an energy source, noting that $H_2$ has not been incorporated as an alternative source of energy, does not exist Regulation of storage, there is a lack of regulations to regulate $H_2$ final applications, such as the case of Solid Oxide Fuel Cells (SOFC) and it is observed that there is no regulation for safety and properties relevant to $H_2$. Public policies in Mexico lack continuity and therefore efficiency, therefore, there is a latent fear that, based on new sexual commitments, the scarce achievements in energy will be left aside, so it is appropriate to propose Public policy strategy the reform of the legal framework to include the $H_2$ as a potential source of alternative energy and the creation of a National Hydrogen Council that will have as its central objective, be a citizen body that seeks to create synergies with the academic, Institutional, economic, governmental and social through the advice and constant recommendation on the use and benefits of the incorporation of the $H_2$ as main energy source.

***Keywords:*** Public policy, legislation, SOFC, National Council of Hydrogen

## 1. Introduction

The need for renewable energy sources that do not depend on time and space and that their storage is feasible is a priority considered by developed countries such as the United States, Holland, Germany, Sweden, Japan, Australia, Canada, etc., To achieve this it was necessary to promote industrial, social, political, economic and legal actions. Faced with these challenges, Mexico, which has a natural wealth recognized worldwide, has the priority of establishing the mechanisms to obtain clean energies that foster development conditions. Certainly, there are legal gaps that the recent administrations have claimed to have corrected, however, legal lags continue to exist that make it impossible to recognize $H_2$ as an alternative energy, but as a way to guarantee clean energy, to date, proposals are mentioned However, few of them have been consolidated as forms of alternative energy, this is essentially due to the legal system lacking links with the social, economic, academic and political sectors, in addition, the limited research done in Mexico on efficiency $H_2$ energy, faces the ignorance, uncertainty and fears facing the industry that could, in the first instance, be the promoter of energy alternatives based on $H_2$.

The literature suggests that using $H_2$ as part of energy solutions leads every nation to move towards the $H_2$ Economy [1], [2] and [3], however, it is not enough to emphasize its efficiency, it is necessary to recognize it Formal way, so that it can promote the mechanisms of solution and linkage. In Mexico, a form of formal recognition is through the Legislative Process that consists of solemn acts that abrogate, add, reform or repeal laws that, by their characteristics, are heteronomous, coercive, external and bilateral. This makes it possible to consolidate efficient laws that recognize $H_2$ as an energy alternative, regulate its storage and make possible its application. The next level is to link to the academic, social and economic sectors, one way to achieve this is by creating a National Hydrogen Council that is a citizen body that seeks and achieves synergies with previous sectors and maintains a dynamic incentive to Research on $H_2$ uses, opening development possibilities for Mexico.

This is more than a priority because of the governmental commitments in Mexico to have at least 35% participation in the generation of non-fossil technologies by 2024 [4]; However, in Mexico the dependence on fossil energy in 2012 was 92%, while in renewable energies of 6.8% [5], a situation that continues to be maintained. Added to this is the fact that the level of proved reserves with which Mexico currently has will only allow hydrocarbon production to be maintained over a period of no more than 10 years [4].

According to the National Energy Balance of 2015 [6], only 9.3% of the primary energy is from renewable sources obtained from firewood and bagasse from sugarcane, a situation that shows the lack of use of other energy sources, especially those Which actually constitute an alternative energy, such as the use of $H_2$, and not only those considered as renewable, while hydrocarbons contributed 87.2% to energy production

In this context, the paradigm of the classification of energies in renewables and alternates, has resulted in Mexican legislation to leave aside the use of $H_2$ as an alternative and clean energy source, betting on the main renewable energy (wind in a 2 %, Thermoelectric in 69%, thermoelectric in 6%, hydroelectric in 1%, photovoltaic in 0%, dual

in 12%, coal in 7% and nucleoelectric in 6%) [5]. This situation is analyzed in this paper, comparing the Mexican legal framework that, in terms of energy, is conformed by the Political Constitution of the United Mexican States (CPEUM); By fourteen laws of the federal order; Two regulations of article 27 of the CPEUM; Ten regulations to the laws of the federal order and an internal regulation of the Secretariat of Energy. Other public actions are located in the National Development Plan 2013-2018; The Fund for Energy Transition and Sustainable Energy Use; The Energy Sector Program; The National Renewable Energy Inventory and the National Energy Balance. All this with the purpose of observing its strengths and weaknesses in the incorporation of the $H_2$ as an energetic alternative; As well as their deficiencies in considering storage and regulated security mechanisms; The final applications of the $H_2$ and mechanisms to encourage its use and application.

Subsequently, it analyzes and discusses the viability of the creation of a consolidated citizen body through the National Hydrogen Council, whose purpose is to advise and recommend actions and proposals that serve as a link between the academy, the social sector, the economic and the political. Highlighting in all this the importance of the use of the $H_2$ as a true alternative source of energy that can improve the conditions of life and with this approach the scheme of sustainable development.

Finally, we present some brief conclusions that show the need to incorporate $H_2$ in the Mexican legal framework and achieve legal efficiency and promote conditions for sustainable development through the creation of the National Hydrogen Council.

## 2. Materials and Methods

The article is based on an inductive-deductive analysis of the Mexican legal framework in the field of energy, in accordance with the legal systems in force, as well as the analysis of the international and national context on energy paradigms propelling sustainable development.

## 3. Results and Discussion

### 1.1. From the international context to the national reality of energy transitions

Since the discovery of fire, mankind has sought incessantly to control and efficiently process production and consumption dependent on energy sources that facilitate processes and meet social requirements. This has led to the search for new methods of energy efficiency, such as those emerging from the Industrial Revolution, which offered not only technological innovation such as the steam engine, but also diversification of energy-use technologies and sources of energy supply, such as the introduction Of the electricity or the internal combustion engine [7]. However, all of this strengthened dependence on oil as a primary energy source, a situation that was exacerbated by the population growth

that, in parallel, brought uncontrolled urbanization, the need for low quality and costly inputs and goods, the growing need for Transportation, etc.

Given this scenario, it was emerging to take measures to address these issues, so countries with a high level of development have opted for research and implementation of other alternative or commonly called conventional sources.

But in Mexico, why has not the use of alternative energies been promoted efficiently? Perhaps the obvious answer is the existence of other social problems that require special attention from decision-makers, such as the Poverty, which according to official figures amounts to 53 million people in such situation [8], is added to it the problem of insecurity, which according to the World Police and Homeland Security Index, Mexico is located in the place 118 of 127 and occupies the thirteenth place of 20 of the most corrupt [9], among other problems such as lack of education; Little investment in research; The indiscriminate use of the natural elements still existing; Unlimited and inefficient access to the health sector; etc.

The transition that Mexico has sought in the energy sector continues to be based on products of fossil origin despite the fact that the discourse shows an efficient transition towards clean and alternate energies. The energy transition policy in Mexico has been based on three conditions:

1. Environmental restrictions such as programs that limit vehicular traffic, mandatory emissions reporting and climate change forums;
2. Express in speeches the economic benefits to be achieved in the transition to renewable energies;
3. The need to reduce risks in energy installations, in the face of possible attacks or failures.

These conditions have neglected the main mechanism of clean development that was fostered in the Kyoto Protocol signed by Mexico in June 1998 and ratified in September 2000. This mechanism seeks to enable projects that benefit developing economies, such as Mexico , Through the use of clean sources; However, Mexico has participated only as a mechanism to receive investment in wind and hydroelectric energy projects [10], despite the fact that the natural elements of Mexico facilitate these mechanisms and do not really offer an alternative energy source, only foreign direct investment.

Another international event that influenced the ideology of energy mechanisms in Mexico was the Bonn Conference of 2004 that sought to promote the global participation of renewable energy as substantial for sustainable development because it provides access to energy especially to those with few Resources, mitigates greenhouse gas emissions and reduces pollution. To achieve this, it was envisaged that developing countries like Mexico would improve their markets, financing, technologies and policies, all under an international cooperation scheme; However, it is worth thinking about how feasible is freedom of decision for Mexico? If the bilateral relationship with the US forces him to remain subordinate and dependent. In the short and long term, the changes necessary to encourage the use of alternative and renewable energies are only an ideology that abandons national political discourses.

It has been argued that, in order to achieve the energy transition under the schemes proposed by the Bonn Conference, political, educational and technological co-participation [11] is required, which raises the question why in Mexico in 2017 Budget for research, innovation and technology instead of promoting better scientific conditions ?, is not educational work a priority issue on the political diary? These questions have undoubtedly aroused the interest of knowing that it is behind the political discourse and showing if the current public policies are effective, so it is advisable to review the legal framework of energy in Mexico under the scheme that laws are, finally, formalization From the entry into force, of public policies [12].

But to do so, it is necessary to recapitulate what has been done in energy world-wide, where it can be seen that since 1975, programs have been decreed to encourage alternative and renewable energies, for example in Brazil, in 1975, Decree 76.593 Concerning the PROALCOHOL Program; In 1981, India encouraged programs for the training of human resources and commissions for additional sources of energy; In 1982 likewise, India creates the Department of Non-Conventional Sources; In 1990, Denmark created the Energy Plans; Finland also issues its Energy Action Plan, which was updated in 2002. In 1992, India created the Ministry of Non-Conventional Sources and in the same year, the Netherlands issued the White Paper on Renewable Energies - Advanced Energies 1998 To 2002 creates the Program of Action for said Book. For the year 1996 Denmark issues a new Energy Plan; In 1997 Spain announces its Plan for the Promotion of Renewable Energies and throughout the European Union the document entitled "Energies for the future: Renewable energy sources" appears and in 2001 the ALTENER program enters into force in the European Union, In the same year of 2001 in Mexico creates the Energy Secretariat and with it the National Energy Program with effect to 2006. In 2002 Brazil publishes the Law that created the Program of Incentives for Alternate Energy Sources. In 2004, Germany modified its Renewable Energy Law, issued in 2000. For 2006, Brazil encourages energy development programs such as ELECTROBRAS and PRODEEM.

Mexico for its part in 2002 publishes the Law of Energy for the Field; In 2008 the Law on the Promotion and Development of Bioenergy and in 2014 enacts the Law of the Energy Regulatory Commission and the Law of the Public Service of Electric Energy and its Regulations (which are currently repealed), however, also publishes In 2014 the Law of Geothermal Energy, the Law of Regulated Regulatory Bodies in Energy Matters; The Hydrocarbons Law; The Law of National Agency of Industrial Safety and Protection of the Environment of the Hydrocarbons Sector and the Law of Revenues on Hydrocarbons, all of them still in force.

In 2015 it publishes the Law for the Use of Renewable Energies and the Financing of Energy Transition and its Regulations, as well as the Law for the sustainable use of energy and its Regulations (currently repealed), however, in the same 2015 Publish other laws that are still in force, such as the Energy Transition Law; Already in 2016 the Federal Law to Prevent and Punish Crimes Committed in the Field of Hydrocarbons is published and in 2017 Mexico launches the 2017-2021 Strategic Program with the support of the National Center for Energy Control.

As can be seen, energy actions generally translate into strategic programs that seek to meet specific needs, few countries have promoted laws that coercively make the energy transition possible, Mexico has not been the exception, however, it is to be recognized That the actions it has undertaken have recently been highlighted and all of them emphasize renewable energy rather than alternative energies. For this reason it is convenient to briefly analyze the scope and limitations of the Mexican legal framework in order to observe the role played by $H_2$.

### 1.2. Scope and Limitations of the Mexican Legal Framework in Energy Matters

As already mentioned, the Mexican legal framework in energy matters is composed of the CPEUM; By fourteen laws of the federal order; Two regulations of article 27 of the CPEUM; Ten regulations to the laws of the federal order and an internal regulation of the Secretariat of Energy. Other public actions are located in the National Development Plan 2013-2018; The Fund for Energy Transition and Sustainable Energy Use; The Energy Sector Program; The National Inventory of Renewable Energies and the National Balance of Energy and to know the role that the $H_2$ plays in these legal systems should be analyzed.

It is observed that, 29% of the federal laws including the CPEUM, make a superficial reference of the $H_2$, without specifying in its forms of use and use, for example, the CPEUM in its article 27 indicates that it corresponds to the Nation the dominance of solid, liquid and gaseous hydrogen carbides; The Law of Petróleos Mexicanos states in its article 5 in general on the exploration and extraction of solid, liquid or gaseous hydrogen carbides. The Organic Law of the Federal Public Administration states in its article 33 that the function of the Energy Secretariat is to regulate and promote the development and use of alternative energy sources to hydrocarbons, and the Energy Transition Law indicates in the sixteenth "The minimum efficiency for the use of hydrogen to be considered a Clean Energy shall not be less than 70% of the lower calorific value of the fuels used in the production of said hydrogen."

The rest of the laws and regulations that emerge from these as the Regulations, do not emphasize the use and use of $H_2$ or alternative forms of energy, focusing on renewable energy and based on fossils.

In this context it is feasible to argue that the legal basis in $H_2$ in Mexico has as its main weakness the legal support, although there are national programs and plans that seek to promote the use of alternative energies, it is not enough that they exist due to their scope Limited that transcend presidential sexennia. This is why the weakness lies in the fact that there is no legal support that promotes the use and utilization of $H_2$ and that, in turn, actually consolidates the energy transition gradually removed from oil.

A strong strength is in the Mexican legal framework is the feasibility of placing through a legal reform, the $H_2$ figure and raise it to a viable and sustainable energy alternative. Based on the scientific research that, although it is scarce, has been developed by researchers in Mexico, as is the case of the proposal of the National Hydrogen Plan, which seeks to offer a vision of the use of the same as energy vector, through the Incentive in infrastructure and training programs for specialized personnel in Mexico, as well as

opportunities for research, development and application of $H_2$ technologies for the benefit of society. In addition, it is necessary to promote hydrogen technologies that offer solutions according to Mexican needs and based on current environmental conditions.

Public energy policies in Mexico have remained in the phase of program, plan, fund or energy balance, without to date have been consolidated into a heteronomous and coercive legislation. It should be remembered that political demands also depend on the valuations of each citizen and each social leader in consideration of an environment according to a given time and space [13]. For what is very true is that it is necessary to promote before the government and financial institutions, projects based on the efficient use of $H_2$ for the purpose of claiming the right to development, [14] however, current governmental actions are reflected in Development plans, transition funds, energy programs, energy inventories and balances.

The National Development Plan 2013-2018 [15] has been one more of the political strategies to seek Mexico's long-awaited development. However, due to internal inconsistencies, it has not had the necessary bases to carry out the actions it proposes, if Well, all are aimed at achieving a decent life for development and well-being under inclusive schemes of peace and responsibility, the truth is that the mechanisms have not been given to achieve these goals. In terms of $H_2$, the National Plan seeks to achieve that energy transition, however, it can not achieve this if it does not translate its actions into laws, to force all social sectors to seek energy alternatives and not only to consider renewable sources of energy.

The Energy Sector Program 2013-2018 [16], published in the Official Gazette of the Federation (DOF) on 13 December 2013, starts with a diagnosis to create a national energy matrix in consideration of the availability of hydrocarbons in the national territory, Recognizes that energy demand in Mexico has been concentrated in fossil energy sources, mainly crude oil and natural gas. Currently, the combined production of oil and natural gas accounts for about 90% of total primary energy production. On the other hand, despite significant progress in the use of non-fossil energies, its share in the energy matrix remains low (7%).

On the other hand, the Fund for Energy Transition and Sustainable Use of Energy [17] seeks to implement actions to carry out the National Strategy for Energy Transition and Sustainable Energy Use, promoting the use, development and The investment of renewable energies and energy efficiency, however, their actions carried out until 2015 indicate that they have been careful to encourage projects to promote the bioeconomy in Mexico, through bioenergetics and agribusiness, where they give continuity to the use Fossil fuels and renewable energies, such as wind projects in Oaxaca and Sonora, those focused on photovoltaic energies in Quinta Roo, geothermal in Michoacán; Other examples promoted by the Fund have been lighting such as ILUMEXICO 2011-2012 and replacement programs for household appliances and light bulbs; among others.

The National Strategy for Energy Transition and Sustainable Energy Utilization 2013-2027 [18], is the mechanism by which the Mexican State will promote policies, programs, actions and projects aimed at achieving greater utilization and exploitation of the sources

of energy. Renewable energy and clean technologies; Promote energy efficiency and sustainability; As well as the reduction of Mexico's dependence on hydrocarbons as a primary source of energy. However, it only addresses the use of $H_2$ by suggesting efficient refineries, making Petróleos Mexicanos (PEMEX) and the Energy Regulatory Commission (CRE) responsible. It is recognized that the Strategy seeks to include the contribution of society under a scheme of legality and equity. Arguments that surely the academic sector will follow closely to know the degree of its application.

On May 31, 2017, the Agreement by which the Energy Secretariat issued the Special Program for Energy Transition was published in the DPF [19]. In Chapter I it deals with clean energies and technological development of talent And value chains. Particularly in section 1 g), it cites:

> *"Clean energies are defined in the Law of the Electrical Industry (LIE), as those sources of energy and processes of generation of electricity whose emissions or residues do not exceed the thresholds established in the regulations that are issued for that purpose. Among the clean energies are considered the following ...*
>
> *g) The energy generated by the use of hydrogen through its combustion or its use in fuel cells, provided that the minimum efficiency established by the CRE and the emission criteria established by SEMARNAT in its life cycle are met ...*

For its part, section 3 regarding technological development, talent and value chains indicates:

> *"All three are fundamental pillars for the full development of clean energy in our country. The use of clean energies is one of the areas of research where the scientific-technological community has devoted considerable efforts for several years. The development of specialized human capital is another area of opportunity and in recent years important efforts have been made to train and raise the quality of professionals and technicians in the sector. Value chains are vital to support the entire energy sector and is another area with great opportunities for improvement, and in at least eight states of the country, the National Institute of Entrepreneurs (INADEM) has identified renewable energy as a strategic sector future".*

As can be seen, recently the agreements of the Energy Units in Mexico have sought to link the potential of natural elements, human resources and external experiences in economic and energy matters to consolidate a true energy transition, missing a great way to go, It is important to avoid restricting the progress achieved so far with a new six-year political scheme and to seek to incorporate these strategies and alternatives into the legal bodies.

A key element that favors the effectiveness of the public policies translated into laws is social participation. For this reason, it is necessary not to opt for an agency that facilitates the rapprochement of all social sectors and contributes to advice, proposals, follow-up and Evaluation of any energy alternative derived from the efficient use of $H_2$. That body must have its own autonomy and operate under its own regulatory schemes.

### 1.3. Viability of the creation of the National Hydrogen Council

The need to have an autonomous body that seeks to encourage the use and use of $H_2$ can be translated into a parastatal sector sector of the Ministry of Energy, comprising a body composed of academic, social, business and government representatives, said body will support the National Council In cooperation with government agencies (Secretaría de Energía, Petróleos Mexicanos, the Federal Electricity Commission, the Energy Regulatory Commission, the National Commission for the Efficient Use of Energy, the Electric Energy Savings Trust, the National Institute of Nuclear Research, Institute of Electrical Research, National Commission for Nuclear Safety and Safeguard), academic and research institutions, civil associations, business and industrial sectors, as well as society in general, will promote as general objective the use and Approve $H_2$, developing research according to social needs, translating these social needs into public policies that, through a legislative process (initiative, discussion, approval, sanction and publication), are transformed into laws that all society must observe, and that in a way Constant and regardless of government periods, will evaluate and improve the proposals for use and use of the $H_2$, being an efficient means of rapprochement and linkage with the business and industrial sector of Mexico to promote the benefits of $H_2$ use in these sectors and strengthen mechanisms of Investment and financing. With this, in parallel, the effectiveness of the use and use of truly alternative energies is achieved without neglecting all current policies that promote renewable energies.

In addition, the National Council will promote the storage of $H_2$, under security mechanisms that can inform and apply through the development and implementation of an $H_2$ management plan, an instrument that will facilitate the storage of the element, its safety conditions and specifications in Case of contingencies. This will not only encourage the use and use of the $H_2$, through the information on their safe use, but will promote the legal framework to seek to link and recognize it properly in alternative energies, reforming and separating, in the first instance, the general definitions of Renewable energies and alternative energies.

In this context, the $H_2$ National Council will be the governing body of public policy that in a binding way will achieve a true incorporation of the $H_2$ as an element that promotes the energy transition in Mexico based on knowledge, economic and technological investment, giving as Result in a quality of life that defines development and well-being.

## 4. Conclusion

The great challenge facing Mexico in the energy transition goes beyond the current effectiveness of public policies, the transition is not only political but also legal, economic, technological, academic and social. It has been observed that Mexico has begun to emphasize the importance of clean energy under the motto of sustainability, however, it is disappointing that the proposed actions do not transcend sexually or governmental periods and that these actions are sustained by the use and exploitation Of fossil sources. Certainly, there are other lags that make it impossible to turn to alternative energies and rethink the political task, such as education, poverty, marginalization, lack of health services, insecurity, etc. However, it is essential to act Parallel and better than supported

by a body that meets social, economic, academic and political needs, seeking to create links between these sectors that may become federal law.

## References


[1] Jeremy, R. (2002). La economía del hidrógeno. editorial Paidós, Buenos aires.

[2] Botas, J. A., Calles, J. A., Dufour, J., y San Miguel, G. (2005). La economía del hidrógeno–Una visión global sobre la revolución energética del siglo XXI. Revista de la Asociación Española de Científicos, 9.

[3] Alvarado F. J. J., Valencia, J. E., y Rodríguez, M. L. Á. (2015). La necesidad de incorporar el hidrógeno como potencial fuente alterna de energía en la legislación mexicana. *Revista Catalana de Dret Ambiental*, *6*(1).

[4] Secretaría de Energía. Prospectiva de Energías Renovables 2012-2026. Recuperado a través de https://www.gob.mx/sener/documentos/prospectivas-del-sector-energetico. accessed 17/07/03.

[5] Vázquez, A. L. (2015). Desarrollo y prospectivas de energía renovable en México. Economía Informa, 390, 132-135.

[6] Secretaría de Energía. Balance Nacional de Energía (2015). Secretaría de Energía, Dirección General de Planeación e Información Energéticas, México, 2016. Recuperado a través de https://www.gob.mx/sener/documentos/balance-nacional-de-energia. accessed 17/07/03.

[7] Nakićenović, N., Grübler, A., y McDonald, A. (Eds.). (1998). *Global energy perspectives*. Cambridge University Press.

[8] Secretaría de Desarrollo Social (2016) recuperado en https://www.gob.mx/sedesol. accessed 17/07/03.

[9] OCDE (Organización para la Cooperación y el Desarrollo Económicos) 2013. Evaluaciones de la OCDE sobre el desempeño ambiental: México 2013, OECD Publishing. De: www.oecd.org/env/country-reviews/mexico2013.htm, accessed 13/11/03.

[10] CDM Watch (2017). Recuperado a través de: http://www.cdmwatch.org/project. accessed 17/07/03.

[11] Internacionale Konferenz für Erneuenbare Energien (2004). Alemania

URL: http://www.renewables2004.de, accessed 04/08/31.

[12] Subirats, J. (2017). Análisis de políticas públicas y eficacia de la administración.

[13] Lindblom, C. (1991). *El proceso de elaboración de políticas públicas*. Grupo Editorial Miguel Ángel Porrúa.

[14] Vieyra, Calderón Juan Manuel (2005). Las políticas públicas y el futuro de la energía en México. Revista: Mundo siglo XXI, ISSN: 1870-2872, junio, número 1, páginas 51-61.

[15] Plan Nacional de desarrollo 2013-2018. *Diario Oficial de la Federación*, *20*13. Recuperado a través de http://pnd.gob.mx/wp-content/uploads/2013/05/PND.pdf. accessed 17/07/03.

[16] Secretaría de Energía. Programa Sectorial de Energía (PROSENER) (2013-2018). Gobierno de la República. Recuperado en https://www.gob.mx/sener/acciones-y-programas/programa-sectorial-de-energia-2013-2018. accessed 17/07/03.

[17] Secretaría de Energía. Fondo para la Transición Energética y el Aprovechamiento Sustentable de la Energía (FOTEASE), 2009-2015. Informe 0, consultado a través de https://www.gob.mx/sener/articulos/el-fondo-para-la-transicion-energetica-y-el-aprovechamiento-sustentable-de-la-energia-es-un-instrumento-de-politica-publica-de-la-secretaria. accessed 17/07/03.

[18] Secretaría de Energía. Estrategia Nacional de Transición Energética y Aprovechamiento Sustentable de la Energía 2013-2027 (ENTEASE) 2013-2027. Recuperado a través de https://www.gob.mx/sener/documentos/estrategia-nacional-de-transicion-energetica-y-aprovechamiento-sustentable-de-la-energia. accessed 17/07/03.

[19] Secretaría de Energía. Programa Especial de la Transición Energética (2017-2018), recuperado en https://www.gob.mx/sener/documentos/programa-especial-de-la-transicion-energetica-2017-2018accessed 17/07/03.

# CHAPTER 8
# Codes, Standards and Safety Issues.

# CHAPTER 9
# Nanostructured Materials

# 9.1 MOF 253- Pt performance electrocatalyst for Oxygen Reduction Reaction

V. Ávila Vázquez, I.L. Escalante-García,V. H. Collins Martínez, S.M. DurónTorres

[1]Universidad Autónoma de Zacatecas, Área de Ciencias Químicas, Carretera Zacatecas-Guadalajara km 6, Ejido "La Escondida", Edificio 6, C.P. 98160, Zacatecas, Zac.
[2]S.C. Depto. de Ingeniería y Química de Materiales, Centro de Investigación en Materiales Avanzados, Miguel de Cervantes 120, Complejo Industrial Chihuahua, 31190 Chihuahua, Mexico

* Corresponding author: duronsm@prodigy.net.mx

## ABSTRACT

Metal organic frameworks (MOFs) are a new class of coordination polymers that have been attractive for clean and efficient energy conversion applications as well as electrocatalyts for energy conversion in fuel cells. Briefly, the MOFs are solid materials formed by metal ions (or clusters) coordinated to multidentate organic molecules. In this investigation, we present the results for the electrochemical and physicochemical characterization of MOF 253 using Pt as metal ion for the Oxygen Reduction Reaction (ORR). The material was synthesized by solvothermal and microwave methods with the aim of optimizing the catalytic load of Pt used in the fuel cell. The results show that the Pt-MOF 253 exhibits electrochemical activity towards the ORR and a namometric particle size. Overall, these materials can be a promising possibility as electrocatalysts for fuel cell.

***Keywords:*** MOF-Pt, Fuel Cell, ORR

## 1. Introduction

Metal−organic frameworks, or MOFs (also known as coordination polymers), have emerged as an extensive class of crystalline materials with ultrahigh porosity (up to 90% free volume) and enormous internal surface areas, extending beyond 6 000 - 10 000 $m^2/g$. These properties, together with the extraordinary degree of variability for both the organic and inorganic components of their structures, make MOFs of interest for potential applications in clean energy, most significantly as storage media for gases such as hydrogen and methane, and as high-capacity adsorbents to meet various separation needs. Additional applications in membranes, thinfilm devices, catalysis, and biomedical imaging are increasingly gaining importance [1-5]

One the novel MOF aplication is the catalysis to fuel cell, an H2/O2 proton exchange membrane (PEM) fuel cell is a generator of electrical power based on the electrochemical oxidation of hydrogen at the anode and the electrochemical reduction of oxygen at the cathode. In these systems, electrocatalysts are necessary to accelerate both half-cell reactions. Today, only platinum and platinum−alloy electrocatalysts are used in all PEM fuel cell prototypes. However, in the context of a strong economy, platinum will always be expensive, hence hindering the large scale commercialization of these clean and efficient electrical energy sources [6-9].

The platinum catalysts account for 33% of the overall stack costs. Due to kinetic limitations for the oxygen reduction reaction (ORR), the required platinum content at the cathode is about order of magnitude larger than at the anode. Therefore, in terms of cost reduction, the replacement of platinum and platinum−alloy catalysts is especially welcome at the cathode [10-13].

The goals of this study are: (i) to compare the activity, performance, and stability of the new Pt- MOF and Ru-MOF in oxygen reduction reaction (ORR) catalysts, (ii) to study the effect of the metal in the reaction; (iii) to try to correlate any improvement in the catalyst stability measured in (ii) to some properties measured for the same catalysts during their physico-chemical and electrochemical characterization.

## 2. Materials and Methods

### 2.1. Synthesis of MOF-Pt and MOF- Ru

Pt and Ru based MOF-253 materials as the electrocatalyst precursor were synthesized in two steps according to the reported procedure [14-16]. For the microwaves synthesis the procedure was followed with the time change: to synthesize MOF-253 (first step), 151 mg of AlCl3:6H2O was dissolved in DMF (10 mL), followed by the addition of 153 mg of 2,20-bipyridine-5,50-dicarboxylic acid (bpydc). The obtained mixture was then placed in a Teflon capped vial and heated at 120 °C for 6 min in microwaves. The resulting white microcrystalline powder was then filtered and washed with DMF. To obtain fully desolvated framework, this powder was subsequently washed with methanol in microwaves for 5 min, then collected by filtration and finally dried at 180 °C under dynamic vacuum for 12 h.

In order to introduce Pt atoms (second step), 500 mg of the desolvated MOF-253 was mixed with 386 mg of $PtCl_2$ $(CH_3CN)_2$ and 400 mg of $Ru_3(CO)_{12}$ respectivily and acetonitrile (15 mL). This mixture was then heated at 85 °C in a Teflon-capped vial for 5 min.

The resulting solid was collected by filtration and immersed in acetonitrile (15 mL). The total immersion time was three days and the solvent was replaced with fresh acetonitrile after each 24 h. Finally, the product (hereafter referred to as Pt-MOF and Ru-MOF) was collected by filtration and dried at 150 °C for 12 h under vacuum.

2.2. Pyrolytic transformation of the Pt-based MOF into electrocatalysts

To prepare the PEMFC electrocatalysts, the Pt-MOF and Ru-MOF materials were heat treated at temperatura 1000°C. A quartz tube (6 mm diameter) containing 100 mg of the sample was weighed and placed inside a furnace. The tuve was sealed airtight and then purged with argon for 1 h prior to the treatment. The materials were typically heated at the ramp rate of 1 °C per min for 4 h under flow of argon at a rate of 20 mL per min. The yield after the heat treatment was normally about 50 wt.

2.3 Physicochemical characterization

A JEOL JEM-2200FS high resolution transmission electron microscope was used for evaluate the size particle, and the specific area of the MOF and Pt-MOF previous pyrolyzed were established by Brunauer – Emmett – Teller (BET) analysis of the nitrogen adsorption-desorption isoterherms recorded at 77 K using a Micromeritics ChemiSorb 2720. All the samples were degassed by heating at 200°C under flow of nitrogen prior to measuring the surface area [17-20].

2.4 Electrochemical characterization

2.4.1 Electrodes preparation

The electrodes were prepared from a catalytic ink comprising 6 µL of Nafion ® (5 wt. %, Aldrich), 10 µL of ethanol spectroscopic grade, 6 mg of Pt-MOF 253. Later, the resulting suspensions were hold in an ultrasonic bath for 0.5 h in aim to gain additional dispersion of mixture. Subsequently, a volume of each ink was deposited on a clean polished glassy carbon disk electrode (GCE) (A = 0.07068 $cm^2$). The coated GCEs were dried in a furnace at 80°C for 10 min. In order to comparison a Pt supported on Vulcan electrode were used. Finally, MOF-253, Ru-MOF and Pt- MOF before pyrolized, Ru-MOF and Pt- MOF pyrolized were used as working electrodes for the ORR kinetic studies. All the current values reported in this paper are normalized to the electrode geometric area.

2.4.2 Electrochemical characterization of electrodes

All the experiments were performed in a double-compartment electrochemical glass cell. An $Hg/Hg_2SO_4$/0.5 M $H_2SO_4$ (ESM = 0.7V vs. NHE) electrode was used as reference which was positioned as close to the working electrode as possible by means of a Luggin capillary. A Pt-mesh was used as counter-electrode and the aqueous electrolytic medium was 0.5 M $H_2SO_4$ at room temperature. The electrochemical measurements were performed using an EG&G PAR VersaSTAT 3 Potentiostat/Galvanostat. In this study, all measured values of potential are reported respect to the normal hydrogen electrode (NHE).

Cyclic voltammetry (CV) was carried out to evaluate the effect of different step of the synthesis for make the Ru-MOF and Pt-MOF, the electrodes by scanning the potential at a rate of 50 mV $s^{-1}$ between -2.2 V and 1.7 V for Pt-MOF and -2 V and 1.8 V. For Ru-MOF under a $N_2$ atmosphere electrolyte solution. Oxygen reduction experiments were performed using rotation speeds of 100, 625, and 1600 rpm in a potential range of 0.5 to -1.4 V at a scan rate of 5 $mVs^{-1}$ in oxygen-saturated $H_2SO_4$. The rotation rate was controlled by a PINE MSRX precision rotating system.

## 3. Results and Discussion

The Table 1 shows the specific surface area and the particle size, the área decrease when the Pt is added may be due to the restructuration betwen Pt and MOF, while the size particle obtained is nanometric [20-21].

**Table 1.** BET specific surface area and size particle of MOF materials

| Sample | $S_{BET}$ ($m^2 gr^{-1}$) | Size particle(nm) |
|---|---|---|
| MOF | 81 | - |
| Pt-MOF previous pyrolyzed | 4 | - |
| Pt-MOF pyrolyzed | - | 8 -12 |

The Figure 1 shows the compares the cyclic voltammograms obtained for the steps the formation of the Pt-MOF, the insert corresponds to the final steps of synthesis, when the Pt-MOF is pyrolyzed present an increase in the current obtained in comparison with the previous steps of formation ( MOF and Pt-MOF previous pyrolyzed) this may indicate an restructuration of the atoms of Pt above carbon support.

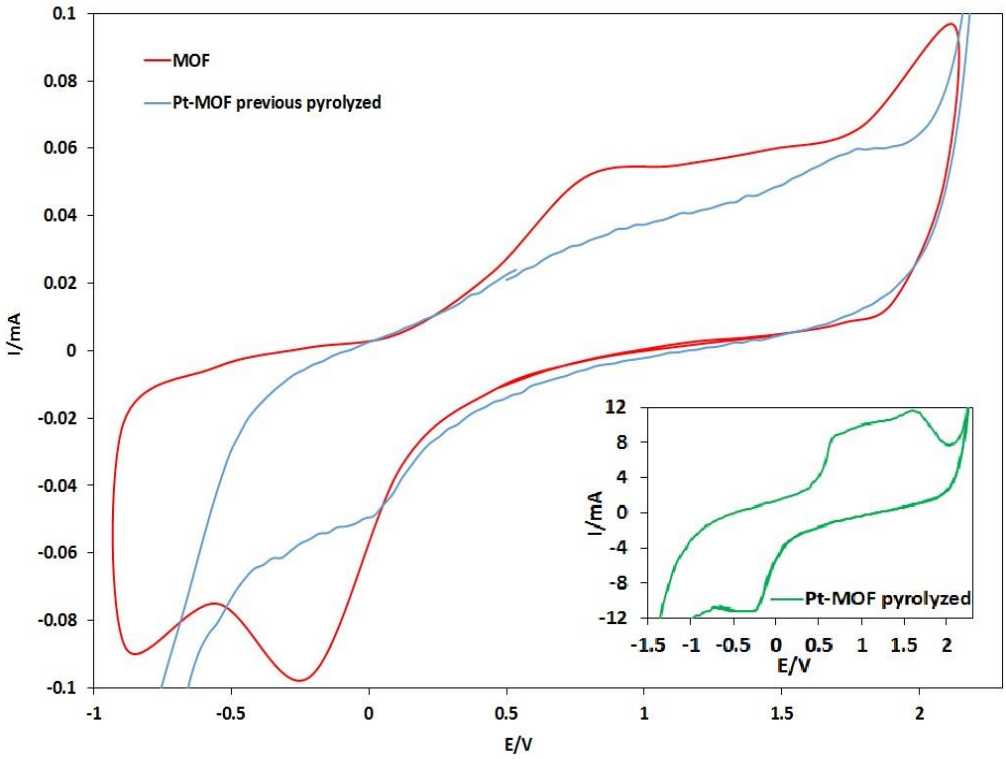


**Fig 1.** Cyclic voltammogram the steps synthesis of Pt-MOF in $N_2$ saturated 0.5 M $H_2SO_4$ and room temperature at 50 mV $s^{-1}$.

The Figure 2 shows the compares the cyclic voltammograms obtained for the steps the formation of the Ru-MOF, the current obtained is less in comparison with the Pt-MOF. The electrochemical behavior of Pt as a electrocatalyst for ORR was already known [22-23], and this was also confirmed with the results presented in this work.

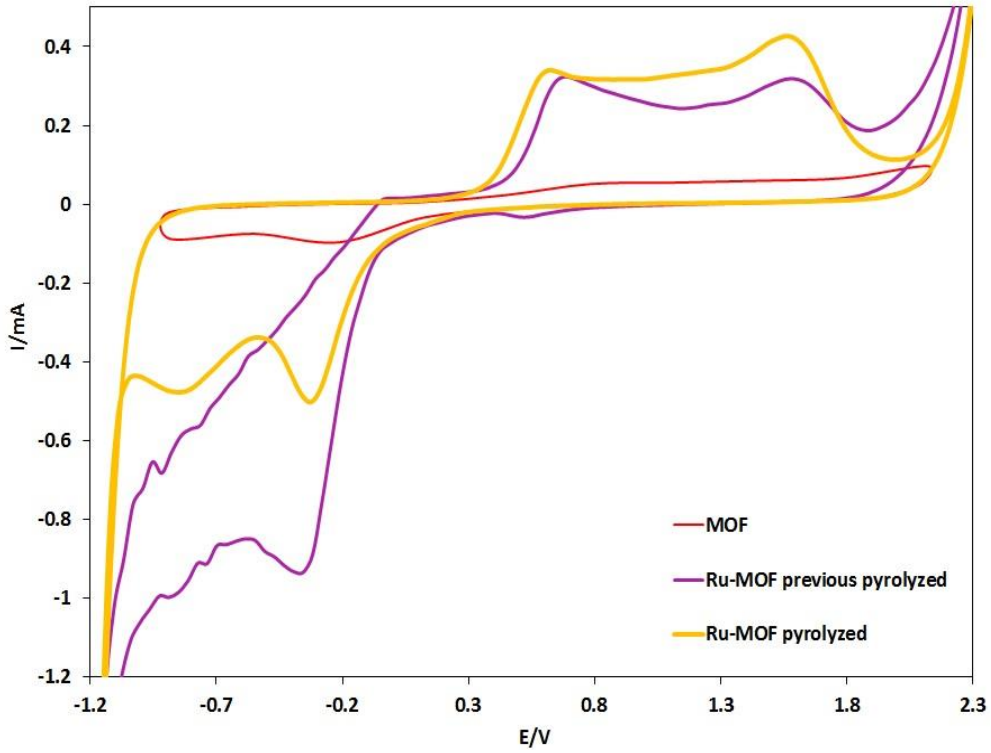


**Fig 2.** Cyclic voltammogram the steps synthesis of Ru-MOF in $N_2$ saturated 0.5 M $H_2SO_4$ and room temperature at 50 mV $s^{-1}$.

The Figure 3 show the comparison electrochemical behavior between the materials synthetized (Pt-MOF and Ru-MOF) and the Pt-Vulcan used who reference, is possible appreciate differences in the typical profile of the behavior of the Pt support on vulcan in acidic medium The window of potential wide suggests that the ORR is more irreversibly and therefore slow in the materials synthetized.

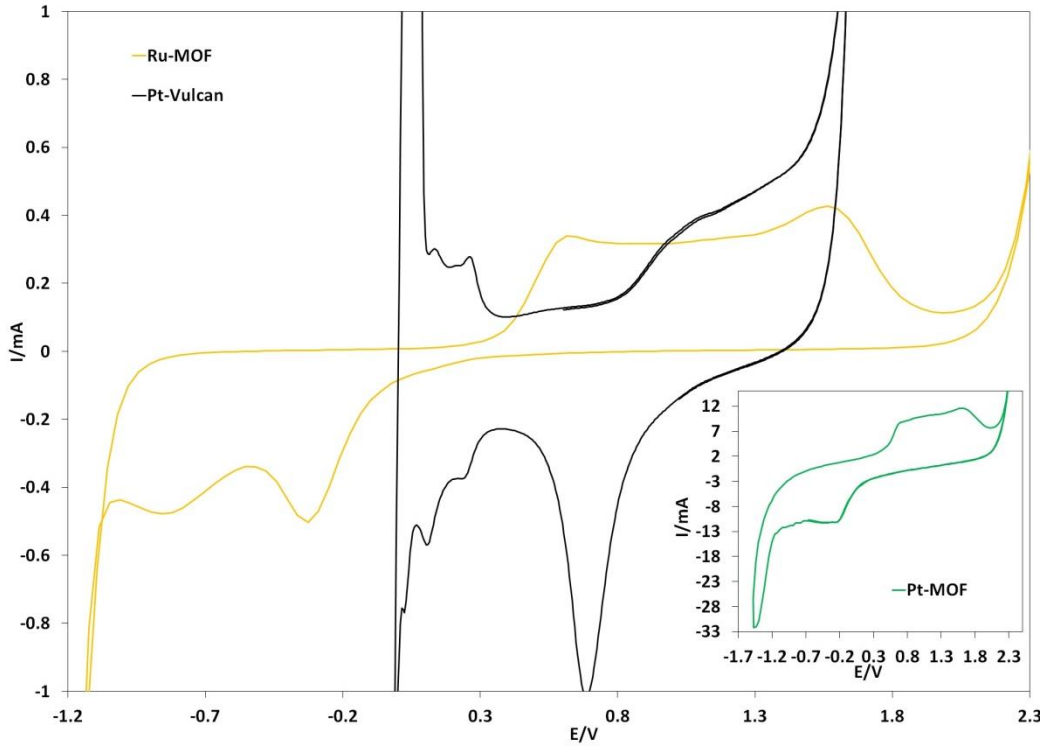


**Fig 3.** Cyclic voltammogram the Pt-vulcan, Pt-MOF and Ru-MOF in $N_2$ saturated 0.5 M $H_2SO_4$ and room

temperature at 50 mV $s^{-1}$.

Figure 4 a) shows the j–E diagrams obtained for Pt-MOF, 4 b) Ru-MOF and 4 c) comparison between Pt-vulcan and material synthetized (only 1600 rpm), for ORR using the RDE technique at a rotating speed of 100, 625 and 1600 rpm (Figure 4 a) and 4 b)). The used this technique confirmed that both materials sinthetized present electrochemical activity for ORR. The difference in the limiting currents for materials compared (Pt-MOF and Ru-MOF) may be attributed a better coverage and electrochemical activity of the Pt catalyst and to the physical properties, such as the porosity and nature of the catalyst-MOF film on the glassy carbon electrode(Figure 4 a) and 4b)). Finally the RDE curves in the Figura 4 c) show the classical mixed, kinetic and diffusion control zones; although these regions are better defined when the Vulcan is used who support, confirmed that the ORR is more slow with the Pt-MOF and Ru-MOF increased the overpotential to which the ORR is carried out.

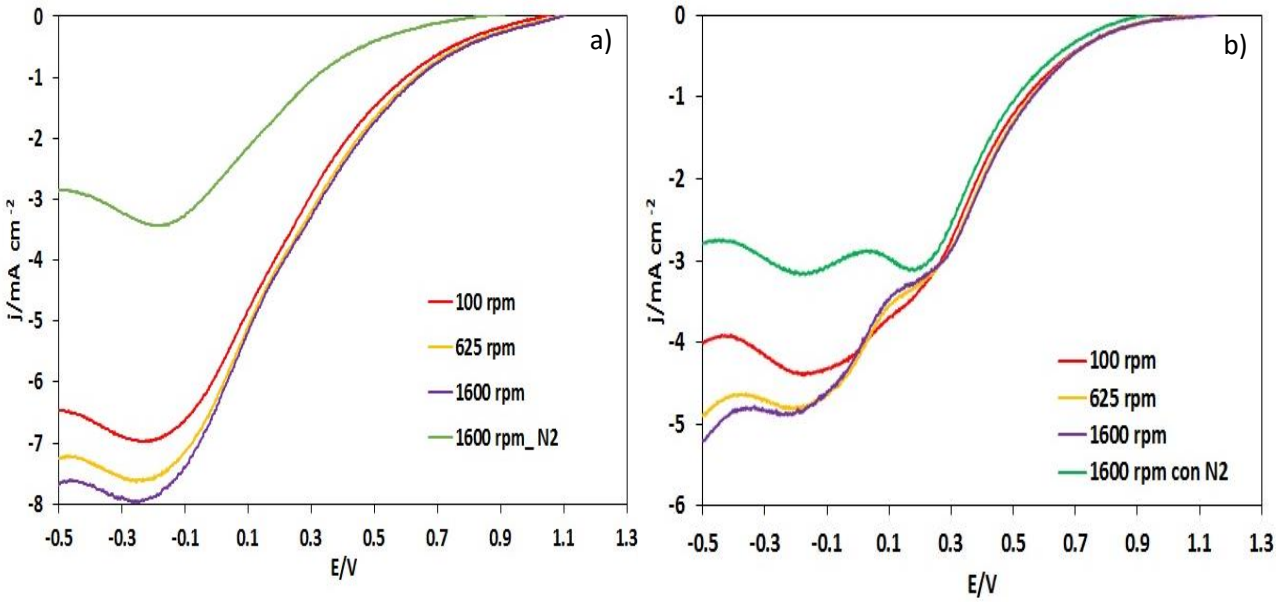


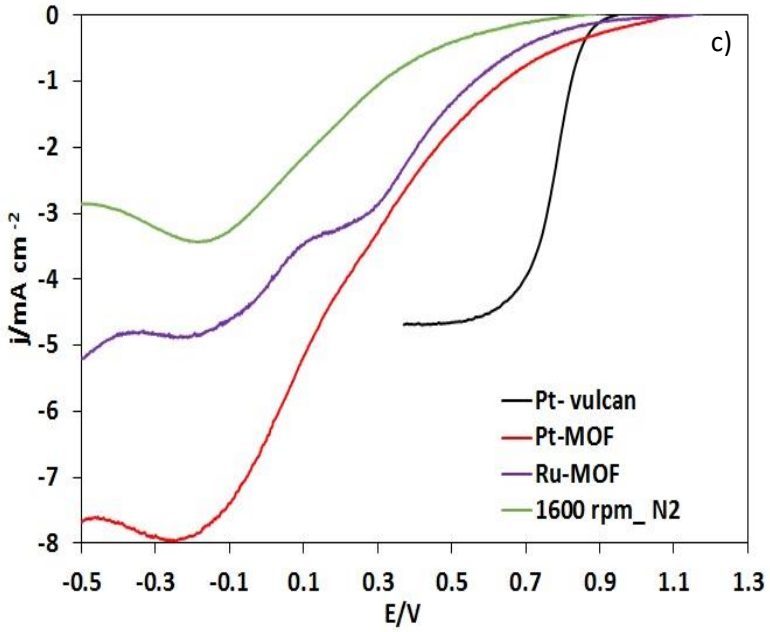


## 4. Conclusion

In this study, it was possible to prepared materials electrocatalytic nanometric of Pt-MOF and Ru-MOF for the ORR in one alone process of synthesys and with a catalytic load of very much minor Pt, compared with Pt traditional electrocatalysts supported on vulcan. This indicates that the materials based on Pt-MOF or Ru-MOF can be an option for use in fuel cell type PEM.

Nevertheless, is necessary to optimize the synthesis and diminish the overpotentials obtained with the use of the MOF.

## Acknowledgements

The authors wish to thank the Mexican CONACyT for financial support of this work and the SMH and XVII International Congress of the Mexican Hydrogen Society.

## References

[1] Janiak Ch., Vieth J. K., *New J. Chem*, 2010:34: 2366-2388.
[2] Zhou Hong-Cai, Long J. R., Yaghi O. M., *Chem. Rev*., 2012:112: 673-674.

[3] Joe Zhoua Hong-Cai, Kitagawa Susumu, *Chem. Soc. Rev*.,2014: 43:5415-5418.

[4] Falcaro P, Ricco R, Doherty C. M., Liang K, Hillb A. J., Stylesb M. J. *Chem. Soc. Rev*., 2014:43:5513-5560..

[5] Gao W-Y, Chrzanwski M., Ma S., *Chem. Soc. Rev.*, 2014:43:5841-5866.

[6] Zhu Q-L., Xu Q., *Chem. Soc. Rev.,* 2014:43, 5468-5512.
[7] Wanga H., Yin F., Li G., Chen B., Wang Z., *Int. J. Hydrogen Energy*, 2014:39:16179-16186.
[8] Luz I., Llabrés i Xamena F.X., Corma A., *J. Catal.*,2010: 276, 134-140.
[9] Aijaz A., Xu Q., *J. Phys. Chem. Lett 2014:* 5: 1400-1411.
[10] Corma A., García H., Llabre´s X. Francesc X. , *Chem. Rev*.,2010:110, 4606-4655.
[11] Yang L., Lorouche N., Chenitz R., Zhang G., Lefèvre M., *Electrochim Acta*,2015:159, 184-197.
[12] Kramm U. I., Lefèvre M., Larouche N., Schmeisser D., Dodelet J.-P., *J. Am. Chem. Soc.*,2014: 136, 978-985.
[13] Morozan A., Sougrati Tahar M., Goellner V., Jones D., Stievano L., Jaouen F., , *Electrochim. Acta*, 2014:119, 192-205.
[14] Ge L., Yang Y., Wang L, Zhou W., Dre M. R. , Chen Z., Zou J, Zhu Z., *Carbón*, 2015:82, 417-424..
[15] Yin F., Li G., Wang H., *Catal. Commun.* 2014:54, 17-21.
[16] Lee J., Jeong B., Ocon J. D., ,*Curr. Appl. Phys.*, 2013:13, 309-321.
[17] Jahan M., Bao Q., Loh P. K., *J. Am. Chem. Soc*., 2012:134, 6707-6713.
[18] Afsahi F, Vinh- Thang H, Mikhailenko S., Kaliaguine S, *J. Power Sources*, 2013:239: 415-423..
[19] Bloch E. D., Britt D., Lee Ch. ,Doonan Ch. J., Uribe-Romo F. J., Furukawa H., Long J. R., Yaghi O. M., *J. Am. Chem. Soc*., 2010:132: 14382-14384.
[20] Ren Y., Chia Hui G., Gao Z., , *Nano Today*, 2013:8: 577-597.
[21] Ma Tian Y., Dai S., Jaroniec M., Qiao Shi Z., *J. Am. Chem. Soc*., 2014:136: 13925-13931.

[22] Zhao S, Yin H., Du L., He L., Zhao K., Chang L., Yin G., Zhao H., Liu S., Tang Z., *ACS Nano,* 2014: 8, 12660-12668.
[23] Xia W., Mahmood A., Zou R., Xu Q., *Energy Environ. Sci.*,2015:8:1837-1866.

# 9.2 Carbon nanotubes supported nano silver electrocatalyst for oxygen reduction reaction in alkaline media

Alfredo Hernández Flores, Carolina Silva Carrillo, Ana Martha Arcila Torres, Sergio Pérez Sicairos, Rosa María Félix Navarro , Irma Lorena Albarrán Sánchez, José Roberto Flores Hernández, and Tatiana Romero Castañón

[1]Centro de Graduados e Investigación en Química, Instituto Tecnológico de Tijuana, Blvd. Alberto Limon Padilla s/n Col. Otay Tecnológico, Tijuana, B. C. 22510, México.

[2]Instituto Nacional de Electricidad y Energías Limpias, Ave. Reforma 113 Col. Palmira. Cuernavaca, Morelos, 62490, México.

* Corresponding author: +52 (777)362-3811, tromero@iie.org.mx

---

## ABSTRACT

This work exhibits the use of nanostructured materials potentially suitable as catalysts for cathodes in alkaline fuel cells. Since platinum´s high cost, silver is considered an affordable alternative for reducing the cost of fuel cell technology. Silver nanoparticles from micro emulsion reaction were deposited on multiwall type carbon nanotubes (Ag/CNT). The electrochemical characterization of Ag/CNT was performed in alkaline solution in a three-electrode-cell. The catalytic activity of Ag/CNT for oxygen reduction reaction (ORR) in 1M KOH was studied by cyclic voltammetry and rotating disk electrode (EDR) to compare kinetics parameters with Pt/CNT. In order to test the catalyst in half cell, the half-membrane-electrode-assembly was prepared using the Ag/CNT deposited on carbon paper diffuser in contact with Neosepta®, an alkaline membrane, to characterize it as cathodic catalytic layer in an alkaline membrane fuel cell. Physicochemical characterization was carried out by SEM, TEM and TGA on Ag/CNT samples.

***Keywords:*** nano silver, carbon nanotubes, alkaline, fuel cell

## 1. Introduction.

The fuel cells are electrochemical devices that generate electricity converting the energy from a fuel, such as hydrogen. The alkaline fuel cells (AFC) offer the benefit of electricity generation with low-cost catalysts, as the alkaline environment allows the use of non-platinum group (NPG) metals as catalyst. Besides, development of a new anion exchange membrane as fuel cell electrolyte has improved the performance and efficiency of such Anion Exchange Membrane Fuel Cells (AEMFC) [1].

For this work, nano particles Ag has been synthesized by microemulsion method and supported on carbon nanotubes (CNT) to be used as cathode catalysts for the oxygen reduction reaction (ORR) in alkaline media. The use of CNT as catalyst support offered a high surface area, reducing metallic particles loading for high catalytic activity [2]. In this work, the electrochemical performance of CNT supported silver nanoparticles (Ag/CNT) was carried out in alkaline media to determine its performance as cathode catalyst by kinetics parameters determination in the ORR, using alkaline solution and Neosepta®, a commercial Anion Exchange Membrane (AEM), as electrolytes.

## 2. Experimental part

The CNT were synthesized by the pyrolysis spray method, this CNT were treated to remove the iron from its surface and also to functionalize the walls of CNT. Synthesis of metallic nanoparticles of Ag / CNT was carried by inverse micro-emulsion, resulting in a 20% metal loading. The catalytic ink was prepared by a mixture of 2.5 mg of Ag/CNT, 1.5 ml of deionized water, 960 µL of ethyl alcohol and 40 µL de Nafion solution (5 wt%, Aldrich). The mixture was sonicated for 2 hours to form a homogenized catalytic ink solution. The catalytic ink was deposited on the surface of a glassy carbon disk (4 drops with 15 µL per drop) previously polished to a mirror finish. The glassy carbon disk of 3 mm in diameter and 2 mm thick was in contact with the steel bar with silver epoxy.

The catalyst ink was electrochemically characterized by EDR using cyclic voltammetry (CV) under inert atmosphere and linear sweep voltammetry (ORR) in oxygen saturated, 1 M KOH solution. Before the ORR testing, the solution was oxygen saturated at room temperature for 30 min. The rotating disk containing the sample acted as working electrode, and a Hg/HgO (0.098V vs EEH) was used as reference electrode; a Pt mesh worked as counter electrode. The tests were performed using a workstation Solartron Schlumberger SI 1253, in a three-electrode glass cell system. The ORR tests were performed varying the rotation rates: 50, 100, 200, 300, 400, 500, 600, 700, 800, 900 and 1000 rpm.

For the half-cell test, the fabrication of the half membrane-electrode assembly was carried out using the same catalytic ink formulation described above, which was spray coated on the surface of a carbon paper acting as gas diffusion layer to form the electrode. The half

membrane electrode assembly (MEA) was maintain together in a screw tightened Teflon made cell; the catalyst coated surface of the electrode was in contact with the Neosepta membrane, a gold current collector was in contact with the back of the electrode. Both sides of the MEA had an exposed active are to the electrolyte 1M KOH solution. Prior to the test, the membrane followed a pre activation treatment: a 1 M KOH solution with 0.5 M $(NH_4)_2SO_4$ was prepared and heated to 60°C in which the membrane was immersed for 2 h. The membrane was left immersed in this solution for 24 hours before the tests.

The half cell test was carried out using a Pt mesh as counter electrode, Hg/HgO (0.098 v vs EEH) with luggin capillary as reference electrode, and the half MEA (Ag/CNT/Neosepta) as working electrode, using a workstation ELECTROCHEMICAL INTERFACE SI 1287 and a PC. The ORR test was performed varying the voltage from 0.6 until -1 V vs EEH with a scan rate of 20 mV/seg in oxygen saturated 1 M KOH at room temperature, with magnetic stirring, as is showed in the diagram of figure 1.

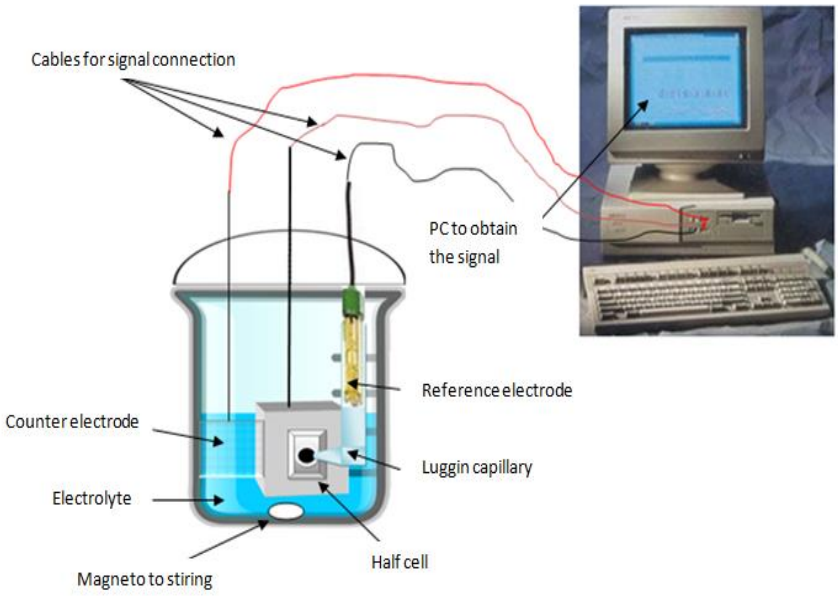


Figure 1. Scheme of half cell system with Pc.

## 3. Result and discussion

### 3.1. Rotating disk electrode

#### 3.1.1 Cyclic voltammetry

The graph in figure 2 shows the cyclic voltammograms obtained from the Ag/CNT catalysts y platinum supported on CNT (Pt/CNT). The voltammograms of Ag/CNT catalyst showed two anodic characteristics peaks similar to the reported literature [3, 4, 5], these peaks are showed at potentials of 0.28 V and the second at 0.37 V vs EEH, the first peak is associated with adsorption of $OH^-$ on silver particles $Ag(OH^-)_2$ (equation 1) this is a step to the second peak associated with formation of $Ag_2O$ (equation 2), while the cathode peak appears at 0.1 V that is associated at reduction of rusty species $Ag_2O$ to come back to its metallic form Ag (equation 3). Anodic peaks represented by the equations [5]:

$$Ag + 2OH^- \rightarrow Ag(OH)_2^- + e^- \qquad \text{equation (1)}$$

$$Ag(OH)_2^- + e^- \rightarrow Ag_2O_{(l)} + H_2O \qquad \text{equation (2)}$$

Anodic peak equation [5]:

$$Ag_2O + H_2O + 2e^- \rightarrow 2Ag + 2OH^- \qquad \text{ecuación (3)}$$

In Pt/CNT catalyst the adsorption and desorption of hydrogen were observed in potentials of -0.95 and -0.8 V vs EEH, respectively, the formation of platinum oxides are observed from the potential of -0.2 V in the anodic zone, and reverts to its metallic form in the cathodic zone and also can be observed the hydroxyls adsorption in potential from -0.12 to -0.45 V vs EEH.

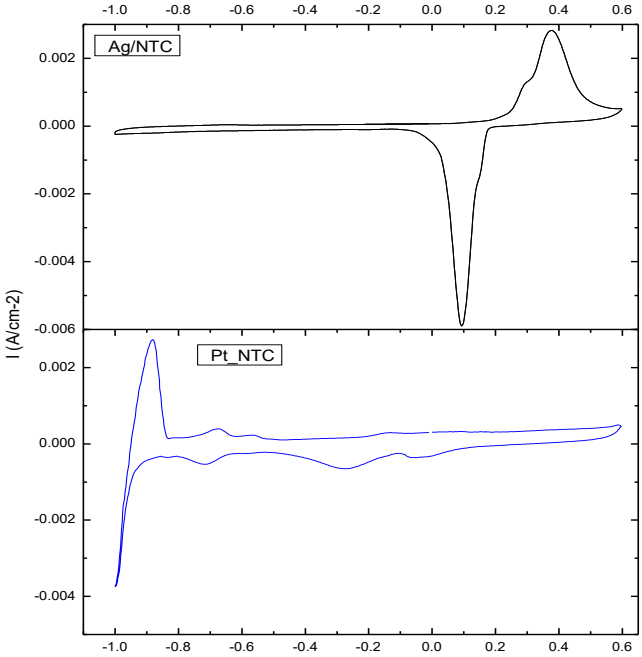


Figure 2. Cyclic voltammograms of Ag/NTC y Pt/NTC obtained in solution 1 M KOH whit scan rate of 20 mV/s in nitrogen saturated.

### 3.1.2 Linear sweep voltammetry

In the linear sweep voltammograms to Pt/CNT (figure 3A) and Ag/CNT (figure 3B) catalysts three different zones are observed due to the type of control from electrochemical process: zone i) it is the kinetic control zone appears to Pt/CNT from 0 to -0.04 V and to Ag/CNT from 0 to -0.09 V vs EEH, approximately, in this zone the rotation rate does not influence the current density; zone ii) appears from -0.04 to -0.13 V and from -0.09 to -0.32 V vs EEH to Pt/CNT and Ag/CNT, respectively, this is the region of mixed control, due to the potential difference that increases the concentration of the species in the surface will be decreased, also in this zone a gradual increase is observed in the current density with the increase of the rotation rate; zone iii) it is presents from -0.13 to -1 V and from -0.32 to -1 V vs EEH to Pt/CNT y Ag/CNT, respectively, it is the zone controlled by the mass transport, where the transfer rate of charge becomes faster in comparing with the contribution of the reagent as the negative potential increases, also is attributed to increase due to rotation of electrode. There is also, an observable increase in the current density proportional to increase of electrode rotation rate due to high mobility of the species in the electrolyte.

The figure 3A corresponding to Pt/CNT catalyst shows a little change in the current density from 50 to 100 rpm and from 100 to 200 rpm, but for rates from 200 to 800 rpm there isn't much observable difference, otherwise in the rates from 800 to 900 and 1000 rpm there is a great increase in the current density with the increase in the electrode rotation rate. In the case of Ag/CNT catalyst (figure 3B) an increase in the current density directly proportional to the increase of the electrode rotation rate, this indicates that to higher electrode rotation rate will obtain an increase in the current density due to the high mobility of species inside the electrolyte. In the figure 3A we can observe that the sample of Pt/CNT catalyst shows a higher density in comparison to Ag/CNT catalyst, this is attributed to the high catalytic activity of Pt.

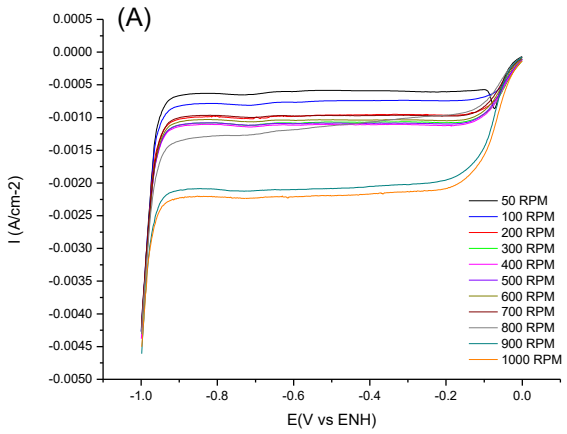


Figura3. Linear sweep voltammograms to A) Pt/NTC y B) Ag/NTC catalysts obtained to several rotation rates in solution 1 M KOH scan rate of 20 mV/s in oxygen saturated.

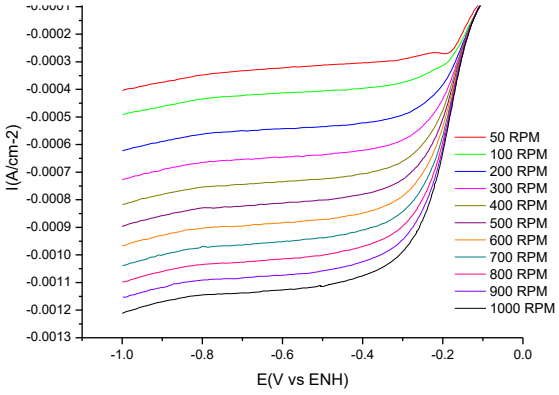


Kinetic parameters were obtained by results of RDE making the correction to the total current by the input of mass transfer, those were obtained at potentials of -0.9 V vs ENH in solution 1 M KOH.

Table 1: Values of experimental slopes, numbers of electrons transferred and constant of rate to RRO obtained by the graphics of Koutecky-Levich to potential of -0.9 V vs ENH.

| Material | *1/B* experimental | n experimental | k (cm s-1) |
|---|---|---|---|
| **Ag/CNT** | -1.29042 | 4.948308 | 0.020059 |
| **Pt/CNT** | -0.57862 | 5.528422 | 0.015226 |

### 3.2. ORR in half-cell

The polarization curve shows the signal obtained by the current-potential of this material, as result of applying a scanning voltage on the electrode in a half cell arrangement, this signal shows a current density with a maxim value of 0.032 $mAcm^{-2}$ approximately, as result of oxygen reduction reaction, figure 4.

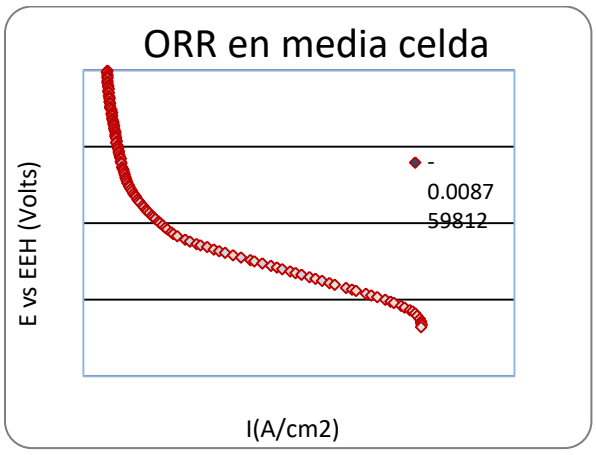


Figure4. Linear sweep voltammogram of Ag/NTC catalyst obtained in solution 1 M KOH. with a scan rate of 20 mV/s in oxygen saturated.

### 4. Conclusions

The analysis of Ag supported on CNT as catalyst of oxygen reduction in alkaline media shows a high catalytic activity through the electrochemical characterization and kinetic parameter analysis. The performance characterization of Ag/CNT in contact with an alkaline membrane in half cell was made, which was the first step in the direction of this

newfangled technology that requires yet I+D to achieve better performance. The alkaline membrane fuel cell allows the reduction of cost in the fabrication and operation of the fuel cell; these first tries allow us to identify the needs of the system at a laboratory level.

## 5. References

[1] Alkaline direct alcohol fuel cells. Journal of Power Sources 195 3431-3450 pp. (2010). E. Antolini, E.R. Gonzalez.

[2] Highly dispersed Ag nanoparticles on functional MWNT surfaces for methanoloxidation in alkaline solution. Carbon 43 (2005) 1259-1264. D. J. Gou, H. L. Li

[3] Synthesis and Evaluation of Carbon Nanotubes Supported Silver Catalyst for Alkaline Fuel Cell. ELECTOANALYSIS, 26, 1-9 pág. november 2014. Fazil A, Raghuram C.

[4] Carbon-Supported Silver as Cathode Electrocatalyst for Alkaline Polymer Electrolyte Membrane Fuel Cells. Electrocatalysis 3, 13-21, 2012. S. Maheswari, P. Sridhar, S. Pitchumani,

[5] Electrochemical Behavior and Reduction Mechanism of High Valence Silver Oxide in Alkaline Solution. Electrochemical and Solid-State Lett. 10(3), F5- F8 (2007) Y. Cheng, M. Yan, Z. Jiang.

# 9.3 Analysis of behavior of Carbon Surfaces Modified with S or N for Oxygen Reduction Reaction

E. Montiel-Macias, Y. Verde-Gomez, A. M. Valenzuela-Muñiz, P. B. Balbuena

[1]TECNM/Instituto Tecnológico de Cancún, Av. Kabah Km 3, Cancún, Q. Roo, 77500, Mexico

[2]Department of Chemical Engineering, Texas A&M University, TAMU 3122, College Station, TX, 77843, USA

+ CONACYT Fellow

Corresponding author: +52 998 880 7432 elizabethmontielmacias@hotmail.com

## ABSTRACT

The challenge to find alternative power sources which are environmental friendly has been a topic of discussion in the last decades. Proton exchange membrane fuel cells (PEMFC) represent electrochemical energy devices that are currently leading the technology for light duty and materials handling vehicles, and also for portable applications. Platinum is the more common material used as catalyst in a PEMFC; however due to its high cost and scarcity, new alternatives had been researched. On this way, the design and synthesis of new materials to reduce or replace platinum materials in the cathode side of low temperature fuel cells has become imperative. Carbon nanomaterials have shown good performance when are used as Pt catalyst supports. Also, it has been investigated that an alternative to enhance the activity of carbon nanomaterials is their modification with heteroatoms such as N or S. On the other hand, first-principles computational methods are useful tools to explain the influence of heteroatoms in doped carbon materials on the adsorption/reaction phenomena associated with the oxygen reduction reaction (ORR). This work presents the density functional theory calculations (DFT) to evaluate the behavior of adsorption/reaction phenomena during the electro catalysis processes on graphene structures modified with dopants. Surfaces models of perfect graphene and graphene with structural defects doped with adsorbed N or S atoms are studied for modelling the surface of carbon materials previously developed experimentally. The electrochemical performance of carbon materials under adsorption of different functional groups that can describe the behavior of ORR are analyzed. The theoretical and experimental results will be discussed.

***Keywords:*** DFT; doped carbon catalysts; ORR

# 9.4 Green microwave assisted synthesis of CdS/ZnS photocatalyst, decorated with AuPd nanoparticles and supported on $CuZnFe_2O$ for $H_2$ production.

M. Ruiz, V. Sánchez

[1]Universidad Autónoma de Chihuahua, Circuito Universitario s/n, Campus II, Chihuahua, Chihuahua, México, 31170.

Tel. +52 (614) 156 0815; e-mail: haitaimega1986@gmail.com

## ABSTRACT

The sustainable approach of water splitting process via photocatalysis uses a photocatalyst and visible light spectrum (λ= 420-670 nm) to split the $H_2O$ molecule into $O_2$ and $H_2$, the later used as energy carrier. Taking advantage of the semiconductor´s properties is possible to obtain a stable photocatalyst with low band-gap for the $H_2$ production. In this work, we propose a microwave assisted synthesis of CdS/ZnS photocatalyst decorated with AuPd nanoparticles following a green approach using garlic skin extract to avoid the use of toxic and dangerous options as $NaBH_4$ or $LiAlH_4$ (Allium sativum L.) as reducing agent, and supporting it on Copper/Zinc ferrite ($CuZnFe_2O$) to take benefit from the magnetic properties and recover the material after each use from the aqueous solution. To produce the expected material, we studied the garlic extract antioxidant capacity via ORAC method, and determined the total phenol content via Folin-Ciocalteu method. AuPd nanoparticles were generated based on a microwave assisted method. In this work it´s shown that the extract was able to reduce $Au^{+3}$ and $Pd^{+2}$ to $Au^0$ and $Pd^0$ thus, generating nanoparticles. Obtained Raman spectra (785nm), proved that in fact the chalcogenide has been produced by observing the characteristic peak around 290 $cm^{-1}$. Based on this results we can confirm that the assisted method and extract used can achieve the proposed synthesis. The current stage of the project is the characterization of the physical as well as the chemical properties of the obtained material by XRD, XRF, TEM, SEM, EDS, BET, and UV-vis

***Keywords:*** Photocatalyst, microwave assisted synthesis, nanoparticles, garlic extract, water splitting.

# 9.5 Green synthesis of $Cu_2O/TiO_2$ for photocatalytic hydrogen production through photoreforming

M. Segovia, V. Sánchez

[1]Universidad Autónoma de Chihuahua, Circuito Universitario s/n, Campus II, Chihuahua, Chihuahua, México, 31170.

* Corresponding author. Phone: 6141153632. e-mail: miguelomar_14@hotmail.com

## ABSTRACT

Photocatalysis is a feasible method for hydrogen production exploiting solar energy directly. Thus far, titanium dioxide ($TiO_2$) has been widely used as a model photocatalyst because it is stable, non-corrosive, environmentally friendly, abundant and cost-effective. However, the main disadvantage relies on its strong absorption in the UV region, which incidentally it is very weak within the solar spectrum. Therefore, to improve its absorption in the visible region of the solar spectrum, $TiO_2$ is usually doped with a co-catalyst. In this context, copper oxide I ($Cu_2O$) has proved to be a suitable dopant. In this work, we synthesized nanoparticles of $Cu_2O$, under microwave radiation, and supported them onto $TiO_2$. To adhere to the green chemistry principles, we used aqueous extract of dry onion skin waste as reducing and stabilizing agent. Based on a Benedict test we propose that reducing sugars from the extract are the active reducing and stabilizing agents, therefore we also carried out a control experiment, by replacing our extract with a 1 % wt glucose solution. UV-Vis spectra allowed us to predict that the size $Cu_2O$ nanoparticles is below of 100 nm, and molecular fluorescence revealed activity of the colloidal suspensions. Infrared spectra also confirmed the occurrence of $Cu_2O$, by the presence of a peak *ca*. 620 $cm^{-1}$, usually assigned to Cu(I)-O vibrations.Through X-ray fluorescence results, we estimated a 1.5 %wt $Cu_2O/TiO_2$. X-ray diffraction and Scanning electron microscopy also verified the occurrence of $Cu_2O$ nanoparticles. Finally, performance assessment to produce hydrogen from glycerol and biomass in a micro photochemical reactor using visible light revealed $Cu_2O$ improves the photocatalytic activity of pure $TiO_2$. In conclusion, this is potentially a rapid and sustainable approach to achieve greener routes of synthesis of effective photocatalysts.

***Keywords:*** Photocatalyst, microwave assisted synthesis, nanoparticles, onion extract, visible light.

# 9.6 Microwave-assisted green synthesis of Ag-Pd and Fe-Pd nanoparticles supported on SiC and $Al_2O_3$ for zinc sulfate decomposition

O. Soto, V. Sánchez, D. Chávez

Universidad Autónoma de Chihuahua, Circuito Universitario s/n, Campus II, Chihuahua, Chihuahua, México, 31170.

Tel. +52 (614) 236 6000; e-mail: a257569@uach.mx

## ABSTRACT

This work focuses on the synthesis of Ag-Pd and Fe-Pd nanoparticles supported on SiC and $Al_2O_3$ as a catalytic material for the zinc sulfate decomposition in the sulfur-ammonium thermochemical cycle. This cycle involves a high temperature reaction for the oxygen production step: a metal sulfate decomposition. To reduce the high energy requirements of this particular step, catalysts are introduced to lower the reaction temperature. Pd catalysts in nanometric scale are one of the most used materials for this purpose. However, the main disadvantages of palladium are its scarcity and high cost. To counteract the previous, the use of Pd-based alloys is being widely investigated. Additionally, it has been reported that the use of Ag and Fe to form Pd-based alloys significantly enhances the catalytic activity.

The synthesis consists in a microwave-assisted method using nutshell extract as chemical reductant and stabilizing agent. Glycerol is used as solvent, its high boiling point (290 °C) will allow to carry the synthesis at higher temperature with respect to aqueous medium (100 °C). The synthesized materials are thermally treated to remove all organic and solvent residues. Finally, the catalytic material is characterized by the BET technique, scanning electron microscopy (SEM), X-ray fluorescence (XRF), transmission electron microscopy (TEM), x-ray diffraction (XRD) and thermogravimetric analysis (TGA).

Results obtained by XRF and Electron Dispersive Spectroscopy (EDS) analysis confirm the presence of the desired metals on the material. Moreover, XRD technique shows a successful Ag-Pd and Fe-Pd alloy.

***Keywords:*** *Glycerol, microwave assisted synthesis, nanoparticles, nutshell extract, sulfur-ammonium cycle.*

## 1. Introduction

Hydrogen is a promising alternative for producing sustainable energy. It has the potential to replace the use of fossil fuels, which are responsible of climate change due to high emissions of greenhouse gases such as $CO_2$ [1].

Basically there are three ways to produce hydrogen from solar energy: electrochemical, photochemical and thermochemically. Thermochemical cycles, which main objective is the dissociation of the water molecule through a series of chemical reactions at different temperatures, have the potential to produce hydrogen with high efficiency in a large scale process [2].

Since the early 1970s there have been more than 400 thermochemical cycles for hydrogen production. Among them, a class of cycles known as thermochemical cycles sulfur family has received special attention [3].

The sulfur-ammonia cycle is a promising technology for the large-scale production of chemical energy from solar energy. It consists of two stages: first, hydrogen production followed of oxygen production.

$$SO_{3\,(g)} + 2NH_{3\,(g)} + H_2O_{\,(l)} \xrightarrow{25°C} (NH_4)_2SO_{3\,(ac)} \qquad (1)$$

$$(NH_4)_2SO_{3\,(ac)} + H_2O_{\,(l)} \xrightarrow{25°C} (NH_4)_2SO_{4\,(ac)} + H_{2\,(g)} \qquad (2)$$

$$(NH_4)_2SO_{4\,(ac)} \xrightarrow{500°C} 2NH_{3\,(g)} + H_2SO_{4(g)} \qquad (3)$$

$$H_2SO_{4(g)} \xrightarrow{900°C} SO_{2\,(g)} + H_2O_{\,(g)} + \frac{1}{2}O_2 \qquad (4)$$

The first step for hydrogen production consists in reactions represented in equations 1 and 2. In the equation 1, the ammonia and sulfur dioxide are chemically absorbed in water to produce ammonium sulfite. In equation 2, hydrogen is produced by a photocatalytic process in which the $SO_3^{2-}$ ions are oxidized to $SO_4^{2-}$. Oxygen production, where solar thermal energy is used for oxygen production, consists in reactions 3 and 4

For the sulfuric acid in (4), very expensive materials to withstand the corrosive nature of this compound at high temperatures are required. As an alternative, the introduction of a metal oxide in the reaction (3) has been proposed. Metal oxides are capable of reacting with sulfate ammonia to produce the corresponding metal sulfate by a catalyzed thermal reaction with energy obtained from solar radiation as shown in (3´). Successively, the formed sulfate is decomposed by the same thermal energy from solar radiation, producing sulfur dioxide and oxygen as described in (4´) [4, 5]

$$y(NH_4)_2SO_{4\,(ac)} + M_xO_y \rightarrow M_x(SO_4)_y + 2y\,NH_3 + y\,H_2O \quad (3')$$

$$M_x(SO_4)_y \rightarrow M_xO_y + ySO_3 \rightarrow M_xO_y + y\,SO_2 + \frac{Y}{2}O_2 \quad (4')$$

The decomposition of metal sulfate formed requires temperatures above 900 ° C. To reduce the high energy requirements of this particular step, catalysts are introduced to lower the reaction temperature. For this purpose, a variety of catalysts has been tasted such Pt [5-7] Pd [8], Cu [9-11] and Fe [12] supported primarily on alumina, silica and silicon carbide due to their known thermal stability.

Microwave assisted synthesis is characterized by a rapid and uniform heating of the reaction medium propitiating homogeneous nucleation with shorter reaction times, small sizes of nanoparticles (nm), monodispersity and high purity with respect to the traditional methods of synthesis [13].

Stabilizing agents, reducers and the reaction medium are three key factors for an efficient metal nanoparticles synthesis. Most commonly used stabilizing agents for the synthesis of metal nanoparticles, such as thiols, triphenylphosphine and/or polyvinylpyrrolidone are toxic, difficult to obtain and minimizes the utility of nanoparticles. Moreover, most of the reducing agents reported include sodium borohydride (NaBH4), which is potentially hazardous to the environment [14]

The use of plant extracts such as *Camellia sinensis* [15], *Azadirachta indica* [16], *Macrotyloma uniflorum* [17] as reducing agents and reactive stabilizers for the green synthesis of nanoparticles has been widely investigated.

It has also been found that the biosynthesis of silver nanoparticles by an assisted microwave method using plant extracts such as *biophytum sensitivum* [13] as reducing agents and stabilizers is a viable method for an easy and fast synthesis.

This work focuses in the synthesis and characterization of Ag-Pd and Fe-Pd nanoparticles supported on SiC and $Al_2O_3$ by a microwave-assisted method using nutshell extract as chemical reductant and stabilizing agent, glycerol as solvent and evaluate their performance for zinc sulfate decomposition.

## 2. Materials and Methods

The required amount of gamma alumina nano powder purchased from Sigma Aldrich was treated at 500 °C in a tubular furnace to remove impurities. A functionalization pretreatment was made for SiC purchased form Sigma Aldrich; this consisted in mixing and heating sulfuric acid and SiC 50% w/v for 30 minutes at 110 °C in a CEM-Discover microwave, using 50 mL of acid per gram of solid. After functionalization time, the mixture was separated by filtration and the recuperated solid was rinsed with distilled water until pH 7 before drying at 80 °C.

### 2.1. Extract and precursor preparation.

1.5 g of milled nutshell (40 mesh) and 30 mL of distillated water in a round flask and heated by microwave for 10 minutes at 80 °C while stirring. The resulting product was filtrated and stored for later use.

$PdCl_2$, $AgNO_3$ (Sigma Aldrich 99.98%) and Fe $(NO_3)_3$ (Golden Bell 98.2%) salts were used as precursors. For this, the required amount of salt to prepare 1mM solution was put in a volumetric flask and graduated at 100 mL with glycerol.

### 2.2. *in-situ* nanoparticles synthesis in MARS 6 microwave.

In a microwave vial, 5 mL of $PdCl_2$ and 5 mL of $AgNO_3$ or Fe $(NO_3)_3$ according to the desired alloy were added. After, 15 milliliters of extract, 5 mL of glycerol and the required amount of support ($Al_2O_3$ or SiC) to obtain a metal load of 7% w/w were added. Additionally, a blank was synthesized replacing the 15 mL of nutshell extract with the same volume of water.

This mixture was heated by microwave at 180 °C during 10 minutes. Finally, the solid was dried at 110°C by 48h and calcinated at 500 °C during 10h

### 2.3. Characterization methods.

BET analysis was used to estimate the superficial area of the supports employed before and after their corresponding treatment. Moreover, bimetallic alloy identification, as well as crystallite size and alloying degree estimation, were carried out by X-ray Diffraction (XRD) analysis. The metallic composition of the materials was assessed by X-ray Fluorescence (XRD).The dispersion of the nanoparticles synthesized was observed by Electron Scattering Microscopy (SEM).

## 3. Results and Discussion

### 3.1. Support characterization.

Characteristic signals for alumina and silicon carbide supports were identified by a XRD analysis. The corresponding peaks of *gamma* alumina phase were indexed in accord with JCPDS PDF 10-0425 crystallographic card [18, 19]. Moreover, signals in 35.6, 41.3, 60.01, 71.8 and 34.1, 34.81, 38.13 in 2Θ were indexed in accord to

JCPDS 029-1129 crystallographic card corresponding to β-SiC and α-SiC phases respectively [20-22]. No changes were observed in XRD pattern for both supports.

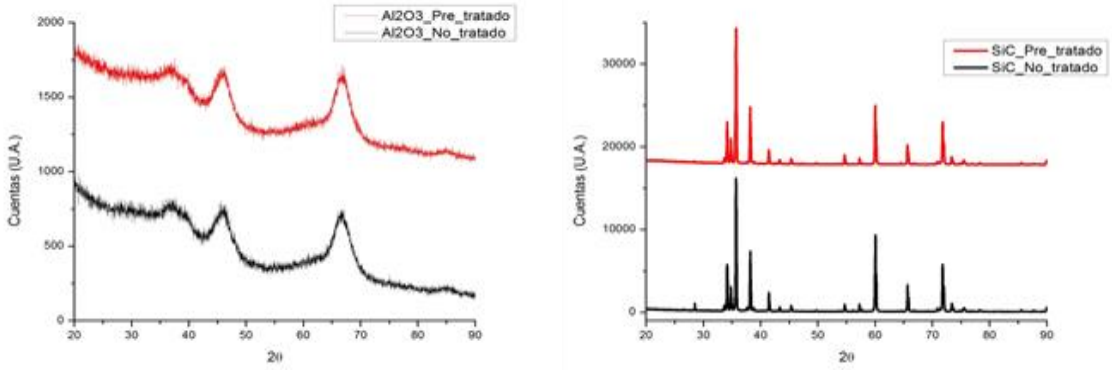


**Figure 3-1** XRD pattern: a) $Al_2O_2$ and b) SiC.

The BET analysis performed on alumina and silicon carbide before and after pretreatment is represented in Figure 3-2. Decrease on superficial area for both materials can be observed: alumina decrease from 475.832 m²/g to 220.946 m²/g and silicon carbide from 27.740 m²/g to 5.285 m²/g after pretreatment.

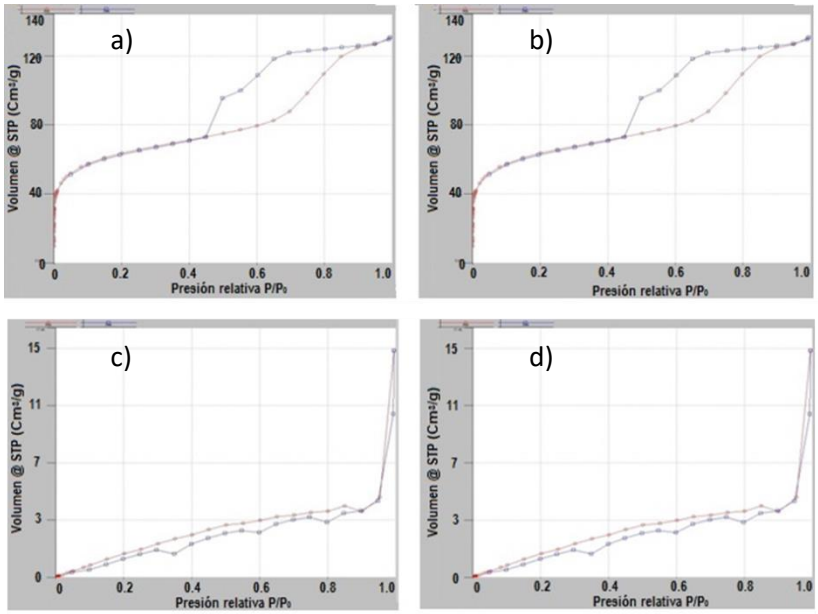


**Figure 3-2** BET adsorption isotherms: a) Al2O3 not pretreated, b) Al2O3 pretreated, c) SiC not pretreated and d) SiC pretreated.

On the other hand, the isotherms presented in Figure 1-2 for alumina, could be classified to a type IV isotherm [18, 19], which is characteristic of mesoporous materials. Moreover, SiC presented a type II-IV isotherm that is characteristic of macroporous and mesoporous materials [20-22].

### 3.2. $AgPd/Al_2O_3$ and $FePd/Al_2O_3$ catalysts characterization.

XRD analyses were made with the objective to identifying the crystallographic phases present in the synthesized materials.

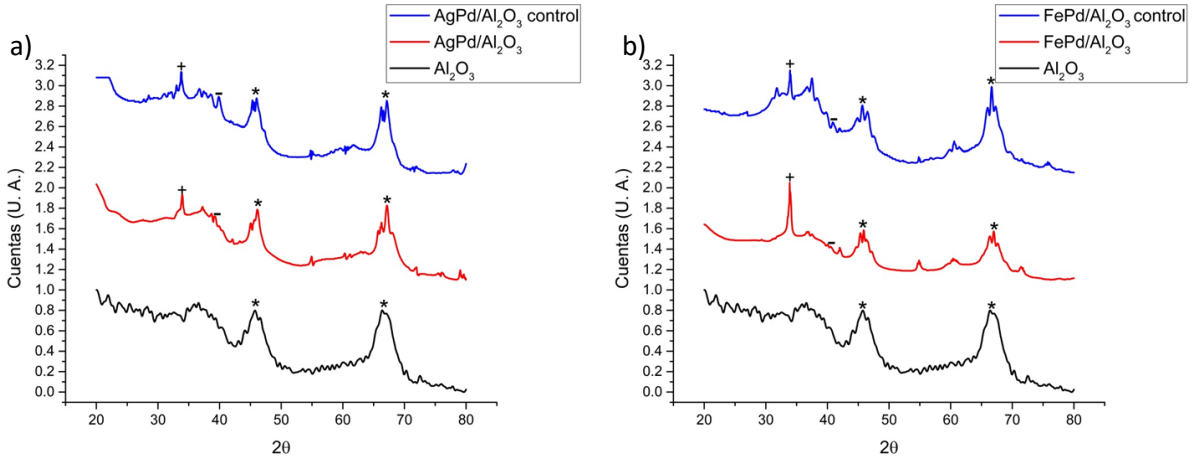


**Figure 3-3.** XRD patterns of: a) $AgPd/Al_2O_3$ and $FePd/Al_2O_3$

The diffraction patterns (Figure 3-1), which were subjected to a refinement by Rietveld method, confirmed the presence of the desired alloys over the support by the identification of a signal at 2Θ value of 39.1° between the characteristic peaks of palladium (JCPDS 05-0681) and Silver (JCPDS 04-0783) corresponding to (111) plane of a FCC structure [23, 24]. Likewise, it was observed a unique signal at 2Θ value of 49.8° between the characteristic peaks of palladium (JCPDS 05-0681) and iron (JCPDS 87-0721), which is an indicative of the successful alloy of both. Crystallite size, calculated by the Scherrer equation, was of 25 nm to $AgPd/Al_2O_3$ and 15 nm for $AgPd/Al_2O_3$ control catalysts. Also, the alloying degree was estimated with the results of the peak fitting analysis of the XRD patterns, resulting in a 49% for AgPd alloy. Otherwise, the particle size estimated for $FePd/Al_2O_3$ and $FePd/Al_2O_3$ control was 24.99 and 17.47 nm respectively with an alloying degree of 24%.

It is also important to remark the presence of palladium oxide (PdO) in the materials. The apparition of this compound cloud be attributed to a fastest reduction of $Pd^{+++}$ than the $Ag^{+}$ and $Fe^{+++}$ ions. It may be due to their oxidoreduction potential, which is 0.9 V for palladium (higher than silver and iron), 0.80 V and -0.44 V for silver an iron respectively. This condition makes the palladium ions more susceptible to be reduced [25]. It has been reported a good catalytic activity by PdO for sulfur trioxide decomposition [8].

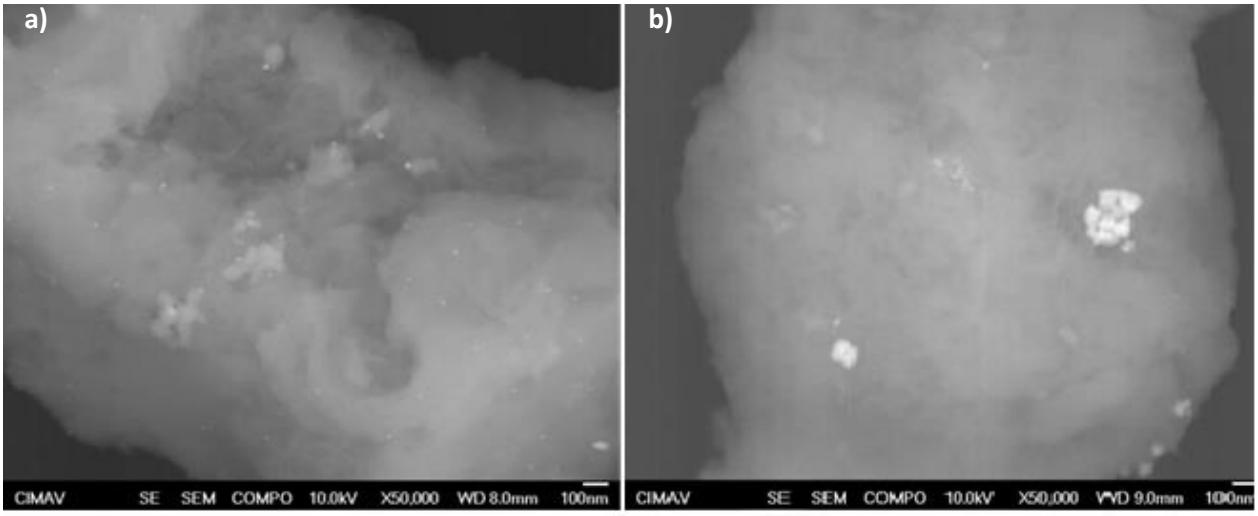


**Figure 3-4.** SEM microscopy for: a) $AgPd/Al_2O_3$ and b)$FePd/Al_2O_3$.

In figure 3-4 we can observe a good dispersion of metals on the support for $AgPd/Al_2O_3$ catalysts, while for $FePd/Al_2O_3$ the formation of some conglomerates is visible. In addition to the previous study, an X ray fluorescence semi quantitative analysis was made. The results of this study can be seen in Table 3-1, where the presence of the desired metals, with an excellent proportion, is confirmed. On the other hand, a considerable amount of other metals in $AgPd/Al_2O_3$ and $FePd/Al_2O_3$ is observed which have been contributed by the nutshell extract. Also, a big percentage of sulfur is present by the $Al_2O_3$.

**Table 3-1.** XRF elemental analysis results.

| Sample | Analysis | Al | K | Ca | S | Ti | Ag | Pd |
|---|---|---|---|---|---|---|---|---|
| **$AgPd/Al_2O_3$** | % weight XRF | 90.71 | 1.182 | 0.787 | 3.02 | 1.328 | 5.945 | 4.463 |
| **$AgPd/Al_2O_3$ control** | % weight XRF | 88.47 | --- | 0.13 | 3.38 | 0.66 | 5.662 | 1.09 |
| **$FePd/Al_2O_3$** | % weight XRF | 81.04 | 2.434 | 0.874 | 2.43 | 1.139 | 5.133 | 5.106 |
| **$FePd/Al_2O_3$ control** | % weight XRF | 92.46 | 0.010 | --- | 3.41 | 0.635 | 1.182 | 1.262 |

3.3. AgPd/SiC and FePd/SiC catalysts characterization.

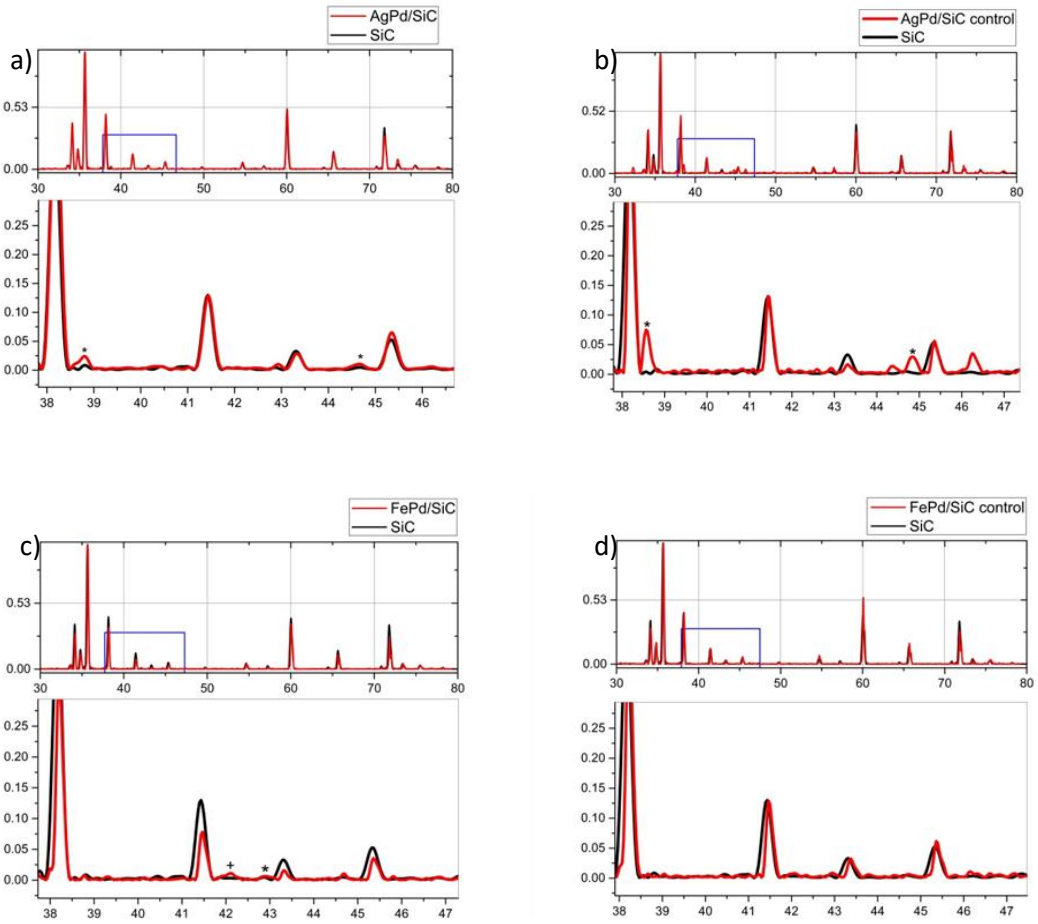


**Figure 3-5.** XRD pattern of: a) AgPd/SiC, b) AgPd/SiC control, c) FePd/SiC and d) FePd/SiC control catalysts.

The diffraction patterns (Figure 3-5), which were subjected to a refinement by Rietveld method, also confirmed the presence of the desired alloys over the support by the identification of a signal at 2Θ value of 38.7° between the characteristic peaks of palladium (JCPDS 05-0681) and Silver (JCPDS 04-0783) corresponding to (111) plane of a FCC structure. Likewise, it was observed a unique signal at 2Θ value of 42.1° between the characteristic peaks of palladium (JCPDS 05-0681) and iron (JCPDS 87-0721), which is an indicative of the successful alloy of both. No signals corresponding to a FePd alloy were identified for control sample. Crystallite size, calculated by using the Scherrer equation, was of 42 nm to AgPd/SiC and 54 nm for AgPd/SiC control catalysts. Also, the alloying degree was estimated by using the results of the peak fitting analysis of the XRD patterns, resulting in a 66% for AgPd alloy 64%. Otherwise, the particle size estimated for FePd/SiC was 39.68 nm with an alloying degree of 24%.

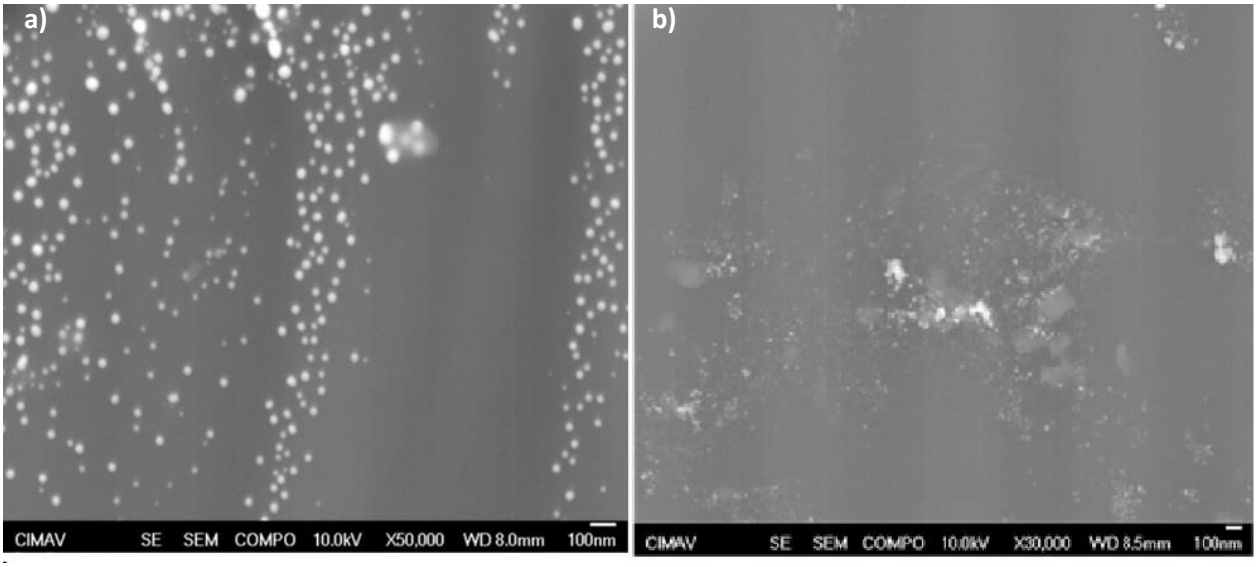


**Figure 3-6.** SEM analysis for: a) AgPd/SiC and b) FePd/SiC.

In figure 3-6 we can observe an excellent dispersion of metals over the support for AgPd/SiC catalysts while for the FePd/SiC the formation of some conglomerates is visible. In addition to the previous study, an Energy dispersive Spectroscopy (EDS) semicuantitative analysis was made. The results of this study can be seen in table 3-2. This study confirms the presence of the deired metals over the support. However, there are considerable differences between the amount of metals, which can be attributed to the way of the study was carried out. Also, a big percentage of potssium is present in AgPd/SiC and FePd/SiC samples wich has been contributed by the nutshell extract.

**Table 3-2.** EDS elemental analysis results.

| Sample | Analysis | Si | K | Ca | Ti | Ag | Pd |
|---|---|---|---|---|---|---|---|
| **AgPd/SiC** | % weight EDS | | | | | | |

| | | | | | | | |
|---|---|---|---|---|---|---|---|
| | | 20.86 | 4.24 | --- | --- | 5.36 | 9.89 |
| **AgPd/SiC control** | % weight EDS | 2.94 | --- | --- | --- | 4.93 | 37.38 |
| **FePd/SiC** | % weight EDS | 0.82 | 4.15 | --- | --- | 3.32 | 41.62 |
| **FePd/SiC control** | % weight EDS | 1.27 | --- | --- | --- | 3.67 | 70.63 |

## 4. Conclusion

Ag-Pd and Fe-Pd nanoparticles supported on $Al_2O_3$ and SiC were synthesized by a green and microwave-assisted method using an aqueous nutshell extract as chemical reductant and stabilizing agent and glycerol as solvent. The XRD analyzes confirm the presence of the Ag-Pd and Fe-Pd bimetallic alloys in the proposed materials. There was not a substantial difference in particle size between the materials synthesized with extract and the blanks. A good dispersion of metals is observed for AgPd/ $Al_2O_3$ and AgPd/SiC catalysts. Some metal conglomerates are present in FePd/$Al_2O_3$ and FePd/SiC materials. The presence and percentage of desired metals was confirmed by XRF and EDS analyzes. The content of other elements like Ca, K, Ti and S was attributed to nutshell extract and supports.

Proposed work for the future:

- Evaluate the performance of the synthesized materials as catalysts for zinc sulfate decomposition.

## References

1. Abanades, S., et al., *Screening of water-splitting thermochemical cycles potentially attractive for hydrogen production by concentrated solar energy.* Energy, 2006. **31**(14): p. 2805-2822.
2. Steinfeld, A., *Solar thermochemical production of hydrogen—a review.* Solar Energy, 2005. **78**(5): p. 603-615.
3. Mao, L., et al., *Thermal decomposition of (NH4)2SO4 in presence of Mn3O4.* International Journal of Hydrogen Energy, 2011. **36**(10): p. 5822-5827.
4. Tizzoni, A.C., et al., *Oxygen production by intermediate metal sulphates in sulphur based thermochemical water splitting cycles.* International Journal of Hydrogen Energy, 2015. **40**(11): p. 4065-4083.
5. Banerjee, A.M., et al., *A comprehensive study on Pt/Al 2 O 3 granular catalyst used for sulfuric acid decomposition step in sulfur–iodine thermochemical cycle: Changes in catalyst structure, morphology and metal-support interaction.* Applied Catalysis B: Environmental, 2015. **162**: p. 327-337.
6. Everson, R.C., et al., *Sulphur trioxide decomposition with supported platinum/palladium on rutile catalysts: 1. Reaction kinetics of catalyst pellets.* International Journal of Hydrogen Energy, 2015. **40**(1): p. 85-94.
7. Noh, S.-C., et al., *Sulfuric acid decomposition on the Pt/n-SiC catalyst for SI cycle to produce hydrogen.* International Journal of Hydrogen Energy, 2014. **39**(9): p. 4181-4188.
8. Barbarossa, V., et al., *Catalytic thermal decomposition of sulphuric acid in sulphur–iodine cycle for hydrogen production.* International Journal of Hydrogen Energy, 2006. **31**(7): p. 883-890.
9. Abimanyu, H., et al., *Preparation and characterization of Fe/Cu/Al2O3-composite granules for SO3 decomposition to assist hydrogen production.* Applied Catalysis A: General, 2008. **343**(1-2): p. 134-141.
10. Kawada, T., et al., *Hydrothermal synthesis of CuV 2 O 6 supported on mesoporous SiO 2 as SO 3 decomposition catalysts for solar thermochemical hydrogen production.* International Journal of Hydrogen Energy, 2014. **39**(35): p. 20646-20651.
11. Nagaraja, B.M., K.D. Jung, and K.S. Yoo, *Synthesis of Cu/Fe/Ti/Al2O3 Composite Granules for SO3 Decomposition in SI Cycle.* Catalysis Letters, 2008. **128**(1-2): p. 248-252.
12. Giaconia, A., et al., *Hydrogen production via sulfur-based thermochemical cycles: Part 2: Performance evaluation of Fe2O3-based catalysts for the sulfuric acid decomposition step.* International Journal of Hydrogen Energy, 2011. **36**(11): p. 6496-6509.
13. Joseph, S. and B. Mathew, *Microwave-assisted green synthesis of silver nanoparticles and the study on catalytic activity in the degradation of dyes.* Journal of Molecular Liquids, 2015. **204**: p. 184-191.
14. Joseph, S. and B. Mathew, *Microwave assisted facile green synthesis of silver and gold nanocatalysts using the leaf extract of Aerva lanata.* Spectrochim Acta A Mol Biomol Spectrosc, 2015. **136 Pt C**: p. 1371-9.

15. Vilchis-Nestor, A.R., et al., *Solventless synthesis and optical properties of Au and Ag nanoparticles using Camellia sinensis extract.* Materials Letters, 2008. **62**(17-18): p. 3103-3105.
16. Shankar, S.S., et al., *Rapid synthesis of Au, Ag, and bimetallic Au core-Ag shell nanoparticles using Neem (Azadirachta indica) leaf broth.* J Colloid Interface Sci, 2004. **275**(2): p. 496-502.
17. Vidhu, V.K., S.A. Aromal, and D. Philip, *Green synthesis of silver nanoparticles using Macrotyloma uniflorum.* Spectrochim Acta A Mol Biomol Spectrosc, 2011. **83**(1): p. 392-7.
18. Patra, A.K., A. Dutta, and A. Bhaumik, *Self-assembled mesoporous gamma-Al2O3 spherical nanoparticles and their efficiency for the removal of arsenic from water.* J Hazard Mater, 2012. **201-202**: p. 170-7.
19. Mrabet, D., et al., *A new route to the shape-controlled synthesis of nano-sized gamma-alumina and Ag/gamma-alumina for selective catalytic reduction of NO in the presence of propene.* J Colloid Interface Sci, 2017. **485**: p. 144-151.
20. Ceballos-Mendivil, L.G., et al., *Synthesis of silicon carbide using concentrated solar energy.* Solar Energy, 2015. **116**: p. 238-246.
21. Najafi, A., et al., *Synthesis and characterization of SiC nano powder with low residual carbon processed by sol–gel method.* Powder Technology, 2012. **219**: p. 202-210.
22. Díaz, J.A., et al., *β-silicon carbide as a catalyst support in the Fischer–Tropsch synthesis: Influence of the modification of the support by a pore agent and acidic treatment.* Applied Catalysis A: General, 2014. **475**: p. 82-89.
23. Casas Hidalgo, A.I., et al., *Sustainable application of pecan nutshell waste: Greener synthesis of Pd-based nanocatalysts for electro-oxidation of methanol.* International Journal of Hydrogen Energy, 2016. **41**(48): p. 23329-23335.
24. Shang, N.-Z., et al., *Ag/Pd nanoparticles supported on amine-functionalized metal–organic framework for catalytic hydrolysis of ammonia borane.* International Journal of Hydrogen Energy, 2016. **41**(2): p. 944-950.
25. Nadagouda, M.N. and R.S. Varma, *Green synthesis of silver and palladium nanoparticles at room temperature using coffee and tea extract.* Green Chemistry, 2008. **10**(8): p. 859-862.

# 9.7 Sulfur-dopedcarbonmadefrom cassava peelbymicrowavefunctionalization as metal-freeelectrocatalysts in alkaline media

D.P. Cetina-Arenas; B, Escobar, C. Mena-Durán , I.L. Alonso-Lemus

[1] Centro de Investigación Científica de Yucatán, Carretera Sierra Papacal – Chuburná Puerto, km 5. Sierra Papacal, Mérida C.P. 97302, Yucatán, México

[2] CONACyT. Centro de Investigación y Estudios Avanzados del IPN Unidad Saltillo, Av. Industria Metalúrgica, Parque Industrial Saltillo-Ramos Arizpe, C.P. 25900, Ramos Arizpe, Coahuila, México

* Corresponding author: beatriz.escobar@cicy.mx; (52) 999-930-07-60 ext 1203

---

## ABSTRACT

Cassava *(Manihotesculenta)* is a starch-derived tubercule regionally grown in Yucatan. Its peel is often discarded because it is not edible; however this part of cassava is mainly composed by cellulose and lignin. In this study, sulfur-doped carbons were synthesized using cassava peel residues as raw material. The electrochemical performance for the oxygen reduction reaction (ORR) in alkaline media was evaluated by rotating disk electrode technique (RDE). This work representsa proposal for an easy, low cost and eco-friendly method to obtain metal-free electrocatalysts. First, cassava residues were collected from a local market in Merida, Yucatan; the peel was separated and washed extensively with distilled water. The peels were dried at 80 °C overnight and ground using a food processor to get a very fine powder (sieve No. 100). Then the clean and dry raw material was pyrolyzed at 800 °C (Cas800) and functionalized by a microwave treatment using a modified microwave oven (800 W). Sulfuric acid and DMSO (dimethyl sulfoxide) were used both as sulfur precursor and solvent, during 15 minutes. After microwave treatment, the surface of the carbon materials was modified attaching sulfur functional groups. Metal-free electrocatalysts were characterized using FT-IR, DRX, Raman, $N_2$ adsorption isotherm with BET analysis and RDE in the presence of oxygen in order to evaluate their physicochemical and electrochemical properties for oxygen reduction reaction in alkaline fuel cells.

***Keywords:*** ORR; metal-free electrocatalyst; *Manihotesculenta*; microwave; sulphur-doped carbon.

# 9.8 PtNi Nanoparticles on Micro-/Nano-Strucutred Carbon for Methanol Electro-Oxidation in Acid Media

D. Macias-Ferrer, J.A. Melo-Banda, R. Silva-Rodrigo, U. Páramo-García, J.Y. Verde-Gómez

[1]Tecnológico Nacional de México/Instituto Tecnológico de Cd. Madero, Cd. Madero, Tamaulipas, 89440, México

[2]Tecnológico Nacional de México/Instituto Tecnológico de Cancún, Cancún, Quintana Roo, 77500, México

* Corresponding author: maestro_macias@hotmail.com

---

## ABSTRACT

In this work, electrocatalyst as micro-/nanostructured carbon (MNC) supported PtNi nanoparticles has been prepared by sequential impregnation reduction method in which Pt and Ni precursors are reduced by sodium borohydride, ammonium hydroxide, citric acid and Ar-$H_2$ static atmosphere at room temperature. MNC sample was synthesized via nanocasting method and pyrolysis at 1273 K using SBA-15 as hard template and refined sugar as carbon source. The prepared materials were characterized by means of $N_2$ physisorption analysis, X-ray Diffraction (XRD), energy dispersive X-ray spectroscopy (EDS), Raman spectroscopy, scanning electron microscopy (SEM) and high resolution transmission electron microscopy (HRTEM). The performance of electrocatalysts for methanol oxidation reaction was measured by cyclic voltammetry (CV), chronoamperometry (CA) and electrochemical impedance spectroscopy (EIS). The characterization techniques revealed that MNC proved to be a negative replica of SBA-15 having a rope-like morphology with carbon nanopipes surrounded turbostratic carbon. On the other hand, the electrocatalyst exhibit high dispersion of spherical nanoparticles with average particle sizes of 4.1 nm. In comparison with commercial catalyst (Pt/XC-72), the PtNi/MNC sample shows higher electrocatalytic specific activity and better resistance to carbonaceous intermediate poison into the methanol oxidation reaction.

***Keywords:*** Electrocatalysts, SBA-15, turbostratic carbon, carbon nanopipes

# 9.9 $Pt_3Fe/C$ bimetallic alloy nanoparticles as electrocatalysts with improved activity for the ORR

M. M. Tellez-Cruz, M.A. Padilla-Islas, H. Cruz-Martínez, O. Solorza-Feria

[1]Departamento de Química, CINVESTAV, Av. Instituto Politécnico Nacional 2508, Cuidad de México, C.P. 07360, México

[2]Programa de Doctorado en Nanociencias y Nanotecnología, CINVESTAV

* Corresponding author: 57473800, mtellez@cinvestav.mx

## ABSTRACT

Fuel cells powered by hydrogen from renewable sources are the ideal solution for non-polluting vehicles due to the to their high efficiency result because the chemical energy is directly converted to electrical energy with low emissions. However, two major technical gaps limit their commercialization: cost and durability. Regarding to the catalysts currently the main challenge in the wide spread of fuel cell technology is to lower or even eliminate Pt-content and other precious metals in catalysts without losing their performances.

For that reason the synthesis of two nano catalyst (octahedral and octapods) of $Pt_3Fe$ for oxygen reduction reaction (ORR) in acid media is presented. Catalysts were prepared through chemical reduction with the properly amount of oleylamine, oleic acid, and precursor salts ($Pt(acac)_2$ and $Fe(acac)_3$). In one of the two synthesis we use dibenzyl ether and tungsten hexacarbonyl (W(CO)6) as solvent and reducing agent respectively. Subsequent, both catalysts were dispersing in a carbon matrix (Vulcan Carbon) previously thermally treated. The presence of the alloy Pt3Fe in the catalysts was proved by XRD. TEM micrographs shown the morphology of the nanoparticles with an average 7-9 for octahedral and 12-14 nm for octapods. The electrochemical performance of $Pt_3Fe/C$ was evaluated by cyclic voltammetry, CO stripping and rotating disk electrode in $HClO_4$ as electrolyte. Octapods of $Pt_3Fe/C$ nanocatalyst showed the best mass activity and octahedral the best specific activity than commercially available 20-wt% Pt /C-Etek® catalyst. Therefore, this finding suggests a methodology for producing a carbon supported octahedral and octapods nanocatalyst, which could be used as a cathode electrode in a PEM fuel cell.

***Keywords:*** Pt3Fe alloy; octapods, octahedral nanoparticles; ORR catalyst; fuel cells.

# 9.10 Micro-mesoporous N-doped carbon materials obtained from biomass for power generation in alcaline fuel cells

L. Verduzco; B. Escobar, C. Mena-Durán; I.L. Alonso-Lemus

[1] Centro de Investigación Científica de Yucatán, Carretera Sierra Papacal – Chuburná Puerto, km 5. Sierra Papacal, Mérida C.P. 97302, Yucatán, México

[2] CONACyT. Centro de Investigación y Estudios Avanzados del IPN Unidad Saltillo, Av. Industria Metalúrgica, Parque Industrial Saltillo-Ramos Arizpe, C.P. 25900, Ramos Arizpe, Coahuila, México

* Corresponding author: beatriz.escobar@cicy.mx; (52) 999-930-07-60 ext 1203

## ABSTRACT

In this work, the synthesis and characterization of metal-free electrocatalysts from *Brosimum alicastrum* wastes as raw material were carried out. Ramon tree (*Brosimum alicastrum)* is native of Yucatan Peninsula, their seed and stalk are often used in industry for both food manufacturing and livestock. In this work, Ramon tree wastes were collected from the Germplasm bank from CICY. First, the wastes were washed with desionized water and dried overnight at 80°C. Then, they were milling to obtain a fine powder (Sieve No. 100). Thermogravimetric analysis (TGA) was performed in order to set the pyrolysis temperature range (400-700 °C) After pyrolysis treatment, the activation was carried outusing potassium hydroxide (KOH) 2:1 weight ratio to increase the surface area of the pyrolyzed materials. In addition, N-doping treatment was performed using hydrazine as nitrogen precursor by solvothermal method. The physicochemical properties were evaluated by the techniques of FT-IR, TGA, DRX, Raman spectroscopy and BET.The electrochemical performance for the Oxygen Reduction Reaction (ORR) was evaluated by rotating disk electrode (RDE) technique in alkaline media. This study is a good approach to obtain metal-free electrocatalysts from biomass residues, which are promising and sustainable alternative to generate low cost and large-scale materials for fuel cells.

***Keywords:*** Biomass, ORR, metal free-electrocatalyst, nitrogen-doped carbon, fuel cells.

# 9.12 CoNi@Pt core-shell electrocatalystswith enhanced activity towards oxygen reduction:computational and experimental contributions

H. Cruz-Martínez, E. Flores-Rojas, M. M. Tellez-Cruz, C. A. Ramírez-Herrera,P. Calaminici, O. Solorza-Feria

[1]Programa de Doctorado en Nanociencias y Nanotecnología, CINVESTAV, Av. Instituto Politécnico Nacional 2508, CP: 07360, Ciudad de México, Mexico.

[2]Departamento de Química, CINVESTAV, Av. Instituto Politécnico Nacional 2508, CP: 07360, Ciudad de México, Mexico.

*Corresponding author: Tel.: +52 (55) 5747 3800, ext. 4473, e-mail: hcruzm@cinvestav.mx

---

## ABSTRACT

CoNi@Ptcore-shellnanoparticles were theoretically studied and experimentally validated for the oxygen reduction reaction (ORR). In the computational section, the objective was to evaluate the effect of the core composition in the CoNi@Ptcore-shell nanoparticles towards the ORR. $Pt_{44}$ and $Co_nNi_{6-n}@Pt_{38}$ ($0 \leq n \leq 6$) octahedron nanoparticles were used as models. The O and OH adsorption energies were used as descriptors of the catalytic activity for this reaction. All calculations were performed using the density functional theory as implemented in the deMon2k code. The experimental validation of the CoNi@Pt core-shell nanoparticles was developed with three compositions (24:56@20, 40:40@20 and 56:24@20 wt.%). A combined synthesis of high energy milling-galvanic displacement was used to produce the CoNi@Pt core-shell nanoparticles. The physical characterization of the electrocatalyst was developed using X-ray diffraction, energy dispersive X-ray spectroscopy and scanning transmission electron microscopy. Cyclic voltammetry and rotating disk electrode techniques were used for the electrochemical characterization of the synthesized nanocatalysts. The O and OH adsorption energies showed that the $Co_nNi_{6-n}@Pt_{38}$ ($0 \leq n \leq 6$) octahedron clusters are better candidates than $Pt_{44}$ octahedron nanoparticles for the ORR. Theoretical results were confirmed electrochemically.

***Keywords:*** High energy milling; Galvanic displacement; Auxiliary density functional theory; Adsorption energy; Active sites

# 9.14 High-Active $MoS_x$-Carbon Electrocatalist Towards Hydrogen Evolution Reaction in Acidic Media

C.A. Campos-Roldán, R.G. Gonzalez-Huerta, N. Alonso-Vante

[1]Instituto Politécnico Nacional-ESIQIE, Laboratorio de Electroquímica y Corrosión, UPALM, 07738, CDMX, México

[2]IC2MP, UMR-CNR 7285, University of Poitiers, 4 rue Michel Brunet, 86022, Poitiers, France

* Corresponding author: rosgonzalez_h@yahoo.com.mx

## ABSTRACT

Herein, we synthetized $MoS_x$-X (X=graphite, multi-walled carbon nanotubes or carbon Vulcan) electrocatalyst by a simple photodeposition method, where the carbon surface chemistry impacts in the material intrinsic activity towards hydrogen evolution reaction (HER) in acidic media. Polarization curves revels the superior activity of $MoS_x$-CNT, meanwhile $MoS_x$-Graphite exhibits the sluggish kinetics towards HER. Electrochemical impedance spectroscopy (EIS) demonstrates the fast electron transfer processes of $MoS_x$-CNT, putting in evidence the high performance of which material. Interestingly, for $MoS_x$-Graphite, EIS revels a different kind of interaction, due to Bode-phase diagram shows two overlap time-constants, suggesting that two electrochemical events posses high-resistive behavior. We expect that electrical conductivity and surface area of carbon substrates leads a kind of interaction, which enhance the activity towards HER in acidic media.

***Keywords:*** $MoS_x$, Hydrogen Evolution Reaction, Electrochemical Impedance Spectroscopy

## 1. INTRODUCTION

Supplying the world's growing population with clean, affordable energy is a critical challenge. Fossil fuels continue to dominate the global energy landscape, but increasing concerns over the effect of anthropogenic carbon dioxide on the earth's climate make sustainable energy technologies, where hydrogen ($H_2$) is a promising option. Water splitting from either light or renewable energy provides the most sustainable supply of $H_2$. Electrochemical hydrogen evolution reaction (HER) in acidic media is most effectively way to produce the mention about, and Pt and its alloys are the best catalyst for this reaction. However, the scarcity and high cost of the Pt group metals prevent wider adoption of this

technology. Recently, molybdenum disulfide ($MoS_2$) has been identified as a promising active and acid-stable catalyst for HER [1-5].

However, the catalytic performance of layered $MoS_2$ structures is highly restricted by the scarcity of metal edges [6] and the low electron transport efficiency in multilayered phases (catalytic activity decreases by a factor of ~4.5 with each additional layer) [7-9]. Improvements in $MoS_2$ catalytic performance have been made by increasing edge exposures (e.g., surface structure engineering) [7], improving electron transport efficiency (e.g., formation of monolayers, 1T metallic monolayers on graphite, and nanoparticles/NPs binding with highly conductive substrates) [8-10], and modulating the electronic structure via chemical doping [11]. Nevertheless, the majority of metal atoms in these particles remain within the basal plane away from particle edges, which unfortunately are catalytically inactive. To overcome these technical challenges, here we systematically studied the effect of a carbon support-material in the $MoS_2$ HER activity in acidic media.

## 2. EXPERIMENTAL

### 2.1. Chemicals

The following precursors were purchased and used without further purification: XC-72 Carbon Vulcan from Carbot (labeled as C), Multi-walled carbon nanotubes from Bayer (labeled as CNT), Graphite powder from Alfa (labeled as Graph), $(NH_4)_2MoS_4$ 99.99% and isopropanol from Sigma-Aldrich.

### 2.2 $MoS_x$ Photo-deposition (PD)

The support material (e.g., C, CNT or Graph) was mixed in Ar-saturated Milli-Q water/isopropanol mixture in a reactor. A solution containing $(NH_4)_2MoS_4$ was added into the reactor and stirred for 4 h under UV light (Xe lamp, 200 mW). To prevent the sample heating, temperature was held at 25 ºC with a water circulator. After the irradiation time, the resulting powder was thoroughly washed with Milli-Q water, vacuum filtered and dried overnight at 80 ºC.

### 2.3 Surface electrochemistry

Hydrogen Evolution Reaction (HER) kinetics was evaluated by electrochemical methods. A catalytic ink was prepared as follows: a mixture containing 5 mg of catalyst and 3 mL of stock solution (20% isopropanol, 0.4 % Nafion® Sigma-Aldrich and 79.6% Milli-Q water) was dispersed in an ultrasonic bath for 30 min. Then, 10 μL of the mixture was dropped onto a glassy carbon electrode (5 mm diameter) and dried at room temperature. The electrochemical measurements were carried out at 25 ºC using a potentiostat/galvanostat (Autolab PGSTAT 30) in a typical one-compartment three-electrode cell with 0.5 M $H_2SO_4$ as electrolyte. A Pt mesh and a reversible hydrogen electrode (RHE) were used as counter and reference electrode, respectively. Cyclic Voltammograms (CVs) were

recorded at 50 $mVs^{-1}$ between 0.05 and 1.2 V to calculate the Electrochemical Surface Area (ECSA). The HER activity activity was measured by the Rotating Disk Electrode technique in Ar saturated 0.5 M $H_2SO_4$, at 1600 rpm, from 0.05→-0.3 V, at 5 mV $s^{-1}$. Electrochemical Impedance Spectroscopy (EIS) was evaluated from 2 MHz→1 mHz, at 5 mV $s^{-1}$, at 0 V, -0.05 V, -0.10 V and -0.15 V.

## 3. RESULTS AND DISCUSSION

To visualize up the active surface area of Graph-$Mo_xS_y$, CNT-$Mo_xS_y$, and C-$Mo_xS_y$ materials, cyclic voltammetry was carried out. Figure 1 depicts the voltammograms of carbon-support materials before and after photodeposition of molybdenum sulfide.

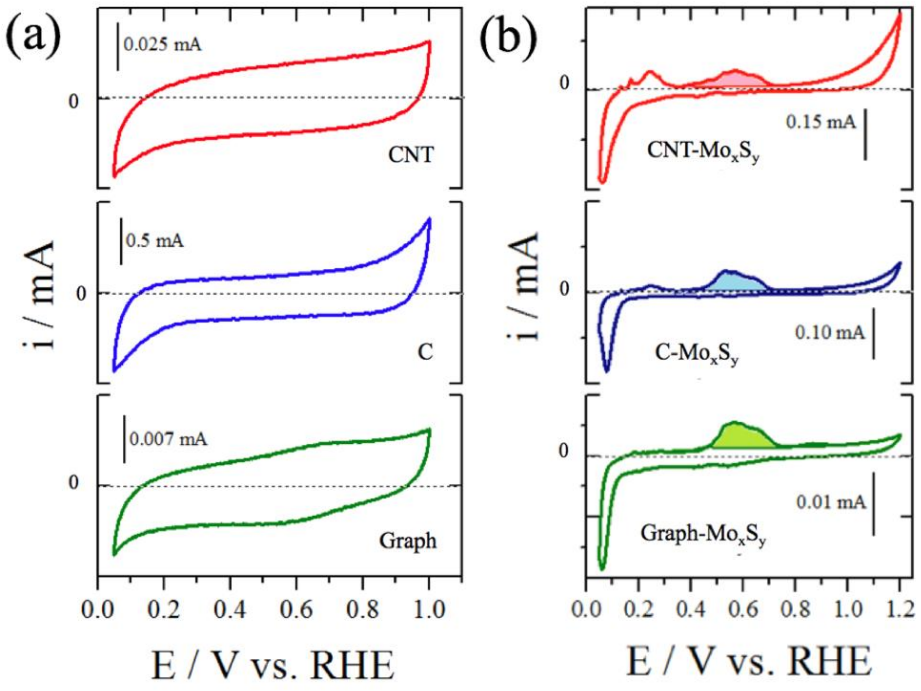


***Figure 1.*** *Cyclic voltammograms of a) Graph, CNT and C; and b) Graph-$Mo_xS_y$, CNT-$Mo_xS_y$ and C-$Mo_xS_y$. Measurements were carried out in Ar-saturated 0.5 M $H_2SO_4$, 50 mV $s^{-1}$, 25 ºC.*

A complete anodic stripping to 1.2 V oxidizes all the $MoS_x$ species to $MoO_x$, which are no HER active. Previous work on nanocrystalline $MoS_2$ has also showed that performing cyclic voltammetry to oxidize parts of the catalyst can result in its deactivation to various degrees [12]. Observing Figure 1a, all carbon-support materials present a rectangular-

shape pseudo-capacitive behavior, which is a typical feature of carbon electrodes under these experimental conditions. After photodeposition, Figure 1b, we can appreciate interfasial processes in all materials. At c.a. 0.2 V, $Mo^0$ is oxidized to $Mo^{3+}$ [13]. Furthermore, in the potential range 0.4-0.8 V, we can appreciate the oxidation of all the $MoS_x$ species to $MoO_x$. The integrated oxidation charge (Q) was calculated from:

$$Q = \frac{1}{v}\int i\ dE \qquad (1)$$

where ν is the scan rate [V $s^{-1}$], i is the measure current [A] and E is the applied potential [V]. The calculated Q for Graph-$Mo_xS_y$, CNT-$Mo_xS_y$ and C-$Mo_xS_y$ are summarized in Table 1. From Table 1, the integrated oxidation charge of Graph-$Mo_xS_y$ is an order of magnitude lower than CNT-$Mo_xS_y$ and C-$Mo_xS_y$ quantities. The Q measure values is governing by the trend CNT-$Mo_xS_y$ > C-$Mo_xS_y$ > Graph-$Mo_xS_y$. Therefore, this feature suggests that this is the trend for the active surface of those catalysts.

Rotating-disk electrode (RDE) technique was used to elucidate the HER kinetic over catalyst surface. Figure 2 depicts the HER polarization curves, as well as their respective Tafel plots, of Graph-$Mo_xS_y$, CNT-$Mo_xS_y$, and C-$Mo_xS_y$ materials. In order to contrast the catalytic center, carbon-support materials HER polarization curves are also shown, as well as a benchmarking Pt/C commercial catalyst.

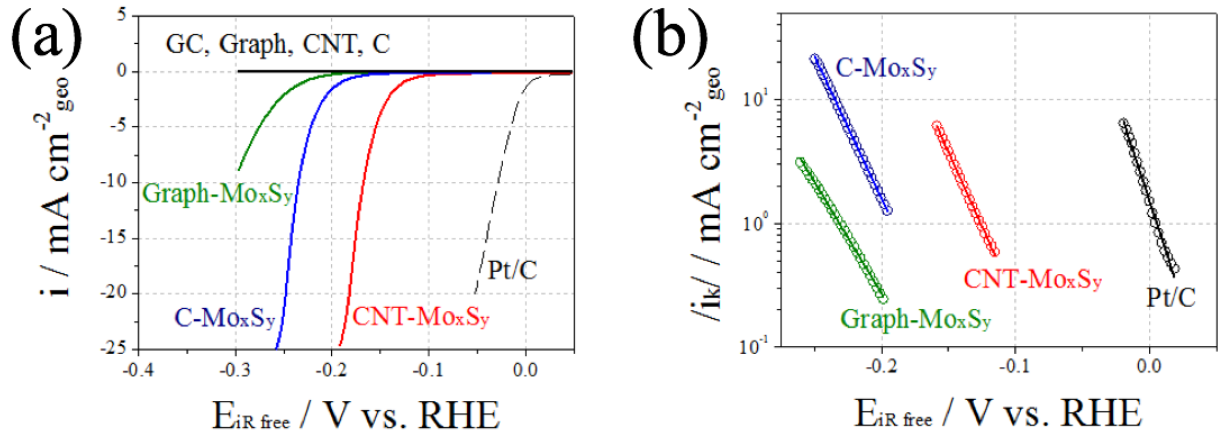


***Figure 2.*** *a) HER polarization curves and b) corresponding Tafel slopes plot of Pt/C (commercial), Graph-$Mo_xS_y$, CNT-$Mo_xS_y$ and C-$Mo_xS_y$. Measurements were carried out in Ar-saturated 0.5 M $H_2SO_4$ with iR correction, 1600 rpm, 5 mV $s^{-1}$, 25 ºC.*

Although Graph, CNT, and C surfaces are inert towards HER, when molybdenum sulfide is

present onto their surfaces, a kinetic HER signal is observed. Thus, all the measured HER current can be attributed to catalysis by the molybdenum sulfide nanostructures. The onset potential ($\eta_{HER}$) increases as follow: CNT-$Mo_xS_y$ (0.10 V) < C-$Mo_xS_y$ (0.16 V) < Graph-$Mo_xS_y$ (0.20 V), suggesting that HER kinetics start faster, namely, less energy barriers, according this trend. To compare the HER activities exhibited by the different $Mo_xS_y$-catalysts, the overpotencial ($\eta_{@10}$) needed to drive a current density of 10 mA $cm^{-2}$ was used as a reference. This parameter increases as CNT-$Mo_xS_y$ (0.16 V) < C-$Mo_xS_y$ (0.23 V) < Graph-$Mo_xS_y$ (>0.30 V), suggesting that HER kinetics on CNT-$Mo_xS_y$ needed the lowest applied-energy to drive 10 mA $cm^{-2}$. Tafel-slope plots, which reflects the HER mechanism (see Figure 1b) increases according to CNT-$Mo_xS_y$ (39.53 mV $dec^{-1}$) < C-$Mo_xS_y$ (43.37 mV $dec^{-1}$) < Graph-$Mo_xS_y$ (45.43 mV $dec^{-1}$). This results suggest that HER goes through a Volmer-Heyrovsky mechanism, being Heyrovsky step the reaction-determining step (RDS), namely, the electrochemical coupling between a $H^+$ and a hydrogen atom adsorbed onto an active site through the electrode surface. This feature is related with a Tafel slope value of 40 mV $dec^{-1}$.

The turnover frequency (TOF) of $H_2$ evolution of Graph-$Mo_xS_y$, CNT-$Mo_xS_y$ and C-$Mo_xS_y$ was evaluated. The number of sites present was estimated by integrated oxidation peak. All HER kinetic parameters are summarizing in Table 1.

***Table 1**. HER kinetic parameters of $Mo_xS_y$-Graph, $Mo_xS_y$-CNT and $Mo_xS_y$-C.*

| | Q (C) | $\eta_{@10mA\ cm^{-2}}$ (V) | $TOF_{@0.20V}$ ($s^{-1}$) | $-b_{RDE}$ (mV $dec^{-1}$) |
|---|---|---|---|---|
| Graph-$Mo_xS_y$ | $4.193x10^{-5}$ | > 0.30 | 0.0818 | 45.43 |
| CNT-$Mo_xS_y$ | $8.7326x10^{-4}$ | 0.16 | 2.7639 | 39.53 |
| C-$Mo_xS_y$ | $5.0998x10^{-4}$ | 0.23 | 0.3099 | 43.37 |

From Table 1, the HER performance is governing according to the follow trend: CNT-$Mo_xS_y$ < C-$Mo_xS_y$ < Graph-$Mo_xS_y$. This behavior could be attributed to carbon-support chemical nature, particles dispersion through carbon-support material, particle size and quantity of sulfur-terminal atoms of molybdenum sulfide.

In order to appreciate the resistances through the electrochemical HER kinetics, electrochemical impedance spectroscopy (EIS) was carried out. Figure 3 shows the EIS fitted results at a representative potential (-0.15 V) of Graph-$Mo_xS_y$, CNT-$Mo_xS_y$, and C-$Mo_xS_y$ materials.

Observing Figure 3a, the Nyquist plots of CNT-$Mo_xS_y$ and C-$Mo_xS_y$ materials revel two loops, suggesting the presence of three impedances (including the resistance solution). However, the loop located at low frequency is potential dependent, whereas the loop

located at high frequency does not depends on the potential. Therefore, the loop at low frequency is associated with the HER kinetics, namely, the charge-transfer resistance. Nevertheless, for Graph-$Mo_xS_y$ material, we can appreciate only the presence of one loop, suggesting the presence of two impedances.

In order to fit the EIS experimental data of CNT-$Mo_xS_y$ and C-$Mo_xS_y$ materials, the transmission line model was used [14]. This model consists of three impedances, which are representing by (i) the electronic transport in the solid phase, (ii) the ionic transport through the electrolyte, and (iii) the electrochemical recombination. The physical interpretation for our systems consists in: (i) the electronic transport through the carbon-support material, assigned to the loop at high frequency, which is related with its porosity, (ii) the 0.5M $H_2SO_4$ solution resistance, and (iii) the HER kinetic recombination, assigned to the loop at low frequency.

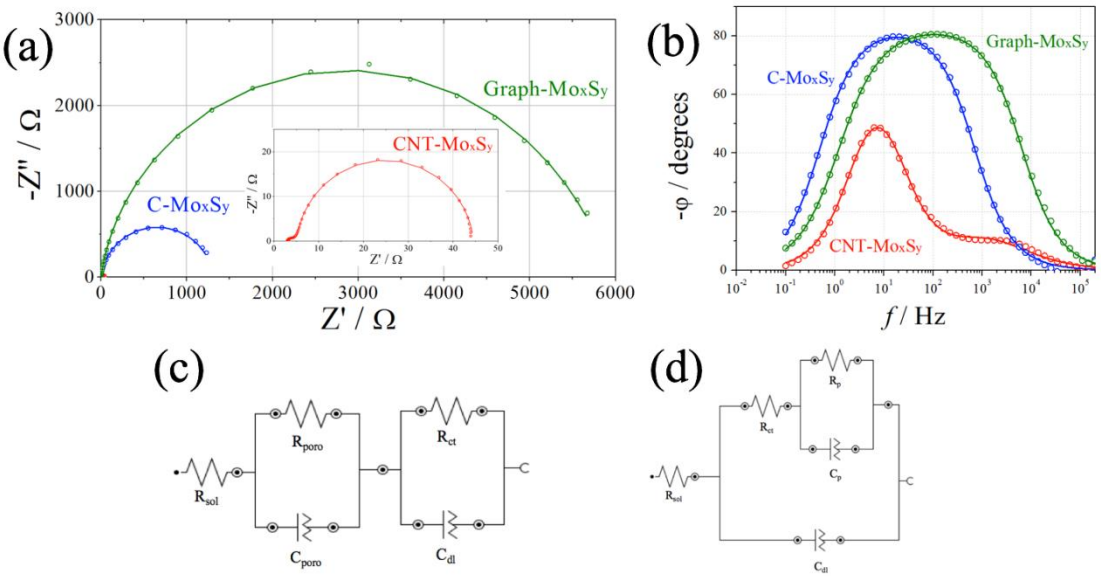


***Figure 3.*** *a) Nyquist diagrams and b) Bode-phase diagrams of Graph-$Mo_xS_y$, CNT-$Mo_xS_y$ and C-$Mo_xS_y$. Measurements were carried out in Ar-saturated 0.5 M $H_2SO_4$, 0.1 Hz→2 MHz, with an amplitude of 10 mV $s^{-1}$, at E=-0.15 V, 25 ºC. Equivalent circuit model of c) CNT-$Mo_xS_y$ and C-$Mo_xS_y$, and d) Graph-$Mo_xS_y$.*

The equivalent-circuit model for CNT-$Mo_xS_y$ and C-$Mo_xS_y$ materials is depicted in Figure 3c. However, for Graph-$Mo_xS_y$ material, the model was modified, due to Bode-phase diagram (see Figure 3b) is wide, suggesting two time-constants overlapped, hence, two overlapped electrochemical processes. In this case, the impedances were representing by: (i) the 0.5M $H_2SO_4$ solution resistance, and (ii) the HER kinetic recombination, which is divided in the $H^+$ adsorption onto electrode surface and its electrochemical coupling. This interpretation was validated by considering the graphite crystalline-character and the slow HER kinetics (see Figure 2). The equivalent-circuit model for Graph-$Mo_xS_y$ material is

depicted in Figure 3c.

## 4. CONCLUSION

Our preliminary results revels how the electrochemical performance towards the HER of supported $MoS_x$ onto different carbon surfaces is influenced by the carbon chemical surface. However, to obtain a better interpretation and discussion, it is necessary the physicochemical characterization of support-materials before and after $MoS_x$-particles deposition.

## ACKNOLEGMENTS

C.A.C.R. acknowledges financial support from CONACYT-Mexico Nr.: MX-561206. The authors would like to acknowledge to the Instituto Politécnico Nacional for the financial support received through the Multidisciplinary project 1820. Also to the CONACYT project CEMIE-Ocean-249795: Transversal Line I-LT1.

## REFERENCES

[1] J. Kibsgaard, T. Jaramillo, F. Besenbacher, Nature Chemistry 2014, 6, 248-253.
[2] H. Wang, P. Skeldon, G. Thompson, Surface and Coating Technology 1997, 91, 200-207.
[3] B. Guichard, M. Roy-Auberger, E. Devers, C. Legens, P. Raybaud, Catalysis Today 2008, 130, 97-108.
[4] T. Weber, J. Muijsers, J. Niemantsverdriet, J. Phys. Chem. 99, 1995, 9194-9200.
[5] T. Weber, J. Muijsers, J. van Wolput, C. Verhagen, J. Niemantsverdriet, J. Phys. Chem. 100, 1996, 14144-14150.
[6] A. Borgschulte, O. Sambalova, R. Delmelle, S. Jenatsch, R. Hany, F. Nuesch, Scientific Reports 2017, 7, 40761.
[7] L. Lin, N. Miao, Y. Wen, S. Zhang, P. Ghosez, Z. Sun, D. Allwood, ACS Nano 2016, 10, 8929-8937.
[8] B. Seo, G. Jung, Y. Sa, H. Jeong, J. Cheon, J. Lee, H. Kim, J. Kim, H. Shin, S. Kwak, S. Joo, ACS Nano 2015, 9, 3728-3739.
[9] H. Wang, Z. Lu, D. Kong, J. Sun, T. Hymel, Y. Cui, ACS Nano 2014, 8, 4940-4947.
[10] S. Gao, X. Wei, H. Liu, K. Geng, H. Wang, H. Moehwald, D. Shchukin, J. Mater. Chem. A 2015, 3, 23376-23384.
[11] T. Jaramillo, J. Bonde, J. Zhang, B. Ooi, K. Anderson, J. Ulstrup, I. Chorkendorff, J. Phys. Chem. C 2008, 112, 17492-17498.
[12] J. Piwek, A. Platek, K. Fic, E. Frackowiak, Electrochimica Acta 2016, 215, 179-186.

[13] L. Lin-Ting, Y. Deng, L. Ma, Y. Zhang, A. Peterson, B. Yeo, ACS Catal. 2016, 6, 861-867.
[14] H. Vrubel, T. Moehl, M. Gratzel, X. Hu, Chem. Commun. 49, 2013, 8985.

# 9.15 Co3O4 spinel as three dimensional ordered macroporous (3-DOM) electrocatlayst for the water splitting in alkaline media

J.E. García-Béjar, E. Ortega-Ortiz, M.P. Gurrolaand, L. G. Arriaga
Centro de Investigación y Desarrollo en Electroquímica

*Corresponding autor: larriaga@cideteq.mx

Oxygen reaction reduction (ORR) and oxygen evolution reaction (OER) still being the key issue of in the water splitting, furthermore the usual catalyst are made of noble metals, like platinum and iridium compounds, that is the reason because developing of no-noble, stable and efficient electrocatalyst has attracted attention of many researchers in the world. This work presents a 3-DOM $Co_3O_4$ spinel characterized by a high relation weight-volume allowing a greater catalytically active area, is a no-noble catalyst and good bifunctional performance. The macroprous structure of 3-DOM was synthetized by colloidal crystal template (CCT) and was physiochemically characterized by (X-ray diffraction) XRD, scanning electron microscopy (SEM), energy dispersive spectroscopy EDS and Brunauer Emmett Teller BET. Characterization results (XRD and EDS) showed the existence of Co3O4 spinel oxide, and the formation of the 3-DOM structure was corroborated by SME, finally BET showed a great superficial area of $32 m^2 g^{-1}$. To evaluate its performance as a bifunctional catalyst the material was compared with Pt/C commercial catalyst; the study was made using cyclic voltammetry and shows that the materials exhibit catalytic activity for OER and ORR as well as good stability. The kinetic parameters were determined by rotating disc electrode (RDE), and the results exhibit a good performance as bifunctional catalyst, like the catalyst that containing noble metals.

***Keywords:*** *3*-DOM, bifunctional catalyst, $Co_3O_4$ spinel.

# 9.16 Styrene-co-butyl acrylate copolymers with potential application as membranes in PEM fuel cell

L. Francisco-Vieira, D. Morales-Acosta, E. Cuara-Diaz, R. Benavides

Centro de Investigación de Química Aplicada, Blvd Enrique Reyna No. 140, Col. San José de los Cerritos, 25290. Saltillo, Coahuila, México

*Tel: +52844-4389830 E-mail: roberto.benavides@ciqa.edu.mx; diana.morales@ciqa.edu.mx

## ABSTRACT

In order to prepare an alternative system to Nafion membranes, Styrene-butyl acrylate (St-BuA) copolymers were obtained by mass copolymerization via free radical reactions, using BPO as initiator. A 70:30 (St:BuA) comonomer composition was selected. Three different molar concentrations of sulfonating agents (50, 100 and 150%) were considered to obtain the sulfonated copolymer (sSt-BuA). Membranes were prepared from sSt-BuA copolymers by casting method. Copolymers were characterized through FTIR, TGA and NMR $^{1}$H. The sSt-BuA sulfonation degree (SD) effect on the ion-exchange capacity (IEC) was also evaluated by titration, while its electrochemical properties through cyclic voltammetry (CV) and electrochemical impedance spectroscopy (EIS). Fourier transformed infrared spectroscopy (FT-IR) and thermal gravimetric analysis (TGA) analysis confirmed the existence of both comonomers and a successful sulfonation near 30%, as well as a good thermal stability under 350 °C. The chemical composition of St-BuA copolymer was also confirmed by proton nuclear magnetic resonance (NMR $^{1}$H) spectroscopy. The IEC values obtained varied from 0.83 to 1.18 meq g$^{-1}$, depending on sulfonation degree. These values are similar to the one obtained for Nafion (0.91 meq g$^{-1}$). The mechanical properties of sSt-BuA membranes were followed by E* (complex modulus) obtained from thermomechanical analysis (TMA). Results showed that these copolymers are promising materials to be used as membranes in fuel cells applications.

***Keywords:*** membranes, styrene-co-butyl acrylate; fuel cells.

## 1. Introduction

In the last decades, fuel cells are regarded as efficient and clean energy sources as alternatives to limited fossil fuel resources. Fuel cells (FC) are the promising energy conversion, devices that convert chemical energy of fuel (hydrogen, methanol, ethanol) to the electrical energy in an efficient and ecofriendly way [1].

The PEMFC and Direct Methanol (DMFC) are based in the technology of Proton Exchange Membrane (PEM), where the principal components are the electrodes and the ion exchange membrane (IEM). In this cell, the fuel feeds the anode (oxidation) producing protons and electrons in the presence of a catalyst, normally platinum. An electrically insulating electrolyte allows protons to pass through to reach the cathode and blocks the electrons, allowing a current flow in the external circuit. At the cathode electrons are combined with protons of oxygen of the air producing water [2].

Perfluorosulfonic acid based membranes have been used in portable and stationary dispositive. Those polymers present an attractive combination of performance, reliability and high durability. Nafion membrane is the most successful commercial membrane used exclusively for PEM, due to superior combination of good chemical and physical stability and high proton conductivity also, in a wide range of moisture level at moderate operating temperatures. However, it presents limited operation at moderate temperatures (0 – 80$^{o}$C), high cost and high permeability in methanol (in DMFC) [3].

In this context, alternative polymers have been developed. Sulfonation of hydrocarbon polymeric materials is a common alternative for preparation of the membranes. They are usually prepared by either direct sulfonation of a polymer matrix with different sulfonating agents, or synthesized from the sulfonated monomers by polymerization [1]. The copolymers based on polystyrene (Ps) are attractive, since it is a common polymer of low cost and facile processability. Ps materials are interesting because of the presence of the benzene ring, which provides the facility to sulfonate and provide the exchange property. In this work, poly(styrene-co-butyl acrylate) (St:BuA) was synthetized by free radical mass polymerization and treated by direct sulfonation, with the general idea of improving the mechanical and thermal properties of the membranes.

## 2. Materials and Methods

### *2.1. Polymerization and sulfonation of the poly(styrene-co-butyl acrylate)*

Styrene and butyl acrylate were synthetized by free radical mass polymerization, using benzoyl peroxide (BPO) as initiator of the reaction. The copolymer was synthesized with a molar ratio of 70:30 (St:BuA).
The sulfonation reaction was carried out by solubilizing the copolymer in chloroform. After the complete solubility, concentrated sulfuric acid ($H_2SO_4$, 98%) was added as the sulfonating agent. The solution was heated to 60 °C for 2h under inert atmosphere ($N_2$). The reaction was stopped by pouring the sulfonated solution into a beaker with distilled water immersed in an ice bath. The solid sulfonated copolymer was washed several times until neutral pH was reached and vacuum oven at 50 $^{o}$C for 48h, to remove residual water. The sulfonating agent was added at concentrations of 50, 100 and 150 mol% relative to the molar amount of benzene rings, theoretically present in each composition. The synthetic route is presented in Scheme 1.

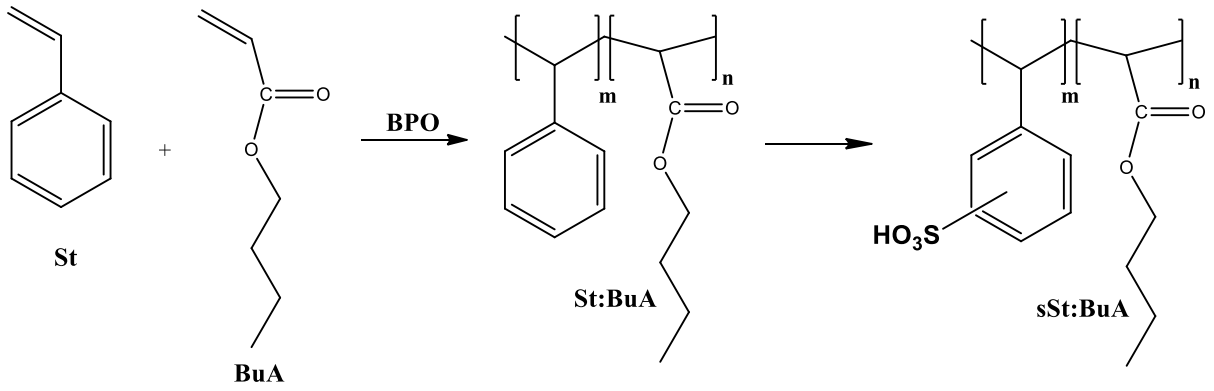


**Scheme 1.** Synthesis of poly (styrene-*co*-butyl acrylate) by free radical mass polymerization and sulfonation reaction of the copolymer with $H_2SO_4$.

*2.2. Preparation of the membranes*

The membranes of St:BuA were prepared by the casting method using toluene as solvent. The solution was prepared of 0.2 $g.mL^{-1}$ copolymer/solvent. The dissolved copolymers were poured into glass molds and dried at room temperature.

*2.3. Characterization of membranes*

The copolymer St:BuA 70:30 was characterized from NMR $^1H$, using a Bruker Avance 3 spectrometer with 500 MHz of frequency. Sample of copolymer was dissolved in $CDCl_3$. FTIR measurements were performed with a spectrophotometer, Nicolet Magna – IR$^{TM}$ Spectrometer 550 at the following conditions: 32 scans, resolution de $4cm^{-1}$ in the region of 4000-400 $cm^{-1}$.
Thermal stability was determined by TGA analysis, using a TA Instruments model Q500 equipment, under nitrogen atmosphere at a heating rate of $10^oC.min^{-1}$, from 30 $^oC$ to 600 $^oC$. The mechanical properties of sSt-BuA membranes were also obtained by thermomechanical analysis (TMA), using a TA Instruments model Q400 instrument. A constant temperature was used at 35ºC, with a force ramp of 0.001 $N.min^{-1}$ from 0.001 N to 0.010 N. The analysis were carried out by the 3-point bending method. The modulus of elasticity in bending ($E_B$) was obtained from the equation:

$$E_B = \frac{L^3.m}{4.b.d^3} \quad (1)$$

where L is the support span (mm), m is slope of the tangent to the initial straight-line portion of the load-deflection curve ($N.mm^{-1}$), b is the width of beam tested (mm) and d is depth of beam tested (mm) [4].

The ion exchange capacity (IEC) of the sulfonated copolymers was evaluated by the titration method. The dried membrane was immersed into a 1M HC solution for 24h. Then it was rinsed and immersed again in a solution of 1M NaCl for 24h. Finally the membrane was rinsed with deionizer water. The number of protons shifted of the membrane was determined using a pHmeter to detect the equivalent point during the titration on the

solution of NaCl with a solution 0.005M of NaOH. The IEC was calculated using the following equation:

$$IEC = \frac{V_{NaOH} \cdot N_{NaOH}}{W_{dry}} \quad (2)$$

where $V_{NaOH}$ (mL) is the volume of the 0.05 M NaOH solution, $N_{NaOH}$ is the concentration of NaOH (mmol.ml$^{-1}$ ~ meq.mL$^{-1}$) and $W_{dry}$ is the dry weight of the copolymer membrane [5].

The sulfonation degree of St:BuA is an important parameter, due to its effect on the physicochemical and thermal properties of the membranes. The sulfonation degree (DS) was calculated considering the values of IEC, through the equation:

$$DS\ (\%) = \frac{IEC.M_{w(St:BuA)}}{1-(IEC.M_{w(SO_3H)})} \quad (3)$$

where $M_{w\ St:BuA}$ (gr.mol$^{-1}$) is molecular weight of the copolymer (St:BuA) and $M_{w\ SO3H}$ (gr.mol$^{-1}$) is molecular weight of the sulfonic group [6].

The proton electrochemical measurements were carried out from electrochemical impedance spectroscopy (EIS) at room temperature in a frequency range 4 MHz- 1 KHz. A diffusion cell with two compartments was used, containing 150 mL 0.5 mol.L$^{-1}$ of $H_2SO_4$ and a Biologic SP-300 potentiostat/galvanostat. A platinum wire was employed as working electrode (WE), the Ag/AgCl electrode was used as the reference electrode (RE) and a steel mesh as the counter electrode (CE). The Pt electrode was placed in compartment B of the cell while Ag/AgCl and steel electrodes were placed in the compartment A. The membranes were positioned between both compartments.

## 3. Results and Discussion

The real composition of the copolymer was obtained by $^1$H NMR analysis. Copolymer composition was calculated by comparison the integral values from signals at 4 - 3.5 ppm, assigned to the two protons of the -$OCH_2$- group of butyl acrylate, and the broad signals at 7.5 - 6.3 ppm, due to the protons (5H per molecule) of the aromatic ring of styrene (Figure 1-1). Figure 1 also shows the FTIR spectrum of polystyrene, which shows a change in the signals confirming the presence of butyl acrylate. The real composition calculated was 75:25, very close to the theoretical composition (70:30) [4].

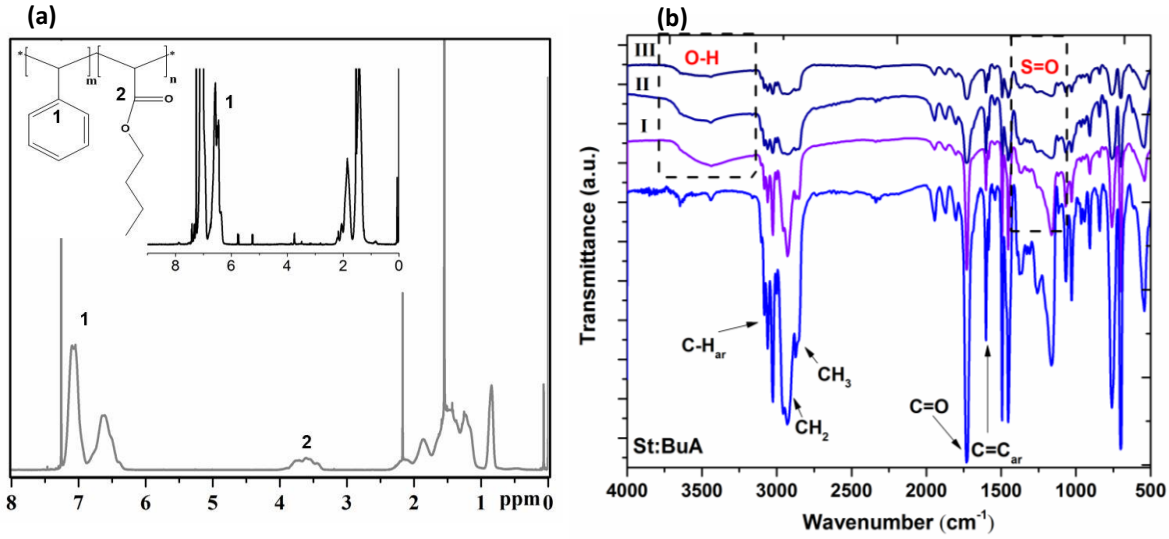


**Figure 1.** (a) $^{1}$H NMR spectrum of St:BuA copolymer. (b) Comparative FTIR spectra of St:BuA and St:BuA sulfonated (sSt:BuA) I – 50%, II – 100%; III – 150%.

The FTIR analysis corroborated the copolymer presence, as well as the existence of sulphonation in the copolymer. Figure 1 (b) shows the spectra of the sulfonated copolymers superimposed on the non-sulfonated St: BuA 70:30 copolymer. It is possible to observe the characteristic bands of the copolymer in the absorption band between 3100-3000 cm$^{-1}$, characteristics of the stretching of the C-$H_{ar}$, while the bands at 2962-2850 cm$^{-1}$ are attributed to the asymmetric and symmetrical deformation, corresponding to the $CH_2$ and $CH_3$ groups present in the polymer chain. The characteristic signal of the ester group present in the BuA monomer is observed as an intense absorption band at 1722 cm$^{-1}$, corresponding to the C=O group. Then at 1140 cm$^{-1}$ the absorption band corresponds to the stretching vibration of O-C (O) -C [5]. Sulfonation is confirmed by the identification of the absorption bands at 1377-1300 cm$^{-1}$, characteristics of the asymmetric stretching of the S=O bond. It is noticeable that with the increase of the concentration of sulfonic groups (50, 100 and 150%) in the polymer chain, an expansion of these bands, in a sequenced way with the level of sulfonant, is observed. These bands originate due to the asymmetric and symmetrical $SO_2$ elongation observed in the absorption bands at 1200 -1168 cm$^{-1}$, respectively. Another notable feature in this system is the decrease in the absorption band of the carbonyl group (C=O) along with the concentration of sulfonating agent.

TGA thermogram of copolymers St:BuA and sSt:BuA are presented in Figure 2. The TGA curves shows good thermal stability for the copolymer St:BuA, since the first decomposition step started at 350$^{o}$C. sSt:BuA copolymers show three weight loss steps: first loss from 100 – 110$^{o}$C is due to the loss of water molecules, may be coming from the process of the neutralization realized after of the sulfonation, or due to the absorption of common moisture in sulfonated copolymers. The second loss, from 150 to 250$^{o}$C, is assigned of the decomposition or desulfonation of the sulfonic groups (-$SO_3H$). The third loss is showed into 350 – 380 $^{o}$C is assigned to degradation of the main chain. All the copolymers presented good thermal stability at temperatures of 300$^{o}$C, with potential for the desired application [7] [8].

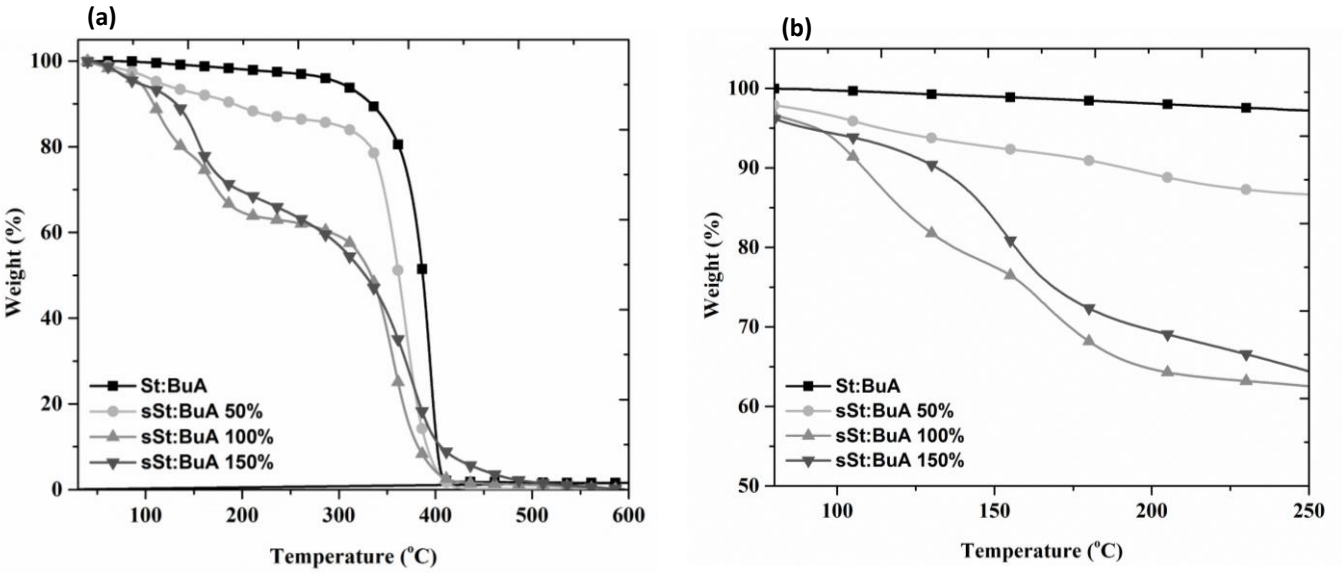


**Figure 2.** (a) TGA curves of copolymers St:BuA and sSt:BuA. (b) Close view of TGA curves

Ion exchange capacity (IEC), degree of sulfonation (DS) and water uptake (WU) obtained for the copolymers are presented in the table 1. The DS calculated from IEC data was compared with the level of sulfonation groups released and observed in the TGA curves during the second decomposition step (150°C to 250°C).

**Table 3.** Properties of copolymers sSt:BuA.

| Sample | IEC (meq $g^{-1}$) | WU (%) | $DS_{IEC}$ (%) | $DS_{TGA}$ |
|---|---|---|---|---|
| **sSt:BuA 50%** | 0.83 | 3 | 20 | 5 |
| **sSt:BuA 100%** | 0.84 | 15 | 21 | 15 |
| **sSt:BuA 150%** | 1.18 | 12 | 30 | 20 |

It is clear to observe that according with the increase in DS, there is also an increase of IEC. It is also noticeable that the copolymer sSt:BuA 150% presented a IEC of 1.18 meq.$g^{-1}$ with DS 30%, comparing with Nafion membranes (0.91 meq.$g^{-1}$) this copolymer of St:BuA is an interesting material for the fuel cell application.

The mechanical properties of the membranes were obtained from thermomechanical analysis (TMA). Figure 3 shows the valor of the modulus of elasticity obtained for the copolymers with and without sulfonation.

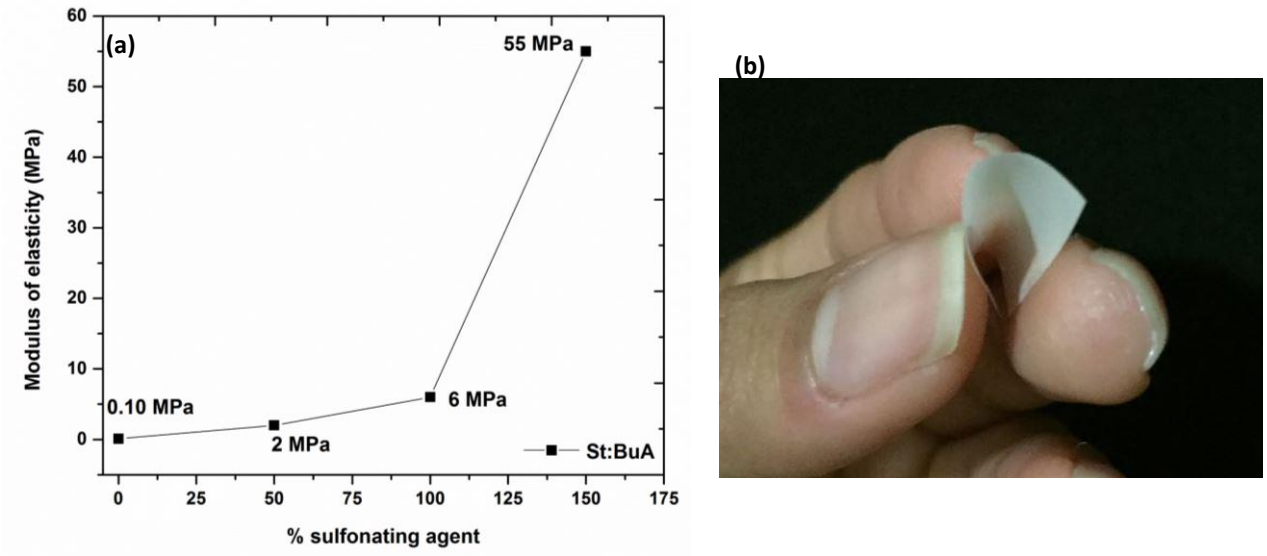


**Figure 3**. (a) Modulus of elasticity vs % sulfonating agent. (b) Picture of the membrane flexibility sSt:BuA 150%.

Figure 3 (a) indicate that as the concentration of sulfonating agent increases, an increase in the rigidity of the material occurs. That is may be associated to the presence of the sulphonic groups in the polymer, promoting less chain mobility, compared to the copolymer. Figure 3 (b) shows the flexibility of the membrane 150% sSt: BuA, with a favorable mechanical properties condition to use in cell devices.

The proton conductivity was measured under completely hydrated condition at room temperature. Nafion membrane was used as standard material, and Nyquist graph is shown in Figure 4.

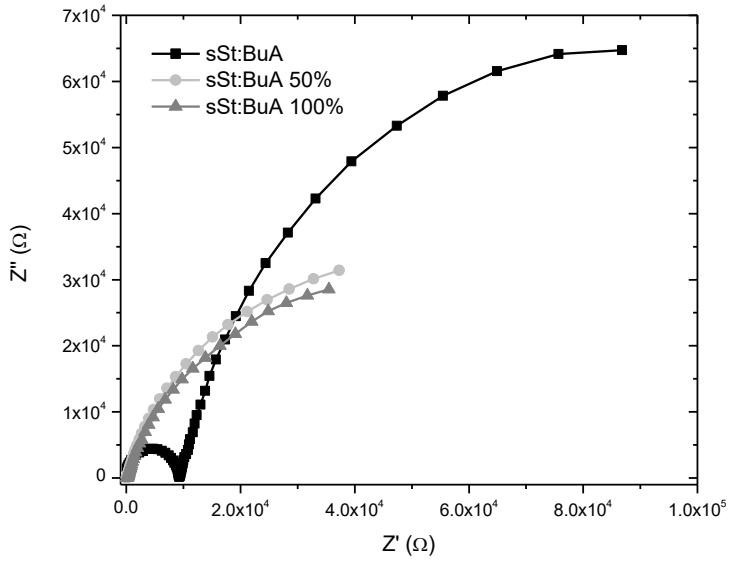


**Figure 4.** (a) Nyquist plot of copolymers St:BuA and sSt:BuA with 50 and 100% of sulfonating agent.

In order to understand the effect of sulfonating process on ionic conductivity processes, electrochemical impedance spectroscopy (EIS) experiments were carried out. The Nyquist plots in figure 4 under OCP conditions. sSt:BuA shows two semicircles, suggesting a particular process related with a different time constant. A lower ionic resistance with sSt:BuA 50% and sSt:BuA 100% was observed, which could be mainly due to its increased proton conduction and ion exchange capacity produced after the sulfonation process. Further, higher water retention from sulfonated material promotes increased transverse ionic conduction across of membrane.

## 4. Conclusion

The copolymers of sSt:BuA are synthetized successfully confirmed by NMR $^{1}H$ and FTIR. The sulfonation was confirmed from FTIR and the degree sulfonation was compared by titration and TGA analysis. The copolymer has good physicochemical characteristics as proton exchange membrane, as confirmed by IEC results (IEC = 1.18 meq.g$^{-1}$). The thermal properties showed good stability above of 300$^{o}$C.

## Acknowledgements

This work has been supported by the Mexican Council for Science and Technology (CONACyT) through grants 25910 and 270214. L. Francisco thanks to CONACyT for MSc Scholarship.

## References


[1] S. Banerjee and K. K. Kar, “Impact of degree of sulfonation on microstructure, thermal, thermomechanical and physicochemical properties of sulfonated poly ether ether ketone,” *Polymer (Guildf).*, vol. 109, pp. 176–186, Jan. 2017.

[2] C. M. Branco, S. Sharma, M. M. de Camargo Forte, and R. Steinberger-Wilckens, “New approaches towards novel composite and multilayer membranes for intermediate temperature-polymer electrolyte fuel cells and direct methanol fuel cells,” *J. Power Sources*, vol. 316, pp. 139–159, Jun. 2016.

[3] E. Moukheiber, G. De Moor, L. Flandin, and C. Bas, “Investigation of ionomer structure through its dependence on ion exchange capacity (IEC),” *J. Memb. Sci.*, vol. 389, pp. 294–304, 2012.

[4] ASTM, “tD790-03-Standard test method for flexural properties of unreinforced and reinforced plastics and electrical insulation materials,” 2015.

[5] T. A. Sherazi, S. Ahmad, M. A. Kashmiri, D. S. Kim, and M. D. Guiver, “Radiation-induced grafting of styrene onto ultra-high molecular weight polyethylene powder for polymer electrolyte fuel cell application,” *J. Memb. Sci.*, vol. 333, no. 1–2, pp. 59–67, May 2009.

[6] A. Basile, L. Paturzo, A. Iulianelli, I. Gatto, and E. Passalacqua, “Sulfonated PEEK-WC membranes for proton-exchange membrane fuel cell: Effect of the increasing level of sulfonation on electrochemical performances,” *J. Memb. Sci.*, vol. 281, no. 1, pp. 377–385, 2006.

[7] L. Unnikrishnan, S. K. Nayak, and S. Mohanty, “Polyethersulfone membranes : the effect of sulfonation on the properties,” *Polym. Plast. Technol. Eng.*, vol. 49:14, pp. 1419–1427, 2010.

[8] L. Unnikrishnan, S. Mohanty, and S. K. Nayak, “Proton exchange membranes from sulfonated poly (ether ether ketone) reinforced with silica nanoparticles,” *High Perform. Polym.*, vol. 25, no. 7, pp. 854–867, 2013.

# 9.17 Optimal resolution of SEM images for characterizing electrode materials

René Ledesma-Alonso, Jaime Ortegón, Romeli Barbosa-Pool

[1]CONACYT-Universidad de Quintana Roo, Boulevar Bahía s/n, Chetumal, 77019, Quintana Roo, México.

[2]Universidad de Quintana Roo, Boulevar Bahía s/n, Chetumal, 77019, Quintana Roo, México.

* Corresponding author: phone number – 983-156-6032

email – romelix1@gmail.com

## ABSTRACT

The characterization and reconstruction heterogeneous materials, such as porous media and electrode materials, involve the application of image processing methods to data acquired by SEM or other microscopy techniques. Among them, binarization and decimation are critical in order to compute the correlation functions that characterize the micro-structure of the above-mentioned materials. In this study, we present a theoretical analysis of the effects of the image size reduction, due to the sequential decimation of the original image. Three different decimation procedures (random, bilinear and bicubic) were implemented and their consequences on the discrete correlation functions (two-points, line-path and pore-size distribution), which are typically employed to characterize statistically and reconstruct heterogeneous materials, are reported and analyzed.

A normalization for each of the discrete correlation functions has been performed. When the loss of statistical information has not been significant for a decimated image, its normalized correlation function is forecast by the trend of the original image (reference function). In contrast, when the decimated image does not represent the statistical evidence of the original one, the normalized correlation function diverts from the reference function. Moreover, the addition of the average of the squared difference, between the discrete correlation functions of the decimated images and the reference functions, leads to a definition of an overall error. During the first stages of the sequential decimation, the error remains relatively small and independent of the decimation procedure. A power law with an exponent of around 1/8, describing the error as a function of the number of decimation steps, is observed. Once the statistical information is lost, the error becomes dependent of the decimation procedure and the exponent of the power law becomes larger, approaching the value of 3/4.

These results may help us to restrict the amount of information that one can afford to loss during a decimation process, in order to reduce the computational and memory cost, when

one aims to diminish the time consumed by a characterization or reconstruction technique, yet maintaining the statistical quality of the sample.

***Keywords:*** heterogeneous media; image resolution; correlation functions.

# 9.18 Reduced graphene oxide: effect of functional groups in the N-doping process and its ORR catalytic activity

N.M. Sánchez-Padilla, E. De-Casas, S. Fernández, R. Benavides, D. Morales-Acosta.

[1]Departamento de Procesos de Transformación de Plásticos, Centro de Investigación de Química Aplicada

[2]Laboratorio Nacional de Materiales Grafénicos, Centro de Investigación de Química Aplicada

Blvd Enrique Reyna No. 140, Col. San José de los Cerritos, 25290. Saltillo, Coahuila, México.

*E-mail: roberto.benavides@ciqa.edu.mx, diana.morales@ciqa.edu.mx

## ABSTRACT

Recently, graphene oxide (GO) doped with heteroatoms such as nitrogen (N-rGO) have attracted the attention to be used as alternative catalysts for the oxygen reduction reaction (ORR) in a fuel cell. The functional groups present in GO must play a critical role in the doping process with nitrogen. In this work, the effect of functional groups percentage in GO on the final N-doping reaction is presented. GO was synthesized by modified Tour's method using graphite as a precursor and two materials with different exfoliation degree were obtained. The N-doped reduced graphene oxide were prepared through a hydrothermal process carried out in an autoclave at 180 °C for 5 hours using amitrol as a nitrogen source; obtaining $DNrGO_{36}$ and $DNrGO_{43}$, respectively. These materials were characterizes through XRD, Raman spectroscopy and SEM-EDS. Furthermore, the catalytic activity for ORR was evaluated by means of cyclic voltammetry in alkaline media. The XRD patterns of the N-doped samples show a peak at ~26 °(2□) related to the plane (002) of graphite, suggesting the turbostatic re-stacking of graphene layers. Raman spectra show an increasing in the $I_D/I_G$ ratio and a downshift of the G peak of the N-doped graphene, comparing with GO, suggesting a successful doping process. Both materials are highly doped and have potential applications as cathodes for oxygen reduction reaction.

***Keywords:*** oxygen reduction reaction, fuel cells, n-doped graphene oxide.

## 1. Introduction

In the last decade, heteroatom-doped graphene has been studied as a promising electrocatalysts for oxygen reduction reaction (ORR)[1]. Heteroatoms like N, S, B and P have been considerate for modification of graphene[2]. Among of these, Nitrogen is one of the most used due to its similar atomic radius to carbon, which facilitates to the incorporation into carbon lattice[3]. Furthermore, the density functional theory (DFT) studies point out that N has the lower limit of overpotential (U) of the other heteroatoms (S, P, B)[2].

Graphene can be obtained by chemical exfoliation of graphite through oxidation process. The final product of this process is graphene oxide (GO) which is a single- or few-layer graphene with many oxygenated groups covalently bonded to carbon. The influence of the type and amount of oxygenated groups may have a critical role during doped process[4].

In this work, two N-doped graphene catalyst with different types of functional groups and different exfoliation degrees were synthesized. The results show that a higher content of stable oxygenated groups and a higher exfoliation degree has a positive effect in the material's catalytic activity for ORR.

## 2. Materials and Methods

Graphene oxide (GO) was synthetized by Tour's method. Typically, graphite powder was dispersed in concentrated mixture $H_2SO_4$:$H_3PO_4$ (9:1 volume ratio) and sonicated for 30 minutes. Then, the dispersion was placed in an ice bath and $KMnO_4$ (3:1 mass ratio respect graphite) were slowly added. The temperature was raised to 69 °C for 30 minutes. The reaction was cooled to room temperature and water was added (1.5:1 volume ratio respect volume of the acid mixture) and continuous stirring for 48 hours. A solution of 3 % $H_2O_2$ solution was added, in order to stop the reaction. The resulting solution was centrifuge and successively washed with water and ethanol to neutral pH and dried. The resulting material was labeled as $GO_{36}$. As comparative, a GO with different exfoliation degree ($GO_{43}$) were provided by Graphene Materials National Laboratory (LMNG).

A mixture that contains GO and 3-amino-1,2,4-triazole (as N source) in a 1:5 mass ratio was hydrothermally treated in a autoclave at 180 °C for 5 h. At the end of the reaction time, the autoclave was allowed to cool down to room temperature. The product was washed and dried at 80 °C for 24 h. The resulting materials were labeled as $DNrGO_{36}$ and $DNrGO_{43}$.

The catalytic activity of doped materials was evaluated for ORR in a SP-300 (Biologic) potenciostat connected to a RDE (Pine Inst.) in a three- electrode system. A modified-glassy was used as working electrode, carbon Pt wire as counter electrode, while Ag/AgCl serve as reference. The working electrode was prepared from catalytic ink as follows: the catalyst powder was dispersed in isopropanol and Nafion (5 □L) by ultrasound to form an

ink with catalyst loading of 10 mg $mL^{-1}$. Then, an aliquot of 20 □L of catalytic ink was deposited onto glassy carbon disk (0.196 $cm^2$ geometrical area), previously polished until mirror-finished surface. After drying, the working electrodes were obtained. All experiments were carried out in alkaline media (0.1 M KOH). After 50 cycles at 50 mV $s^{-1}$ cyclic voltammetry (CV) activation and CV profile at 20 mV $s^{-1}$, the ORR activity was measured at different rotation rates (400, 800, 1200, 1600 and 2000 rpm) in a $O_2$-saturated electrolyte.

## 3. Results and Discussion

Fig. 1 shows the experimental diffraction patterns from the graphite precursor (a), the synthetized materials $GO_{36}$ (b) and $GO_{43}$ (c), and doped materials $DNrGO_{36}$ (d) and $DNrGO_{43}$. The graphite precursor (Fig. 1a) shows a sharp peak at 26.5 °2□, related to the (002) plane of graphite (JCPDS 41-1487) with an interlayer spacing ($d_{(002)}$) of 0.335 nm. For $GO_{36}$ sample (Fig. 1b), a shift to smaller angles (10.65 °2□) of the (002) plane indicates an increment in the $d_{(002)}$ until 0.829 nm due to the exfoliation of graphite sheets caused during the oxidation process[5]. A second peak although low intensity at 26.5 °2□ indicates that a small fraction of graphite remains unoxidized. For $GO_{43}$ sample (Fig. 1c) the downshift is greater than $GO_{36}$ (9.58 °2□) with $d_{(002)}$=0.923 nm. The greater $d_{(002)}$ value in $GO_{43}$ indicated that $GO_{36}$ was more exfoliated during Tour's method[6]. After the hydrothermal treatment and doping, the experimental pattern shows the reappearance of a broad peak near to 25°2□ ((002) plane of graphite). This is due to the reduction process that cause a rehybridization $sp^3$□$sp^2$ from GO to its reduce form rGO.

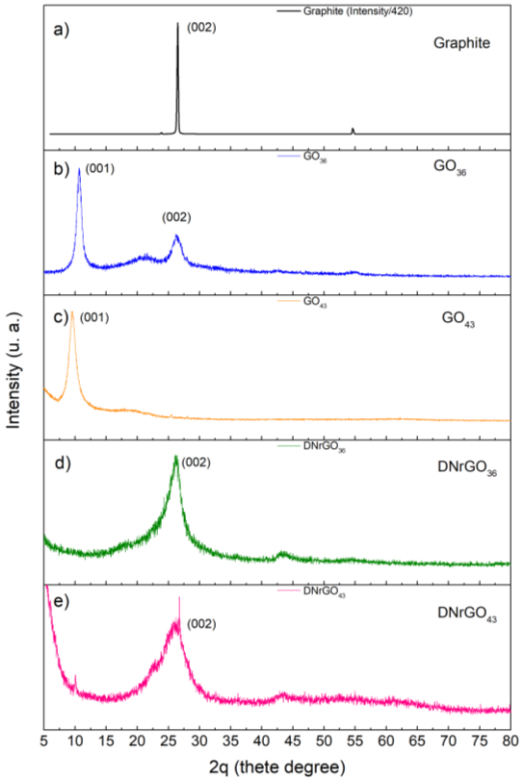


**Figure 7.** Difractograms of a) graphite, b) $GO_{36}$, c) $GO_{43}$, d) $DNrGO_{36}$ and e) $DNrGO_{43}$.

Fig. 2 shows the FT-IR spectra for the starting materials ($GO_{43}$ and $GO_{36}$) and after both hydrothermal and doping processes ($DNrGO_{36}$ and $DNrGO_{43}$). For $GO_{43}$ and $GO_{36}$ the same five bands are observed, corresponding to the functional groups incorporated due to the oxidation process. A broad peak between 3000 and 3700 $cm^{-1}$ is commonly attributed to stretching modes from hydroxyl groups (O-H). At 1750 $cm^{-1}$ the band can be associated to stretching vibration of carbonyl group (C=O) and at 1630 $cm^{-1}$, stretching modes for C=C or vibration of aromatics related to $sp^2$ hybridization in GO. More peaks can be identified including C-O stretching vibration (at 1070 $cm^{-1}$) and stretching vibrations in epoxides (C-O-C at 850 $cm^{-1}$)[7]. For $DNrGO_{36}$ and $DNrGO_{43}$, the displacement of the band related with C=C (1630 $cm^{-1}$), suggests the incorporation of N in the carbon lattice due the overlapping of the vibrations of C=C and C=N (1560 $cm^{-1}$)[8]. Also, the appearance of a band at 1200 $cm^{-1}$ related to the C-N bond suggests that the N atoms were covalently bonded to graphene lattice.

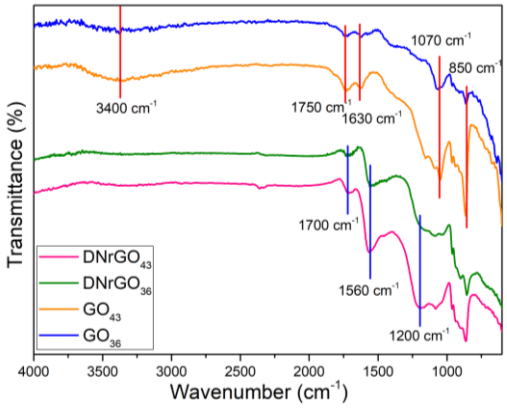


**Figure 8.** FT-IR spectra of $GO_{36}$, $GO_{43}$, $DNrGO_{36}$ and $DNrGO_{43}$.

TGA curves are shown in Fig. 3. For $GO_{36}$ and $GO_{43}$ a major weight loss close at ~150 °C is observed, due to the release of labile functional groups incorporated to GO [9]. A second weight loss between 220 and 600 °C, is related with the pyrolysis of more stable oxygen containing groups. For $GO_{36}$ the first weight loss belongs to 36.7 %, while for $GO_{43}$ is lower (30 %). The second weight loss is 6 and 11 %, for $GO_{36}$ and $GO_{43,}$ respectively. The above indicate that $GO_{43}$ has more stable functional groups than $GO_{36}$. For $DNrGO_{36}$ and $DNrGO_{43}$, a slight weigh loss is observed between 25 and 600 °C indicating an improved thermal stability due to the hydrothermal treatment and the doping process suggesting a successful covalent functionalization with N[10].

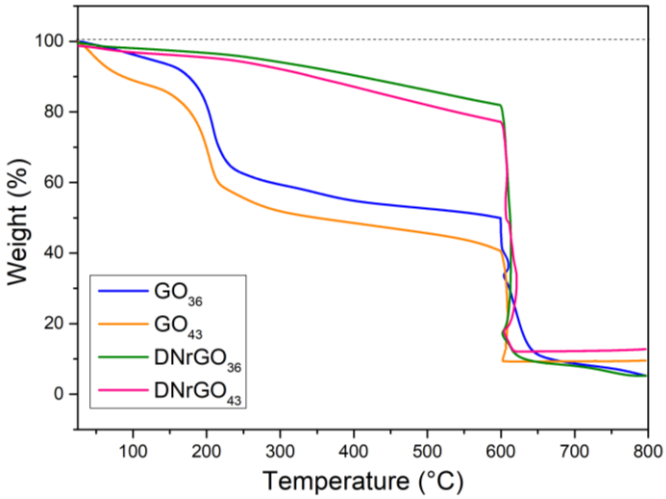


**Figure 9.** TGA curves of $GO_{36}$, $GO_{43}$, $DNrGO_{36}$ and $DNrGO_{43}$.

Fig. 4 shows the cyclic voltammograms of $DNrGO_{36}$ and $DNrGO_{43}$. Both materials shows a near-rectangular shape voltammogram which can be related to the increment in

the surface area after the N-doping process, this is due to N atoms in a carbon lattice improve the wettability of the material enhancing the electrochemical performance for redox reactions[11]. $DNrGO_{43}$ shows a reversible humps ~0.4 V related to the contribution of remaining oxygen groups in the surface of the material. The insert in Fig. 4 shows the CV for $GO_{36}$ and $GO_{43}$ which has current densities in the order of □A $cm^{-2}$ and two signals in 0.82 V and 0.65 V associated to electrooxidation of quinone-hydroquinone groups in the carbon surfaces[12]. The increment in current density of N-doped materials confirms the successfully N-doping process. The observed results suggest that on $DNrGO_{43}$ the charge transference processes are more efficient than $DNrGO_{36}$.

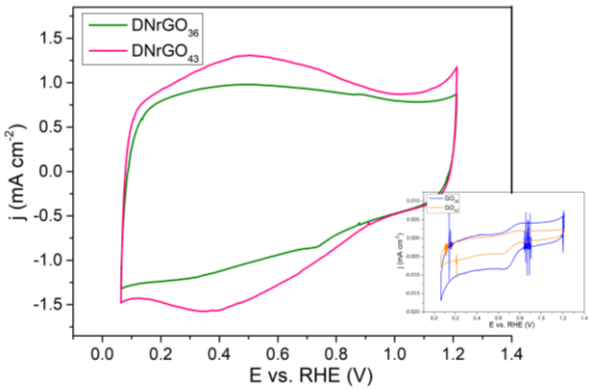


**Figure 10.** Cyclic voltammograms of $GO_{36}$, $GO_{43}$, $DNrGO_{36}$ and $DNrGO_{43}$. Electrolyte: KOH 0.1 M $N_2$-saturated, □ = 20 mV $s^{-1}$.

The polarization curves at 2000 rpm are shown in Fig. 5. The capability of all materials for ORR is confirmed and three distinguishable potential regions are revealed: kinetic (E > 0.8 V), mixed (0.6 < E < 0.8) and diffusion controlled (E < 0.6 V). $GO_{36}$ and $GO_{43}$ exhibits a similar onset potential value ($E_{ORR}$) 0.8 V and a current density (J) of 0.7 and 0.5 mA $cm^{-2}$, respectively. For nitrogen-doped reduced graphene oxide materials the $E_{ORR}$ decrease at 0.87 V, and J increased considerably 4.5 mA $cm^{-2}$ for $DNrGO_{43}$ and 3.7 mA $cm^{-2}$ and $DNrGO_{36}$. The remarkably enhancement of doped materials confirms the successes incorporation of N-atoms in the C-lattice. Furthermore, the higher J recorded at $DNrGO_{43}$ electrode, suggests that a higher exfoliation degree in $GO_{43}$ facilitate the N-doped compared to $DNrGO_{36}$. The electrochemical behavior of $DNrGO_{43}$ and $DNrGO_{36}$ for RRO is comparable with previously reported for cathodes based on Pt[13], indicating that they are potential candidates for the replacement of catalysts based on Noble metals.

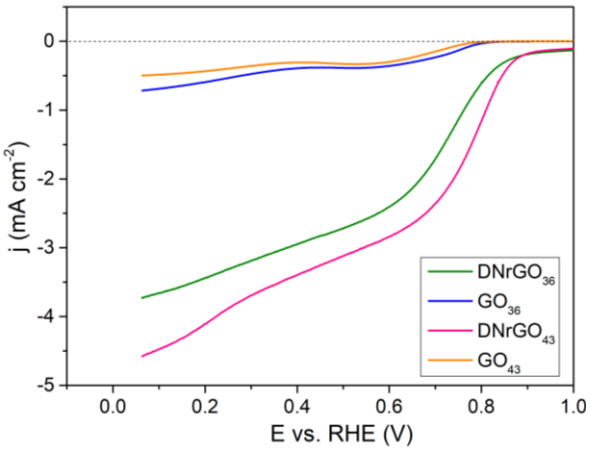


**Figure 11.** Polarization curves of $GO_{36}$, $GO_{43}$, $DNrGO_{36}$ and $DNrGO_{43}$. Electrolyte: KOH 0.1 M $O_2$-saturated, □□□ 2000 rpm, □ = 5 mV $s^{-1}$.

## 4. Conclusion

Two N-doped graphene catalyst were successfully synthetized through a hydrothermal route. A high current density was observed for both materials in comparison with un-doped GO materials. Nevertheless, $DNrGO_{43}$ shows a higher value of onset potential (0.87 V) and higher current density (4.5 mA $cm^{-2}$) than $DNrGO_{36}$ which suggests that the degree of exfoliation and the type of functional groups in GO has a big role in N-doping process.

## Acknowledgements

The authors are grateful to the National Council of Science and Technology (Conacyt) through the 259010, 270214. NMSP is thankful to Conacyt for the PhD scholarship. Authors also are grateful to Graphene Materials National Laboratory (LNMG) to the facilities provided for the use of some of its installations.

## References

[1] R. Ma, X. Ren, B.Y. Xia, Y. Zhou, C. Sun, Q. Liu, et al., Novel synthesis of N-doped graphene as an efficient electrocatalyst towards oxygen reduction, Nano Res. 9 (2016) 808–819. doi:10.1007/s12274-015-0960-2.

[2] Z. Zhao, M. Li, L. Zhang, L. Dai, Z. Xia, Design Principles for Heteroatom-Doped Carbon Nanomaterials as Highly Efficient Catalysts for Fuel Cells and Metal-Air Batteries, Adv. Mater. 27 (2015) 6834–6840. doi:10.1002/adma.201503211.

[3] B. Grzyb, S. Gryglewicz, A. Sliwak, N. Diez, J. Machnikowski, G. Gryglewicz, Guanidine, amitrole and imidazole as nitrogen dopants for the synthesis of N-graphenes, RSC Adv. 6

(2016) 15782–15787. doi:10.1039/C5RA24624E.

[4] Y. Chen, B. Xie, Y. Ren, M. Yu, Y. Qu, T. Xie, et al., Designed nitrogen doping of few-layer graphene functionalized by selective oxygenic groups, Nanoscale Res. Lett. 9 (2014) 646. doi:10.1186/1556-276X-9-646.

[5] C. Botas, P. ??Lvarez, P. Blanco, M. Granda, C. Blanco, R. Santamar??a, et al., Graphene materials with different structures prepared from the same graphite by the Hummers and Brodie methods, Carbon N. Y. 65 (2013) 156–164. doi:10.1016/j.carbon.2013.08.009.

[6] D.C. Marcano, D. V. Kosynkin, J.M. Berlin, A. Sinitskii, Z. Sun, A. Slesarev, et al., Improved synthesis of graphene oxide, ACS Nano. 4 (2010) 4806–4814. doi:10.1021/nn1006368.

[7] J. Chen, B. Yao, C. Li, G. Shi, An improved Hummers method for eco-friendly synthesis of graphene oxide, Carbon N. Y. 64 (2013) 225–229. doi:10.1016/j.carbon.2013.07.055.

[8] Y.K. Zhang, Z. Sun, H. Wang, Y.D. Wang, M. Liang, S. Xue, Nitrogen-doped graphene as a cathode material for dye-sensitized solar cells: effects of hydrothermal reaction and annealing on electrocatalytic performance, RSC Adv. 5 (2015) 10430–10439. doi:10.1039/c4ra13224f.

[9] M. Fan, C. Zhu, J. Yang, D. Sun, Facile self-assembly N-doped graphene quantum dots/graphene for oxygen reduction reaction, Electrochim. Acta. 216 (2016) 102–109. doi:10.1016/j.electacta.2016.09.014.

[10] M. Barrejón, A. Primo, M.J. Gómez-Escalonilla, J.L.G. Fierro, H. García, F. Langa, Covalent functionalization of N-doped graphene by N-alkylation, Chem. Commun. 51 (2015) 16916–16919. doi:10.1039/C5CC06285C.

[11] A. Śliwak, B. Grzyb, N. Díez, G. Gryglewicz, Nitrogen-doped reduced graphene oxide as electrode material for high rate supercapacitors, Appl. Surf. Sci. 399 (2017) 265–271. doi:10.1016/j.apsusc.2016.12.060.

[12] K. Kinoshita, J.A.S. Bett, Potentiodynamic analysis of surface oxides on carbon blacks, Carbon N. Y. 11 (1973) 403–411. doi:10.1016/0008-6223(73)90080-8.

[13] N.M. Sánchez-Padilla, D. Morales-Acosta, M.D. Morales-Acosta, S.M. Montemayor, F.J. Rodríguez-Varela, Catalytic activity and selectivity for the ORR of rapidly synthesized M@Pt (M = Pd, Fe3O4, Ru) core–shell nanostructures, Int. J. Hydrogen Energy. (2014) 1–9. doi:10.1016/j.ijhydene.2014.03.223.

# 9.19 Opportunities of porous silicon in energy renewable technology applications

Edith Osorio, René Ledesma, Beatriz Escobar and Romeli Barbosa

[1]CONACYT-Universidad de Quintana Roo, Boulevard Bahía s/n esq. Ignacio Comonfort, C.P. 77019, Chetumal, Quintana Roo, México.

[2] CONACYT, Centro de Investigación Científica de Yucatán, Carretera Sierra Papacal– Chuburná Puerto, Km. 5, Sierra Papacal, Mérida 97302, México

[3] Universidad de Quintana Roo, Boulevard Bahía s/n esq. Ignacio Comonfort, C.P. 77019, Chetumal, Quintana Roo, México.

---

## ABSTRACT

Technologies for utilizing hydrogen as clean source of energy are considered to assume an important position in order to overcome problems of lack of energy and environment in future. The storage energy or of reduced-size devices constitutes the crucial points in the development of the hydrogen technology. In particular, reduced-size of fuel cells can offer a possibility in the field of small energy sources. Proton exchange membrane-type fuel cell is alternative and attractive option for production of clean energy for portable and transportation applications. Many silicon-based technologies can be used to perform micro-fuel cells and, in particular, porous silicon. This material is a nanocomposite promised to use in hydrogen technology to versatility and compatible with micro-fabrication technology. Moreover, high porosity of porous silicon and very large surface-to-volume ratio ensures the high proton conductivity comparable with that of polymer membrane. In the other hand, porous silicon is material has been a natural candidate to be used as an anode active material for batteries, due which contain “preset” voids to accommodate volume expansion of the Si particles so that the dimensional variations of the entire electrode layer can be mitigated. In this work, we describe the state of the art of porous silicon integration in micro-fuel cells and storage energy. We show how porous silicon has arisen as a promising material to perform many functions necessary to the core fuel cell such as proton exchange membrane, gas diffusion layer and catalyst support. The performances of the several final devices reported in the literature are discussed.

***Keywords:*** porous silicon; hydrogen technology

# 9.20 Heterostructured materials synthesized via AACVD applied for direct water splitting irradiated with an AAA solar Simulator

P. Pizá-Ruiz, A. Sáenz-Trevizo, Y. Verde-Gómez, V. Collins-Martínez, M. Meléndez-Zaragoza , J. Salinas- Gutiérrez , and M. Miki-Yoshida

[a] Centro de Investigación en Materiales Avanzados S.C., Miguel de Cervantes 120, C.P. 31136, Chihuahua, Chihuahua, México

[b] Instituto Tecnológico de Cancún, Ave. Kabah, Km. 3, C.P. 77515, Cancún, Quintana Roo, México

* 52-614-4391114, Mario.miki@cimav.edu.mx

## ABSTRACT

Binary metal oxides have been recently applied for electrocatalytic and photocatalytic water splitting. Common metal oxides are synthesized using earth's crust abundant elements such as Ti, Cu, Fe and Zn in order to reduce costs.On the other hand, ternary oxides as those of the delafossite group, have also proved to be suitable for direct water splitting. In either case, metal oxide materials intend to replace the utilization of noble metals for the generation of $H_2$. According to literature, the efficiencies obtained using noble metal nanoparticles, carbon based materials or several metal oxides coupled in a tandem configuration are superior than those obtained using a single metal oxide layer. Nevertheless, the synthesis process often requires the utilization of various techniques in order to obtain the desired heterostructured configuration. Besides, since surface area plays a determining role in direct water splitting, it is believed that the utilization of various nanostructured morphologies will result in an increase of the $H_2$ production.

Hence, this work presents an heterostructured material comprised of different layers distributed onto borosilicate glass following this order: BGS/$TiO_2$/ZnO/$CuFeO_2$/$SnO_2$/Pt. Zinc oxide was grown following a nanorod morphology while Pt was synthesized in the form of nanoparticles. All nanostructured layers were synthesized by a sequential five-stage method using solely the aerosol assisted CVD technique. The synthesized sample was characterized by means of electron microscopy, UV-Vis-Nir spectroscopy and grazing incidence x-ray diffraction. A customized batch reactor was used to measure the $H_2$ produced when the sample was immersed into a solution of water and 2% of methanol and irradiated with an AAA solar simulator. The obtained efficiencies were compared to those using individual layers of $TiO_2$, $TiO_2$/$CuFeO_2$ and $TiO_2$/$CuFeO_2$/$SnO_2$.

***Keywords:*** Direct Water Splitting, Delafossite, AACVD

# 9.21 Use of the $Ti_xCu_yO_z$ oxide catalyst in water electrolysis

A. Velázquez-Osorio; J.L. Reyes-Rodríguez; F.D. Fernández-Galván; O. Solorza-Feria; H.Yee-Madeira

[1]Escuela Superior de Física y Matemáticas - Instituto Politécnico Nacional SN, Av. Instituto Politécnico Nacional SN, U.P. Adolfo López Mateos, San Pedro Zacatenco, De. Gustavo A. Madero, 07738, CDMX. Mexico.

[2]Centro de Investigación y Estudios Avanzados CINVESTAV-IPN, Av. Instituto Politécnico Nacional 2508, San Pedro Zacatenco, Del. Gustavo A. Madero, 07738, CDMX. Mexico

* Corresponding author: +52-55-5729-6000 ext. 55156, contact@adrianvelazquez.com

---

## ABSTRACT

Transition from fossil fuels to renewable energy is of paramount importance to halt the growing pollution associated to conventional energy production. A long-term and sustainable alternative to fossil fuels is the use of fuel cell technology. Fuel cells are devices capable of transforming chemical energy into electricity in a very clean and efficient manner. However, their operation is conditioned by the continuous supply of oxygen O2, and hydrogen H2. Presently, these gasses are obtained from complex and contaminant gas reformation and purification processes. Through water electrolysis, it is possible to produce O2 and H2 without the harmful carbon emissions implicit to gas reformation. A challenge in mass electrolysis implementation is that electrolyzers require the use of catalytic materials; often transition metal groups like Pt, Pd, and Ir are used. However, their scarcity and restrictive costs limit the possibilities of water electrolysis. This work presents a synthesis of a $Ti_xCu_yO_z$ catalyst with excellent activity compared to pure platinum in the oxygen evolution reaction. High-energy ball milling of Ti and Cu powders was performed for 2, 4, 6, 8, and 10 h; afterwards, the milled powders were subjected to a thermal treatment at air atmosphere and characterized through X-Ray diffraction (XRD), scanning electron microscopy (SEM), elemental chemical characterization (SEM-EDS), and voltammetries (cyclic, linear, and cronoamperometry).

***Keywords:*** $Ti_xCu_yO_z$ catalyst, oxygen, electrolysis

# 9.22 Synthesis and characterization of ni-mo$_2$c catalysts supported on hydroxyapatite for hydrogen production reactions

Jonathan Jesús Malpica Maldonado, José Aarón Melo Banda, Ana Lidia Martínez Salazar, Margarita García Hernández

[1] Centro de Investigación en Petroquímica Secundaria, Instituto Tecnológico de Ciudad Madero, Prol. Bahía del Aldair, Av. de las Bahías. Parque Industrial Tecnia, Altamira, Tamaulipas, México, 89608.

*833-261-13-32, jonathan-jesus15@hotmail.com

## ABSTRACT

The search for new catalytic material to hydrogen production is very important for generation of new more efficient process and low cost. On the other hand, biomass is a renewable source for hydrogen production by green methods. Also, the green methods for hydrogen production are not emitting greenhouse gases. So, these methods can be considered friendly with the environment. Several studies have demonstrated Ni-$Mo_2C$ catalysts exhibits high activity and selectivity in hydrogen production processes. While the molybdenum carbide has shown a catalytic behavior similar as some noble metals, the loads of nickel act as a promoter increasing selectivity and stability of the materials.

In this research, Ni-$Mo_2C$ nanoparticles were synthesized by carburization of nickel and molybdenum oxides as precursors using sucrose as a carbon source. The carburization condition was varied in function of temperature (873 K to 1073 K), under Ar/$H_2$ flow. Hydroxyapatite was used as a support due its main constituent is CaO, which improve selectivity by CO adsorption capacity in the cases of hydrogen production processes with CO presence as a byproduct. All samples were characterized by Infrared Spectroscopy with Fourier Transform (FTIR), Scanning Transmission Electron Microscopy (STEM) and X-Ray Diffraction (XRD) to confirm the structure of the nanoparticles and observe the effects of thermal treatment in the thermal stability of the materials. The catalyst Ni-$Mo_2C$ supported on hydroxyapatite could be a very well option to be used in green processes for hydrogen production. The properties of active phase and the properties catalytic support make the catalytic material have excellent thermal and mechanical stability.

***Keywords :*** Ni-$Mo_2C$ Catalyst, $Mo_2C$ nanoparticule, hydrogen production, hydroxyapatite.

## 1. Introduction

The necessity of use more energy every day, is a big problem because in the actually the most used energy sources are hydrocarbons. The use of hydrocarbons increases greenhouse gases by the combustion of hydrocarbons. Hydrogen could be an alternative energy source from renewable resources, also, the use hydrogen as clean fuels has benefits in the environment, because it doesn´t emit greenhouse gases.

The main processes for hydrogen production implicate the use hydrocarbons; being the natural gas the main source for hydrogen production through reforming steam methane [1-2].

Transition metal carbides have shown a special catalytic behavior similar to the noble metals [3-5]. Transition metals carbide have been using at extreme conditions of pressure and temperature [6]. The use at extreme conditions of these carbides is because of their great strength and durability. The physical and mechanical properties of carbides are similar to that of ceramic.

The physical and chemical properties of transition metal carbides including high thermal stability and mechanical hardness, superconductivity and show catalytic activity similar to those of metals noble in various catalytic reaction for hydrogen production as methane reforming, conversion biomass, water gas shift reaction, among other reaction [5,7].

The actual methods for the synthesis of molybdenum carbide involve direct carbonization of molybdenum at high temperature (> 1000 °C). Some authors [8,9] studied the effect of temperature on the synthesis of molybdenum carbide and concluded that the optimum temperature for the synthesis of molybdenum carbide is around 800 °C.

The modification of traditional catalysts $Mo_2C$ with Ni shows an increase in thermal and mechanical stability, as well as in the catalytic activity of materials. The catalytic activity increase respect to the increases in the amount of Ni, but the Ni increase causes an oxidation of the material [10].

Some research [11 - 14] shows the use of calcium oxide to remove emissions of $CO_2$ in reaction for hydrogen production, also, CaO increase the hydrogen production. On the other hand, materials as hydroxyapatite have a high content of calcium oxide [15] and other compounds that give a high mechanical and thermal stability.

## 2. Materials and Methods

### 2.1 Preparation of $Mo_2C$

The preparation of $Mo_2C$ precursors were prepared by an aqueous solution of ammonium heptamolybdate tetrahydrate [$(NH_4)_6Mo_7O_{24}$ $4H_2O$] and an aqueous solution of sucrose with a molar ratio of C/Mo = 2 to form the hexagonal crystalline

structure of molybdenum carbide (β-$Mo_2C$) [16,17]. Then homogenize the two solutions the sucrose solution was added over ammonium heptamolybdate tetrahydrate solution stirring constantly for 15 min. the final solution was dried at room temperature at 120 °C for 24 h.

The $Mo_2C$ precursors were thermally treated in situ in a quartz fix bed reactor under a reducing atmosphere of $Ar/H_2$ to get $Mo_2C$. The temperature was increased linearly at ₁0 °C/min, the conditions of reactor are show in the table 1.

**Table 1.** Carburization conditions used on the quartz fix bed reactor on $Mo_2C$ precursors

| Sample | Temperature (°C) | Pressure (atm) | Flow ($Ar/H_2$) (l/min) | Ramp (°C/min) | Time (min) |
|---|---|---|---|---|---|
| **1** | 700 | 1 | 4 | 10 | 120 |
| **2** | 800 | 1 | 4 | 10 | 120 |
| **3** | 900 | 1 | 4 | 10 | 120 |

## 2.2 Preparation of Ni-$Mo_2C$ catalysts

The synthesis of Ni-$Mo_2C$ is similar to $Mo_2C$. The Ni-$Mo_2C$ precursors were prepared by aqueous solution using nickel nitrate dihydrate as source of nickel. The load of nickel on the materials is 15 wt% and molar ratio C/Mo = 2. The nickel solution was added over ammonium heptamolybdate tetrahydrate solution stirring constantly for 4 h. the final solution was dried at temperature room at 120 °C for 24 h

The powder was dissolved using the minimum amount of water possible. The solution of sucrose was added over powder solution stirring constantly for 1 h the final solution was dried at temperature room at 120 °C for 24 h

The $Mo_2C$ precursors were thermally treated in situ in a quartz fix bed reactor under a reducing atmosphere of $Ar/H_2$ to get Ni-$Mo_2C$. The temperature was increase linearly at of 10 °C/min, for 2 h and the temperature of reactor was 800 °C.

## 2.3 Extraction of hydroxyapatite

For extraction of hydroxyapatite were used bovine bones following the methodology of C.K. Rojas-Mayorga [18] by thermal decomposition.

### 2.3.1 Bovine bone preparation

The bovine bones were cleansed by water and acetone to remove the impurities and fasts. After clean the bovine bones were reduced to size of 1 mm. The powder was dried at 120 for 24 h The bovine bones were thermally treated (pyrolysis) in quartz reactor by synthesis of bone char. The synthesis of bone char needs specific condition of heating rate, temperature and time of thermal treatment. For the pyrolysis process, nitrogen gas (400 ml/min) was used to

provide an inert atmosphere during the thermal treatment. The conditions of synthesis are show in table 2.

**Table 2**. Synthesis of hydroxyapatite

| Sample | Temperature (°c) | Pressure (atm) | Flow ($Ar/H_2$) (ml/min) | Ramp (°c/min) | Time (min) |
|---|---|---|---|---|---|
| **1** | 700 | 1 | 400 | 10 | 120 |
| **2** | 800 | 1 | 400 | 10 | 120 |
| **3** | 900 | 1 | 400 | 10 | 120 |

## 3. Results and Discussion

### 3.1 X-ray diffraction

Fig. 1 shows the experimental x-ray diffraction patterns of $Mo_2C$ synthesized at different temperature of carbonization and also shows the experimental x-ray diffraction patterns of $Mo_2C$ precursor.

According with the fig. 1 the experimental x-ray diffraction patterns correspond with hexagonal structure of $Mo_2C$ [17]. $Mo_2C$ presented XRD patterns with different diffraction peaks at 34.40°, 38.10°, 52.26°, 61.78°, 69.77°, 74.94° and 75.98 of 2θ, corresponding to the (021), (200), (221), (023), (321), (223) and (104) diffraction planes. The crystallite size was calculated with Scherrer Equation; the table 3 shows the crystallite size of $Mo_2C$ sample at different carbonization temperature.

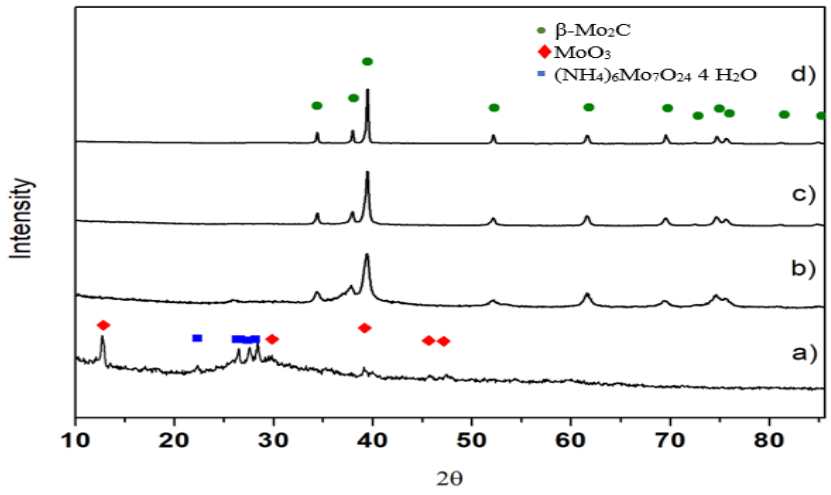


**Fig. 1**. Experimental X-ray diffraction patterns of $Mo_2C$ a) $Mo_2C$ precursor b) $Mo_2C$ synthesized at 700 °C, c) $Mo_2C$

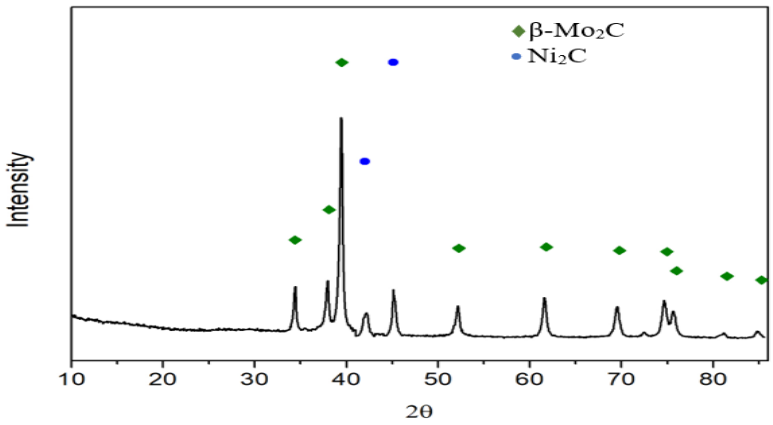


Table 3. Crystallite Size of $Mo_2C$

| Sample | Temperature (°c) | Crystallite size (nm) |
|---|---|---|
| **1** | 700 | 1.9335 |
| **2** | 800 | 3.6169 |
| **3** | 900 | 5.7199 |

Also, the experimental x-ray diffraction patterns of $Mo_2C$ show a high thermal stability by showing the same diffraction patterns at different temperature synthesis

of $Mo_2C$. According to Malinee Kaewpanha et al. [19] the optimal temperature to synthesis of $Mo_2C$ is at 800 °C.

Fig. 2 shows the experimental x-ray diffraction pattern of Ni-$Mo_2C$ synthesized at 800 °C. According with experimental x-ray diffraction patterns the crystalline structure of $Mo_2C$ corresponds with hexagonal. Also, the experimental x-ray diffraction patterns show that the crystalline structure of $Ni_3C$ correspond with hexagonal.

Fig. 3 shows the experimental x-ray diffraction pattern of hydroxyapatite extracted from bovine bone and heat treatment at different temperature.

The XRD patterns show a gradual increase in the degree of sharpness of peak with heat treatment [15]. P. Shipman [20] reported that results of XRD patterns in terms of alteration in crystal size. They found that there was gradual increase in hydroxyapatite crystal size associated with increased heat-treating temperature. This alteration in hydroxyapatite crystal size could be for a recrystallization [15].

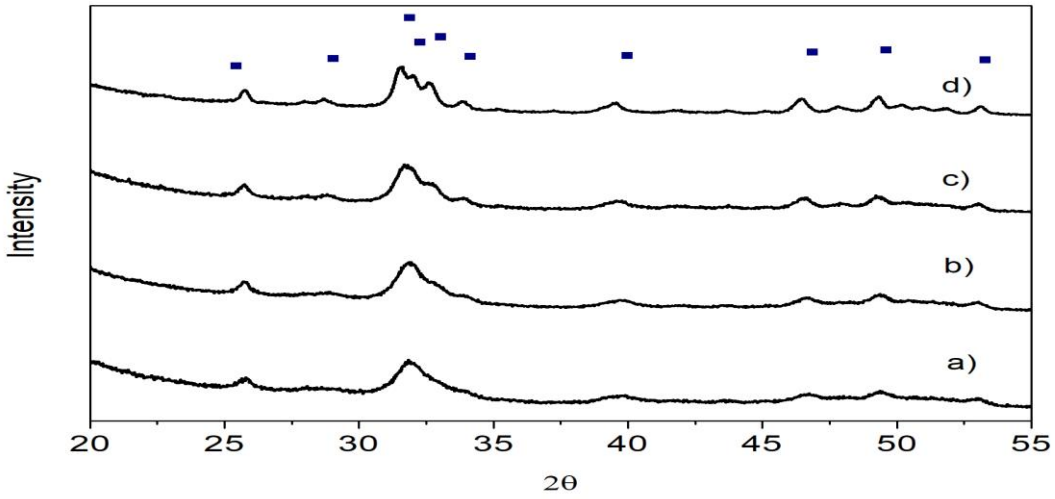


**Fig. 3.** Experimental X-ray patterns diffraction of precursor and bone chars obtained at different pyrolysis

### 3.2 FT-IR analysis

The FT-IR spectra show a decomposition of organic material and a dihydroxylation on bovine bone by effect of heat treatment staring at 700 °C. But the structure remains almost point Fig. 4 shows spectra of bovine bones and bone char after the pyrolysis process, and In table 4 shows the compounds / bond of FT-IR spectrum.

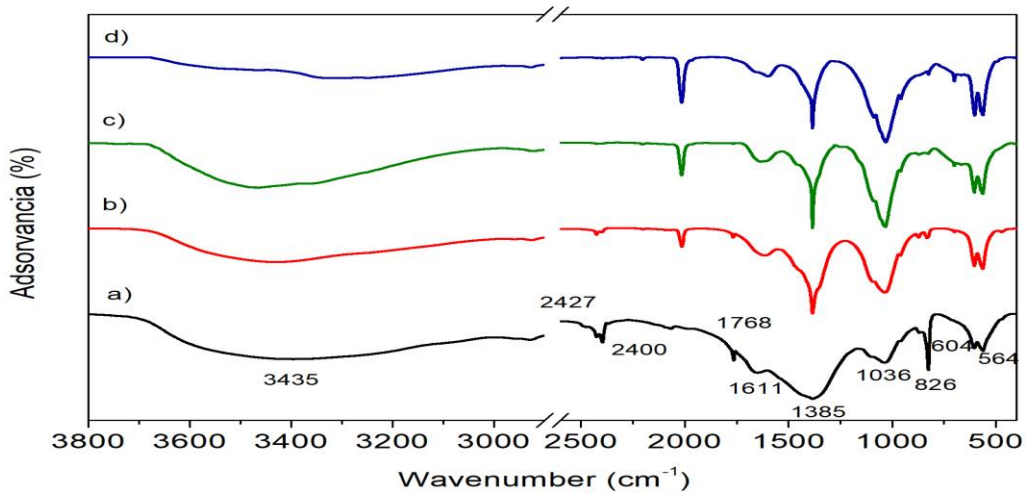


**Fig. 4**. FT-IR spectra of precursor and bone chars obtained at different pyrolysis temperature. a).

**Table 4**. bands of FT-IR spectra

| Band ($cm^{-1}$) | Bond | Band ($cm^{-1}$) | Bond |
|---|---|---|---|
| 3435 | Group O-H | 826 | $CO_3^{-2}$ |
| 2427 | P | 604 | $PO_4^{-3}$ |
| 2400 | P | 564 | $CO_3^{-2}$ |
| 1768 | -C=O | ---- | -- |
| 1611 | -NH | ---- | -- |
| 1385 | $CO_3^{-2}$ | ---- | -- |
| 1036 | $PO_4^{-3}$ | ---- | --- |

## 3.3 Scanning Electron Microscopy (SEM) and Energy-dispersive X-ray spectroscopy analysis

Fig. 5 shows the SEM images and EDS analysis of samples $Mo_2C$ synthesized at different temperature. As it can be seen in the figure 5 the carbide is composed of large particle which seem the particles to be covered with some small particles.

The EDS analysis shows the composition of three samples corresponds to molybdenum carbide. The Results of EDS are shows in table 5.

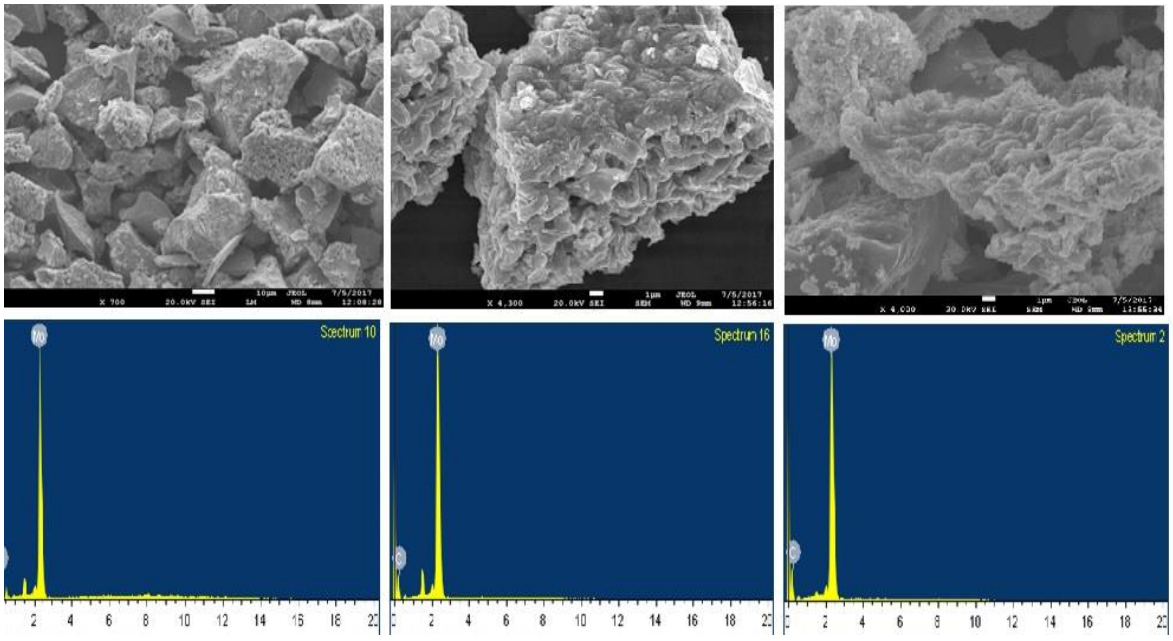


a) b) c)

**Fig. 5.** SEM images and EDS analysis of $Mo_2C$ samples synthesized at different temperature. a) $Mo_2C$T-700

**Table 5.** EDS analysis of $Mo_2C$ samples.

| *Sample* | *Element* | *Weight%* | *Atomic%* |
|---|---|---|---|
| *a)* | Mo | 80.70 | 34.29 |
| | C | 19.30 | 65.31 |
| *b)* | Mo | 80.00 | 40.13 |
| | C | 20.00 | 59.86 |
| *c)* | Mo | 80.19 | 38.91 |
| | C | 19.61 | 61.12 |

## 4. Conclusion

The method of $Mo_2C$ synthesis using sucrose as carbon source is effective to synthesize $Mo_2C$ with hexagonal structure, also, it is show that $Mo_2C$ has a high thermal stability, and it is confirmed that the optimal temperature of $Mo_2C$ synthesis is at 800 °C.

The variation of this method is effective for doping Ni in $Mo_2C$.

The results of hydroxyapatite extraction showed the heat treatment remove organic materials, and the hydroxyapatite has a thermal and mechanical stability to be used as a catalytic support.

## Acknowledgements

The Authors want to acknowledge the Instituto Tecnológico de Ciudad Madero – Centro de Investigación en Petroquímica by resources and equipment provided for this research.

## References

[1] Mohamm Asadullah, Shin-ichi Ito, Kimio Kunimori, Muneyoshi Yamada, Keiichi Tomishinge. Biomass gasification to hydrogen and syngas at low temperature: Novel catalytic system using fluidized-bed reactor. Journal of catalysis. 2002;255:259-208

[2] Kamel Bennaceur, Brian Clark, Franklin M. Orr, Jr, T. S. Ramakrishan, Claude Roulet, Ellen Stout. El hidrógeno: ¿un future portador energético? 2005;35:47.

[3] L. Delannoy, J.- Giraudon, P. Granger, L. Leclercq, G. Leclercq. Group VI transition metal carbides as alternatives in the hydrodechlorination of chlorofluorocarbons. Catalysis Today. 2000;231:240-59.

[4] M. J. Ledoux, Cuong Pham Huu, Jean Guille, H. Dunlop. Compared Activities of platinum and high specific superface area $Mo_2C$ and WC Catalysts for reforming reactions. Journal of catalysis. 1982;383:398-134.

[5] Yufei Ma., Guoquing Guan, Xiaogang Hao, Ji Cao, Abulitu Abudula. Molybdenum carbide as alternative catalyst for hydrogen production – A review. Renewable and Sustainable Energy Review. 2017;1101:1129-75.

[6] S. Ted Oyama. The chemistry of transition metal carbides and nitrides. New York: BLACKIE ACADEMIC & PROFESSIONAL; 2012

[7] Hua-Min Wang, Xiao-Hui Wang, Ming-hui Zhang, Xiao-Young Du, Wei Li, Ke-Yi Tao. Synthesis of Bulk and supported molybdenum carbide by a single-step thermal carburization method. Chem Mater. 2007;1801:1807-19.

[8]. Franco C, Pinto F, Gulyurtlu I, Cabrita I. The study of reactions influencing the biomass steam gasification process. Fuel. 2003;835:842-82.

[9] Alex C.C. Chang, Hsin-Fu Chang, Fon-jou Lin, Kuo-Hsin Lin, Chi-Hung Chen. Biomass gasification for hydrogen production. Hydrogen Energy. 2011;1452:14260-36.

[10] Chuan shi, Anjie Zhang, Xiosong Li, Shaohua Zhang, Amimin Zhu, Yufei Ma. Chaktong Au. Ni-modified $Mo_2C$ catalysts for methane dry reforming. Applied catalysis A: General. 2012. 431:432.

[11] Nicholas H. Florin, Andrew T. Harris. Enhanced hydrogen production from biomass with in situ carbon dioxide captre using calcium oxide sobernts. Chemical Engineering Science. 2008;287:316-63.

[12] Piyarat weerachanchai, Masayuki Horio, Chaiyot Tangsathitkulchai. Effects of gasifyng conditions and bed materials on fluidized bed steam gasification of wood biomass. Bioresource Technology. 2009;1419:1427-100.

[13] Bishnu Acharya, Animesh Dutta, Prabir Basu. An investigation into steam gasification of biomass for hydrogen enriched gas production in presence of CaO. 2010;1582:1589-35.

[14] Bing-shun huang, Hsin-Yi Chen, Kui-Hao Chuang, Ren-Xuan Yang, Ming-Yen Wey. Hydrogen production by biomass gasification in a fluidized-bed reactor promoted by and Fe/CaO catalyst. 2012;6511:6518-37.

[15] M. Younesi, S. Javadpur, M. E. Bharolooom. Effect of heat treatment temperature on chemical compositions of extracted hydroxyapatite from bovine none ash. Journal of Materials Engineering and Performance. 2011;1484:1490-20.

[16] G. Vitale, M.L. Frauwallner, C. E.Scott, Prereira-Almao. PRepatation and characterization of low-temperature nano-crystalline cubic molybdenum carbides and insights on thei r structure. Applied catalysis A: General. 2011;178:186-48.

[17] Gerardo Vitalea, Héctor Guzmán, Maria L. Frauwallner, Carlos E. Scott, Pedro Pereira-Almao. Synthesis of nanocrystalline molybdenum carbide materials and their characterization. Catalysis Today. 2015;123:133-250.

[18] C.K. Rojas-Mayorga, A. Bonilla-Petriciolet. I. A. Aguayo-Villareal, V. Hernández-Montoya, M.R. Moreno-Virgen, R. Tovar-Gómez, M.A. Montes Morán. Optimization of pyrolysis conditions and adsorption properties f bone char for fluoride removal from water. Journal of Analytical and Applied pyrolysis. 2013;10:18-104.

[19] Malinee Kaewpanha, Guoqing Guan, Yufei Ma., Xiaogang Hao, Zhonglin Zhang, Prasert Reubroychareon, Katsuki Kusakabe, Abuliti Abudula. Hydrogen production by steam reforming of biomass tar over biomass char supported molybdenum carbide catalyst. International journal of hydrogen energy. 2015;7974:7982-40.

[20] P. Shipman, G. Foster, and M. Schoeninger. Burnt Bones and Teeth: an Experimental Study of Color, Morphology, Crystal Structure and Shrinkage. Journal of Archaeological Science. 1984;307:325-11.

# 9.23 Interfacial-redox interaction of $NO_x$ species in alkaline conditions at palladium nanoparticles supported on carbon Vulcan

J. Soto-Hernandez, C. R. Santiago-Ramirez, E. Ramirez-Meneses, T. Poznyak, A. Manzo-Robledo.

[1]*Instituto Politécnico Nacional. DIQI-ESIQIE. Laboratorio de Electroquímica y Corrosión. Av. Luis Enrique Erro S/N, Unidad Profesional Adolfo López Mateos, Zacatenco, Delegación Gustavo A. Madero, C.P. 07738, Ciudad de México, México*

[2]*Departamento de Ingeniería y Ciencias Químicas, Universidad Iberoamericana, Prolongación Paseo de la Reforma 880, Lomas de Santa Fe, 01219 Ciudad de México, México.*

**corresponding author: amanzor@ipn.mx*

---

## ABSTRACT

Electrochemical reduction of $NO_x$ ($NO_2^-$, $NO_3^-$, $NO_{2(g)}$ and $NO_{(g)}$) in alkaline solutions (0.5M NaOH) was studied on palladium supported catalysts, synthetized by alcohol reduction route and supported on carbon Vulcan (3%wt. Pd). XRD, XPS and TEM techniques were employed to characterize the morphological and structural properties. The obtaining mean particle size using XRD was 12 nm as also demonstrated by TEM. In addition, a well-defined semi-spherical nano-particles were observed. On the other hand, XPS analysis was carried out to identify the chemical binding states and composition of Pd/C catalyst; it was found that palladium species at metallic state was 50%wt, with some traces of other Pd-oxidation states. The catalysts were evaluated by electrochemical approaches in the nitrate electro-reduction (NER), having reduction process in all cases, including the hydrogen evolution reaction (HER). The obtained results show that the NER is favored at solutions of $NO_3^-$ ions saturated with $NO_{(g)}$ and $NO_{2(g)}$. Whereas, at nitrite-based solutions saturated with $NO_{(g)}$ and/or $NO_{2(g)}$, the HER process take place with more current-intensity when compared with nitrate-based solutions.

***Keywords:*** Electro-catalysis, $NO_x$, redox-process, pollution, nanoparticles, reduction.

# 9.24 Oxygen Reduction Reaction over Graphene Nanosheets Metal-Free Cathode Electrocatalysts

M.Z. Figueroa-Torres, I.L. Alonso-Lemus, F.J. Rodríguez-Varela, B. Escobar-Morales, A. Fernández-Fuentes.

[1]Universidad Autónoma de Nuevo León (UANL), Facultad de Ingeniería Civil, Av. Universidad s/n, Ciudad Universitaria, San Nicolás de los Garza, Nuevo León C.P. 66455, México.

[2]Centro de Investigación y Estudios Avanzados del Instituto Politécnico Nacional Unidad Saltillo, (CINVESTAV-Saltillo). Parque Industrial Saltillo-Ramos Arizpe. Ramos Arizpe, Coahuila, México, C.P. 25900.

[3]Centro de Investigación Científica de Yucatán (CICY). Unidad de Energía Renovable. Calle 43 No. 130 Col. Chuburná de Hidalgo, Mérida, Yucatán, México. C. P. 97200. ł Conacyt Research Fellow

* Corresponding author: Phone +52 01 8329400 ext. 7286 e-mail: m_zyzlila@yahoo.com.mx

## ABSTRACT

Fuel Cells are attractive devices to supply clean energy and reduce the consumption of fossil fuels. However, Large-scale applications of fuel cells have been limited by the slow kinetics characteristic of the cathodic oxygen reduction reaction (ORR) and the use of Pt as active electrocatalyst. Thereby, intense research has been focused on the development of non-noble metal or metal-free electrocatalysts to replace Pt and to reduce the cost of a fuel cell. Graphene based nanomaterials are of great interest for energy devices due to their extraordinary physical and chemical properties. This investigation reports a fast and simple method to prepare graphene nanosheets through ultrasound exfoliation of graphite in an aqueous solution of Pluronic (P123®). Ultrasonic time were variated in the range of 30 to 120 minutes. The influence of the ultrasonic time on the physicochemical characteristics of graphene nanosheets and their electrocatalytic performance for the ORR were discussed. Physicochemical characterization was performed by using Scanning Electron Microscopy and Raman spectroscopy. Results demonstrated that a good exfoliation of graphite was achieved and graphene nanosheets with an average thickness of 15 nm were obtained. Moreover, Raman results showed graphene nanosheets has a molecular structure composed by a mixture of few and multilayer sheets with a defective lattice. The electrochemical performance of the material for ORR was tested by rotation disk electrode technique. Results demonstrate that ultrasonication time is a key parameter to control the yield and size of graphene, when sonication time was higher than 60 minutes the production of graphene decreased. Electrochemical evaluation revealed that these materials are electroactive for ORR in alkaline media showing almost a four-electrons transfer process.

***Keywords:*** Liquid-phase exfoliation; Carbon nanomaterials; Ultrasound; Sonochemical synthesis.

# CHAPTER 10
# Environmental Aspects.

# 10.1 Methylene Blue Degradation by TiO2 Nanoparticles on Multiwalled Carbon Nanotubes Under Visible Light Irradiation

G. Rosado, N. Alonso-Vante, Y. Verde-Gómez, A. M. Valenzuela-Muñiz

[1] Instituto Tecnológico de Cancún, Av. Kabah Km. 3, 77500, Cancún, Quintana Roo, México.

[2] Université de Poitiers, UMR-CNRS6503, 40 Av. du Recteur Pineau, 86022, Poitiers Cedex, France.

*Catedrático CONACYT,

* Corresponding author: +52 (998) 8807432 ext. 2018, anavalenzuelam@yahoo.com

---

## ABSTRACT

$TiO_2$ is a low cost, environmental friendly and one of the most attractive photocatalyst for dye degradation in aqueous media. The rapid recombination of electron-hole pairs, as well as the fact that $TiO_2$ is only active under UV light irradiation (only 4% of solar radiation), are problems to solve in order to use the material for the degradation of organic pollutants under visible light radiation. These disadvantages could be solved by adding a dopant or a support, for example, using carbonaceous materials like multiwalled carbon nanotubes (MWCNT).

The carbon nanotubes can work as an electron captor and active sites provider due to the good conductivity and high surface area. In this research work, $TiO_2$ nanoparticles were synthetized by sol-gel method using a titanium isopropoxide precursor (TTIP) and deposited over MWCNT. A solution of TTIP was mixed with MWCNT by ultrasonication. The suspension was kept in an ice bath near $0^0$C, and a certain amount of water was added for the hydrolysis reaction. Finally, in order to obtain $TiO_2$ nanoparticles in anatase phase, a thermal treatment was performed at $400^0$C during two hours. On the other hand, to get a mix of anatase-rutile phases, the thermal treatment was done in $N_2$ atmosphere at $700^0$C for two hours. The theoretical percentages of $TiO_2$ added to the carbon nanotubes were 12, 30 and 50% wt. The obtained materials were characterized physically and chemically using scanning and transmission electron microscopy, energy dispersive spectroscopy, thermogravimetric analysis (TGA) and X-ray diffraction.

The photocatalysts performances were evaluated towards the photodegradation of methylene blue, in solution (0.01g/L) under visible light irradiation. The evolution of dye degradation was monitored at different times during one hour, and the concentration was measured using a UV-VIS spectrometer. The results confirm an improvement in the photocatalysts performance when the MWCNT were incorporated; compare to $TiO_2$ nanoparticles (without support). In addition, the materials in anatase phase showed a

better photocatalytic activity than the ones presenting a mix of anatase-rutile phases. More results and the discussion will be presented at the conference.

***Keywords***: $TiO_2$ nanoparticles, carbon nanotubes, photocatalyst

# 10.2 Synthesis and characterization of hematite nanoparticles for arsenite removal in aqueous médium

Herlys Viltres Cobas, Oscar F. Odio Chacón, Susel Del Sol Fernández, Raul Borja Urby, Edilso Reguera Ruiz

[1]Centro de Investigación en Ciencia Aplicada y Tecnología Avanzada-Unidad Legaria, Instituto Politécnico Nacional, Ciudad de México, Distrito Federal, México.

[2]Instituto de Ciencia y Tecnología de Materiales, La Habana, Cuba.

[3]Centro de Nanociencias y Micro-Nanotecnologías, Instituto Politécnico Nacional, Ciudad de México, Distrito Federal, México.

* Corresponding author: 5545031145 and herlysvc.231289@gmail.com

---

## ABSTRACT

Arsenic is one of the most widespread inorganic pollutants worldwide and represents a significant potential risk to human health and the biosphere. It is well known that arsenic is highly toxic and carcinogenic; at present, there are reports of diverse countries with arsenic concentrations in drinking water higher than those proposed by the World Health Organization (10 µg/L). Nanomaterials and nanotechnologies inspire new possible solutions to major environmental issues nowadays. It has been reported that adsorption strategies using nanoparticles as hematite proved to be very efficient for the removal of arsenic in drinking water. However, the adsorption mechanism is not yet clear. In order to shed light on this subject, we attempt to study the interactions between arsenic species and α-$Fe_2O_3$ nanoparticles in aqueous medium.

The iron oxide nanoparticles were prepared using a solvothermal method. As-synthesized hematite nanoparticles were put in contact with $As_2O_3$ solutions at room temperature at pH 4 and 7. The nanoparticles were characterized by FTIR, XRD, UV-vis, XRF and XPS. The results showed that synthesized nanoparticles had an average diameter of crystallite of 30 nm. The presence of arsenic on particles surface was confirmed, which is more remarkable when pH= 7 condition is employed. On the other hand, after adsorption experiment, it was evident from FTIR and XPS that once arsenic species interact with the nanoparticles, they form mono and bidentate surface complexes.

***Keywords:*** nanoparticles, hematite, adsorption, arsenic

# 10.3 Bioelectrochemical System with a Proton Exchange Membrane for Wastewater Treatment

R.A Chacón-Carrera, A. López-Ortiz, V. Collins-Martínez, V.H. Ramos-Sánchez

[1] Centro de Investigación en Materiales Avanzados, S.C., Miguel de Cervantes #120, Complejo Industrial Chihuahua, Chihuahua, Chih., México. C.P. 31109.

[2] Facultad de Ciencias Químicas, Universidad Autónoma de Chihuahua, Nuevo Campus Universitario, Circuito Universitario, Chihuahua, Chih., México. C.P. 31125

* Corresponding author: vramos@uach.mx (614) 183-10-68

---

## ABSTRACT

Microbial electrolysis cells (MECs) are bioelectrochemical devices where organic matter is oxidized to hydrogen through exoelectrogenic bacteria, this process is a new alternative to energy crisis and to mitigate climate change. Microorganisms are attached to the anode where the oxidation is carried out producing carbon dioxide ($CO_2$), electrons ($e^-$), and protons ($H^+$), while at the cathode protons and electrons are chemically reduced to finally produced biohydrogen. This is not a spontaneous reaction; thus, the minimum required voltage is ≥ 0.2 V, which is substantially lower than the needed for conventional water electrolysis. MECs have some advantages over other biohydrogen processes from biomass: a higher conversion efficiency, high purity of gas, and have proved to be a robust technology able to treat a wide range of organic substrates, wastewater included. Most of the studies of MECs have reported double chamber designs, where the anode and cathode are separated by an ion exchange membrane. The importance of the membrane is to regulate the ionic flux between both chambers since low migration rates of ionic species could affect the pH balance in the system affecting the performance of the system. Nafion is a proton exchange membrane widely used to study MECs, however, there is little information about bipolar membranes (BPM) in these systems. In this study, a double-chambered MEC was constructed to evaluate the performance of the system using Nafion 117 as a proton exchange membrane, and a bipolar membrane (FUMASEP-FBM). The biofilm formation was monitored by cyclic voltammetry and open circuit voltage (OCV) while the electrochemical performance was characterized by polarization curves and power density curves. The kinetics of COD removal were evaluated over a period of 3 hours with a percentage of removal of 39%.

***Keywords:*** biohydrogen, wastewater treatment, bipolar membrane.

## 1. Introduction

### *1.1 Energy Demand.*

The use of fossil fuels in recent years has brought with it many problems of high environmental impact. According to the IEA, fossil fuels represent 86% of global energy consumption [1]. However, the use of energy from petroleum has serious disadvantages, the main one of which is that they are finite sources, which means they will eventually be terminated. According to some predictions [2], crude oil reserves will last at least 50 years at the current rate of consumption. In addition to this, the burning of hydrocarbons is directly related to the emission of gases to promote the greenhouse effect, mainly by the emission of carbon dioxide ($CO_2$) [3]. Increasing the concentration of greenhouse gases (GHG), different phenomena have been observed such as: increased of the global average temperature, consequently, the melting of the polar caps and changes in the precipitation pattern. Energy consumption today is estimated at 22 trillion kWh by 2020 [4].

### *1.2 Hydrogen as an energy carrier.*

Hydrogen ($H_2$) is known to be an energy carrier, since it needs to be produced through some method and then used in other process. Hydrogen has become the central axis of new technologies for the generation of energy due to the characteristics it presents, mainly the energy density. It is reported that the energy released in the case of $H_2$ is 120 MJ/kg, which far exceeds hydrocarbons such as 50 MJ/kg of natural gas, 44 MJ/kg of oil and 20 MJ/kg of methane [1].

The biological production is considered the most efficient and friendly with the environment process, compared to the electrolysis and thermal processes. Some microorganisms possess the ability to produced hydrogen by means of enzymes such as dehydrogenase and nitrogenase [5]. Although there is a wide variety of methods for producing hydrogen, not all are fully sustainable. Currently, more than 96% of the production of hydrogen is produced by using fossil fuels. Therefore, despite the benefits of hydrogen, its production by these processes does not solve the problem of the emissions of GHG.

### *1.3 Microbial Electrochemical Systems.*

Microbial electrochemical systems (MES) use microorganisms to convert the chemical energy stored in biodegradable materials to direct electric current and chemicals. Compared to traditional methods, these technologies offer a new solution for integrated waste treatment and energy and resource recovery. An example of this technologies is the microbial fuel cells (MFC) which can use carbon sources present in different wastewater (municipal and industrial wastewater) as fuel to produce electricity, also these devices can be used to treat wastewater. A conventional MFC consists of an anodic chamber and a

cathodic chamber which are separated by a membrane, usually a protonic exchange membrane. The anodic chamber is under anaerobic conditions, while the cathode has an oxygen inlet. Inside the anodic chamber, the oxidation of the organic matter is carried out releasing protons, electrons and $CO_2$. Electrons travel through an external circuit from the anode to the cathode, while protons migrate through the solution and reach the cathode chamber to combine with oxygen and form water.

A new technology to produce hydrogen from biomass is the microbial electrolysis cell (MEC), which are a modification of the MFC that offers a viable option for the sustainable generation of an energy carrier from a wide variety of substrates such as wastewater [4]. Compared to conventional processes for producing hydrogen (dark fermentation, biomass gasification, etc.), MECs have several advantages, one of them and the most attractive is that the energy requirements are low approximately 0.6 - 1 kWh/$m^3H_2$, which is less than the traditional water electrolysis (4.5 – 50.6 kWh/$m^3H_2$) [5].

Traditionally, the components of a MEC consist of: anodic chamber, cathodic chamber, an ion exchange membrane, electrochemically active microorganisms and a power source. Microorganisms colonize the anode and oxidize organic matter by decomposing into $CO_2$, electrons ($e^-$) and protons ($H^+$) as part of its metabolism. Electrons are released from the microbial cell pass to the anode where they travel through an external circuit to the cathode, while protons migrate through the solution and the membrane to finally recombine with the electrons and form hydrogen. Figure 1 schematize the operation of a MEC.

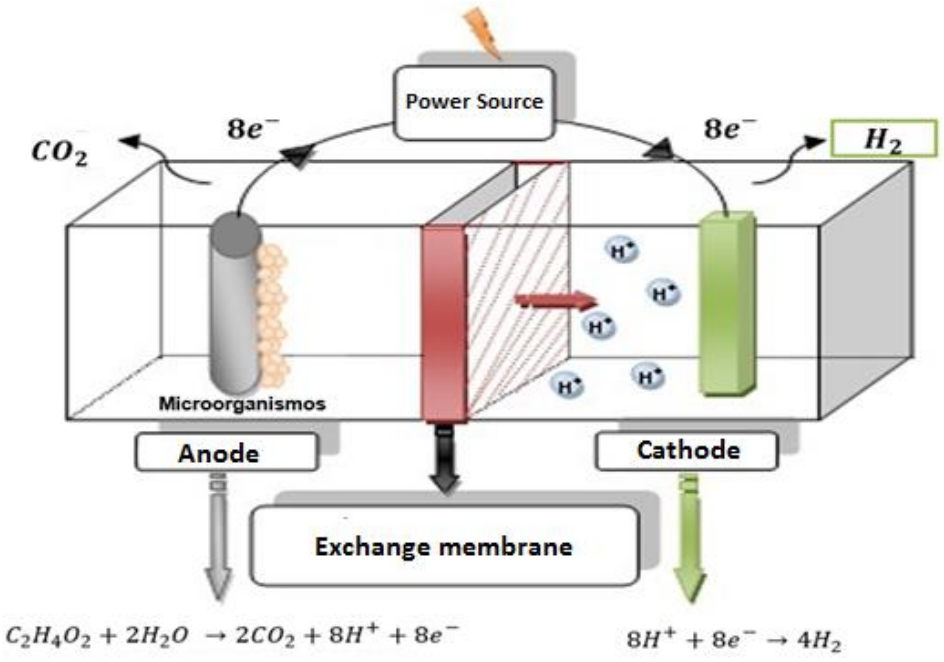


**Figure 12. Diagram of the operation of an MEC.**

*1.3.1 Ion Exchange Membranes.*

The use of an ion exchange membrane is used in two-chamber systems and presents the advantage that the hydrogen produced has a high purity, also the presence of a membrane avoids the consumption of the gas by microbial action and additionally is used to avoid short circuits [6]. The ion exchange membranes can be divided by: cationic, anionic and bipolar [6].

Cationic exchange membranes have negatively charged functional groups, such as: $SO_3^{2-}$, COO-, $PO_3^{2-}$, or $PO_3H^-$, these groups allow the migrations of cations. Among the most used membranes are the proton exchange membranes (PEM), as its name indicates, allows only the migrations of $H^+$. The most used PEM is Nafion, which offers high proton conductivity due to the sulfonic groups attached to the inert structure of polytetrafluoroethylene.

Bipolar membranes (BPM) are formed by a cation exchange layer and an anionic exchange layer attached, forming a wet bonding interface. In some cases, the wet layer is considered a third layer. Through the effect of an electric field, the water splits forming protons and hydroxyl ions [7]. Theoretically, the voltage required for the operation of some BPM is 0.83 V.

In this study, the effect of a BPM was evaluated in a MEC, using as substrate wastewater from the Treatment Plant which was enriched with sodium acetate 20 mM, and chloride sodium 100 mM as catholyte. The parameters that were analyzed to evaluate the performance of the MEC were: the conductivity, the presence of metals, the pH, the removal of COD, as well as the gas produced.

## 2. Materials and Methods

### *2.1 Design and Construction of the Bioelectrochemical Reactor.*

The bioreactor was desing by using Solid Works with an architecture of a two chambered MEC, each chamber has a volume of 500 mL. The material used was nylamid, since the material provides the necessary characteristic of manipulation and resistance to operate the electrochemical system. The anode chamber has four inputs, mainly to place the anode and for another attachment for pH monitoring, electrical conductivity or for sampling. The cathode chamber only has one input to place the cathode and has a gas manifold with a volume of 250 mL.

### *2.2 Physicochemical characterization of wastewater*

#### *2.2.1 COD quantification.*

The consumption of the organic matter was evaluated through the COD. The quantification of COD was performed according to the NMX-AA-030/2-SCFI-2011 norm, which is a spectrophotometric analysis [8]. Residual water contained COD between 400 and 680 mg COD/mL. Sodium acetate was added to enriched the wastewater at a concentration of 20 mM. Once the characterization was carried out, the percentage of COD removal of each batch evaluated as MFC was calculated using the following formula:

$$\%\ COD\ removal = \frac{COD_i - COD_f}{COD_i} x\ 100$$

Where:

$COD_i$= initial concentration

$COD_f$= final concentration

The degradation kinetics of the COD were carried out at different intervals. The first kinetics were carried out in 3.5 hours, a sample of water from the anode chamber was taken every 30 minutes. The residual water was enriched with 20 mM sodium acetate, which was considered as a contribution to the COD.

*2.2.2 Elemental analysis of metals by XRF.*

The analysis for the identification and quantification of metals was carried out in the Faculty of Chemical Sciences in the laboratory of Physical Chemistry. A volume of 20 mL of waste water was filtered using a 0.45 µm filter to avoid the passage of organic material. Then, 995 µL of waste water and 5 µL of gallium standard (Ga) were taken and both were mixed. Quartz disks were used, which were rinsed with acetone. Once dried, 10 µL of sample was taken and placed in the center of the disk, 4 measurements were made. The discs were then placed on a heating grill to evaporate the water. Finally, the already dried discs were installed on the reading reel where the irradiation time of each sample was 300 seconds.

*2.2.3 Conductivity and pH.*

The pH and conductivity parameters were measured using the EXTECH Instruments Oyster pH-conductivity-TDS potentiometer. Calibration to measure pH was performed with buffer solutions of pH 7 and pH 4. The electrode was rinsed with deionized water and the

solution temperature was adjusted to approximately 25 ° C. The electrode was then rinsed and dried to introduce it into the value buffer 7 until it stabilized. It was then rinsed and dried to pH 4 buffer until stabilized. Finally, the pH value in the residual water sample was measured.

The calibration to measure conductivity was carried out by placing the electrode in tap water. The potentiometer was then adjusted to measure conductivity (µS / cm) and the conductivity of the waste water was measured.

### 2.3 Electrochemical evaluation.

*2.3.1 Cyclic Voltammetry.*

The electrochemical evaluation was carried out using the following configuration: graphite as working electrode (anode for biofilm formation), Pt as cathode (1 $cm^2$) and as counter electrode. A velocity of 10 mV / s for 2 cycles was used in a potential window of -1.1 to 1.1 V using Nafion 117 ion exchange membrane.

*2.3.2 Polarization and Power Curves.*

The Polarization and Power curve for the first experimental part was carried out using the Nafion 117 membrane using the linear scanning voltammetry technique [9] at a scanning speed of 1 mV / s. The technique was performed every 48 hours to monitor the power increase.

## 3. Results

*3.1 Design and Construction.*

.

The three-dimensional design of the bioelectrochemical system is shown in Figure 2. It can be observed that the bioreactor has a two-chamber architecture separated by a flange where the membrane to be evaluated.

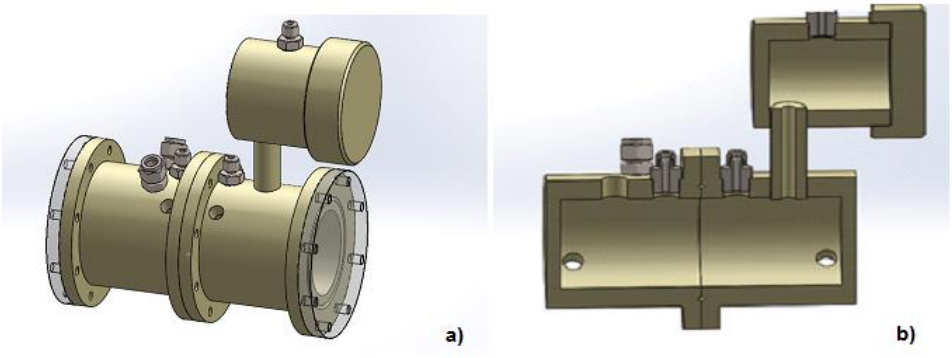


**Figure 13. a) Front view; b) interior view**

The construction of the biochemical system was developed in the CIMAV prototypes workshop. Figure 3 shows the bioreactor.

**Figure 14. Microbial Electrolysis Cell.**

*3.2 Physicochemical analysis of Wastewater.*

The analyzes for the detection of metals do not show the presence of heavy metals. The elements found correspond to the typical load of a domestic wastewater. With respect to COD the measured values are between 620 and 400 mg/L on average. With respect to COD the measured values are between 620 and 400 mg / L on average. The pH and conductivity are also within the parameters already reported for domestic wastewater. Table 1 shows the results of the analyzes performed.

***Tabla 1. Values of the evaluated parameters.***

| Element | Concentration (mg/L) | COD (mg/L) | pH | Conductivity (µS/cm) |
|---|---|---|---|---|
| **Na** | 163.36 | 613.5 | 7.81 | 1385 |
| **P** | 6.285 | | | |
| **S** | 64.21 | | | |
| **Cl** | 135.72 | | | |
| **K** | 26.46 | | | |
| **Ca** | 77.31 | | | |
| **Ti** | 0.165 | | | |
| **Mn** | 0.065 | | | |
| **Fe** | 0.401 | | | |
| **Sr** | 0.617 | | | |

### *3.2.1 COD removal*

The initial COD concentration was 406 mg/L considering the contribution of sodium acetate. After 3.5 hours, the COD decreased to 246 mg/L. The percentage of removal for this experiment of 3.5 hours was of 39.41%, this percentage is considered good since in other works [10,11] the percentages reached in 120 hours reached 45-48%. Figure 4 shows the curve for COD removal.

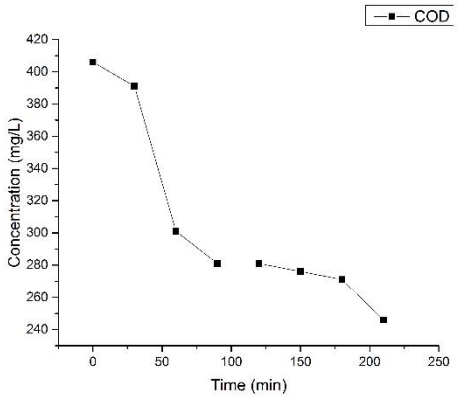


**Figure 15. COD Removal**

*3.3 Electrochemical Evaluation.*

3.3.1 Cyclic Voltammetry.

The results of the cyclic voltammetry allow monitoring the formation of the biofilm at the anode by increasing the generation of electric current. Figure 5 shows the curves obtained when the anode is not colonized, at 15 and 45 days after colonization.

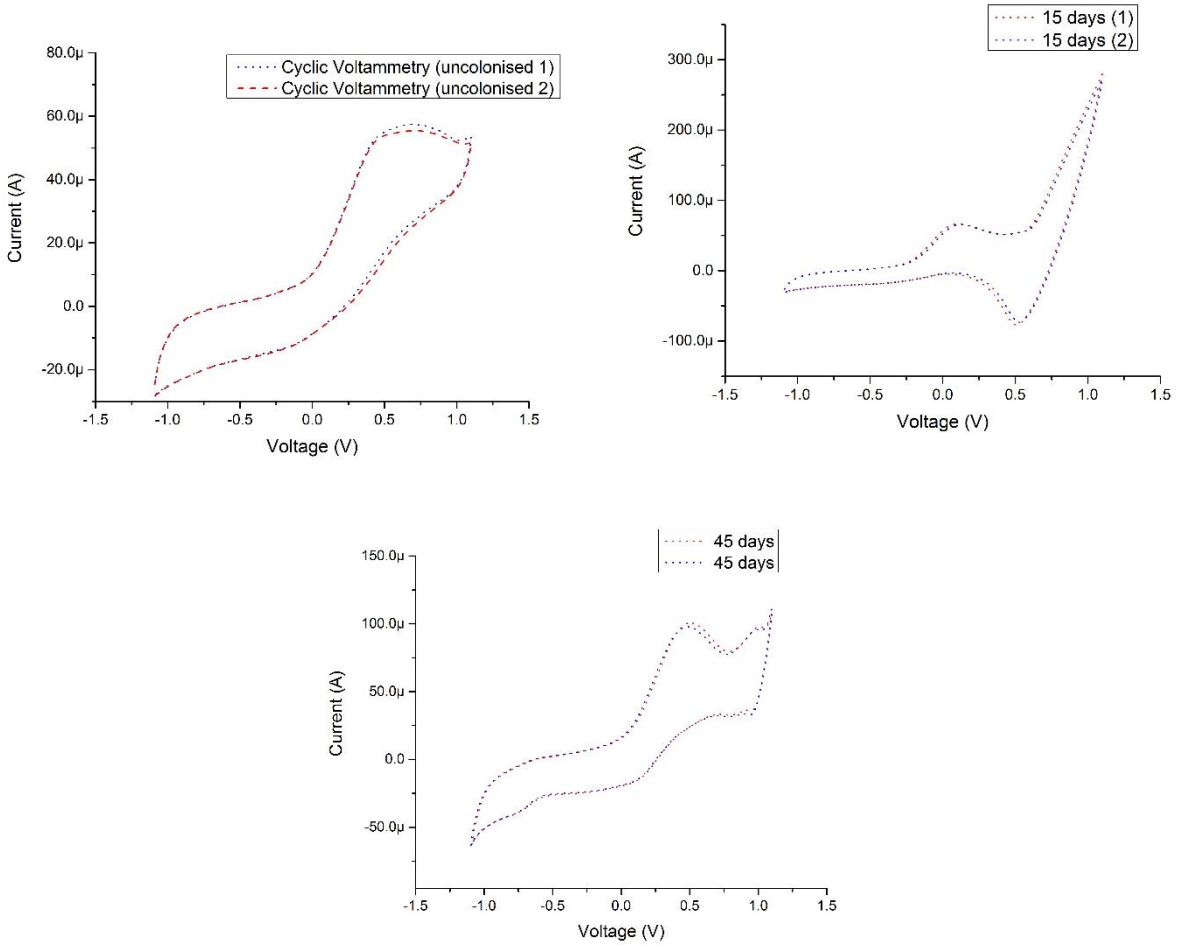


**Figure 16. Cyclic Voltammetry at different stages 1) uncolonised, 2) 15 days after, 3) 45 days after.**

The first curve obtained shows that the electrochemical activity is almost null, which confirms that no exoelectrogenic bacteria are present. In our case, the oxidation peak is observed around 0.5 V with a current generation of 57.45 μA.

After 15 and 45 days, a cyclic voltammetry was performed on the anode to compare the bioelectrochemical activity. These results suggest that the formation of the biofilm is taking place on seeing an increase in current.

3.3.2 Polarization and Power Curves.

The first graph shown was performed at time 0, the second graph corresponds to the curve performed at 48 hours and the third image represents the curve at 96 hours after the experiment was started. Figure 6 shows the curves.

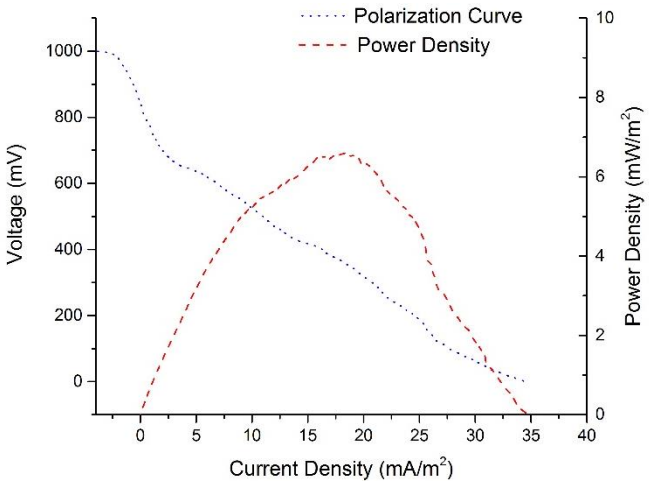


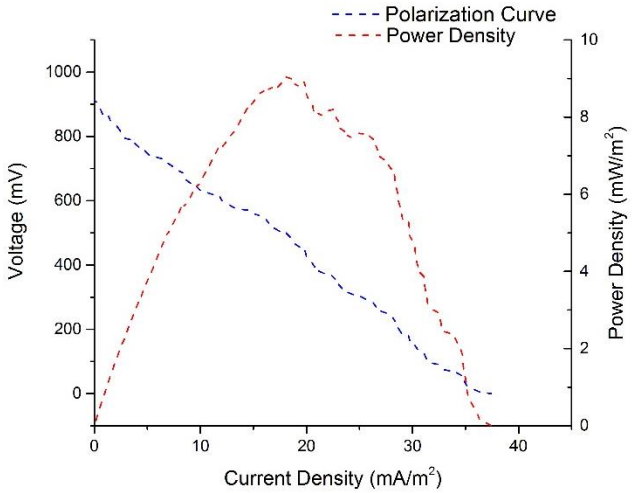


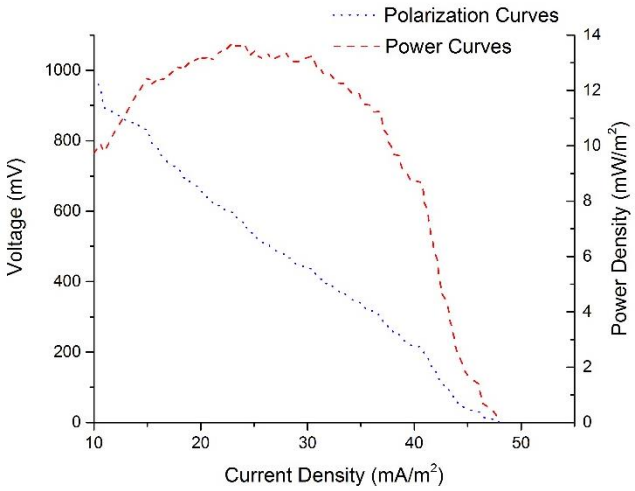

**Figure 6. Polarization and Power Curves: 1) 0 time, 2) 48 h, 3) 9 h**

Power curves show behavior that increases over time. The maximum reported potencies were: a) for the time 0: 6.51 mW/m$^2$, b) at 48 hours: 8.22 mW/m$^2$ and c) at 96 hours: 13.24 mW/m$^2$.

## 4. Conclusion

The performance of the bioelectrochemical system showed a progressive increase as microbial activity was established. The formation of the biofilm is a process that is given continuously, through cyclic voltammetry was observed as this activity is increasing as the days pass.

The percentage of COD removal was 40%, however, it took about three weeks for the colonization of the anode and to be able to perform the purification. It is expected to monitor the kinetics for 8 hours to be able to compare with the reported literature.

The maximum power generated was reached at 96 hours of operation, this suggests that the microbial consortium continues in formation.

Gas measurement and evaluation of the bipolar membrane is being carried out.

## Acknowledgements

We thank CONACyT for the support granted through the scholarship and the SMH for the acceptance of the project in poster mode.

## References

[1] Kadier, A. Yibadatihan, S, Peyman, A., Nadia, K. Chandrasekhar, Mohd S, Kalil, A comprehensive review of microbial electrolysis cells (MEC) reactor designs and configurations for sustainable hydrogen gas production, Alexandria Engineering Journal, 2016, Pages 427-443

[2] Lamb, R. When will we run out of oil, and what happens then? Website: ⟨http://science.howstuffworks.com/environmental/energy/run-out-of-oil. htm⟩ 2010.

[3] Cucu A.. "Microbial Electrolysis Cell: Hydrogen Production Using Microbial Consortia From Romanian Waters." Digest Journal of Nanomaterials and Biostructures. 2013 8(3): 1179-1190.

[4] Boden, T.A., G. Marland, and R.J. Andres. 2016. Global, Regional, and National Fossil-Fuel CO2 Emissions. Carbon Dioxide Information Analysis Center, Oak Ridge National Laboratory, U.S.

[5] A. Escapa, R. Mateos, E.J. Martínez, J. Blanes, Microbial electrolysis cells: An emerging technology for wastewater treatment and energy recovery. From laboratory to pilot plant and beyond, Renewable and Sustainable Energy Reviews, 2016 (55) Pages 942-956

[6] Oliot M., Galier S., Roux de Balmann H., Bergel A. Ion transport in microbial fuel cells: key roles, theory and critical review. Appl Energy 2016; 188; 1682-1704.

[7] Yossan S, Xiao L, Prasertsan P, He Z. Hydrogen production in microbial electrolysis cells: choice of catholyte. Int J Hydrogen Energy 2013; 38: 9619–24.

[8] Norma Mexicana NMX-AA-030-2-SCFI-2011
https://www.gob.mx/cms/uploads/attachment/file/166775/NMX-AA-030-2-SCFI-2011.pdf

[9] Liu, L., Tsyganova O., Lee D., Su A., Chang J.S., Wang A., Ren N. Anodic biofilm in single chamber microbial fuel cells cultivated under different temperatures. International Journal of Hydrogen Energy, 37, 15972-15800.

# 10.4 Synthesis of $MFe_2O_4$ nanoparticles by the Oil-in-Water microemulsion reaction method and its exploration for photocatalytic water splitting

Arturo Adrián Rodríguez Rodríguez, Maira Berenice Moreno Trejo, Miguel de Jesús Meléndez Zaragoza, Virginia Collins Martínez, Alejandro López Ortíz, Eduardo Martínez Guerra, Margarita Sánchez Domínguez.

[1] Centro de Investigación en Materiales Avanzados, S. C. (CIMAV), Unidad Monterrey, Alianza Norte 202, Parque de Investigación e Innovación Tecnológica, 66628 Apodaca, México.

[2] CIMAV Unidad Chihuahua, Av. Miguel de Cervantes Saavedra 120, Complejo Industrial Chihuahua, 31136 Chihuahua, Chih. México.

* Corresponding author: (+52) 8448073209, arturo.rodriguez@cimav.edu.mx, margarita.sanchez@cimav.edu.mx

## ABSTRACT

Spinel-type ferrites have the molecular formula $MFe_2O_4$, where M represents a divalent metallic cation, such as $Co^{2+}$, $Ni^{2+}$ and $Zn^{2+}$ for $CoFe_2O_4$, $NiFe_2O_4$ and $ZnFe_2O_4$, respectively. As photocatalyst, spinel-type ferrites have shown an efficient visible light absorption, high sorption capacity, thermal stability, and low toxicity. Moreover its magnetic response allows their easy recovery from the liquid reaction media. Thanks to these features, $MFe_2O_4$ compounds are a promising option for the photocatalytic water-splitting, a clean and simple technology to obtain $H_2$, which has not been fully explored for $MFe_2O_4$ nanoparticles, especially those synthesized by microemulsion. In light of this, we prepared cobalt, nickel and zinc ferrites employing the novel oil-in-water microemulsion reaction method and explored its $H_2$ evolution through water splitting reaction. In order to perform the photocatalytic experiments, a dispersion of nanoparticles in water (2% MeOH) was prepared inside a quartz tube reactor; this system was sealed, and then illuminated with a 250 W white mercurial lamp. $H_2$ production was monitored by gas chromatography. Prior to photocatalytic evaluation, as-synthesized nanomaterials were thermally treated and characterized. Characterization results showed globular nanoparticles with a cubic spinel-type crystalline structure, adequate textural properties for photocatalytic applications and UV-visible light absorption. In regard to light-driven $H_2$ production, the photoactivity of these oxides was successfully demonstrated; photocatalytic water splitting evaluation of $ZnFe_2O_4$ yielded a higher amount of hydrogen (354 $\mu molH_2g^{-1}$) compared with $Co^{2+}$ and $Ni^{2+}$ ferrites in an 8 h experiment. Broadly, this work represents a new contribution to the studies of spinel-type ferrites for the photocatalytic production of $H_2$.

***Keywords:*** ferrites nanoparticles; oil-in-water microemulsion; $H_2$ production; photocatalytic water-splitting

## 1. Introduction

Nowadays, owing the search of alternative and green energy sources, molecular hydrogen ($H_2$) has become a strong candidate to replace fossil fuels. As a consequence, the implementation of clean technologies, as the photocatalytic splitting of water molecule, are being envisaged as promising techniques to produce $H_2$. [1-3] The photocatalytic water splitting involves the use of a powder photocatalyst, well-dispersed in water (usually with a sacrificial agent as methanol), and contained in a sealed reactor, irradiated by a photon energy source. The photocatalyst, generally an inorganic semiconductor material, must meet the energetic requirements for either reduction of protons ($H^+$ / $H_2$, 0 V vs NHE a pH=0) and/or oxidation of water ($O_2$ / $H_2O$, 1.23 V vs NHE pH=0), in order to provoque the splitting of $H_2O$ molecule into $H_2$ and ½ O.[4-7] Several types of inorganic nanomaterials have been studied for photocatalytic water splitting [8-13], among them spinel-type ferrites nanoparticles have gained great interest due its remarkable properties [14-16]. Spinel-type ferrites are a group of iron oxides with the molecular formula $MFe_2O_4$, where M represents a divalent metallic cation, such as $Co^{2+}$, $Ni^{2+}$ and $Zn^{2+}$, in the case of cobalt ($CoFe_2O_4$), nickel ($NiFe_2O_4$) and zinc ferrites ($ZnFe_2O_4$). As photocatalyst, $CoFe_2O_4$, $NiFe_2O_4$ and $ZnFe_2O_4$ nanoparticles have shown an efficient visible light absorption (which promotes the photocatalytic redox reactions) due its relative low bandgaps (<2 eV), good electrical conductivity (favorable for the transfer of electrons and holes), high molecular adsorption-desorption capability, stability against photocorrosion, low toxicity, and easy and low cost preparation; moreover its magnetic response (moderate magnetic saturation, and low magnetic remanence) allows to recover them from the liquid reaction media, by the application of an external magnetic field [17-20]. Although the increasing interest of spinel-type ferrites in regard photocatalytic production of $H_2$, the capacity of this family of iron oxides has not been fully explored yet, especially with $MFe_2O_4$ nanoparticles synthesized by microemulsion methods such as the oil-in-water (O/W) microemulsion reaction method, which has been used recently to synthesize photocatalyst nanoparticles for the degradation of water pollutants [21, 22]. Roughly, the O/W microemulsion reaction method consist in the use of oil droplets (2-50 nm), in which organometallic precursors are dissolved, stabilized by a surfactant, and dispersed in a continuous aqueous phase. When a precipitating agent is added, the reagents will contact each other at the interface, and they will react to form precipitates of nanometric size, the nanoparticles. The benefits of using this method are mainly the possibility to obtain very small particles with good textural properties and homogeneous composition at mild conditions. More information about the O/W microemulsion reaction method can be found in our previous works. [23, 24] In this context, the present work represents a new contribution to the studies of $CoFe_2O_4$

$NiFe_2O_4$, and $ZnFe_2O_4$ spinel-type ferrites, for the light driven production of $H_2$ by water splitting reaction. Detailed characterization of prepared and thermal treated nanoparticles, in terms of structure, morphology, textural and optical properties were a valuable tool to the understanding of spinel-type ferrites photocatalytic activity.

## 2. Materials and Methods

### 2.1 Materials

#### 2.1.1 $MFe_2O_4$ (M: $Co^{2+}$, $Ni^{2+}$ and $Zn^{2+}$) nanoparticles synthesis

Iron (III) 2-ethylhexanoate ($C_{24}H_{45}FeO_6$, nominally 50% in mineral spirits) and zinc (II) 2-ethylhexanoate ($C_{16}H_{30}ZnO_4$, nominally 50% in mineral spirits) were purchased from Alfa Aesar. Cobalt (II) 2-ethylhexanoate ($C_{16}H_{30}CoO_4$, 65 wt% solution in mineral spirits), nickel (II) 2-ethylhexanoate ($C_{16}H_{30}NiO_4$, 78 % in 2-ethylhexanoic acid), isooctane ($C_8H_{18}$, CHROMASOLV® Plus for HPLC, $\geq$ 99.5%), tetramethylammonium hydroxide pentahydrate TMAH ($C_4H_{13}NO{\cdot}5H_2O$, $\geq$ 97 %) were purchased from Sigma-Aldrich. Synperonic$^{TM}$ 91/5 ($C_{19}O_6H_{40}$) was purchased from CRODA.

#### 2.1.2 Photocatalytic water splitting evaluation

Distilled water ($H_2O$) and methanol ($CH_4O$, HPLC grade) were purchased from J.T. Baker. Ultrapure gaseous nitrogen ($N_2$: $\geq$ 99.998 %), used as gas carrier for chromatography.

### 2.2 Methods

#### 2.1 $MFe_2O_4$ (M: $Co^{2+}$, $Ni^{2+}$ and $Zn^{2+}$) nanoparticles synthesis

Three compositions of spinel-type ferrite nanoparticles were similarly synthesized, employing the oil-in-water microemulsion reaction method. For this purpose an oil/surfactant/deionized water pseudo-ternary system, with a 20/20/60 weight percent ratio (wt %) composition, was prepared. Isooctane was used as oil, in which Fe (III) 2-EH, and Co (II) 2-EH; for $CoFe_2O_4$, or Ni (II) 2-ethylhexanoate; for $NiFe_2O_4$, or Zn (II) 2-ethylhexanoate; for $ZnFe_2O_4$, in stoichiometric proportions (M:Fe 1:2), were previously dissolved, and further incorporated to the surfactant and deionized water. As surface active agent, synperonic$^{TM}$ 91/5 was employed. Pseudo-ternary system constituents were properly weighted on glass vessels, closed and then placed in a water bath with controlled temperature and magnetic stirring. Raising-up temperature close to 40 °C, led to the

corresponding oil-in-water microemulsion formation, as depicted by the apparition of dark-brown translucent solutions. The O/W microemulsion reactions were carried out at 46 °C; in the case of cobalt ferrite, and 41 °C and 40 °C; in the case of nickel and zinc ferrites respectively, by continuous addition of a 1 M TMAH solution (under magnetic stirring) until reaching a pH of 12-12.45. Nanoparticles presence was indicated by the formation of a dark solid. Magnetic stirring and temperature conditions were maintained for 24 hours. The obtained solids were washed several times with water (until neutral pH was achieved), isopropanol and chloroform, to remove by-products. Finally, products were dried at 70 °C for 24 hours, and thermally treated at 500 °C for 5 hours.

### 2.3 $MFe_2O_4$ (M: $Co^{2+}$, $Ni^{2+}$ and $Zn^{2+}$) nanoparticles characterization

Crystalline phases of as-prepared and thermally treated $MFe_2O_4$ nanoparticles were identified by X-ray diffraction (XRD), on a PANalytical Empyrean diffractometer with $CuK_\alpha$ radiation; diffractograms were recorded with a step size of 0.0167113° and a time per step of 59.69 s. The morphology of thermal treated nanoparticles was studied by high-resolution transmission electron microscopy in scanning mode (HRTEM-STEM), employing a field emission transmission electron microscope JEM-2200FS, operated at 200 kV. Textural properties were determined by nitrogen adsorption–desorption isotherms (at 77 K), employing an automatic Quantachrome Autosorb instrument; prior to $N_2$ adsorption, all the samples were outgassed. Specific surface area was calculated using the Brunauer-Emmet-Teller (BET) method. Optical properties were determined by diffuse reflectance (DR) UV-Vis measurements, using an UV-Vis-NIR spectrophotometer from Perkin Elmer, with an integrating sphere configuration.

### 2.3 Photocatalytic water splitting

In order to perform photocatalytic water splitting experiments, a dispersion of $MFe_2O_4$ nanoparticles (200 mg) in 200 mL of water (with a 2% of methanol, MeOH) was prepared inside a quartz tube reactor (photoreactor); this system was closed by two aluminum flanges bolted together by threaded rods, and properly sealed to avoid gas leaks. Photoreactor was then illuminated with a white mercurial lamp of 250 Watts (Philips MH/U 250W/640). $H_2$ evolution was monitored hourly (for 8 h) by a Clarus 580 Perkin Elmer gas chromatograph equipped with a thermal conductivity detector. Evolved gas sampling was carried out through a septum port located on the top of the photoreactor, and then transferred to the chromatograph (1 mL) by injection using a precision analytical syringe (VICI precision sampling, inc.) for gases.

## 3. Results and Discussion

### 3.1 $MFe_2O_4$ (M: $Co^{2+}$, $Ni^{2+}$ and $Zn^{2+}$) nanoparticles characterization

#### 3.1.1 X-ray diffraction (XRD)

Fig. 1 (left) shows the XRD patterns of as-obtained ($Co^{2+}$, $Ni^{2+}$ and $Zn^{2+}$) ferrites. First, as it can be seen $CoFe_2O_4$ pattern displays typical peaks of a polycrystalline material, whose positions and relative intensities at specific 2Θ (°) values can be matched with the (111), (220), (311), (400), (511), and (440) crystalline planes of cubic spinel-type cobalt ferrite (*, JCPDS 04-006-4150). Secondly, $ZnFe_2O_4$ ferrite pattern shows a more broadened and less defined profile compared with $Co^{2+}$ composition; however, it is still possible to identify the main cubic $MFe_2O_4$ spinel-type peaks, matched with the (220), (311), (400), (511), and (440) crystalline planes. Finally, $NiFe_2O_4$ shows the broadest and low intensity peaks among synthesized ferrites, even though it also displays the (311), (400) and (440) crystalline planes related to spinel-type structure. Broadly, the depicted diffractograms have a typical profile for nanoparticles. After treating the as-obtained materials at 500 °C for 5h (fig. 1, right), the samples patterns clearly revealed sharper profiles and an increment of crystalline peaks, indicating an enhanced crystallinity as a result of the atomic ordering promoted by thermal treatment. The identified signals confirm again the formation of pure cobalt ferrite, as well as the nickel (+, ICDD 00-044-1485) and zinc cubic spinel-type structures (∧, ICSD 98-011-6750). Comparing the ($Co^{2+}$, $Ni^{2+}$ and $Zn^{2+}$) ferrites patterns, it is possible to observe slight displacements in main crystalline planes, in part due the ionic radii of divalent metals ($Zn^{2+}$: 0.88 Å = $Co^{2+}$: 0.838 Å > $Ni^{2+}$: 0.731 Å [25]) that composes the crystalline $M^{2+}Fe_2O_4$ structure. Based on experimental and reference diffractograms, Rietveld refinement was performed to estimate the crystallite mean size ($d_{XRD}$) and lattice parameter of prepared ferrites. In regard obtained values, $ZnFe_2O_4$ has the higher $d_{XRD}$: 10 nm, followed by $CoFe_2O_4$ ferrite $d_{XRD}$: 8 nm and $NiFe_2O_4$ $d_{XRD}$: 4 nm. Calculated lattice parameter values ($ZnFe_2O_4$: 8.4370 Å, $CoFe_2O_4$: 8.3961, $NiFe_2O_4$: 8.3393 Å) are in agreement with the reported for identified crystalline phases ($ZnFe_2O_4$: 8.4379 Å, $CoFe_2O_4$: 8.3961 Å, $NiFe_2O_4$: 8.3393 Å). XRD results probes the capacity of the O/W microemulsion method to produce semicrystalline ($Co^{2+}$, $Zn^{2+}$, $Ni^{2+}$)$Fe_2O_4$ ferrites at mild conditions using TMAH 1M solution as precipitation agent, and although a thermal treatment is needed to enhance nanomaterials crystallinity, the employed conditions are not as high as commonly needed in other synthesis methods [26, 27].

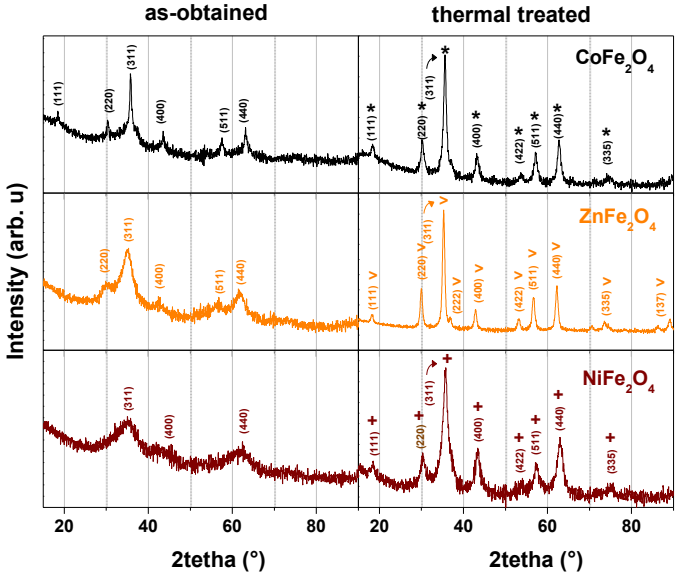


**Fig. 1.** X-Ray diffraction patterns of $(Co^{2+}, Zn^{2+}, Ni^{2+})Fe_2O_4$ nanoparticles: before (as-obtained) and after thermal treatment.

### 3.1.2 High-resolution transmission electron microscopy in scanning mode (HRTEM-STEM)

Fig. 2 displays bright field HRTEM-STEM electron micrographs of thermally treated nanoparticles: (a) cobalt, (b) nickel and (c) zinc ferrites. As evident, $CoFe_2O_4$ analyzed zone shows agglomerated globular nanoparticles, with sizes around 20 nm; similarly, $NiFe_2O_4$ and $ZnFe_2O_4$ micrographs exhibits agglomerated globular nanoparticles but with smaller sizes (around 14 nm) and apparently a more defined morphology. Cobalt ferrite nanoparticles are larger since, as evidenced by XRD, the $CoFe_2O_4$ crystalline phase was already formed before thermal treatment (in comparison with nickel and zinc ferrites), and thus when the samples were treated at 500 °C for 5 h, the growth of nanoparticles was more favored. Corresponding inset images display nanocrystals, which composes ferrite nanoparticles. The observed lattice fringes makes evident the crystallinity of prepared $MFe_2O_4$ structures; the measured interplanar spacings ($CoFe_2O_4$ (022) = ~ 2.9 Å, $NiFe_2O_4$ (111) = ~ 4.8 Å and $ZnFe_2O_4$ (311) = ~ 2.5 Å) are in good accordance with cubic-spinel phases of cobalt (JCPDS 04-006-4150), nickel (ICDD 00-044-1485) and zinc (ICSD 98-011-6750) ferrites. As demonstrated, HRTEM-STEM results confirms the successful formation of crystalline ferrite nanoparticles using the employed preparation method.

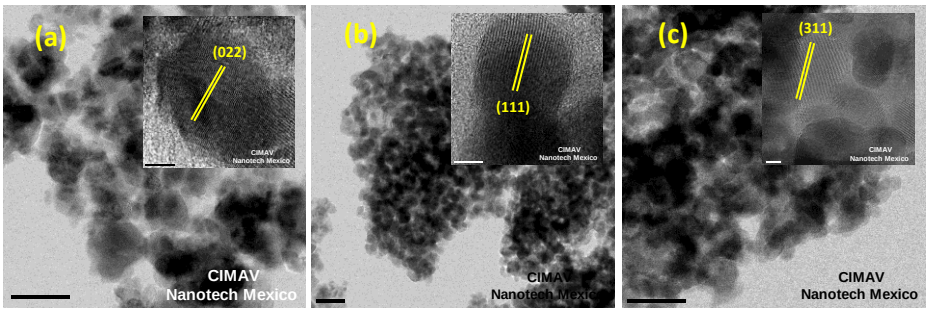


**Fig. 2.** HRTEM-STEM images of thermal treated samples: (a) $CoFe_2O_4$, (b) $NiFe_2O_4$ and (c) $ZnFe_2O_4$.

### 3.1.3 Textural properties

$N_2$ adsorption/desorption isotherm curves of thermal treated ($Co^{2+}$, $Ni^{2+}$ and $Zn^{2+}$)$Fe_2O_4$ nanoparticles are presented on fig. 3. In the case of cobalt ferrite, the gas sorption measuring depicts a type-IV curve (IUPAC classification), with a hysteresis loop characteristic of a presumably mesoporous material (pore sizes between 2-50 nm) in the 0.6-1 range of relative pressure [28]. Similarly, nickel and zinc ferrites sorption processes exhibit type-IV curves (with hysteresis loops), but with an apparently higher amount of $N_2$ sorption than cobalt ferrite, and in a distinct relative pressure scale. These differences can be associated to the texture of prepared nanoparticles, as well to the peculiar interparticle arrangements of each system, achieved from packing of neighbouring nanoparticles (observed by HRTEM-STEM). Additionally, specific surface areas (SSA) were calculated by BET method, values of 63.823 $m^2/g$, 64.699 $m^2/g$ and 49.311 $m^2/g$ were obtained for $Co^{2+}$, $Ni^{2+}$, and $Zn^{2+}$ ferrites, respectively. Obtained textural properties demonstrate the capacity of the O/W microemulsion to produce materials with adequate surface areas and sorption capability for catalytic applications.

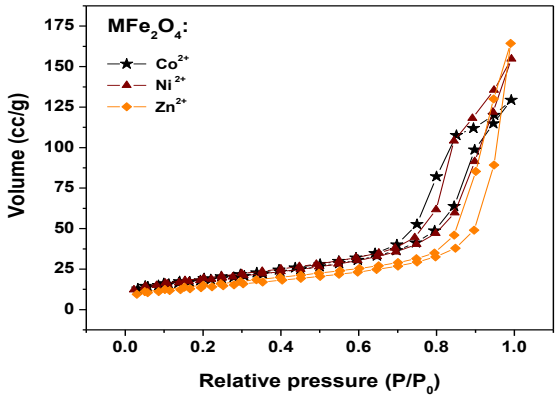


**Fig. 3.** $N_2$ adsorption/desorption isotherms of thermal treated ($Co^{2+}$, $Zn^{2+}$, $Ni^{2+}$)$Fe_2O_4$ nanoparticles.

### 3.1.4 Diffuse Reflectance UV-Vis spectroscopy (DR UV-Vis)

In fig. 4a the absorbance spectra of thermally treated ($Co^{2+}$, $Ni^{2+}$ and $Zn^{2+}$)$Fe_2O_4$ nanoparticles, measured by diffuse reflectance UV-Vis experiments, are presented. The broader spectra corresponds to the $CoFe_2O_4$ nanoparticles, and as it can be inferred, this material strongly absorbs photons from UV and visible-light region. In comparison, $NiFe_2O_4$ and $ZnFe_2O_4$ nanoparticles spectras exhibit also UV- visible light absorption, but within a shorter visible-light range, as depicted in an absorption decrement in the 500-700 nm wavelength. Moreover, in the case of nickel ferrite spectra it is possible to observe a shoulder-type band around 750 nm, which according to other works is typical of $NiFe_2O_4$, and it can be attributed to the d–d transition from Ni3d-$t_{2g}$ to Ni3d-$e_g$ [29]. To the best of our knowledge, this band has not been reported for $Co^{2+}$ and $Zn^{2+}$ compositions. The light absorption properties of thermally treated $MFe_2O_4$ nanoparticles, is related to the presence of $Co^{2+}$, $Ni^{2+}$ or $Zn^{2+}$ cations in the cubic spinel-type crystalline structure, which implies structural changes (as demonstrated by XRD results), and thus different electronic band structures. The latter, can be assumed due to the estimated optical bandgap energies (Eg): ~1.39 eV for $CoFe_2O_4$, ~1.9 eV for $ZnFe_2O_4$, and ~1.79 eV for $NiFe_2O_4$, calculated by the Tauc method, employing the UV-Vis diffuse reflectance data and considering an indirect transition (F(R)*hv^2, fig. 4b). According to the estimated Eg values, the three spinel-type ferrite nanoparticles possess appropriate forbidden band energies for photocatalytic water splitting (driven by UV or visible light), which requires a minimum theoretical band gap of 1.23 eV [6]. Obtained values are also in accordance with the reported for $CoFe_2O_4$, $NiFe_2O_4$ and $ZnFe_2O_4$ phases [17, 27, 29-31].

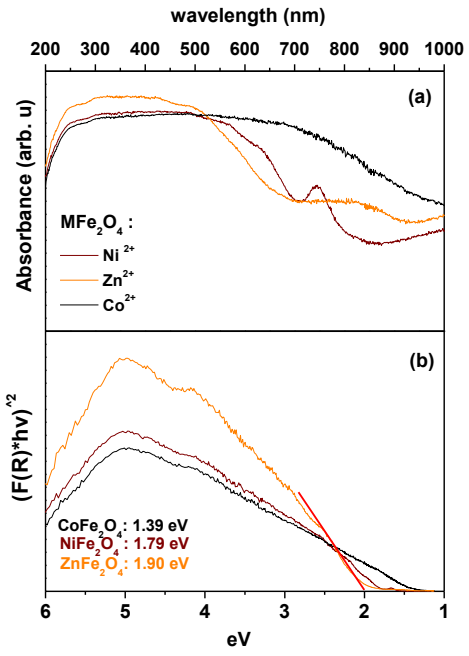


**Fig. 4.** (a) DR UV-Vis absorption spectra of thermal treated ($Co^{2+}$, $Zn^{2+}$, $Ni^{2+}$)$Fe_2O_4$ nanoparticles, and corresponding (b) Tauc plots for Eg determination.

### 3.2 $MFe_2O_4$ (M: $Co^{2+}$, $Ni^{2+}$ and $Zn^{2+}$) nanoparticles: photocatalytic water splitting

Fig. 5 depicts the $H_2$ evolution profiles for $Co^{2+}$, $Ni^{2+}$ and $Zn^{2+}$ ferrites nanoparticles, photoassisted by white mercurial lamp illumination, as a function of time and using MeOH as sacrificial agent. As can be seen, zinc ferrite has a higher performance from the second hour of photocatalytic evaluation, in comparison with cobalt and nickel ferrites, which display a similar performance. After 8 h of illumination $CoFe_2O_4$, $NiFe_2O_4$ and $ZnFe_2O_4$ yielded the following amounts: 128.00 $\mu molH_2/g$, 128.64 $\mu molH_2/g$, and 353.53 $\mu molH_2/g$, respectively. It is possible to assume that $Zn^{2+}$ ferrite superior $H_2$ production was achieved because a combination of good crystallinity, small particle size, higher sorption ability, and more importantly suitable bandgap and band edges positions (reported to be around +1.65 V and -0.25 V vs NHE [14]). On the other hand, $Co^{2+}$ and $Ni^{2+}$ ferrites similar photoresponse can be ascribed to its resemblance on textural properties. Comparing with previous scientific reports, T. Peng et al. prepared $NiFe_2O_4$ [29] and $ZnFe_2O_4$ [32] , by a 30 h hydrothermal process, followed by a 500 °C thermal treatment. Regarding photocatalytic water splitting evaluation, zinc ferrite produced 237.87 $\mu molH_2/g$, while nickel ferrite only produced 15.45 $\mu molH_2/g$ after 5 h of reaction. As evident, O/W microemulsion synthesized ferrites presented the same trend, being zinc ferrite as better photocatalyst for $H_2$ production. In the case of cobalt ferrite evaluation, Y. Ortega-López [27] demonstrated an outstanding performance of $CoFe_2O_4$, using co-precipitation (2540 $\mu molH_2/g$) and ball-milling (3490 $\mu molH_2/g$) as preparation methods, and although in the present study a less promising behavior was observed (128 $\mu molH_2/g$), even compared with O/W microemulsion synthesized $ZnFe_2O_4$, it still represents a new contribution to the investigation studies of $MFe_2O_4$ ferrites as light driven $H_2$ producers. Based on ferrites behavior at this test, it was confirmed that spinel-type ferrites (using MeOH) meet the needed conditions for carrying electron-hole pair reactions, in order to promote hydrogen ion reduction to $H_2$, and possibly MeOH oxidation (to be studied). Thus, it also implies that the employed light source provided enough energy to cause charge separation whereupon photoredox reactions took place.

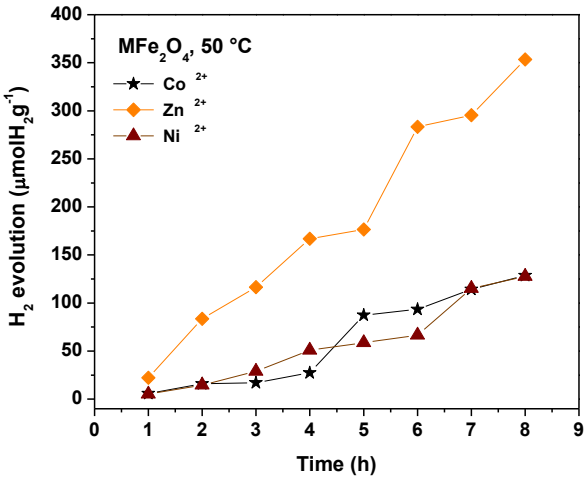


**Fig. 5.** Hydrogen evolution profile for thermal treated ($Co^{2+}$, $Zn^{2+}$, $Ni^{2+}$)$Fe_2O_4$ nanoparticles in function of time (8 h experiment).

## 4. Conclusion

In summary, the presented results demonstrated the successful synthesis of globular nanoparticles (< 20 nm) with a cubic $MFe_2O_4$ (M: $Co^{2+}$, $Ni^{2+}$ and $Zn^{2+}$) spinel-type crystalline structure (after thermal treatment) through the feasible oil-in-water microemulsion method. The prepared nanoparticles exhibited textural properties adequate for surface molecular sorption (e.g. $H_2O$). UV-Vis measurements displayed a good light absorption capability of the spinel-type ferrites, and according to the estimated bandgaps (< 2 eV) these compounds can accomplish both, ultraviolet and visible light absorption. In regard to light-driven $H_2$ production, the obtained results provided experimental evidence that $MFe_2O_4$ meet the requirements to reduce protons to generate molecular hydrogen, in the presence of methanol as a sacrificial agent and under white mercurial light illumination. Among the explored compositions, $ZnFe_2O_4$ yielded a higher amount of $H_2$ compared with $Co^{2+}$ and $Ni^{2+}$ ferrites in an 8 h experiment, due to the combination of its structural, textural and electronic features. The obtained results highlight the usefulness of microemulsion method for the straightforward synthesis of cobalt, nickel and zinc spinel-type ferrites, whose valuable properties can be boosted to the development of novel photocatalysts for water splitting reaction.

## Acknowledgements

We are grateful to CONACYT for financial support (CB project grant number CB2011/166649 and Proyecto Redes Temáticas No. 194451). Authors also acknowledge Enrique Longoria (CIMAV Monterrey), Cesar Leyva (CIMAV Chihuahua) and Luis de la Torre Sáenz (CIMAV Chihuahua) for their assistance with XRD, HRTEM-STEM and BET and DR UV-Vis measurements, respectively.

## References

[1] T. Jafari, E. Moharreri, A.S. Amin, R. Miao, W. Song, S.L. Suib, Molecules, 21 (2016) 900.
[2] A. López Ortiz, M.J. Meléndez Zaragoza, V. Collins-Martínez, International Journal of Hydrogen Energy, 41 (2016) 23363-23379.
[3] R. Li, Chinese Journal of Catalysis, 38 (2017) 5-12.
[4] H. Ahmad, S.K. Kamarudin, L.J. Minggu, M. Kassim, Renewable and Sustainable Energy Reviews, 43 (2015) 599-610.
[5] K. Maeda, Journal of Photochemistry and Photobiology C: Photochemistry Reviews, 12 (2011) 237-268.
[6] D.J. Martin, Introduction: Fundamentals of Water Splitting and Literature Survey, Investigation into High Efficiency Visible Light Photocatalysts for Water Reduction and Oxidation, Springer International Publishing, Cham, 2015, pp. 1-53.

[7] A.A. Ismail, D.W. Bahnemann, Solar Energy Materials and Solar Cells, 128 (2014) 85-101.
[8] M. Ni, M.K.H. Leung, D.Y.C. Leung, K. Sumathy, Renewable and Sustainable Energy Reviews, 11 (2007) 401-425.
[9] S. Oros-Ruiz, A. Hernández-Gordillo, C. García-Mendoza, A.A. Rodríguez-Rodríguez, R. Gómez, Journal of Chemical Technology & Biotechnology, 91 (2016) 2205-2210.
[10] A. Pérez-Larios, R. Lopez, A. Hernández-Gordillo, F. Tzompantzi, R. Gómez, L.M. Torres-Guerra, Fuel, 100 (2012) 139-143.
[11] Y. Liu, L. Xie, Y. Li, R. Yang, J. Qu, Y. Li, X. Li, Journal of Power Sources, 183 (2008) 701-707.
[12] S. Sun, W. Wang, D. Li, L. Zhang, D. Jiang, ACS Catalysis, 4 (2014) 3498-3503.
[13] C. Zeng, T. Hu, N. Hou, S. Liu, W. Gao, R. Cong, T. Yang, Materials Research Bulletin, 61 (2015) 481-485.
[14] R. Dillert, D.H. Taffa, M. Wark, T. Bredow, D.W. Bahnemann, APL Mater., 3 (2015) 104001.
[15] P.A. Mangrulkar, V. Polshettiwar, N.K. Labhsetwar, R.S. Varma, S.S. Rayalu, Nanoscale, 4 (2012) 5202-5209.
[16] B. Ren, Y. Huang, C. Han, M.N. Nadagouda, D.D. Dionysiou, Ferrites as Photocatalysts for Water Splitting and Degradation of Contaminants, Ferrites and Ferrates: Chemistry and Applications in Sustainable Energy and Environmental Remediation, American Chemical Society, 2016, pp. 79-112.
[17] D. Hong, Y. Yamada, M. Sheehan, S. Shikano, C.-H. Kuo, M. Tian, C.-K. Tsung, S. Fukuzumi, ACS Sustainable Chemistry & Engineering, 2 (2014) 2588-2594.
[18] A. Boudjemaa, I. Popescu, T. Juzsakova, M. Kebir, N. Helaili, K. Bachari, I.-C. Marcu, International Journal of Hydrogen Energy, 41 (2016) 11108-11118.
[19] X. Gao, X. Liu, Z. Zhu, X. Wang, Z. Xie, Scientific Reports, 6 (2016) 30543.
[20] H.M. Gobara, I.M. Nassar, A.M.A. El Naggar, G. Eshaq, Energy, 118 (2017) 1234-1242.
[21] K. Pemartin-Biernath, A. Vela-González, M. Moreno-Trejo, C. Leyva-Porras, I. Castañeda-Reyna, I. Juárez-Ramírez, C. Solans, M. Sánchez-Domínguez, Materials, 9 (2016) 480.
[22] M. Sanchez-Dominguez, G. Morales-Mendoza, M.J. Rodriguez-Vargas, C.C. Ibarra-Malo, A.A. Rodriguez-Rodriguez, A.V. Vela-Gonzalez, S.A. Perez-Garcia, R. Gomez, Journal of Environmental Chemical Engineering, 3 (2015) 3037-3047.
[23] M. Sanchez-Dominguez, M. Boutonnet, C. Solans, Journal of Nanoparticle Research, 11 (2009) 1823-1829.
[24] M. Sanchez-Dominguez, K. Pemartin, M. Boutonnet, Current Opinion in Colloid & Interface Science, 17 (2012) 297-305.
[25] C. Singh, Devika, R. Malik, V. Kumar, S. Singhal, RSC Advances, 5 (2015) 89327-89337.
[26] P. Borse, J. Jang, S. Hong, J.S. Lee, J. Jung, T. Hong, C. Ahn, E. Jeong, K. Hong, J. Yoon, (2009).

[27] Y. Ortega Lopez, H. Medina Vazquez, J. Salinas Gutierrez, V. Guzman Velderrain, A. Lopez Ortiz, V. Collins Martinez, Journal of Nanomaterials, 2015 (2015) 9.
[28] Z.A. ALOthman, Materials, 5 (2012) 2874-2902.
[29] T. Peng, X. Zhang, H. Lv, L. Zan, Catalysis Communications, 28 (2012) 116-119.
[30] R. Dillert, D.H. Taffa, M. Wark, T. Bredow, D.W. Bahnemann, APL Materials, 3 (2015) 104001.
[31] R. Dom, R. Subasri, N.Y. Hebalkar, A.S. Chary, P.H. Borse, RSC Advances, 2 (2012) 12782-12791.
[32] H. Lv, L. Ma, P. Zeng, D. Ke, T. Peng, Journal of Materials Chemistry, 20 (2010) 3665-3672.

[i]Sun, Y., Wu, J., Tian, J., Jin, C., & Yang, R. (2015). Sulfur-doped carbon spheres as efficient metal-free electrocatalysts for oxygen reduction reaction. *ElectrochimicaActa*, *178*, 806-812.

Wang, S., Zhang, L., Xia, Z., Roy, A., Chang, D. W., Baek, J. B., & Dai, L. (2012). BCN graphene as efficient metal-free electrocatalyst for the oxygen reduction reaction. *AngewandteChemie International Edition*, *51*(17), 4209-4212.

[iii]Shui, J., Wang, M., Du, F., & Dai, L. (2015). N-doped carbon nanomaterials are durable catalysts for oxygen reduction reaction in acidic fuel cells. *Science advances*, *1*(1), e1400129.

Wang, S., Dai, C., Li, J., Zhao, L., Ren, Z., Ren, Y., Qui, Y.& Yu, J. (2015). The effect of different nitrogen sources on the electrocatalytic properties of nitrogen-doped electrospun carbon nanofibers for the oxygen reduction reaction. *International Journal of Hydrogen Energy*, *40*(13), 4673-4682.

Zahoor, A., Christy, M., Hwang, Y. J., Lim, Y. R., Kim, P., &Nahm, K. S. (2014). Improved electrocatalytic activity of carbon materials by nitrogen doping. *Applied Catalysis B: Environmental*, *147*, 633-641.

Soo, L. T., Loh, K. S., Mohamad, A. B., Daud, W. R. W., & Wong, W. Y. (2015). An overview of the electrochemical performance of modified graphene used as an electrocatalyst and as a catalyst support in fuel cells. *Applied Catalysis A: General*, *497*, 198-210.

[vii] Wang, S., Zhang, L., Xia, Z., Roy, A., Chang, D. W., Baek, J. B., & Dai, L. (2012). BCN graphene as efficient metal-free electrocatalyst for the oxygen reduction reaction. AngewandteChemie International Edition, 51(17), 4209-4212.

[viii]Yu, L., Pan, X., Cao, X., Hu, P., &Bao, X. (2011). Oxygen reduction reaction mechanism on nitrogen-doped graphene: A density functional theory study. *Journal of catalysis*, *282*(1), 183-190.

[ix]Okamoto, Y. (2009). First-principles molecular dynamics simulation of O 2 reduction on nitrogen-doped carbon. Applied Surface Science, 256(1), 335-341.

[x]Bell, R. P. (2013). The tunnel effect in chemistry. Springer.

[xi]Aquino, N., Campoy, G., &Yee-Madeira, H. (1998). The inversion potential for NH 3 using a DFT approach. *Chemical physics letters*, *296*(1), 111-116.

[xii]Miyasato, T., Kawakami, Y., Kawano, T., &Hiraki, A. (1984). Preparation of sp3-rich amorphous carbon film by hydrogen gas reactive RF-sputtering of graphite, and its properties. Japanese Journal of Applied Physics, 23(4A), L234.

[xiii]Li, Y., Zhang, S., Song, H., Chen, X., Zhou, J., & Hong, S. (2015). New insight into the heteroatom-doped carbon as the electrode material for supercapacitors. *ElectrochimicaActa*, *180*, 879-886.

[xiv]Sanchez-Bojorge, N. A., Rodriguez-Valdez, L. M., Glossman-Mitnik, D., & Flores-Holguin, N. (2015). Theoretical calculation of the maximum absorption wavelength for Cyanidin molecules with several methodologies. *Computational and Theoretical Chemistry*, *1067*, 129-134.

[xv]Hernández-Paredes, J., Glossman-Mitnik, D., Duarte-Moller, A., & Flores-Holguín, N. (2009). Theoretical calculations of molecular dipole moment, polarizability, and first hyperpolarizability of glycine–sodium nitrate. *Journal of Molecular Structure: THEOCHEM*, *905*(1), 76-80.

[xvi]Cervantes-Navarro, F., &Glossman-Mitnik, D. (2013). Density functional theory study of indigo and its derivatives as photosensitizers for dye-sensitized solar cells. *Journal of Photochemistry and Photobiology A: Chemistry*, *255*, 24-26.

[xvii]Ioniţă, M., Vlăsceanu, G. M., Watzlawek, A. A., Voicu, S. I., Burns, J. S., &Iovu, H. (2017). Graphene and functionalized graphene: Extraordinary prospects for nanobiocomposite materials. *Composites Part B: Engineering*.